



# **Swansea University** **Prifysgol Abertawe**

## **Disentangling the Effects of Nitrogen Dioxide and Particulates in Air Pollution on Human Health: A Mechanistic Toxicological Approach**

Submitted to Swansea University in partial  
fulfilment of the requirements for the Degree of  
Doctor of Philosophy

**Joshua William Paul Bateman, MSc, BSc Hons**

## Summary

---

The ambient levels of particulate matter (PM) and nitrogen dioxide (NO<sub>2</sub>), two major pollutants within both outdoor and indoor air, are typically proportional given that they are often emitted from the same sources, such as motor vehicles and industry. Epidemiological studies have linked inhalation exposure of each pollutant to adverse pulmonary health effects, although difficulty lies in distinguishing the pollutant-specific effects due to their co-emission. These health effects could be determined by assessing either pollutant type within the same experimental system.

To address this research gap, an *in vitro* co-culture model of the alveolar barrier comprising alveolar type 1 cells (hAELVi), alveolar type 2 cells (NCI-H441) and alveolar macrophages (differentiated THP-1) was characterised. Through culturing at the air-liquid interface, the co-culture was examined after pollutant co-exposures to PM (aerosol exposure) and NO<sub>2</sub> (using a novel NO<sub>2</sub> exposure unit). Standardised PM samples of carbon black, urban dust, indoor dust, as well as freshly captured diesel emission particles were chosen based on their relevance to human exposure. The ability of each pollutant to affect cytotoxicity, barrier function, pro-inflammatory responses, oxidative stress, and the transcriptome (*via* RNA sequencing) was evaluated.

The results showed that both PM and NO<sub>2</sub> can act in a pro-inflammatory manner, shown through IL6 and IL8 release (*via* ELISA). In contrast, confocal microscopy revealed that NO<sub>2</sub> induced morphological changes, which could be indicative of phenotypic alterations, especially in NCI-H441 cells. Co-exposure of PM samples with NO<sub>2</sub> was shown to amplify PM-induced cytotoxicity and the pro-inflammatory response. RNA-sequencing uncovered a potential synergistic mechanism behind this effect, where NO<sub>2</sub> inhibits anti-inflammatory mechanisms, allowing PM to induce an augmented pro-inflammatory response.

In conclusion, this work suggests that differing constituents of air pollution may be able to act synergistically to amplify airway inflammation. However, this was shown to be dependent upon the source of the PM. These results highlight the importance of considering the toxicological effects of air pollution both independently and in relation to each other, an important factor when considering the reduction of air pollution exposure to improve the burden upon public health.

## Declaration and Statements

---

This work has not previously been accepted in substance for any degree and is not being concurrently submitted in candidature for any degree.

Signed..  .....

Date 27 March 2024

This thesis is the result of my own investigations, except where otherwise stated. Other sources are acknowledged by footnotes giving explicit references. A bibliography is appended.

Signed..  .....

Date 27 March 2024

I hereby give consent for my thesis, if accepted, to be available for photocopying and for inter-library loan, and for the title and summary to be made available to outside organisations.

Signed..  .....

Date 27 March 2024

The University's ethical procedures have been followed and, where appropriate, that ethical approval has been granted.

Signed..  .....

Date 27 March 2024

## Acknowledgements

---

Firstly, I would like to express my sincerest gratitude to my primary supervisor, Prof. Martin Clift, for guiding me through this project with profound support, expertise, and enthusiasm. I will forever be grateful for the opportunity to undertake a PhD within his group. The opportunities Martin has given me over the years have allowed me to evolve as a scientist, and I thank him dearly for that. I would also like to thank my principal supervisor, Dr Rachel Smith, for the opportunity to undertake a UK Health Security Agency-funded PhD. I appreciate the guidance, advice, and inspiration she has provided during this project.

I am incredibly thankful to the rest of my supervisory team, Prof. Shareen Doak, Dr Alison Buckley, Dr Matthew Wright and Dr Sarah Robertson, for their feedback, guidance and knowledge. I especially want to thank Alison for her immense time working with the nitrogen dioxide exposure system and her support and expertise in many aspects of the exposure characterisation used in this work. Further, I would like to thank Martin Leonard for assisting with the statistical analysis of the RNA sequencing data.

Committing to this PhD would have been impossible without support from the laboratory. Therefore, I would like to give special thanks to all those within the PhD and Postdoc offices for maintaining my sanity. In particular, I would like to thank Dr Kirsty Meldrum for her help with many aspects of the laboratory work and her endless patience and support.

I also would not have been able to complete this PhD without encouragement and support from home. Therefore, I dedicate this thesis to Mum, Dad, Dan, Sam, and the rest of my family for guiding me through the ups and downs of this PhD and always being there for me.

To Ellie, thank you for backing me every step of the way and for the encouragement and patience you have shown; I will always be sincerely grateful.



## Table of Contents

---

Summary .....	i
Declaration and Statements .....	ii
Acknowledgements .....	iii
Table of Contents .....	iv
List of Figures .....	12
List of Tables .....	21
Abbreviations and Acronyms .....	23
Chapter 1: Introduction .....	28
1.1 Air Pollution .....	29
1.1.1 Background .....	29
1.1.2 Gaseous Pollutants .....	33
1.1.3 Particulate Matter .....	36
1.1.4 Heavy Metals.....	37
1.1.5 Persistent Organic Pollutants .....	38
1.2 Public Health and Epidemiology .....	39
1.3 Anatomy and Physiology of the Human Respiratory System .....	47
1.3.1 Anatomy of the Human Lung.....	47
1.3.2 Innate Lung Defences Against Air Pollution and Mechanisms of Toxicity .....	50
1.4 Particulate Matter .....	63
1.4.1 Particulate Matter Induced Oxidative Stress .....	67
1.4.2 Particulate Matter Induced Inflammatory Response .....	70
1.4.3 Non-Pulmonary Effects .....	71
1.5 Nitrogen Dioxide .....	72
1.6 Research Aims .....	79
Chapter 2: Materials and Methods .....	82

2.1 Materials, Chemicals, Reagents and Equipment .....	84
2.2 Cell Culture .....	87
2.2.1 hAELVi Cell Culture .....	87
2.2.2 NCI-H441 Cell Culture .....	89
2.2.3 THP-1 Cell Culture .....	91
2.3 Cell Counts and Viability .....	93
2.4 Seeding onto Transwell Inserts .....	95
2.5 Immunocytochemistry and Confocal Microscopy .....	95
2.5.1 Sample Fixation and Storage .....	95
2.5.2 Immunocytochemistry .....	96
2.5.3 Confocal Imaging .....	98
2.6 Membrane Integrity .....	98
2.6.1 Blue Dextran .....	98
2.7 Pro-Inflammatory Response .....	99
2.8 Data and Statistical Analysis .....	102
Chapter 3: Development and Characterisation of an <i>In Vitro</i> Alveolar Barrier Model .....	103
3.1 Introduction .....	104
3.1.1 Aims and Objectives .....	105
3.2 Materials and Methods .....	106
3.2.1 Experimental Design .....	106
3.2.2 Chemicals and Reagents .....	106
3.2.3 Cell Culture .....	106
3.2.4 Cell Count and Viability .....	107
3.2.5 Seeding onto Transwell Inserts .....	107
3.2.6 Immunocytochemistry and Confocal Microscopy .....	107
3.2.7 CellTracker™ Staining and Determination of Co/Triple Culture Seeding Ratio .....	108

3.2.8 Membrane Integrity .....	111
3.2.9 Pro-Inflammatory Response.....	112
3.2.10 Data and Statistical Analysis .....	112
3.3 Results and Discussion.....	113
3.3.1 hAELVi Characterisation .....	113
3.3.2 NCI-H441 Compatibility with huAEC Coating.....	129
3.3.3 Growth and Viability of hAELVi/NCI-H441 Co-Culture at the Air-Liquid Interface.....	131
3.3.4 Barrier Integrity of Submerged hAELVi/NCI-H441 Co-Culture at the Air-Liquid interface .....	133
3.3.5 Co-Culture Seeding Density Optimisation.....	134
3.3.6 Deducing Seeding Concentrations of hAELVi and NCI-H441 Co-Cultures .....	135
3.3.7 Adherence Efficiency of dTHP-1 Cells to Alveolar Epithelial Cells at the Air-Liquid Interface and Quantification of dTHP-1 Density in the Triple Cell Co-Culture .....	138
3.3.8 Assessment of dTHP-1 Activation within the Triple Cell Co-Culture ....	142
3.4 Summary and Outlook .....	144
Chapter 4: Particulate Matter and Nitrogen Dioxide Exposure Systems .....	147
4.1 Introduction .....	148
4.1.1 Aims and Objectives.....	149
4.2 Materials and Methods .....	151
4.2.1 Experimental Design .....	151
4.2.2 Particulate Matter Samples.....	151
4.2.3 VitroCell Cloud 12 .....	156
4.2.4 Scanning Electron Microscopy .....	160
4.2.5 Nitrogen Dioxide Exposure Chamber .....	162

4.2.6 Transporting Samples between Swansea University and The Radiation, Chemical and Environmental Hazards Directorate .....	164
4.2.7 Data and Statistical Analysis .....	165
4.3 Results .....	166
4.3.1 Printex® 90 Carbon Black exposure characterisation .....	166
4.3.2 NIST Urban Dust SRM 1649b exposure characterisation .....	172
4.3.3 NIST Indoor Dust SRM 2583 exposure characterisation.....	177
4.3.4 Actual Deposited Concentrations .....	182
4.3.5 Nitrogen Dioxide Exposure Chamber Parameters .....	183
4.3.6 Simulated Transportation of Samples between Swansea University and The Radiation, Chemical and Environmental Hazards Directorate .....	184
4.4 Discussion .....	185
4.4.1 VitroCell Cloud .....	186
4.4.2 Nitrogen Dioxide Exposure Chamber .....	189
4.5 Summary and Outlook .....	191
Chapter 5: Exposure of Advanced <i>In Vitro</i> Models to Particulate Matter.....	192
5.1 Introduction .....	193
5.1.1 Aims and Objectives.....	194
5.2 Materials and Methods.....	195
5.2.1 Experimental Design .....	195
5.2.2 Chemical and Reagents .....	196
5.2.3 Cell Culture .....	196
5.2.4 Exposure of <i>In Vitro</i> Models to PM Samples .....	197
5.2.5 Cell Count and Viability .....	198
5.2.6 Blue Dextran .....	198
5.2.7 Pro-Inflammatory Response.....	198
5.2.8 Immunocytochemistry and Confocal Microscopy .....	198
5.2.9 Data and Statistical Analysis .....	198

5.3 Results .....	199
5.3.1 hAELVi Monoculture Exposure to Printex® 90, Urban Dust and Indoor Dust .....	199
5.3.2 NCI-H441 Monoculture Exposure to Printex® 90, 1649b and 2583 .....	203
5.3.3 hAELVi & NCI-H441 Co-Culture Exposure to Printex® 90, 1649b and 2583 .....	208
5.3.4 hAELVi & dTHP-1 Co-Culture Exposure to Printex® 90, 1649b and 2583 .....	214
5.3.5 NCI-H441 & dTHP-1 Co-Culture Exposure to Printex® 90, 1649b and 2583 .....	219
5.3.6 Triple Cell Co-Culture Exposure to Printex® 90, 1649b and 2583 .....	226
5.3.7 Triple Cell Co-Culture Exposure to Diesel Emission Particles .....	231
5.4 Discussion .....	236
5.4.1 Monoculture Exposures .....	237
5.4.2 Co-Culture Exposures .....	240
5.4.3 Triple Culture Exposures .....	244
5.5 Summary and Outlook .....	247
Chapter 6: Co-exposure of Advanced <i>In Vitro</i> Models to Nitrogen Dioxide and Particulate Matter .....	249
6.1 Introduction .....	250
6.1.1 NO <sub>2</sub> and PM co-exposure parameters .....	250
6.1.2 Aims and Objectives .....	251
6.2 Materials and Methods .....	253
6.2.1 Experimental Design .....	253
6.2.2 Chemicals and Reagents .....	254
6.2.3 Cell Culture .....	254
6.2.4 Impact of Geography on Cell Cultures and their exposure to pollutants .....	254
6.2.5 Exposure of <i>In Vitro</i> Models to Nitrogen Dioxide .....	255

6.2.6 Exposure of <i>In Vitro</i> Models to PM and/or Nitrogen Dioxide .....	255
6.2.7 Cell Count and Viability .....	256
6.2.8 Blue Dextran .....	256
6.2.9 Pro-Inflammatory Response.....	256
6.2.10 Oxidative Stress.....	257
6.2.11 Immunocytochemistry and Confocal Microscopy .....	259
6.2.12 Quantitative Polymerase Chain Reaction.....	259
6.2.13 Data and Statistical Analysis .....	264
6.3 Results .....	266
6.3.1 NCI-H441 Response to Nitrogen Dioxide Exposure .....	266
6.3.2 hAELVi Response to Nitrogen Dioxide Exposure .....	269
6.3.3 Alveolar Triple Cell Co-Culture Response to Nitrogen Dioxide Exposure .....	270
6.3.4 Assessing for Interaction Between Nitrogen Dioxide and Negative Particle Controls .....	272
6.3.5 NCI-H441 Co-Exposure to Printex® 90 and Nitrogen Dioxide .....	274
6.3.6 Triple Cell Co-Culture Co-Exposure to Printex® 90 and Nitrogen Dioxide .....	276
6.3.7 Triple Cell Co-Culture Co-Exposure to Indoor/Urban Dust and Nitrogen Dioxide .....	278
6.3.8 Triple Cell Co-Culture Co-Exposure to Diesel Emission Particles and Nitrogen Dioxide .....	281
6.4 Discussion .....	285
6.4.1 Effects of Nitrogen Dioxide Exposure on NCI-H441 and hAELVi Monocultures and the Triple Cell Co-Culture.....	285
6.4.2 Co-exposure of NCI-H441 Monoculture and Triple Cell Co-Culture to Nitrogen Dioxide and Carbon Black .....	289
6.4.3 Co-exposure of the Triple Cell Co-Culture to Nitrogen Dioxide and Urban/Indoor Dust (SRM 1649b & SRM 2583).....	292

6.4.4 Co-exposure of Triple Cell Co-Culture to Nitrogen Dioxide and Diesel Emission Particles .....	294
6.5 Summary and Outlook .....	298
Chapter 7: Transcriptomic Response to Nitrogen Dioxide and Particulate Matter Co-exposure .....	299
7.1 Introduction .....	300
7.1.1 Aims and Objectives.....	301
7.2 Methods .....	303
7.2.1 Triple Cell Co-Culture Protocol .....	303
7.2.2 Indoor Dust/Diesel Emission Particle and Nitrogen Dioxide Exposures	303
7.2.3 RNA Sequencing Analysis .....	303
7.2.4 RNA Extraction .....	303
7.2.5 Library Preparation and Next-Generation Sequencing .....	303
7.2.6 Data Analysis.....	304
7.3 Results .....	305
7.3.1 Transcriptomic Changes Following Co-Exposure of Indoor Dust or Diesel Emission Particles with Nitrogen Dioxide .....	305
7.3.2 Enriched Processes Following Exposure to DEP and Nitrogen Dioxide Co-Exposure.....	308
7.3.3 Single Gene Analysis of Indoor Dust, DEP and Nitrogen Dioxide Exposures .....	317
7.4 Discussion .....	325
7.4.1 Inflammation .....	326
7.4.2 Oxidative Stress.....	331
7.4.3 Metabolism and Detoxification .....	332
7.4.4 Surfactant Proteins .....	333
7.5 Summary and Outlook .....	334
Chapter 8: Discussion.....	336

8.1 Summary of Introduction and Aims .....	337
8.2 Summary Development of the Alveolar Triple Cell Co-Culture.....	337
8.3 Summary of the Characterisation of Particulate Matter and Nitrogen Dioxide Exposure Methods .....	338
8.4 Summary of Effects of Particulate Matter Exposure .....	339
8.5 Summary of the Effects of Particle Matter and Nitrogen Dioxide (Co-) Exposure in Alveolar Models .....	340
8.6 Conclusion.....	347
8.7 Future Perspectives .....	349
Chapter 9: Appendices .....	350
9.1 Appendix 1 .....	351
9.2 Appendix 2 .....	356
9.3 Appendix 3 .....	357
Chapter 10: References .....	395



## List of Figures

---

<b>Figure 1.1</b> Timeline of notable events in the history of air pollution in the UK .....	29
<b>Figure 1.2</b> Major emitters of air pollution .....	32
<b>Figure 1.3</b> An anterior view of the lung, .....	48
<b>Figure 1.4</b> Histology of the epithelial lung lining .....	50
<b>Figure 1.5</b> An overview of pro-inflammatory pathways involved within the alveolar regions of the lung. ....	57
<b>Figure 1.6</b> Schematic of the metabolism of benzo(a)pyrene .....	63
<b>Figure 1.7</b> Relative sizes of different PM fractions.....	64
<b>Figure 1.8</b> Outline of questions aimed to be answered within this work. ....	79
<b>Figure 2.1</b> An overview of the experimental methodology carried out within this work. ....	83
<b>Figure 2.2</b> Trypan blue procedure .....	93
<b>Figure 2.3</b> Example of flagging of viable/non-viable cells using LUNA II.....	94
<b>Figure 2.4</b> Method for indirect staining of antigens (proteins of interest) on transwell inserts .....	97
<b>Figure 2.5</b> Blue dextran assay .....	99
<b>Figure 2.6</b> Schematic describing the molecular basis behind the sandwich ELISAs .....	100
<b>Figure 3.1</b> Scheme to illustrate how each alveolar epithelial cell type were distinguished and quantified.....	111
<b>Figure 3.2</b> Location for TEER readings on a single insert. ....	112
<b>Figure 3.3</b> Total cell counts and viability of hAELVi cells cultured under submerged conditions .....	113
<b>Figure 3.4</b> Barrier properties of hAELVi cells cultured under submerged conditions measured.....	114
<b>Figure 3.5</b> Light microscopy images of hAELVi cells grown in a T75.....	116
<b>Figure 3.6</b> LSM images of submerged hAELVi cells.....	121
<b>Figure 3.7</b> IL6 and IL8 release from hAELVi cells cultured in submerged conditions .....	122
<b>Figure 3.8</b> Total cell counts and viability of hAELVi cells cultured every 24 hours using LUNAII automated cell counter under submerged conditions for 72 hours before being exposed to ALI .....	123

<b>Figure 3.9</b> Barrier properties of hAELVi cells cultured under ALI conditions .....	125
<b>Figure 3.10</b> LSM images of hAELVi cells at the ALI .....	128
<b>Figure 3.11</b> IL6 and IL8 release from hAELVi cells cultured in submerged conditions for 72 hours before being exposed to ALI.....	129
<b>Figure 3.12</b> Total cell count, viability, barrier integrity, IL6 release and IL8 release from NCI-H441 cells cultured at ALI in either uncoated or huAEC coated transwell .....	130
<b>Figure 3.13</b> LSM images of NCI-H441 cells cultured in uncoated wells and huAEC coated wells. ....	131
<b>Figure 3.14</b> Total cell counts and viability of hAELVi and NCI-H441 (H441) co-cultures at 96 hours post seeding.....	132
<b>Figure 3.15</b> Barrier properties measured using blue dextran of hAELVi and NCI-H441 (H441) co-cultures 96 hours post seeding.....	133
<b>Figure 3.16</b> Total cell count, viability and blue dextran for co-cultures seeded at $2.5 \times 10^5$ or $5 \times 10^5$ cell/mL .....	134
<b>Figure 3.17</b> Caveolin-1 LSM images of hAELVi or NCI-H441 monocultures .....	136
<b>Figure 3.18</b> CellTracker™ staining of hAELVi and NCI-H441 co-cultures .....	137
<b>Figure 3.19</b> CellTracker staining of hAELVi and NCI-H441.....	138
<b>Figure 3.20</b> Viable cell counts using the LUNA II on media removed when cells were exposed to ALI 2 hours following the addition of dTHP-1 cells .....	139
<b>Figure 3.21</b> CellTracker™ staining of dTHP-1 in the triple cell co-culture .....	141
<b>Figure 3.22</b> TNF- $\alpha$ and IL8 release following LPS stimulation of epithelial co-cultures or triple cell co-cultures.....	142
<b>Figure 3.23</b> Schematic of the method for culturing the alveolar triple cell co-culture. ....	146
<b>Figure 4.1</b> Methods of PM exposure using submerged, qALI and aerosol (VibroCell Cloud) techniques.....	149
<b>Figure 4.2</b> Macroscopic images of carbon black suspensions.....	153
<b>Figure 4.3</b> Macroscopic images of NIST SRM 1649b suspensions. ....	154
<b>Figure 4.4</b> Macroscopic images of NIST SRM 2583 suspensions. ....	155
<b>Figure 4.5</b> The VibroCell® Cloud12 unit. ....	157
<b>Figure 4.6</b> A typical QCM curve .....	158
<b>Figure 4.7</b> The TEM grid holder .....	160
<b>Figure 4.8</b> Blank TEM grid and TEM grid immediately after dropcasting.....	160

<b>Figure 4.9</b> Aerosol sampling from the VitroCell® Cloud .....	161
<b>Figure 4.10</b> The NO <sub>2</sub> exposure chamber .....	163
<b>Figure 4.11</b> Schematic of the NO <sub>2</sub> system feedback mechanism to maintain the user set NO <sub>2</sub> concentration.....	164
<b>Figure 4.12</b> QCM data from nebulisation CB suspensions .....	166
<b>Figure 4.13</b> Deposition of CB for each feed concentration.....	167
<b>Figure 4.14</b> SEM images of dropcast CB suspensions used for characterising CB deposition using the VitroCell® Cloud .....	168
<b>Figure 4.15</b> SEM images of CB aerosol captured 30s after nebulisation of various feed concentrations of CB.....	169
<b>Figure 4.16</b> SEM images of CB deposited after nebulisation with the VitroCell® Cloud .....	170
<b>Figure 4.17</b> SEM images of CB deposited after nebulisation with the VitroCell® Cloud .....	171
These are the deposited concentrations that will be utilised in the in vitro experiments. ....	171
<b>Figure 4.18</b> QCM data from nebulisation of SRM 1649b suspensions.....	172
<b>Figure 4.19</b> Deposition of NIST SRM 1649b for each feed concentration. ....	172
<b>Figure 4.20</b> SEM images of dropcast NIST SRM 1649b suspensions used for characterising 1649b deposition using the VitroCell® Cloud.....	173
<b>Figure 4.21</b> SEM images of NIST SRM 1649b aerosol captured 30s after nebulisation of various feed concentrations of 1649b .....	174
<b>Figure 4.22</b> SEM images of NIST SRM 1649b deposited after nebulisation with the VitroCell® Cloud .....	175
<b>Figure 4.23</b> SEM images of NIST SRM 1649b deposited after nebulisation with the VitroCell® Cloud on copper carbon-coated TEM grids. These are the deposited concentrations that will be utilised in the in vitro experiments.....	176
<b>Figure 4.24</b> QCM data from nebulisation NIST SRM 2583 suspension.....	177
<b>Figure 4.25</b> Deposition of NIST SRM 2583 for each feed concentration .....	177
<b>Figure 4.26</b> SEM images of dropcast NIST SRM 2583 suspensions used for characterising 2583 deposition using the VitroCell® Cloud.....	178
<b>Figure 4.27</b> SEM images of NIST SRM 2583 aerosol captured 30s after nebulisation of various feed concentrations of 2583 within the VitroCell® Cloud .....	179
<b>Figure 4.28</b> SEM images of NIST SRM 2583 deposited after nebulisation with the VitroCell® Cloud .....	180

<b>Figure 4.29</b> SEM images of NIST SRM 2583 deposited after nebulisation with the VitroCell® Cloud on copper carbon-coated TEM grids. These are the deposited concentrations that will be utilised in the in vitro experiments.....	181
<b>Figure 4.30</b> Actual deposited concentrations of CB, 1649b and 2583 .....	182
<b>Figure 4.31</b> Parameters to be controlled over the duration of exposure within the NO <sub>2</sub> chamber. ....	183
<b>Figure 4.32</b> An example NO <sub>2</sub> exposure concentration trend across a 24-hour period.. .....	184
<b>Figure 4.33</b> Viability, barrier function and IL6 and IL8 release from NCI-H441 monocultures exposed to simulated travel conditions.....	185
<b>Figure 5.1</b> In vitro models used within this chapter. ....	195
<b>Figure 5.2</b> Proposed exposure plan for PM exposure to various in vitro models ...	196
<b>Figure 5.3</b> Schematic of hAELVi monoculture used in Section 5.3.1.....	199
<b>Figure 5.4</b> Viability, total cell count, blue dextran, IL6 concentration and IL8 concentration of hAELVi monocultures exposed to CB .....	199
<b>Figure 5.5</b> Confocal microscopy images of hAELVi monocultures exposed to CB .....	200
<b>Figure 5.6</b> Viability, total cell count, blue dextran, IL6 concentration and IL8 concentration of hAELVi monocultures exposed to 1649b.....	201
<b>Figure 5.7</b> Confocal microscopy images of hAELVi monocultures exposed to 1649b .....	201
<b>Figure 5.8</b> Viability, total cell count, blue dextran, IL6 concentration and IL8 concentration of hAELVi monocultures exposed to 2583.....	202
<b>Figure 5.9</b> Confocal microscopy images of hAELVi monocultures exposed to 2583 .....	202
<b>Figure 5.10</b> Schematic of NCI-H441 monoculture used in Section 5.3.1. ....	203
<b>Figure 5.11</b> Viability, total cell count, blue dextran, IL6 concentration and IL8 concentration of NCI-H441 monocultures exposed to CB .....	203
<b>Figure 5.12</b> Confocal microscopy images of NCI-H441 monocultures exposed to CB. ....	204
<b>Figure 5.13</b> Viability, total cell count, blue dextran, IL6 concentration and IL8 concentration of NCI-H441 monocultures exposed to 1649b.....	205
<b>Figure 5.14</b> Confocal microscopy images of NCI-H441 monocultures exposed to 1649b.....	205

<b>Figure 5.15</b> Viability, total cell count, blue dextran, IL6 concentration and IL8 concentration of NCI-H441 monocultures exposed to 2583 .....	206
<b>Figure 5.16</b> Confocal microscopy images of NCI-H441 monocultures exposed to 2583 .....	207
<b>Figure 5.17</b> Schematic of hAELVi + NCI-H441 monoculture used in Section 5.3.3. ....	208
<b>Figure 5.18</b> Viability, total cell count, blue dextran, IL6 concentration and IL8 concentration of hAELVi + NCI-H441 co-cultures exposed to CB .....	208
<b>Figure 5.19</b> Confocal microscopy images of hAELVi + NCI-H441 co-cultures exposed to CB .....	209
<b>Figure 5.20</b> Viability, total cell count, blue dextran, IL6 concentration and IL8 concentration of hAELVi + NCI-H441 co-cultures exposed to 1649b .....	210
<b>Figure 5.21</b> Confocal microscopy images of hAELVi + NCI-H441 co-cultures exposed to 1649b .....	211
<b>Figure 5.22</b> Viability, total cell count, blue dextran, IL6 concentration and IL8 concentration of hAELVi + NCI-H441 co-cultures exposed to 2583 .....	212
<b>Figure 5.23</b> Confocal microscopy images of hAELVi + NCI-H441 co-cultures exposed to 2583 .....	213
<b>Figure 5.24</b> Schematic of hAELVi + dTHP-1 co-culture used in Section 5.3.4.....	214
<b>Figure 5.25</b> Viability, total cell count, blue dextran, IL6 concentration and IL8 concentration of hAELVi + dTHP-1 co-cultures exposed to CB .....	214
<b>Figure 5.26</b> Confocal microscopy images of hAELVi + dTHP-1 co-cultures exposed to CB .....	215
<b>Figure 5.27</b> Viability, total cell count, blue dextran, IL6 concentration and IL8 concentration of hAELVi + dTHP-1 co-cultures exposed to 1649b .....	216
<b>Figure 5.28</b> Confocal microscopy images of hAELVi + dTHP-1 co-cultures exposed to 1649b .....	217
<b>Figure 5.29</b> Viability, total cell count, blue dextran, IL6 concentration and IL8 concentration of hAELVi + dTHP-1 co-cultures exposed to 2583 .....	218
<b>Figure 5.30</b> Confocal microscopy images of hAELVi + dTHP-1 co-cultures exposed to 2583 .....	219
<b>Figure 5.31</b> Schematic of NCI-H441 + dTHP-1 co-culture used in Section 5.3.5..	220
<b>Figure 5.32</b> Viability, total cell count, blue dextran, IL6 concentration and IL8 concentration of NCI-H441 + dTHP-1 co-cultures exposed to CB .....	220

<b>Figure 5.33</b> Confocal microscopy images of NCI-H441 + dTHP-1 co-cultures exposed to CB .....	221
<b>Figure 5.34</b> Viability, total cell count, blue dextran, IL6 concentration and IL8 concentration of NCI-H441 + dTHP-1 co-cultures exposed to 1649b .....	222
<b>Figure 5.35</b> Confocal microscopy images of NCI-H441 + dTHP-1 co-cultures exposed to 1649b.....	223
<b>Figure 5.36</b> Viability, total cell count, blue dextran, IL6 concentration and IL8 concentration of NCI-H441 + dTHP-1 co-cultures exposed to 2583 .....	224
<b>Figure 5.37</b> Confocal microscopy images of NCI-H441 + dTHP-1 co-cultures exposed to 2583.....	225
<b>Figure 5.38</b> Schematic of the triple cell co-culture used in Section 5.3.6. ....	226
<b>Figure 5.39</b> Viability, total cell count, blue dextran, IL6 concentration and IL8 concentration of the triple cell co-culture exposed to CB.....	226
<b>Figure 5.40</b> Confocal microscopy images of the triple cell co-culture exposed to CB. ....	227
<b>Figure 5.41</b> Viability, total cell count, blue dextran, IL6 concentration and IL8 concentration of the triple cell co-culture exposed to 1649b .....	228
<b>Figure 5.42</b> Confocal microscopy images of the triple cell co-culture exposed to 1649b .....	229
<b>Figure 5.43</b> Viability, total cell count, blue dextran, IL6 concentration and IL8 concentration of the triple cell co-culture exposed to 2583 .....	230
<b>Figure 5.44</b> Confocal microscopy images of the triple cell co-culture exposed to 2583 .....	231
<b>Figure 5.45</b> Viability, total cell count, blue dextran, IL6 concentration and IL8 concentration, of the triple cell co-culture exposed to diesel emission particles at 9.8, 13 or 17% engine oxygen intake .....	232
<b>Figure 5.46</b> Confocal microscopy images of the triple cell co-culture exposed to diesel emission particles at 9.8, 13 or 17% engine oxygen intake .....	235
<b>Figure 6.1</b> Proposed exposure plan for NO <sub>2</sub> ± PM exposure to various in vitro models. ....	253
<b>Figure 6.2</b> Primer validation data for SOD1, HPRT1 and GAPDH primers.....	263
<b>Figure 6.3</b> Viability, total cell count, barrier integrity, IL6 concentration, IL8 concentration, SOD1 expression and morphology of NCI-H441 monocultures exposed to NO <sub>2</sub> (5 ppm) for 4 hours .....	266

<b>Figure 6.4</b> Viability, total cell count, barrier integrity, IL6 concentration, IL8 concentration and SOD1 expression of NCI-H441 monocultures exposed to either 1, 2.5 or 5 ppm NO <sub>2</sub> for 24 hours.....	267
<b>Figure 6.5</b> Morphological analysis of NCI-H441 monocultures exposed to either 1, 2.5 or 5 ppm NO <sub>2</sub> for 24 hours.....	268
<b>Figure 6.6</b> Viability, total cell count, barrier integrity, IL6 concentration, IL8 concentration and SOD1 expression of hAELVi monocultures exposed to either 1, 2.5 or 5 ppm NO <sub>2</sub> for 24 hours.....	269
<b>Figure 6.7</b> Morphological analysis of hAELVi monocultures exposed to either 1, 2.5 or 5 ppm NO <sub>2</sub> for 24 hours.....	270
<b>Figure 6.8</b> Viability, total cell count, barrier integrity, IL6 concentration, IL8 concentration, SOD1 expression, protein concentration and GSH concentration of alveolar triple cell co-cultures exposed to either 1, 2.5 or 5 ppm NO <sub>2</sub> for 24 hours .....	271
<b>Figure 6.9</b> Morphological analysis of triple cell co-cultures exposed to either 1, 2.5 or 5 ppm NO <sub>2</sub> for 24 hours .....	272
<b>Figure 6.10</b> Viability, total cell count, barrier integrity, IL6 concentration and IL8 concentration of alveolar NCI-H441 monocultures exposed to either NaCl at 0.009%, or 0.0009% (1:10) via VitroCell® Cloud, then either incubated in 5 ppm NO <sub>2</sub> or not for 24 hours .....	273
<b>Figure 6.11</b> Viability, total cell count, barrier integrity, IL6 concentration, IL8 concentration and SOD1 expression of alveolar NCI-H441 monocultures exposed to either CB (780 ng/cm <sup>2</sup> ) then either incubated in 5 ppm NO <sub>2</sub> , or not, for 24 hours..	274
<b>Figure 6.12</b> Morphological analysis of NCI-H441 monocultures exposed to 780 ng/cm <sup>2</sup> CB ± NO <sub>2</sub> at 5 ppm.....	275
<b>Figure 6.13</b> Viability, total cell count, barrier integrity, IL6 concentration and IL8 concentration of alveolar triple cell co-cultures exposed to either CB (780 ng/cm <sup>2</sup> ) then either incubated in 2.5 ppm NO <sub>2</sub> or at normal incubator conditions, for 24 hours..	276
<b>Figure 6.14</b> Morphological analysis of triple cell co-cultures exposed to 780 ng/cm <sup>2</sup> CB ± NO <sub>2</sub> at 2.5 ppm.....	277
<b>Figure 6.15</b> Viability, total cell count, barrier integrity, IL6 concentration and IL8 concentration of alveolar triple cell co-cultures exposed to either 1649b/2583 (780 ng/cm <sup>2</sup> ) then either incubated in 2.5 ppm NO <sub>2</sub> or at normal incubator conditions, for 24 hours .....	279

<b>Figure 6.16</b> Morphological analysis of triple cell co-cultures exposed to 780 ng/cm <sup>2</sup> 1649b/2583 ± NO <sub>2</sub> at 2.5 ppm .....	280
<b>Figure 6.17</b> Viability, total cell count, barrier integrity, IL6 concentration and IL8 concentration expression of alveolar triple cell co-cultures exposed to either DEPs (from 9.8, 13 and 17% engine O <sub>2</sub> intake) (exposed via qALI) then either incubated in 2.5 ppm NO <sub>2</sub> or at normal incubator conditions, for 24 hours.....	281
<b>Figure 6.18</b> Morphological analysis of triple cell co-cultures exposed to 780 ng/cm <sup>2</sup> DEPs (from 9.8, 13 and 17% engine O <sub>2</sub> intake) (exposed via qALI) ± NO <sub>2</sub> at 2.5 ppm. ....	284
<b>Figure 7.1</b> Schematic of RNA-Seq methodology. ....	300
<b>Figure 7.2</b> Volcano plots of gene expression changes after triple cell co-culture exposure to (A) NaCl, (B) NO <sub>2</sub> , (C) 2583, (D) 2583 + NO <sub>2</sub> , (E) DEP 17% or (F) DEP 17% + NO <sub>2</sub> .....	305
<b>Figure 7.3</b> Volcano plots of gene expression changes after triple cell co-culture exposure to (A) 2583 + NO <sub>2</sub> co-exposure against 2583 single pollutant exposure and (B) DEP 17% + NO <sub>2</sub> co-exposure against DEP 17% single pollutant exposure.....	306
<b>Figure 7.4</b> Number of overlapping or different DEGs for each exposure .....	307
<b>Figure 7.5</b> STRING analysis of DEGs resulting from NO <sub>2</sub> exposure (against incubator control) .....	310
<b>Figure 7.6</b> GO terms for Biological Processes, Cellular Component and Molecular Function shown for NO <sub>2</sub> exposures (against incubator control) .....	311
<b>Figure 7.7</b> STRING analysis of DEGs resulting from DEP exposure (against NaCl control) .....	312
<b>Figure 7.8</b> GO terms for Biological Processes, Cellular Component and Molecular Function shown for DEP 17% exposure (compared to NaCl control) .....	313
<b>Figure 7.9</b> STRING analysis of DEGs resulting from DEP+ NO <sub>2</sub> co-exposure (against NaCl control) .....	314
<b>Figure 7.10</b> GO terms for Biological Processes, Cellular Component and Molecular Function shown for DEP 17% + NO <sub>2</sub> co-exposure .....	315
<b>Figure 7.11</b> STRING analysis of DEGs resulting from DEP + NO <sub>2</sub> co-exposure (against DEP single pollutant exposure) .....	316
<b>Figure 7.12</b> GO terms for Biological Processes, Cellular Component and Molecular Function shown for DEP 17% + NO <sub>2</sub> co-exposure (compared to DEP 17% single pollutant exposure) .....	316



<b>Figure 7.13</b> Gene expression of chemokines following exposure to DEP 17% or 2583 $\pm$ NO <sub>2</sub> .....	318
<b>Figure 7.14</b> Gene expression of guanylate binding protein following exposure to DEP 17% or 2583 $\pm$ NO <sub>2</sub> .....	319
<b>Figure 7.15</b> Gene expression of cytokines (or related proteins) following exposure to DEP 17% or 2583 $\pm$ NO <sub>2</sub> .....	320
<b>Figure 7.16</b> Gene expression of inflammatory related proteins following exposure to DEP 17% or 2583 $\pm$ NO <sub>2</sub> .....	321
<b>Figure 7.17</b> Gene expression oxidative stress related proteins following exposure to DEP 17% or 2583 $\pm$ NO <sub>2</sub> .....	322
<b>Figure 7.18</b> Gene expression surfactant proteins following exposure to DEP 17% or 2583 $\pm$ NO <sub>2</sub> .....	323
<b>Figure 7.19</b> Gene expression MUC 21, SLC11A1, MMP9 and CYP1A1 following exposure to DEP 17% or 2583 $\pm$ NO <sub>2</sub> .....	324
<b>Figure 7.20</b> TNF signalling pathway. ....	330
<b>Figure 7.21</b> IL17C transduction pathway.....	331
<b>Figure 8.1</b> Toxicological effects caused by either PM or NO <sub>2</sub> within the alveolar models used in this work .....	341
<b>Figure 8.2</b> Possible routes of toxicity caused by PM and NO <sub>2</sub> co-exposure implicated within this work.....	345
<b>Figure 8.3</b> Possible routes of toxicity caused by PM and NO <sub>2</sub> co-exposure implicated within this work, put into the context with published literature.....	346
<b>Figure 9.1</b> VitroCell® Cloud systems within Swansea University (IVTG) and RCE (UKHSA) were compared using CB to model deposition. ....	356

## List of Tables

---

<b>Table 1.1</b> Sources of gaseous pollutants and their respective limit levels .....	33
<b>Table 1.2</b> Maximal accepted levels of PM fractions.....	37
<b>Table 1.3</b> A list of genes activated through Nrf2 transactivation.....	60
<b>Table 1.4</b> Characteristics and prevalence of significant sources of PM .....	64
<b>Table 2.1</b> Cell lines, reagents, chemicals, kits and equipment used within this work. .....	84
<b>Table 2.2</b> Settings used on LUNA II to count cells and analyse viability. ....	94
<b>Table 2.3</b> Primary antibodies used within this work.....	98
<b>Table 2.4</b> Reagents used in IL6, IL8 and TNF $\alpha$ ELISAs.....	100
<b>Table 3.1</b> Cell seeding densities used to characterise the hAELVi cells shown as cell/mL, cell/well and cell/cm <sup>2</sup> .....	107
<b>Table 3.2</b> Seeding Densities investigated for use within the alveolar epithelial co- culture. ....	109
<b>Table 3.3</b> Adherence of dTHP-1 cells to various alveolar epithelial models.....	139
<b>Table 3.4</b> Key conclusions and findings from Chapter 3 .....	144
<b>Table 4.1</b> Physical and chemical characterisation of PM samples used within this work .....	151
<b>Table 4.2</b> Volumes used to dilute each concentration of CB, 1649b or 2548 .....	159
<b>Table 4.3</b> Actual exposure concentrations of CB, 1649b and 2583 when targeting 390, 780 and 3100 ng/cm <sup>2</sup> .....	182
<b>Table 4.4</b> Key conclusions and findings from Chapter 4.....	191
<b>Table 5.1</b> Seeding densities and media used within various in vitro models. ....	197
<b>Table 5.2</b> Main effects observed with differing alveolar models following exposure to CB, 1649b, 2583 and DEPs.....	236
<b>Table 5.3</b> Key conclusions and findings from Chapter 5.....	247
<b>Table 6.1</b> BSA concentrations used to create the standard curve within the DC protein quantification assay. ....	257
<b>Table 6.2</b> DNase Master Mix Constituents .....	261
<b>Table 6.3</b> Constituents of the reaction mixture for the first thermal cyclor run for cDNA synthesis. ....	261
<b>Table 6.4</b> DNase reaction thermal cyclor protocol. ....	261
<b>Table 6.5</b> cDNA synthesis reaction thermal cyclor protocol .....	262

<b>Table 6.6</b> Sequences of primers used in this work. ....	262
<b>Table 6.7</b> Constituents of the SYBR Green supermix .....	262
<b>Table 6.8</b> Summary of the main effects observed following NO <sub>2</sub> exposure within hAELVi cells, NCI-H441 cells or the alveolar triple cell co-culture. ....	284
<b>Table 6.9</b> Summary of the main effects observed on the triple cell co-culture following co-exposures of PM samples: CB, 1649, 2583 or DEPs with NO <sub>2</sub> .....	284
<b>Table 6.10</b> Key conclusions and findings from Chapter 7.....	298
<b>Table 7.1</b> Number of DEGs resulting from each exposure using thresholds of a Log <sub>2</sub> fold change of 1.5 and a p-value of < 0.05.....	307
<b>Table 7.2</b> Summary of key findings and conclusions from Chapter 7.....	334
<b>Table 9.1</b> Pre-published Chemical Properties for CB, 1349b, 2583, and DEP 9.8, 13 and 17%.....	351
<b>Table 9.2</b> DEGs from NO <sub>2</sub> , 2583, DEP (17%), NO <sub>2</sub> + 2583 and NO <sub>2</sub> + DEP (17%). ....	357

## Abbreviations and Acronyms

---

<b>2583</b>	NIST SRM 2583 Trace Element in Indoor Dust
<b>1649b</b>	NIST SRM 1649b Urban Dust
<b>16HBE14o–</b>	Human Bronchial Epithelial Cell Line
<b>A549</b>	ATII Cell Line
<b>ALI</b>	Air-Liquid Interface
<b>AM</b>	Alveolar Macrophage
<b>AMP</b>	Antimicrobial Peptides
<b>ANOVA</b>	Analysis of Variance
<b>ANSES</b>	French Agency for Food, Environment and Occupational Health and Safety
<b>APHEA</b>	Air Pollution and Health: a European Approach Air Pollution and Health: A Combined European and North American
<b>APHENA</b>	Approach
<b>AQG</b>	Air Quality Guidelines
<b>ARE</b>	Antioxidant Response Element
<b>ATCC</b>	The American Type Culture Collection
<b>ATI</b>	Alveolar Type 1 Cell
<b>ATII</b>	Alveolar Type 2 Cell
<b>BAL(F)</b>	Bronchoalveolar Lavage (Fluid)
<b>BC</b>	Black Carbon
<b>BEAS-2B</b>	Human Bronchial Epithelial Cell Line
<b>BMI</b>	Body Mass Index
<b>BSA</b>	Bovine Serum Albumin
<b>Caco-2</b>	Colon Carcinoma Cell Line
<b>CB</b>	Printex® 90 Carbon Black
<b>CCL</b>	C-C Motif Chemokine Ligand
<b>CCM</b>	Cell Culture Media
<b>CD11β</b>	Integrin Subunit Alpha M
<b>CD3</b>	Cluster of Differentiation 3
<b>CD69</b>	Cluster of Differentiation 69
<b>cDNA</b>	Copy/Complementary DNA
<b>CI</b>	Confidence Interval
<b>CO</b>	Carbon Monoxide
<b>CO<sub>2</sub></b>	Carbon Dioxide
<b>COMEAP</b>	Committee on the Medical Effects of Air Pollutants
<b>COPD</b>	Chronic Obstructive Pulmonary Disease
<b>CRP</b>	C-Reactive Protein
<b>CXCL</b>	CXC Motif Chemokine Ligand

<b>CYP</b>	Cytochrome P450 Enzyme
<b>DAPI</b>	4',6-diamidino-2-phenylindole (DNA Probe)
<b>DC</b>	Detergent Compatible
<b>DEFRA</b>	Department for Environment, Food and Rural Affairs
<b>DEGs</b>	Differentially Expressed Genes
<b>DEP</b>	Diesel Emission Particle
<b>DEP 13%</b>	Diesel Emission Particle from 13% O2 Engine Intake
<b>DEP 17%</b>	Diesel Emission Particle from 17% O2 Engine Intake
<b>DEP 9.8%</b>	Diesel Emission Particle from 9.8% O2 Engine Intake
<b>DMEM</b>	Dulbecco's Modified Eagle Medium
<b>DMSO</b>	Dimethylsulfoxide
<b>DNA</b>	Deoxyribonucleic Acid
<b>dTHP-1</b>	Differentiated THP-1 Cell
<b>EA.hy 926</b>	Vascular Endothelial Cell Line
<b>EC</b>	European Commission
<b>EDTA</b>	Ethylenediaminetetraacetic Acid
<b>EF<sub>50</sub></b>	Mid-tidal Expiratory Flow
<b>EGFR</b>	Epidermal Growth Factor Receptor
<b>ELAPSE</b>	Effects of Low-Level Air Pollution: A Study in Europe
<b>ELISA</b>	Enzyme-Linked Immunosorbent Assay
<b>EMT</b>	Epithelial-Mesenchymal Transition
<b>EPA</b>	Environmental Protection Agency
<b>ESCAPE</b>	The European Study of Cohorts for Air Pollution Effects
<b>FBS</b>	Foetal Bovine Serum
<b>FEV1</b>	Forced Expiratory Volume
<b>FMT</b>	Fibroblast-Mesenchymal Transition
<b>FOV</b>	Field of View
<b>GAPDH</b>	Glyceraldehyde-3-Phosphate Dehydrogenase
<b>GBP</b>	Guanylate Binding Protein
<b>GCL</b>	Glutamine-Cysteine Ligase
<b>GIVIMP</b>	Guidance Document on Good In Vitro Method Practices
<b>GSH</b>	Reduced Glutathione
<b>GSSG</b>	Oxidised Glutathione
<b>H<sub>2</sub>O<sub>2</sub></b>	Hydrogen Peroxide
<b>H<sub>2</sub>SO<sub>4</sub></b>	Sulfuric Acid
<b>hAELVi</b>	Human Alveolar Epithelial Lentivirus Immortalized Cells
<b>hBD</b>	Human Beta-Defensin
<b>HBEC</b>	Human Bronchial Epithelial Cells

<b>HEPES</b>	4-(2-Hydroxyethyl)-1-Piperazineethanesulfonic Acid
<b>HMC-1</b>	Human Mast Cell Line
<b>HMOX1</b>	Haem Oxygenase-1
<b>HO•</b>	Hydroxyl Radical
<b>HPRT1</b>	Hypoxanthine Phosphoribosyltransferase 1
<b>HR</b>	Hazard Ratio
<b>HRP</b>	Horseradish Peroxidase
<b>huAEC</b>	human Alveolar Epithelial Cell
<b>IFN<math>\gamma</math></b>	Interferon Gamma
<b>I<math>\kappa</math>B<math>\alpha</math></b>	NF $\kappa$ B Inhibitor Alpha
<b>IL</b>	Interleukin
<b>IL10</b>	Interleukin 10
<b>IL10R</b>	Interleukin 10 Receptor
<b>IL1<math>\alpha</math></b>	Interleukin 1 alpha
<b>IL1<math>\beta</math></b>	Interleukin 1 beta
<b>IL1R</b>	Interleukin 1 Receptor
<b>IL6</b>	Interleukin 6
<b>IL8</b>	Interleukin 8
<b>iNOS</b>	Inducible Nitrogen Oxide Synthase
<b>IRAK</b>	IL1R-Activated Protein Kinase
<b>ISA</b>	Integrated Science Assessment
<b>JAK</b>	Janus Kinase
<b>JNK</b>	c-Jun N-terminal Kinase
<b>Keap1</b>	Kelch-like ECH-associated Protein 1
<b>LDH</b>	Lactate Dehydrogenase
<b>LPS</b>	Lipopolysaccharide
<b>LSM</b>	Laser Scanning Microscope
<b>MAPK</b>	Mitogen-activated Protein Kinase
<b>MMP</b>	Matrix Metalloproteinase
<b>mRNA</b>	Messenger RNA
<b>MT2A</b>	Metallothionein-2
<b>MT1G</b>	Metallothionein 1G
<b>N<math>_2</math></b>	Nitrogen
<b>NaCl</b>	Sodium Chloride
<b>NCI-H441</b>	Lung adenocarcinoma Cell Line
<b>NF<math>\kappa</math>B</b>	Nuclear Factor-Kappa B
<b>NH<math>_3</math></b>	Ammonia
<b>NIST</b>	National Institute of Standards and Technology

<b>NLR</b>	NOD-like Receptor
<b>NLRP3</b>	NOD-, LRR- and Pyrin Domain-containing Protein 3
<b>NMMAPS</b>	National Mortality, Morbidity and Air Pollution Studies
<b>NO•</b>	Nitric Oxide Radical
<b>NO<sub>2</sub></b>	Nitrogen Dioxide
<b>NOS</b>	Nitric Oxide Synthase
<b>NO<sub>x</sub></b>	Oxides of Nitrogen
<b>NQO1</b>	NDAPH-Quinone Oxidoreductase 1
<b>NRC</b>	No-Reverse Transcriptase Control
<b>Nrf2</b>	Nuclear Factor Erythroid 2-related Factor
<b>NTC</b>	No-Template Control
<b>O<sub>2</sub></b>	Oxygen
<b>O<sub>2</sub>•-</b>	Superoxide Radical
<b>O<sub>3</sub></b>	Ozone
<b>OECD</b>	The Organisation for Economic Co-operation and Development
<b>PAH</b>	Polycyclic Aromatic Hydrocarbon
<b>P<sub>app</sub></b>	Permeability Coefficient
<b>PBS</b>	Phosphate Buffered Saline
<b>PCB</b>	Polychlorinated Biphenyl
<b>PCDD</b>	Polychlorinated Dibenzo-dioxin
<b>PCDF</b>	Polychlorinated Dibenzo-furan
<b>PCR</b>	Polymerase Chain Reaction
<b>PFA</b>	Paraformaldehyde
<b>PM</b>	Particulate Matter
<b>PM<sub>0.1</sub></b>	Particulate Matter below 0.1 micrometers in aerodynamic diameter
<b>PM<sub>10</sub></b>	Particulate Matter below 10 micrometers in aerodynamic diameter
<b>PM<sub>2.5</sub></b>	Particulate Matter below 2.5 micrometers in aerodynamic diameter
<b>PMA</b>	Phorbol 12-Myristate 13-Acetate
<b>PRR</b>	Pattern Recognition Receptors
<b>PTEN</b>	Phosphatase and Tensin Homolog
<b>PTGS2</b>	Prostaglandin-Endoperoxide Synthase 2
<b>qALI</b>	Quasi-Air-Liquid Interface
<b>QCM</b>	Quartz Crystal Microbalance
<b>qPCR</b>	Quantitative PCR
<b>RCE</b>	UKHSA Radiation Chemical and Environmental Hazards Directorate
<b>RCF</b>	Relative Centrifugal Force
<b>RCP</b>	Royal College of Physicians
<b>REVIHAAP</b>	Review of Evidence on Health Aspects of Air Pollution

<b>RMPI-1640</b>	Roswell Park Memorial Institute 1640 Media
<b>RNA</b>	Ribonucleic Acid
<b>RNA-Seq</b>	RNA Sequencing
<b>ROS</b>	Reactive Oxygen Species
<b>SEM</b>	Scanning Electron Microscope
<b>SFTP</b>	Surfactant Protein
<b>SO<sub>2</sub></b>	Sulphur Dioxide
<b>SOD1</b>	Superoxide Dismutase 1
<b>SOD2</b>	Superoxide Dismutase 2
<b>SP</b>	Surfactant Protein
<b>SR-A</b>	Class A Scavenger Receptor
<b>SRM</b>	Standard Reference Material
<b>SRM 2975</b>	NIST SRM Diesel Particulate Matter
<b>STAT</b>	Signal Transducer and Activator or Transcription
<b>TCA</b>	Trichloroacetic Acid
<b>TEER</b>	Transepithelial Electrical Resistance
<b>TEM</b>	Transmission Electron Microscopy
<b>THP-1</b>	Human Monocytic Cell Line
<b>TiO<sub>2</sub></b>	Titanium Dioxide
<b>TLR</b>	Toll-like Receptor
<b>TNF<math>\alpha</math></b>	Tumour Necrosis Factor Alpha
<b>TRAF</b>	TNF Receptor-associated Factor
<b>TT1</b>	Transformed Type 1 Cells
<b>TUBA1C</b>	Tubulin Alpha 1C
<b>UFP</b>	Ultrafine Particles (See PM0.1)
<b>UK</b>	United Kingdom
<b>UKHSA</b>	UK Health Security Agency
<b>US</b>	United States
<b>VOC</b>	Volatile Organic Compound
<b>WHO</b>	World Health Organization
<b>ZO-1</b>	Zonula Occludens-1



## Chapter 1: Introduction

---

## 1.1 Air Pollution

### 1.1.1 Background

The human health risks and socioeconomic burdens associated with air pollution are well defined and well recognised by governmental and public health bodies globally, including the World Health Organisation (WHO), European Commission (EC) and Environmental Protection Agency (EPA) (RCP, 2016; World Health Organization, 2021). Further, air pollution has an extensive history in the United Kingdom (**Figure 1.1**). Key events that have driven increases in air pollution include the transition from wood to bituminous coal in the 11<sup>th</sup> – 12<sup>th</sup> centuries and the Industrial Revolution in the 19<sup>th</sup> – 20<sup>th</sup> centuries. However, no event should be considered more important than the Great London Smog of 1952.

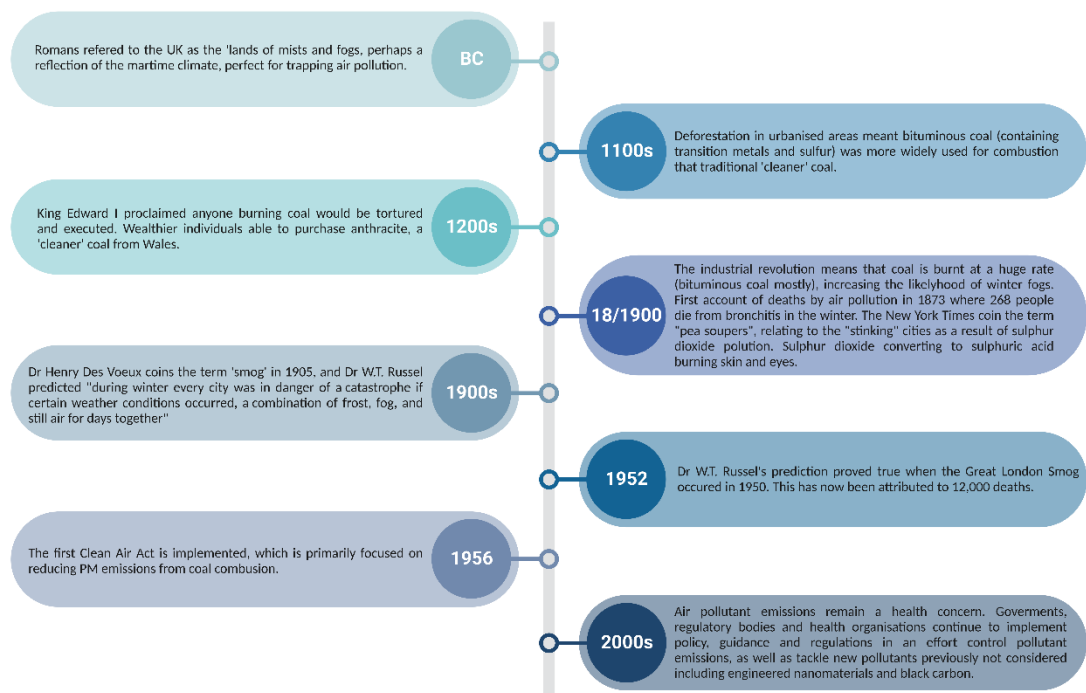


*Figure 1.1 Timeline of notable events in the history of air pollution in the UK. Created using BioRender.com*

From 5<sup>th</sup> December to 9<sup>th</sup> December 1952, London was plunged into darkness due to a massive build-up of smog (described as a mixture of smoke and fog). Due to cold winter weather, the combustion of high-sulphur coal for personal heating was high, and emissions from other sources of air pollution were growing. Increased emissions, combined with a meteorological temperature inversion, whereby stagnant warm air sat above land level cold air trapping air pollution at a lower altitude, is thought to be the leading cause of this smog event (Laskin, 2006).

On December 4<sup>th</sup>, 1952, before the smog, smoke was measured (by collection on a filter and assessment of ‘blackness’) to be 0.49 mg/m<sup>3</sup>. The smoke increased almost ten-fold by December 7<sup>th</sup> and 8<sup>th</sup> to 4.46 mg/m<sup>3</sup> (Wilkins, 1954). During this time, visibility was reported to be less than 10 metres, resulting in profound social impact and mortality (Polivka, 2018). An estimated 12,000 deaths can now be attributed to the acute and persisting effects of the Great London Smog (Bell & Davis, 2001). The Great London Smog led to a significant public outcry and subsequent governmental action.

In response, over 3 years, the UK Government enacted the first Clean Air Act of 1956, intending to control public exposure to air pollution (RCP, 2016), which aimed to curb air pollution emissions through a range of control measures, including a push for the use of smokeless fuels and more effective chimneys (Parliament of the United Kingdom, 1956). These changes were largely successful in reducing the emissions of pollutants sulphur dioxide (SO<sub>2</sub>) and particulate matter (PM) (in the form of black smoke). However, other gaseous pollutants, such as oxides of nitrogen (NO<sub>x</sub>) and ozone (O<sub>3</sub>), remained unchanged (Ayres, 1997). To date, global governments strategize to include advances and evolution in technology, scientific understandings, and fuel sources within policy. For example, the UK banned the sale of pre-packaged bituminous house coal and wet wood in 2021 (DEFRA, 2020). Further, there is an intention to suspend the sale of non-electric cars from 2035 (Department for Transport, 2020). Although there have been two iterations of the Clean Air Act between 1956 and the present date (1968 and 1993), the UK Government's Department for Environment, Food and Rural Affairs (DEFRA) published the most recent Clean Air ‘Strategy’ in 2019. This strategy acknowledges the issues arising from air pollution and sets forward goals to be reached to combat this. Further, the Environmental Act 2021 outlines laws to improve many aspects of environmental health. This includes improving air quality through measures such as pushing local authorities to prepare action plans to target air pollution, and the implementation of penalties for emitting smoke within smoke-controlled areas.

Although there have been improvements in air quality since the Great London Smog, air pollution is still recognised as the fourth largest global human health risk factor, behind blood pressure, dietary risks and smoking (Juginović et al., 2021). Air pollution contributes to 9 million premature deaths per year worldwide (Fuller et al., 2022) and

costs the UK economy over £20 billion per year in health care and loss of work (RCP, 2016). Within the UK alone, long-term exposure to air pollution is estimated to be directly attributable to 28,000 to 36,000 deaths annually (COMEAP, 2018). It has been observed that exposure to indoor and ambient air pollutants can increase the risk of morbidities such as cardiovascular disease (Brook et al., 2004; Poloniecki et al., 1997), acute cardiovascular events (Mittleman & Mostofsky, 2011; Peters et al., 2001), asthma (Jiang et al., 2016), chronic obstructive pulmonary disease (COPD) (Song et al., 2014) and lung cancer (Chen et al., 2016). Therefore, there is an urgent need for improvements in policy and technology in this area to improve public health and reduce the pressure on healthcare systems.

Policy decisions are difficult as the complexities of air pollution must be considered. Air pollution is a heterogeneous mixture of gaseous and particulate components, which can each elicit independent toxicological impacts within biological systems (Kampa & Castanas, 2008). Therefore, when developing and adopting policy, careful consideration should be given to the pollutant emitters, the geographical location (*e.g.*, rural settings will have differing air qualities to urban) and timing (*e.g.*, pollutant levels may fluctuate on a seasonal and daily basis). A fundamental challenge of air pollution research is deriving and isolating constituents of air pollution that cause specific adverse outcomes. For example, particulate aerosols have been highly associated with cardiovascular and respiratory endpoints (Bosson et al., 2019). However, in long-term and epidemiological studies, it can be challenging to correlate specific adverse outcomes to single elements of air pollution due to confounding pollutant exposures. The requirement to better understand the synergy between multipollutant exposure and human health was further highlighted in the Chief Medical Officers Annual Report in 2022, which stated “another area that requires greater understanding is the effect of synergistic co-exposures of multiple air pollutants on people’s health” (CMO, 2022). An example of where this has been difficult is during research into the health impacts of nitrogen dioxide (NO<sub>2</sub>), due to its correlation with PM emissions.

NO<sub>2</sub> is a gaseous pollutant, often found at high concentrations in urban environments due to traffic and industrial emissions (DEFRA, 2019), as well as indoors due to tobacco smoke, as well as fossil fuel powered stoves, ovens and heaters (WHO, 2010). Numerous epidemiological reports have associated NO<sub>2</sub> inhalation with increased risk of morbidity and mortality (Faustini et al., 2014). There is difficulty, however, with

extracting trends relevant to NO<sub>2</sub> from trends that could be relevant to other pollutants, such as PM. As NO<sub>2</sub> and PM are emitted from similar sources, their concentrations are often proportional. Therefore, those exposed to high NO<sub>2</sub> levels are also exposed to high PM levels (COMEAP, 2018). There is a vital call to research to address this gap in the knowledge through the comparison of the toxicity of both NO<sub>2</sub> and PM within the same experimental system, so the toxicological impact of each can be derived. Further, the tragic death of a child in London due to NO<sub>2</sub> exposure underscores the requirement for this research. Through the possession of more in-depth knowledge of the health impacts of air pollution, a greater push can be made into controlling it, feeding into policy generation and ultimately safeguarding of public health.

Before focussing on the interplay between NO<sub>2</sub> and PM and the known toxicological information of these pollutants, air pollution will be discussed holistically to gain

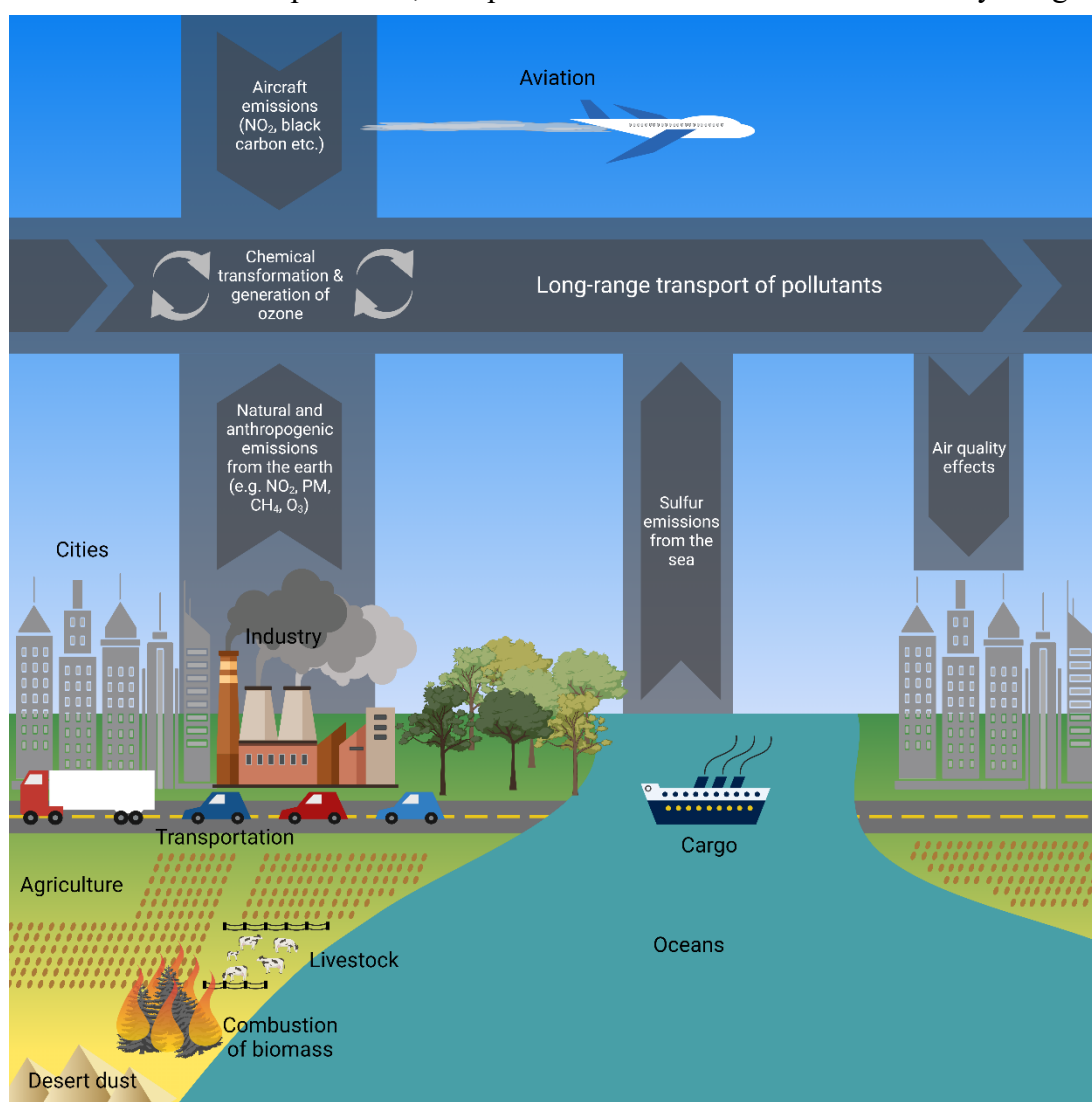


**Figure 1.2** Major emitters of air pollution, such as transportation and industry, produce inhalable pollutants that can travel large distances, impacting air quality over large regions. Created using BioRender.com

insight into its complexity and diversity. As mentioned, air pollution is a complex, heterogenous mixture of gaseous, particulate, and chemical pollutants. Sources of air pollution are vast and consist not only of anthropogenic emitters but also of natural emitters, such as sea salt, Saharan dust and wildfires (Thompson, 2018) (**Figure 1.2**). These pollutants can be split into four categories: 1. Gaseous, 2. Particulate matter, 3. Heavy metals (*e.g.*, lead, mercury) and 4. Persistent organic pollutants (*e.g.*, dioxins) (Kampa & Castanas, 2008).

### 1.1.2 Gaseous Pollutants

Gaseous pollutants, vapour-phase compounds, and secondary pollutants constitute more than 90% of the pollutant mass (Münzel et al., 2018). Gaseous pollutants are vast and vary in terms of their chemistry, emission sources, and toxicology. Prevalent gaseous pollutants include ammonia (NH<sub>3</sub>), sulphur dioxide (SO<sub>2</sub>), carbon monoxide (CO), volatile organic compounds (VOCs) and oxides of nitrogen (NO<sub>x</sub>). A significant source of gaseous pollutants is the combustion of fossil fuels, often emitted by motor transport and industry. Combustion of fossil fuels results in the release of gases such as nitrogen monoxide (NO) (which reacts with ozone and free radicals to rapidly form

*Table 1.1 Sources of gaseous pollutants and their respective limit levels*

Gas	Emission Sources	Maximal Accepted Concentration
Ammonia	Agriculture (animal husbandry and synthetic fertilisers) <sup>1</sup>	N/A
	Biomass combustion <sup>1</sup>	
	Vehicles <sup>2</sup>	
Carbon Monoxide	Incomplete combustion of hydrocarbons <sup>3</sup>	WHO AQG 2021 - 7 mg/m <sup>3</sup> (24 hr average) Directive 2008/50/EC - 10 mg/m <sup>3</sup> (8 hr average)
Nitrogen Oxides	Combustion within ambient air <sup>4</sup>	WHO AQG 2021 - 10 µg/m <sup>3</sup> (annual average) (NO <sub>2</sub> ) WHO AQG 2021 - 25 µg/m <sup>3</sup> (24 hr average) (NO <sub>2</sub> ) Directive 2008/50/EC - 200 µg/m <sup>3</sup> (1 hr average) (NO <sub>2</sub> ) Directive 2008/50/EC - 40 µg/m <sup>3</sup> (annual average) (NO <sub>2</sub> )
Ozone	Secondary pollutant from photochemical reactions of VOCs <sup>5</sup>	WHO AQG 2021 - 60 µg/m <sup>3</sup> (peak season) WHO AQG 2021 - 100 µg/m <sup>3</sup> (8 hr average) Directive 2008/50/EC - 120 µg/m <sup>3</sup> (8 hr average)
Sulphur Dioxide	Combustion of sulphur containing fuel ( <i>e.g.</i> coal and oil) <sup>6</sup>	WHO AQG 2021 - 40 µg/m <sup>3</sup> (24 hr average) Directive 2008/50/EC - 350 µg/m <sup>3</sup> (1 hr average) Directive 2008/50/EC - 125 µg/m <sup>3</sup> (24 hr average)
Volatile Organic Compounds	Household products ( <i>e.g.</i> paint, cleaning aerosols, pesticides) <sup>7</sup> Combustion of hydrocarbons <sup>8</sup> Combustion of waste <sup>8</sup>	Directive 2008/50/EC - 5 µg/m <sup>3</sup> (annual average) (benzene)

<sup>1</sup>Behera *et al.* (2013), <sup>2</sup>Wang *et al.* (2023), <sup>3</sup>Bleecker (2015), <sup>4</sup>World Health Organization (2018), <sup>5</sup>Wang *et al.* (2015), <sup>6</sup>Chen *et al.* (2007), <sup>7</sup>Environmental Protection Agency (2023b), <sup>8</sup>David and Niculescu. (2021)

NO<sub>2</sub>), CO (through incomplete combustion), ozone (O<sub>3</sub>) (through photochemical reactions involving NO<sub>2</sub>, VOCs and sunlight), SO<sub>2</sub> (thorough combustion of sulphur containing fossil fuels, such as coal and heavy oil), and VOCs (organic chemicals such as benzene) (Katsouyanni, 2003). However, ammonia is primarily released through agricultural processes (DEFRA, 2019). **Table 1.1** outlines emitters and accepted levels of each of these main gaseous pollutants.

It is essential to realise that although NO<sub>2</sub> (and its associated co-exposure with PM) will be the focus of this work and examined in greater detail in Sections 1.4 and 1.5, there is still a degree of co-exposure that would occur between all the aforementioned gases. CO and SO<sub>2</sub> are, for example, both associated with combustion sources (along with NO<sub>2</sub> and PM), whereas O<sub>3</sub> and NH<sub>3</sub> are often related to rural settings. Therefore, although these gases are often discussed as singular entities, their relative concentrations should be considered when consulting epidemiological evidence. Although this work will examine NO<sub>2</sub> and PM co-exposure, there are still many other pollutants that could benefit from being investigated within a situational setting. This means that the relative levels of each pollutant should be considered and accounted for to deduce pollutant-specific effects. This should also be considered within exposure studies, where, from a public health perspective, it would be beneficial to consider these pollutants as a heterogeneous mixture exposed at concentrations that are applicable to real-life exposures.

CO is a colourless gas released from the incomplete combustion of hydrocarbons. Inhaled CO can translocate into circulation, where it binds with haemoglobin, forming carboxyhaemoglobin, reducing the blood's efficiency of delivering oxygen to tissue (Bateman, 2012). Unintentional non-fire related CO poisoning results in 25 deaths per year within the UK (Health and Safety Executive, 2022). However, this is usually due to indoor environments lacking proper ventilation, properly maintained combustion equipment and non-functional CO alarms (Roca-Barceló et al., 2020). The US EPA reported a considerable reduction in CO concentration at a national level, from approximately 10 ppm to less than 1 ppm (annual 2<sup>nd</sup> maximal 8-hour average) between 1980 and 2022 (Environmental Protection Agency, 2023a). This change is likely due to the increased use of catalytic converters on car exhausts (Hutchinson Emma & Pearson Peter, 2004).

Levels of SO<sub>2</sub>, a crucial pollutant in the London smog event of 1952, increased in Europe throughout the 1900s, especially after the Second World War. However, levels of this gas have been decreasing since 1980 (Mylona, 1996). The WHO has suggested that a maximal daily average SO<sub>2</sub> concentration should not exceed 40 µg/m<sup>3</sup>. For comparison, the effects that led to the London smog saw SO<sub>2</sub> in the range of 3000 to 4000 µg/m<sup>3</sup> (Greater London Authority, 2022). More recently, however, levels have been within single digits of µg/m<sup>3</sup> (DEFRA, 2024). This decrease is likely due to a change in the attitude towards fuel usage, a reduction in coal use for energy generation and a limit placed on the sulphur content of liquid fuels (DEFRA, 2023b). Epidemiological evidence has linked SO<sub>2</sub> exposure with increased all-cause and respiratory mortality (Orellano et al., 2021), respiratory infection, asthma and COPD (Carlsen et al., 2021).

Tropospheric O<sub>3</sub> is a secondary pollutant, so is not emitted directly but is instead generated through photochemical reactions between NO<sub>x</sub>, VOCs and methane. For this reason, O<sub>3</sub> is often found at high levels within cities (due to the high levels of the precursor pollutants) (Anbari et al., 2022). However, O<sub>3</sub> can often be found at higher levels within rural areas. This is because NO<sub>x</sub>, which is less abundant in rural locations, can also cause the breakdown of O<sub>3</sub>. O<sub>3</sub> can also travel long distances from the initial source of precursor pollutants, potentially moving from urban to rural regions. It is for this reason that many urban areas saw increased O<sub>3</sub> concentrations during the COVID-19 lockdowns, whilst most other air pollutant levels decreased (Wang et al., 2020). Within the UK, rural O<sub>3</sub> concentrations have remained unchanged since 1987; however, urban concentrations have been increasing since 1992, likely due to a reduction in NO<sub>x</sub> emissions and increased hot (summer) weather (DEFRA, 2023c). O<sub>3</sub> exposure has been linked with a plethora of toxic outcomes such as asthma onset, exacerbation of asthma, emphysema, COPD and respiratory mortality. The mechanisms by which O<sub>3</sub> exerts these effects are likely through oxidative stress and inflammatory responses within the pulmonary tissues (Zhang et al., 2019). With O<sub>3</sub> levels expected to increase further, consideration should be given to mitigation measures, especially when implementing policies that will reduce NO<sub>x</sub> emissions.

NH<sub>3</sub> is a pollutant mainly associated with agricultural areas, which contribute 81% of global NH<sub>3</sub> emissions, and is often released during the use of artificial fertilisers and



through animal husbandry (manure generation, storage and application) (Wyer et al., 2022).  $\text{NH}_3$  is able to have independent toxic effects on the human body (Sundblad et al., 2004). The US Environmental Protection Agency (2016) has reviewed inhalation exposure to  $\text{NH}_3$ , finding associations with increased respiratory symptoms, reductions in lung function and asthma exacerbation, although, other studies have shown little effect of ammonia inhalation within agricultural settings.  $\text{NH}_3$  can also react with aerosol acids, generating  $\text{PM}_{2.5}$  as ammonium sulphate, ammonium nitrate and ammonium chloride, which are known to have toxic effects (discussed in detail in Section 1.4) It is estimated that  $\text{NH}_3$  contributed to 30% and 50% of all  $\text{PM}_{2.5}$  in the US and Europe, respectively (Wyer et al., 2022). The co-benefits of mechanisms to control  $\text{NH}_3$  release are well established, such as reducing unwanted nutrient release into rivers, and therefore should be directed through relevant policies such as EU directive 92/43/EEC. However,  $\text{NH}_3$  pollution is still attributable to 50% of  $\text{PM}_{2.5}$  in Europe (Erisman & Schaap, 2004).

VOCs, consisting of reactive compounds such as benzene and propylene glycol, are a less discussed form of gaseous air pollutants. VOCs are often found in household products, such as solvents and aerosols used for cleaning and DIY, meaning they pose a significant threat to indoor air quality (Environmental Protection Agency, 2023b). As VOCs represent a whole class of pollutants, their toxic effects are varied depending on the emission source and chemistry. However, they are often able to react with the surface of the airway to induce a pro-inflammatory response and regulate immune system activities (Ogbodo et al., 2022; Wang et al., 2012). Although recognised as a source of air pollution within the home, the WHO Air Quality Guidelines 2021 do not refer to a maximal recommended VOC level. However, EU directive 92/43/EEC does suggest a maximum level for benzene (**Table 1.1**). Within the US, anthropogenic VOC emissions have decreased by 47% between 1990 and 2014, likely due to cleaner transport and industrial fuel sources (Environmental Protection Agency, 2018).

### **1.1.3 Particulate Matter**

Particulate matter (PM) will be a crucial pollutant focused on within this work, especially its co-emission/co-exposure with  $\text{NO}_2$ . PM is a term used to describe a wide range of air pollutants that consist of solid or liquid particles suspended within the air. These particles vary in size, composition, surface area, surface charge, and

agglomeration, amongst other physical and chemical characteristics. The impacts, therefore, on human health are diverse (COMEAP, 2022; Poschl, 2005). PM sources are highly varied but include natural and anthropogenic sources, such as industry,

*Table 1.2 Maximal accepted levels of PM fractions*

PM Type	Maximal Accepted Concentration
PM <sub>10</sub>	WHO AQG 2021 - 15 µg/m <sup>3</sup> (annual average)
	WHO AQG 2021 - 45 µg/m <sup>3</sup> (24 hr average)
	Directive 2008/50/EC - 40 µg/m <sup>3</sup> (annual average)
	Directive 2008/50/EC - 50 µg/m <sup>3</sup> (daily average)
	Directive 2008/50/EC - 35 µg/m <sup>3</sup> (no more than 35 times a year)
PM <sub>2.5</sub>	WHO AQG 2021 - 5 µg/m <sup>3</sup> (annual average)
	WHO AQG 2021 - 15 µg/m <sup>3</sup> (24 hr average)
	Directive 2008/50/EC - 20 µg/m <sup>3</sup> (annual average)

traffic vehicles (through exhaust emissions and non-exhaust emissions (*e.g.*, brake dust and tyre debris)), dust, sea salt, fires, and organic matter (*e.g.*, pollen and insect parts). PM is usually classified based on size, such as PM<sub>10</sub> and PM<sub>2.5</sub>, distinguishing PM below 10 µm and 2.5µm, respectively. PM can also be defined as ultrafine (UFP or PM<sub>0.1</sub>), with an aerodynamic diameter of less than 0.1 µm (Kwon et al., 2020).

Similar to gaseous air pollutants, the WHO has included maximum PM<sub>10</sub> and PM<sub>2.5</sub> level guidelines in their 2021 report. The European Directive 2008/50/EC has also suggested maximal levels. Recommended maximal levels are shown in **Table 1.2**. Although the WHO AQG 2021 does not specify a maximal level for UFPs, black carbon and sand and dust storms, it provides good practice statements. These statements acknowledge the risks of each pollutant type whilst simultaneously acknowledging the research gaps that require addressing to enable exposure-level guidance to be created. The inherent complexities of PM are explored in greater detail in Section 1.4.

#### **1.1.4 Heavy Metals**

Heavy metals are natural components of the earth's crust, commonly defined as those having a specific density greater than 5 g/cm<sup>3</sup> (Järup, 2003). Heavy metal emissions into the environment occur through various processes, including release from air (*e.g.*, combustion), soil and water. Many heavy metal pollutants, such as cadmium, lead, mercury, arsenic, and vanadium, each carry their own impacts on biological systems. Biologically, many heavy metals are required in trace amounts to support healthy

metabolic and enzymatic functions; however, higher concentrations of these heavy metals can result in toxicity (Järup, 2003) and are often the subject of bioaccumulation (Kampa & Castanas, 2008). Cadmium is an example of a common environmental contaminant, and emissions into the air occur through various natural processes such as the erosion of cadmium-containing rocks, volcanic activity, and sea spray. Anthropogenic processes, including tobacco smoking, the combustion of fossil fuels, the incineration of waste and the mining and refinement of zinc-containing ores, also release cadmium (Pan et al., 2010). Cadmium is retained at much higher proportions through inhalation, compared to ingestion, with the main target of toxicity being the kidneys (WHO, 2008). Cadmium has been classed as carcinogenic by the International Agency for Research on Cancer (Straif et al., 2009) with association with many cancer types, including lung cancer (Nawrot et al., 2015), potentially through increased oxidative stress and inhibited DNA repair (Hartwig, 2010).

Another heavy metal air pollutant, lead, is regulated by EU Directive 2008/50/EC at an annual maximal average of  $0.5 \mu\text{g}/\text{m}^3$ . Lead can be inhaled following exposure to leaded fuels, using lead-based paints, printing and industrial processes (such as lead smelting) (Wani et al., 2016). Within the UK, lead emissions have decreased by 96% since 1990, likely due to the implementation of unleaded petrol in the 1980s. Before this, leaded petrol contributed 73% of lead emissions, which has been reduced to 0.5% since 2000 (National Atmospheric Emissions Inventory, 2021). Approximately 30-40% of inhaled lead will enter the bloodstream (Philip & Gerson, 1994), where it can interrupt haem synthesis, reducing the haemoglobin content within a human's blood. Lead has also been shown to cause nervous system effects, though it may induce oxidative stress at a pulmonary level, resulting in DNA, membrane and protein damage (Patrick, 2006; Vaziri & Sica, 2004; Wani et al., 2016).

### **1.1.5 Persistent Organic Pollutants**

Persistent organic pollutants are a group of toxic chemicals, which, hence the name, persist in the environment for long periods. Persistent organic pollutants include polychlorinated dibenzo-dioxins (PCDDs), polychlorinated dibenzo-furans (PCDFs), often referred to as “dioxins”, and polychlorinated biphenyls (PCBs), often referred to as “dioxin-like compounds”. Generally, dioxins are formed through incomplete combustion of organic material (Bumb et al., 1980) and the combustion of chlorine-

containing materials, such as plastics (Kampa & Castanas, 2008). There are 210 distinct chemically different PCDD/Fs, each with varying toxicological profiles (Hites, 2011). There are many instances in recent history where dioxin exposure has profoundly impacted public and environmental health. An example of this is ‘Agent Orange’, a herbicide used by the US military during the Vietnam War, which was contaminated with the dioxin 2378-TCDD. The National Academies for Sciences Engineering and Medicine (2018) have reviewed the evidence from the event and have associated 2378-TCDD exposure with non-Hodgkin’s lymphoma, Hodgkin’s disease, soft-tissue sarcoma and chronic lymphatic leukaemia, among other conditions.

From the above discussion, it is evident that, at any one time, air may contain pollutants belonging to many or all of these categories at varying levels and proportions which can give rise to an array of pathologies and disease states. The make-up of air pollution is determined by many factors, including geographic location, weather, environmental pressures, human activity, time of day and time of year (Bhatnagar, 2017). It is, therefore, a challenge for epidemiologists to wholly determine the impacts of individual pollutants on human health due to the risk of confounding pollutants also having health effects.

## **1.2 Public Health and Epidemiology**

The UK government has called air pollution the ‘single biggest environmental threat to health in the UK’ (Environmental Agency, 2023). In 2012, of human-generated social burdens, outdoor air pollution alone was within the top 10 of those that took an economic toll, accounting for a share of 1.3% of the gross domestic product. These figures are supported by a plethora of epidemiological data demonstrating an association between air pollution exposure and mortality (COMEAP, 2018; Ghio et al., 2018).

### **1.2.1 Short-Term Impacts of Air Pollution**

Many studies have investigated the impact of short-term air pollution on human health (Manisalidis et al., 2020). These have been in the form of cohort studies that have examined hospital admissions and mortality, and panel studies on volunteers to deduce the impacts of disease symptoms and progression. In the 1990s, the Air Pollution and Health: a European Approach (APHEA) studies (Atkinson et al., 2001; Katsouyanni

et al., 1996; Katsouyanni et al., 2001) uncovered robust evidence to associate short-term PM<sub>10</sub> exposure with unfavourable outcomes. The APHEA studies were conducted across 29 European cities and accounted for 43 million individuals, which were studied across a period of 5 years, investigating analytics associated with PM<sub>10</sub>, NO<sub>2</sub>, SO<sub>2</sub>, and O<sub>3</sub> exposure levels. Combining data from 21 cities, the studies uncovered an increase in PM<sub>10</sub> by 10 µg/m<sup>3</sup>, increasing all-cause mortality by 0.6%.

Furthermore, across 8 cities, the same rise in PM<sub>10</sub> levels resulted in an increase in hospital admissions in a population of those older than 65 years for COPD and asthma by 1.0% and cardiovascular disease by 0.5%. In the same group, hospital admissions for cardiovascular disease were increased by 1.1% per 10 µg/m<sup>3</sup> increase in PM<sub>10</sub>. Across 6 cities, a 50 µg/m<sup>3</sup> increase in maximal O<sub>3</sub> and NO<sub>2</sub> levels was associated with a 2.9% and 1.3% increase in daily mortality, respectively (Touloumi et al., 1997). This study, however, raised the issue that the impact of NO<sub>2</sub> on mortality may be confounded by other vehicle-derived pollutants, such as PM, which have both been shown to be primarily released from diesel vehicles (Smit, 2014). This study, in particular, showed a high correlation between NO<sub>2</sub> and black smoke levels and stresses the requirement for further investigation into the impacts of NO<sub>2</sub>. Analysis of the APHEA data has been thorough and published in many articles (Katsouyanni, 2006); overall, this data clearly shows that short-term exposure to air pollutants is associated with increased respiratory and cardiovascular disease and mortality.

Similar large-scale epidemiological studies have been performed in the USA to examine the short-term effects of air pollutants. Between 1987 and 1994, the National Mortality, Morbidity and Air Pollution Studies (NMMAPS) investigated the largest 20 metropolitan areas of the USA, containing a total of 50 million inhabitants (Samet, Dominici, Zeger, et al., 2000). Closely resembling results seen within Europe, all-cause mortality increases by 0.5% for each 10 µg/m<sup>3</sup> increase in PM<sub>10</sub> (Samet, Dominici, Curriero, et al., 2000). The same rise in PM<sub>10</sub> was also associated with a 1.5% and 1.1% increase in COPD and cardiovascular disease hospital admissions, respectively. Dissimilar to their European counterparts, the NMMAPS study found little evidence of mortality changes associated with NO<sub>2</sub> and SO<sub>2</sub> after adjustment for PM<sub>10</sub> and O<sub>3</sub> (O<sub>3</sub> was found to have weak effects in summertime but no impact during winter) (Zanobetti et al., 2000).

More recently, the Air Pollution and Health: A Combined European and North American Approach (APHENA) study has aimed to bring together the data from APHEA and NMMAPS, along with the inclusion of Canadian data, to investigate coherence between the datasets through the development of a standard approach to the analysis of the data. The associations between PM<sub>10</sub> and mortality determined through APHENA were generally compatible with those reported by both APHEA and NMMAPS, supporting these findings (Samoli et al., 2008). Similarly, findings from APHENA regarding O<sub>3</sub> and mortality were comparable to the previously reported results. However, it was also concluded that there were no intense effect modifications by age or ecological variations in the analysis (Peng et al., 2013).

Studies on a smaller scale have been carried out to investigate the impacts of short-term air pollution. For example, Pope *et al.* (1991) examined 55 individuals split into a relatively healthy, school-based group of primary school-aged children and a patient-based group of those aged 8 to 72 years who had asthma. Participants were given a peak flow meter and a diary to record symptoms and medical care. It was found that elevated PM<sub>10</sub> levels were associated with decreased lung function, identified through reduced peak expiratory flow, increased respiratory disease symptoms and asthma medication use. It was reported that levels of SO<sub>2</sub>, NO<sub>2</sub>, acid aerosols and O<sub>3</sub> were very low, and they attribute the observed results to PM<sub>10</sub> exposure alone. However, the findings were reliant on participant collaboration. They consisted of a small dataset, with little analysis of the potential effects of medications, such as those used to treat asthma.

Nonetheless, the data is contextualised by non-epidemiological data which found a reduction in lung function when mice were acutely exposed to low doses of urban PM<sub>2.5</sub> *via* intranasal instillation. PM<sub>2.5</sub> exposure increased lung impedance and alveolar collapse, though it also increased elastic and viscoelastic components of the lung mechanics. The onset of tissue inflammation and oxidative stress was also noted (Riva et al., 2011). Additionally, the correlation between short-term exposure to SO<sub>2</sub> and cardiorespiratory mortality has been observed (Wang et al., 2018), as well as an association between acute exposure to higher O<sub>3</sub> levels and increased non-accidental mortality, cardiovascular disease, hypertension, coronary disease and stroke (Yin et al., 2017).

### **1.2.2 Long-Term Impacts of Air Pollution**

The long-term impacts are less well established than the short-term effects, although some have tried to elucidate the longer-term implications. For example, a series of Swiss studies investigated how an area's air quality could alter the population's lung function. Through its mountainous landscape, Switzerland possesses high contrast in terms of air pollution concentration between regions, allowing effective comparisons to be drawn. Adult populations over a total of 8 regions were investigated, where it was found that lung function was significantly reduced in regions that had increased NO<sub>2</sub>, SO<sub>2</sub>, and, most profoundly, PM<sub>10</sub> (Ackermann-Lieblich et al., 1997). Further, it was found that pollutant exposure was associated with bronchitis symptoms, including chronic cough and phlegm production, breathlessness when at rest, and dyspnoea on exertion. They found no association with asthma symptoms and found no associations correlated with O<sub>3</sub> levels (Zemp et al., 1999). These results have been mirrored in a similar study which examined the long-term impacts of air pollution across 10 Swiss regions (Braun-Fahrlander et al., 1997).

#### **1.2.2.1 The European Study of Cohorts for Air Pollution Effects**

More recently, The European Study of Cohorts for Air Pollution Effects (ESCAPE) has investigated the long-term health implications of air pollution across 13 nations, pooling subjects from 22 cohorts, involving approximately 370,000 participants that were, on average, followed for 14 years. PM and NO<sub>x</sub>, along with traffic volume, were the key pollutants analysed during ESCAPE, directly relating to the research performed within this work. A plethora of papers emerged from the data collected by ESCAPE, which implicate air pollution in many aspects of pathogenesis, disease progression and mortality. Notably, both PM and NO<sub>2</sub> were associated with increased asthma incidence (Jacquemin et al., 2015), COPD prevalence and incidence (Schikowski et al., 2014) and respiratory infection (MacIntyre et al., 2014).

Many respiratory effects were observed in these studies. For example, associations between PM<sub>2.5</sub> and NO<sub>2</sub> levels and COPD were observed (HR 1.10 and 1.05, respectively, for a 10 µg/m<sup>3</sup> increase) (Schikowski et al., 2014). PM<sub>10</sub> and NO<sub>2</sub> are associated with the onset of respiratory infections, specifically pneumonia, otitis media and croup, with pneumonia odds ratios of 1.30 and 1.76 per 10 µg/m<sup>3</sup> increase in PM<sub>10</sub>

and NO<sub>2</sub>, respectively. Interestingly, only NO<sub>2</sub> increased the risk of otitis media and croup with an OR of 1.09 per for each (MacIntyre et al., 2014). It was found that a 10 µg/m<sup>3</sup> increase in PM<sub>10</sub> and a 5 µg/m<sup>3</sup> increase in PM<sub>2.5</sub> were correlated with a significant increase in lung cancer risk (HRs 1.22 and 1.18, respectively). Additionally, 5 µg/m<sup>3</sup> increases in PM<sub>10</sub> and PM<sub>2.5</sub> were associated with a significantly increased risk of lung adenocarcinomas (HRs 1.51 and 1.55, respectively). However, the study showed no association between NO<sub>2</sub> exposure and lung cancer (Raaschou-Nielsen et al., 2013). Potentially through similar toxicological mechanisms, a 10 µg/m<sup>3</sup> increase in NO<sub>2</sub> and PM<sub>10</sub> and a 5 µg/m<sup>3</sup> increase in PM<sub>2.5</sub> were associated with a -1.05%, -0.67% and -1.77% change in FEV<sub>1</sub>, respectively. It is hypothesised that these changes are brought about through oxidative stress and inflammation to the airways (Gehring et al., 2013). This could be aligned with findings from Lanki *et al.* (2015), where participants who lived near busy roads (whereby more than 10,000 cars passed per day) had significantly higher C-reactive protein levels (CRP) compared to those who lived near quieter roads (less than 1,000 cars passed per day). Increased annual NO<sub>x</sub> concentration was also found to be associated with higher CRP levels. CRP is a clinically established marker of systemic inflammation, showing a potential link between traffic and NO<sub>x</sub> exposure and the onset of inflammation. Systemic inflammation is then known to be a factor in cardiovascular effects. Indeed, it was found that a 5 µg/m<sup>3</sup> increase in PM<sub>2.5</sub> and a 10 µg/m<sup>3</sup> increase in PM<sub>10</sub> were associated with a 13% and 12% increased risk of coronary events (such as myocardial infarction or unstable angina), respectively (Cesaroni et al., 2014). These effects could impact mortality, which has been widely reported. In the ESCAPE trials, Beelen *et al.* (2014) associated air pollution exposure with all-cause mortality, with a significant increase in hazard ratio per 5 µg/m<sup>3</sup> increase in PM<sub>2.5</sub> (HR = 1.07). Although not determined to be a significant increase, the HR for a 10 µg/m<sup>3</sup> increase in PM<sub>10</sub> and NO<sub>2</sub> were 1.08 and 1.01, respectively. Furthermore, an association between cardiovascular mortality and PM<sub>2.5</sub> (HR 1.21 per 5 µg/m<sup>3</sup> increase) and PM<sub>10</sub> (HR 1.22 per 10 µg/m<sup>3</sup> increase) was shown.

However, a drawback of many of the ESCAPE datasets is the inability to effectively distinguish the individual effects of PM and NO<sub>2</sub> as single pollutants, though, single/multi-pollutant modelling were used in an attempt to adjust for confounding pollutants. It was found that the impact of NO<sub>2</sub> on natural-cause mortality was not



altered when adjusting for PM<sub>2.5</sub>, though the impact of NO<sub>2</sub> was reduced by course PM (Beelen et al., 2014).

### **1.2.2.2 Review of Evidence on Health Aspects of Air Pollution (REVIHAAP)**

More recently, various agencies have attempted to combine toxicological evidence about air pollution exposure and toxicological outputs to collate the data and provide a rationale for policy adoption. In 2013, for example, the WHO (2007) produced the 'Review of Evidence on Health Aspects of Air Pollution' (REVIHAAP) report. Within this, a panel reviewed and discussed up-to-date evidence in the field and attempted to answer 24 questions about the health effects of PM, O<sub>3</sub>, and traffic-related air pollution (including NO<sub>2</sub>, black carbon, PAHs, *etc.*) within European regions. The European Commission posed these questions to advise their policy decisions. Amongst the discussion, it was agreed that the newer evidence supports the WHO's 2005 air quality guidelines (World Health Organization, 2006). However, it also supports the theory that these guidelines may not go far enough and that toxic outcomes are occurring below the suggested limits. This was later confirmed in the Effects of Low-Level Air Pollution: A Study in Europe (ELAPSE) project. The project intended to assess the health effects of air pollution at levels below those recommended by the EU, US EPA and WHO. Through the analysis of a cohort in regions below these levels, there was a positive correlation between PM<sub>2.5</sub>, NO<sub>2</sub> and BC and natural-cause, respiratory, cardiovascular and diabetes mortality and hospital admissions for stroke, asthma, and COPD. There was no evidence of a threshold at which no association between pollutant exposure and health effects could be found (Brunekreef et al., 2021). This was pivotal as it showed that even previously accepted air pollution levels were detrimental to human health. As such, WHO updated their air quality guidelines in 2021 (World Health Organization, 2021), advising lower PM and NO<sub>2</sub> levels compared to their 2005 guidelines.

The ELAPSE study again noted correlated pollutant levels as a potential confounder within the data, and therefore attempted to use two-pollutant models to adjust for this. It was found that PM<sub>2.5</sub> HR for natural-cause mortality was lost when adjusting for NO<sub>2</sub>, whereas the NO<sub>2</sub> effect was not lost when adjusting for PM<sub>2.5</sub>. This is potentially due to the fact that the two-pollutant model only accounts for PM<sub>2.5</sub> co-emitted with NO<sub>2</sub>, and does not adjust for UFPs (Brunekreef et al., 2021)

### **1.2.2.3 Air pollution: new insights into ambient air particulate matter and the impact of road traffic (ANSES)**

Since the REVIHAAP report, the French Agency for Food, Environment and Occupational Health and Safety (ANSES) have produced the report, 'Air pollution: new insights into ambient air particulate matter and the impact of road traffic' (2019). This report aims to expand on the REVIHAAP report, though specifically examining the particulate component of air pollution within human and *in vivo* exposures. The report explicitly attempts to disentangle particle-specific toxicological outputs depending on emission sources, particle morphology, and chemical characteristics. The report distinguishes between PM's coarse and fine fractions, finding that coarse particles may be more linked with respiratory health and all-cause mortality. In contrast, the fine particles may be linked with cardiovascular health.

Further, the ANSES report examines the impact of BC and elemental carbon (EC), suggesting an association between exposure and various health effects, including respiratory health, cardiovascular health, all-cause mortality, all-cause hospitalisation, neurological health, and pre-natal health. It is suggested that some of these outcomes could align with PAH exposure due to their co-emission with PM, although the evidence is comparatively lacking. In addition, sulphate- and nitrate-rich inorganic aerosols are considered, and exposure to them is associated with low birth weight, respiratory health, cardiovascular health, and all-cause mortality. It is thought that sulphate and nitrate presence in PM could influence the toxicity of the PM, rather than impart toxicity themselves. For example, suggestions are made that sulphate-rich aerosols could acidify particles, increasing their iron dissolution capacity and as such iron bioavailability (Reiss et al., 2007). Along a similar inorganic theme, the transition metals nickel and vanadium were found to impact cardiovascular and respiratory health, where iron was associated with all-cause mortality. The report acknowledges difficulty in assessing the effects of metal exposure within singular components, however. This is because metals have large overlaps in their emission sources, for example, brake and tyre wear particles may contain iron, zinc, and copper together. The report highlights an essential aspect of the heterogeneity of PM, and the subsequent ability of different particles to induce a differential effect on human health. As such, the report recommends that air quality measures should be implemented that

focus on unregulated particulate fractions, such as UFPs and BC (ANSES, 2019). Since then, the WHO have included good practice statements in their 2021 air quality guidelines. However, clarity of maximal accepted exposure levels requires further focus.

#### **1.2.2.4 Integrated Science Assessment for Particulate Matter**

The US EPA also attempted to expand on the REVIHAAP report in Integrated Science Assessment (ISA) for Particulate Matter (Environmental Protection Agency, 2019). Similarly to the ANSES report, this ISA attempted to examine the health effects of PM in depth by reviewing evidence from the date of the REVIHAAP report through to 2019. Outcomes are broken down into specific health effects, with deleterious effects found in the fields of respiratory effects, cardiovascular effects, metabolic effects, nervous system effects, reproductive and developmental effects, cancer, and mortality. Based on the available evidence, the ISA found that PM<sub>2.5</sub> could be responsible for many health effects compared to PM<sub>10</sub>. However, it acknowledges a lack of evidence on PM<sub>0.1</sub>/UFP, which requires further focus.

To examine the respiratory effects specifically, the ISA concludes that there is sufficient evidence of a likely causal relationship between short-term PM<sub>2.5</sub> exposure and asthma exacerbation, COPD and combined respiratory diseases, even after adjusting for confounding effects such as weather. It concludes that the *in vivo* studies back up the epidemiological findings, demonstrating similar asthma and COPD responses and enhancing lung injury, increasing respiratory infections and irritant effects. Though limited, controlled human exposure studies support this, showing decreased lung function and increased inflammation following PM<sub>2.5</sub> exposure. The ISA finds that long-term effects of PM<sub>2.5</sub> are associated with similar outcomes but also include the onset of asthma in children and pulmonary inflammation. However, the ISA concedes that the evidence for the long-term effects is comparatively lacking when compared to the short-term due to the heterogeneity of exposure as well as the confounding impact of co-pollutants. *In vivo*, PM<sub>2.5</sub> exposure (pre- or postnatal) was associated with impaired lung development, with enhanced allergic phenotype, perhaps indicating a mechanism behind the increase in asthma prevalence in the epidemiological studies. Further, increased oxidative stress and inflammation within *in vivo* exposure studies could support this theory. These outcomes culminate in

increased respiratory mortality when PM<sub>2.5</sub> exposure is heightened, for which this ISA found supporting consistent evidence.

COMEAP (2022) supplemented the ANSES report and the ISA for PM with evidence through to December 2020 in their ‘Statement on the differential toxicity of particulate matter according to source or constituents: 2022’. Through analysis of the available research, it is concluded that PM containing different constituents and from differing sources likely elicit conflicting toxicological actions. Pertinent to the PM exposure studies conducted within this work, the statement suggests that there is a requirement to compare PM of different compositions and from various sources within the same research, using relevant *in vitro* models and exposure approaches. Further, these studies could benefit from the use of ‘real world’ samples. In addition, it is noted that many studies focus on traffic-related air pollution, though they do not factor in the potential confounding effect of NO<sub>2</sub>. The work within this thesis aims to address this knowledge gap. However, before this topic is explored, it is essential to understand the cellular mechanisms of the region of the lung which will be the focus of this work.

### **1.3 Anatomy and Physiology of the Human Respiratory System**

#### **1.3.1 Anatomy of the Human Lung**

Each breath we take exposes us to various toxic materials, including gaseous and particulate pollutants and biologics, such as microorganisms and allergens. Each possesses a potentially harmful effect, and the lung often becomes the primary region targeted when these pollutants are inhaled. It is, therefore, vital that the anatomy and physiology of the lungs during health are understood as this enables the determination of toxic effects of air pollutants to be better derived.

Responsible for respiration, the lung is supplied by blood from the pulmonary circulation. It provides an interface to facilitate gaseous exchange between environmental air and the bloodstream, whereby oxygen is absorbed, and carbon dioxide is removed from the blood (Martini et al., 2018).

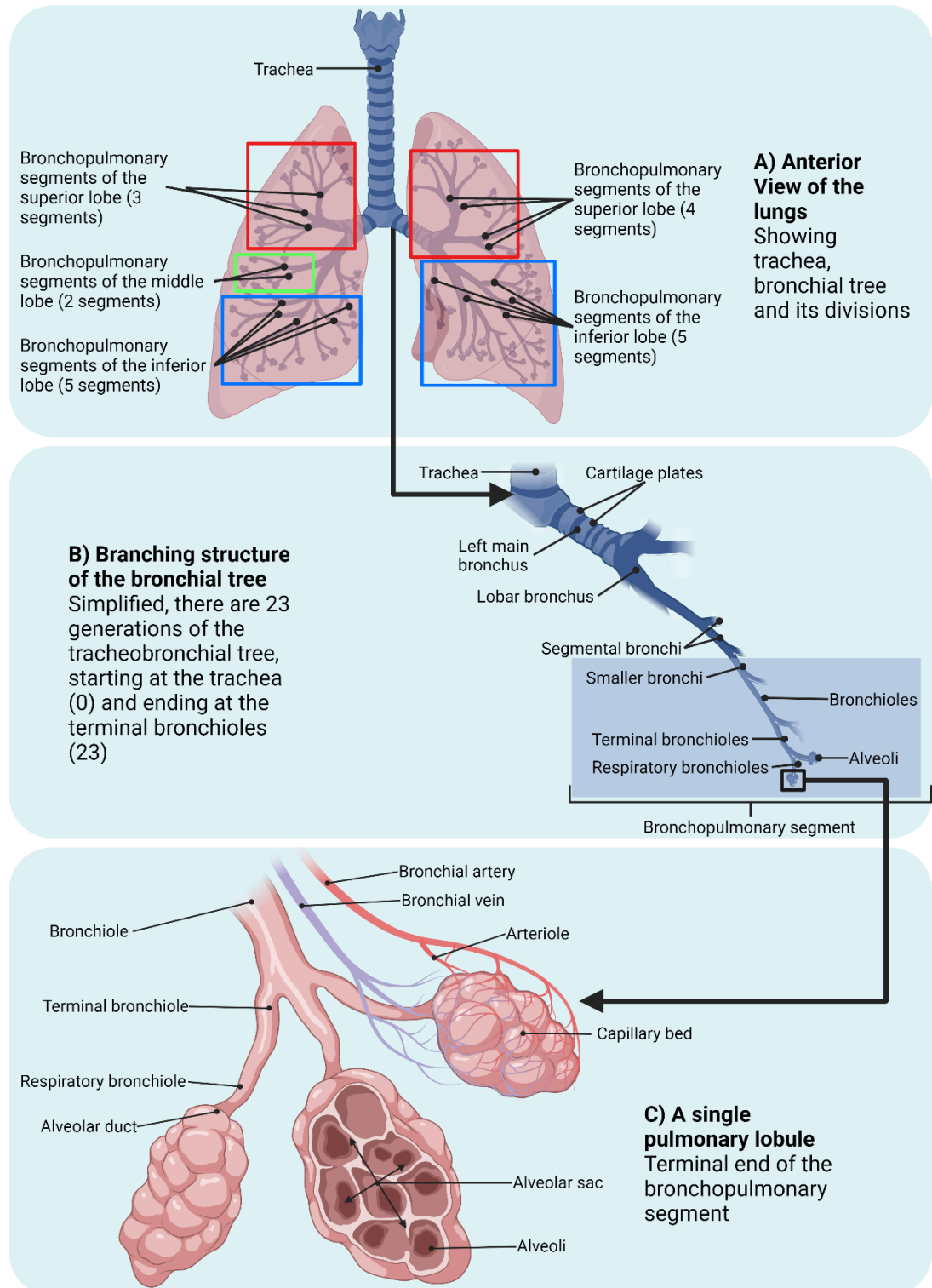


**Figure 1.3** An anterior view of the lung, showing branches of the bronchial tree. Individual lobes can be visualised and correspond with the number of secondary bronchiole branches. The left lung possesses 1 less lobe due to the presence of the cardiac notch. Created using BioRender.com

During breathing at rest, air will typically enter through the nose, allowing effective heating and humidification before the air reaches the lungs. However, during activity, the mouth may be used for inhalation as this offers a path of lower resistance to allow a greater ventilation rate to reach respiratory demands. After entering the nose or mouth, air will travel from the pharynx to the larynx before entering the branching lung at the trachea. There are 23 branches of the lung starting in the upper chest, the trachea (branch 0) branches into two primary bronchi (branch 1) (one for each left and right lung). The larger right bronchi then split into 3 secondary bronchi and the smaller left into 2 secondary bronchi, one for each of the lobes of the lung (branch 2) (**Figure 1.3A**). Each secondary bronchi then splits into two tertiary bronchi. Each tertiary bronchus ultimately provides air to single bronchopulmonary segments, specific regions of each lung. Within their respective bronchopulmonary segments, the tertiary bronchi branch numerous times, giving rise to bronchioles, which further branch into terminal bronchioles (**Figure 1.3B**) (branches 3-16). Each tertiary bronchus has an estimated 6,500 terminal bronchioles (Martini, Nath and Bartholomew, 2018). The terminal bronchiole, which supplies air to a single pulmonary lobule, further splits into respiratory bronchioles (branches 17-19). The respiratory bronchioles then connect to individual alveoli (the site of gaseous exchange) and alveolar ducts, which in turn connect to alveolar sacs, which terminate in multiple individual alveoli (branches 10-23) (**Figure 1.3C**). Each lung possesses an estimated 150 million alveoli (Martini et al., 2018).

The lung airways are lined with an epithelial layer that forms a tight barrier to prevent the passage of contaminants into the underlying tissues, therefore acting as the first line of defence against inhaled hazardous pollutants. The epithelial layer is highly differentiated and varies in structure and function depending on location. Broadly, the epithelial layer within the lungs can be split into the conducting airway (*i.e.*, bronchi and bronchioles) epithelium and the alveolar epithelium.

The conducting airway acts as a conduit for transporting oxygen-containing air into and carbon dioxide out of the alveoli. The pseudostratified epithelial layer of the conducting airway is comprised of a range of cell types, namely goblet cells (which produce mucus), ciliated cells, non-ciliated club cells, neuroendocrine cells and basal cells (Crapo et al., 1982).

The alveolar epithelium, in contrast, is comprised of 3 cell types: alveolar type 1 cells (ATI), alveolar type 2 cells (ATII) and alveolar macrophages (AMs) (**Figure 1.4**). Squamous ATI occupies approximately 90-95% of the alveolar surface and facilitates gas movement between the alveoli's lumen and the blood. This is made optimal through the extremely thin nature of ATI at 0.2  $\mu\text{m}$  (Crapo et al., 1982). Cuboidal ATII vary vastly in function and are easily identified through electron microscopy by numerous lamellar bodies, which store surfactant to be secreted into the alveolar epithelium. This surfactant is needed to reduce alveolar surface tension, preventing alveolar collapse and maintaining normal lung function (Knudsen & Ochs, 2018).

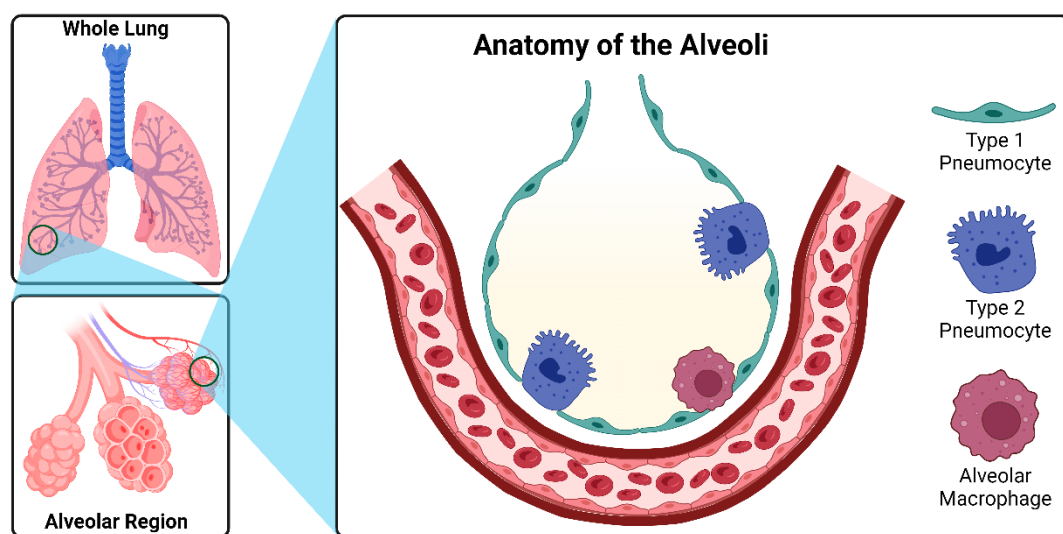


*Figure 1.4 Histology of the epithelial lung lining comprising ATI, ATII and AMs. Created using BioRender.com*

### 1.3.2 Innate Lung Defences Against Air Pollution and Mechanisms of Toxicity

#### 1.3.2.1 Epithelial Lining Fluid

Epithelial lining fluid, a thin fluid layer, coats the airway epithelium and, again, is variable depending on the area of the lung in question. Epithelial lining fluid of the conducting airways consists of 2 layers: the periciliary layer and the mucus layer (Whitsett, 2018). The periciliary layer is a low-viscosity polyanionic gel, the thickness of which is similar to the length of the cilia on the epithelial cells (7  $\mu\text{m}$  approximately). This layer, therefore, provides lubrication and facilitates the beating of the cilia of ciliated cells. Additionally, the periciliary layer can play a defensive role against inhaled toxicants by restricting access of particles to the cells' surface (Button et al., 2012).

Atop the periciliary layer sits a mucus layer (2 – 5  $\mu\text{m}$  thick). The major component of mucus is mucin glycoproteins such as MUC5AC and MUC5B, encoded by the *MUC* genes, which are highly expressed in goblet cells and mucosal cells of submucosal glands (Groneberg et al., 2002). The sticky mucus can trap inhaled particles and aerosols, which, through the rhythmic beating of the cilia, are propelled, along with the mucus, in a cephalad direction in a process called mucociliary clearance (Brooks & Wallingford, 2014; Rose & Voynow, 2006). This mucociliary clearance process, therefore, is an essential first line of defence against inhaled particles (Brooks & Wallingford, 2014). Goblet cells are mainly responsible for mucus secretion within the bronchi and primary bronchioles. However, beyond generations 15/16 of the bronchioles, club cells become the primary secretory cells and possess a much lower ability of mucous secretion (Widdicombe & Wine, 2015).

The alveoli are coated with a layer of alveolar surface liquid that contains pulmonary surfactant secreted by ATII cells. The surfactant is made up of approximately 90% phospholipids. Of these phospholipids, 70-80% are dipalmitoylphosphatidylcholine, which gives surfactant the ability to lower surface tension (Nkadi et al., 2009). The remaining 10% of surfactant comprises proteins: surfactant protein (SP)-A, SP-B, SP-C and SP-D. SP-B and SP-C are required for the stabilisation of the surfactant monolayer. SP-A and SP-D, however, have been shown to play a role in regulating surfactant release (Veldhuizen & Haagsman, 2000) as well as providing antiviral defence properties (Watson et al., 2021).

### **1.3.2.2 Antimicrobial Peptides**

Another mechanism by which the airway and alveolar epithelium can protect against inhaled pathogens is through the release of antimicrobial peptides (AMPs). These peptides can be genetically coded or produced through proteolytic cleavage of larger proteins and are approximately 10 – 15 amino acid residues. AMPs target viral, bacterial, and fungal inhaled toxins *via* their antimicrobial properties. AMPs can broadly be split into two families: defensins or cathelicidins (Hiemstra et al., 2015).

Although there are various groups of defensins,  $\beta$ -defensins are produced by airway epithelial cells.  $\beta$ -defensins can again be divided into 4 specific proteins, human  $\beta$ -defensin 1, 2, 3 and 4 (hBD1/2/3/4). hBD1 is secreted constitutively. In contrast, hBD2, 3 and 4 require activation of toll-like receptors (TLR) or the NF- $\kappa$ B pathway,



or the presence of pro-inflammatory mediators.  $\beta$ -defensins are thought to exert their antimicrobial effect through interactions with microbial lipids (Hiemstra et al., 2015). However, they have also been shown to possess chemoattractant characteristics, which could attract immune cells, contributing to the onset of inflammation and triggering immune response (Yang et al., 1999). hBDs may, however, only be a first-line defence, having shown increased activation in acute but not chronic inflammation (Herr et al., 2009).

Humans only express one of the next group of AMPs, cathelicidins: hCAP-18, encoded by the *CAMP* gene. Many cells within the lung produce hCAP-18, including epithelial cells, neutrophils and macrophages (Bals et al., 1998). The positive charge of hCAP-18 allows its association with negatively charged lipid membranes and subsequent membrane penetration due to the unilateral hydrophobicity of an  $\alpha$ -helix domain, resulting in bacterial lysis (Bucki & Janmey, 2006).

### 1.3.2.3 Endocytic Uptake

In some events, pathogens and inhaled particles are not effectively removed *via* mucociliary clearance or detoxified by AMPs; this is especially common for smaller particles, such as PM<sub>2.5</sub> and PM<sub>0.1</sub>, which can be deposited into the alveolar space. Alveolar macrophages (AM), the resident dominant phagocytes of the lung (Patel et al., 2015), can uptake PM (as can bronchial epithelial cells to a lesser degree) and constitute an essential mechanism of disposal of inhaled foreign material (Saxena et al., 2008). Complement, mannose, and scavenger receptors are known to play a role in phagocytic uptake through the recognition of inhaled foreign material (Geiser, 2010). The binding of these receptors activates them, which triggers the restructuring of the cytoskeleton through an actin-dependant manner, as shown by Stringer *et al.* (1995), who still observed AM ingestion of PM after treatment with cytochalasin-D, an inhibitor of actin polymerisation. This cytoskeletal remodelling forms pseudopods which engulf the particle. Internalisation through endocytosis will then occur, where the phagosome (Haberzettl et al., 2007) will fuse with a lysosome, forming a phagolysosome allowing the material to be digested *via* lysosomal acidification and enzymatic activity (Patel et al., 2015). Alveolar inflammation (discussed in Section 1.3.2.4) has been shown to increase the rate of phagocytosis (Patel et al., 2015), where AMs can inactivate, ingest and degrade inhaled bacteria within 8 hours. However, the

presence of inhaled pollutants can impair the speed of bacterial clearance (Gordon & Read, 2002).

Although the internalisation of foreign matter into AMs mainly occurs through endocytosis, other non-phagocytic uptake mechanisms can also be utilised, specifically micropinocytosis and pinocytosis (Geiser, 2010). Interestingly, alveolar epithelial cells have also been shown to act through pinocytosis in clathrin and caveolin-dependent manners (Soni et al., 2022).

Although the lung possesses many defences, there are instances where these defences can cause unwanted effects or become overloaded. These mechanisms are subsequently discussed.

#### **1.3.2.4 Inflammatory Response**

Inflammation can be in response to direct tissue injury (Bagloli et al., 2006) and as part of an immune response to targeting infiltrating pathogens (Alessandri et al., 2013) and environmental pollutants, such as inhaled air pollution (de Souza et al., 2014). Although acute inflammation is a beneficial process, in the case of chronic inflammation without relief, as could be the case during long-term exposure to air pollutants, tissue damage can be caused. Pathogenic processes, namely carcinogenesis and autoimmunity, can then be initiated (Alessandri et al., 2013), as well as asthma (Nathan & Ding, 2010). PM exposure has been directly linked to an inflammatory response in humans; for example, through exhaled breath analysis, exposure to PM has been associated with increased fractions of exhaled nitric oxide and hydrogen sulphide, both markers of pulmonary inflammation (Gong et al., 2014; Wu et al., 2016). Furthermore, within a cohort study, exposure to PM<sub>2.5</sub> was associated with increased percentages of inflammatory-associated neutrophils and IL8 within nasal lavages (B. Y. Chen et al., 2012).

The mechanisms by which PM triggers inflammation are varied; however, it could involve activations of pathways through toll-like receptors (TLRs). Humans possess thirteen identified TLRs (namely, TLR1 – TLR13). TLR2 and TLR4 are thought to induce a signal cascade in response to PM due to their ability to bind gram-positive and gram-negative bacteria, respectively (Bauer et al., 2002), which could be on the surface of inhaled particulates. This was shown through heat treatment of PM to

inactivate biological activity on the surface of PM, which was found to attenuate macrophage response, possibly through TLR2 and TLR4 (Alexis et al., 2006). PM size has also been shown to play a role in activation, with PM<sub>10</sub> known to contain more endotoxin (Heinrich et al., 2003), mainly activating TLR4, which is at highest density on AMs, whereas PM<sub>2.5</sub> is largely TLR2-dependant and is more readily handled by bronchial epithelial cells (Shoenfelt et al., 2009). It has also been shown that TLRs may play a significant role in the pro-inflammatory response as well. Through inhibiting activation of each *in vitro*, it has been found that a reduction in TLR2 activation inhibited PM-induced production of IL8, whereas blocking TLR4 inhibited PM-induced production of IL6 (Becker et al., 2005). Furthermore, *in vivo*, TLR2/4 knockout studies showed a significant decrease in IL6 and tumour necrosis factor- $\alpha$  (TNF- $\alpha$ ) upon PM exposure (Shoenfelt et al., 2009), and mutations in TLR2/4 are associated with a higher risk of asthma exacerbation in children (Kerkhof et al., 2010). TLRs are classified as signalling pattern recognition receptors (PRRs) due to their ability to recognise clusters of molecules rather than specific molecules and subsequently promote intracellular signalling. However, AMs also express the class A scavenger receptor (SR-A), which is classified as an endocytic PRR. SR-A can recognise the inorganic components of PM and can promote intracellular signalling and drive attachment, engulfment and digestion of PM (Palecanda & Kobzik, 2001).

Interestingly, it has been found that SR-A activation has the opposite effect on TLRs following PM exposure by reducing pro-inflammatory cytokine production and the influx of polymorphonuclear neutrophils into the lung tissue. This has been shown through *in vivo* studies of SR-A knockout mice exposed to silica and titanium dioxide PM (Arredouani et al., 2006; Beamer & Holian, 2005). The mechanism behind this is unclear but could be a result of TLR4 pro-inflammatory response inhibition through interaction with TNF receptor-associated factor 6 (TRAF6) (Yu et al., 2011), which prevents the overproduction of pro-inflammatory cytokines, therefore protecting the tissue from damage (Haworth et al., 1997).

Therefore, the pro-inflammatory activity of the airways is expected to rely on TLR activity. However, as previously stated, TLRs primarily identify pathogens, yet inflammation has been observed in response to ambient UFP, which lacks substantial endotoxin content (Samet et al., 2009). It has, therefore, been shown that TLRs on AMs could mount pro-inflammatory responses to oxidised lipids. Oxidation of lipids

within the pulmonary surfactant, hyaluronan fragments (due to the breakdown of high molecular weight hyaluronan by free radicals), and heat shock proteins (which have shown to be induced by diesel emission particles) could therefore cause an inflammatory response in the absence of endotoxins (Jung et al., 2007; Kampfrath et al., 2011; Sato et al., 2001).

Activation of TLR is known to subsequently activate NF $\kappa$ B, which itself exists within a heterodimer with Rel and p50 proteins, as well as an inhibitory protein I $\kappa$ B $\alpha$ , within the cytosol. Stimulation of NF $\kappa$ B allows dissociation of I $\kappa$ B $\alpha$ , enabling translocation of NF $\kappa$ B into the nucleus. Numerous studies have implicated PM exposure in NF $\kappa$ B activation (Jiang et al., 2014; Li et al., 2018; Shukla et al., 2000), potentially mediated by TLRs, in numerous types of airway cells. ROS generation and increased cytosolic calcium have also been shown to play a role in NF- $\kappa$ B activation (Sakamoto et al., 2007; Shukla et al., 2000). Once NF $\kappa$ B has translocated into the nucleus, it can bind to the promoter on NF $\kappa$ B responsive genes, which generally drives the transactivation of cytokines, chemokines and cell adhesion molecules (Schuliga, 2015). Within airway epithelial cells, activation of NF $\kappa$ B has been associated with the production of IL6, IL8 and B2-defensins (Platz et al., 2004). In contrast, pro-inflammatory mediators produced by the alveolar epithelium are more generally IL1 $\beta$  and TNF $\alpha$ , which are produced by the resident AMs (Riches & Martin, 2018).

Alveolar macrophages and epithelial cells express IL1 $\beta$  in response to invading pathogens through NF- $\kappa$ B signalling. IL1 $\beta$  is released in an inactive pro-protein form and cleaved into its active form by inflammasome protein caspase-1. Caspase-1 is also produced as a pro-protein but is activated when integrated into NLRP3 inflammasomes. IL1 $\beta$  is then released from cells, likely through several mechanisms such as exocytosis, proptosis or microvesicle release (Lopez-Castejon & Brough, 2011). IL1 $\beta$  will then bind to the ubiquitously expressed IL1 receptor (IL1R), which induces intracellular signalling through proteins IL1RacP, myeloid differentiation primary response gene 88 (MyD88) and IL1R-activated protein kinase (IRAK) 4. IRAK4 can subsequently phosphorylate IRAK 1 and 2, which recruit TNF-associated factor 6 (TRAF6) into a complex that activates NF- $\kappa$ B, c-Jun N-terminal kinase (JNK) and MAPK. Signalling through NF- $\kappa$ B, JNK, and MAPK are then able to induce the expression of pro-inflammatory mediators such as IL6 and IL8 (Weber et al., 2010).

IL6 is subsequently released from epithelial cells and macrophages, where it can bind to IL6 receptors in either a soluble or membrane-bound form. Through the Janus kinase (JAK) signal transducer and activator of transcription (STAT) pathway (Johnson et al., 2018), IL6 receptors will signal to increase transcription of genes involved with cytokine release, proliferation and angiogenesis (Mihara et al., 2011). IL6 has been implicated in fibrosis by inducing fibroblast-to-mesenchymal transition (FMT) (Kumar et al., 2019) and epithelial-to-mesenchymal transition (EMT) (Yang et al., 1999). Indeed, IL6 is upregulated in idiopathic lung fibrosis patients (Zhou et al., 2010), and through blocking IL6 signalling, PM<sub>2.5</sub>-induced EMT could be reversed (C.-H. Lin et al., 2021). Further, STAT3 inhibitors were found to reduce AII damage, which contributes to lung fibrosis. These data indicate a role of IL6 in pulmonary damage, fibrosis, and reduction in lung function.

IL8 is a CXC chemokine that induces neutrophil migration into tissue from the bloodstream. IL8 modulates the presentation of adherence molecules on the surface of endothelial cells, aiding in leukocyte adherence and extravasation from the blood. In a dual-action, leukocytes follow a chemokine gradient containing IL8 to the site of infection or damage. IL8 induces its actions through binding to CXC receptors 1 and 2 (Pease & Sabroe, 2002). Augmented IL8 release has been shown to play a role in allergic disease, with higher concentrations in the serum of asthma patients. IL8 has been suggested as a biomarker for accurately identifying uncontrolled asthma (Marc-Malovrh et al., 2020).

A further aspect of innate immunity to inhaled PM involves the influx of neutrophils and monocytes from the circulation into the airspace, which plays an additional role in detoxification, although, in the case of intense/prolonged exposures, could release further ROS contributing to tissue damage and epithelial injury (Kondo et al., 1994; Sittipunt et al., 2001). An overview of these pathways is outlined in **Figure 1.5**.

Although the above discussion has addressed the hazardous consequences to the pulmonary system specifically (of which, the pulmonary system will also be the focus of the research to be conducted), particles of a smaller diameter, such as UFPs, have been shown to cross the alveolar membrane of the lung. This subsequently causes systemic responses (Miller et al., 2017), with PM exposure resulting in heightened superoxide anion radicals ( $O_2^{\cdot-}$ ) and inflammation and vasoconstrictor responses in *in*

*vivo* models. A mechanism of action may be that the vasodilator nitric oxide is scavenged by  $O_2^{\cdot-}$ , reducing the vascular effects of nitric oxide (Cherng et al., 2011). Therefore, the onset of systemic toxicity can cause effects within organs distant from the lungs. For example, Gurgueira *et al.* (2002) showed ambient  $PM_{2.5}$  is detectable within the heart following short-term (5 hr) exposures. This is likely linked with oxidative stress observed within the heart following PM exposure, which could contribute to adaptive responses, such as cardiac hypertrophy, which has also been seen following chronic  $PM_{2.5}$  exposure (Su et al., 2020). Furthermore, exposure to PM

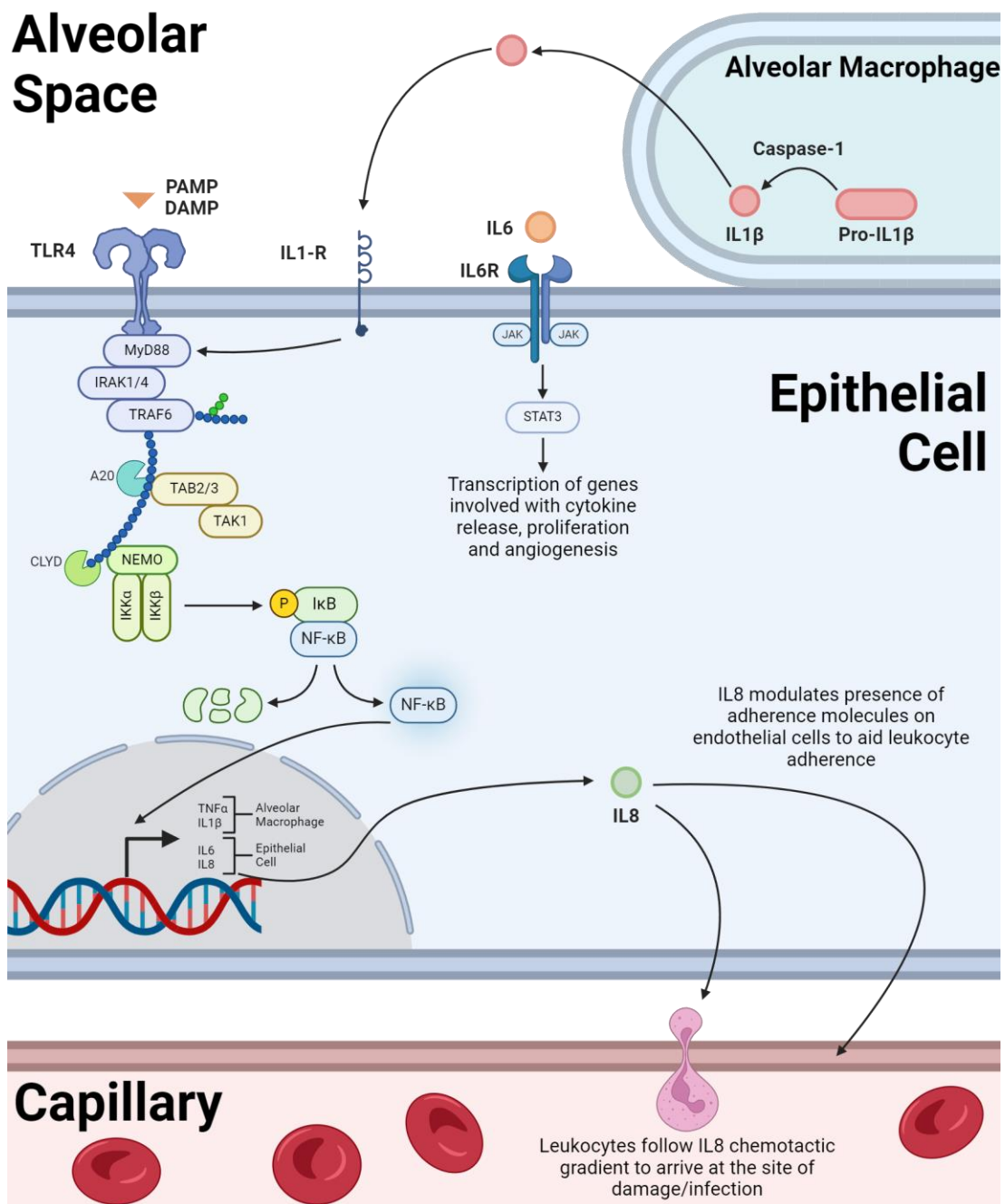


Figure 1.5 An overview of pro-inflammatory pathways involved within the alveolar regions of the lung.

for 15 weeks was associated with increased heart weight, blood pressure and cardiac fibrosis and lowered stroke volume in rats (Qin et al., 2018; Ying et al., 2015). Of which, the onset of fibrosis indicates the presence of chronic inflammation, a phenomenon supported by Du *et al.* (2019) which detected increased circulating inflammatory markers following PM<sub>2.5</sub> exposure for 16-weeks in mouse models.

The mechanism by which inhalation of PM causes systemic inflammation is not entirely characterised. However, it could involve the release of inflammatory cytokines and chemokines into the circulation from immune cells of the lung (Goto et al., 2004). AMs could play a significant role in this as they have been shown to increase cytokine production following phagocytosis (van Eeden et al., 2001). Furthermore, it has been demonstrated that the supernatant from AMs cultured with inert carbon particles induced a quicker release of immune cells from the bone marrow compared to AMs that were untreated (van Eeden et al., 2001). In addition, activation of the autonomic nervous system results from PM exposure, which causes an increase in heart rate and vasoconstriction, increasing the chance of arrhythmias (Wu et al., 2018).

### **1.3.2.5 Antioxidative Defence and Oxidative Stress**

It has often been reported that exposure to inhaled toxins has been associated with the onset of pulmonary oxidative stress, which causes subsequent DNA, protein and phospholipid damage (Kaspar et al., 2009). Therefore, these cells require a means of protecting themselves against the accumulation of reactive species and electrophiles. This is achieved through an antioxidant defence system, which regulates the redox status of cells. A vital example of this is mechanisms that are activated through nuclear factor erythroid 2-related factor (Nrf2), encoded by the *Nfe2l2* gene. Nrf2 is a transcription factor that can regulate redox balance through the transactivation of antioxidants and plays a role in detoxification during Phase II reactions (Kensler et al., 2007). This is achieved through the binding of Nrf2 to antioxidant response elements (ARE) on DNA, allowing regulation of antioxidants such as glutamine-cysteine ligase (GCL), thioredoxin reductase 1 (Txnrd1), NADPH-quinone oxidoreductase 1 (NQO1) and haem oxygenase-1 (HMOX1). This will initiate a cascade of events, ultimately providing a level of protection to cells against oxidative challenges (Kansanen et al., 2013). Nrf2 possesses 6 function Neh domains (Neh1-6). Neh2 is particularly important due to its ability to bind Kelch-like ECH-associated protein 1 (Keap1).

Keap1, under physiological conditions, binds to Nrf2 at Neh2 within the cytosol, targeting Nrf2 for ubiquitination and subsequent degradation (Kang et al., 2004). This is a rapid process that, in turn, leaves Nrf2 with a half-life of approximately 20 minutes (Kobayashi & Yamamoto, 2006). Under cellular oxidative stress, however, as could be the case when inhaled pollutants have affected cells, electrophiles modify cysteine residues on Keap1, resulting in inactivation, Nrf2 release and subsequent Nrf2 stabilisation (Kobayashi et al., 2006), increasing Nrf2's half-life to up to 200 minutes (Canning et al., 2015). Nrf2 can then translocate to the nucleus, where it can bind at an ARE and the small Maf, their transcriptional partner, *via* Neh1 (due to the presence of a bZip domain). Neh3, 4 and 5 allow the recruitment of transcriptional coactivators, such as CREB-binding protein, enhancing transcriptional activity (Sykiotis & Bohmann, 2010). Cytoprotective genes transactivated through this mechanism are summarised in **Table 1.3**.

Superoxide dismutase (SOD) is of particular interest in this work as its expression can be investigated to indicate the antioxidative response of the cell. There are 3 isoforms of SOD (1, 2 and 3). Nrf2 activation can drive *sod1* transcription, where the SOD1 protein then localises to the cytosol or intermitochondrial membrane (Okado-Matsumoto & Fridovich, 2001). SOD1 can catalyse the conversion of  $O_2^{\cdot-}$  to  $H_2O_2$  and  $O_2$  using a copper/zinc active centre. Catalase or glutathione peroxidase can then reduce  $H_2O_2$  to  $H_2O$  and  $O_2$ . This is an example of an antioxidative mechanism; however, when catalase or glutathione peroxidase are unavailable, SOD1 could prove pro-oxidative due to the accumulation of  $H_2O_2$  (Singh et al., 2017). As such, the transcription of SOD1 can be used as a marker of oxidative stress, and has found to be increased which is increased by DEP exposure (Farina et al., 2017).

SOD2 on the other hand is localised to the mitochondrial matrix and contains manganese as its active centre, whereas SOD3 is a secreted, extracellular SOD containing copper/zinc. Each SOD catalise the same reaction involving  $O_2^{\cdot-}$ .



**Table 1.3** A list of genes activated through Nrf2 transactivation. Table adapted from Loboda et al. (2016)

Gene	Major Function
Ferritin	Sequesters free iron
Glucose-6-phosphate dehydrogenase	Provides NADPH to glutathione reductase
Glutathione peroxidase	Detoxifies peroxides and hydroperoxides
Glutathione S-transferase	Catalyses the conjugation of the reduces from of glutathione to xenobiotic substrates
Glutathione reductase	Catalyses the reduction of glutathione disulphide to the sulfhydryl form of glutathione
$\gamma$ -Glutamylcysteine ligase	Catalyses the rate limiting step in the cellular glutathione biosynthesis pathway
Haeme oxygenase-1	Degrades haeme and generates the antioxidant molecules, biliverdin and CO
NADPH-quinone oxidoreductase 1	FAD-binding protein, reduces quinones to hydroquinone's
Sulfotransferases	Catalyse sulphation of many xenobiotics
Superoxide dismutase	Catalyses the dismutation of the superoxide radical ( $O_2^{\cdot-}$ ) into molecular oxygen ( $O_2$ ) or hydrogen peroxide ( $H_2O_2$ )
Thioredoxin reductase	Reduces thioredoxin
UDP-glucose dehydrogenase	Converts UDP-glucose to UDP-glucuronate

### 1.3.2.6 Genotoxicity and Carcinogenicity

Typically, the inhalation of pollutants is linked with carcinogenicity. For example, exposure to tobacco smoke or asbestos is a well-established risk factor for small cell lung cancer and mesothelioma, respectively (Gaudino et al., 2020; Tseng et al., 2022). The global burden of disease concludes that air pollution is a major driver of lung cancers, with particular emphasis on  $PM_{2.5}$  as an oncogenic driver (Ebrahimi et al., 2021). This is further exemplified by the fact that DEPs and woodburning have been listed as group 1 and 2a carcinogens, respectively (International Agency for Research on Cancer, 2024).

The mechanisms of action underpinning air pollution exposure and carcinogenesis are complex and varied, partially due to the complex nature of air pollution and the many

mechanistic effects that these can have on cells and biological systems. For example, exposure to lower concentrations of ambient air pollution has been associated with an increased risk of peripheral lung adenocarcinoma, yet as air pollution concentration increases, there is an increased ratio of a person developing central squamous cell carcinoma (Ge et al., 2020). This is potentially due to high PM concentrations causing cilia dysfunction, reducing the lungs' ability to clear the particles.

That being said, some pathways are likely general regardless of the PM type or location of action. For example, PM is known to bind PAHs to its surface (Cassee et al., 2013). There are many different PAHs, many of which are known to be carcinogenic. Dibenzo[def,p]chrysene, present on PM from smoky coal, is known to be genotoxic (Mumford et al., 1995). Dibenzo[def,p]chrysene is metabolised by CYP enzymes to form thiol-epoxide derivatives, which can covalently bond directly to DNA, forming DNA adducts (Mahadevan et al., 2006). Typically, cells have systems in place to repair these DNA adducts; however, in situations where repair does not occur effectively or DNA adduct quantity is beyond the repair capacity, it may cause mutations to occur during DNA replication. Activation or deleterious mutations in oncogenes and tumour suppressors, respectively, can then lead to carcinogenesis (Ma et al., 2019).

Air pollution may also act through secondary genotoxicity. The ability of air pollution to induce oxidative stress has already been discussed in the context of both ATI and ATII cells, but AMs are especially capable of producing ROS. The generation of ROS is then able to subsequently cause damage to nucleic acids through DNA-protein crosslinking, alteration of purine and pyridine base structures and single/double-strand breaks, potentially inducing oncogenic mutations. This could lead to cellular proliferation, evasion of cell death, angiogenesis and metastasis, contributing to cancer initiation and progression. Further, ROS can alter gene expression and epigenetic mechanisms, which could induce these effects (Gruber et al., 2018). Indeed, PM<sub>2.5</sub> exposure has been linked to the downregulation of tumour suppressors p53, retinoblastoma protein and PTEN (Abbas et al., 2010; Chao et al., 2020). Further, elements within air pollution, such as iron, could induce antiapoptotic events through Nrf2-mediated mechanisms (Lovera-Leroux et al., 2015).

Interestingly, lung cancer in never smokers, which is subsequently linked to air pollution exposure, lacks a distinct mutational signature (Zhang et al., 2021), perhaps

suggesting a non-genotoxic route of carcinogenesis. In a landmark study, Hill *et al.* (2023) have suggested that PM exposure can promote tumorigenesis and tumour progression in lung tissue harbouring pre-existing EGFR mutations. Further, it was shown *in vivo* that an immune response was required to observe this effect. Specifically, IL1 $\beta$  released from alveolar macrophages, which caused a phenotypic change in ATII, promoting lung cancer. This, therefore, suggests that inflammation could be a driving factor of air pollution-induced lung cancer, though a pre-existing driver mutation may be required. This mutation could be induced through pollutant exposure but could also result from random change or ageing.

### **1.3.2.7 Detoxification and Metabolism**

The mechanisms of defence against inhaled toxins described previously, such as endocytic uptake and TLR activation, may be effective in the response to inhaled PM and pathogens, though may not be effective in targeting the effects of inhaled gases, which might not trigger these responses. To combat this, bronchial and bronchiolar epithelial cells, club cells, ATII and AMs express xenobiotic-metabolising cytochrome P450 enzymes (CYPs). CYPs possess a broad substrate specificity and can act on many potential toxicants. The enzymes catalyse a variety of oxidation and reduction reactions, such as hydroxylation, heteroatom oxygenation, dealkylation, epoxidation, desaturation, and haem destruction, with the overall goal of introducing functional groups to xenobiotics in what is known as a Phase I reaction (Manikandan & Nagini, 2018). Phase I reactions increase the target molecules' reactivity and polarity through the addition of polar groups such as hydroxyls, carboxylic acids, amines and thiols (Zhao *et al.*, 2021). There is an abundance of CYPs within the human lung, each possessing various mechanisms of action and reaction pathways (Castell *et al.*, 2005). After the changes resulting from the Phase I reactions, xenobiotics undergo Phase II reactions, whereby endogenous molecules are conjugated to the toxicant, causing further detoxification. These reactions aim to increase polarity and solubility to allow excretion *via* the kidneys or bile (Riechelmann, 2004).

However, it is important to note that reactive, potentially harmful metabolites may be produced during this process in a phenomenon called bioactivation (**Figure 1.6**). Studies have implicated metabolism by some CYPs present in the human lung with the activation of pulmonary toxins. The PAH benzo(a)pyrene, found in diesel exhaust emissions and cigarette smoke, for example, is metabolised by CYP1A1 to form benzo(a)pyrene-7,8-epoxide, which is subsequently hydrated to form benzo(a)pyrene-7,8-diol by epoxide hydrolase. Benzo(a)pyrene-7,8-diol is then either detoxified in a Phase II reaction by glutathione S-transferase (GST- $\mu$ ) (Rebbeck, 1997) or is further metabolised by CYP1A1 to form benzo(a)pyrene-7,8-diol-9,10-epoxide, a reactive species with the ability to bind to DNA, leading to mutations and carcinogenesis (Li et al., 2001). It is, therefore, clear that problems arise when an individual may possess a mutation to the GST- $\mu$  gene (Garte et al., 2001).

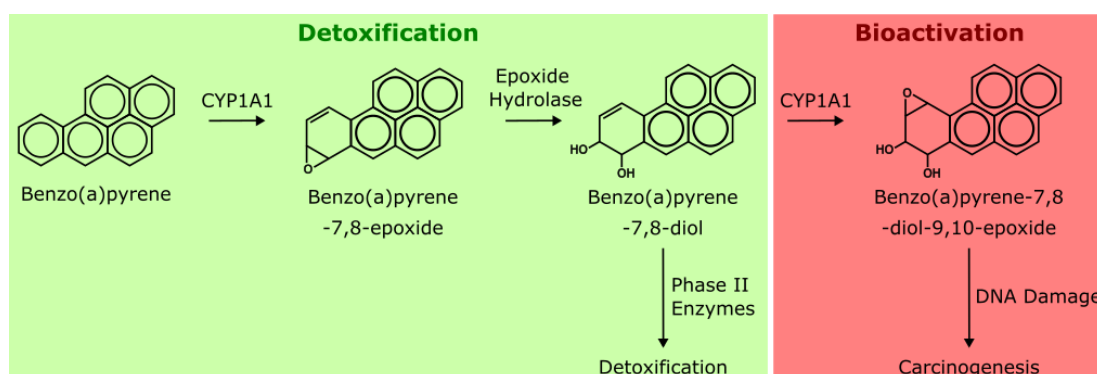


**Figure 1.6** Schematic of the metabolism of benzo(a)pyrene, present in diesel exhaust emissions and cigarette smoke. Green indicates the physiological detoxification pathway that will normally be followed. Red shows the bioactivation pathway that will be followed in the case that enzymes, such as GST- $\mu$ , cannot meet the detoxification demand.

## 1.4 Particulate Matter

PM is highly diverse in its characteristics, many of which influence its toxicity, including their dispersion, agglomeration and aggregation in different environments and biological media, as well as source of emission (Stone et al., 2017). As previously mentioned, however, the primary method by which PM is classified is by size. PM<sub>10</sub> is defined as particles smaller than 10  $\mu\text{m}$  in aerodynamic diameter. PM<sub>2.5</sub> encompasses PM smaller than 2.5  $\mu\text{m}$  in aerodynamic diameter. Additionally, particles below 100 nm exist and are defined as UFPs or PM<sub>0.1</sub> (**Figure 1.7**). PM is a complex mixture of organic, inorganic or organometallic, solid, liquid or mixed phased particles originating from natural and anthropogenic sources. For example, black carbon or soot particles, produced during incomplete combustion, could be released from forest fires

or the burning of fossil fuels to power personal transport (Thompson, 2018). Some major PM types are summarised in **Table 1.4**.

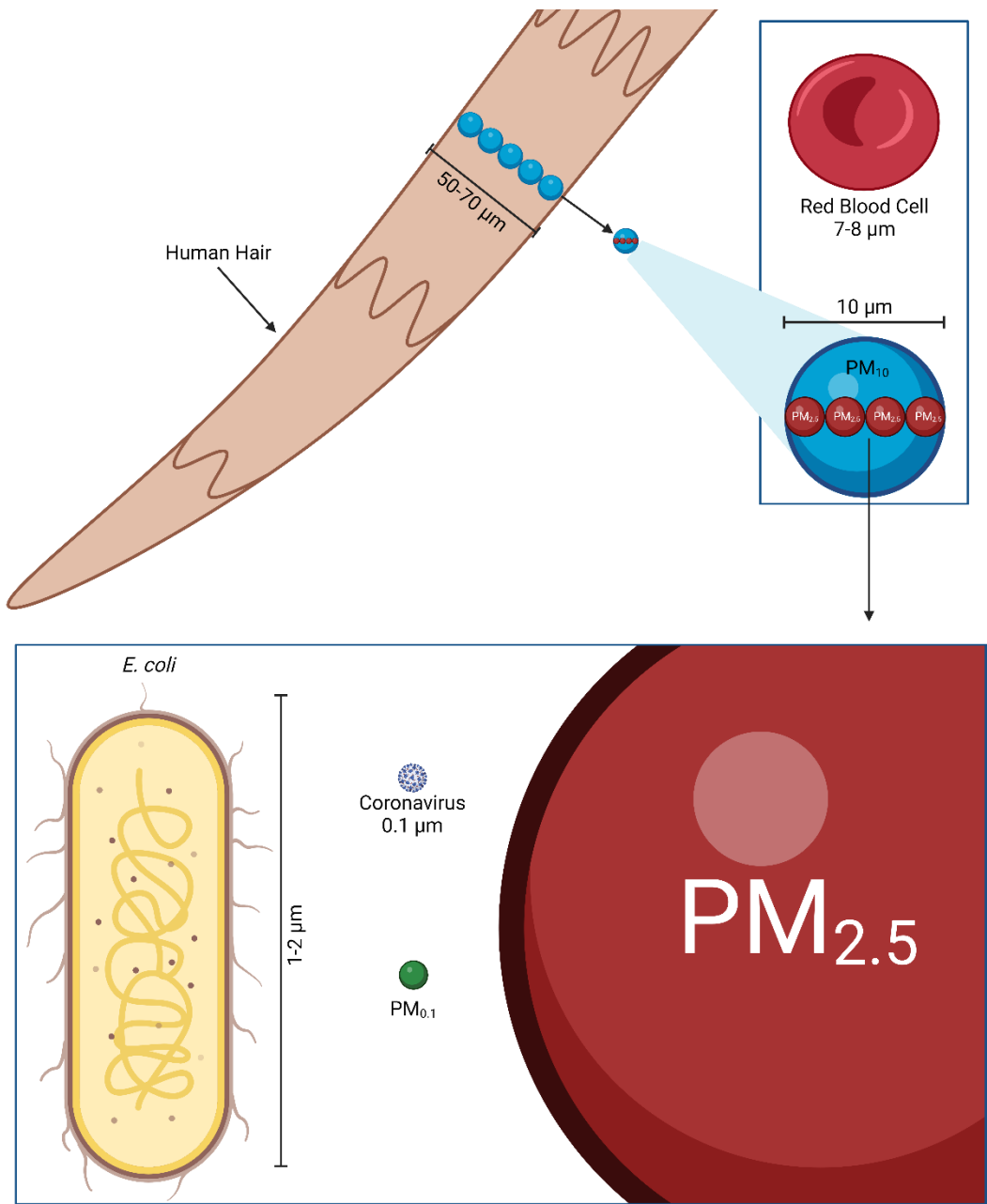


**Figure 1.7** Relative sizes of different PM fractions. PM10 particles are of a similar size to a human erythrocyte, a fraction of the width of a human hair. PM2.5 is a quarter of the size of this. PM0.1 is again a fraction of this size, similar in size to a coronavirus. Created using BioRender.com.

**Table 1.4** Characteristics and prevalence of significant sources of PM

Marine aerosol	Primary marine aerosols are produced through the action of bubbles bursting during the breaking of waves, and capillary action is produced through wind moving across the surface of the water; thus, the amount of marine PM produced is
----------------	-------------------------------------------------------------------------------------------------------------------------------------------------------------------------------------------------------------------------------------------

	<p>proportionate to wind speed, but has also been shown to be proportional to the temperature as well as sea salinity (Salter et al., 2015). The main aerosol emitted during this is sea salt, although it has been shown that organic matter, such as fatty acids, may also be incorporated (Bargner &amp; Garrett, 1970), as well as dimethylsulphide, produced by phytoplankton (Charlson et al., 1987).</p>
Mineral dust	<p>Mineral dust originates from natural and anthropogenic sources (at an estimated proportion of 75% and 25%, respectively) (Ginoux et al., 2012). Of the many natural sources of mineral dust, Saharan dust is the most prominent source and is responsible for almost half of annual mineral dust globally (Karanasiou et al., 2012) and may drastically increase PM levels recorded during the monitoring of air quality (Querol et al., 2009). Regardless, Saharan-derived PM<sub>2.5</sub> is not significantly associated with total or cause-specific mortality. Perez <i>et al.</i> (2008), for example, only saw a non-significant 1.5% increase in mortality per 10 µg/m<sup>3</sup> increase in PM<sub>2.5</sub>. These results were mirrored by Tobias <i>et al.</i> (2011), who only reported a 0.3% increase in mortality on days when Saharan dust was present. There is contention regarding the health impact of PM<sub>10</sub> originating from Saharan dust. For example, Sajani et al. (2011) did not find an association between PM<sub>10</sub> and mortality during dust and non-dust events, whereas Mallone <i>et al.</i> (2011) reported an 8.9% cardiac mortality on dust days compared to non-dust days where cardiac mortality was 1.9%.</p>
Primary biological aerosol particles (PBAPs)	<p>As the name suggests, PBAPs are emitted directly from natural sources into the atmosphere. PBAPs are highly diverse in size and composition, such as viruses that can be from tens of nanometres in aerodynamic diameter, in contrast with plant debris, which can exceed 100 micrometres (Jaenicke, 2005). The diversity of PBABs allows for a wide range of biological</p>

	<p>responses to their exposure; for example, bacteria and viruses are of particular importance to public health (<i>e.g.</i>, in light of the COVID-19 pandemic) due to their risk of inducing infection and disease (Gordon et al., 2014). Natural airborne allergens, such as pollen and fungal spores, cause discomfort to those who develop allergic reactions and have also been implicated in the acute exacerbation of asthma (Burge &amp; Rogers, 2000). PBAPs such as oncogenic viruses, wood dust, and fungi-derived molecules such as aflatoxin and ochratoxin A (usually only inhaled during certain types of industry work, <i>e.g.</i>, peanut processing) have also been associated with the onset of cancer (Douwes et al., 2003).</p>
Combustion of wood	<p>Wood combustion is widely utilised for residential heating and, as such, is the largest source of PM<sub>2.5</sub> in many European countries (Amann et al., 2018). PM<sub>2.5</sub> from wood combustion has been implicated as one of the most highly concerning air pollutants in urban environments (Karagulian et al., 2015). Respiratory symptoms and exacerbations have been associated with exposure to wood combustion PM, especially in children, although cardiovascular symptoms are less apparent (Naeher et al., 2007). Additionally, wood smoke contains polycyclic aromatic hydrocarbons, which are known carcinogens. Hosgood <i>et al.</i> (2010) have also implicated indoor exposure to wood smoke with increased cancer incidence.</p>
Diesel emission particles	<p>Particles originating from the combustion of diesel are highly prevalent due to the reliance of diesel to power private transportation. Diesel emission particles often consist of a elemental carbon core (10-30 nm in diameter). This is then layered with unburn lubricants and fuel oils, as well as metals from fuel additives, oils and engine wear. Further, during the combustion process and when interacting with other pollutants within the air, the particles are able to bind PAHs (Steiner et al., 2016). Inhalation of diesel emission particles has shown to</p>

cause pulmonary inflammation, oxidative stress and genotoxicity (Bendtsen et al., 2020), and as such, has been categorised as a group 1 carcinogen (International Agency for Research on Cancer, 2024).

Inhalation of PM is associated with morbidity and mortality, the severity of which has been shown in a systematic literature review by Morakinyo et al. (2016) to be directly influenced by the quantity and duration of PM exposure, mirrored by epidemiological data as previously discussed in Section 1.2. Due to the aerosolised nature of PM, it has the ability to infiltrate the human respiratory system, the depth of penetration of which is dependent on the aerodynamic diameter of the PM. PM<sub>10</sub> is generally deposited within the major airways of the lung, whereas PM<sub>2.5</sub> can penetrate deeper into the lung and be deposited as far as the alveolar region. PM<sub>2.5</sub> (as well as UFPs) can also deposit within the alveoli themselves, as well as show a degree of lung permeation and translocation into the bloodstream (Brunekreef & Holgate, 2002), with particles detected at distant organs such as the liver, kidney, heart and brain (Aalapati et al., 2014). Due to the diversity in PM characteristics, mechanistic biological responses to particular PM sources are varied; however, ubiquitous responses are notably inflammation, either in the presence of or absence of oxidative stress or *vice versa*.

#### **1.4.1 Particulate Matter Induced Oxidative Stress**

Oxidative stress arises from the imbalance in redox homeostasis, the equilibrium between oxidants and antioxidants. A disproportionate increase in oxidants produces reactive oxygen species (ROS) and reactive nitrogen species (RNS). These are molecules classed due to their absence of a complete electron pair in their outer valence. Typically, ROS include O<sub>2</sub><sup>·-</sup>, hydrogen peroxide H<sub>2</sub>O<sub>2</sub> and hydroxyl radicals (HO<sup>·</sup>), whereas the most abundant RNS is nitric oxide (NO<sup>·</sup>) (Kaspar et al., 2009), and are produced during aerobic cellular respiration. ROS provide beneficial effects at physiological levels, including cellular signal transduction, enzymatic activation and gene expression; however, at higher levels, ROS can induce oxidative damage to all major cellular structures such as phospholipid membrane, proteins and DNA (Dröge, 2002). To defend against oxidative damage, aerobic organisms have developed an antioxidant system which acts to neutralise free radicals and prevent cellular oxidative



stress (Sena & Chandel, 2012). Oxidative stress results when reactive species are continually produced beyond the antioxidants' capacity or when antioxidants are depleted (Ottaviano et al., 2008).

Naturally, since PM is inhaled, a significant site of oxidative stress is within the pulmonary system, specifically, the epithelial lining of the lung. Oxidative stress is considered an initial factor in pulmonary pathology, potentially driven by subsequent inflammation (Ghio et al., 2012). This could be through activation of the redox-sensitive transcription factors mitogen-activated protein kinase (MAPK) (Tamaoki et al., 2004) and nuclear NFκB (Jiménez et al., 2000), pathways of which have been implicated in the inflammatory process and apoptosis (programmed cell death), proliferation, transformation and differentiation of cells (Terzano et al., 2010).

The mechanisms by which PM can induce reactive species formation are under contention and vary depending on the composition of the PM in question. For example, *via* a reaction called the Fenton reaction, particulates containing a proportion of heavy metal are able to induce the production of HO· from H<sub>2</sub>O<sub>2</sub> (In the case of PM containing iron:  $\text{Fe}^{2+} + \text{H}_2\text{O}_2 \rightarrow \text{Fe}^{3+} + \text{HO}^- + \text{HO}\cdot$ ) (Donaldson et al., 1997). The hydroxyl radicals have been shown to act as potent disruptors of DNA structure and induce lipid peroxidation (Shi et al., 2006). In a different mechanism, diesel exhaust particles, which are a large component of PM<sub>2.5</sub> (in terms of particle number), can be engulfed by alveolar macrophages in a phagocytotic matter. Diesel combustion originated PM, which consists of a carbonaceous core coated with various burnt petrochemicals, including PAHs, halogenated aromatic hydrocarbons (HAHs), and redox-active quinones. AMs contain an abundance of cytochrome P450 enzymes which possess the capability of metabolising the burnt petrochemicals, resulting in reactive species formation, and has been experimentally shown to increase apoptosis *in vitro* (Hiura et al., 1999). These mechanisms are not mutually exclusive; the metabolism of PAHs, for example, could result in the release of O<sub>2</sub>·<sup>-</sup> (or O<sub>2</sub>·<sup>-</sup> could be released from the particle itself), which has been shown to lead to the production of H<sub>2</sub>O<sub>2</sub>, which can subsequently produce HO· through the Fenton reaction (Prahalad et al., 1999).

Reactive species can impact DNA, potentially through damage to purine and pyrimidine bases or cleavage of phosphodiester bonds. This occurs both in nuclear

DNA and mitochondrial DNA, of which mitochondrial DNA could be more susceptible due to its exposed nature. If DNA repair cannot keep up with the damage induced by PM, carcinogenesis may follow (Jakubczyk et al., 2020). Furthermore, it has been demonstrated that the heavy metals within PM and the subsequently formed reactive species can suppress natural DNA repair mechanisms of the cell, such as nucleotide excision repair. It has also been shown that PM exposure could promote the replication of damaged DNA (Mehta et al., 2008). The above evidence, therefore, provides a clear mechanism for PM-induced carcinogenesis and cancer progression, an observation supported by epidemiological evidence (Pope et al., 2002).

ROS has also been shown to attack lipid membranes in a process called lipid peroxidation, with the main target being fatty acid residues within lipids of the plasma membrane (Montuschi et al., 2004). Lipid peroxidation has been shown to increase in response to PM<sub>2.5</sub> exposure. Ambroz *et al.* (2016), demonstrated this link this through identifying an increase in 15-F2t-isoprostane (a marker of lipid peroxidation) driven by the ambient air pollution levels at the residence of mothers and new-borns. Lipid peroxidation by reactive species ultimately disrupts the phospholipid membrane integrity through alterations in lipid-lipid interactions, membrane permeability, ion gradients and membrane fluidity (Catalá & Díaz, 2016). This has also been shown to trigger inflammation and immune responses (Ackermann et al., 2017), potentially through macrophage recognition (Wong-Ekkabut et al., 2007). Consequently, membrane disruption could cause aberrations in the cellular calcium (Ca<sup>2+</sup>) homeostasis due to the loss of the ability of mitochondria and endoplasmic reticulum to sequester cytosolic Ca<sup>2+</sup> (Pompella et al., 2019). This ultimately results in an increase in intracellular Ca<sup>2+</sup>, which, in turn, has been shown to lead to increased free radical production (Kim et al., 1997). Brown *et al.* (2004) have shown that, through UFP exposure, a ROS-mediated mechanism of intracellular Ca<sup>2+</sup> concentration modulation could be involved in onset of inflammation through activation of transcription factors such as NF-κB and activator protein 1 (AP-1). Furthermore, it has been shown that increased cytosolic Ca<sup>2+</sup> levels could lead to cell apoptosis and necrosis (Xing et al., 2011), therefore proposing a mechanism that PM exposure could cause direct tissue injury.

### 1.4.2 Particulate Matter Induced Inflammatory Response

The mechanisms underpinning airway inflammation have been discussed in Section 1.3.2.4. Exposure of the airways to PM has been associated with the onset of inflammation, likely through various mechanisms, such as the presence of xenobiotics on the surface of PM that could activate TLR4 or through phagocytic uptake into lysosomes, subsequently causing cathepsin D release and NLRP3 inflammasome activation, allowing the cleavage of pro-IL1 $\beta$  to active IL1 $\beta$  (Gairola et al., 2023) and subsequent downstream signalling.

Cerium oxide is a nanoparticle (in the PM<sub>0.1</sub> range) and diesel additive that increases combustion efficiency. *In vivo* studies have linked cerium oxide exposure to increased neutrophil infiltration into the lung and release of TNF $\alpha$  and IL1 $\beta$  (Aalapati et al., 2014). Generally, DEP exposure has been associated with the onset of pulmonary inflammation. Within mice, for example, intratracheal instillation of DEPs induced the influx of neutrophils and an increase in IL6 within BAL (Nemmar et al., 2011) and has been shown to increase TNF $\alpha$ , IL1 $\beta$ , IL6 and IL8 production in alveolar macrophages and epithelial cells (Ohtoshi et al., 1998). This could be associated with a reduction in FEV<sub>1</sub> observed in human exposures to traffic-related air pollution (McCreanor et al., 2007) and the onset and progression of asthma (Pandya et al., 2002).

Again, due to the heterogeneity of PM, as highlighted by COMEAP (2022), the mechanisms by which PM induces an inflammatory response are likely varied, although they have been suggested to act through TLR4 (due to the presence of gram-negative bacteria on the PM surface). Indeed, inhibiting/knocking out TLR4 attenuated IL6 and TNF $\alpha$  production in PM<sub>10</sub>-exposed AMs (Alexis et al., 2006; Becker et al., 2005). If TLR4 were being activated, it would be expected that an associated increase in NF $\kappa$ B activation would follow, which has been indicated by Shukla *et al.* (2000) when exposing ATII to PM<sub>2.5</sub>. NF $\kappa$ B could also be activated through PM-induced ROS production, as discussed in Section 1.3.2.5. ROS could trigger the release of calcium ions from the endoplasmic reticulum, which can alter NF $\kappa$ B activation (Sakamoto et al., 2007). In line with activation of the NF $\kappa$ B, PM has been found to stimulate the release of pro-inflammatory mediators IL1 $\beta$ , TNF $\alpha$ , IL6 and IL8 from AMs (Ishii et al., 2004), which promote neutrophilia (Simons et al., 1996) and potentially systemic

inflammation (Tedgui & Mallat, 2006). This could explain some of the non-pulmonary effects described in Section 1.4.3.

It has been widely reported that PM<sub>0.1</sub> could possess a greater toxic potential than its larger fraction counterparts, though, the data is inconsistent (Environmental Protection Agency, 2019). However, Becker (2003) showed that PM<sub>10</sub> induced a larger pro-inflammatory response in AMs than PM<sub>2.5/0.1</sub>, potentially due to the greater ability to harbour pathogens, though the ability for each particle size to deposit at the alveolar level requires thought (as these exposures occurred *in vitro*). Given the larger systemic effects observed for PM<sub>0.1</sub> in meta-analyses of the broad health effects of PM, such as the US EPA ISA for PM, it could suggest a greater systemic effect of the fine fraction of PM beyond systemic pro-inflammatory mediator release. This could perhaps be due to particle translocation into the circulation.

### **1.4.3 Non-Pulmonary Effects**

Although health effects relating to pulmonary and cardiovascular health are perhaps the most well-understood, evidence has linked PM exposure with health impacts in an additional number of the body's organs. For example, inhalation exposure to PM and subsequent swallowing of mucociliary clearance products has been linked with lipid metabolism dysfunctions and intestinal villi shortening (Li et al., 2015). Additionally, transport of PM to the brain could occur through a variety of processes, including transport across the blood-brain barrier, perineural transport into the cerebral spinal fluid, axonal transport from the olfactory mucosa or *via* the lymphatic pathway (Loane et al., 2013). Exposure to PM has therefore been loosely linked to neurodegeneration (Amor et al., 2010), as well as spatial learning and memory deficits and ventral enlargement in mice (Allen, Liu, Pelkowski, et al., 2014; Allen, Liu, Weston, et al., 2014; Fonken et al., 2011), and reduced cognitive function and autism in humans (Freire et al., 2010; Ranft et al., 2009; Volk et al., 2013).

Further, exposure to PM has been associated with a decline in reproductive health, showing the ability to accumulate within reproductive organs and alter hormone levels (Wang et al., 2021). PM<sub>2.5</sub> has also been associated with increased prevalence of chronic kidney disease (Wathanavasin et al., 2024), liver cancer, liver cirrhosis and fatty liver disease (Sui et al., 2022). Additionally, maternal exposure to PM<sub>2.5</sub> has

shown to reduce birth weight (Tapia et al., 2020) and increased risk of post-natal allergic rhinitis development (Lin et al., 2021).

There is an abundance of mechanistic, toxicological evidence linking PM exposure to a plethora of adverse outcomes, *in vitro*, *in vivo* and in human subjects. However, it is unlikely that PM exposure occurs independently, and humans are likely exposed to numerous pollutants simultaneously. Thus, there is a requirement to deduce the single pollutant effects as well as the combined effect of these pollutants. The project aims to ‘disentangle’ the PM impacts from those of NO<sub>2</sub>, given that epidemiological studies have had difficulty doing this in the past due to their correlated levels within ambient air.

### **1.5 Nitrogen Dioxide**

NO<sub>2</sub> is a gaseous pollutant that is primarily released through the combustion of fossil fuels. Road traffic emissions contribute 34% of total NO<sub>2</sub> emissions (although at roadsides, 80% of NO<sub>2</sub> can be attributed to emissions deriving from road traffic), as well as during energy generation, such as power plants (22%), domestic and industrial combustion (19%) and from other forms of transport, such as ships and trains (17%) (DEFRA, 2019; WHO, 2013). As NO<sub>2</sub> is emitted mainly through road traffic, it has been, in the past, and is often to this day, used as a marker for traffic-based air pollution (Hamra et al., 2015). It has even become practice to align hazardous outcomes associated with NO<sub>2</sub> levels directly with the source of pollution (*i.e.*, combustion of petrol/diesel) and/or associated PM level (which is emitting from the same combustion sources), rather than thinking of these pollutants as singular entities (Bosson et al., 2019). Methodologically, this approach should be used with caution given evidence shows that away from the roadside, road-traffic-originated NO<sub>2</sub> only comprised approximately a third of total NO<sub>2</sub>.

Furthermore, Wooding *et al.* (2019) showed an association of diesel exhaust aerosols with respiratory outcomes, even after the removal of particulate matter from the aerosol, perhaps indicating a toxic role of other substances emitted by traffic, including NO<sub>2</sub>. Currently, the UK does not fully comply with the Air Quality Standard Regulations, with 9 regions exceeding mean annual levels for NO<sub>2</sub> (DEFRA, 2023a). This is despite a concerted effort and resources being made available from a local to a governmental level to combat this (DEFRA, 2019). Although the ultralow emission

zone (ULEZ) within London has resulted in a 23% reduction in NO<sub>x</sub> emissions since 2019, which is estimated to have reduced NO<sub>2</sub> concentrations by 21% and 56% in inner and central London, respectively, compared to if there were no implementation of a ULEZ zone (Mayor of London, 2023).

It has been heavily reported by several epidemiological studies that ambient NO<sub>2</sub> concentration is correlated with an increased risk of morbidity and mortality (COMEAP, 2018; WHO, 2013). For example, Carey *et al.* (2013) reported that within an English cohort, an increase in NO<sub>2</sub> levels by 10.7 µg/m<sup>3</sup> was correlated with an increase in all-cause mortality, lung cancer mortality, circulatory mortality and respiratory mortality (HRs, 1.07, 1.06, 1.05 and 1.17 respectively after adjustment for age, sex, smoking status and BMI). Similar results were reported by Fischer *et al.* (2015), which found associations between NO<sub>2</sub> exposure and non-accidental mortality, respiratory and lung cancer mortality, but not circulatory mortality (HR, 1.03, 1.02, 1.10 and 1.00, respectively, after adjustments for socioeconomic parameters).

Alas, the above epidemiological evidence cannot be attributed to NO<sub>2</sub> alone. As previously stated, NO<sub>2</sub> levels are closely correlated with other pollutants, especially PM, as they are often emitted from similar sources (Bourdrel *et al.*, 2017). Both Carey *et al.* (2013) and Fischer *et al.* (2015) also reported a close correlation between NO<sub>2</sub> and PM exposure in their cohorts. Therefore, it remains inconclusive as to whether the effects observed within the epidemiological studies are a result of exposure to NO<sub>2</sub> alone, exposure to the various other pollutants that are correlated with NO<sub>2</sub> (*e.g.*, PM), or combined exposure to several pollutants that work additively, or synergistically to elicit the observed ‘toxic’ response.

The toxic effects of PM are well established (see Section 1.4); however, comparatively, the toxicological response by the body to NO<sub>2</sub> as a single pollutant is limited. Wooding *et al.* (2019) have implicated the importance of the NO<sub>2</sub> constituent of diesel emissions through particle depletion studies. It has previously been shown in both animal and human studies that sensitisation and immune response to allergens, such as ovalbumin, Japanese cedar pollen and ragweed, were increased when allergens were co-exposed with diesel-exhaust particles (Diaz-Sanchez *et al.*, 2000; Diaz-Sanchez *et al.*, 1997; Miyabara *et al.*, 1998; Muranaka *et al.*, 1986). Wooding *et al.* hypothesised that removing diesel exhaust particles would protect against heightened allergenic

responses. Allergen-sensitised patients were exposed to 4 conditions (4 weeks were allowed between each exposure): filtered air + 0.9% saline (used as a negative control); filtered air + allergen; diesel emissions diluted to 300 µg/ml of PM<sub>2.5</sub> + allergen; or particle-depleted diesel emissions + allergen for 2 hours. Despite a 94% effectiveness of particle removal, the predicted hypothesis proved incorrect, and removal of diesel-exhaust particles did not protect against allergic response; those subjects exposed to the particle-depleted diesel emissions showed a significant reduction in FEV<sub>1</sub> compared to the diesel-exhaust that had not been filtered. Although particle depletion reduced the fraction of particles, VOCs and other gases within the diesel emissions, it increased the fraction of NO<sub>2</sub> 3.5-fold (data confirmed by Carslaw (2005), demonstrating environmental NO<sub>2</sub> increase with increased diesel particulate filter use). This strongly implicated NO<sub>2</sub> as a pollutant that could enhance allergic sensitisation in human subjects. However, further work is required to confirm that the response observed is directly due to NO<sub>2</sub>, it could be the case that other gases are being relatively increased during the filtering process. The results also require verification on a larger scale, as this study only analysed 14 subjects.

Work by a group, mainly performed in the 1980s, implicated NO<sub>2</sub> exposure with a plethora of toxic outcomes in *in vivo* models. For example, Ichinose *et al.* (1982) showed that the exposure of NO<sub>2</sub> (at concentrations of 0, 0.4, 1.2 and 4.0 ppm) to rats over 4 months was associated with a dose-dependent increase in lipid peroxidation, measured through ethane exhalation and thiobarbituric acid reaction on lung homogenates, which was vastly increased within the first 1-2 weeks, before decreasing to base levels. A similar pattern was followed by antioxidant protective enzymes, which showed an initial increase in the first 4 weeks before gradually decreasing. Overall, this demonstrates that with long-term NO<sub>2</sub> exposure, cells lose their ability to protect against oxidative stress, leading to increased lipid peroxidation as the activity of antioxidative enzymes decreases. The same group then ran a similar study but ran a more extended exposure period of up to 27 months. The previous findings were confirmed, showing longer exposures being associated with a decrease in the antioxidative protective abilities of cells, shown through a reduction in enzymatic activity such as glutathione peroxidase and glutathione S-transferase, along with a simultaneous increase in lipid peroxidation, indicative of cellular oxidative stress (Sagai *et al.*, 1984). It is suggested that the loss of antioxidative protection during long-

term exposure to NO<sub>2</sub> could lead to chronic lung damage, such as lung fibrosis and an increase in alveolar wall thickness, as shown by Kubota *et al.* (1987). This could contribute to the NO<sub>2</sub> exposure-associated reduction in arterial blood oxygenation observed by Suzuki *et al.* (1983).

Additionally, for lung fibrosis, exposure to 4 ppm NO<sub>2</sub> for 9 months was associated with bronchial epithelial proliferation and hyperplasia, which further increased after 18 months. There was also simultaneous proliferation and hypertrophy of the epithelia lining the terminal airways, ATI and ATII cells. Additionally, there was an increase in interstitial oedema (Kubota *et al.*, 1987).

The above study by Kubota *et al.* reported no sign of inflammatory cell infiltration, enlargement of the lymphatic system, or emphysema, perhaps indicating no direct role for NO<sub>2</sub> in mediating inflammatory cascades. However, more recent evidence is contrasting. Work by Wegmann *et al.* (2002) exposed C57BL/6 mice (chosen due to their deficiency in  $\alpha$ 1-antitrypsin serum levels, a factor known to lead to respiratory diseases such as COPD and emphysema in humans (Stoller & Aboussouan, 2005)) to varying concentrations of NO<sub>2</sub> for 14 hours each for up to 25 days (controls were exposed to room air). Exposure to 20 ppm NO<sub>2</sub> for 15 days significantly increased leukocyte count within bronchoalveolar lavage samples, indicative of the onset of inflammation, which was shown to be both intraluminal and peribronchial. Additionally, histological findings show goblet cell hyperplasia, increased mucus production and areas of focal inflammation, and an increase in collagen fibres, perhaps indicating a link between inflammation and fibrosis. This was backed up by an investigation into lung inflation, which revealed that those exposed to NO<sub>2</sub> had larger lung volumes, showing a loss of lung elastic recoil. Head-out body plethysmography on live mice demonstrated that the inflammation and structural changes to the lung as a result of NO<sub>2</sub> exposure could be associated with a decrease in mid-expiratory airflow (EF<sub>50</sub>), indicative of impaired lung function, which could be associated with respiratory diseases, such as COPD.

It must be noted that the concentrations of NO<sub>2</sub> used within the above *in vivo* studies are often much higher than those observed in realistic human exposures, and magnitudes higher than the WHO 2021 Air Quality Guidelines. Though, it could be



useful to use these concentrations when observing toxicological events occurring over an acute exposure duration.

Within an *in vitro* setting, NO<sub>2</sub> has been shown to induce numerous effects on cells that could explain some of the mechanisms underpinning the morbidity and mortality demonstrated by epidemiological evidence. However, the number of *in vitro* studies is comparatively small and often uses concentrations beyond what would be expected during real live exposures. Bronchial epithelial cells, for example, had an enhanced ability to move chromium-51 and carbon-14-labelled bovine serum albumin across the membrane following exposure to 800 ppb NO<sub>2</sub>, compared to a clean air negative control. This could suggest lower barrier integrity and increased barrier permeability, which could be indicative of morbidities (Devalia et al., 1993). Also, 45 ppm NO<sub>2</sub> exposure was associated with a caspase-3 independent increase in apoptotic and necrotic cell death within bronchial epithelial cells. The rate of cell death was increased through pre-treatment of bronchial cells with pro-inflammatory mediators TNF $\alpha$ , IFN $\gamma$  and IL8. This could indicate an enhanced health effect of NO<sub>2</sub> within individuals with pre-existing inflammatory health conditions, such as asthma (Ayyagari et al., 2007). Tsukue *et al.* (2010) used diesel emissions (containing NO<sub>2</sub> and PM). It was found that A549 cells exposed to high NO<sub>2</sub>/low PM emissions had greater cell death compared to high NO<sub>2</sub>/high PM, although high NO<sub>2</sub>/high PM did increase HMOX1 expression and increased oncogene activation. In further NO<sub>2</sub> PM co-exposure studies, where quartz was used as a PM model particle, NO<sub>2</sub> was found to have an immunosuppressive effect shown through a decrease in TNF $\alpha$  response in bovine alveolar macrophages. NO<sub>2</sub> was also found to attenuate the TNF $\alpha$  observed in quartz only exposures (Polzer et al., 1994). The difference in response to NO<sub>2</sub> between different cell types may reflect the requirement for a human relevant *in vitro* model, comprising numerous cell types to give greater indication as to the health effect at a system level.

Of course, there is no argument that the most relevant model to assess human response to air pollutant exposures would be within humans themselves. Indeed, human exposure to NO<sub>2</sub> has been associated with increased expression of IL5, IL10 and IL13 (WHO, 2010). Perhaps in part explaining an increase in leukocyte, B lymphocytes, CD3<sup>+</sup> and CD69<sup>+</sup> lymphocytes, natural killer cells count within bronchial lavage following NO<sub>2</sub> exposure (Blomberg et al., 1997; Frampton et al., 2002; Helleday et al.,

1994). This increase in immune invasion could indicate disease states such as asthma. Indeed, asthmatics exposed to 1 ppm NO<sub>2</sub> were found to increase the production of thromboxane B<sub>2</sub> and prostaglandin D<sub>2</sub> (inflammatory mediators), whilst the bronchodilator 6 keto-prostaglandin and FEV<sub>1</sub> were decreased (Jorres et al., 1995). As was discussed in Section 1.3.2, inflammation and oxidative stress often arise synergistically. Exposure to 2 ppm NO<sub>2</sub> for 4 hours increased antioxidant factors in the bronchial and bronchioalveolar lavage, shown through increases in uric acid, ascorbic acid and glutathione (Kelly et al., 1996).

Considering the above evidence, NO<sub>2</sub> is expected to contribute to some of the toxicological outcomes associated with exposure to certain air pollutions, such as traffic emissions, although the extent to which NO<sub>2</sub> causes health implications is yet to be confirmed. This is explained in a report by the Committee on the Medical Effects of Air Pollution (COMEAP) which states:

*“the evidence now suggests that it would be sensible to regard NO<sub>2</sub> as causing some of the health impacts found to be associated with it in epidemiological studies. Nonetheless, it is likely, to some extent, NO<sub>2</sub> acts as a marker of the effects of other traffic related air pollution” (COMEAP, 2015).*

To further assess the relationship between NO<sub>2</sub> exposure and health implications, COMEAP undertook a systematic review of cohort studies that associated long-term exposure with increased all-cause mortality (COMEAP, 2018). This included studies that adjusted for confounding health impacts caused by correlated pollutants, such as PM (multi-pollutant models), and studies that made associations between NO<sub>2</sub> and mortality without accounting for other pollutants (single-pollutant models). Meta-analysis of the single-pollutant models showed a mortality rate of 1.023 (95% CI:1.008, 1.037) per 10 µg/m<sup>3</sup> increase in NO<sub>2</sub> as an annual average, though, this does not adjust for potential confounding pollutants. Therefore multi-pollutant models were utilised, though, large, unexplained heterogeneity was noted. Regardless, the majority of the committee agreed that there was an association between long-term NO<sub>2</sub> exposure and mortality, especially given greater effects were observed in specific age groups and at-risk groups. Greater associations were also observed when comparing NO<sub>2</sub> concentration with respiratory or cardiovascular mortality. As such, the majority of the committee members believe that NO<sub>2</sub> contributes, at least in part, to the health

effects observed in the epidemiological studies, with effects mainly targeted at the respiratory system. COMEAP calculated an adjusted coefficient mortality risk of 1.006-1.013 per 10  $\mu\text{g}/\text{m}^3$  increase in  $\text{NO}_2$  after adjusting the single-pollutant model coefficient for confounding effects of PM and other traffic related air pollutants (such as CO, black carbon, PAHs). This means a 1  $\mu\text{g}/\text{m}^3$  decrease in  $\text{NO}_2$  concentration could increase average life expectancy by 2-5 days, resulting in 420,000 to 903,000 more life years in the next 106 years (from 2018). This does not taken into account the potential co-benefits reducing  $\text{NO}_2$  would likely have on all traffic-related air pollutants (*i.e.* reducing  $\text{NO}_2$  emissions would likely also reduce PM emissions), which likely aligns with the unadjusted single pollutant model of  $\text{NO}_2$  (1.023) (essentially using  $\text{NO}_2$  as a marker of traffic-related air pollution). It is calculated that a 1  $\mu\text{g}/\text{m}^3$  reduction in traffic-related air pollution could increase average life expectancy by 8 days (1.6 million life years in the next 106 years, from 2018). COMEAP however have recognised that there is a degree of uncertainty in the data, to the point that some committee members do not believe there is enough information available to implicate  $\text{NO}_2$  exposure with an increase in mortality. As such COMEAP have recommended further toxicological studies to identify adverse effects of  $\text{NO}_2$  and compare these effects to other pollutants within the same experimental system to allow robust comparisons between pollutants to be drawn.

Therefore, it is imperative to establish the ability of  $\text{NO}_2$ , PM, and combined exposure of the two pollutants to cause direct and indirect health impacts on the human respiratory system. By approaching this issue from a mechanistic perspective, an understanding of which pollutant may possess a driving effect or whether the pollutants can act synergistically or additively to alter the toxicological response can be established. This would provide essential toxicological and health-related knowledge and further indicate a rationale towards potential legislative and infrastructural changes, allowing an effective cost-benefit analysis on future strategies and answering an urgent call to research.

## 1.6 Research Aims

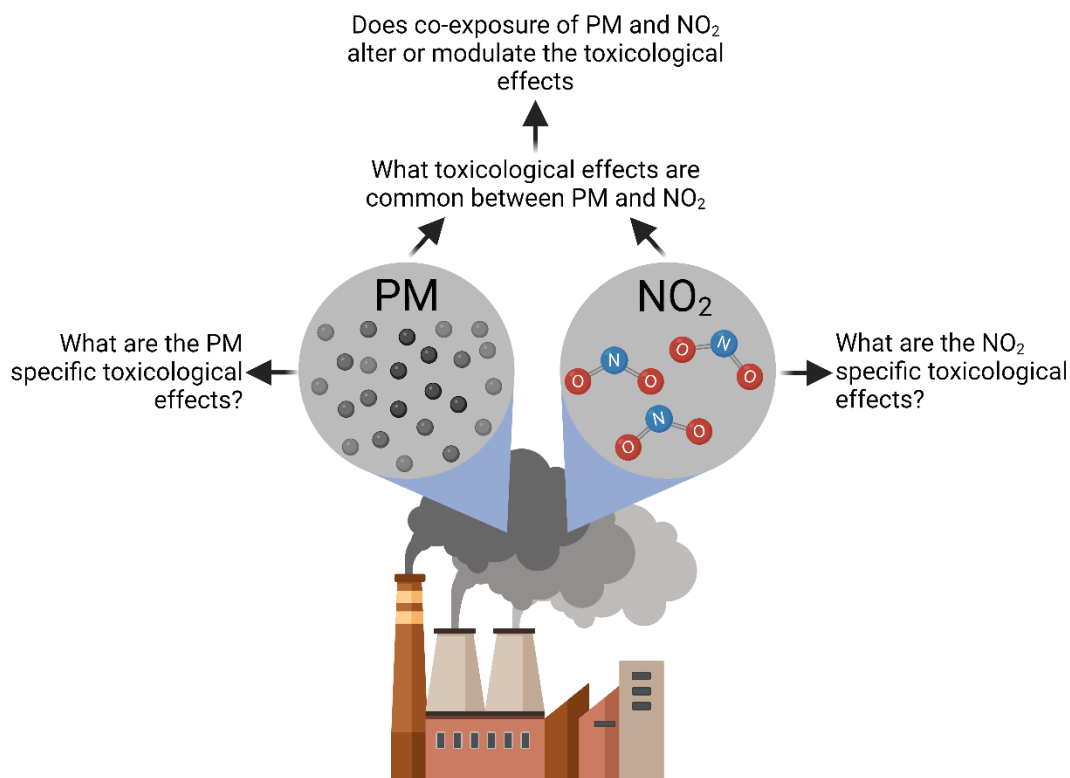


*Figure 1.8* Outline of questions aimed to be answered within this work.

As explained above, there is a vital need to clarify and ‘disentangle’ the potentially toxic effects of PM and NO<sub>2</sub> on human health (**Figure 1.8**).

Therefore, this research proposes to address this issue by undertaking purposeful, mechanistic-based toxicity studies to compare the potency of NO<sub>2</sub> ± PM within the alveolar lung region. The work will initially utilise appropriate, advanced *in vitro* cell culture models to identify relevant biological endpoints that are reflective of adverse respiratory health effects in humans, considering potential mechanistic pathways described previously. Throughout, realistic concentrations of NO<sub>2</sub> and PM will be used as best as possible to ensure findings apply to the general population, as this has been a considerable drawback of prior research that has demonstrated the toxic effects of NO<sub>2</sub>. The project aims to:

1. Develop an advanced *in vitro* model of the alveolar barrier. This model will constitute a co-culture model comprising ATI, ATII and AMs. Although the ATII and AM cell lines have been previously characterised, the ATI cells will require characterisation initially before the co-culture is assembled.

2. Characterise the exposure methods of the relevant cell culture models to either PM or NO<sub>2</sub>. This includes deposition and morphological analysis of VitroCell® Cloud PM exposures and NO<sub>2</sub> concentration analysis using a novel NO<sub>2</sub> exposure chamber.
3. Assess the toxicological response of mono and co-cultures to relevant PM samples. This includes carbon black (used as a model PM particle), indoor dust, urban dust, and diesel emission particles. These will be exposed to cultures at the air-liquid interface *via* aerosol or quasi-air-liquid interface exposures.
4. Investigate single pollutant NO<sub>2</sub> exposure within mono and co-culture models before investigating potential additive or synergistic toxic effects by combining NO<sub>2</sub> and PM exposures.
5. Assess NO<sub>2</sub> ± PM exposure from a transcriptomic perspective.

Through a mechanistic toxicological approach, this project intends to compare the potency of NO<sub>2</sub> exposure with and without PM exposure (standardised and fresh) at relevant concentrations within a relevant complex *in vitro* model. The project will supplement and add context to the findings of various epidemiological studies that have previously demonstrated the toxic effects of NO<sub>2</sub> and answer a crucial call to research regarding our lack of understanding of specific pollutant toxicological profiles.

### 1.6.1 Hypotheses

Based on the aims of this work, it is hypothesised that:

1. ATI, ATII and AMs will be able to be successfully co-cultured at anatomically relevant ratios allowing PM and/or NO<sub>2</sub> exposures to be conducted at the air-liquid interface. The model will also be capable of mounting a pro-inflammatory response when challenged with a pro-inflammatory stimulus.
2. The VitroCell® Cloud will allow exposure to PM at environmentally relevant concentrations whereas a novel NO<sub>2</sub> exposure chamber will be able to maintain a set NO<sub>2</sub> concentration. These systems will be able to be used in tandem to allow PM and NO<sub>2</sub> co-exposures.
3. Exposure of the anatomically relevant triple cell co-culture to PM samples will cause a dose-dependent decrease in cell viability, and increase in IL6 and IL8 release.

Furthermore, it is hypothesised that there will be cell specific effects observed when comparing exposure of each cell type to PM, where ATII could be more prone to a loss of barrier function.

4. NO<sub>2</sub> will induce a pro-inflammatory and oxidative stress effect within the triple cell co-culture. Co-exposure of NO<sub>2</sub> with PM will further amplify these effects.
5. Co-exposure of NO<sub>2</sub> and PM will cause transcriptomic changes to the triple cell co-culture, increasing the number of differentially expressed genes compared to either single pollutant exposures.

## Chapter 2: Materials and Methods

---

This chapter gives details of materials and methods used across more than one data collection chapter. Any alterations made to the methods outlined in this chapter will be made clear in the methods sections of the subsequent data chapters (Chapters 4-7). **Figure 2.1** gives an overview of the experimental procedure to be carried out, where *in vitro* cultures will be exposed to  $\text{NO}_2 \pm \text{PM}$ , and various endpoint analyses will be undertaken, the methods of which will be discussed subsequently.

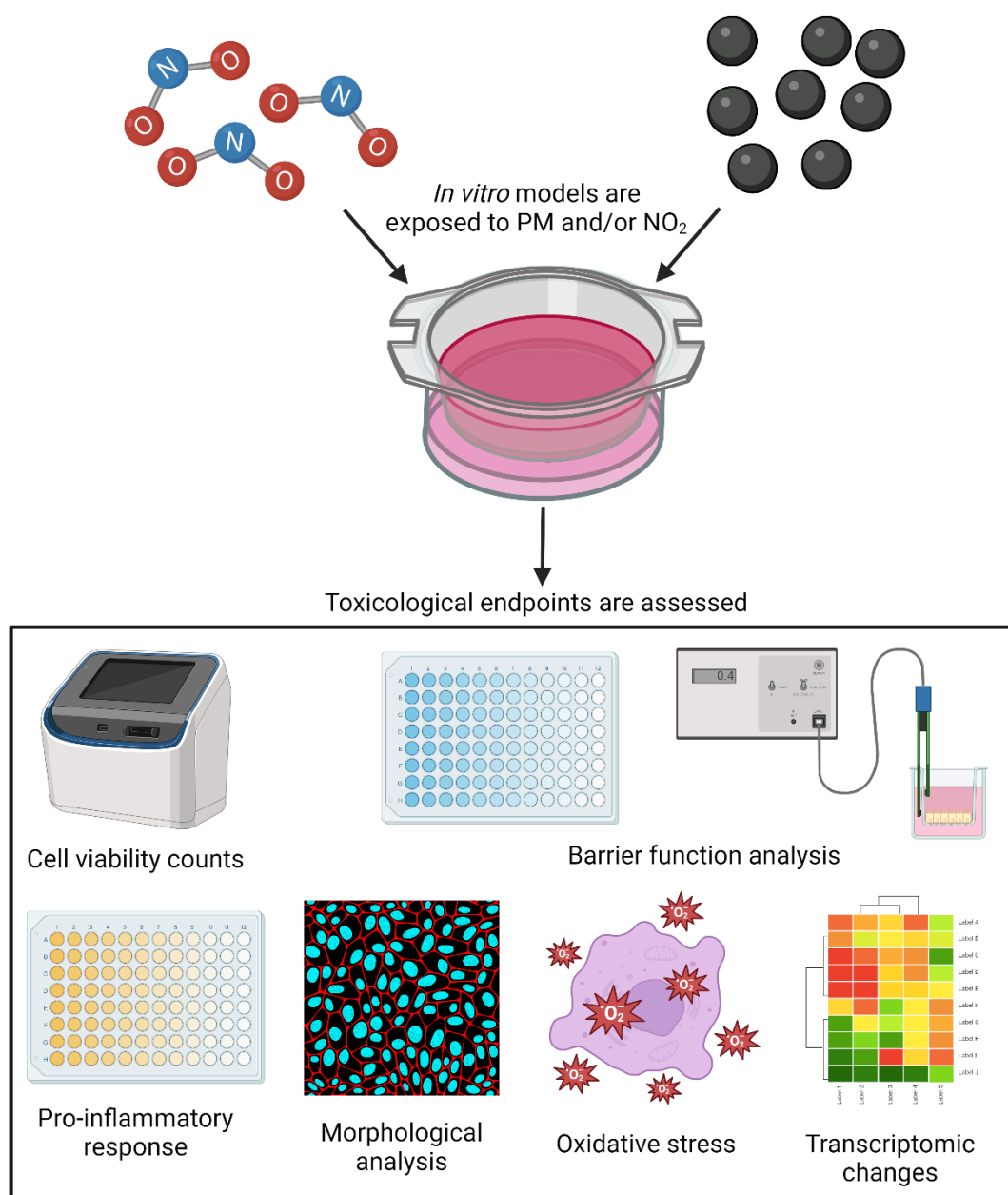


**Figure 2.1** An overview of the experimental methodology carried out within this work.



## 2.1 Materials, Chemicals, Reagents and Equipment

Unless otherwise specified, all chemicals and reagents were purchased from Sigma-Aldrich. **Table 2.1** identifies cell lines, materials, chemicals, reagents and equipment used within this work.

*Table 2.1 Cell lines, reagents, chemicals, kits and equipment used within this work.*

Chemical/Reagent	Supplier	Reference Number
<b>Cell Lines</b>		
hAELVi	InSCREENeX, Germany	INS-CL-1015
NCI-H441	ATCC, USA	TIB-202
THP-1	ATCC, USA	HTB-174
<b>Cell Culture</b>		
huAEC Medium	InSCREENeX, Germany	INS-ME-1013
huAEC Coating Solution	InSCREENeX, Germany	INS-SU-1018
huAEC Freezing Medium	InSCREENeX, Germany	INS-SU-1004
RPMI 1640 (for NCI-H441)	Gibco, UK	A1049-01
RPMI 1640 (for THP-1)	Gibco, UK	31870-025
Foetal Bovine Serum (Heat Inactivated)	Gibco, UK	16140071
L-Glutamine	Gibco, UK	25030-024
Penicillin/Streptomycin	Gibco, UK	15140-122
Trypsin-EDTA (0.05%) + Phenol Red	Gibco, UK	25300062
Accutase® Solution	Merck, UK	A6964
Bovine Serum Albumin	Merck, UK	A2153
Phorbol 12-Myristate 13-Acetate (PMA)	Merck, UK	P8239
Phosphate Buffered Saline (1X) (Sterile)	Gibco, UK	10010015
<b>Assay Kits</b>		
DC Protein Assay Kit	Bio-Rad, UK	500111
Interleukin-6 ELISA Kit	R&D Systems, UK	DY206
Interleukin-8 ELISA Kit	R&D Systems, UK	DY208
Tumour Necrosis Factor- $\alpha$ ELISA Kit	R&D Systems, UK	DY210
RNeasy® Mini Kit	QIAGEN, UK	74104
QIAshredder Columns	QIAGEN, UK	79656
iScript gDNA Clear cDNA Kit	Bio-Rad, UK	1725035
Deproteinization Sample Preparation Kit	Abcam, UK	ab204708
GSH/GSSG Ratio Detection Assay Kit	Abcam, UK	ab205811
<b>Chemicals</b>		

Blue Dextran	General Electrics	Y2-9MJ-17-0360-01
Mammalian Lysis Buffer (5X)	Abcam, UK	ab179835
Triton X-100	Merck, UK	X100PC
Paraformaldehyde	Merck, UK	158127
Glycine	Merck, UK	G7126
DPX	Thermo Fisher Scientific, UK	D/5330/05
Trizma Base	Merck, UK	T4661
Tween-20	Fisher Bioreagents, UK	BP337-100
Sodium Chloride	Fisher Chemical, UK	S/3120/63
Ethanol	Fisher Chemical, UK	E/640DF/17
PBS Tablets	VWR, UK	E404
Dimethylsulfoxide (DMSO)	Merck, UK	5.89569
Sulfuric Acid	Merck, UK	258105
SsoAdvanced Universal SYBR® Green Supermix	Bio-Rad, UK	1725274
RNase-Free Water	Invitrogen, UK	AM9930
Trypan Blue Solution (0.4%)	Gibco, UK	11538886
Lipopolysaccharide	Merck, UK	L4391
Recombinant tumour necrosis factor- $\alpha$	Bio-Techne, UK	NBP2-35076
<b>Antibodies and Fluorescent Probes</b>		
DAPI	Merck, UK	D9541
Alexa Fluor™ 633 Phalloidin	Invitrogen, UK	A22284
ZO-1 Monoclonal Antibody (ZO1-1A12)	Invitrogen, UK	33-9100
Recombinant Anti-CD11 $\beta$ Antibody (EPR1344)	Abcam, UK	Ab133357
Caveolin 1 Monoclonal Antibody (7C8)	Thermo Fisher Scientific, UK	MA3-600
Goat Anti-Mouse Alexa Fluor™ 488	Invitrogen, UK	A32723
Donkey Anti-Rabbit Alexa Fluor™ 555	Invitrogen, UK	A31572
CellTracker® Deep Red	Invitrogen, UK	C34565
CellTracker® Violet BMQC	Invitrogen, UK	C10094
<b>Equipment</b>		
12 Well Transwell Inserts	Falcon, UK	353181
12 Well Companion Plate	Falcon, UK	535503
T25 Cell Culture Flask	Greiner Bio-One, UK	690175
T75 Cell Culture Flask	Greiner Bio-One, UK	658175
T175 Cell Culture Flask	Greiner Bio-One, UK	660175
96 Well Plate	ThermoScientific, UK	442404
Black, Clear Bottom, 96 Well Plate	Invitrogen, UK	M33089
10 $\mu$ L Pipette Tips	TipOne Starlab, Germany	S1111-3810
200 $\mu$ L Pipette Tips	TipOne Starlab, Germany	S1111-1706

1000 µL Pipette Tips	TipOne Starlab, Germany	S1111-6701
5 mL Serological Pipettes	Greiner Bio-One, UK	606180
10 mL Serological Pipettes	Greiner Bio-One, UK	607180
25 mL Serological Pipettes	Greiner Bio-One, UK	760180
200 µL Centrifuge Tube	Fisher Scientific, UK	14230225
500 µL Centrifuge Tube	Fisher Scientific, UK	14230200
1.5 mL Centrifuge Tube	Greiner Bio-One, UK	616202
2 mL Centrifuge Tube	Eppendorf, UK	0030 123.344
15 mL Centrifuge Tube	Greiner Bio-One, UK	188271
50 mL Centrifuge Tube	Greiner Bio-One, UK	227261
Cryovials	Elkay Laboratory Products, UK	T311-2
Microscope Slides	RS France, France	BPB019
Cover Slips	Fisher Scientific, UK	11961988
Pasteur Pipettes	VWR, UK	617-4497
Blue Role	WypAll, UK	7225
Virkon	Lanxess, Germany	Rely+On
Centrifuge (Cell Culture)	VWR, UK	CT6E
Centrifuge	Eppendorf, UK	5415 D
Microcentrifuge	Smart Instruments	N/A
Sonicator	Branson, Ireland	550
Sonicator Probe	Branson, Ireland	102C
Scale (for PM samples)	Ohaus, Switzerland	EX125M
Scale (non-toxic)	Sartorius, Germany	R180 D
Scale (non-toxic)	Sartorius, Germany	TE3102s
Incubator	NuAire, UK	NU-5700
Class II Biological Safety Cabinet	Scanlaf, Denmark	N/A
Water Bath	Grant, UK	JBN18
Cell Culture Light Microscope	Zeiss, UK	40C
Confocal Microscope	Zeiss, UK	LSM 980
-80 °C Freezer	Haier Biomedical, UK	DW-86L728ST
LUNA II Automated Cell Counter	Logos Biosystem, France	L40002
LUNA II Reusable Slide	Logos Biosystem, France	L12011
Voltohmmeter (for TEER)	Merck, UK	ERS-2
Chopstick Electrode	Merck, UK	STX01
NanoPhotometer®	IMPLEN GmbH, Germany	NP80
PCR Plate	Bio-Rad, UK	E1403-0209-C
Microseals	Bio-Rad, UK	MSB1001
Scanning Electron Microscope	Hitachi, Germany	S-4800
VitroCell® Cloud 12	VitroCell®, Germany	N/A
Nebuliser (4-6 µm)	Aerogen, Germany	AG-AL1000
Nebuliser (12 µm)	Tekcelio, France	P&S T45
TEM Grids (400 Mesh, Carbon Coated)	Agar Scientific, UK	AGS160
Lacy Carbon TEM Grids (400 Mesh)	Agar Scientific, UK	AGS166
TEM Grid SEM Stub	EM-Tec, UL	12-000379

Bijous	Merck, UK	Z190519
Plate Reader (Absorbance)	Tecan, Switzerland	Sunrise
Plate Reader (Fluorescence)	BMG LabTech, Germany	FLUOstar Omega
Mini particle sampler	Ecomesure, France	N/A
GilAir Plus Pump	Sensidyne, USA	N/A
Inline Filter	Parker, USA	9922-11-BQ
Adapted Hypoxia Chamber	Coy, USA	N/A
NO <sub>2</sub> Analyser	Aeris, UK	AE2041U
Thermohygrometer	Traceable, USA	4800
Thermal Cycler	Bio-Rad, UK	T100
Real-Time qPCR Machine	Bio-Rad, UK	N/A

## 2.2 Cell Culture

This work utilised immortalised cell lines to allow higher throughput toxicological examination and to avoid donor-to-donor variability. Further, through the model produced in Chapter 3, the immortalised cell lines are intended to mirror human anatomy as accurately as possible. hAELVi cells (INS-CI-1015, passage 6) were purchased from InSCREENeX (Brunswick, Germany). NCI-H441 (HTB-174™, passage 50) and THP-1 (TIB-202™) cells were purchased from ATCC.

All cell culture work and all work required to take place under sterile conditions was conducted within a Class II laminar flow hood. Immediately before laminar flow hood use, all surfaces were cleaned with 70% ethanol. Approximately 30 minutes before use, cell culture medium and trypsin-EDTA were pre-warmed within a 37°C water bath before the bottles were decontaminated with 70% ethanol and put into the laminar flow hood. Any other equipment/reagent bottles used within cell culture were decontaminated with 70% ethanol before being placed inside a laminar flow hood to reduce cell contamination risk.

Cell cultures were stored within a 37°C, humidified, 5% CO<sub>2</sub> incubator. Cells were checked daily for functionality, confluence and contamination using an Axiovert light microscope.

### 2.2.1 hAELVi Cell Culture

#### 2.2.1.1 hAELVi Cell Introduction

hAELVi cells were used as a model cell for alveolar type 1 cells. ATI cells cover the majority of the alveolar epithelial surface and are responsible for forming a tight

barrier and facilitating gaseous exchange (Kuehn et al., 2016). Previous *in vitro* inhalation toxicological work has often used alveolar models comprising cell lines with an ATII-like phenotype, such as A549 cells. Recent work, however, has focused on the more prevalent ATI cells, using cell lines such as transformed type 1 cells (Mitchell, 2022) or hAELVi cells (Kuehn et al., 2016).

hAELVi cells were isolated and immortalised from alveolar cells from patients undergoing lung tumour resection and shown to possess tight junctions and can form a tight barrier when grown at the ALI (Kuehn et al., 2016), making them ideal to use within the present work. Further, real-time PCR has demonstrated that hAELVi cells possess ATI markers, such as the expression of caveolin-1 and the absence of surfactant protein C (Kuehn et al., 2016).

#### **2.2.1.2 hAELVi Cell Culture and Passage**

All cell culture techniques took place under sterile conditions. hAELVi cells were cultured in huAEC medium containing 10% huAEC supplements (provided by the supplier) and 1% penicillin (100 µg/ml) / 1% streptomycin (100 µg/ml). Before seeding hAELVi cells, the receiving flask/plate was coated in huAEC coating solution and placed in a tissue culture incubator for a minimum of 2 hours, up to overnight. The coated flasks/plates were then washed with PBS and could then be stored for up to a week at 4 °C before adding hAELVi cells.

Cell culture was started by thawing hAELVi cells (passage number 6) from liquid nitrogen storage. A single cryovial containing the cryopreserved hAELVi cells was quickly thawed in a 37°C water bath until only a few ice crystals were visible. The vial was disinfected using 70% ethanol and transferred to the laminar flow hood. The thawed cell suspension was transferred to a 15 ml tube containing 4 ml pre-warmed cell culture media. This suspension of cells was centrifuged at 200 RCF for 4 minutes. The supernatant was discarded, and the cell pellet was resuspended in 1 mL cell culture media. This suspension was transferred to a pre-coated T25 cell culture flask containing 4 mL pre-warmed cell culture media, checked for the presence of cells using a light microscope and placed into a cell culture incubator. Cell culture media was replaced every 48-72 hours. Once cells were 70-90% confluent, cells were transferred to a T75 flask with 15 mL media to continue culturing of cells.

To subculture hAELVi cells, media was discarded, and the flask was washed with PBS. PBS was discarded, and 2 mL trypsin-EDTA was added to the flask, which was incubated for 5-10 minutes until cells had detached (detachment of cells from the surface of the flask was confirmed *via* light microscopy). Media (3 mL) was added to the flask, mixed, and transferred to a 15 mL centrifuge tube. Generally, when subculturing, the split ratio was 1:5, whereby 1 ml of the cell suspension was transferred to a new, pre-coated T75 flask containing 14 mL pre-warmed cell culture media.

### **2.2.1.3 Cryopreservation of hAELVi Cells**

To cryopreserve hAELVi cells, they were grown to 90% confluency. The media was discarded, and the flask was washed with PBS. Cells were detached from the flask using 2 ml trypsin-EDTA for 5-10 minutes and were ensured to have detached *via* light microscopy. Cells were resuspended in 8 ml of a 2% FBS in PBS solution and transferred to a 15 mL centrifuge tube. The cell suspension was centrifuged at 200 RCF for 4 minutes. The supernatant was discarded, and the pellet was resuspended in huAEC freezing medium to a  $1 \times 10^6$  cell/mL solution. The suspension was transferred to cryovials (1 mL per vial), and cryovials were placed into a cryopreservation chamber, which was placed into a -80 °C freezer for 24 hours. The cryovials were then transferred to liquid nitrogen for long-term storage. Stored vials were between cell passages 8 and 15.

### **2.2.2 NCI-H441 Cell Culture**

#### **2.2.2.1 NCI-H441 Cell Introduction**

Often, A549 cells are used as a model of ATII cells, though A549 do not possess the ability to form strong barriers as would be expected in healthy physiology as they lack tight junctions (Ren et al., 2016). NCI-H441 cells were derived from the pericardial fluid of a patient with lung papillary adenocarcinoma in 1982 (ATCC, 2024a). NCI-H441 express tight junction proteins ZO-1 and e-cadherin and can form a tight barrier at the ALI, making them a valuable model for exposure studies (Salomon et al., 2014). Although not as strong as the hAELVi cells, the NCI-H441 barrier properties are enhanced compared to A549, with TEER values of over 1000, 529, and 28  $\Omega \cdot \text{cm}^2$ , respectively (Kuehn et al., 2016; Ren et al., 2016). Further, NCI-H441 cells express

surfactant proteins A, B, C and D, as would be expected by ATII in ‘normal’ physiology (Schiefermeier-Mach et al., 2023).

#### **2.2.2.2 NCI-H441 Cell Culture and Passage**

All cell culture techniques took place under sterile conditions. NCI-H441 cells were cultured in RPMI 1640 cell culture media containing D-glucose, (4.5 g/L), HEPES buffer (2.3383 g/L), L-glutamine (1%), sodium bicarbonate (1.5 g/L) and sodium pyruvate (110 mg/L). The media was additionally supplemented with foetal bovine serum (FBS) (10%) and 1% penicillin (100 µg/ml) / 1% streptomycin (100 µg/ml).

NCI-H441 cell culture was started by thawing cells from long-term liquid nitrogen storage by placing a vial in a 37°C water bath. Once defrosted, the cell suspension from the vial was pipetted into a 15 mL centrifuge tube containing 9 mL of pre-warmed complete cell culture media and centrifuged at 340 RCF for 5 minutes. The supernatant was discarded, and the cell pellet was resuspended in a 1 mL complete media. The cell suspension was then added to a T75 flask containing 10 mL of complete cell culture media. The presence of cells within the flask was confirmed *via* light microscopy, and the flask was placed into a humidified cell culture incubator at 37 °C, 5% CO<sub>2</sub>. Routinely (every 48-72 hours), the media was aspirated from the flask, and the remaining media was removed by washing with 7 mL PBS and replaced with 10 mL fresh cell culture media. This would occur until the cells reached 80% confluency and required passaging.

To passage NCI-H441, all media was aspirated from the flask, and the flask was washed with 7 mL PBS. PBS was removed, and 4 mL of trypsin-EDTA was added to the flask. The flask was placed into the incubator for approximately 5 minutes so that the cells could detach from the surface of the flask. Cell detachment was confirmed through light microscopy. Cells were washed down with 6 mL of complete media, and the cell suspension was transferred to a 15 mL centrifuge tube and centrifuged at 340 RCF for 5 minutes. Following this, the supernatant was discarded from the tube, and the cell pellet was resuspended in 1 mL of complete media. Flasks were split at a ratio of 1:3 into new T75 flasks, with the presence of cells being confirmed *via* light microscopy before being put into the incubator. NCI-H441 passages were kept within the range of 4-30 for the duration of this work.

### **2.2.2.3 Cryopreservation of NCI-H441 Cells**

NCI-H441 freezing media was made by adding 5% (v/v) (dimethylsulfoxide) DMSO to complete cell culture media. To cryopreserve cells, the cell passaging protocol was followed to the point that the cells were pelleted in the centrifuge tube; however, here, cells were diluted to  $1 \times 10^6$  cell/mL using freezing medium. Each cryovial received 1 mL of cell suspension and was then placed into a cryopreservation chamber, which was stored at -80 °C for 24 hours. The cryovials were then transferred to liquid nitrogen for long-term storage.

### **2.2.3 THP-1 Cell Culture**

THP-1 cells are a monocytic cell line derived from the blood of a patient with leukaemia (ATCC, 2024b) and are often used in immunological studies. Although kept as monocytic THP-1 cells when within general cell culture, THP-1 cells were differentiated into a macrophage-like phenotype before use at the ALI in alveolar models (Section 2.2.3.3).

#### **2.2.3.1 THP-1 Cell Culture and Passage**

THP-1 cells were stored in liquid nitrogen until required for use. All cell culture techniques took place under sterile conditions. THP-1 cells were cultured in RPMI 1640 cell culture media supplemented with foetal bovine serum (FBS) (10%), L-glutamine (1%) and 1% penicillin (100 µg/ml) / 1% streptomycin (100 µg/ml).

THP-1 cell culture was started by thawing cells from long-term liquid nitrogen storage by placing a vial in a 37 °C water bath. Once defrosted, the cell suspension from the vial was pipetted into a 15 mL centrifuge tube containing 9 mL of pre-warmed complete cell culture media and centrifuged at 340 RCF for 5 minutes. The supernatant was discarded, and the cell pellet was resuspended in 1 mL complete media. The cell suspension was then added to a T75 flask containing 14 mL of complete cell culture media. The presence of cells within the flask was confirmed *via* light microscopy, and the flask was placed into a humidified cell culture incubator at 37 °C, 5% CO<sub>2</sub>. Routinely (every 48-72 hours), cell culture media was replenished by transferring cell suspension from the flask to a 15 mL centrifuge tube and centrifuging at 340 RCF for



5 minutes. The supernatant was removed, and the cell pellet was resuspended in 15 mL of fresh media and transferred back to the T75 flask.

To passage, the above media change process was followed. However, the pellet was resuspended in 5 mL of cell culture media, and the cells were counted using a LUNA II Automated Cell Counter. The cells were seeded into new T75 flasks at a concentration of  $2 \times 10^5$  cell/mL and were used within a passage range of 4-30 for this work.

#### **2.2.3.2 Cryopreservation of THP-1 Cells**

THP-1 freezing media was made by adding 5% (v/v) DMSO to complete cell culture media. To cryopreserve cells, the cell passaging protocol was followed to the point that the cells were pelleted in the centrifuge tube; however, here, cells were diluted to  $1 \times 10^6$  cell/mL using freezing medium. Cell suspension (1 mL) was then added to cryovials. The cryovials were placed into a cryopreservation chamber, which was placed in a  $-70^\circ\text{C}$  freezer for 24 hours. The cryovials were then transferred to liquid nitrogen for long-term storage.

#### **2.2.3.3 Differentiation of THP-1 Cells into Macrophages (dTHP-1)**

Prior to use within exposure studies THP-1 were differentiated into a macrophage-like phenotype using phorbol 12-myristate 13-acetate (PMA) (Meldrum et al., 2020). Exposing THP-1 to PMA before allowing a recovery period from PMA has been found to increase macrophage markers and has, therefore, been implemented within the following protocol. Risby (2022) previously optimised the following protocol within the laboratory.

To differentiate THP-1 to dTHP-1, the THP-1 passage protocol was followed (Section 2.2.3.1); however, THP-1 cells were seeded into T75 flasks at a concentration of  $1 \times 10^5$  cell/mL (15 mL total). PMA was stored in 100  $\mu\text{L}$  aliquots at a concentration of 10  $\mu\text{M}$  (dissolved in DMSO) at  $-20^\circ\text{C}$ . The working concentration of PMA was 20 nM. Therefore, 30  $\mu\text{L}$  of PMA was added to a T75 flask of THP-1 cells. Flasks containing THP-1 cells and PMA were kept inside a tissue culture incubator.

THP-1 cells were allowed 48 hours to differentiate, where they were then checked for adherence *via* light microscopy, which would confirm a macrophage-like phenotype.

The PMA-containing media was discarded from these flasks and replaced with complete THP-1 cell culture media (without PMA). Flasks were left inside a tissue culture incubator for 24 hours before they were ready to be added to epithelial cell cultures.

To add to an epithelial cell culture, the media was aspirated from the flask containing the dTHP-1 cells. The flask was washed with PBS, and 4 mL of accutase was added. The flask was placed inside a tissue culture incubator to allow dTHP-1 to detach. The flask was checked for adherence every 5-10 minutes. If the cells were not detaching, the flask was gently tapped by hand to assist in detachment. Once detached, the cell suspension was made up to 10 mL by adding 6 mL of cell culture media and transferred to a 15 mL centrifuge tube. This was centrifuged at 340 RCF for 5 minutes. The supernatant was discarded, the pellet resuspended in 1 mL cell culture media, and cells were counted using the LUNA II automated cell counter. The dTHP-1 cells were then diluted to concentration (dTHP-1 seeding concentrations are discussed in Chapter 3) using cell culture media.

## 2.3 Cell Counts and Viability

Throughout this work, the ability to assess cell viability and count the number of cells in a given cell suspension was vital. This included when calculating seeding

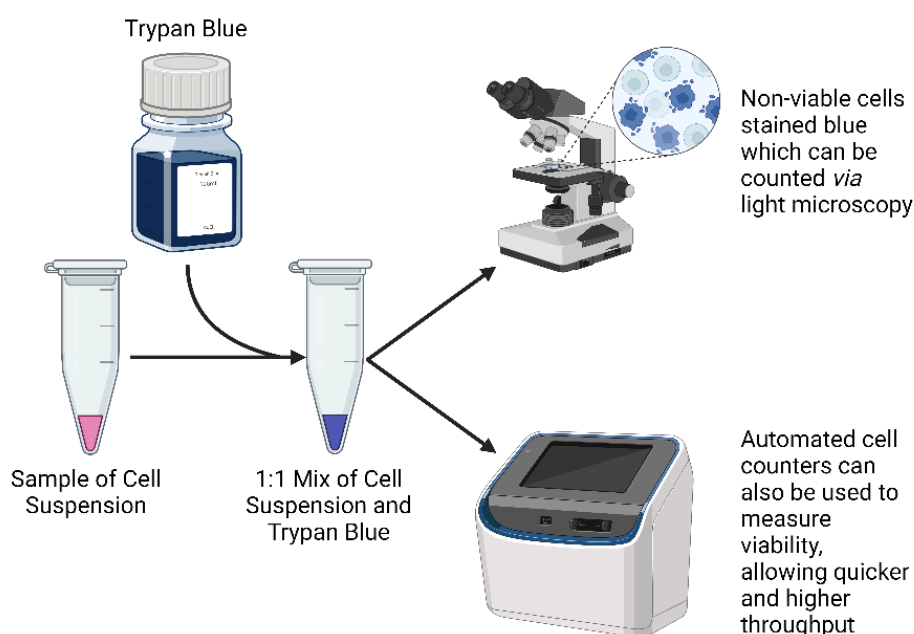


**Figure 2.2** Trypan blue is added to a sample of cell suspension in a 1:1 ratio. Non-viable cells take up the blue dye and appear blue compared to the lighter viable cells. Live and dead cell populations can then be quantified either manually by light microscopy, or automatically using the LUNA II.

concentration for experiments or for use as an endpoint to detect cell viability. Viability was assessed through trypan blue exclusion assay (**Table 2.2**). Trypan blue is a dye absorbed into the cytoplasm of non-viable cells due to non-viable cells' lack of membrane integrity. Conversely, live cells with intact membranes do not uptake the dye (Avelar-Freitas et al., 2014). Light microscopy can then be used to distinguish viable and non-viable cells by counting white or blue cell populations, respectively (**Figure 2.2**).

To perform the trypan blue assay, an aliquot of cell suspension was mixed 1:1 with 0.4% trypan blue. Viability was assessed using a LUNA II automated cell counter. LUNA II settings are displayed in **Table 2.2**. As a cell viability positive control, cell cultures had their media aspirated and were exposed to an environment of -80°C before cells were detached using trypsin-EDTA and mixed with trypan blue solution.

LUNA II reports the following parameters: raw total cell count, raw viable cell count, raw non-viable cell count, total cell/mL, viable cell/mL, non-viable cell/mL, viability percentage and average cell size. Flagging was checked to ensure the chosen setting encompassed all visible cells and classified them correctly (**Figure 2.3**).

**Table 2.2** Settings used on LUNA II to count cells and analyse viability.

Setting	Value
Dilution Factor	2
Noise Reduction	5
Live Cell Sensitivity	1
Roundness	60
Minimum Cell Size	10
Maximum Cell Size	30
Declustering Level	Medium

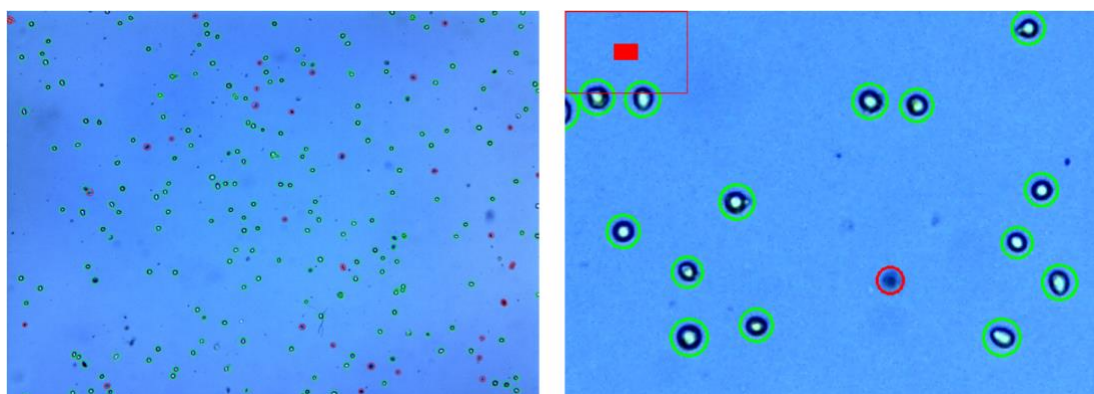


**Figure 2.3** Example of flagging of viable/non-viable cells using LUNA II as determined by settings outlined in Table 1. Green circles indicate viable cells whereas red circles indicate non-viable cells.

## 2.4 Seeding onto Transwell Inserts

hAELVi, NCI-H441 and dTHP-1 cells were seeded onto polyethene terephthalate 12 well transwell inserts possessing 3  $\mu\text{m}$  pores, which were placed within insert companion plates. Before seeding, cell suspensions were counted using the LUNA II (Section 2.3) and diluted to the required density. Within each basal well, 1.5 mL of media was added, with 500  $\mu\text{L}$  of epithelial cell suspension added to the apical insert. Cells growing within transwell inserts were routinely checked for functionality, confluency, and contamination *via* light microscopy. After 72 hours, basal media was removed and replaced with 1.5 mL fresh cell culture media. Cells were also taken to ALI at this time point by directly aspirating and discarding the apical media. If dTHP-1 cells were implemented within the culture, 100  $\mu\text{L}$  of dTHP-1 suspension was added to the apical well and allowed 2 hours for the dTHP-1 cells to adhere. After allowing for cell adherence, apical media was then aspirated to take the cultures to the ALI. Seeding densities of each cell type used are characterised and discussed in Chapter 3. Once the cultures had been at the ALI for 24 hours, they were ready for exposure, the characterisation of which is described in Chapter 4.

## 2.5 Immunocytochemistry and Confocal Microscopy

Assessing cellular morphology allows a qualitative understanding of cell stress, cell-cell interactions, monolayer formation, and barrier function (S. Chen et al., 2012). Further, immunolabelling of proteins of interest allows them to be visualised, either in fixed or live cells, by fluorescent or confocal microscopy. This allows specific morphological or protein localisation/co-localisation changes in response to stimuli to be established (**Figure 2.4**). Within this work, cells were fixed at the end of the pollutant exposure duration using 3% paraformaldehyde (PFA) diluted in 1X PBS. PFA covalently crosslinks biological molecules (Irgen-Gioro et al., 2022), essentially freezing the cell at that point in time, allowing the cells to be subsequently permeabilised and intracellular proteins stained with fluorophores *via* direct or indirect fluorescence.

### 2.5.1 Sample Fixation and Storage

Cell culture supernatant was removed from both the apical and basal compartments of the transwell insert, and each was washed with 1 mL PBS three times. Cells were then

fixed by adding 1 mL of 3% PFA to the apical and basal compartments for 15 minutes. The PFA was removed, and wells were washed three times with PBS. Wells were then stored for future use by adding 1 mL glycine (0.1 M) to the basal and apical compartments to quench PFA activity (Hoffman et al., 2015), and stored at 4°C for up to 1 month before immunostaining.

### **2.5.2 Immunocytochemistry**

Glycine was removed from the stored wells, and wells were washed three times with 1 mL PBS to both the apical and basal compartments. The insert membrane was cut out from the plastic scaffold and placed cell side up in wells of a 12-well plate. Cells were then permeabilised by adding 1 ml 0.2% Triton X-100 (diluted in 1X PBS) to the insert membranes for 15 minutes. Following this, cells were again washed three times with PBS (1 mL for each membrane) before being blocked with 1% BSA diluted in 1X PBS (1 ml for each membrane) for one hour. Wells were again washed 3 times with PBS. Primary antibodies were added next by adding a 10 µL drop of primary antibody(s) diluted in 1% BSA in PBS to the surface of a piece of parafilm. The insert membrane was then placed onto the drop, cell side down, and then 10 µL of primary antibody solution was pipetted on top of the insert membrane. This was incubated at room temperature for 1 hour. The membranes were then transferred back to the 12-well plate and were washed three times with PBS.

The secondary antibody, as well as DAPI and phalloidin fluorescent stains, were next added. Secondary antibodies, phalloidin (1:100) and DAPI (1:100), were diluted to working concentration in 1% BSA. With the same method as the primary antibody, transwell membranes were placed into a 10 µL drop of secondary antibody(s) on the surface of a piece of parafilm. An additional 10 µL of antibody solution was added on top of the insert membrane and incubated at room temperature for 1 hour. The membranes were then transferred back to the 12-well plate and washed with PBS three times before being placed cell side up on labelled microscope slides. A drop of DPX mounting medium was added on top of each membrane, and a coverslip was added

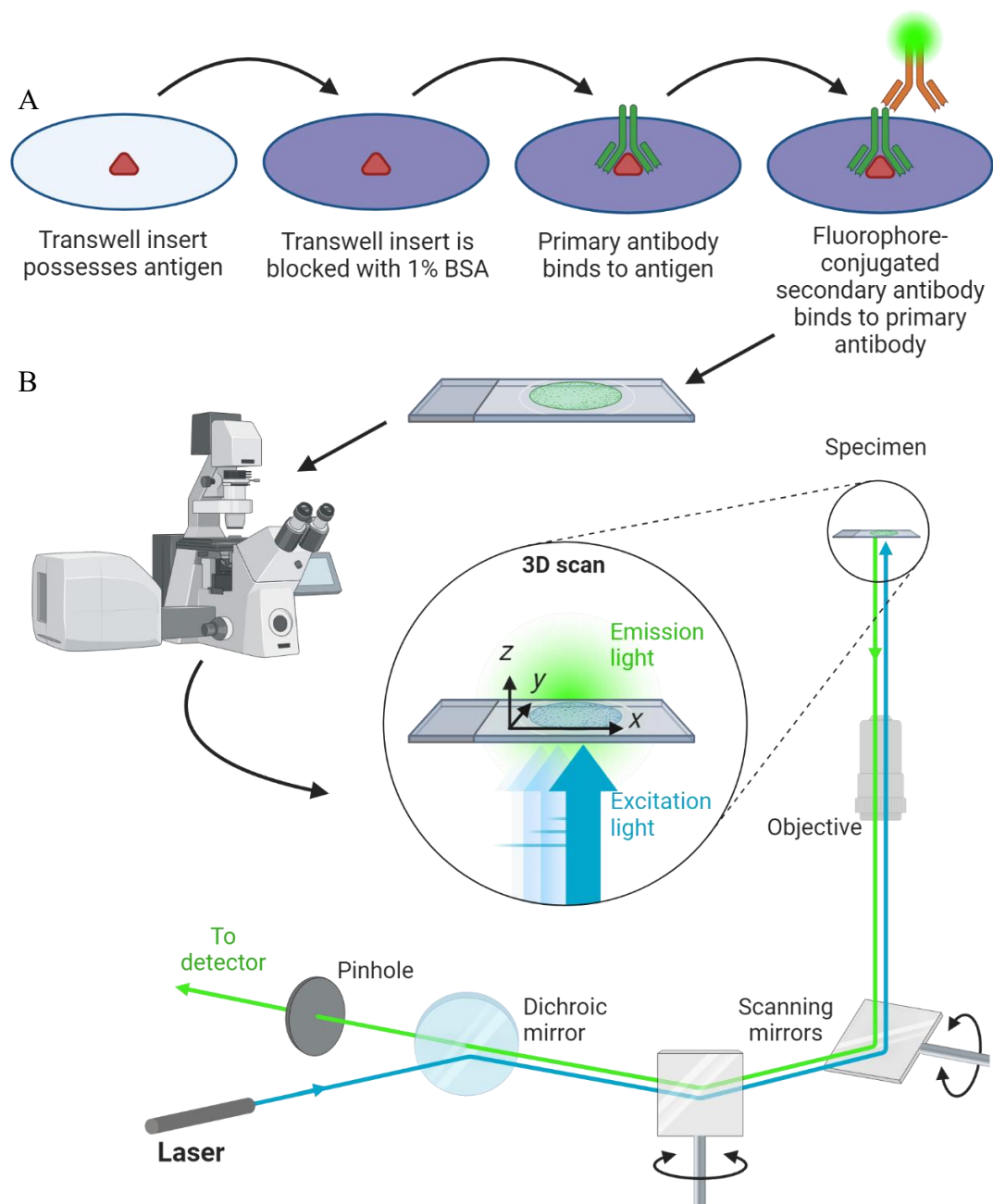


**Figure 2.4** (A) Method for indirect staining of antigens (proteins of interest) on transwell inserts. The primary antibody binds to the antigen, then the primary antibody is bound by a secondary antibody that is reactive against the species in which the primary antibody was raised in. The secondary antibody is also conjugated to a fluorophore allowing excitation at a specific wavelength. (B) lasers of different wavelengths within the laser scanning confocal microscope can excite these fluorophores, causing fluorescence. This fluorescence is measured by a detector allowing an image to be generated.

and gently pressed down. The DPX was allowed overnight to harden before the slides were stored and protected from light at 4°C (**Figure 2.4A**).

If staining with only DAPI and phalloidin (*i.e.*, antibodies were not used), the above protocol was followed where cells were permeabilised with Triton X-100, but the cells were not blocked with 1% BSA. Instead, DAPI (1:1000) and phalloidin (1:100) were diluted in 1X PBS, and a 10 µL drop was placed on the surface of a piece of parafilm.

The insert membrane was then placed cell side down in this drop, and 10  $\mu$ L of DAPI and phalloidin solution was added to the top of the membrane. This was then incubated at room temperature for an hour before being transferred to a 12-well plate and washed with PBS three times. The inserts were then mounted to the slides as above.

**Table 2.3** shows the primary and secondary antibody combinations and concentrations used.

*Table 2.3 Primary antibodies used within this work. The respective secondary antibody used in conjunction is shown adjacent.*

Target	Primary				Secondary				
	Host	Concentration	Supplier	Reference	Host	Reactivity	Conjugate	Concentration	Supplier
Caveolin-1	Mouse	1:100	Thermo Fisher Scientific	MA3-600	Goat	Mouse	Alexa Fluor 488	1:100	Invitrogen
ZO-1	Mouse	1:100	Abcam	ab133357	Goat	Mouse	Alexa Fluor 488	1:100	Invitrogen
CD11 $\beta$	Rabbit	1:1000	Invitrogen	33-9100	Donkey	Rabbit	Alexa Fluor 555	1:100	Invitrogen

### 2.5.3 Confocal Imaging

Fluorescently labelled slides were imaged on a Zeiss LSM 980 equipped with x10, x20, x40 and x63 objective lenses and 405, 445, 488, 514, 561 and 639 nm lasers. For each experiment, laser power and gain were set when imaging the incubator control, and settings were kept for the rest of the imaging to allow comparison of fluorescent intensity. Over/underexposure was checked using the ‘range indicator’ function of the Zen Blue software. Single-slice images were captured at 1024 x 1024 or 2048 x 2048 resolution with 16-line averaging. Z-stacks were captured at 512 x 512 resolution with 8-line averaging (**Figure 2.4B**).

## 2.6 Barrier Integrity

### 2.6.1 Blue Dextran

Blue dextran is a polymer of anhydroglucose containing a blue dye. Due to blue dextrans’ ability to travel paracellularly, it was used to assay the barrier integrity of cell cultures grown within transwell inserts in this instance. By placing blue dextran into the apical transwell, the movement of blue dextran into the basal well could be quantified, indicating the level of barrier integrity (**Figure 2.5**).

Basal media was removed and replaced with 1 mL of fresh media to do this. If present, media was removed from the apical insert (not required if cells are at ALI), and 250  $\mu$ L blue dextran (2000 kDa) was added to the apical insert. Cells were then incubated for 2 hours.

Following this, 200  $\mu$ L of basal media was transferred to wells of a 96-well plate (3 technical repeats for each transwell). The absorbance of the plate was then read using a Tecan Sunrise plate reader at 600 nm. Transwell inserts containing no cells, or cell cultures treated with EDTA (for as long as needed for cells to round but not detach) were used as positive controls.

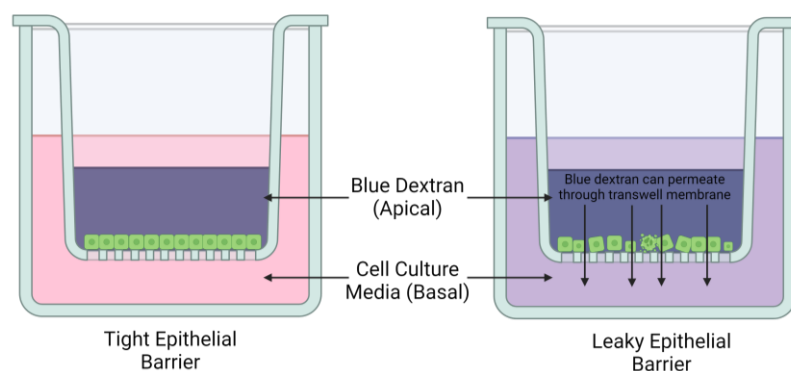


**Figure 2.5** Blue dextran is added to the apical compartment of the transwell insert and allowed 2 hours to permeate through the insert membrane. Cultures with a reduced barrier function will allow more dye through to the basal compartment, turning it blue. This can then be quantified with a plate reader.

## 2.7 Pro-Inflammatory Response

Inflammation is a well-established marker of several morbidities related to air pollution exposure, such as COPD (El-Shimy et al., 2014) and asthma (Murdoch & Lloyd, 2010). Studying the production of pro-inflammatory mediators *in vitro*, therefore, proves invaluable for assessing inhalation toxicological hazards. Within this work, TNF- $\alpha$ , IL6 and IL8 were measured. The role these pro-inflammatory mediators play in airway toxicology is discussed in Section 1.3.2.4.

As pro-inflammatory positive controls, cultures were treated with LPS (1  $\mu$ g/mL) if dTHP-1 cells were present in the culture, or if no dTHP-1 cells were present, then recombinant TNF $\alpha$  (1  $\mu$ g/mL) was instead used. This was done by adding LPS/TNF $\alpha$  to the basal media.



Sandwich enzyme-linked immunosorbent assays (ELISAs) were performed on supernatants collected from cell cultures (**Figure 2.6**). The supernatants were collected and stored at -20°C before being used in the ELISA. If the samples exceeded the concentration of the standards, the samples were diluted in 1:10 in reagent diluent.

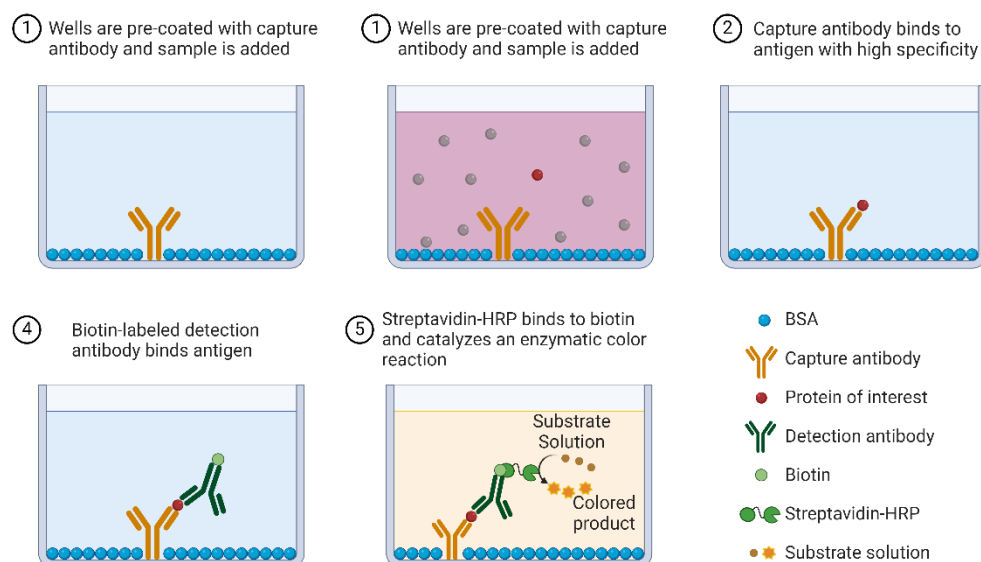


**Figure 2.6** Schematic describing the molecular basis behind the sandwich ELISAs performed within this work.

**Table 2.4** Reagents used in IL6, IL8 and TNF $\alpha$  ELISAs

Reagent	Composition
Wash Buffer	0.05% Tween® 20 in PBS
Block Buffer	1% BSA in PBS
IL6/TNF $\alpha$ Reagent Diluent	1% BSA in PBS
IL8 Reagent Diluent	0.1% BSA, 0.05% Tween® 20 in Tris-buffered Saline (20 mM Trizma base, 150 mM NaCl in water)
Streptavidin-HRP	Streptavidin conjugated to horseradish-peroxidase (included in ELISA kit), diluted in reagent diluent
Substrate Solution	1:1 mixture of H <sub>2</sub> O <sub>2</sub> (colour reagent A) and tetramethylbenzidine (colour reagent B) (R&D Systems)
Stop Solution	2N H <sub>2</sub> SO <sub>4</sub> in water

### 2.7.1.1 Interleukin-6 ELISA

IL6 release was measured using a Human IL-6 DuoSet ELISA kit (R & D Systems, USA) where the product instructions were followed, although half area 96-well plates were used, so the volume of each reagent was reduced by half. Briefly, the 96-well plate was coated using IL6 capture antibody diluted to concentration in PBS. This was left overnight before the plate was washed 3 times in wash buffer (**Table 2.4**). The plates were then blocked using block buffer (**Table 2.4**) for at least 1 hour. The plates were again washed 3 times with wash buffer before 50  $\mu$ L of IL6 standard (diluted in IL6 reagent diluent (**Table 2.4**)), or supernatant sample was added to the required

wells. If required, samples were diluted using IL6 reagent diluent. This was then incubated for 2 hours at room temperature. Plates were washed 3 times with wash buffer before 50  $\mu$ L of biotinylated IL6 detection antibody diluted in IL6 reagent diluent was added to each well. This was allowed to incubate for 2 hours at room temperature. The wells were washed with wash buffer before 50  $\mu$ L of a working concentration of streptavidin-HRP (diluted in IL6 reagent diluent) was added to each well and allowed to incubate at room temperature for 20 minutes. Wells were again washed with wash buffer before 50  $\mu$ L of substrate solution was added to each well. A colour change from colourless to blue occurred, the intensity of which was dictated by the IL6 concentration. This was allowed to incubate at room temperature for 20 minutes before 25  $\mu$ L of stop solution was added to each well (**Table 2.4**). The plate was tapped to mix, and the optical density was read on a FLUOstar Omega Plate Reader at a wavelength of 450 nm. Four parameter logistical curves were generated from the standards of each plate and used to calculate the IL6 concentration of the samples. The lower limit of detection for the IL6 ELISA was 9.38 pg/mL.

#### **2.7.1.2 Interleukin-8 ELISA**

IL8 release was measured using a Human IL8/CXCL8 DuoSet ELISA kit (R & D Systems, USA), and the product instructions were followed. IL8 ELISA protocol was the same as the IL6 ELISA (Section 2.7.1.1), although the IL8 ELISA had a different reagent diluent, capture antibody and detection antibody (**Table 2.4**). The lower limit of detection for the IL8 ELISA was 31.3 pg/mL.

#### **2.7.1.3 TNF- $\alpha$ ELISA**

TNF $\alpha$  release was measured using the Human TNF- $\alpha$  DuoSet ELISA kit (R & D Systems, USA), where the product instructions were followed. TNF $\alpha$  ELISA protocol was the same as the IL6 ELISA (Section 2.7.1.1), although the TNF $\alpha$  ELISA had a different capture antibody and detection antibody (**Table 2.4**). The lower limit of detection for the TNF- $\alpha$  ELISA was 15.6 pg/mL (as indicated by the manufacturer), although lower concentrations of standards were used if necessary.

## **2.8 Data and Statistical Analysis**

Raw data was initially recorded in Microsoft Excel and was transferred to GraphPad Prism (Version 10.1.1) (USA) for data and statistical analysis. Generally, statistical significance for pollutant exposure studies utilised one-way ANOVAs, although the details of specific statistical analyses will be outlined within the methods section of subsequent chapters. Normality was assessed *via* a Shapiro-Wilk test in GraphPad Prism.

Graphs and other data visualisations were produced in GraphPad Prism (Version 10.1.1) unless otherwise stated within the methods section of subsequent chapters.

Confocal microscopy images were analysed using Zen Blue (Version 3.3) (Carl Zeiss, UK).

## **Chapter 3: Development and Characterisation of an *In Vitro* Alveolar Barrier Model**

---

### 3.1 Introduction

As discussed in Chapter 1, the alveoli are a primary location exposed to air pollutants, specifically, the alveolar epithelial barrier, which can be targetted by both PM and NO<sub>2</sub> (Brunekreef & Holgate, 2002; Müller et al., 1998).

Historically, *in vivo* approaches, especially those involving the use of rodent models, have been a critical methodology in inhalation toxicological studies. However, the use of such models does come with drawbacks. Firstly, the ethical consideration of *in vivo* studies must be acknowledged, and as such, their use must be justified. Within the EU, for example, cosmetic testing on animals has been banned since 2004 (European Union, 2009), whilst groups such as People for the Ethical Treatment of Animals (PETA) are striving to broaden the ban to many other areas, such as chemical and drug testing. Other groups, such as NC3Rs, aim to improve the ethical framework surrounding *in vivo* studies, with explicit emphasis on the replacement, reduction, and refinement of animal testing. Secondly, there are significant differences between the lungs of a human compared to the lungs of a rodent. Anatomically, the lungs vastly differ. For example, human lungs possess 23 branching generations, whereas mouse lungs possess 16, altering the deposited fraction of PM at the alveolar level. Further, the histological composition of a rodent lung differs in terms of its cell ratios and cell types compared to a human lung (Faber & McCullough, 2018; Moura et al., 2023).

In line with the ‘replacement’ portion of the 3Rs, *in vitro* models could be implemented within air pollution exposure studies, providing data that can be extrapolated to real-life human exposures (Dvorak et al., 2011). To allow this, however, there is the requirement that these *in vitro* models accurately represent the tissue which they intend to represent. This can be done firstly through the use of co-culture models, compared to monoculture models. Co-culture models allow numerous cell types to be cultured within the same system, resembling the cellular components that would be present within an *in vivo* system. Cells pertinent to the alveolar epithelial barrier include ATI, ATII and AMs, and therefore, could be co-cultured to produce a relevant model for the toxicological assessment of inhaled pollutants. Further, culturing these cells at the air-liquid interface has been shown to push airway cells towards a phenotype more applicable to *in vivo* conditions than submerged cultures (de Jong et al., 1994). The Guidance Document on Good *In Vitro* Method Practices (GIVIMP) gives information

on Good Cell Culture Practice (GCCP) and has specific guidance for cultures that are used at the ALI, *i.e.*, lung, eye and skin models, as well as exposure methods specific to inhalation toxicology (OECD, 2018), and will therefore be adhered to in this chapter.

This chapter describes the development of an alveolar triple cell co-culture to implement within PM  $\pm$  NO<sub>2</sub> co-exposure studies within subsequent chapters. hAELVi, NCI-H441 and dTHP-1 cells will be used as ATI, ATII and AMs, respectively. Previously, hAELVi and NCI-H441 were used in co-culture, although the respective cell ratios were not discussed (Brookes et al., 2021). dTHP-1 cells have also been used within alveolar co-cultures previously, altering the pro-inflammatory response (Meldrum, Evans, et al., 2022).

### **3.1.1 Aims and Objectives**

This chapter aims to characterise and develop an *in vitro* alveolar triple cell-co-culture that will be subsequently implicated within PM  $\pm$  NO<sub>2</sub> co-exposures. To achieve this, a number of objectives will be fulfilled:

1. hAELVi cells will be characterised in terms of their growth, viability, barrier function, morphology and pro-inflammatory response in both submerged and ALI conditions.
2. A co-culture of hAELVi and NCI-H441 cells will be characterised to ensure that an anatomically relevant ratio of each cell type are present within the co-culture.
3. An assessment of the number of dTHP-1 within the triple cell co-culture will be undertaken again to ensure relevance to the anatomy of the human lung. The functionality of the culture will then be assessed using a pro-inflammatory stimulus.

## **3.2 Materials and Methods**

### **3.2.1 Experimental Design**

Firstly, hAELVi cells were required to be characterised in monoculture, according to GIVIMP guidelines, both in submerged and ALI conditions (NCI-H441 and dTHP-1 have been characterised previously by Mitchell (2022) and Risby (2022), respectively).

Once the baseline characteristics of each of the cell lines individually are understood, they can then be implemented together within a triple cell co-culture that will be characterised at anatomically accurate cell type ratios, possess a tight barrier, and have functional macrophages.

Several issues need to be addressed throughout the chapter to ensure the functionality of this system, such as which cell culture media is most suitable, how well the dTHP-1 cells adhere to the culture, and how many cells must be seeded to ensure a confluent monolayer.

### **3.2.2 Chemicals and Reagents**

Chemicals and reagents used are described in Chapter 2, Section 2.1.

### **3.2.3 Cell Culture**

Cell culture is described in Chapter 2, Section 2.2.

#### **3.2.3.1 hAELVi Cell Culture**

General hAELVi cell culture is described in Chapter 2, Section 2.2.1.

Within this chapter, hAELVi cells are characterised in terms of their growth, viability, TEER, barrier function, morphology and basal IL6 and IL8 release. hAELVi cells were seeded on transwell inserts at concentrations of  $6.25 \times 10^4$ ,  $1.25 \times 10^5$ ,  $2.5 \times 10^5$  and  $5 \times 10^5$  cell/mL.

Throughout this chapter, the initial seeding concentration (in cell/mL) will be used to distinguish different cell densities. Although, it is important to note that there was 0.5 mL cell suspension seeded per well over a  $0.9 \text{ cm}^2$  transwell insert. These different

seeding metrics are outlined in **Table 3.1** to allow readability across different transwell insert sizes.

Assays were undertaken every 24 hours post-initial seeding for a maximum of 144 hours. This was done in both submerged and ALI conditions, where cultures were taken to ALI at the 72 hour time point. Additionally, if a basal media change was conducted at the 72 hour time point, a consideration that must be given when examining the IL6 and IL8 release data.

Understanding these characteristics allow informed decisions when implementing these cells within the co-culture model.

*Table 3.1 Cell seeding densities used to characterise the hAELVi cells shown as cell/mL, cell/well and cell/cm<sup>2</sup>*

Cell/mL	Cell/Well	Cell/cm <sup>2</sup>
6.250 x 10 <sup>4</sup>	3.125 x 10 <sup>4</sup>	3.472 x 10 <sup>4</sup>
1.250 x 10 <sup>5</sup>	6.250 x 10 <sup>4</sup>	6.944 x 10 <sup>4</sup>
2.500 x 10 <sup>5</sup>	1.250 x 10 <sup>5</sup>	1.388 x 10 <sup>5</sup>
5.000 x 10 <sup>5</sup>	2.500 x 10 <sup>5</sup>	2.777 x 10 <sup>5</sup>

### **3.2.3.2 NCI-H441 Cell Culture**

NCI-H441 cell culture is described in Chapter 2, Section 2.2.2.

### **3.2.3.3 THP-1 Cell Culture**

THP-1 cell culture is described in Chapter 2, Section 2.2.3.

### **3.2.4 Cell Count and Viability**

Methods for counting cells and assessing viability are described in Chapter 2 Methods, Section 2.3.

### **3.2.5 Seeding onto Transwell Inserts**

Transwell insert seeding is described in Chapter 2, Section 2.4.

### **3.2.6 Immunocytochemistry and Confocal Microscopy**

General principles of sample fixation and storage, immunocytochemistry and confocal microscopy are described in Chapter 2, Section 2.5.



### **3.2.7 CellTracker™ Staining and Determination of Co/Triple Culture Seeding Ratio**

The relative density of each cell type within the triple cell co-culture is crucial to ensuring relevance to a human system. However, growth rates of each cell type vary, requiring each cell to be fully characterised before implementation. Through investigation of normal human lungs obtained during autopsy, Crapo *et al.* (1982) reported a 13:1 – 16:1 surface coverage of ATI:ATII within the alveoli. To confirm the surface coverage of each cell type, hAELVi and NCI-H441 cells were pre-stained using CellTracker™ Deep Red dye and CellTracker™ Violet BMQC dye, respectively. CellTrackers™ were prepared according to the product datasheet through the addition of 20 µL and 30 µL of DMSO to the Deep Red and Violet stains, forming 1 mM and 10 mM solutions, respectively.

To stain the cells, hAELVi and NCI-H441 cells were detached from their flasks, centrifuged, and resuspended in fresh cell culture media. Cells were counted (Section 2.3) to ensure adequate cell count and resuspended with cell culture media in a 15 mL centrifuge tube. Deep Red and Violet CellTracker™ were added to each cell suspension to form a final CellTracker™ concentration of 10 µM and 20 µM, respectively (here, hAELVi were stained with the violet CellTracker™, whereas NCI-H441 were stained deep red). Suspensions were then incubated for 30 minutes at 37°C, 5% CO<sub>2</sub> and gently mixed every 10 minutes. Suspensions were then centrifuged at 340 RCF before being resuspended in 1 mL fresh cell culture media, centrifuged again at 340 RCF, and resuspended in 1 mL fresh CCM. A sample of these pre-stained cells was then counted before dilution to the final seeding concentration and seeded within 12-well transwell inserts.

After 72 hours, the basal media was replaced with fresh cell culture media and the cells were taken to ALI. At 96 hours, all media was removed, and cells were fixed and stored according to Section 2.5.1.

Based on the growth curves of each cell type within the epithelial cell co-culture (hAELVI ((Kuehn et al., 2016)) and NCI-H441 (Mitchell, 2022)), theoretical seeding densities of each cell type were calculated to achieve the desired surface coverage ratio (Table 3.2). Based on the findings from these seeding densities, seeding densities were optimised to reach a surface coverage ratio closer to the target.

*Table 3.2 Seeding Densities investigated for use within the alveolar epithelial co-culture.*

Cell Type	Cell Concentration Seeded (cell/mL)		
	Ratio 1	Ratio 2	Ratio 3
<b>hAELVi</b>	$4 \times 10^5$	$4.25 \times 10^5$	$4.5 \times 10^5$
<b>NCI-H441</b>	$1 \times 10^5$	$7.5 \times 10^4$	$5 \times 10^4$

Images of the pre-stained epithelial co-cultures were captured *via* confocal microscopy (Section 2.5.3) utilising the x20 lens. An 8x8 tile scan was captured for each seeding ratio rep. From this 8x8 tile scan, a  $1 \times 10^6 \mu\text{m}^2$  region of interest was defined using Fiji ImageJ software. The blue (hAELVi) and red (NCI-H441) colour channels were then split and converted to black and white images using the ‘Threshold’ tool. Once a black and white image was generated, Fiji’s integrated ‘Analyse particles’ tool was used to quantify the surface area of the black within the image. This gave the surface area covered by either cell type (**Figure 3.1**).

Stone *et al.* (1992) investigated the surface area of the alveolar epithelium and the associated number of epithelial cell types in various species. A total average alveolar surface area of  $102.2 \text{ m}^2$  was reported with  $5990 \times 10^6$  alveolar macrophages per alveolar region. The number of alveolar macrophages per  $\mu\text{m}^2$  can, therefore, be determined using the below calculations:

$$\begin{aligned}
& 5990 \times 10^6 \text{ Alveolar Macrophages per } 102.2 \text{ m}^2 \\
& = \frac{5990 \times 10^6}{102.2} = 58610567 \text{ Alveolar Macrophages per m}^2 \\
& = 58610567 \text{ Alveolar Macrophages per } 1 \times 10^{12} \mu\text{m}^2 \\
& = 58610567 \times 10^{-12} \text{ Alveolar Macrophages per } \mu\text{m}^2 \\
& = 1.05499 \text{ Alveolar Macrophages per } 18 \times 10^3 \mu\text{m}^2
\end{aligned}$$

This calculation was confirmed by Bhattacharya and Westphalen (2016), who reported 1 alveolar macrophage per  $18 \times 10^3 \mu\text{m}^2$ . These quantitative anatomical and histological studies give clear targets and specifications for what is required in the end-product of the development of an alveolar triple cell co-culture.

CellTrackers™ were also used to quantify the number of dTHP-1 cells in the triple-cell co-culture after cultures had been taken to ALI. Triple-cell co-cultures were seeded as in Sections 3.3.5. However, before the seeding of dTHP-1 cells onto the epithelial co-culture, dTHP-1 cells were pre-stained with CellTracker™ Deep Red using the same protocol as used with the NCI-H441 cells previously. dTHP-1 cells were then seeded at concentrations of 5000, 6430 and 30,000 dTHP-1/well (within 100 µL cell culture media), allowed to adhere for 2 hours before apical media was discarded and cultures were taken to ALI. These cultures were incubated for 24 hours before wells were fixed with PFA and mounted to slides as above. Slides were imaged *via* confocal microscopy again, utilising the x20 lens and an 8x8 tile scan. Within the Fiji software, the Cell Counter function was used to count the fluorescent cells amongst the non-fluorescent cells manually (made visible through brightfield imaging) across the entire tile scan (1,891,307 µm<sup>2</sup>) (**Figure 3.1**).

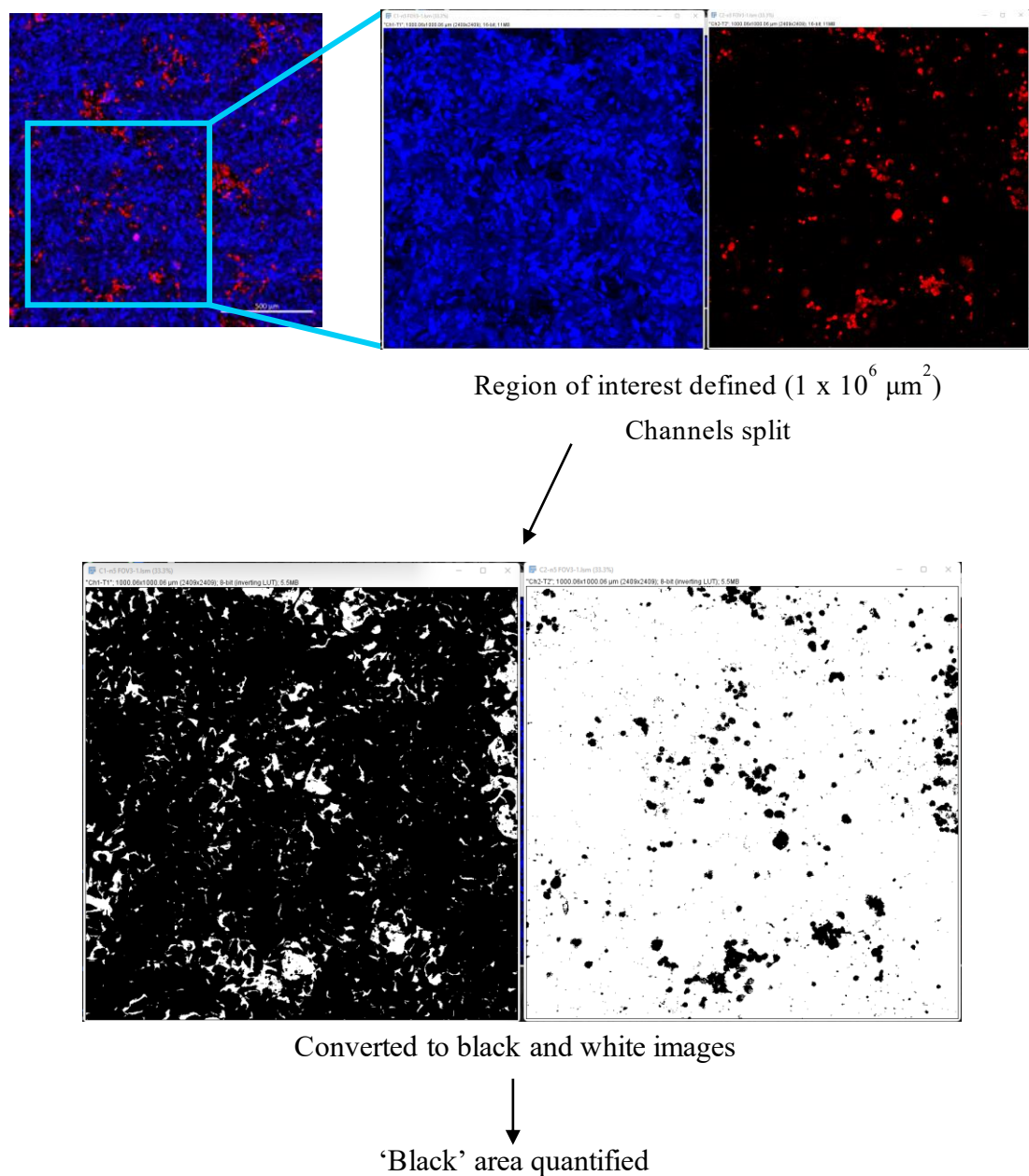


**Figure 3.1** Scheme to illustrate how each alveolar epithelial cell type were distinguished and quantified. Initially, a tile scan image was assigned a  $1 \times 10^6 \mu\text{m}^2$  region of interest, before the blue and red channels were split and converted to black and white images. The black area was then quantified to assess surface coverage of each cell type.

### 3.2.8 Barrier Integrity

#### 3.2.8.1 Blue Dextran

Methods for measuring barrier integrity using blue dextran are described in Chapter 2, Section 2.6.1.

### 3.2.8.2 Trans-Epithelial Electrical Resistance

Trans-epithelial electrical resistance (TEER) was measured using a MilliCell® ERS-2 voltohmmeter equipped with a chopstick STX01 electrode. TEER measurements were only performed in submerged cultures during hAELVi cell characterisation. To perform a reading, the electrode was placed so that one side of the electrode was within the apical insert and the other side was in the basal well. A current is then passed between the two electrodes through the cell culture, allowing for a TEER value to be determined. For each repetition, 4 readings were taken, 1 at each corner of the transwell insert (**Figure 3.2**). TEER values were expressed as ohm by  $\text{cm}^2$  ( $\Omega\cdot\text{cm}^2$ ) by multiplying the resistance by the surface area of the transwell insert.

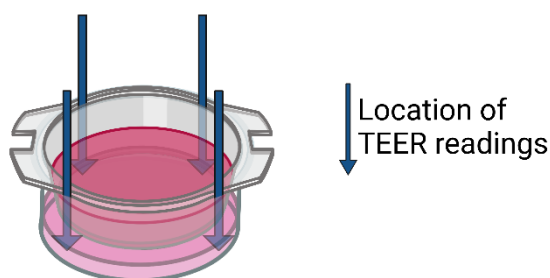


*Figure 3.2 Location for TEER readings on a single insert.*

### 3.2.9 Pro-Inflammatory Response

Methods for measuring pro-inflammatory response are described in Chapter 2, Section 2.7.

### 3.2.10 Data and Statistical Analysis

Raw data was initially recorded in Microsoft Excel and was transferred to GraphPad Prism (Version 10.1.1) (USA) for data and statistical analysis. Statistically significant differences were measured using one-way ANOVAs, two-way ANOVAs and t-tests, with appropriate post hoc tests used. Figure legends specify which statistical tests were used for each data set.

Graphs and other data visualisations were produced in GraphPad Prism (Version 10.1.1) unless otherwise stated within the methods section of subsequent chapters.

Confocal microscopy images were analysed using Zen Blue (Version 3.3) (Carl Zeiss, UK).

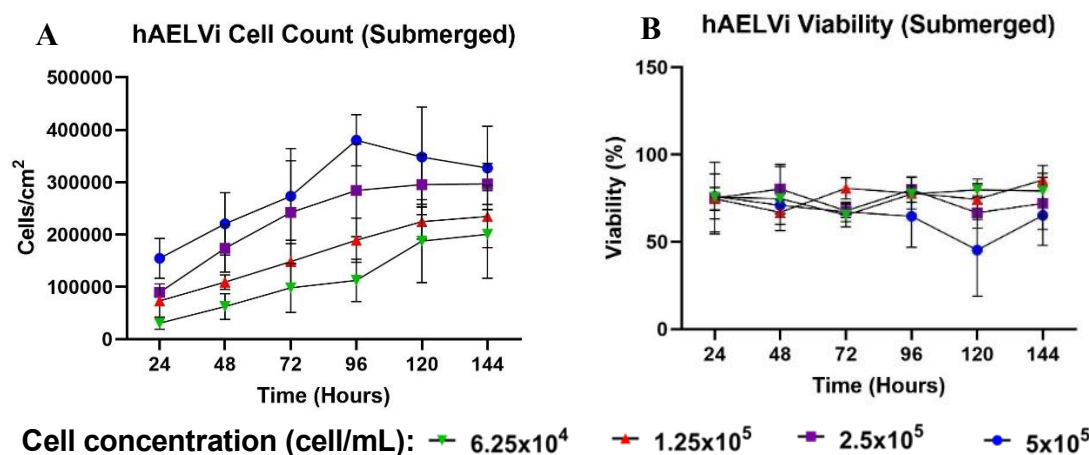
### 3.3 Results and Discussion

This section combines results and discussion into a single section, to allow context behind the decisions made during the development of this model.

#### 3.3.1 hAELVi Characterisation

##### 3.3.1.1 Growth and Viability of Submerged hAELVi Cells

Within submerged conditions, total hAELVi cell count at all initial seeding densities increased every 24 hours, except for the highest seeding density ( $5 \times 10^5$  cell/mL), which slightly decreased after the 96-hour mark. This was associated with a decrease in viability at the same time point, although viability remained at approximately 75% for all other seeding densities (Figure 3.3).



Cell concentration (cell/mL):  $6.25 \times 10^4$   $1.25 \times 10^5$   $2.5 \times 10^5$   $5 \times 10^5$

**Figure 3.3** Total cell counts (A) and viability (B) of hAELVi cells cultured under submerged conditions every 24 hours using a LUNAII automated cell counter. The mean reading of 3 biological replicates is plotted with SEM error bars.

The growth rate of hAELVi cells was consistent regardless of seeding density in submerged conditions. Following 144 hours of culture time, cell counts revealed a direct proportion between the number of cells and initial growth rate, and there was not a specific cell density where growth attenuated. However, the highest cell count (and a decreased percentage viability) was recorded at 96 hours of culture of  $5 \times 10^5$  cell/mL, perhaps indicating a cytotoxic effect when cells are in densely populated culture conditions. Based on this,  $5 \times 10^5$  cell/mL seeding density should be avoided to reduce toxic effects in the absence of particles. Work by Kuehn *et al.* (2016) reported a sigmoidal growth curve with a distinct lag, exponential and stationary phase. This stereotypical growth curve is not as evident in the data presented here; however, this is potentially due to higher seeding densities used within this research and the fact that

growth was only monitored for 144 hours, whereas Kuehn *et al.* recorded growth over 216 hours. It could be argued that growth had slowed to a stationary phase from 96 hours in the  $5 \times 10^5$  and  $2.5 \times 10^5$  cell/mL seeding densities and from 120 hours in the  $1.25 \times 10^5$  and  $6.25 \times 10^4$  cell/mL seeding densities but an extension of the culturing period of the study would be required to confirm this. Leibrock *et al.* (2019) investigated hAELVi growth in submerged conditions over 96 hours and found a similar trend as observed here for the first 96 hours, with a population doubling time of 28 hours.

### 3.3.1.2 Barrier Integrity of Submerged hAELVi Cells

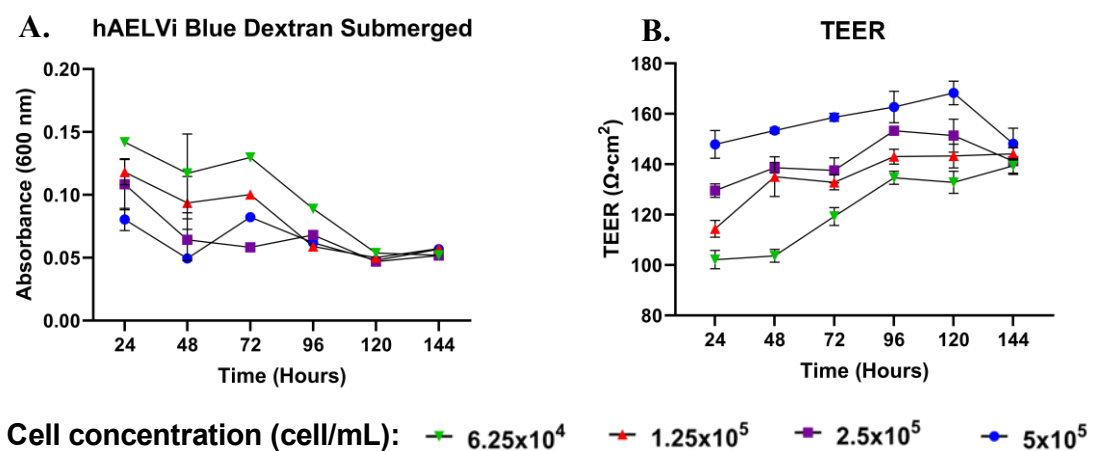


**Figure 3.4** Barrier properties of hAELVi cells cultured under submerged conditions measured using blue dextran (A) and TEER (B). Data points are mean values of 3 independent biological replicates with SEM error bars. When error bars cannot be seen, this is because the SEM is smaller than the size of the data icon.

The barrier integrity of submerged hAELVi cells (**Figure 3.4A**) increases every 24 hours, as shown by a decrease in blue dextran in the basal supernatant and an increased. Regardless of seeding density, blue dextran showed maximal barrier integrity after 120 hours at an absorbance reading (600 nm) of approximately 0.05. These values remained consistent at the 144-hour time point. Before this, a degree of permeability was observed for all initial seeding densities, with lower seeding densities showing a reduced barrier function.

TEER readings showed more variation than blue dextran readings but followed an overall similar trend (**Figure 3.4B**). At a seeding density of  $5 \times 10^5$  cell/mL, maximal TEER readings were observed after 120 hours at  $168 \Omega \cdot \text{cm}^2$ . After 140 hours, resistance was not significantly different, falling between  $139 - 148 \Omega \cdot \text{cm}^2$  (for initial seeding densities of  $6.25 \times 10^4$  and  $5 \times 10^5$  cell/mL, respectively).

As well as increased variation in the TEER readings, compared to the blue dextran data, the data do not follow the same trend. Blue dextran shows maximal barrier formation for all seeding densities at 120 hours, whereas this does not occur until 144 hours within the TEER readings. The TEER readings show an apparent increase at all time points up until 120 hours as the seeding density increases.

Tight barrier properties are a defining characteristic of ATIs and a characteristic of hAELVi cells. Kuehn *et al.* (2016) monitored TEER over 25 days in hAELVi cells. TEER saw significant increases from day 6 to day 17, beyond the time length conducted within this work. In the present work, TEER reached its upper limit at approximately  $170 \Omega \cdot \text{cm}^2$  in the  $5 \times 10^5$  cell/mL seeding density after 120 hours. Similar results were seen by Kuehn *et al.* within the same periods. However, when extending this experiment duration, TEER values dramatically increased beyond  $2000 \Omega \cdot \text{cm}^2$ . A review of alveolar model developments by Srinivasan *et al.* (2015) found models consisting of a variety of alveolar cell types possessed TEER values of between 1000 and  $2000 \Omega \cdot \text{cm}^2$ , a resistance approximately 10-fold higher than recorded here and vastly higher than the TEER observed within hAELVi cells under lower culture time. Kuehn *et al.* (2016) confirmed the presence of tight junction proteins zona occludens-1 (ZO-1) and occluding in the membrane of hAELVi cells which likely contribute to the tight barrier and high TEER values (at least compared to some other immortalised alveolar epithelial cells, such as A549 which display TEER values in the range of  $120\text{-}195 \Omega \cdot \text{cm}^2$  after 21 days in culture (Nalayanda et al., 2009)). Given that TEER remained constant after 96 hours in this study, it is likely that exposures would need to occur at 96 hours onwards.

Assessment of barrier integrity found that the cultures' permeability depended on initial seeding density at the lower time points, with lower seeding densities associated with increased permeation of blue dextran into the basal compartment. Within the 3 highest seeding densities, the lowest permeability rates were observed after 96 hours in culture, whereas this was only reached in the lowest seeding density after 120 hours. Interestingly, the blue dextran and TEER readings do not strictly align, perhaps indicating differences in the speed at which barrier integrity and permeability are established within *in vitro* culture. Kuehn assessed permeability after 7 days of hAELVi culture using sodium fluorescein, which travels paracellularly similarly to blue dextran. They found hAELVi cells had an apparent permeability coefficient ( $P_{\text{app}}$ )



of approximately  $2 \times 10^6$  cm/s after 7 days in submerged conditions, which was increased to  $12 \times 10^6$  cm/s when cultures were treated with EDTA.  $P_{app}$  was generally found to be lower in ALI conditions, suggesting a tighter barrier in these conditions.

In this study, given that maximal barrier integrity was reached in all but the lowest seeding density after 96 hours, this indicated the earliest time point at which ALI could be introduced and maintained.

### 3.3.1.3 Morphology of submerged hAELVi Cells

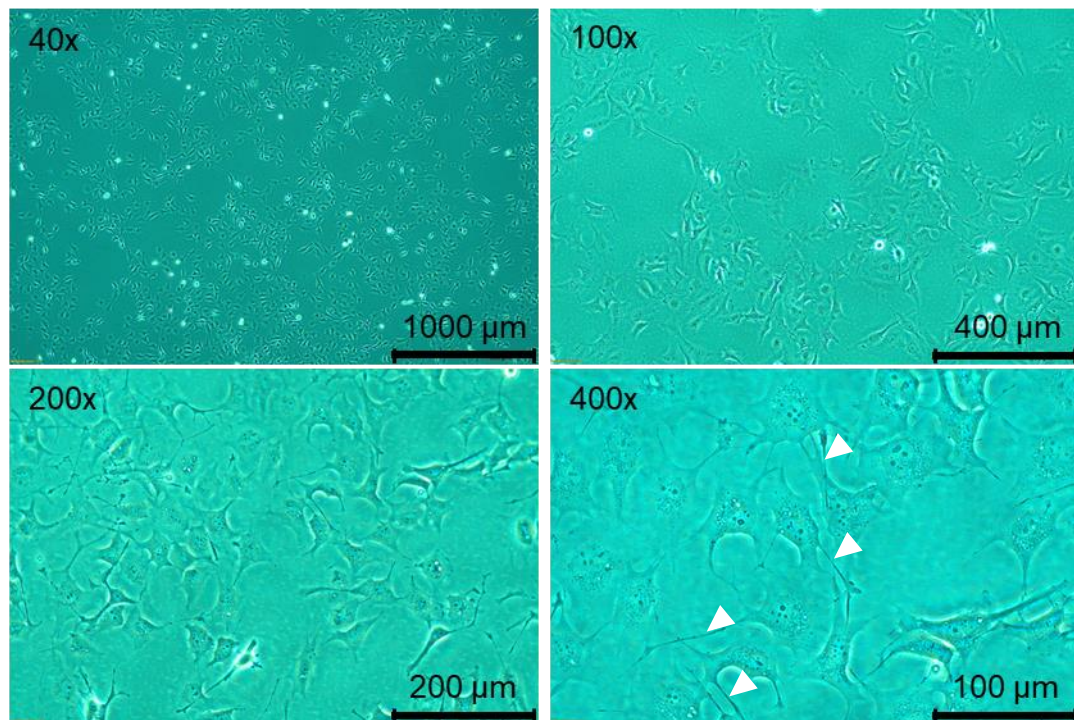


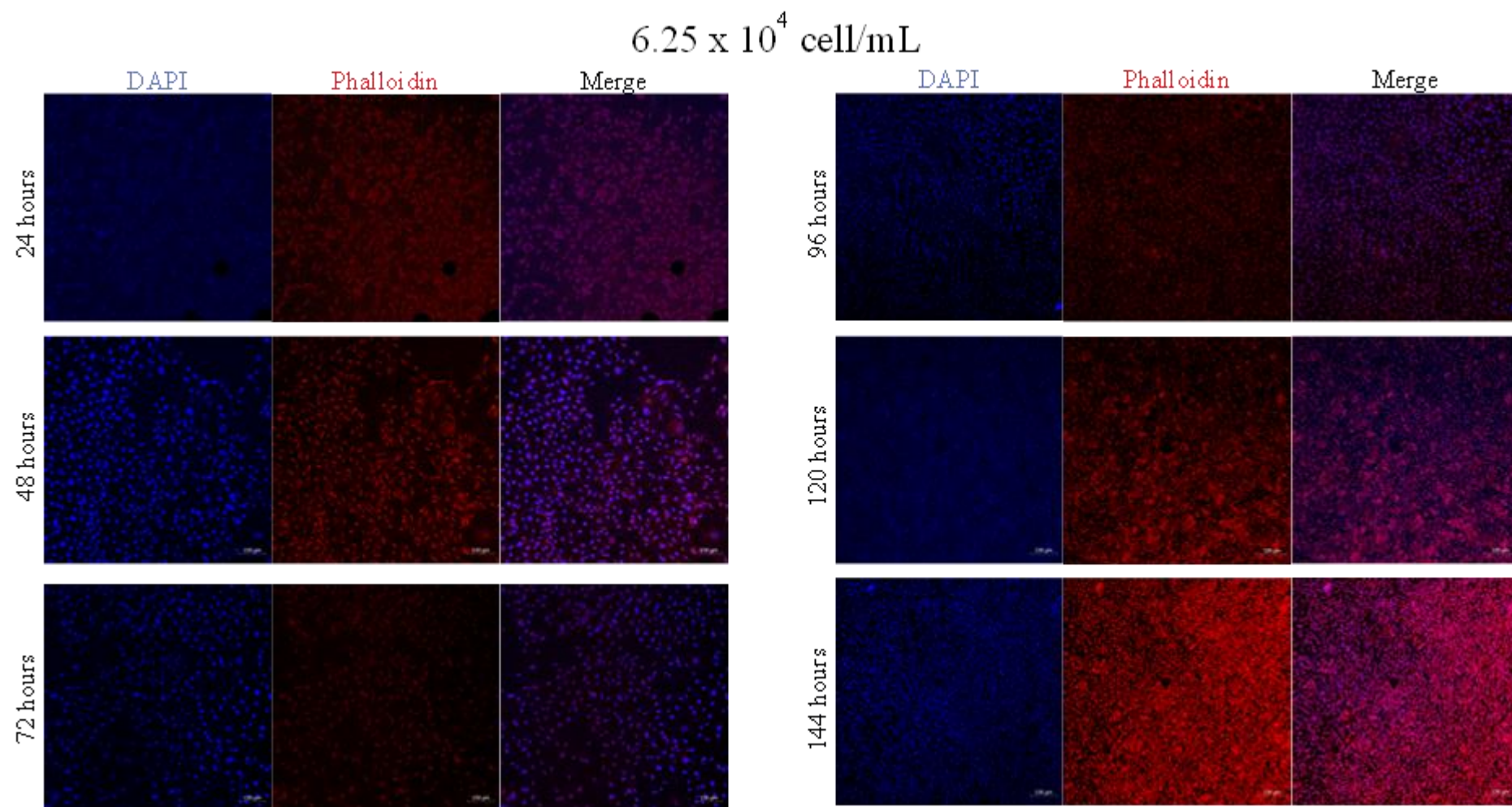
**Figure 3.5** Light microscopy images of hAELVi cells grown in a T75 using 4x, 10x, 20x and 40x lenses on an Invitrogen Evos XL Core. White arrows indicate cell narrow projections.

hAELVi cells grown within pre-coated T75 flasks were imaged *via* light microscopy (**Figure 3.5**). hAELVi cells appeared healthy *via* light microscopy, with most cells attached to the flask's surface. Morphologically, when reaching confluency, cells appeared to be densely packed together, with narrow, elongated projections (Figure 3.6, white arrow heads). Some circular subcellular structures can be seen.

When grown within transwell inserts, the time taken for hAELVi to become confluent changes based on the initial seeding density and the time in culture. When seeded at  $6.25 \times 10^4$  cell/mL, confluency is reached after approximately 96 hours. This is reduced to approximately 72 hours when seeded at  $1.25 \times 10^5$  and  $2.5 \times 10^5$  cell/mL

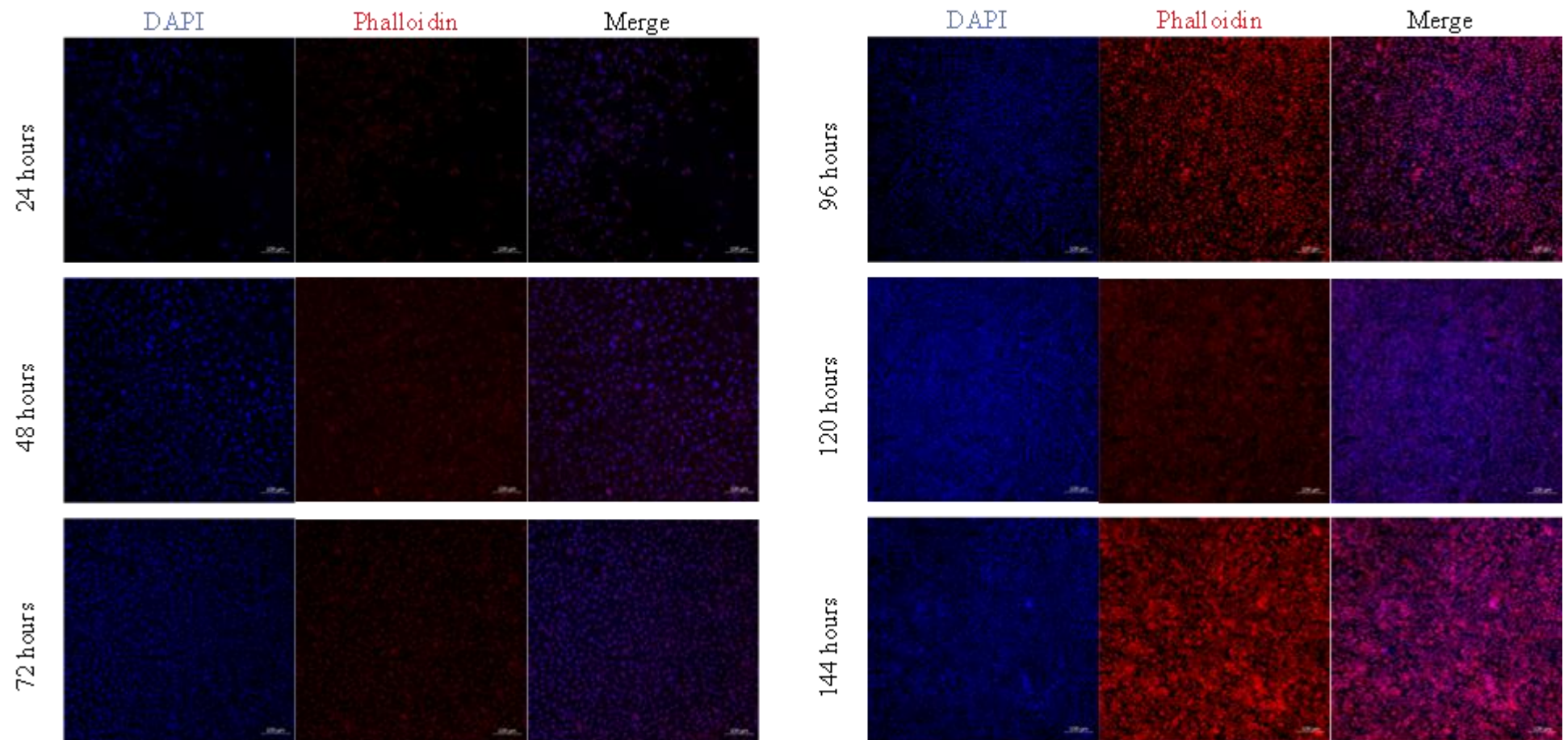
and within 48 hours when seeded at  $5 \times 10^5$  (**Figure 3.6**), shown across subsequent pages).

hAELVi cells, as shown by confocal imaging, form a tight mosaic structure when confluency is reached. The time taken for confluency, however, depends on the seeding density and aligns with the growth curves shown in Section 3.3.1.1. The morphology of hAELVi cells depicted here is comparable to previously published images of hAELVi cells showing a confluent monolayer with few gaps (Kletting et al., 2018; Kuehn et al., 2016). Non-confluent hAELVi cells (as depicted at earlier time points in lower seeding densities) appear as oblong cells with narrow projections, as Diem et al. (2020) also reported.

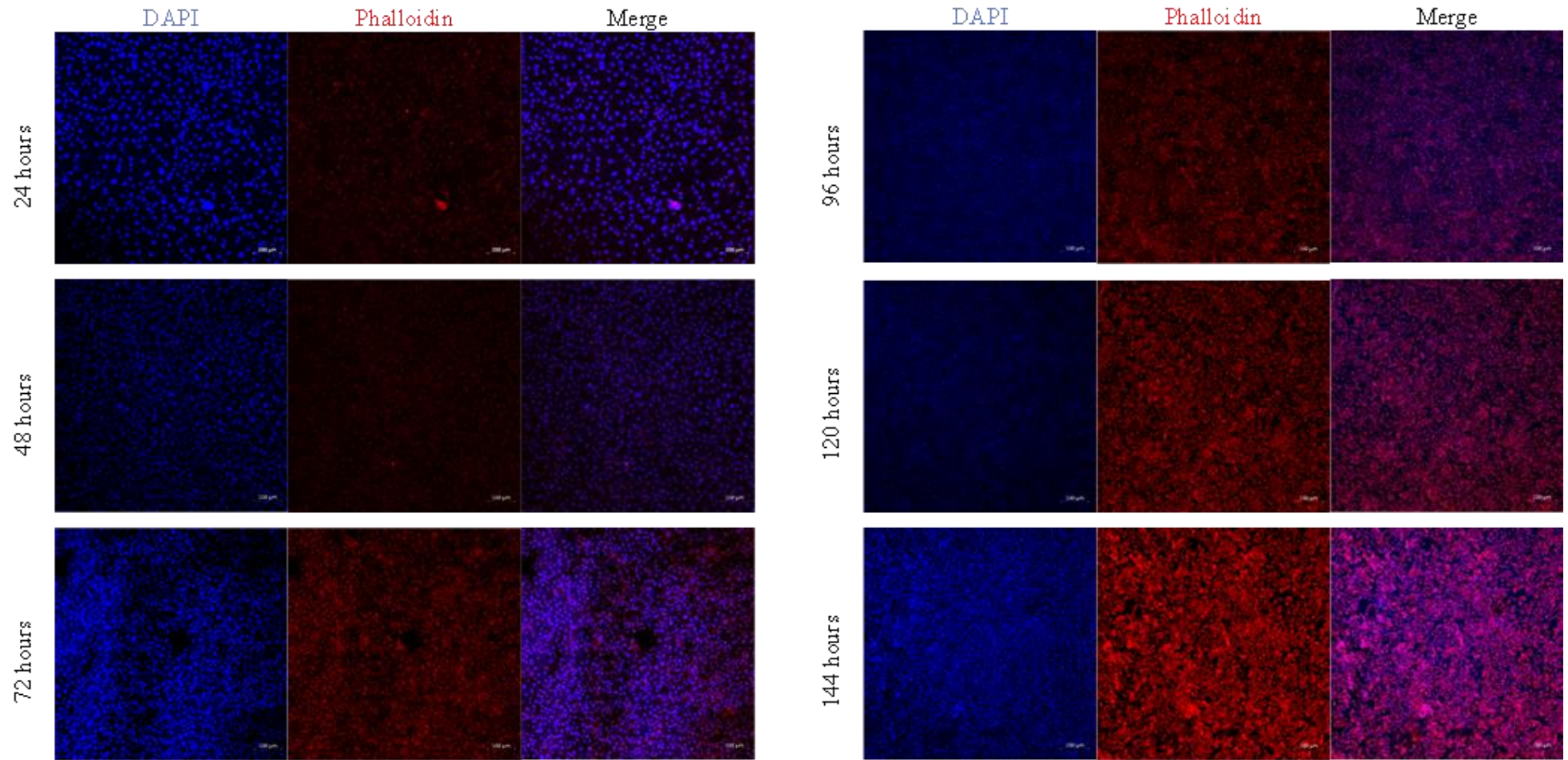




$1.25 \times 10^5$  cell/mL



$2.5 \times 10^5$  cell/mL





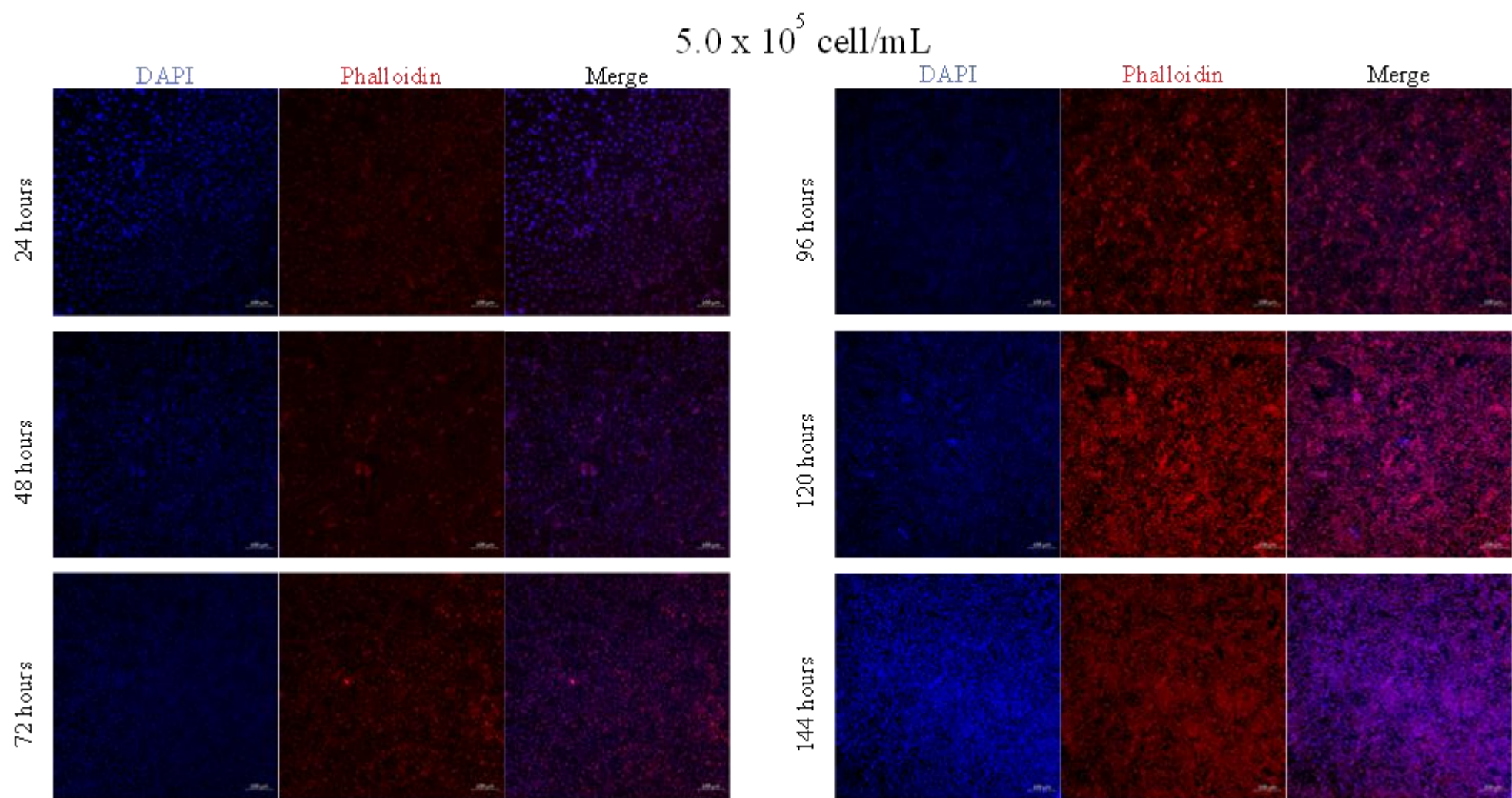


**Figure 3.6** (Previous pages) LSM images of submerged hAELVi cells were captured using 20x objective lens at 24-hour intervals. hAELVi cells were stained using DAPI (nuclei) and phalloidin F-actin).

### 3.3.1.4 Pro-Inflammatory Profile of Submerged hAELVi Cells

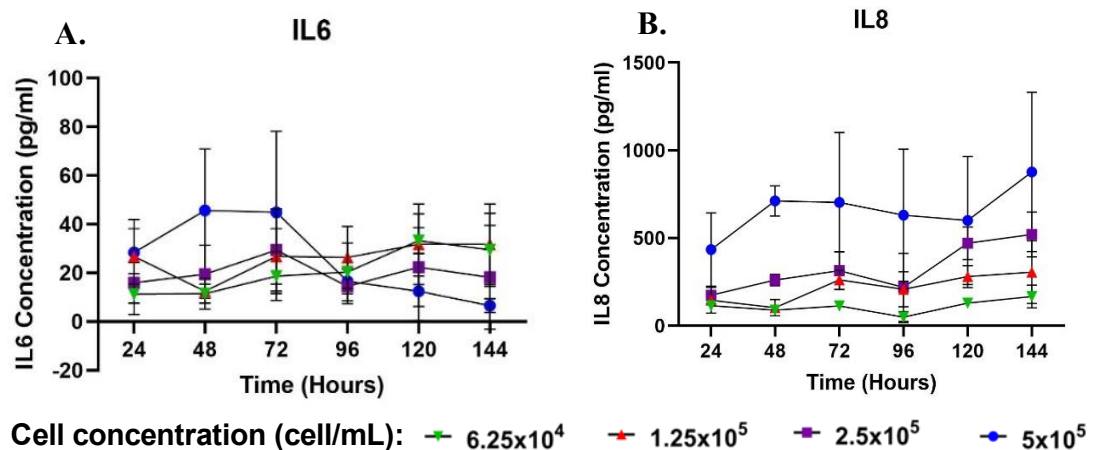


**Figure 3.7** IL6 (A) and IL8 (B) release from hAELVi cells cultured in submerged conditions. IL6/8 was detected in supernatant collected from the cultured cells via sandwich ELISA. Media was changed at 72 hours which should be noted for IL6/8 concentration from 96 hours onwards. Data points show a mean of 3 biological replicates with SEM error bars. Where error bars cannot be seen, the range was smaller than the data icon.

hAELVi monocultures secrete IL6 and IL8 in unstimulated submerged growth conditions (**Figure 3.7**). The concentrations of IL6 and IL8 detected in the supernatant are directly related to the initial seeding density of the cells, where the higher the seeding density generally the more IL6/IL8 detected. An exception to this case is that after the media was changed at 72 hours, IL6 detection drops in the hAELVi cells seeded at  $5 \times 10^5$  cell/mL. IL6 detection does not significantly change over the incubation time in cells seeded at lower densities. IL8 is heightened in hAELVi monocultures seeded at  $5 \times 10^5$  cell/mL compared to lower seeding densities, which remain below the 500 pg/mL level throughout the culture period. The detection of IL8 drops at 96 hours, following the basal media change at 72 hours, similar in trend to IL6 detection. Following 144 hours in culture, there is an apparent increase in IL8 presence in the supernatant, which is in line with the initial seeding density.

In addition to their barrier and gaseous exchange roles, the epithelium of the alveoli plays an essential role in innate immune defence, namely, in the onset of inflammation. By releasing inflammatory proteins, the inflammatory process aims to neutralise invading pathogens and initiate tissue repair (Moldoveanu et al., 2009). Excessive or chronic inflammation, however, can be detrimental. For example, levels of IL6, IL8 and TNF $\alpha$  have been upregulated in the serum and bronchoalveolar lavage of COPD patients (El-Shimy et al., 2014). The alveolar epithelium is a source of IL6 and IL8 (Kobayashi et al., 2015; Wickremasinghe et al., 1999). Further, exposure to NO<sub>2</sub> and

PM has been associated augmented with IL6 and IL8 release (Becker et al., 2005; B. Y. Chen et al., 2012; Garn et al., 2003).

The data presented herein suggest that cells are not undergoing a high degree of inflammatory stress under a submerged culture, and the fact that there are no increasing trends in pro-inflammatory cytokine concentration over the 144 hours suggests that these cells grow with minimal stress in the culture setting. These results can be taken forward to exposure studies and allow a background idea of pro-inflammatory cytokine release to be known so that changes associated with NO<sub>2</sub>/PM exposure can be established.

### 3.3.1.5 Growth and Viability of hAELVi Cells at Air-Liquid Interface

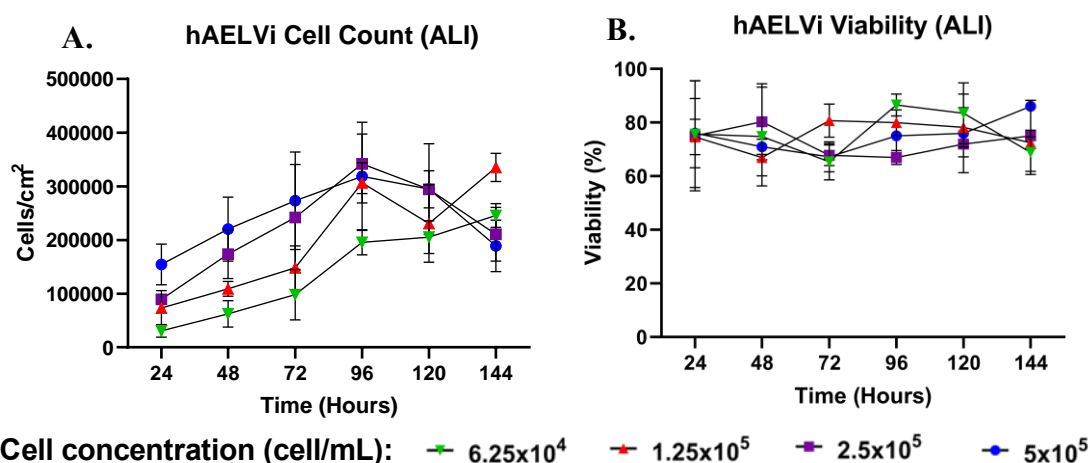


**Figure 3.8** Total cell counts (A) and viability (B) of hAELVi cells cultured every 24 hours using LUNA II automated cell counter under submerged conditions for 72 hours before being exposed to ALI. The mean reading of 3 biological replicated is plotted with SEM error bars.

When hAELVi monocultures are grown within transwell inserts at ALI, growth appears to attenuate once cultures reach between 3-3.5 x 10<sup>5</sup> cell/cm<sup>2</sup> (**Figure 3.8**). This density was reached by cells seeded at 1.25 x 10<sup>5</sup>, 2.5 x 10<sup>5</sup> and 5 x 10<sup>5</sup> cell/mL at the 96-hour time point (cells seeded at 6.25 x 10<sup>5</sup> cell/mL did not reach this density, even after 144 hrs). When at this point, all cells saw a subsequent decrease in cell count at 120 hours and 144 hours (except for cells seeded at 1.25 x 10<sup>5</sup> cell/mL, which rebounded back to the upper limit at 144 hr). Viability remained consistent throughout the study, although it was somewhat low, ranging between 65% and 86%. Specific trends in viability were not seen nor related to the growth data. In many cases, the media change performed at 72 hours appeared to prompt a significant increase in growth at the 96-hour point.



It must be noted that in this instance, hAELVi cells were grown under submerged conditions for 72 hours before apical media was removed and cells were taken to ALI. Endpoints were then assessed every 24 hours for the following 72 hours. It was chosen to take cells to ALI at 72 hours based on the findings of the submerged cultures, knowing that the cells would grow effectively and possess an impermeable monolayer 24 hours later when pollutant exposures could occur. In addition, taking hAELVi cells to ALI at 72 hours allows these cells to be directly implemented into a co-culture with type 2 alveolar NCI-H441 cells. This would allow these two well-characterised alveolar epithelial cells to be used in the same model.

Data here confirms that when taken to ALI, hAELVi cells remain as viable as when grown in submerged conditions. Interestingly, compared to the submerged conditions, the growth rate in the  $5 \times 10^5$  and  $2.5 \times 10^5$  cell/mL begins to decline at 120 and 144-hour time points. Given that a degree of overgrowth is observed in these cultures at these time points, as shown by LSM imaging (Section 3.3.1.7), it could be speculated that some cells may not receive adequate nutrients from the basal media. However, this is not backed up by the viability data that remains constant throughout.

The viability was recorded following all pollutant exposures in subsequent data chapters. This was vital to ensure that exposures were not altering viability to an extent where other assays were impacted, and to allow adjustment if this were the case (*i.e.* reducing dose, or normalising for loss of cell count).

### 3.3.1.6 Barrier Integrity of hAELVi Cells at Air-Liquid Interface

Similarly to hAELVi cells grown in submerged conditions, maximal barrier integrity was reached after approximately 120 hours, regardless of the initial seeding density shown through the blue dextran assay (**Figure 3.9**). All 4 seeding densities display an apparent increase in barrier function through the time points. At the earliest time points, cultures with lower seeding densities have a decreased barrier function. A slight decrease in barrier integrity is seen in the highest seeding density ( $5 \times 10^5$  cell/mL) at the 72 and 96-hour time points, a similar trend to the submerged hAELVi cultures.

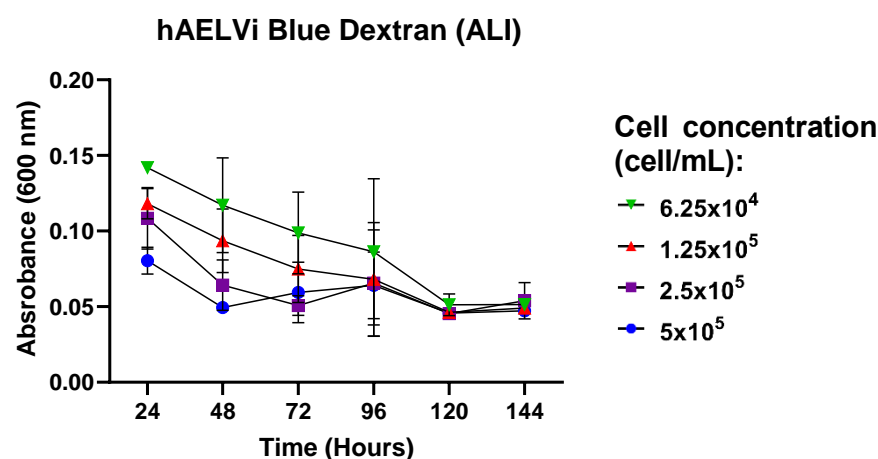


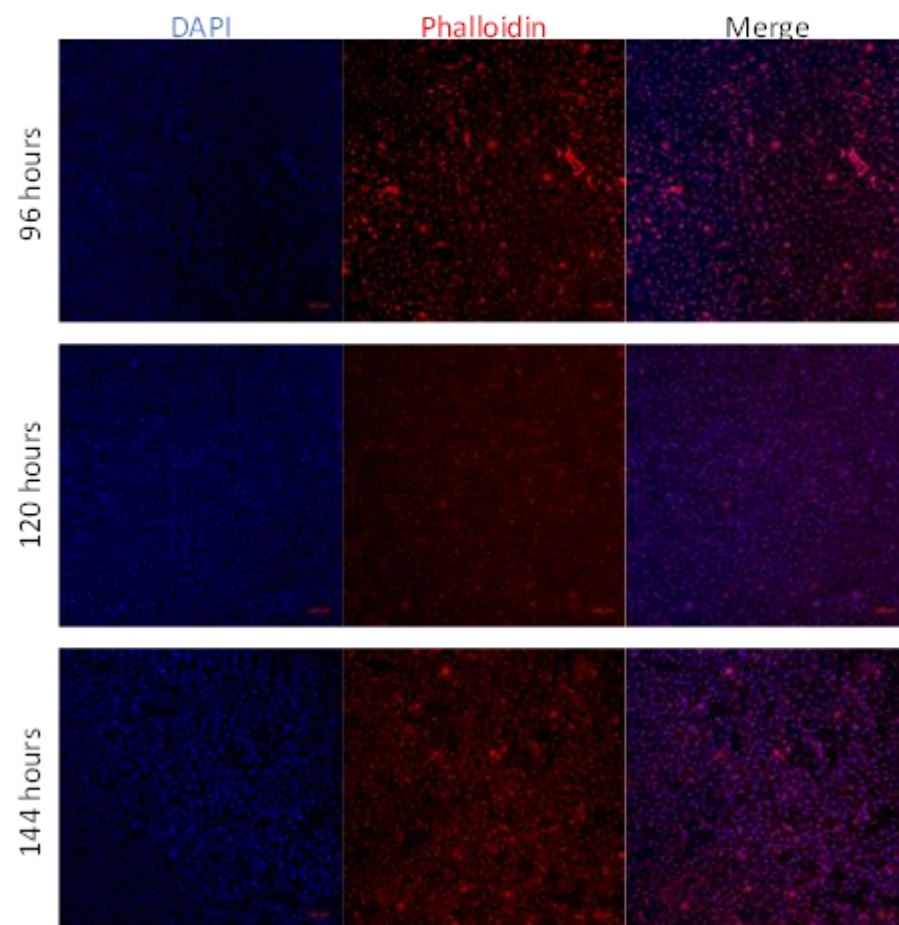
**Figure 3.9** Barrier properties of hAELVi cells cultured under ALI conditions from 72 hours measured using blue dextran. Data points are mean values of 3 independent biological replicates with SEM error bars. When error bar cannot be seen, this is because the SEM is smaller than the size of the data icon.

Although hAELVi cells have not been extensively characterised at ALI by other groups, Kuehn *et al.* (2016) reported significantly higher TEER in 7-9 days compared to submerged cultures. Changes in TEER were insignificant within shorter periods. This is supported by Leibrock *et al.* (2019), who found little difference in TEER between submerged and ALI hAELVi cultures for the first 8-10 days after seeding. Culturing for extended periods (up to 17 days) resulted in modest but comparable TEER increases in both cultures. Due to the lack of apical media, TEER was not measured in ALI cultures. Blue dextran showed similar findings between the submerged and ALI conditions within the 6 days of culture. It remains to be seen whether the barrier function would significantly alter if grown for increased time periods, as it appears that the lower limit of absorbance has been achieved. This again agrees with permeability findings by Kuehn *et al.* (2016), which found little difference in  $P_{app}$  using sodium fluorescein after 7 days in either submerged or ALI cultures.

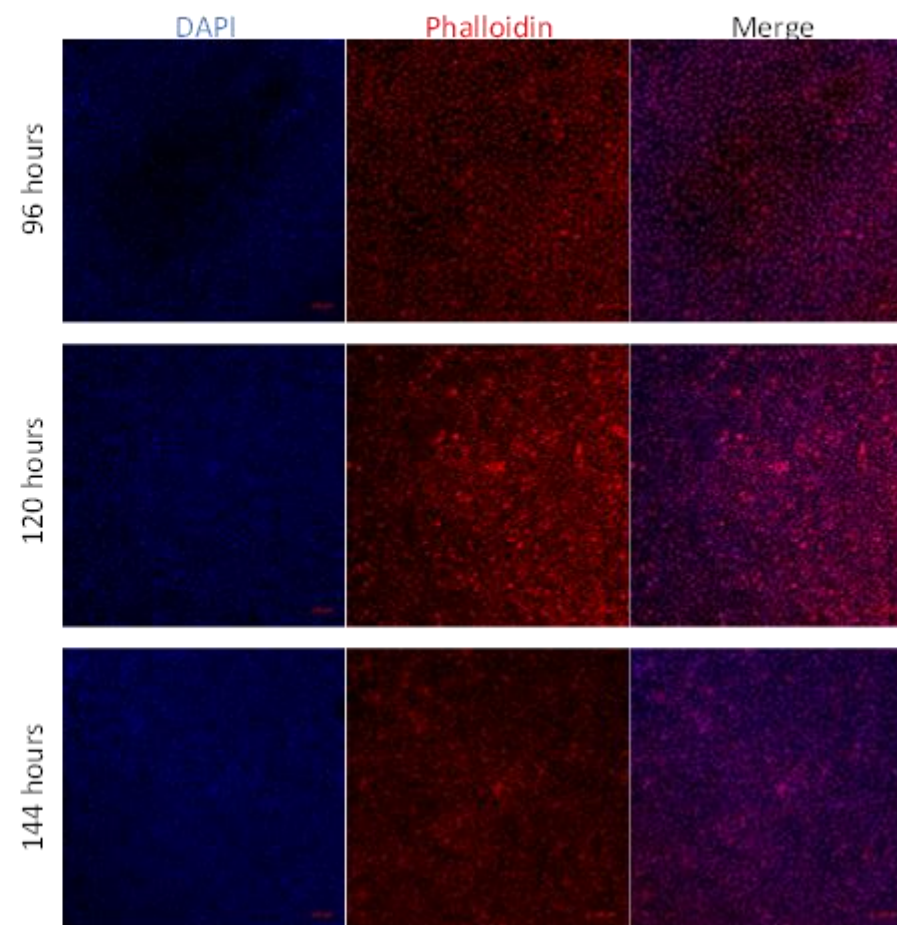
### 3.3.1.7 Morphology of hAELVi Cells at Air-Liquid Interface

When taken to the air-liquid interface at 96 hours, monolayer formation is complete in initial seeding densities of  $1.25 \times 10^5$ ,  $2.5 \times 10^5$  and  $5 \times 10^5$  cell/mL (**Figure 3.10**, shown across subsequent pages). Gaps in the monolayer can be seen at 96 hours in  $6.25 \times 10^4$  cell/mL seeding density. However, a confluent monolayer is reached at the 120-hour time point. After 144 hours, overgrowth is observed in the  $2.5 \times 10^5$  and  $5 \times 10^5$  cell/mL seeding densities, which is not as evident in the  $6.25 \times 10^4$  and  $1.25 \times 10^5$  cell/mL seeding densities. Phalloidin staining of F-actin reveals that hAELVi cells form a mosaic monolayer with few gaps between cells.

$6.25 \times 10^4$  cell/mL



$1.25 \times 10^5$  cell/mL



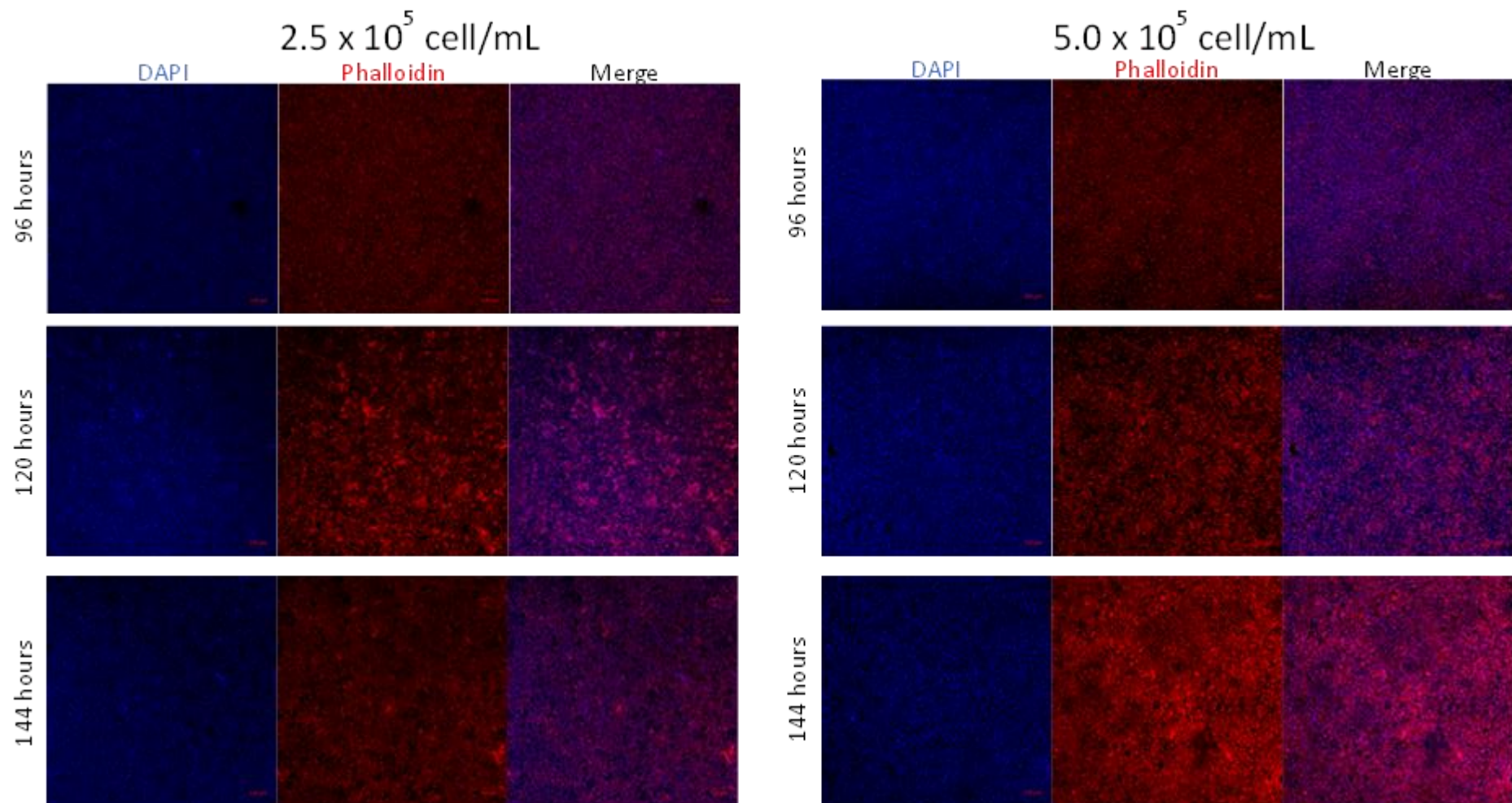


**Figure 3.10** (Previous pages) LSM images of hAELVi cells at the ALI were captured using a 20x objective lens at 24-hour intervals. hAELVi cells were stained using DAPI (nuclei) and phalloidin (F-actin).

### 3.3.1.8 Pro-Inflammatory Profile of hAELVi Cells at Air-Liquid Interface

Detected IL6 levels were initially directly proportional to seeding density and increased within the first 72 hours up to approximately 45 pg/mL in the  $5 \times 10^5$  cell/mL seeding density wells (**Figure 3.11**). Once media had been changed at the 72-hour time point, IL6 release was seen to drop dramatically in the two highest seeding densities, whereas IL6 continued to increase in the lowest seeding densities.

Similarly, IL8 detection was increased in line with an increase in initial seeding density, rising to approximately 750 pg/mL after 72 hours in the  $5 \times 10^5$  cell/mL seeded cells. There was a slow increase of IL8 over the first 72 hours in the lower 3 seeding densities. Upon changing media at 72 hours, IL8 detection initially decreased for the 96-hour time point but then continued to rise over the next 48 hours.

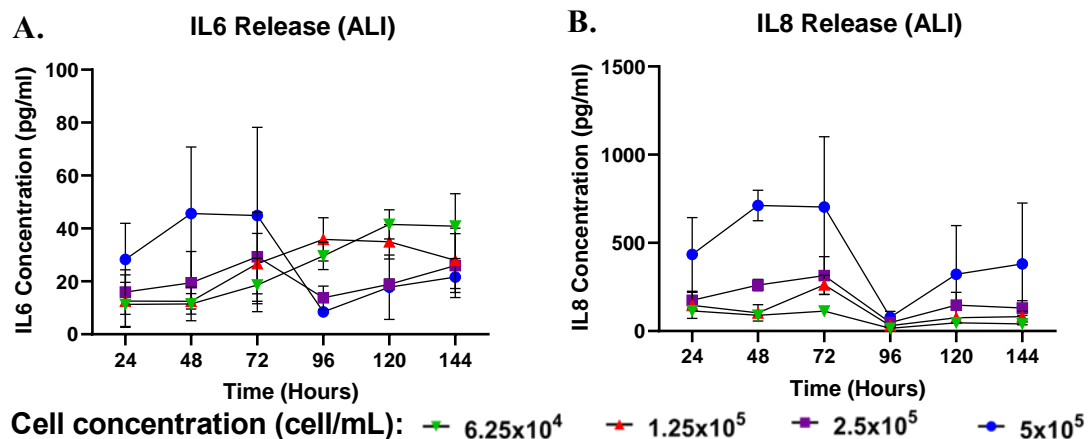


**Figure 3.11** IL6 (A) and IL8 (B) release from hAELVi cells cultured in submerged conditions for 72 hours before being exposed to ALI. IL6/8 was detected in supernatant collected from the cultured cells via sandwich ELISA. Media was changed at 72 hours which should be noted for IL6/8 concentration from 96 hours onwards. Data points show a mean of 3 biological replicates with SEM error bars. Where error bars cannot be seen, the range was smaller than the data icon.

The data presented here confirms that hAELVi cells are viable and continue growing (initial seeding density dependent), maintain an integral membrane, and do not release pro-inflammatory cytokines in a manner that would indicate inflammatory stress. hAELVi cells also visually maintain an air-liquid interface effectively. This evidence justifies the inclusion of hAELVi cells within an advanced in vitro alveolar model.

### 3.3.2 NCI-H441 Compatibility with huAEC Coating

Prior to seeding hAELVi cells within transwell inserts, the inserts were required to be coated with huAEC coating solution to ensure cell adherence. NCI-H441 cells did not require this coating for adherence and growth and have not been characterised in



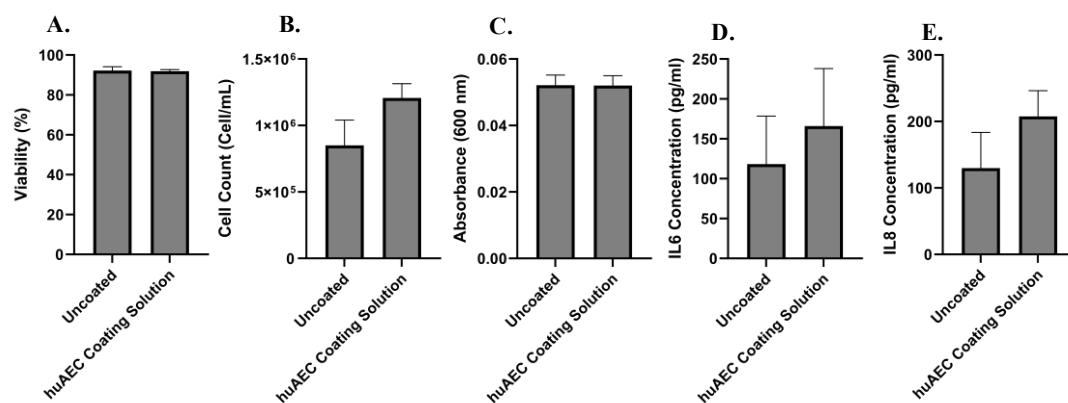


**Figure 3.12** Total cell count (A), viability (B), barrier integrity (C), IL6 release (D) and IL8 release (E) from NCI-H441 cells cultured at ALI in either uncoated or huAEC coated transwell inserts. Averages of 3 technical repeats are reported for each biological replicate (data points). Bars show mean across 3 biological replicates. Error bars show SEM. Unpaired *t*-tests showed no significant difference in any of the measured parameters between coated and uncoated wells.

monoculture with this coating. Therefore, it was pertinent to ensure that NCI-H441 cells did not differ in their growth or inflammatory response when grown on huAEC-coated transwell inserts, which would subsequently allow them to be used in co-culture with the hAELVi cells.

NCI-H441 cells show no significant difference ( $p > 0.05$ ) in growth, viability, barrier integrity and pro-inflammatory cytokine release (**Figure 3.12**). Morphological analysis of NCI-H441 cells cultured in either uncoated wells or coated wells reveals no changes (**Figure 3.13**).

Although there are no instances in the literature of NCI-H441 cells being grown on surfaces coated with huAEC coating solution, hAELVi cells have been found to grow effectively on surfaces coated with collagen I. NCI-H441 cells also grew effectively on the collagen I-treated surface, further indicating compatibility between NCI-H441 and extracellular matrix component-coated surfaces (Brookes et al., 2021). Work here showed no significant difference in cell growth, viability, membrane permeability, IL6/IL8 release or morphology. This gives the rationale for utilising NCI-H441 characterisation by Michell (2022) to implement the NCI-H441 cells into co-culture with hAELVi cells.

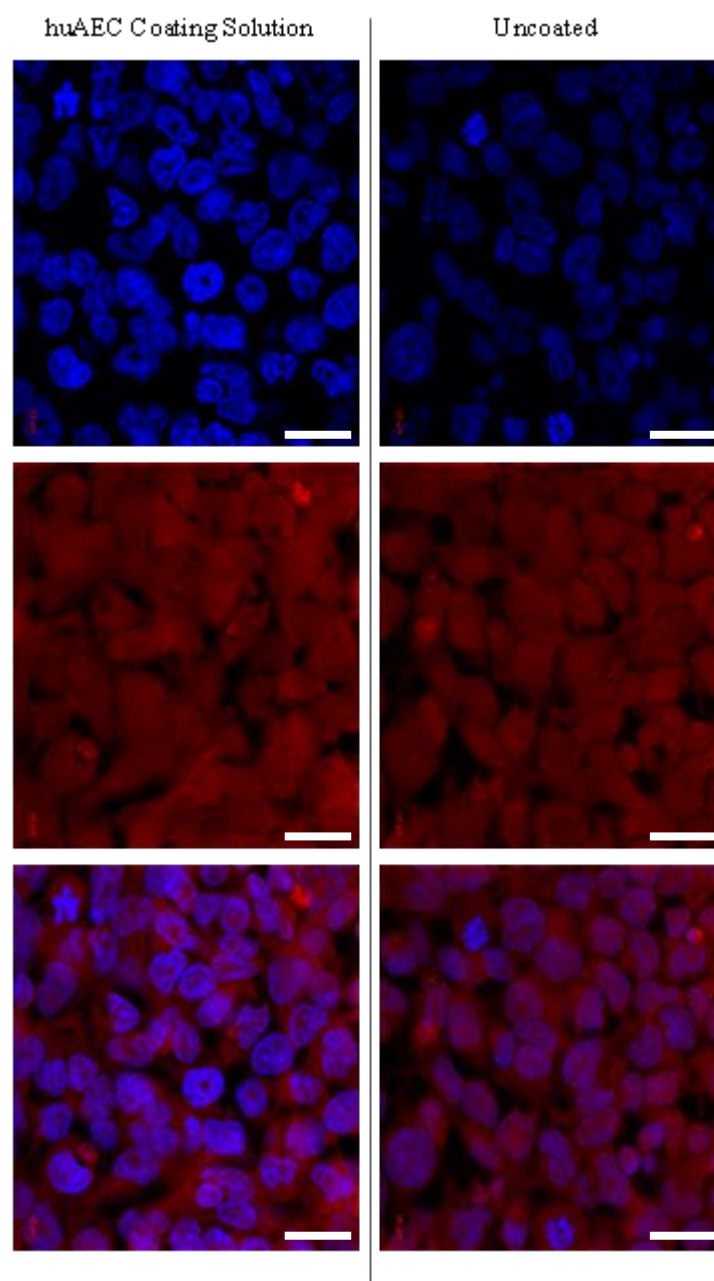


**Figure 3.13** NCI-H441 cells cultured in uncoated wells (top) and huAEC coated well (bottom) for 72 hours before being exposed to ALI for 24 hours. F-actin is shown through phalloidin staining (red) and nuclei were stained with DAPI (blue) using a 40x objective lens. Scale bar = 40  $\mu$ m.

### 3.3.3 Growth and Viability of hAELVi/NCI-H441 Co-Culture at the Air-Liquid Interface

Co-culture seeding density was determined through analysis of the monoculture characterisation of the hAELVi cells (Section 3.3.1) and NCI-H441 cell characterisation, which was carried out by Mitchell (2022). These calculations gave a theoretical seeding density that would need to be utilised to reach a 13-16:1 ratio of



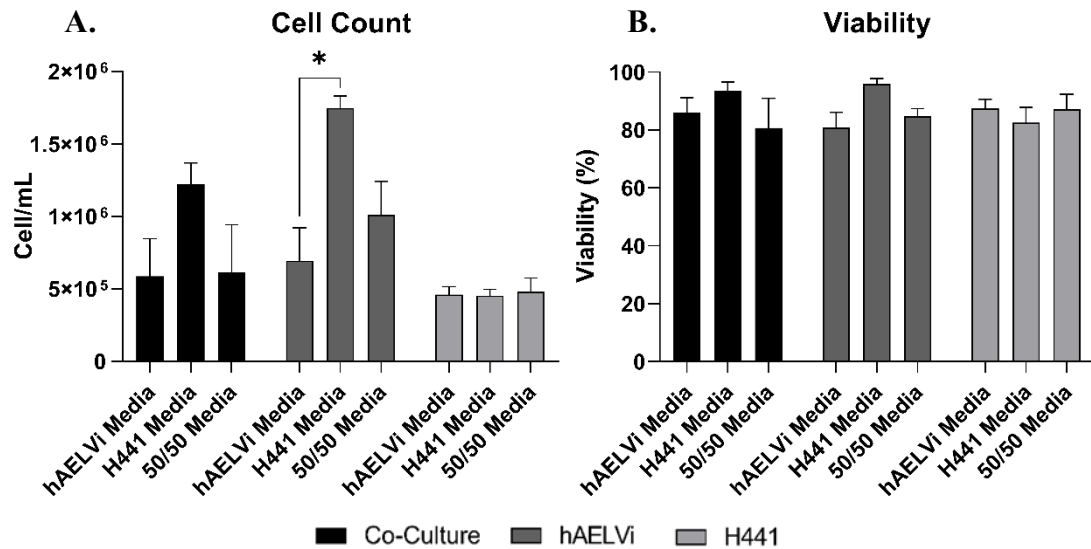


**Figure 3.14** Total cell counts (A) and viability (B) of hAELVi and NCI-H441 (H441) co-cultures at 96 hours post seeding using LUNA II automated cell counter under submerged conditions for 72 hours before being exposed to ALI. Co-cultures were cultured in either RPMI 1640 (NCI-H441 media), huAEC media (hAELVi media), or a 50/50 mixture of the two media types (50/50 media). The mean reading of 3 biological replicates is plotted with SEM error bars. Difference was assessed for via two-way ANOVA utilising a Tukeys post hoc test.

ATI to ATII. However, the media type required for optimal co-culture growth must be determined. Here, huAEC, RPMI 1640 or a 50/50 mix of the two was utilised.

hAELVi and NCI-H441 use huAEC and RPMI 1640 media, respectively. When seeded in co-culture at the theoretical seeding density, cells appeared to increase more rapidly after 72 hours submerged and 24 hours at ALI in RPMI 1640 (NCI-H441) media compared to hAELVi media, or 50/50 media (**Figure 3.14**). Monoculture analysis reveals that hAELVi cells grow significantly more rapidly in NCI-H441 media than NCI-H441 cells, which were not impacted by media type and, therefore, are likely attributable to the change observed in the co-culture cell numbers. A mixture of the two media types had an insignificant increase in growth rate in the hAELVi cells, with the cell count laying between the cell counts for hAELVi cells grown in huAEC or RPMI 1640 medium, though this was not replicated in the co-cultured cells.

Media type did not significantly impact viability in either monocultures or co-cultures. Viability remained approximately 80% or above throughout. Brookes *et al.* (2021) is the only study to date to co-culture hAELVi and NCI-H441 cells, where they have utilised each cell line seeded at equal densities within Advanced DMEM (Gibco) media. The growth of each cell line was not quantified independently; however, cells were found to grow effectively in this media type.

Based on these findings, media choice does not impact cell viability; therefore, media choice to take forward falls onto the impact of growth and how this affects the targeted 13-16:1 ratio, as well as the barrier function of the cultures.

### 3.3.4 Barrier Integrity of Submerged hAELVi/NCI-H441 Co-Culture at the Air-Liquid interface

The media type did not significantly impact barrier integrity in either monoculture or within the co-culture (**Figure 3.15**). However, visual observation of the co-culture and hAELVi monoculture at ALI revealed an inability to maintain ALI conditions when cultured in huAEC or 50/50 media. Basal media was found to leak through the transwell membrane into the apical compartment of the insert during all repetitions. This was not seen when co-cultures or hAELVi monocultures were cultured in NCI-H441 media.

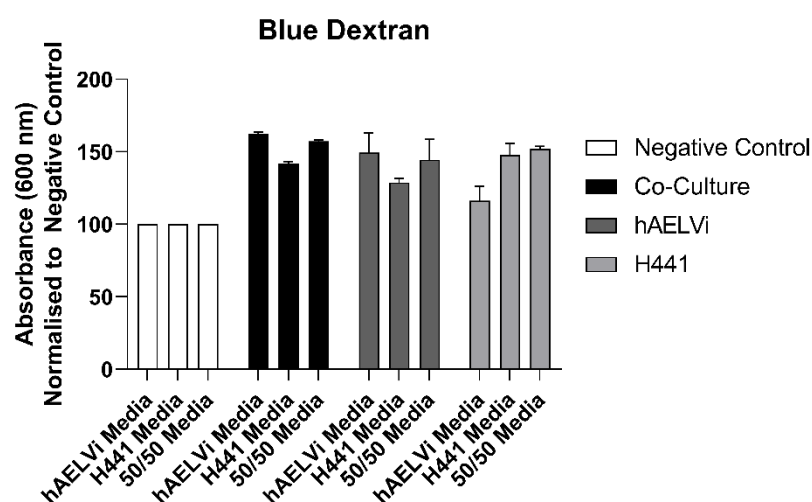


**Figure 3.15** Barrier properties measured using blue dextran of hAELVi and NCI-H441 (H441) co-cultures 96 hours post seeding. Cultures were taken to ALI at 72 hours. Bars show average mean values of 3 independent biological replicates with SEM error bars. Values have been standardised to a negative control of a transwell insert containing no cells for each media type (as each media was different in colour and so had different background absorbances).

Blue dextran revealed that membrane permeability was not significantly different in any culture regardless of media type. However, NCI-H441 cells grown in hAELVi media showed a non-significant increase in barrier function. When taken into the co-culture, however, this effect is lost, likely due to the reduced number of NCI-H441 cells compared to hAELVi cells.

Co-cultures and hAELVi monocultures cultured at ALI were not possible to maintain, with media rapidly translocating from the basal compartment to the apical

compartment. This phenomenon is not indicated in the blue dextran studies, perhaps indicating 1-way transport of solutes (given that monolayer was observed *via* light microscopy).

Based on the findings within this section and Section 3.3.3, a 50/50 media mix was chosen for future characterisation. This was due to the fact that the growth rate was not significantly altered, which did occur when hAELVi cells were cultured in RPMI 1640. Further, changes in the barrier function of hAELVi cells or co-cultures cultured in huAEC media were reduced. The 50/50 media results in growth, viability, and barrier function (*via* blue dextran) that are non-significantly different from if the cells were grown in their own typical media.

### 3.3.5 Co-Culture Seeding Density Optimisation

Given the inability to culture these cells in 50/50 media at the ALI due to the permeation of basal media into the apical compartment, it was thought that perhaps the 50/50 media mix may be increasing the time taken for a strong barrier formation. Whether due to the media type or the interaction between cell types in the co-culture,

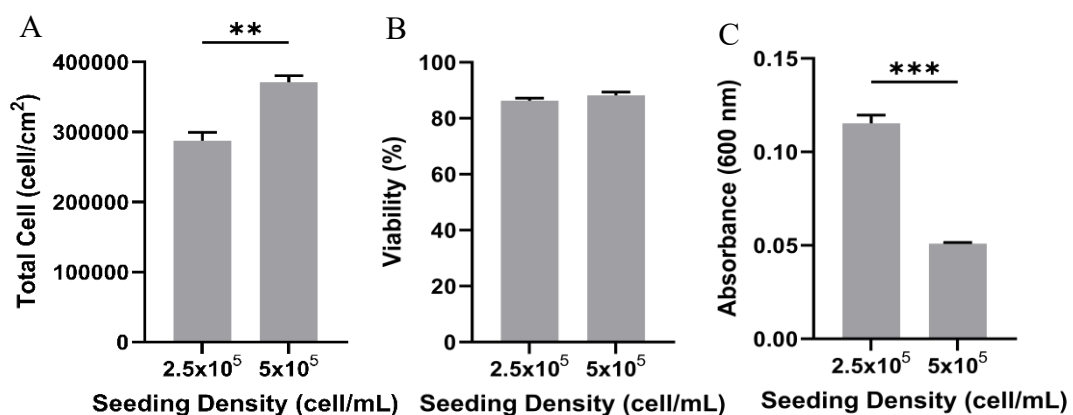


**Figure 3.16** Total cell count (A), viability (B) and blue dextran (C) for co-cultures seeded at  $2.5 \times 10^5$  or  $5 \times 10^5$  cell/mL ( $2.5 \times 10^5 - 2.25 \times 10^5$  hAELVi &  $2.5 \times 10^4$  NCI-H441.  $5 \times 10^5 - 4.5 \times 10^5$  hAELVi and  $5 \times 10^5$  NCI-H441). Bars show mean  $\pm$  SEM. \*\* =  $p \leq 0.01$ , \*\*\* =  $p \leq 0.001$ , shown through unpaired t-test.

it was found that the co-culture was incapable of maintaining tight barrier formation when a total of  $2.5 \times 10^5$  cell/mL were seeded. Therefore, increasing the initial seeding density was investigated to assess whether this could further increase barrier function, allowing a co-culture to be maintained at the ALI. Doubling the seeding density to  $5 \times 10^5$  cell/mL ensured enough cells were present to form a strong barrier, as shown in the blue dextran data (**Figure 3.16**).

Monocultures of either NCI-H441 or hAELVi have previously been characterised to form a confluent, tight monolayer at a 96-hour time point when seeded at  $2.5 \times 10^5$  cell/mL. **Figure 3.16** shows that when seeding at  $5 \times 10^5$  cell/mL, compared to  $2.5 \times 10^5$  cell/mL in the co-culture, cultures contain significantly more cells and form a significantly tighter barrier whilst maintaining similar percentage viability (85-90%).

This issue of co-cultures not maintaining an ALI when seeded at a typical monoculture seeding density has arisen in the past during the development of a transformed type-1 (TT1) and NCI-H441 co-culture at anatomically relevant ratios. Compared to respective monocultures, co-cultures had to be seeded at twice the density to ensure that the ALI could be maintained (Mitchell, 2022).

### **3.3.6 Deducing Seeding Concentrations of hAELVi and NCI-H441 Co-Cultures**

Human surface coverage ratios of ATI:ATII are 13-16:1 (Crapo et al., 1982). Although a theoretical seeding density had been calculated to obtain a 13-16:1 ratio at the time of the exposure based on the growth rate of each cell type in monoculture, reaching this ratio was not as straightforward. Many reasons likely contributed to this. The first is that each cell type likely grows at different rates. Although this was accounted for in the calculations based on the monoculture characterisation data, many factors can alter cell culture growth, such as temperature, pH, CO<sub>2</sub> and O<sub>2</sub> concentrations, and availability of fresh media (Segeritz & Vallier, 2017). Further, monocultures of hAELVi and NCI-H441 were characterised in huAEC and RMPI 1640, respectively, though the co-culture uses a 50/50 mix of the two. Given that different cell types require differing factors for growth, it is conceivable that altering the media would, therefore, change the growth rate (Vis et al., 2020). Further, media supplements such as FBS (used in the RMPI 1640) have been shown to have reproducibility issues, which could contribute further to this (van der Valk et al., 2018).

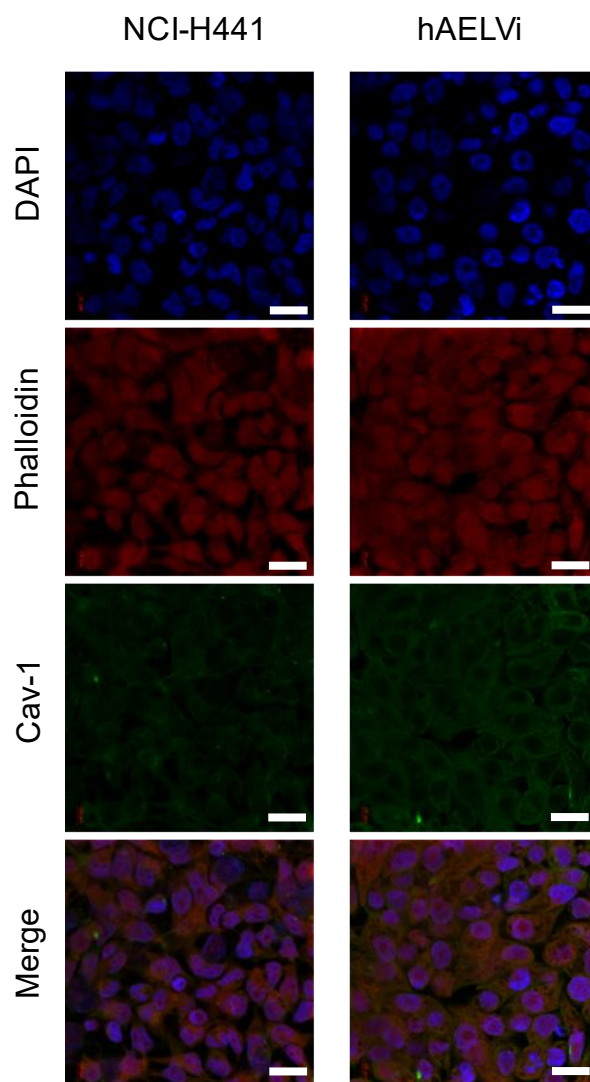


*Figure 3.17 LSM images of hAELVi or NCI-H441 monocultures using x63 objective lens to assess suitability for Cav-1 use in identification of hAELVi in co-culture. Scale bar = 100  $\mu$ m.*

As described previously, the model was required to achieve a hAELVi:NCI-H441 surface coverage ratio of 13-16:1. Initially, ATI and ATII-specific targets were identified and targeted using antibodies. Caveolin 1 was recognised as an ATI-specific marker. However, when tested, caveolin-1 staining intensity appeared to be similar in hAELVi compared to NCI-H441 and, therefore, was unsuitable for use in deducing specific cell populations in co-culture (**Figure 3.17**).

For this reason, the cells were instead pre-stained prior to seeding 3 differing ratios of hAELVi and NCI-H441 (described in **Table 3.2**) to assess what seeding densities would closely resemble the 13-16:1 ratio at 96 hours.

Using CellTrackers™ to quantify the surface coverage of each cell type, seeding ratio 1, ratio 2 and ratio 3 had 4.8, 6.9 and 13.6  $\mu$ m<sup>2</sup> of hAELVi cell coverage, respectively,

for every 1  $\mu\text{m}^2$  of NCI-H441 cell coverage (**Figure 3.18**). Based on this, ratio 3 was taken forward, which had seeding ratios of  $4.5 \times 10^5$  and  $5 \times 10^4$  cell/mL hAELVi and NCI-H441, respectively, which was found to give the ratio at 13.6:1. This is close to the initially targeted ratio based on human anatomy data from Crapo *et al.* (1982).

Further investigation of ratio 3 over 5 biological replicates (using 3 FOVs per replicate) found the average ratio of hAELVi:NCI-H441 was  $16.44:1 \pm 3.29$  (**Figure 3.19**). This seeding ratio confirmed the initial findings and was therefore taken forward into future exposure studies.

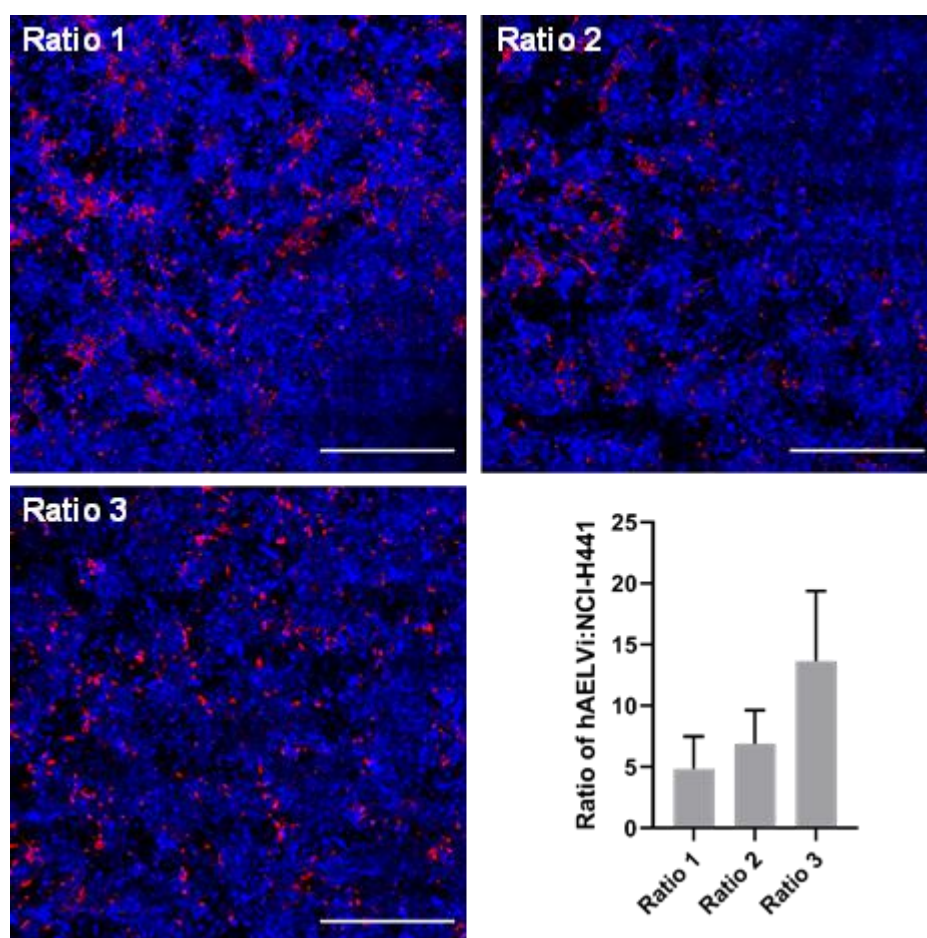


**Figure 3.18** CellTracker™ staining of hAELVi and NCI-H441 co-cultures seeded at ratio 1, ratio 2 and ratio 3 (hAELVi (red) and NCI-H441 (blue) respectively) (scale bar = 5000  $\mu\text{m}$ ). Average ratio across the 3 replicates is shown. Each bar shows average across 3 FOVs  $\pm$  SEM. Scale bars – 500  $\mu\text{m}$

Here, it has been shown that it is essential to track changes to the ratio of each cell type as the cultures grow, as the ratio at the time of exposure will likely not match the ratio of seeded cells. This area is not always reported or explored when co-cultures are utilised, or the relevance to human anatomy is not commented on. For example, Brookes *et al.* (2021) used equal seeding ratios of hAELVi and NCI-H441, though does



not go on to state whether this ratio changes at the time of exposure/endpoint assessment.

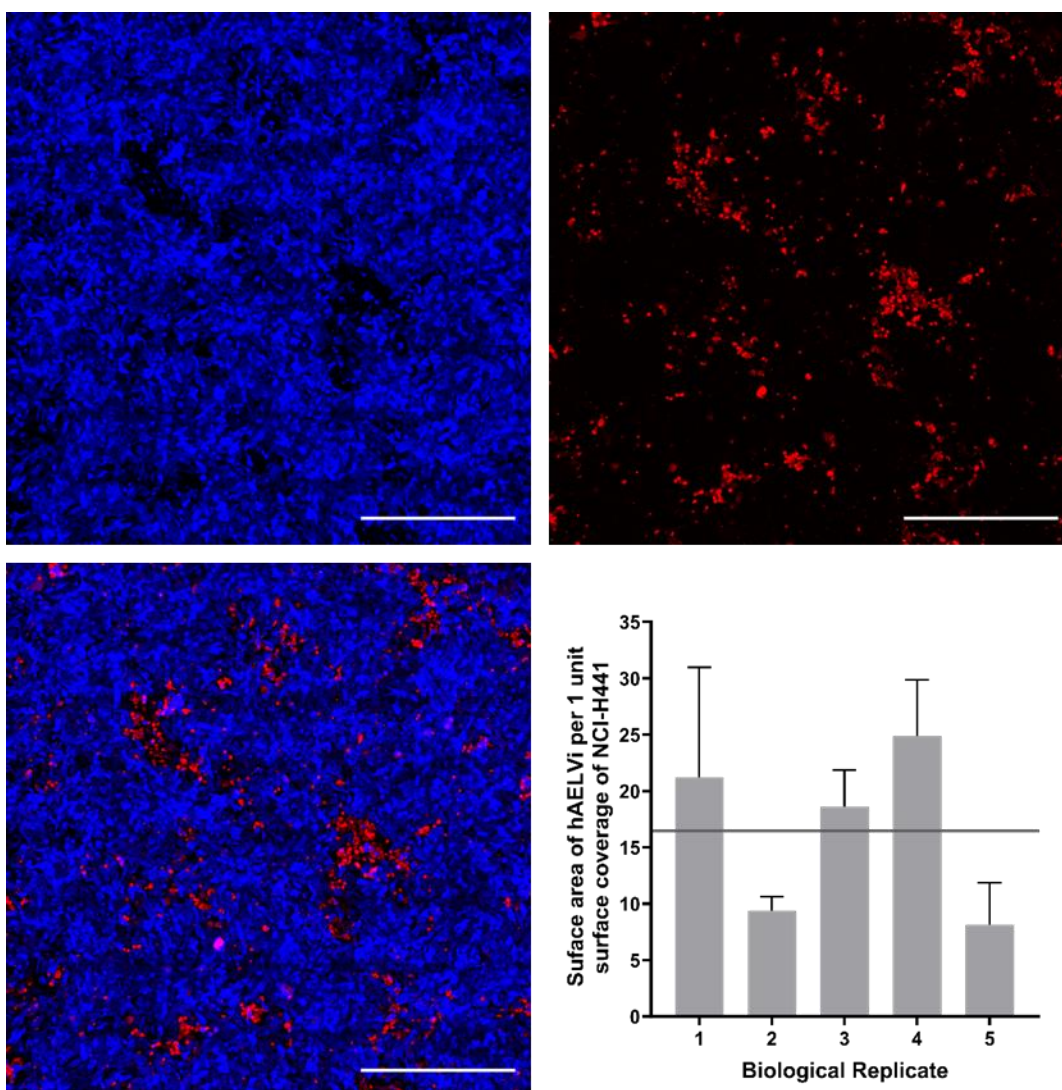


**Figure 3.19** CellTracker staining of hAELVi and NCI-H441 co-cultures seeded at  $4.5 \times 10^5$  and  $5 \times 10^4$  cell/mL (hAELVi (red) and NCI-H441 (blue) respectively) (scale bar = 5000  $\mu\text{m}$ ). Average ratio across the 5 replicates was 16.44:1, with a targeted ratio of 16:1 (grey line). Each bar shows average across 3 FOVs  $\pm$  SEM. Scale bars – 500  $\mu\text{m}$ .

### 3.3.7 Adherence Efficiency of dTHP-1 Cells to Alveolar Epithelial Cells at the Air-Liquid Interface and Quantification of dTHP-1 Density in the Triple Cell Co-Culture

There should be 1 dTHP-1 per  $18 \times 10^3 \mu\text{m}^2$  (Stone et al., 1992) on the apical surface of the culture. During the seeding of this model, dTHP-1 cells are added to an epithelial co-culture, allowed to adhere for 2 hours, and then taken to the ALI (by removing the apical media). It could not be assumed that during this 2-hour adherence period 100% of the dTHP-1 cells would adhere. Therefore, the number of the cells in the apical

media (removed when taken to the ALI) was counted to assess how many dTHP-1 would adhere. This was compared to cultures that had been cultured for the 2 hours in dTHP-1-free to allow for confounding detached epithelial cells.

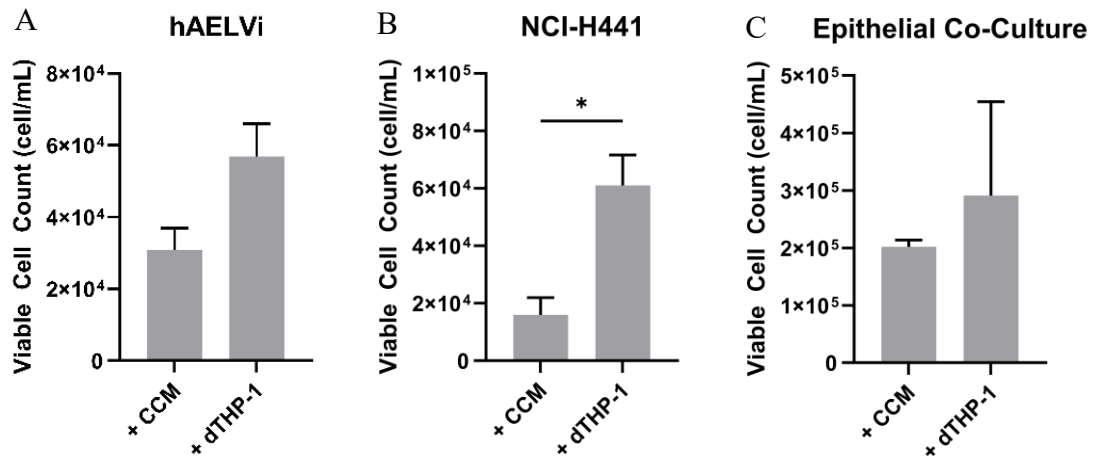


**Figure 3.20** Viable cell counts using the LUNA II on media removed when cells were exposed to ALI 2 hours following the addition of dTHP-1 cells or cell-free media (CCM). Bars show mean  $\pm$  SEM. Significance evaluated using unpaired t-test. \* =  $p \leq 0.05$ .

**Table 3.3** Adherence of dTHP-1 cells to various alveolar epithelial models

	hAELVi	NCI-H441	Epithelial Co-Culture
Net non-attached dTHP-1 (Viable count from +dTHP-1 – Viable count from +CCM) (cell/mL in 50 $\mu$ L total)	$2.61 \times 10^4$	$4.51 \times 10^4$	$4.26 \times 10^4$
Number of dTHP-1 not attached in 100 $\mu$ L (cell/mL in 100 $\mu$ L total)	$1.30 \times 10^4$	$2.26 \times 10^4$	$2.13 \times 10^4$
Total number of dTHP-1 in 100 $\mu$ L (cells)	$1.30 \times 10^3$	$2.26 \times 10^3$	$2.13 \times 10^3$
<b>dTHP-1 Adherence (of initial <math>1 \times 10^4</math> added) (%)</b>	<b>86.96</b>	<b>77.44</b>	<b>78.68</b>

When cultured on top of either hAELVi, NCI-H441 or epithelial co-cultures, there were always more viable cells counted in the discarded media after the addition of dTHP-1 cells (only reaching significance when cultured on top of NCI-H441 cells) (**Figure 3.20**). Viable cell counts enabled the percentage of adhered dTHP-1 to be calculated (**Table 3.3**). Within this triple cell co-culture, macrophages are added on top of the hAELVi + NCI-H441 co-culture, which showed an adherence efficiency of 78.68%, therefore a loss of 21.32% of the dTHP-1 cells when taken to the ALI.

Given a requirement to have 1 dTHP-1 per  $18 \times 10^3 \mu\text{m}^2$  (Stone et al., 1992), it was therefore calculated that 6430 dTHP-1s were needed to be added per well to reach the targeted density whilst accounting for the loss of non-adhered cells.



Using CellTrackers™ to pre-stain the dTHP-1 cells, it was found that actually 30000 dTHP-1 cells needed to be seeded to achieve 1.13 dTHP-1 per  $18 \times 10^3 \mu\text{m}^2$ . Seeding with 5000 or 6430 dTHP-1 resulted in 0.06 and 0.24 dTHP-1 per  $18 \times 10^3 \mu\text{m}^2$ , respectively. Therefore, 30000 dTHP-1 cells per well were instead utilised for seeding this culture throughout this work (**Figure 3.21**).

The number of dTHP-1 required to be seeded was almost five times higher than expected, even taking into account non-adhered cells. This was interesting as when the dTHP-1 cells were added, they were checked for viability and cell suspensions were diluted based on the viable cell count. Using co-cultures of calu-3 cells and dTHP-1, He *et al.* (2021) found that dTHP-1 numbers decreased over 9 days with increased apoptotic bodies. This could suggest that dTHP-1 do not maintain viability at ALI, perhaps explaining why a higher seeding density was required to reach the desired density 24 hours later, though this study examined longer time durations than those used here. The study also demonstrated that giving dTHP-1 cells 24 hours to adhere to the epithelial cells before taking to the ALI resulted in increased formation of extensive multinucleated cell fusions compared to a 4-hour adherence period. In this model, a 2-hour adherence time was used, so the risk of this occurring is reduced here.

The co-culture model from He *et al.* utilised  $1.0 \times 10^4$  dTHP-1/cm<sup>2</sup> (approx. 1 dTHP-1 per  $1 \times 10^4 \mu\text{m}^2$ ), almost half as many macrophages per unit area than the model produced here, though this is a co-culture model of the conducting airway using macrophage histology data that is likely different from alveolar histology (Grashoff *et al.*, 1997). Kletting *et al.* (2018) utilised hAELVi and THP-1 cells at a ratio of 3:1 based on work by Stone *et al.* (1992); hAELVi were grown for 14 days before the addition of dTHP-1 cells which were suspended in 6  $\mu\text{L}$  of media and incubated, without the removal of the additional apical media to form an ALI culture, or were added suspended in 500  $\mu\text{L}$  media to form a submerged culture. It was found that there were fewer cells in the ALI culture, though the viability data for unexposed cultures was not shown. This, perhaps, again shows why more dTHP-1 cells than exposed were required to be added to the co-culture.

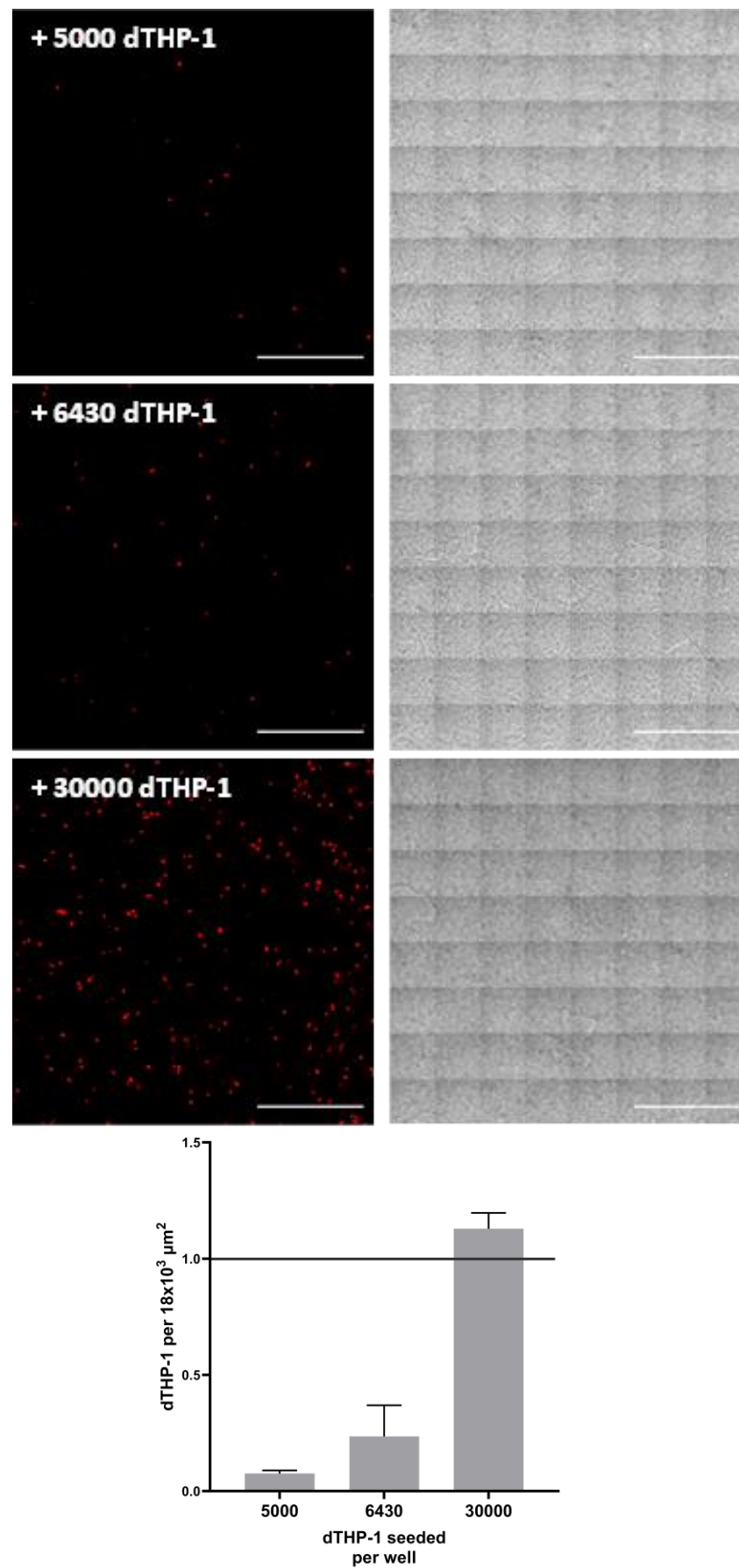


**Figure 3.21** CellTracker™ staining (left) of dTHP-1 in the triple cell co-culture using transmitted light (right) to confirm the presence of non-stained epithelial cells. Number of dTHP-1 per  $18 \times 10^3 \mu\text{m}^2$  shown as mean  $\pm$  SEM ( $n = 2$  for 5000 and 6430,  $n=3$  for 30000). Scale bars =  $500 \mu\text{m}$ .

### 3.3.8 Assessment of dTHP-1 Activation within the Triple Cell Co-Culture

Once the correct number of dTHP-1 was confirmed within the triple cell co-culture, the models' ability to react to an inflammatory stimulus was assessed. When epithelial co-cultures or triple cell co-cultures were exposed to LPS, it was found that TNF- $\alpha$  levels increased in both epithelial cell co-cultures and the triple cell co-culture, though to a much greater extent in the latter. LPS also induced significant increases in IL8 secretion in the triple-cell co-culture compared to epithelial cell co-cultures exposed to LPS and unexposed triple-cell co-cultures (**Figure 3.22**).

Although the fate of dTHP-1 cultured at the ALI is uncertain, the ability of the triple cell co-culture to mount a larger pro-inflammatory response to an inflammatory stimulus, compared to untreated triple cell co-cultures or epithelial co-cultures (lacking dTHP-1 cells) treated with LPS has been shown. He *et al.* (2021) similarly found that co-cultures of Calu-3 and dTHP-1 at ALI produced significantly more apical TNF $\alpha$ , IL1 $\beta$  and IL10 compared to monocultures of Calu-3 when exposed to LPS, though these cells were exposed *via* aerosol rather than through the basal media (as performed here). Given that the triple cell co-culture forms a tight monolayer, aerosol exposure is perhaps more relevant as basal LPS might not reach the dTHP-1 cells that are apical to the epithelial cells. Regardless, a pro-inflammatory response was seen. IL8 levels were increased largely compared to TNF $\alpha$  following LPS exposure here.

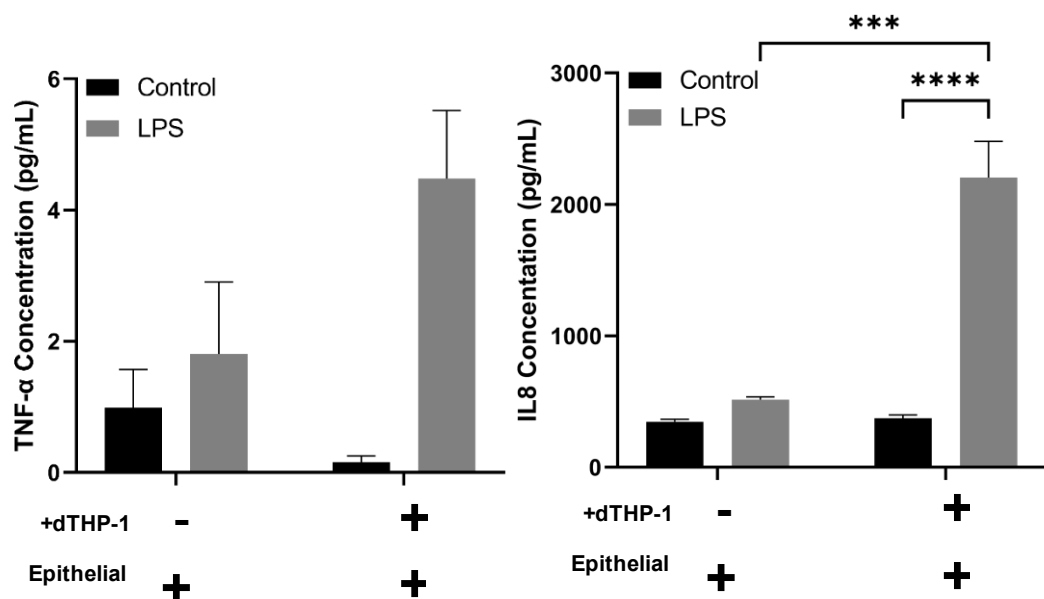


**Figure 3.22** TNF- $\alpha$  and IL8 release following LPS stimulation of epithelial co-cultures or triple cell co-cultures. Bars show mean of 3 biological replicates  $\pm$  SEM. Difference assessed via one way ANOVA. \*\*\* =  $p \leq 0.001$ , \*\*\*\* =  $p \leq 0.0001$ .

Given that TNF $\alpha$  binds to the TNF $\alpha$  receptor (TNFR), which is present in epithelial cells (Yan et al., 2004), sequestering of the protein on the receptor could be the reason lower TNF $\alpha$  concentrations are seen, generally. IL8 (which would be released in response to downstream TNFR signalling), on the other hand, was released at a significantly higher level following LPS exposure. This has been tested experimentally in epithelial cells where TNF $\alpha$  exposure directly induces IL8 release (O'Hara et al., 2009). Co-cultures of A549 and dTHP-1 can react to gaseous stimulants, with co-cultures releasing more IL8 than A549 monocultures when exposed to ozone (Bauer et al., 2014). Similarly, co-cultures were more sensitive than monocultures when exposed to hematite, quartz and silica particles, shown through augmented IL6 and IL8 release (Wottrich et al., 2004). Given that these models are reactive to both gases and particles, it warrants using such models within this research to assess NO<sub>2</sub> and PM co-exposure. This further shows that these cells can communicate within an *in vitro* culture to modulate pro-inflammatory response.

Given that the epithelial co-culture was characterised at a relevant ratio, and the number of dTHP-1 at the time of exposure was counted to be applicable, this method will be taken forward within the PM and NO<sub>2</sub> exposures discussed in subsequent chapters.

### 3.4 Summary and Outlook

*Table 3.4 Key conclusions and findings from Chapter 3*

<b>Chapter Conclusions</b>	<ul style="list-style-type: none"> <li>▪ hAELVi cells can be grown on transwell inserts at the ALI, forming a tight barrier.</li> <li>▪ A physiologically relevant ratio of hAELVi (ATI) to NCI-H441 (ATII) cells can be cultured through seeding 500 <math>\mu\text{L}</math> of cell suspension at <math>4.5 \times 10^5</math> and <math>5 \times 10^4</math> cell/mL, respectively.</li> <li>▪ Through seeding dTHP-1 cells (AMs) at <math>3 \times 10^5</math> cell/mL (100 <math>\mu\text{L}</math> of cell suspension), a physiologically relevant density of AMs can be achieved in this culture.</li> <li>▪ This triple cell co-culture forms a tight barrier.</li> <li>▪ This triple cell co-culture can respond to a pro-inflammatory stimulus.</li> </ul>
<b>Project Impact</b>	<b>A physiologically relevant triple cell co-culture of the alveolar barrier has been developed and characterised within this chapter. This advanced <i>in vitro</i> model can be taken forward within the project and implemented within PM and NO<sub>2</sub> co-exposure toxicological studies.</b>

A triple cell co-culture has been developed and highly characterised, ensuring that studies which have characterised human anatomy were used as the basis to inform the direction during the co-culture development.

The triple cell co-culture comprises 3 cell types: ATI, ATII, and alveolar macrophages (hAELVi, NCI-H441 and dTHP-1, respectively). Understanding the exact cellular constituents and the time of exposure, as opposed to the time of seeding, is vital in understanding cell-specific effects. Given that this model will be used in inhalation exposure studies, the data presented within this chapter will be pivotal when deducing mechanistic toxicological effects of particles or gases. Though not characterised to the same extent, different combinations of cells within the triple cell co-culture can be utilised in co-culture going forward. This will allow investigation into further cell specific effects and interactions.

Regardless, the model has been shown to possess an anatomically relevant ratio of ATI:ATII and an anatomically relevant number of dTHP-1 per unit area. The model possesses a functional tight barrier and can react to a pro-inflammatory stimulus. Although in this study, the model will be utilised within air pollution exposure studies, this model could also be used when looking at a range of emerging inhalation exposure

hazards, such as engineered nanomaterial or micro/nanoplastics, used when assessing occupational risk hazard, or used when looking at effects of respiratory pathogens (*e.g.*, Covid-19) and inhaled therapeutics (**Figure 3.23**).

## Day 0 - Seeding Epithelial Cells and Differentiating THP-1

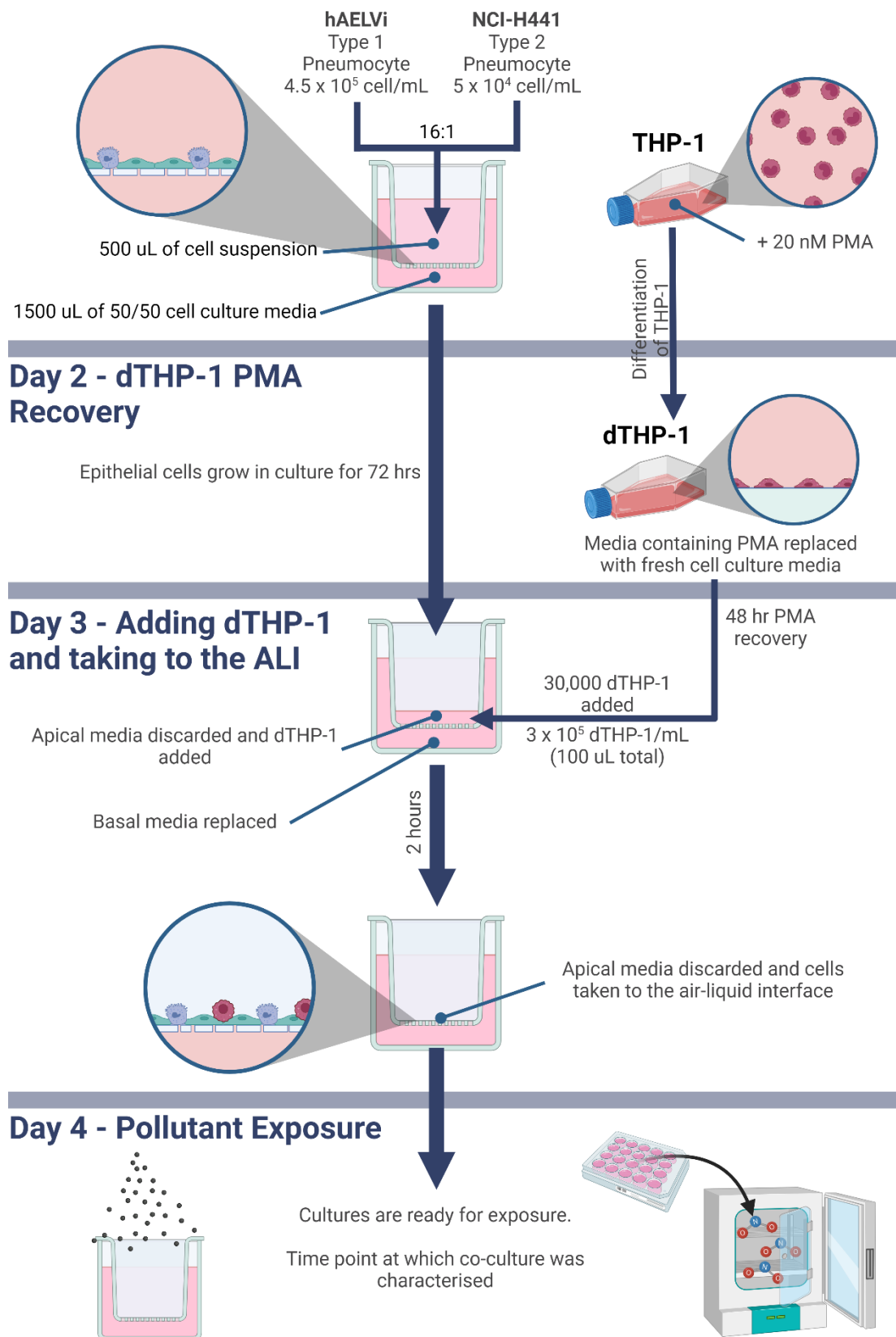


Figure 3.23 Schematic of the method for culturing the alveolar triple cell co-culture.

## **Chapter 4: Particulate Matter and Nitrogen Dioxide Exposure Systems**

---



## 4.1 Introduction

The broad heterogeneous nature of air pollution has been discussed in Chapter 1. In addition to emission sources, these pollutants may differ significantly in their physical and chemical characteristics. The physical and chemical characteristics of particles as a whole are vitally important in determining how the particles could interact with biological interfaces and their subsequent biological impact. For example, when considering PM size exclusively, smaller particles generally permeate deeper into the lungs, impacting the cells and proteins the particles will first encounter. Further, particle size plays a role in determining how PM interacts with biological material and, thus, can alter the toxicological response (Mirowsky et al., 2013). Other particle characteristics that can alter interactions with biological material include chemical composition, shape, agglomeration, dispersion, charge, surface chemistry (Llewellyn et al., 2022), corona formation (especially important when considering interaction with serum within *in vitro* exposure conditions) (Bhattacharya et al., 2016). Although present for nanoparticle research, the impact of PM's physical and chemical characteristics on toxicology is not as well-defined (Stone et al., 2017). Further investigation and reporting of these characteristics in PM exposure studies would allow the identification of hazardous properties that could aid decision-making in the future, as well as create specific structure-activity relationships (*e.g.*, as seen in the fibre paradigm (Poland et al., 2008)).

As well as characterising the material, the exposure method also requires intense focus since this could alter particle characteristics that could, therefore, change their subsequent interactions with biological systems. As such, there is a requirement to ensure that exposure methods are realistic to the exposure that is intended to be replicated. In *in vitro* inhalation toxicology, exposure methods can be broadly summarised into 3 classifications: submerged, quasi-ALI (qALI), or at ALI (**Figure 4.1**). Though each system has benefits and drawbacks, within the studies presented in this work, exposures intend to mimic human exposure conditions. Therefore, most assessments will utilise cells cultured at the ALI combined aerosol exposure using the

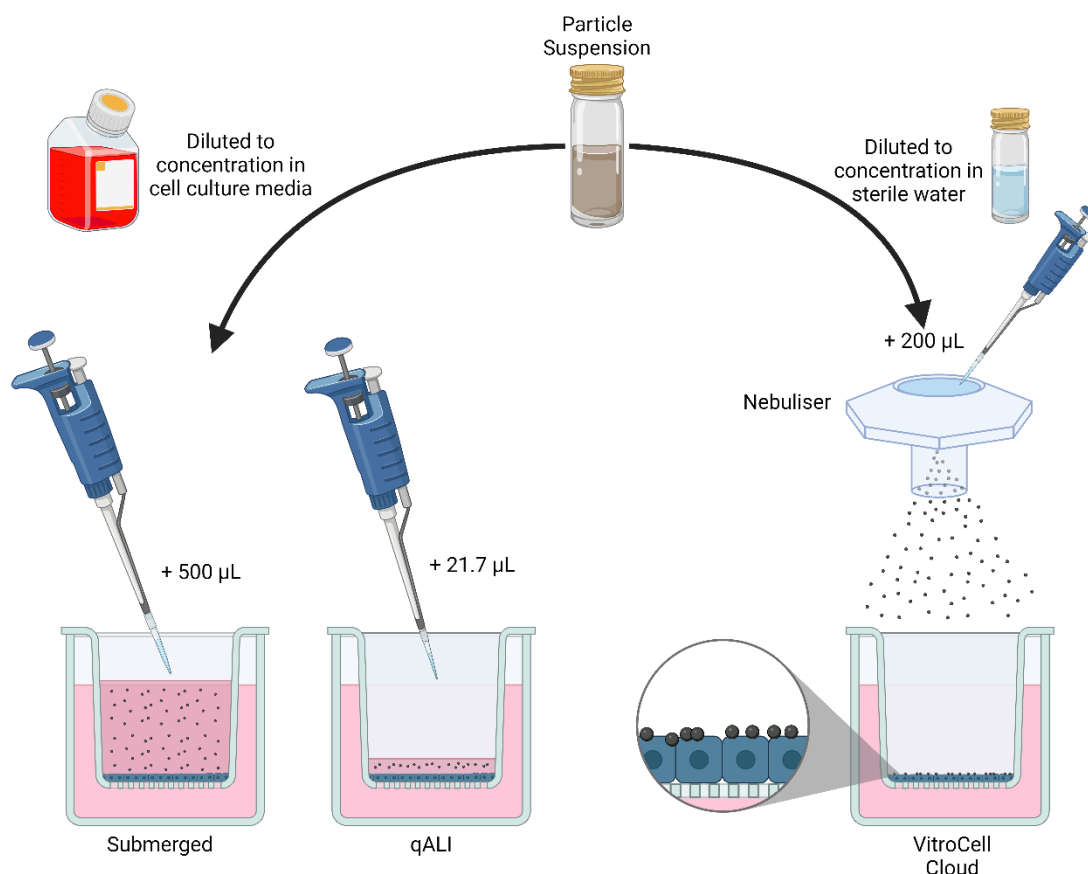


**Figure 4.1** Methods of PM exposure using submerged, qALI and aerosol (VibroCell Cloud) techniques.

VibroCell® Cloud 12. This was chosen as healthy humans would not be exposed to pollutants in submerged conditions.

The exposure method must be strongly considered within air pollutant exposure studies; for example, submerged and aerosol exposures using nanoparticles induce different *in vitro* biological effects. A549 cells show an increase and decrease in HMOX1 and IL8 expression, respectively, when exposed to zinc oxide nanoparticles at the ALI compared to submerged (Lenz et al., 2009). This chapter, therefore, intends to characterise the PM samples that will be exposed to the alveolar models using microscopy techniques and attempts to understand how these particles will act within the VibroCell® Cloud12 regarding deposition efficiency. This is important as it allows refined and guided exposures when moving into the *in vitro* studies.

#### 4.1.1 Aims and Objectives

Though the triple cell co-culture has been well characterised in Chapter 3, there is a requirement to characterise the exposure methods and particles that will be used when

the alveolar model is exposed to air pollutants. This chapter, therefore, aims to assess the morphology of pollutant samples to be used when exposed *via* VitroCell Cloud12 or dropcast and then also assess the deposition efficiency of pollutant suspensions through the VitroCell nebuliser at different nebulised (feed) concentrations.

The NO<sub>2</sub> exposure chambers' development will be discussed, and initial testing of the chamber to assess feasibility in *in vitro* exposures will be investigated.

## 4.2 Materials and Methods

### 4.2.1 Experimental Design

Two main exposure systems will be used in this work. Firstly, the VitroCell® Cloud will aerosolise and deposit PM onto alveolar models. Secondly, a system is required that will allow models to be exposed to NO<sub>2</sub>. Each exposure method requires characterisation prior to implementation within toxicological evaluations. Therefore, this chapter intends to first characterise the deposition of CB, 1649b and 2583 *via* the VitroCell® Cloud through analysis of deposited concentration and morphological analysis using SEM. Then, a state-of-the-art NO<sub>2</sub> exposure system will be described, and a critical assessment of the ability for NO<sub>2</sub> exposure and confounding variables will be conducted.

**Table 4.1** Physical and chemical characterisation of PM samples used within this work. <sup>a</sup> Saber et al. (2005), <sup>b</sup> Saber et al. (2012), <sup>c</sup> Jacobsen et al. (2008), <sup>d</sup> Kong et al. (2013), <sup>e</sup> Bendtsen et al. (2020), <sup>f</sup> NIST (2023).

	Printex 90	NIST Urban Dust (1649b)	NIST Trace Elements in Indoor Dust (2583)	Diesel Emission Particles (9.7%) <sup>e</sup>	Diesel Emission Particles (13%) <sup>e</sup>	Diesel Emission Particles (17%) <sup>e</sup>
<b>Primary Mean Particle Diameter (nm)</b>	65 (carbon spheres) <sup>a</sup>	105 <sup>f</sup>	-	22	17	16
<b>Particle Mobility (Agglomerate) Diameter (nm)</b>	200 <sup>b</sup>	-	-	55 ± 9	104 ± 7	62 ± 4
<b>Specific Surface Area (m<sup>2</sup>/g)</b>	295-338 <sup>a, c</sup>	-	-	152	191	207
<b>Z-average (nm)</b>	~140	-	-	-	-	-
<b>Zeta Potential (mV)</b>	-17.6 (in cell culture media) <sup>d</sup>	-	-	-	-	-
<b>Hydrodynamic Number (nm)</b>	50-60	-	-	-	-	-
<b>Elemental to Total Carbon</b>	-	-	-	0.35	0.88	0.6
<b>Organic to Total Carbon</b>	-	-	-	0.65	0.65	0.4
<b>Intake O<sub>2</sub> (%)</b>	N/A	N/A	N/A	9.7	13	17

### 4.2.2 Particulate Matter Samples

Work within this project will utilise a range of realistic PM samples. Namely, Printex® 90 Carbon Black (CB), which will be used as a surrogate model particle of PM, as well as urban dust and indoor dust from the National Institute of Standards and Technology (NIST) (standard reference material (SRM) 1649b and 2583 respectively). Fuel emission particles from the combustion of diesel (DEP) were also used. The published

physical and chemical characteristics of each PM type are available in **Table 4.1** (and further detailed in Appendix 1).

#### **4.2.2.1 Particle preparation**

PM samples were stored dry at room temperature. When required for use, 8.9 mg of powder was weighed into a bijoux tube. The powder was then pre-wetted with 25  $\mu$ L ethanol (100%) before being suspended in 2.575 mL sterile Milli-Q water, forming a suspension at 3.4 mg/mL. The PM samples are pre-wetted with ethanol to allow dispersion of hydrophobic materials within water-based systems.

The particle suspension was dispersed using a Branson 550 sonicator (equipped with a Branon 102C sonication probe). The suspension was sonicated at 10% power for 4 minutes total sonication time using 10 seconds on 10 seconds off pattern. The sonicator was thoroughly cleaned between uses by sonicating the probe in 70% ethanol twice.

After sonicating, the particle suspension was diluted to a working concentration using sterile Milli-Q water.

#### **4.2.2.2 Printex® 90 Carbon Black**

When considering air pollution, many people think of soot from combustion sources. Regardless of origin, these soot particles often comprise a carbonaceous core with a corona of attached compounds such as PAHs (Jackson et al., 2012). CB can represent the carbonaceous core and has been characterised as containing less than 1% of the impurities often found in air pollution samples (Jacobsen et al., 2007). CB has, therefore, been utilised as a surrogate test material in toxicological studies to assess the hazard associated with PAH naïve combustion particles previously (Jackson et al., 2012).

CB, a group 2B carcinogen (possibly carcinogenic to humans) (Baan et al., 2006), has been implicated in a range of *in vitro* toxicological studies (Beck-Speier et al., 2005; Di Ianni et al., 2021; Drumm et al., 1998). Given the analogy that can be made to DEPs, the available high masses, and the fact that CB is a well-used particle within the field of toxicology, allowing interlaboratory comparisons to be established, it has been utilised within this study.

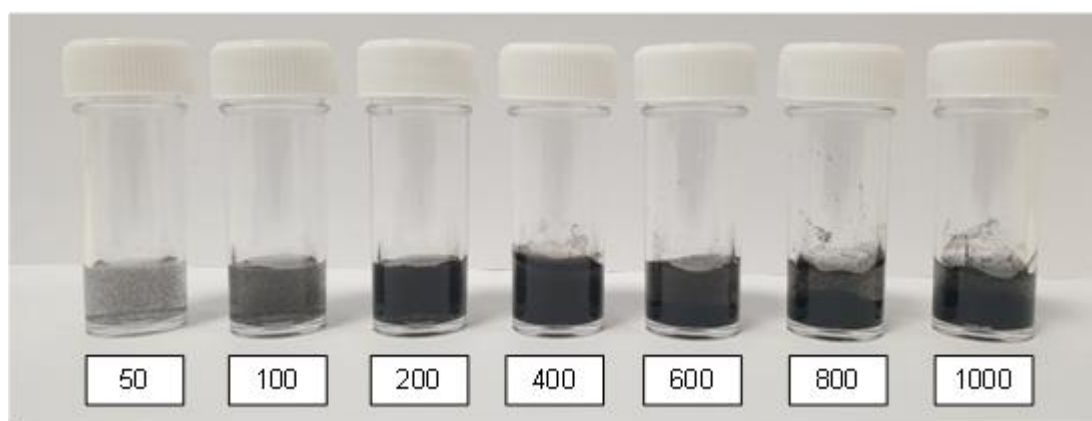


**Figure 4.2** Macroscopic images of carbon black stock solution at 3.4 mg/mL, diluted to working concentrations of 50, 100, 200, 400, 600, 800 and 1000  $\mu\text{g/mL}$ .

CB was diluted to concentrations outlined in **Table 4.2**, forming a black suspension that increased in turbidity as the concentration increased (**Figure 4.2**). At higher concentrations (600 and higher), sedimentation of the suspension was visible at the bottom of the bijoux, whereas CB appeared more evenly dispersed in the lower concentrations. Higher concentrations also caused the surface of the suspension to become irregular compared to lower concentrations, often leaving a tide mark of CB deposited on the inside surface of the bijoux.

#### 4.2.2.3 SRM 1649b Urban Dust

Urban dust was collected in Washington, DC, USA, in 1976 and 1977 over a period > 12 months (NIST, 2023). The SRM is intended to act as a standard for general atmospheric particulate matter and not be representative of the area in which the particles were collected, though for this work, it may be important to consider this considering the emission sources of urban PM have changed vastly in the recent

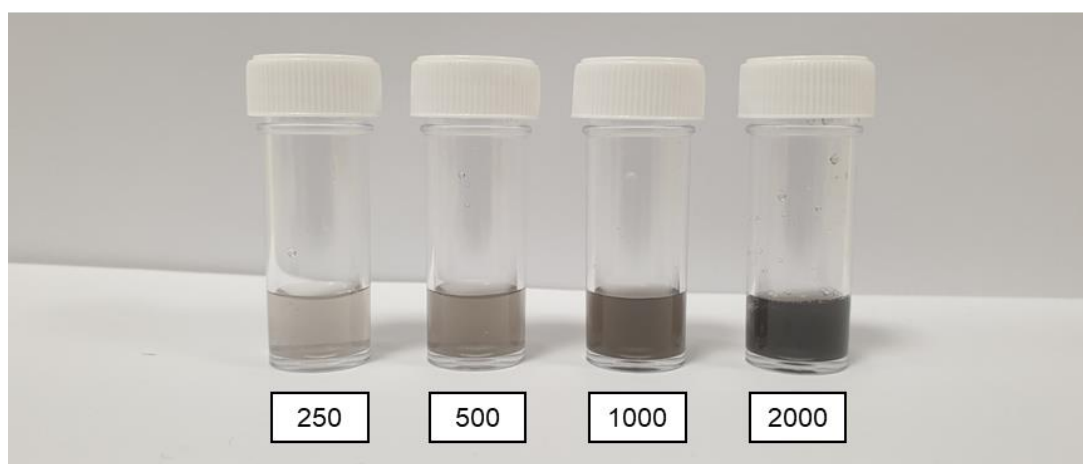


**Figure 4.3** Macroscopic images of NIST SRM 1649b stock solution at 3.4 mg/mL, diluted to working concentrations of 250, 500, 1000 and 2000  $\mu\text{g/mL}$ .

decades (DEFRA, 2019). The sample was collected using baghouse filter bags and passed through a 63  $\mu\text{m}$  sieve to remove filter bag fibres.

NIST has quantified a range of chemicals, including PAHs, nitro-PAHs and heavy metals, to be present within 1649b, which could contribute to inhalation hazards. However, the *in vitro* effects of 1649b have been scarcely reported, though, within the last 5 years, increased efforts have been focused on this PM. It is important to note that 1649b is a replacement for NISTs original 1649a, which was implicated within toxicological studies; however, NIST does not consider these two SRMs identical, so a comparison has not been drawn here. The range of particle sizes in this SRM is 0.2-100  $\mu\text{m}$  (NIST, 2023); however, this size exposed to the cells might differ following nebulisation.

SRM 1649b has been used in this study as a realistic outdoor PM sample. The fact that it is from NIST is beneficial as it allows interlaboratory comparison and can be purchased in large quantities.

In contrast to the CB, 1649b is greyer in colour, especially when diluted, though the stock solution appears almost black. When viewing macroscopically, the presentations of aggregates are minimal again in contrast to CB. The urban dust does not appear to interact with the water in the same manner as CB, where the surface of the water is flat in the bijoux (**Figure 4.3**).

#### 4.2.2.4 SRM 2583 Trace Elements in Indoor Dust

Indoor dust was collected from vacuum cleaner bags used within households, motels, hotels and cleaning services in various US states. Relative to 1649b, 2583 has little physical and chemical characterisation and has not been used in toxicological studies, though it does contain heavy metals such as lead and arsenic (NIST, 2016).

SRM 2583 has been used in this study as a realistic indoor PM sample. The fact that it is from NIST is beneficial as it allows interlaboratory comparison and can be purchased in large quantities.

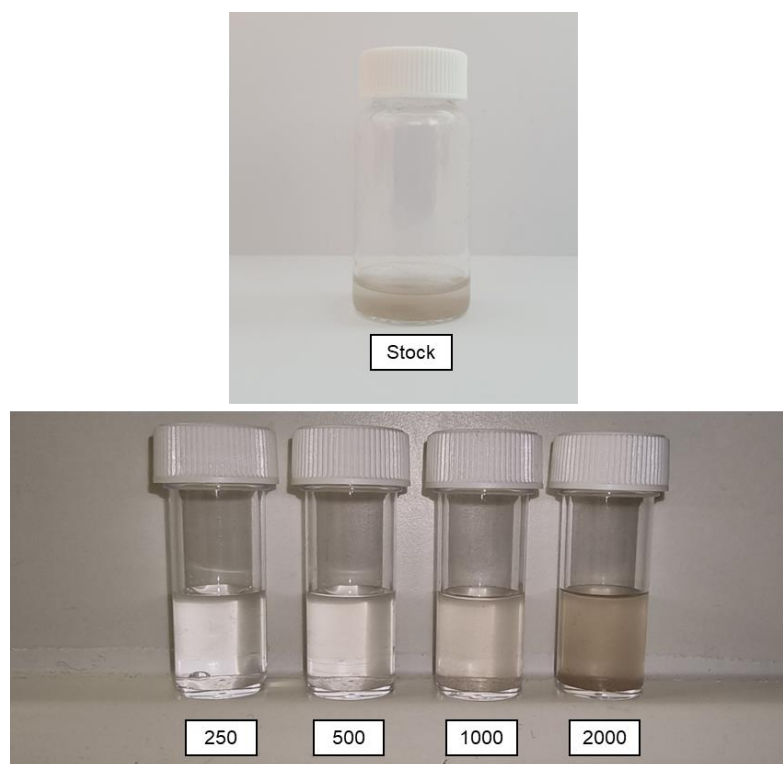


*Figure 4.4 Macroscopic images of NIST SRM 2583 stock solution at 3.4 mg/mL, diluted to working concentrations of 250, 500, 1000 and 2000  $\mu\text{g/mL}$ .*



The 3.4 mg/mL stock solution of 2583 forms a brown/beige solution, which, when diluted, almost forms a clear solution. Compared to the 1649b, the 2583 suspension more readily sediments at the bottom of the bijoux (**Figure 4.4**).

#### **4.2.2.5 Diesel Emission Particles**

DEPs were used to examine the toxicology of fuel emission particles, which could be co-emitted with NO<sub>2</sub>. Three different DEPs were used based on different oxygen concentrations of the air intake, specifically. 9.7, 13 and 17%. Engines have the ability to recirculate exhaust gases (which possess a lower oxygen concentration) in an attempt to reduce NO<sub>x</sub> emissions. Reducing the oxygen intake subsequently increases soot formation, and alters the physical and chemical characteristics of the DEPs produced.

The DEPs were collected from a modern 6-cylinder ignition engine using Teflon filters and extracted using methanol, according to Gren *et al.* (2020). Total extracted mass was recorded and the particles were then stored dried at room temperature until required for use. When required, DEPs were suspended in 1 mL of distilled water to form a stock solution, which was subsequently diluted in distilled water to exposure concentrations of 16.4, 32.8 and 130.4 µg/mL. The diesel particles were exposed *via* qALI.

The ROS-forming potential of the DEPs was higher as the oxygen intake percentage increased (Gren *et al.*, 2020), and these particles have been implicated with acute phase response, inflammation and genotoxicity when intratracheally instilled within mice (Bendtsen *et al.*, 2020). Further, Gren *et al.*, 2020 compared these DEPs to a standard DEP (NIST SRM 2975), finding a greater level of PAHs which may be reflective of the fact these are fresher samples than the standardised counterparts.

#### **4.2.3 VitroCell Cloud 12**

The VitroCell Cloud can fit various nebulisers with various mesh sizes, allowing different particle sizes to be efficiently aerosolised. Here, a 4.0 – 6.0 µm mesh Aerogen nebuliser was used for CB exposures, whereas a 12 µm mesh Tekceleo nebuliser was used for NIST particle exposures. Although mesh size differed between nebulisers (and therefore aerosol particle), the method in which each nebuliser was used was the same.

That being said, the Tekceleo nebuliser had an extra setting, allowing the flow rate to be adjusted (this is not an option on the Aerogen nebuliser). Work by VitroCell using sodium fluoresceine found the greatest deposition efficiency when using a flow rate of 10-30%, and comparisons in the lab found that a flow rate of 30% most closely matched the nebulisation time for the Aerogen nebuliser. The Tekceleo was, therefore, always used at a 30% flow rate (**Figure 4.5**).

The VitroCell software receives data from a quartz crystal microbalance (QCM), which reports deposition data in unit weight/cm<sup>2</sup> with a reading taken every 1 second.

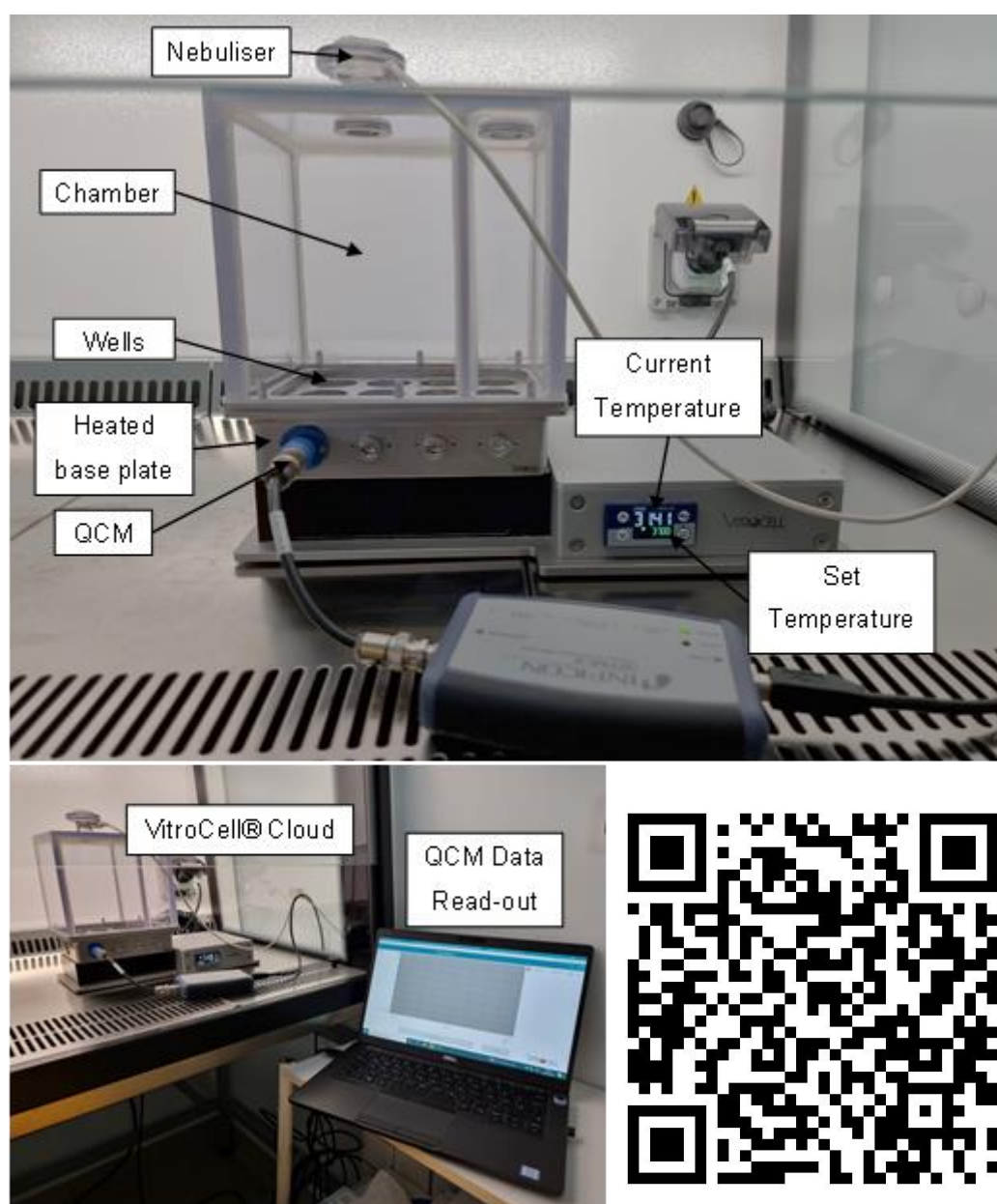


**Figure 4.5** The VitroCell® Cloud12 unit. Is housed in a biological safety cabinet, and the temperature of the baseplate can be set. QCM data is collected via USB on a laptop. The QR code links to a video demonstration of the Cloud in use.

Before each nebulisation, it was ensured that the QCM was set to zero and the reading was stable (not deviating by greater than 25 ng/cm<sup>2</sup> over 30s).

#### 4.2.3.1 Nebulising particle suspensions

Before nebulisation, particle suspensions were spiked with 1% of a 0.9% NaCl solution, which aids nebulisation efficiency. Then, 200  $\mu$ L of particle suspension was nebulised. When nebulising suspensions, the time taken to nebulise was monitored to ensure that it was between 10 and 60 seconds and did not exceed 10% of the original nebulisation (which could indicate a nebulised blockage). Once the 200  $\mu$ L had finished nebulising, 6 minutes was timed, allowing the particles to settle and the associated drop in QCM reading. The chamber was then removed for 1 minute to allow the QCM to dry before the chamber was replaced for 2 minutes, and data acquisition was stopped. The mean of the final 30 seconds was taken as the deposited concentration. Typical QCM data from a nebulisation cycle is shown in **Figure 4.6**.

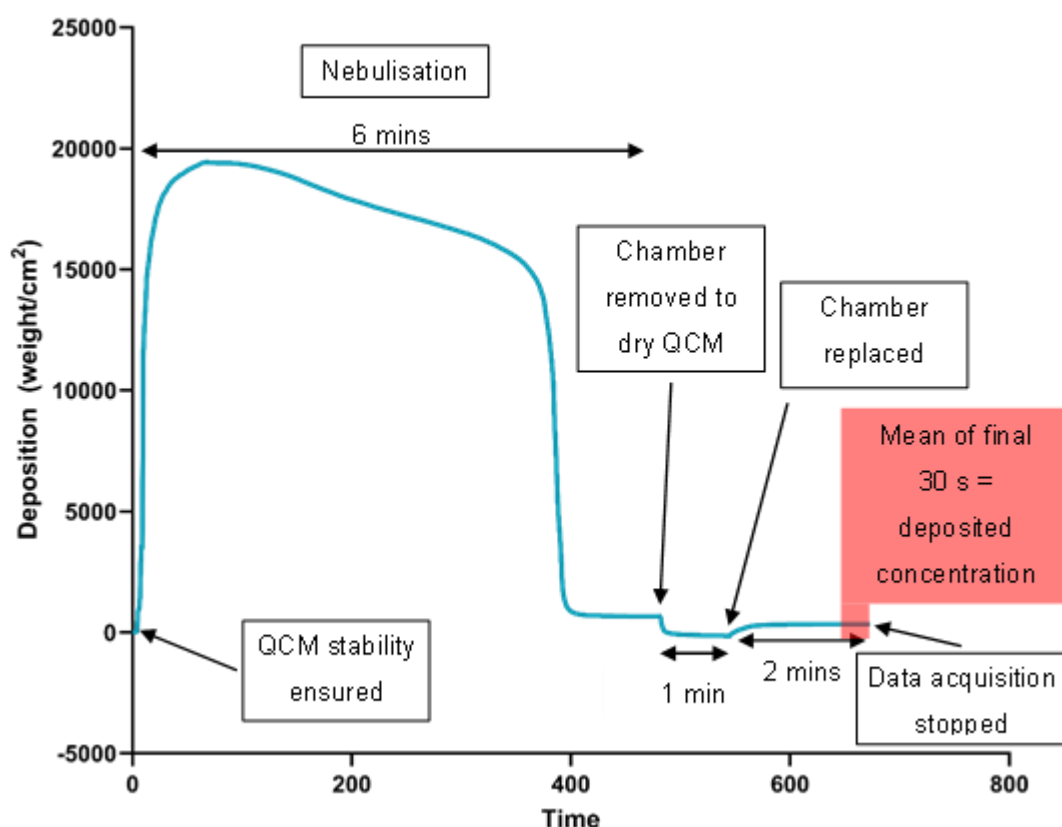


*Figure 4.6 A typical QCM curve after nebulisation of a particle suspension. Every deposition is checked to follow this pattern, though, there can be variability at the top of the curve due to high humidity interference with the QCM. However, what is important is that the final 2 minutes are stable allowing an accurate deposition to be calculated.*

#### 4.2.3.2 Cleaning the VitroCell Cloud

Although a separate nebuliser was used for each particle, nebulisers were cleaned by nebulising 200  $\mu$ L of 0.9% NaCl 3 times after use. If the nebuliser got blocked, the Aerogen nebulisers were cleaned by submerging in 70% ethanol and sonicating at 21% power for 10 minutes. The Tekcelo nebulisers could be cleaned by nebulising a 0.9% NaCl + 1% ethanoic acid solution.

The chamber and the heating block of the VitroCell® were thoroughly cleaned with 70% ethanol before and after every use. During use, if there was a significant humidity build-up, the inside of the chamber could be wiped dry with tissue wetted with 70% ethanol.

The QCM was cleaned before and after each exposure using a cotton bud soaked in 70% ethanol. This could also be done between nebulisations/exposures if there was particle buildup on the QCM.

#### 4.2.3.3 VitroCell Cloud 12 deposition curve generation

A deposition curve was generated for each particle to advise the exposure studies. This was done by nebulising a range of feed concentrations (a volume of 200  $\mu$ L was always used). Concentrations used for each particle are displayed in **Table 4.2**. For each

*Table 4.2 Volumes used to dilute each concentration of CB, 1649b or 2548 are shown (to the nearest  $\mu$ L).*

Volumes required to make 1 mL of suspension ( $\mu$ L)					
	Concentration ( $\mu$ g/mL)	Stock suspension	H <sub>2</sub> O	0.9% NaCl	Total
Printex 90 Carbon Black	50	15	975	10	1000
	100	29	961	10	1000
	200	59	931	10	1000
	400	118	872	10	1000
	600	176	814	10	1000
	800	235	755	10	1000
	1000	294	696	10	1000
NIST SRM 1649b/2583	250	74	916	10	1000
	500	147	843	10	1000
	1000	294	696	10	1000
	2000	588	402	10	1000

concentration of each particle, 10 repetitions were performed due to the high variability of the QCM data.

#### 4.2.4 Scanning Electron Microscopy

To assess the morphology, aggregation, and dispersion of PM in various systems, PM samples were collected on copper grid (400 mesh) carbon-coated TEM grids. TEM grids were taken from the deposited PM in the bottom of a VitroCell Cloud well, *via* aerosol sampling of the chamber mid-run or *via* dropcast of the particle suspension.

##### 4.2.4.1 Generating scanning electron microscopy samples



**Figure 4.7** Blank TEM grid (left) and TEM grid immediately after dropcasting 5  $\mu\text{L}$  of particle suspension (right).

To dropcast particle suspensions onto TEM grids, the carbon-coated TEM grids were placed on tissue within a petri dish. Carefully, 5  $\mu\text{L}$  of particle suspension was pipetted directly on top of the grid (**Figure 4.7**). It was ensured that the droplet was sitting on top of the TEM grid before being left to dry overnight.

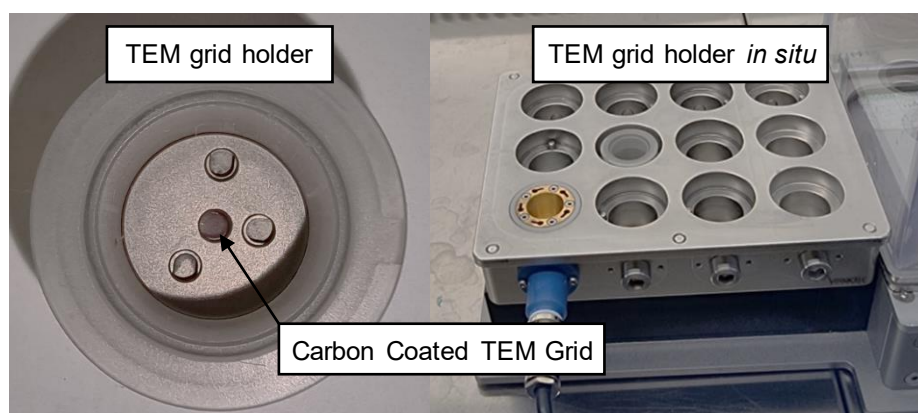


**Figure 4.8** The TEM grid holder can hold 4 grids at one time and fits within the wells of the Cloud, at the same depth that exposed cells would be.

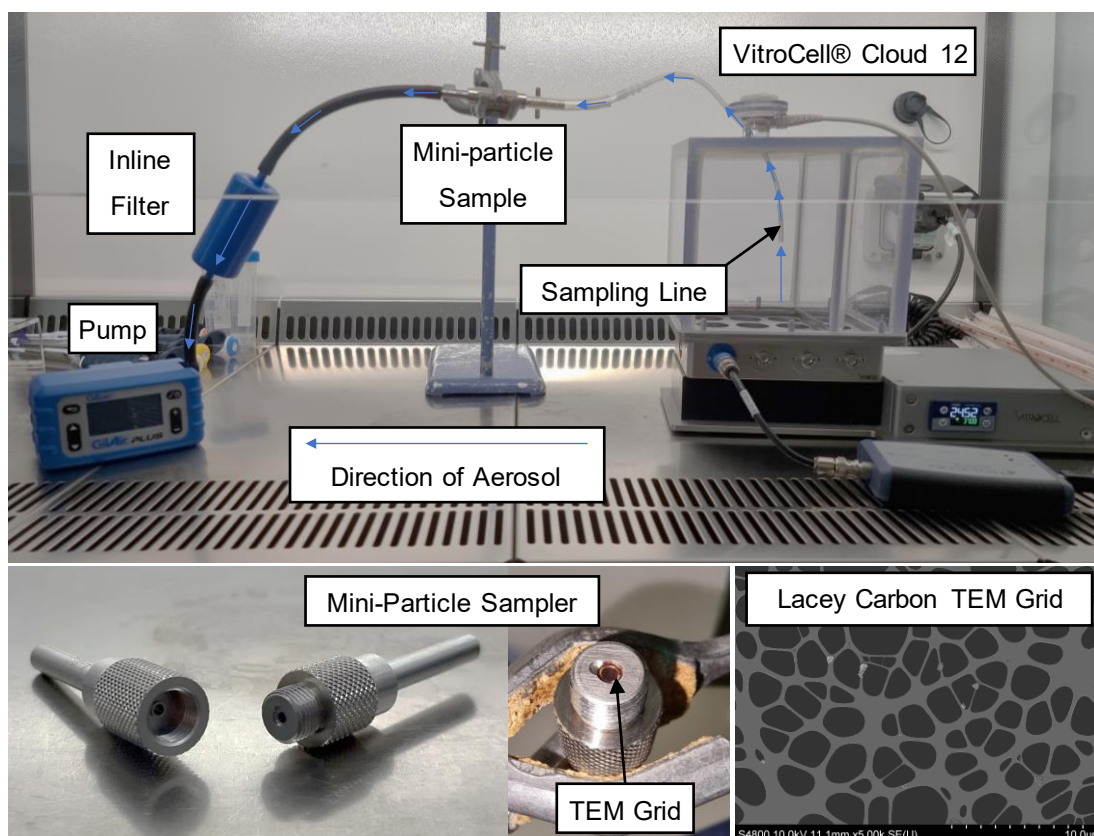


**Figure 4.9** Aerosol sampling from the VitroCell® Cloud. A sampling line is placed half-way down the Cloud chamber; when a flow is drawn by the pump the aerosol could pass through the mini particle sampler which housed a lacey carbon TEM grid to capture particles.

To sample deposited PM, a TEM grid holder was placed in one of the VitroCell Cloud wells and left *in situ* during the particle deposition procedure (**Figure 4.8**). Where numerous nebulisations were required to reach a specific targeted concentration, the TEM grid was left until the end of the final nebulisation before being removed.

A pump was used to draw the sample aerosol onto the TEM grid using a sampling line within the Cloud chamber. Thirty seconds after the suspension had finished nebulising, a GilAir Plus air sampling pump was switched on, and 0.005 L of volume was sampled. The pump draws a gas/aerosol sample through a mini particle sampler, which houses a lacey carbon film copper TEM grid (**Figure 4.9**). This TEM grid type allows gases/aerosols to pass through (*i.e.*, not to block the sampling line), though it still captures the pollutant particles). Behind the mini-particle sampler is an inline filter, which captures particles that pass through the TEM grid to stop them from entering the pump.

Regardless of how the PM was deposited onto the TEM grids, grids were allowed to dry overnight in a petri dish before being stored in a TEM grid holder.



#### 4.2.4.2 Imaging using Scanning Electron Microscopy (SEM)

To image, TEM grids were loaded into a TEM grid holder SEM stub. TEM grids were imaged on a Hitachi S4800 scanning electron microscope (SEM). For each sample, the following parameters were used: acceleration voltage of 10 kV, 10  $\mu$ A and magnifications of 1000x, 5000x and 15000x.

#### 4.2.5 Nitrogen Dioxide Exposure Chamber

As well as the various PM samples, the *in vitro* models will be exposed to NO<sub>2</sub> using a novel nitrogen exposure chamber. As part of this project, several specifications were required to ensure exposures were realistic, relevant, and feasible when developing this exposure system. For example, the NO<sub>2</sub> concentration must be controllable and hold steady over chronic exposure durations (over 24 hrs), and the chamber must be able to house companion plates for transwell inserts. Other factors must also be considered to allow direct comparison to non-exposed inserts in a ‘normal’ tissue culture incubator (*i.e.*, humidified and comparable oxygen and CO<sub>2</sub> levels).

The NO<sub>2</sub> exposure chamber was created through the adaption of a chamber typically used for hypoxia studies. The chamber was adapted to have extra ports for NO<sub>2</sub> input and to connect to a NO<sub>2</sub> gas concentration analyser. The chamber was placed inside a tissue culture incubator, which was used to control the temperature. The O<sub>2</sub> and CO<sub>2</sub> concentrations within the chamber were set to 18% and 5%, respectively, to ensure alignment with ‘normal’ tissue culture incubator concentrations. A tray at the bottom of the chamber allowed humidification, and a fan at the top ensured that gases could be mixed (**Figure 4.10**).

The NO<sub>2</sub> sensor is connected to a PC that controls the NO<sub>2</sub> pump unit, allowing extra NO<sub>2</sub> to be input (or, in the case of too high NO<sub>2</sub> concentrations, N<sub>2</sub> could be pumped into the chamber). Either trickle or purge valves did this depending on how substantially off the NO<sub>2</sub> concentration was compared to the set point. The software allowed the user to define the NO<sub>2</sub> concentration set point and the tolerance. The user can also define the distance from the set point where either the trickle or purge valves would be used and how long the system pumps gas through the valve (**Figure 4.11**). The NO<sub>2</sub> sensor connected to the chamber is an electrochemical sensor that measures every 26 seconds, feeding back to the software, which determines which valve to open

(if any). However, fluctuations in electrochemical sensor sensitivity can arise when there are variabilities in temperature and relative humidity.

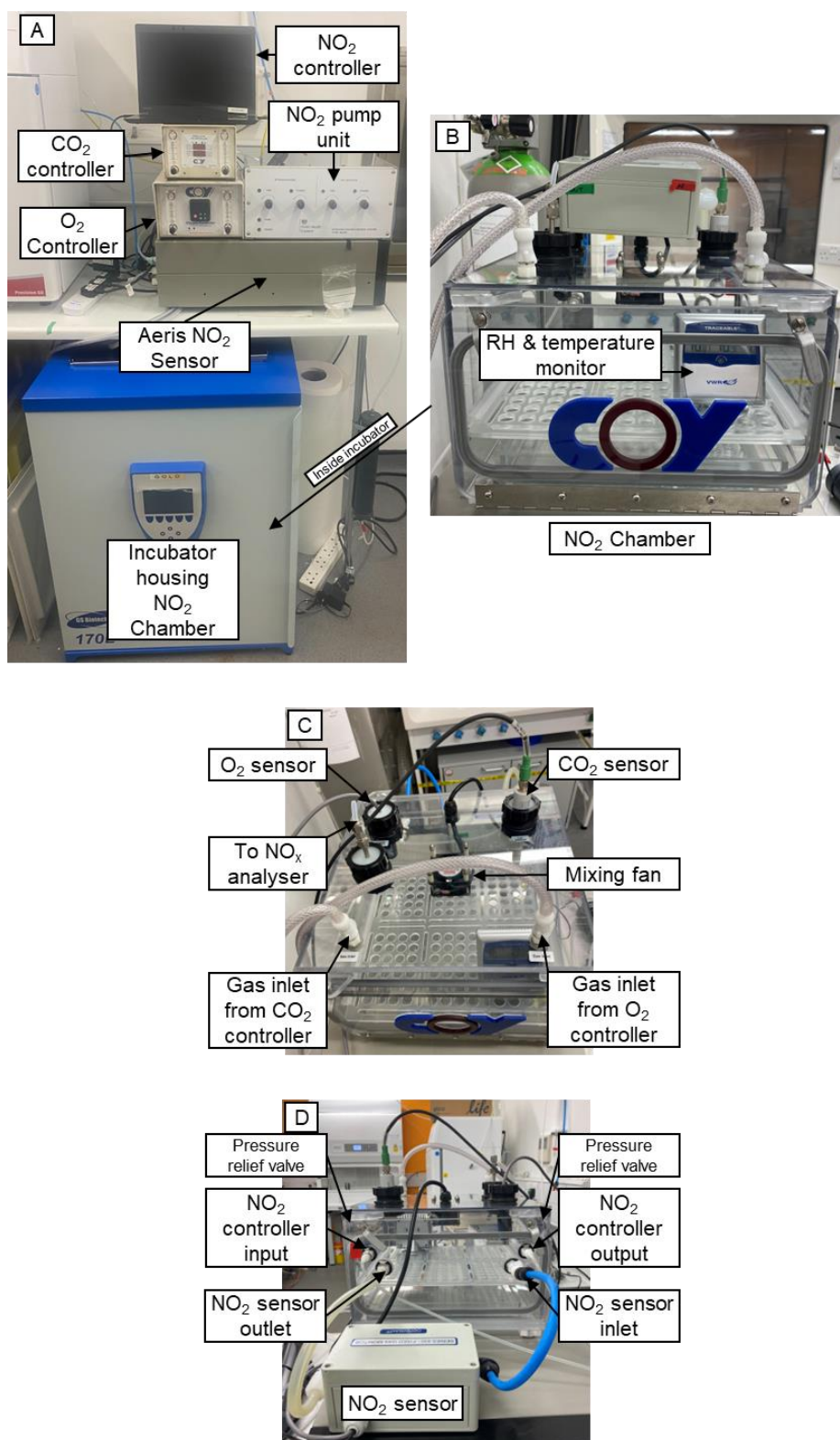


**Figure 4.10** The NO<sub>2</sub> exposure chamber normally housed within the incubator whilst in use, connected to controllers and analysers for O<sub>2</sub>, CO<sub>2</sub> and NO<sub>2</sub> (a). Front, top and rear views of the chamber are shown in (b), (c) and (d) respectively.



For this reason, an Aeris® AE2041U nitrogen oxide analyser was used to calibrate the NO<sub>2</sub> sensor within the system. The Aeris® is a chemiluminescent sensor that should not be altered by temperature or humidity and could also give NO and NO<sub>x</sub> concentrations. The Aeris® analyser was only used transiently to ensure that the system kept to the correct concentration since this analyser requires a flow. Continually drawing a flow from the chamber would affect the gas concentrations and relative humidity, so it was not run constantly. Temperature and relative humidity within the chamber were continually measured using a thermohygrometer (Traceable, USA).

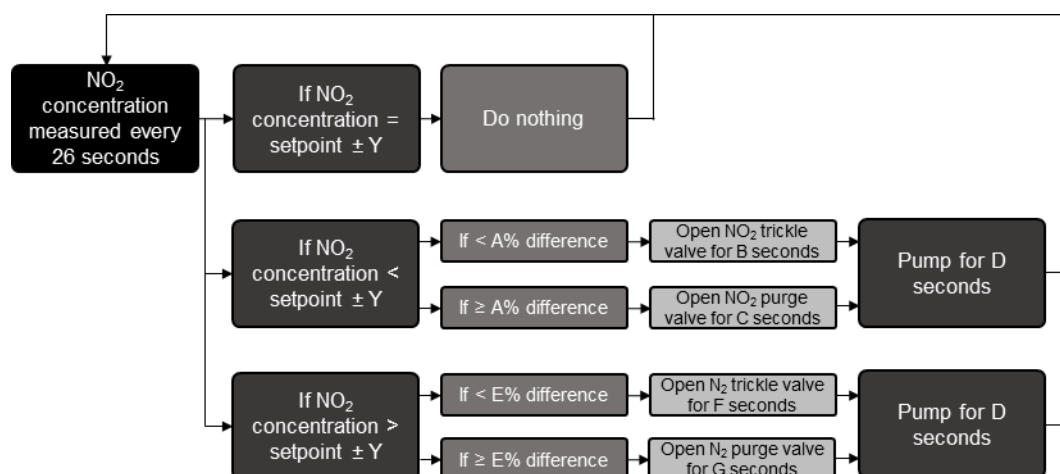


**Figure 4.11** Schematic of the NO<sub>2</sub> system feedback mechanism to maintain the user set NO<sub>2</sub> concentration (y). Parameters a, b, c, d, e, f and g are defined by the user.

#### 4.2.6 Transporting Samples between Swansea University and The Radiation, Chemical and Environmental Hazards Directorate

Seeding of cultures onto transwell inserts was undertaken at Swansea University; however, the NO<sub>2</sub> exposure chamber was located at the Radiation, Chemical and Environmental Hazards Directorate (RCE), UK Health Security Agency. Therefore, seeded transwell inserts must be transported between sites between seeding and exposure. Inserts were transported under submerged conditions within a pre-sterilised polystyrene box packed with packaging air bags/bubble wrap to ensure plates stayed upright and did not spill. Once cultures arrived at RCE, cultures were taken to the ALI, and exposures could commence 24 hours later. Endpoint assessments that were required to be performed immediately following exposure (trypan blue exclusion assay and blue dextran) were carried out at RCE. Supernatants for ELISA and lysates (PCR and glutathione quantification) were collected in RCE and frozen before being transported to Swansea University in ice within a polystyrene box for processing.

Fixed wells were stored at RCE at 4°C and were transported for processing on ice within a polystyrene box.

Before commencing NO<sub>2</sub> exposures, it was ensured that travel would not impact measured toxicological response. The journey between Swansea University and RCE is 2.5 hours. Therefore, NCI-H441 monocultures were packaged as if to be transported and either left on a bench or placed on a rocker to simulate driving conditions. Cell viability, barrier function and IL6/IL8 release were then assayed at the time post-cell seeding as if they had been used within pollutant exposures.

Further, the VitroCell® Cloud systems between Swansea University and RCE differed. Swansea University possess the Cloud 12, and RCE possess a Cloud 6 with adapter rings to accommodate 12 well inserts. It is known that there are inter-laboratory differences between VitroCell® Cloud exposure concentrations (Bannuscher et al., 2022); therefore, a comparison of PM deposition was conducted to ensure exposures could be conducted accurately (Appendix 2).

#### **4.2.7 Data and Statistical Analysis**

Raw data was initially recorded in Microsoft Excel and was transferred to GraphPad Prism (Version 10.1.1) (USA) for data and statistical analysis. Statistically significant differences were measured using one-way ANOVAs, with appropriate post hoc tests used. Figure legends specify which statistical tests were used for each data set.

Graphs and other data visualisations were produced in GraphPad Prism (Version 10.1.1) unless otherwise stated within the methods section of subsequent chapters.

## 4.3 Results

### 4.3.1 Printex® 90 Carbon Black exposure characterisation

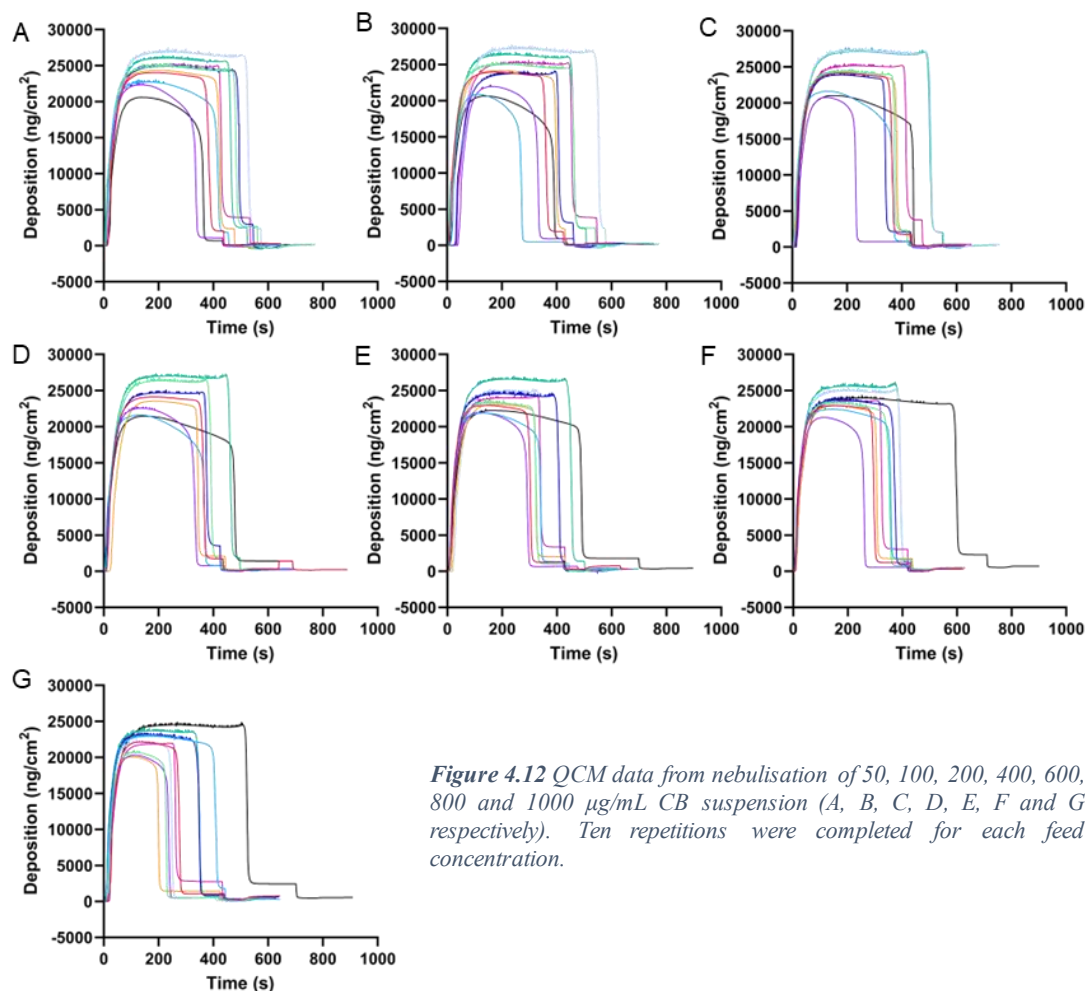


*Figure 4.12 QCM data from nebulisation of 50, 100, 200, 400, 600, 800 and 1000 µg/mL CB suspension (A, B, C, D, E, F and G respectively). Ten repetitions were completed for each feed concentration.*

Nebulising CB resulted in QCM curves (**Figure 4.12**) broadly following what would be expected (Section 4.2.3.1) for each concentration. Final deposited concentrations of CB (**Figure 4.13**) are seen to increase as the feed concentration increases from 150 ng/cm<sup>2</sup> at 50 µg/mL feed concentration to 450 ng/cm<sup>2</sup> for 1000 µg/mL. Broadly, variation in deposition increased as the feed concentration increased.

SEM imaging of dropcast CB suspensions (**Figure 4.14**) shows that at 50 µg/mL, CB forms large agglomerates (from 1-10 µm in width). From 100 µg/mL and up, CB agglomerates into one large mass that gets thicker as the concentration increases. The entire TEM grid is covered underneath a thick agglomeration at the highest CB concentration.

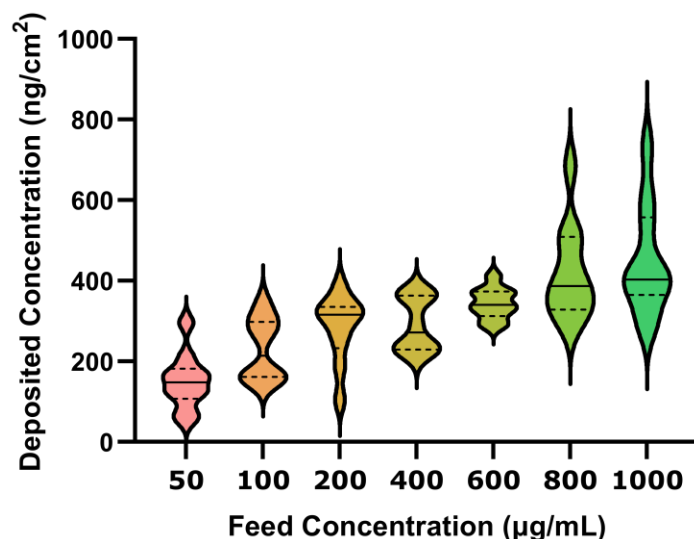


**Figure 4.13** Deposition of CB for each feed concentration. The width of the violins demonstrates the distribution of the data. The solid line shows the median whereas the dashes lines show the upper and lower quartiles, whilst the height of the violins show the range.  $n=10$ .

In contrast, aerosol sampling shows that carbon black agglomerates in the water droplets are highly variable (**Figure 4.15**). For example, in the aerosol from nebulising CB at 50 µg/mL, some single CB particles can be seen in the nanometre range, whilst agglomerations 1-2 µm can also be seen. The number and size of the agglomerations tend to increase as the feed concentration increases. Though instances of single particles are visible, they become scarcer at higher concentrations.

Following the trend of the QCM data, more particles are deposited at higher feed concentrations of CB (**Figure 4.16**). Though forming agglomerations of varying size and shape, deposition is generally evenly dispersed over the TEM grid. Agglomeration size and number appear to increase as the feed concentration increases. Agglomerations at the 50 µg/mL feed concentration appear to be 1 µm or smaller, though steadily increase to agglomerations of 10-20 µm in the 1000 µg/mL feed concentration. However, each deposition has a range of agglomeration sizes spanning nanometres to tens of microns in diameter.

SEM imaging of CB at exposure concentrations of 390, 780 and 3100 ng/cm<sup>2</sup> shows greater particle number and agglomeration size as the deposited concentration increases (**Figure 4.17**).

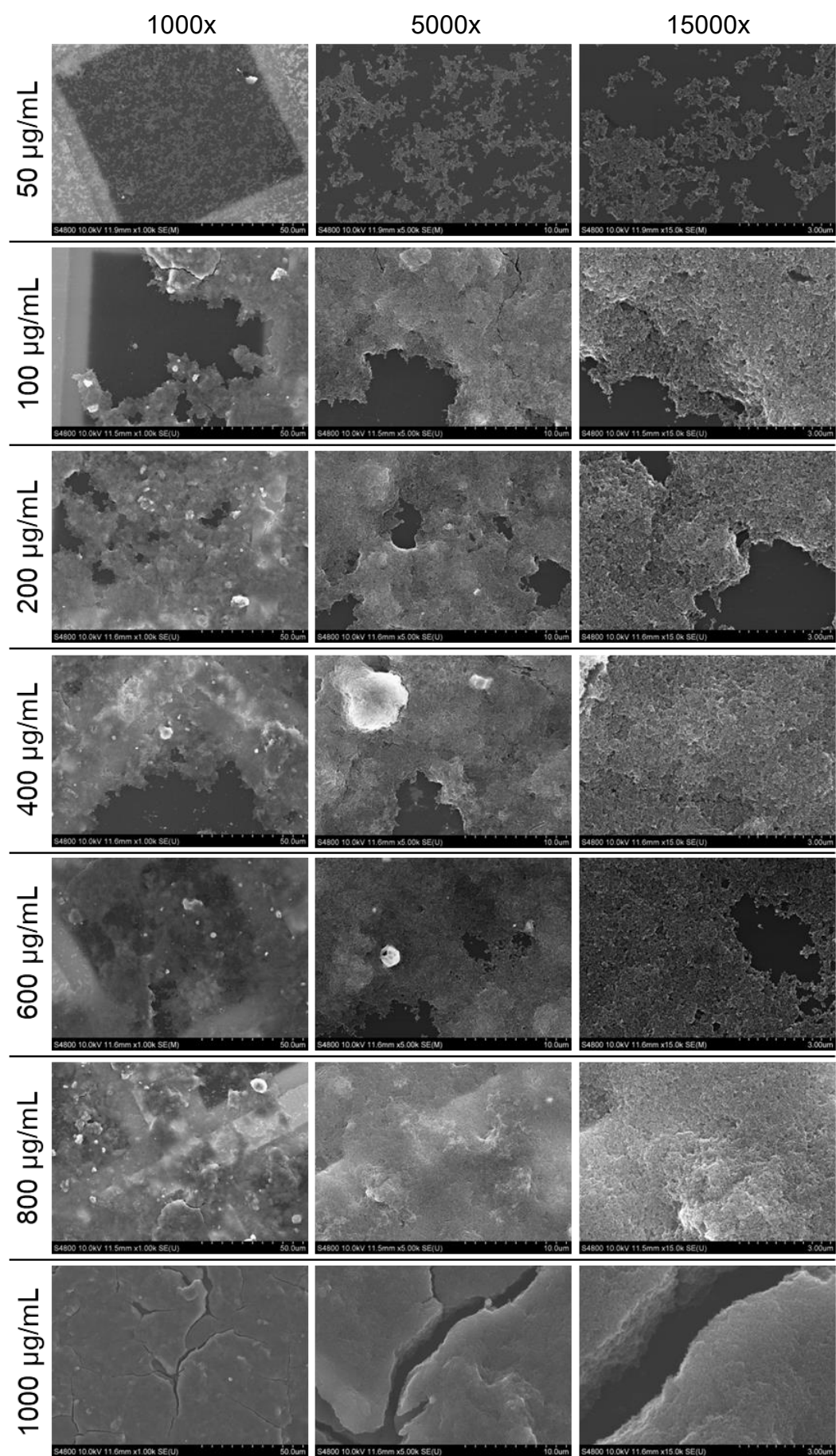


*Figure 4.14 SEM images of dropcast CB suspensions used for characterising CB deposition using the VitroCell® Cloud. Magnification is shown above each column.*



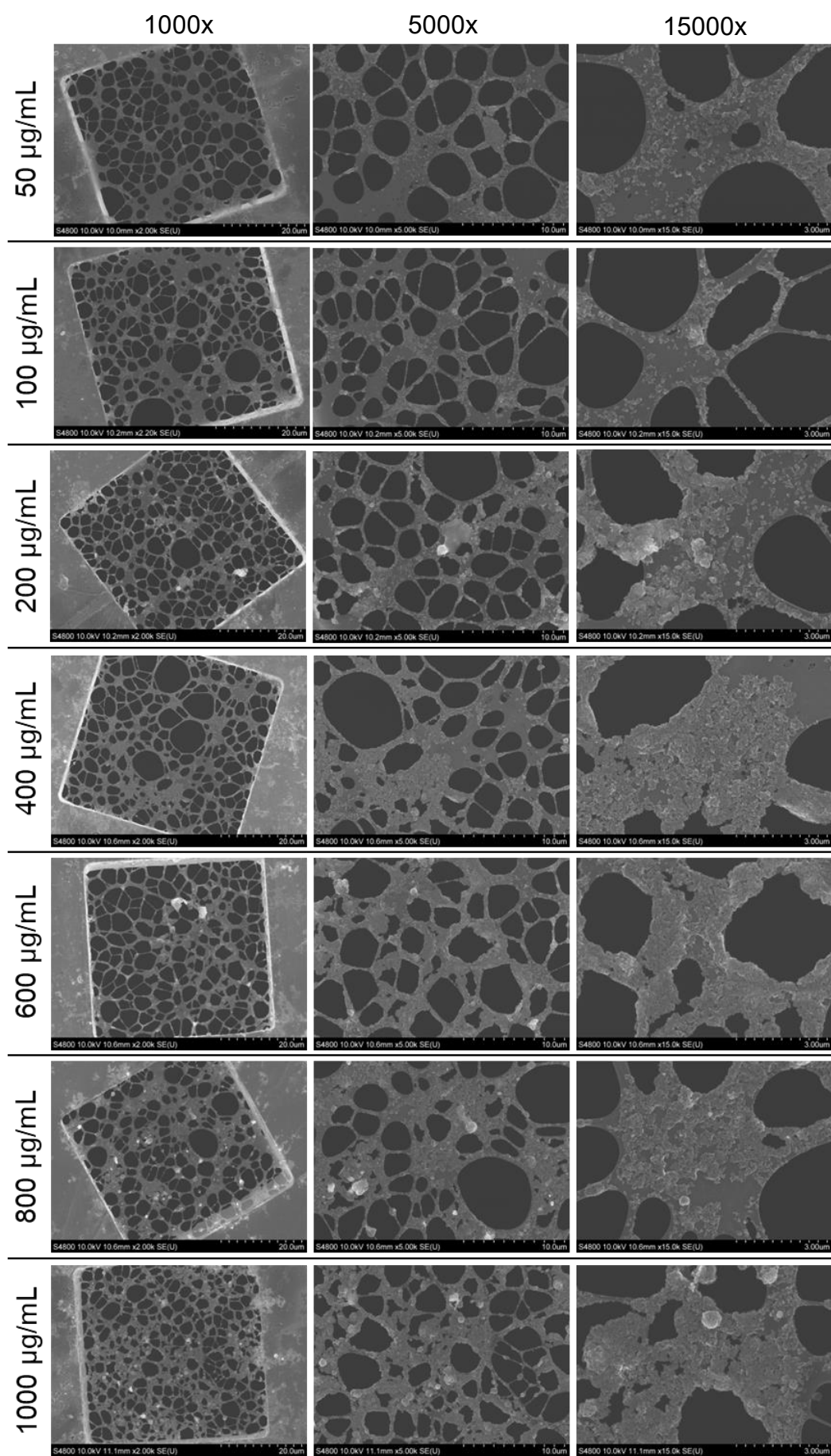


**Figure 4.15** SEM images of CB aerosol captured 30s after nebulisation of various feed concentrations of CB within the VitroCell® Cloud. Particles were captured on lacey carbon coated TEM grids. Magnification is shown above each column.

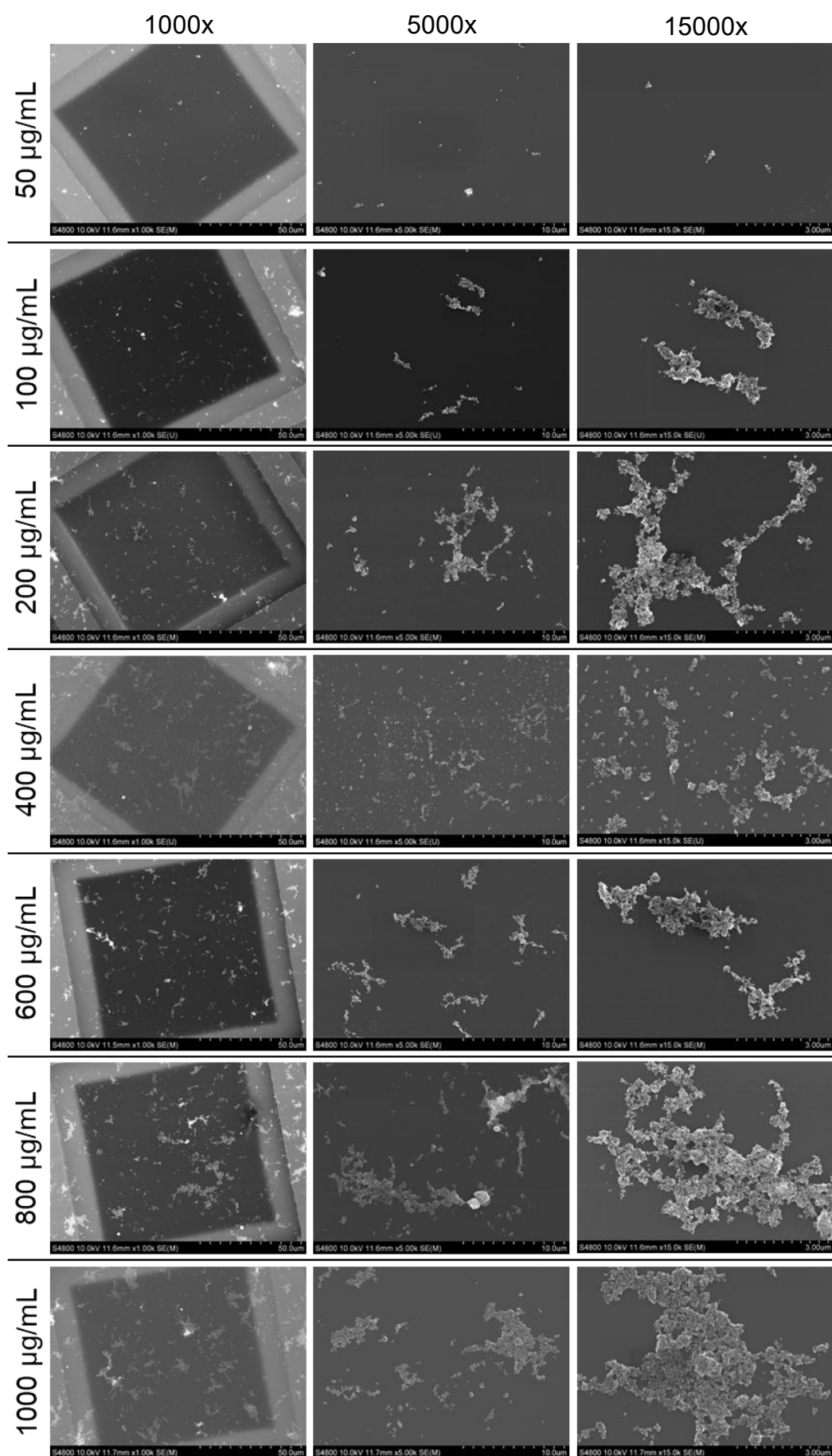


**Figure 4.16** SEM images of CB deposited after nebulisation with the *VitroCell®* Cloud on copper carbon-coated TEM grids. Magnification is shown above each column.

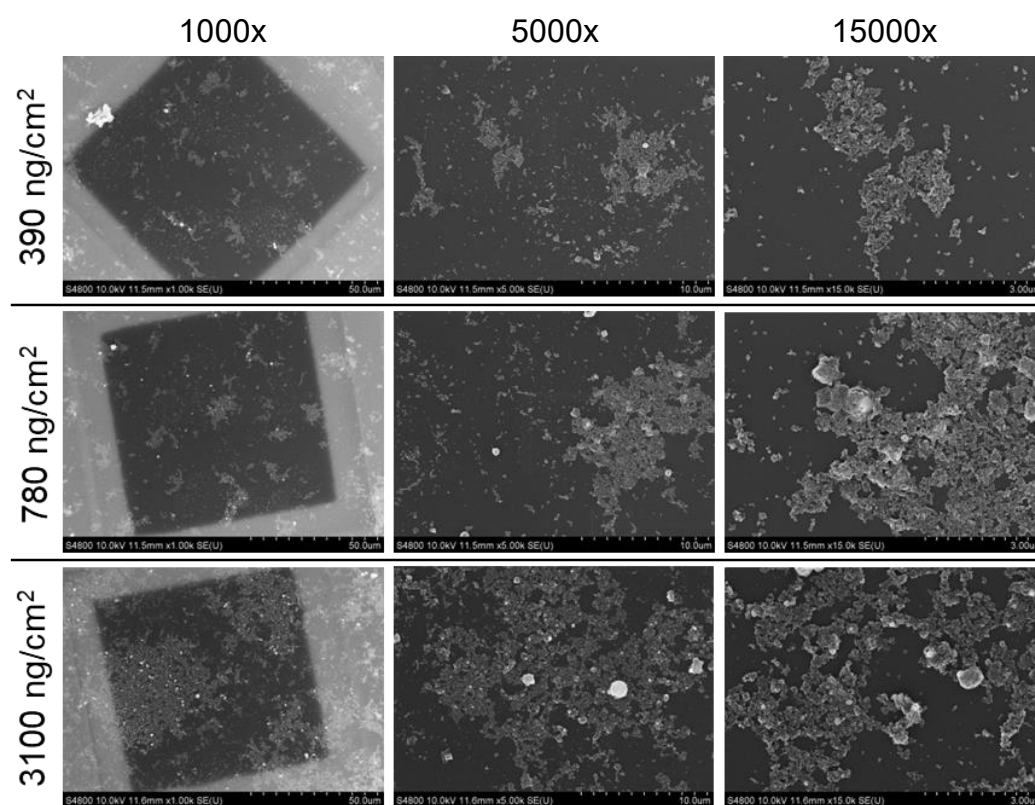


**Figure 4.17** SEM images of CB deposited after nebulisation with the VitroCell® Cloud on copper carbon-coated TEM grids. These are the deposited concentrations that will be utilised in the in vitro experiments. Magnification is shown above each column.



### 4.3.2 NIST Urban Dust SRM 1649b exposure characterisation

QCM data from 1649b nebulisations are as would be expected, though, at the top of the curves, there are regular variations in the QCM data (**Figure 4.18**). What is important, however, is that the final 30 seconds of reading is steady, allowing a deposition to be calculated. The final deposition of each concentration does not substantially change between feed concentrations from 250, 500 and 1000  $\mu\text{g/mL}$ , with mean depositions of 565, 524 and 577  $\text{ng/cm}^2$ , respectively. Deposition does increase with a feed concentration of 2000  $\mu\text{g/mL}$  with a deposition of 846  $\text{ng/cm}^2$ . Interestingly, the 250  $\mu\text{g/mL}$  shows the highest degree of variability in deposition (**Figure 4.19**).

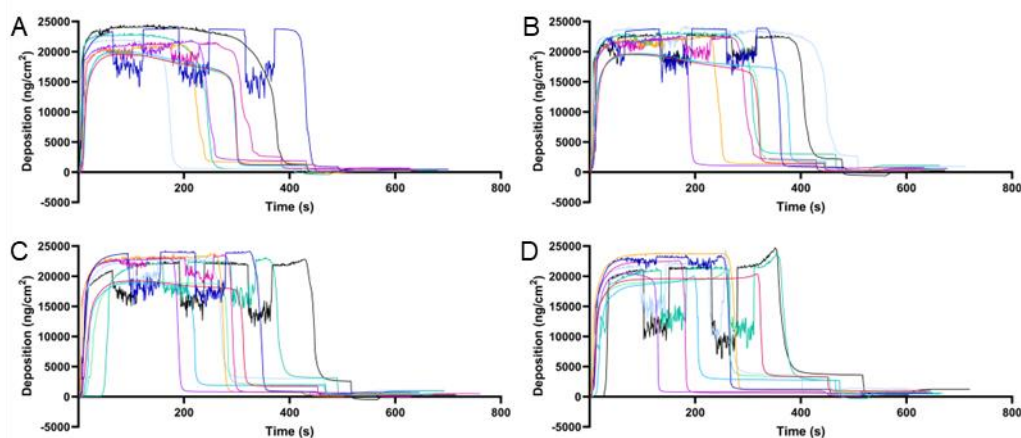


**Figure 4.18** QCM data from nebulisation of 250, 500, 1000 and 2000  $\mu\text{g/mL}$  NIST SRM 1649b suspension (A, B, C and D respectively). Ten repetitions were completed for each feed concentration.

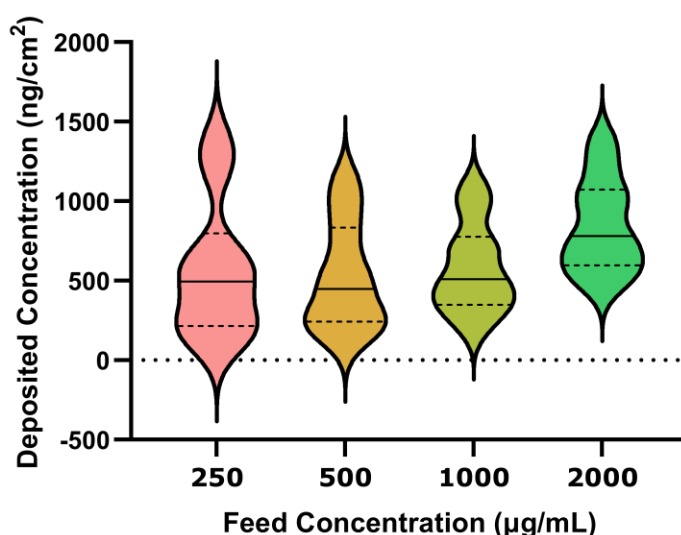


**Figure 4.19** Deposition of NIST SRM 1649b for each feed concentration. The width of the violins demonstrate the distribution of the data. The solid line shows the median whereas the dashed lines show the upper and lower quartiles, whilst the height of the violins show the range.  $n=10$ .

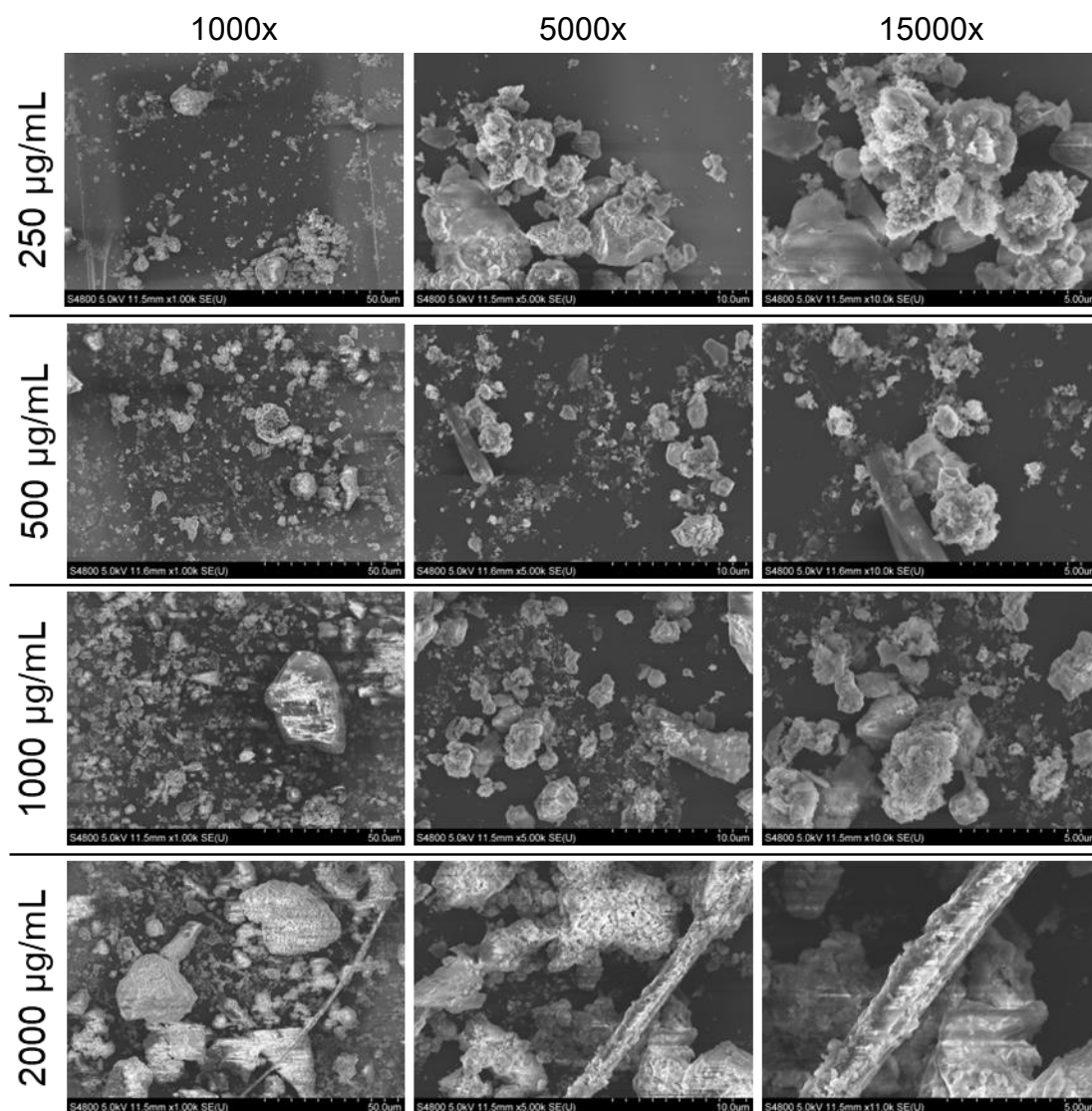


**Figure 4.20** SEM images of dropcast NIST SRM 1649b suspensions used for characterising 1649b deposition using the VitroCell® Cloud. Magnification is shown above each imcolumnage.

SEM images of dropcast 1649b (**Figure 4.20**) reveal a very heterogeneous mixture of particles. These particles range in size from the nano range up to 30-40 µm, though fibres are present (as seen in the 2000 µg/mL images,) which can exceed 50 µm. Many of the particles have irregular round shapes. Predictably, as the concentration increases, the number of particles increases. Many of the particles are large enough that they have caused artefacts in the image when interacting with the electron beam during image acquisition. The larger particles (beyond 2-3 µm) do not seem to agglomerate with each other. However, smaller particles seem to adhere to the surface, which themselves agglomerate to each other.

The number of particles within the aerosol after nebulisation is much reduced compared to the dropcast images (**Figure 4.21**). Most particles captured in the aerosol are about 0.5-1  $\mu\text{m}$  in diameter and are an irregular round shape. The morphology of the particles varies, with some particles appearing to be made of 1 large particle and others being made up of agglomerations of smaller particles (see 500  $\mu\text{g/mL}$ ).

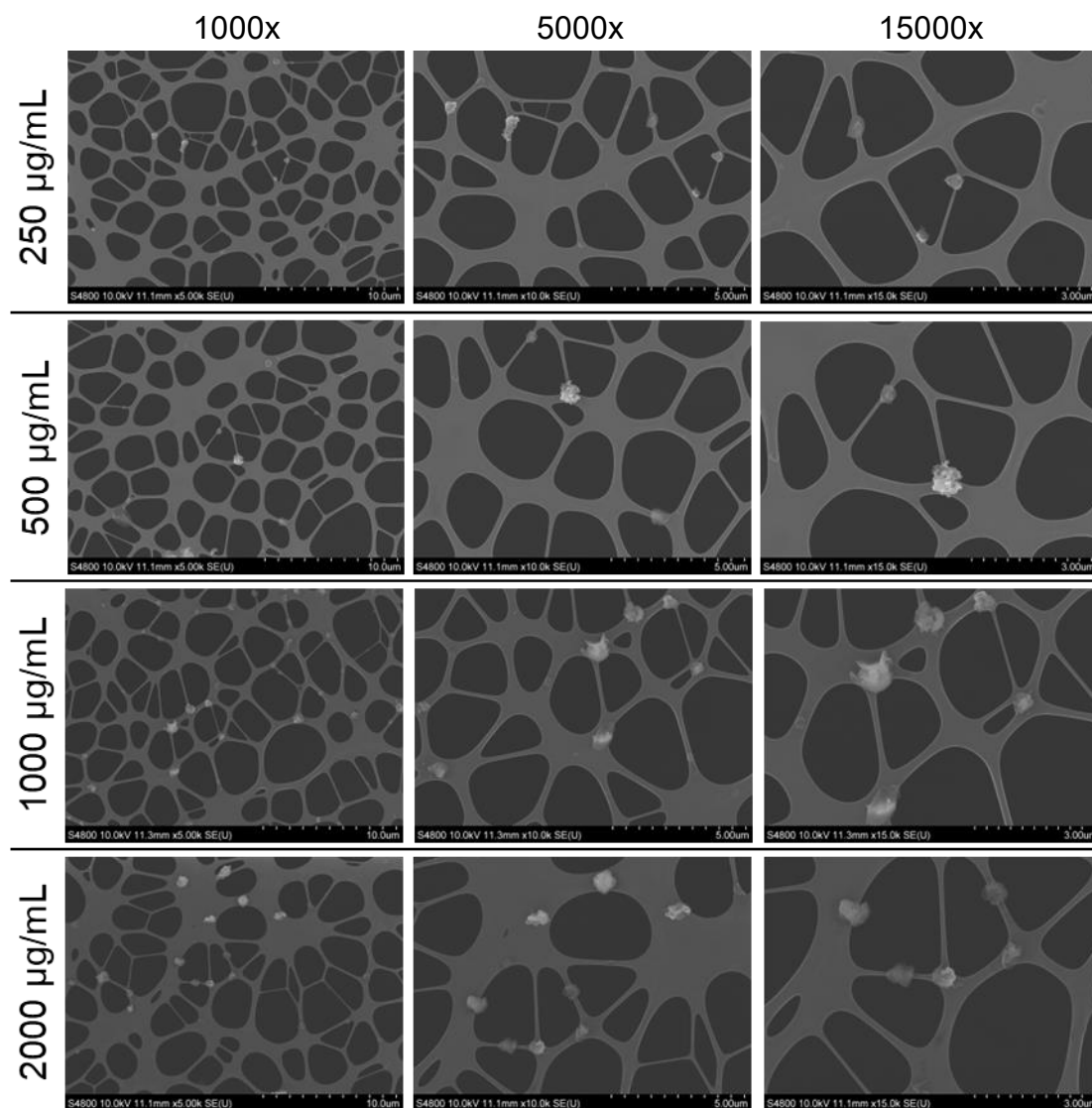


**Figure 4.21** SEM images of NIST SRM 1649b aerosol captured 30s after nebulisation of various feed concentrations of 1649b within the VitroCell® Cloud. Particles were captured on lacey carbon coated TEM grids. Magnification is shown above each column.

When examining deposited 1649b from the bottom of the VitroCell® Cloud, there appears to be no discernible difference in particle count as the feed concentration increases (**Figure 4.22**). Deposited particles appear to lose the irregular round morphology seen in the dropcast and aerosol images and instead often appear much more irregular and heterogeneous in shape and size. A range of particle sizes is again evident, ranging from nanometre range up to 5  $\mu\text{m}$ . A border of smaller particles often

surrounds a large particle. This could be due to the drying of a droplet containing a particle.

When looking at deposited 1649b at the concentrations used in the in vitro exposures, particle deposition shows an apparent increase as the deposited concentration changes (**Figure 4.23**). At 390 ng/cm<sup>2</sup>, particle deposition does not seem evenly distributed across the TEM grid; however, as the concentration increases, the dispersion across the TEM grid becomes more homogeneous. At 3100 ng/cm<sup>2</sup> there seem to be some larger particles (10-20 µm), though most particles fall in the 0-5 µm range.

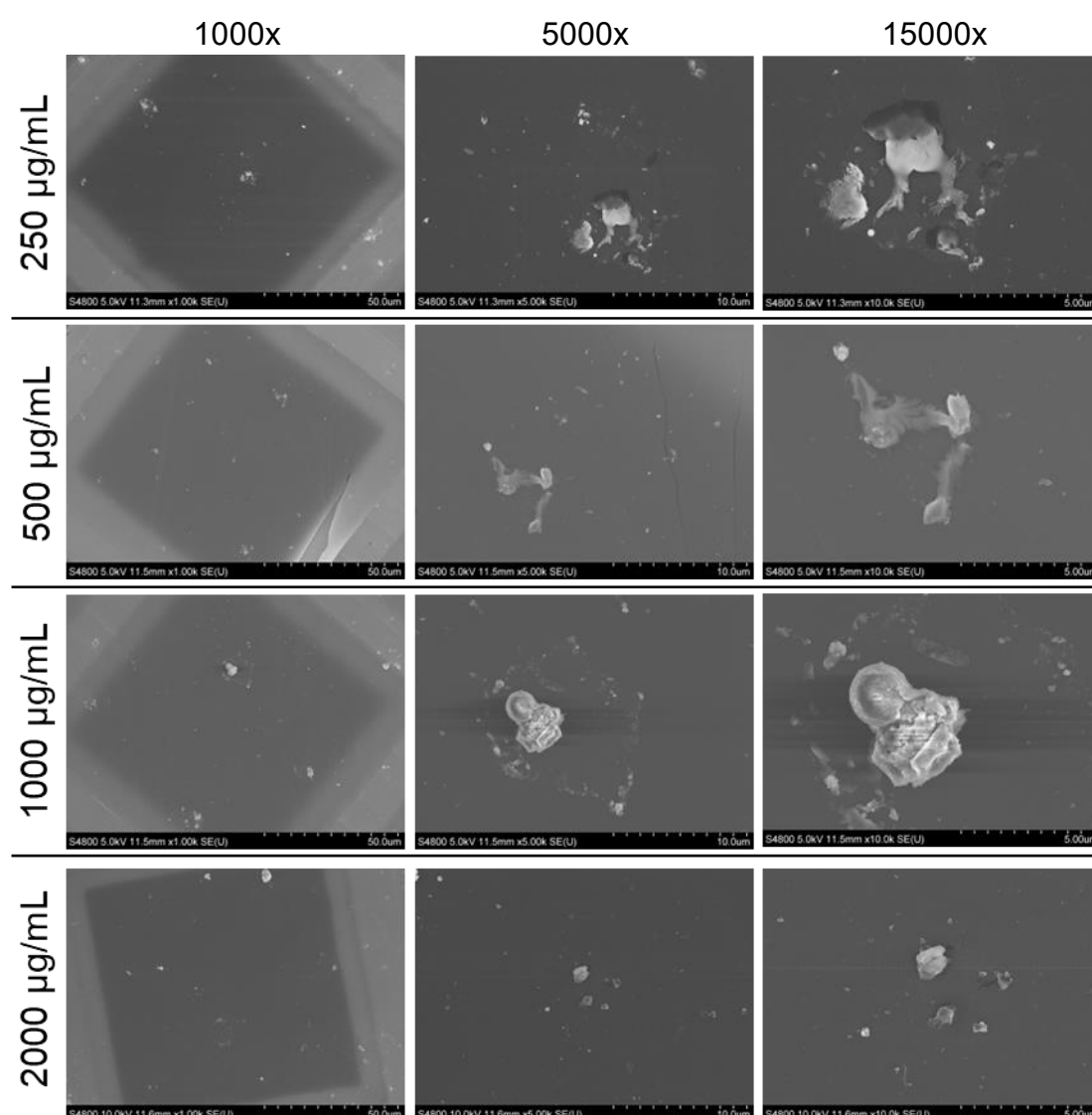


**Figure 4.22** SEM images of NIST SRM 1649b deposited after nebulisation with the VitroCell® Cloud on copper carbon-coated TEM grids. Magnification is shown above each column.

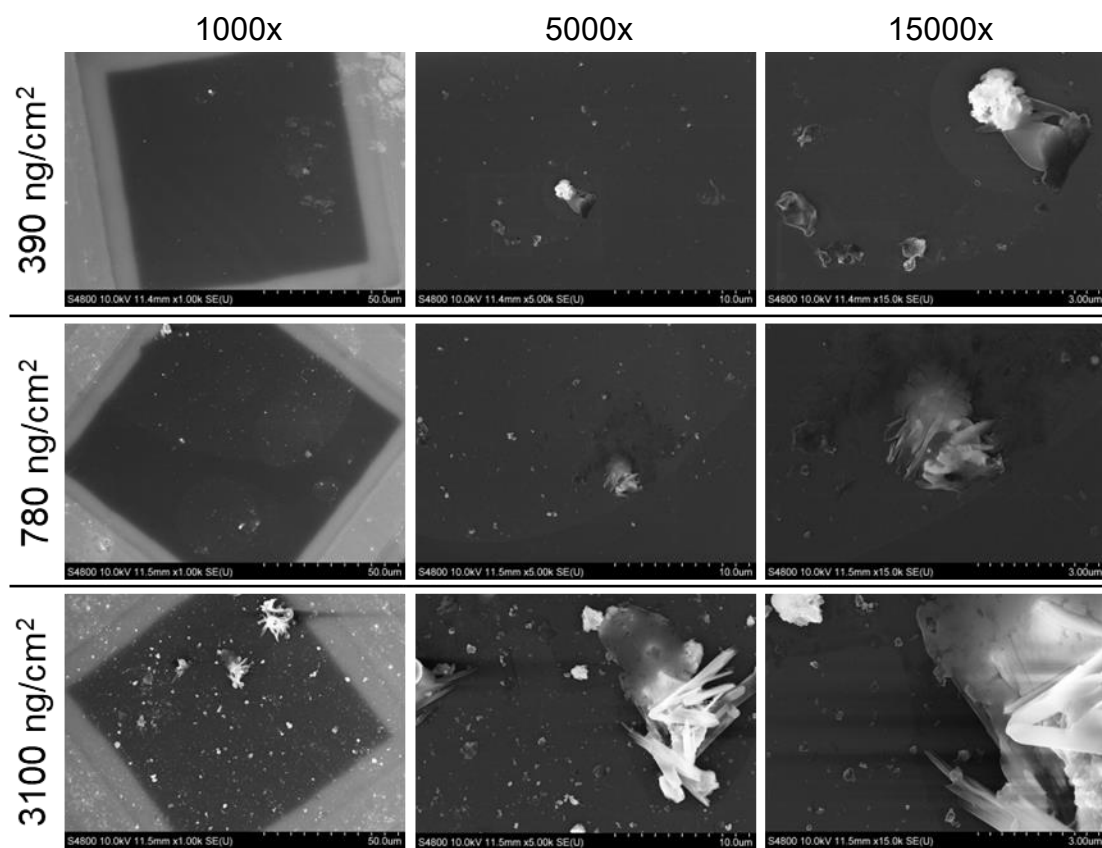


**Figure 4.23** SEM images of NIST SRM 1649b deposited after nebulisation with the VitroCell® Cloud on copper carbon-coated TEM grids. These are the deposited concentrations that will be utilised in the in vitro experiments. Magnification is shown above each column.



### 4.3.3 NIST Indoor Dust SRM 2583 exposure characterisation

When nebulised, the QCM data again follows a similar trend to what is expected, though at the top of the curve, there are regular QCM interruptions (**Figure 4.24**). What is essential, however, is that the final 30 seconds are stable, which is seen for every replicate (**Figure 4.4**). Cloud deposition for 2583 shows a general increasing trend as the feed concentration increases, with mean depositions for 250, 500, 1000 and 2000  $\mu\text{g/mL}$  being 211, 332, 512 and 839  $\text{ng/cm}^2$  respectively (**Figure 4.25**). There is less variability in the deposited concentration compared to 1649b, especially at the lower concentrations. Variability in deposition appears to increase as the feed concentration increases.

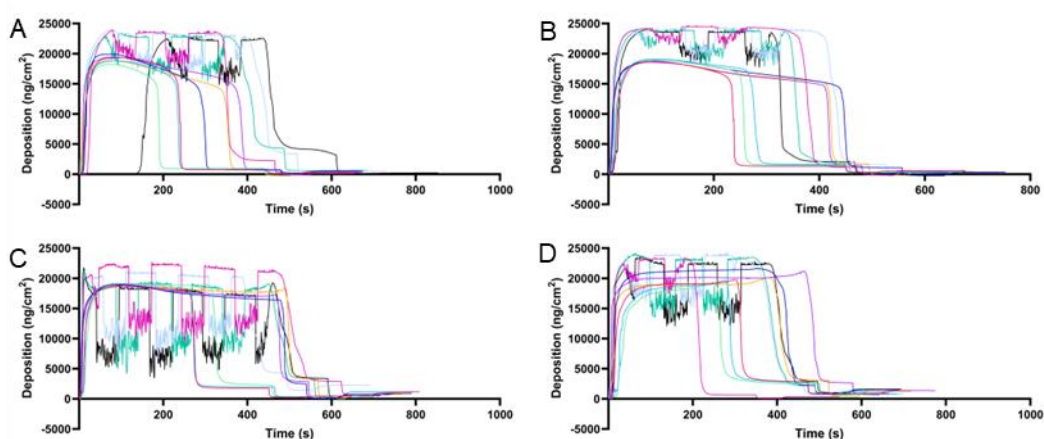


**Figure 4.24** QCM data from nebulisation of 250, 500, 1000 and 2000  $\mu\text{g/mL}$  NIST SRM 2583 suspension (A, B, C and D respectively). Ten repetitions were completed for each feed concentration.

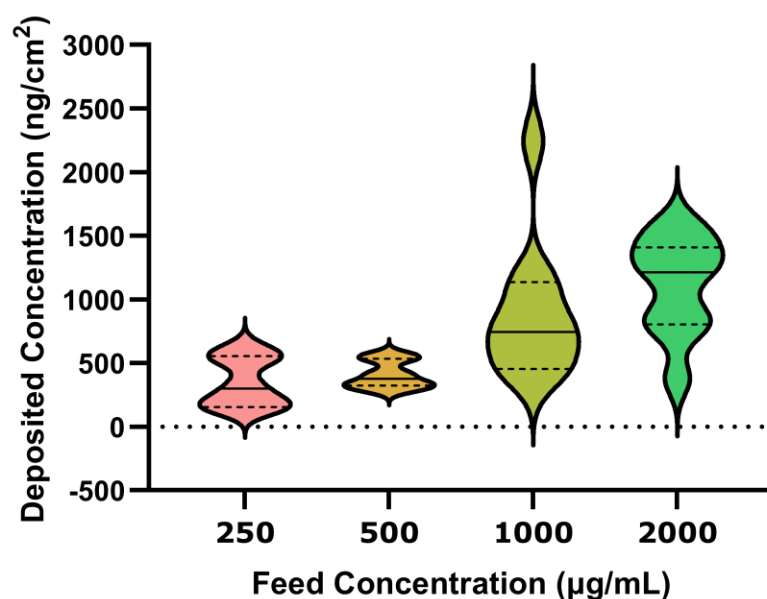


**Figure 4.25** Deposition of NIST SRM 2583 for each feed concentration. The width of the violins demonstrate the distribution of the data. The solid line shows the median whereas the dashed lines show the upper and lower quartiles, whilst the height of the violins show the range.  $n=10$ .

When these feed concentrations were dropcast onto TEM grids (**Figure 4.26**), more particles were present as the concentration increased. However, relative to the other particles used, these particles were larger, often over 10  $\mu\text{m}$ . However, the use of higher magnification of these larger particles reveals that often, these particles are made of agglomerations of smaller particles (see 2000  $\mu\text{g/mL}$  at 15,000x). Like the 1649b, most particles are rounded but have irregular edges.

Increasing the feed concentration did not appear to alter the number or size of the particles captured when sampling the aerosol (**Figure 4.27**). Particles captured appeared to range from 0.5-5  $\mu\text{m}$  in diameter, though the morphology of the particles was variable.

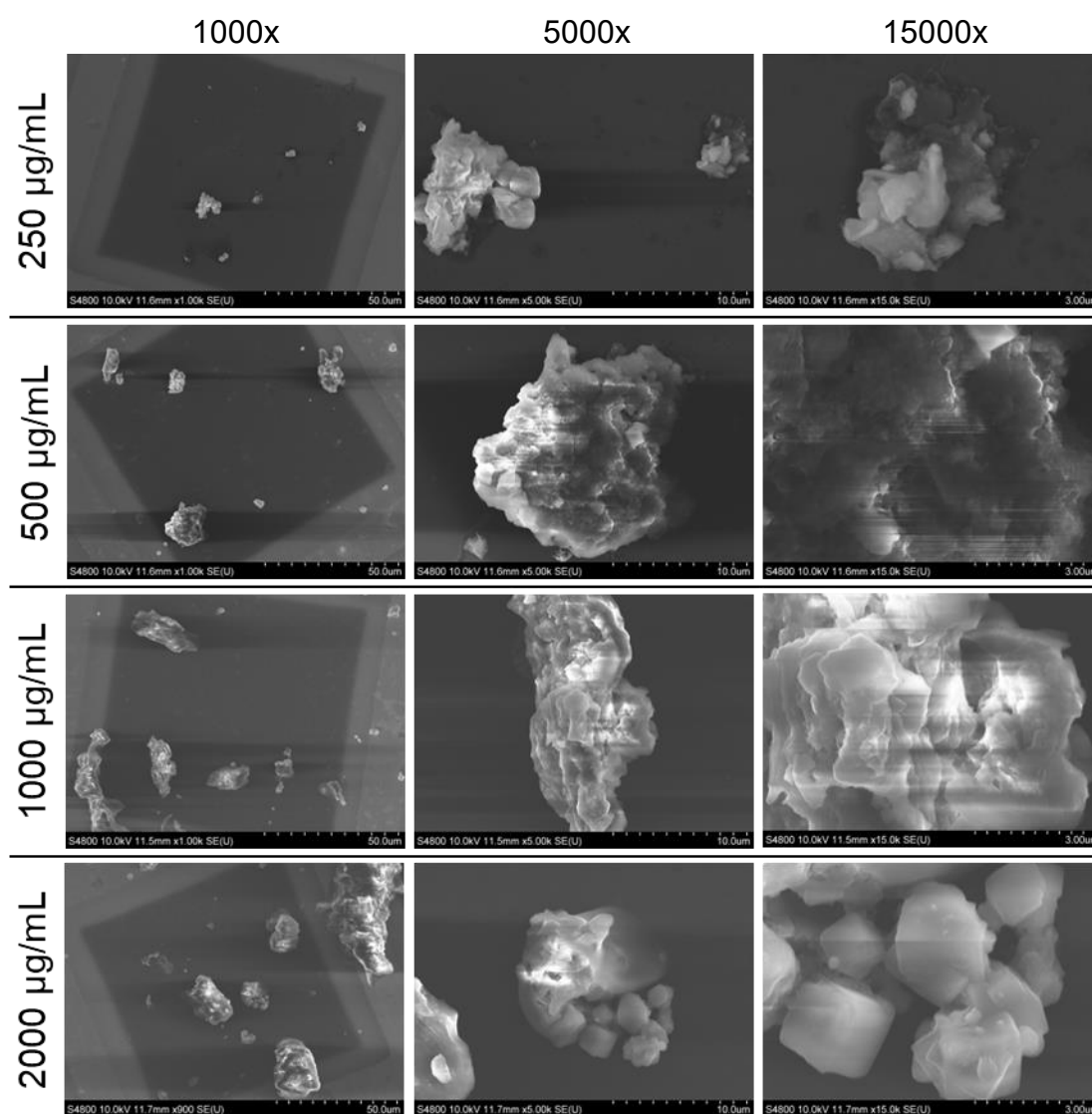


**Figure 4.26** SEM images of dropcast NIST SRM 2583 suspensions used for characterising 2583 deposition using the ViroCell® Cloud. Magnification is shown above each column.

When examining the deposition of 2583, the number of particles deposited increases with the feed concentration (**Figure 4.28**). Again, a border around each of the larger particles perhaps indicates the droplet size and deposition that occurred as the droplet dried. In many cases, these droplets contain smaller particles in the nanometre range. Particles generally did not exceed 5  $\mu\text{m}$  in diameter, with most larger particles again being made up of smaller particle agglomeration when examined at 15,000x magnification. Morphology is very similar in the SEM images of exposure concentrations of 390, 780 and 3100  $\text{ng}/\text{cm}^2$ , with more particles visible as the deposited concentration increases (**Figure 4.30**).

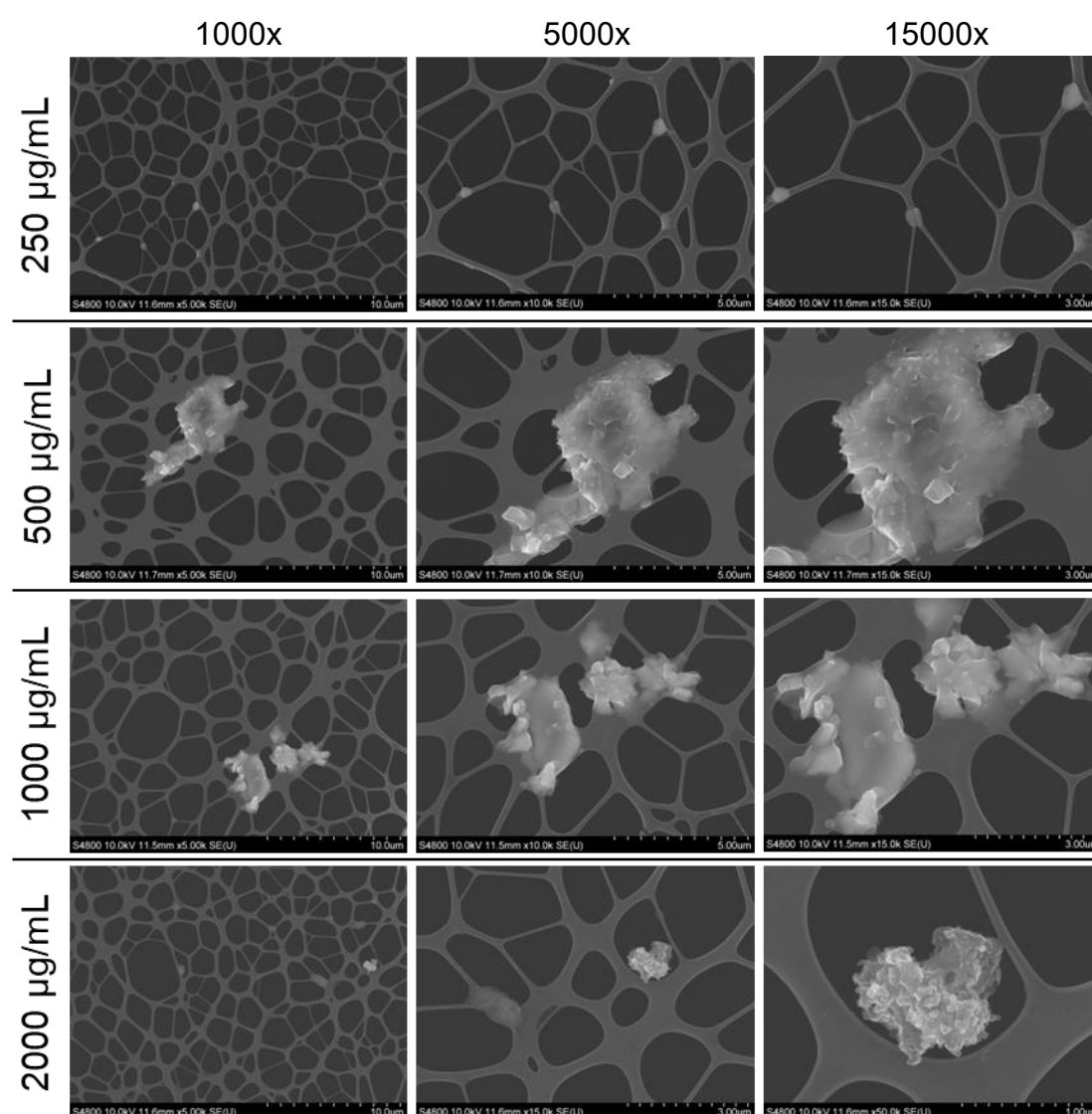


**Figure 4.27** SEM images of NIST SRM 2583 aerosol captured 30s after nebulisation of various feed concentrations of 2583 within the VitroCell® Cloud. Particles were captured on lacey carbon coated TEM grids. Magnification is shown above each column.



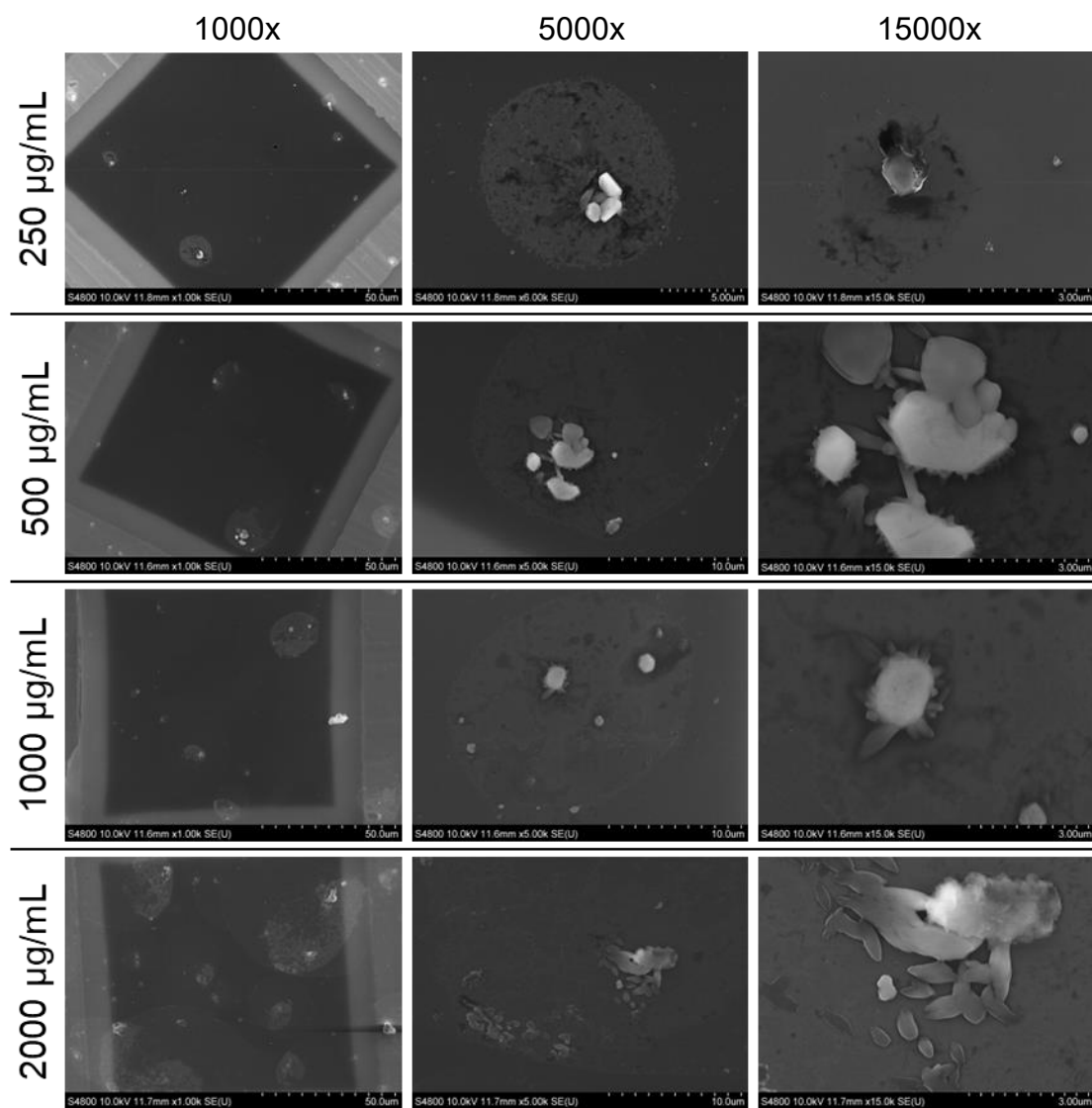


*Figure 4.28 SEM images of NIST SRM 2583 deposited after nebulisation with the VitroCell® Cloud on copper carbon-coated TEM grids. Magnification is shown above each column.*

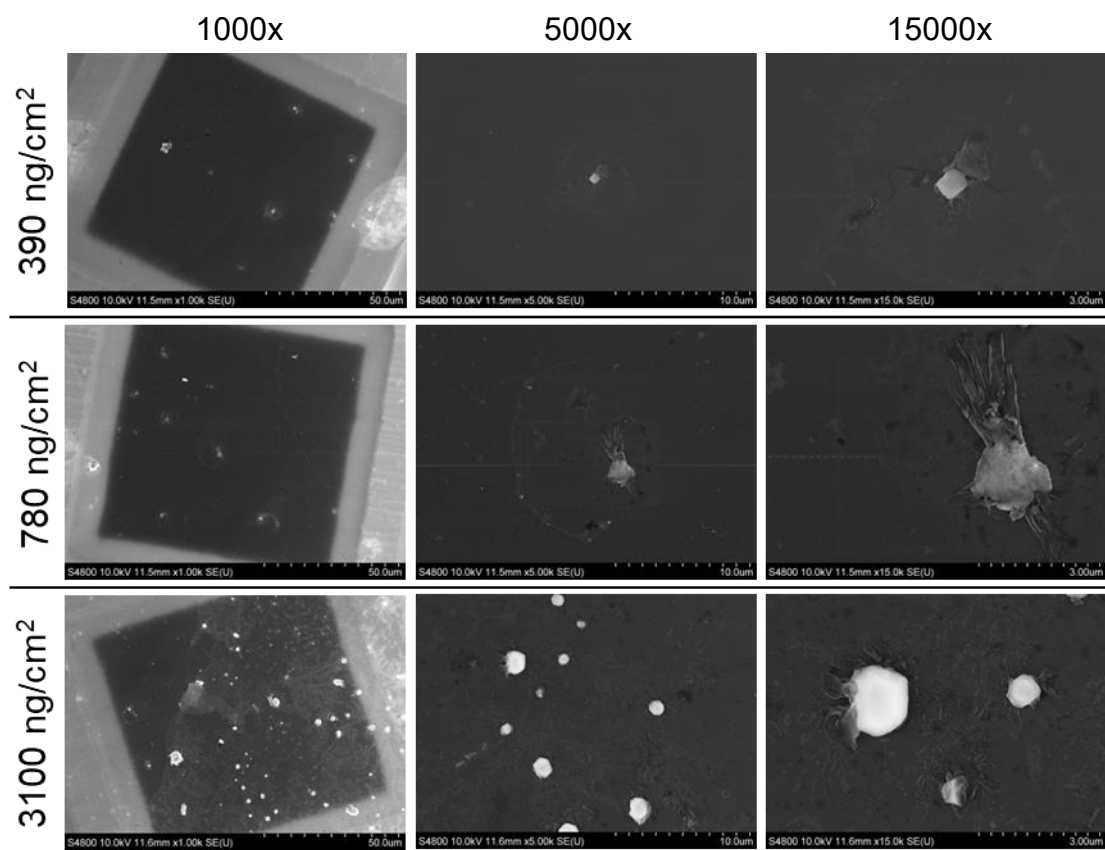


*Figure 4.29 SEM images of NIST SRM 2583 deposited after nebulisation with the VitroCell® Cloud on copper carbon-coated TEM grids. These are the deposited concentrations that will be utilised in the in vitro experiments. Magnification is shown above each column.*

#### 4.3.4 Actual Deposited Concentrations

Due to the nature of this exposure method, it is difficult to achieve 100% accurate PM depositions. The above characterisation, however, advises on feed concentrations to achieve a specified deposited exposure concentration. As mentioned, the targeted concentrations used here are 390, 780 and 3100 ng/cm<sup>2</sup>. **Table 4.3** and **Figure 4.30** show that across 10 independent exposure repetitions, the final deposited concentrations are within 1 SD for each particle used.

*Table 4.3 Actual exposure concentrations of CB, 1649b and 2583 when targeting 390, 780 and 3100 ng/cm<sup>2</sup>. Average exposure duration (i.e., time that cell cultures will spend inside of the VitroCell) are also shown. Deposition values are shown as the mean of 10 independent replicates.*

Targeted (ng/cm <sup>2</sup> )	Carbon Black			SRM 1649b			SRM 2583		
	390	780	3100	390	780	3100	390	780	3100
Deposited (ng/cm <sup>2</sup> )	381.08	753.58	3141.14	378.70	744.85	3124.27	381.17	776.63	3152.56
SD	41.72	80.02	268.91	63.14	109.81	118.17	54.66	114.30	205.63
SEM	13.19	25.31	85.04	19.97	34.73	37.37	17.28	36.14	65.02
Mean Deposition Time (mm.ss)	18.18	31.37	57.38	13.29	16.49	37.54	16.10	14.47	33.14

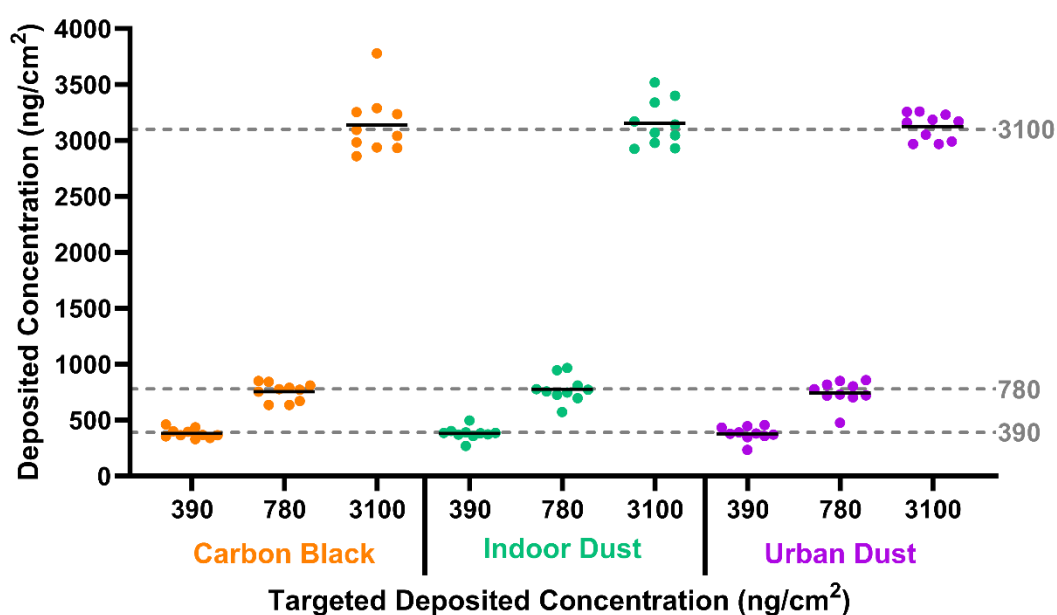


*Figure 4.30 Actual deposited concentrations of CB, 1649b and 2583 are shown by individual data points, with the black line showing the mean across 10 individual replicates. Dotted grey lines show the targeted deposited concentrations.*

### 4.3.5 Nitrogen Dioxide Exposure Chamber Parameters

Given that the NO<sub>2</sub> exposure chamber is required to balance the O<sub>2</sub>, CO<sub>2</sub>, NO<sub>2</sub> and N<sub>2</sub> concentrations, it was essential to ensure that these 4 gases could be controlled and maintained at the desired concentration. Over 24 hours, the O<sub>2</sub> and CO<sub>2</sub> concentration was controlled and maintained at 18% and 5%, respectively and was frequently monitored using the Coy O<sub>2</sub> and CO<sub>2</sub> controllers. During this time, the temperature and relative humidity were monitored and found to average  $37.4 \pm 0.63$  °C and  $86.03 \pm 2.157$  % across the 24 hours (**Figure 4.31**).

This work utilised three different NO<sub>2</sub> concentrations: 1, 2.5, and 5 ppm (1960, 4900, 9800 µg/m<sup>3</sup>). During exposures, the NO<sub>2</sub> concentration was routinely monitored using the Aeris® NO<sub>x</sub> sensor, allowing chamber/pump parameters to be adjusted if required. **Figure 4.32** shows an example of a 24-hour exposure period for each concentration. It is observed that although there is a degree of fluctuation occurring, the mean concentration is close to the set concentrations (within 1 SD). There is greater fluctuation at the higher exposure concentrations and overnight (approximately from hour 8 to hour 18) when the system was monitored less frequently.

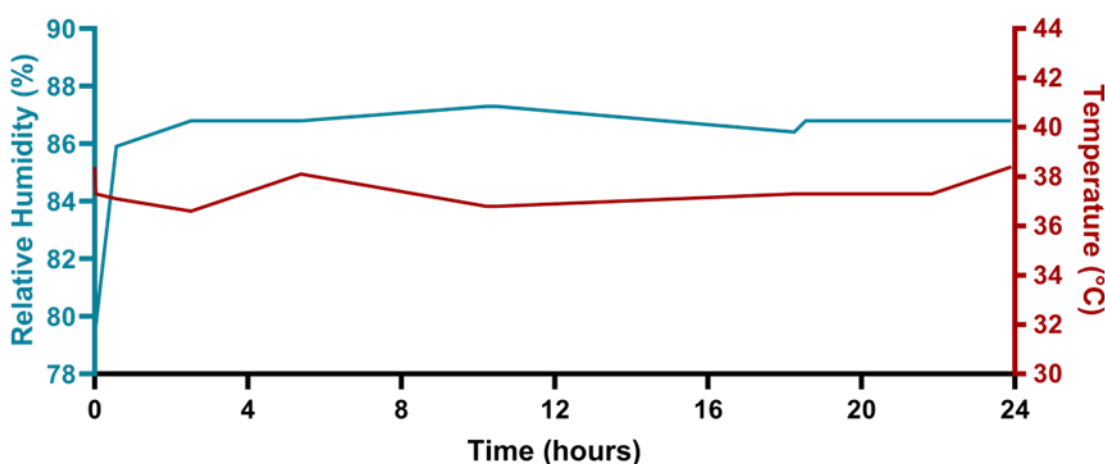


*Figure 4.31 Parameters to be controlled over the duration of exposure within the NO<sub>2</sub> chamber: Relative humidity and temperature measured within the chamber using a thermohygrometer.*

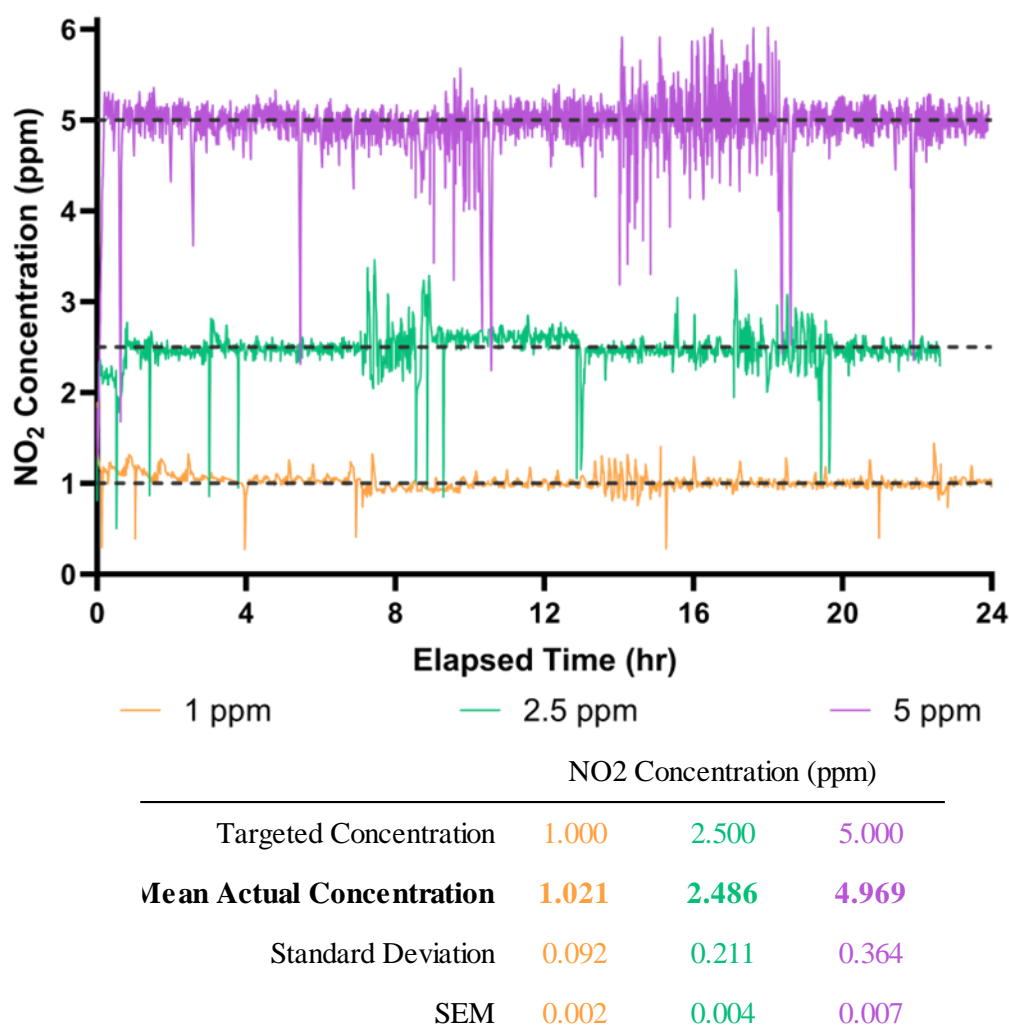


**Figure 4.32** An example exposure concentration trend across a 24-hour period. Targeted concentrations of 1 (yellow), 2.5 (green) and 5 (purple) are shown, with dotted lines indicating these targeted concentrations. The monitor produces a reading ever 26 seconds, this is reflected within this data where every data read is plotted (i.e., there is no rolling average).

#### 4.3.6 Simulated Transportation of Samples between Swansea University and The Radiation, Chemical and Environmental Hazards Directorate

Given that the NO<sub>2</sub> exposure system is in RCE, 2.5 hours away from where the cell cultures would initially be seeded in Swansea University, the impact on travel was assessed by placing seeded NCI-H441 monocultures within a polystyrene box and then either left on the bench or shaken/rocked to simulate driving. It was shown that simulated driving conditions did not alter cytotoxicity, barrier function, IL6 or IL8 release **Figure 4.33**.

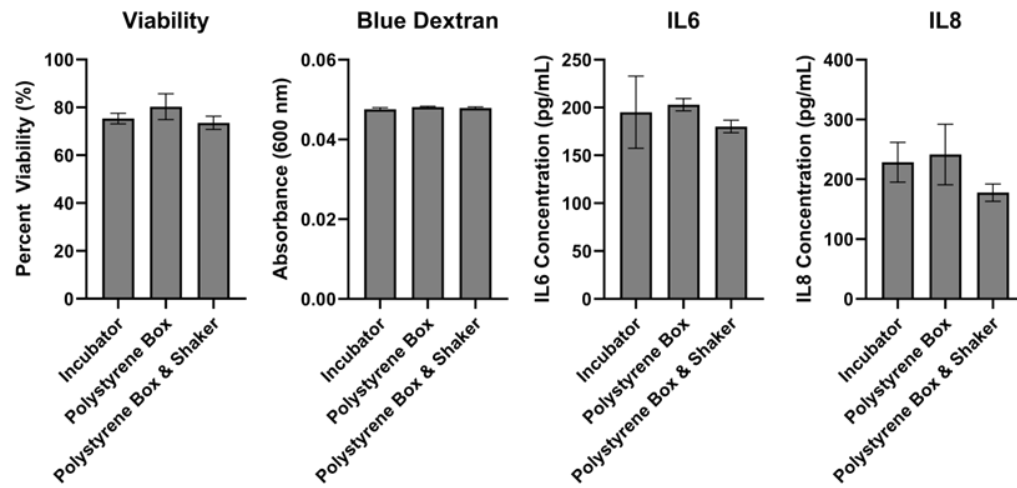


**Figure 4.33** Viability, barrier function and IL6 and IL8 release from NCI-H441 monocultures exposed to simulated travel conditions. Statistical significance was analysed via one-way ANOVA, with a Tukeys post hoc test.

## 4.4 Discussion

### 4.4.1 VitroCell Cloud

Alveolar epithelial cells cultured at the ALI compared to submerged conditions have shown to have contrasting phenotypes, which may be more realistic to *in vivo* conditions (Öhlinger et al., 2019). Traditionally, pollutant exposures have been conducted using submerged exposure techniques. The development of exposure systems allowing cell cultures to be exposed at ALI has meant that more physically relevant *in vitro* models (as discussed in Chapter 3) can be utilised within exposure studies. Companies such as VitroCell and Cultex® produce systems that allow *in vitro* models cultured at ALI to be exposed to particles through aerosol or dry powder exposure.

Not only are ALI exposure systems allowing cells to be exposed in a method that is more comparable to *in vivo* conditions, but also dosimetry can be measured *via* a QCM, in this case, allowing delivered particles to be measured down to  $\text{ng/cm}^2$  resolution (Ding et al., 2020). This is useful as it can be applied directly to alveolar deposition in real-life circumstances, compared to submerged exposures when deposition must mathematically convert from a suspension concentration aligned with the cell growth surface area, and even then, this is an assumption that 100% of the particles are depositing onto the cell monolayer.

Furthermore, it has been shown that the particles intended to be used in this study can be effectively suspended and nebulised in water with no additives. If cells were exposed to these PM samples through submerged conditions, the first proteins the particles would encounter would be those comprising cell culture media components. This would not be the case in real inhalation exposures, where the likely first proteins of interaction would be those present within the surfactant (surfactant proteins, albumin, and immunoglobulins) or alveolar cell surface proteins themselves. Nanoparticles within serum have been shown to develop a protein corona, which can affect particle size (Schaefer et al., 2012), surface charge (Lundqvist et al., 2008) and hydrophobicity (Walkey et al., 2014). This would alter biological interactions, influencing toxicity (Wohlleben et al., 2016). The fact that particles used within this study are nebulised in milli-Q water avoids unwanted interaction with other proteins/lipids, and a more representative interaction is to be established.

As mentioned previously, numerous systems allow exposure at ALI. However, the mechanisms by which exposures are facilitated may differ and have become more advanced over time. An early system for ALI exposures was reported by Voisin *et al.* (1977), where cells were grown on a microporous insert and fed nutrients basally and exposed to a test atmosphere (where gases/particulates could be controlled) apically (like how transwell inserts were used within this work). As these systems have been developed, different deposition methods have been implemented. For example, an electrostatic deposition has been used when examining charged particle toxicity (Paur *et al.*, 2011) or by directly spraying aerosols onto the cultures (Blank *et al.*, 2007). However, the majority of the systems previously developed have relied on gravity to deposit particulate material (Paur *et al.*, 2011). This is how the particles used here are deposited using the VitroCell Cloud.

The nebuliser within the Cloud contains a vibrating mesh cloud generator at the top of the chamber in a central position, generating a particle containing droplets. As a cloud is nebulised into the chamber, air drag causes droplets to be diverted horizontally in all directions, mixing with the air in the chamber. The vortices generated allow a homogenous distribution of droplets through the entire chamber. This means that when the droplets sediment, they are uniformly distributed across the entire surface of the chamber. For this reason, there should be no difference in exposure concentration of transwell inserts placed in different wells within the Cloud system. Indeed, when this was tested experimentally using fluorescein and a surrogate drug, similar depositions were recorded within each base plate (4.3% variability between wells across 18 repetitions) (Lenz *et al.*, 2014).

Exposure studies utilising the Cloud discussed later have focused on exposure concentrations of 390, 780 and 3100 ng/cm<sup>2</sup>. These exposure concentrations were based on previous occupation exposure and *in vivo* studies, which found these concentrations to be the 8-hour exposure burden for 1, 3 and 9 days, respectively (Søs Poulsen *et al.*, 2013). It has been shown that these deposited concentrations are achievable, though it can take up to 5 nebulisations to reach the top concentration. This means the transwell inserts could be within the VitroCell chamber for up to an hour. Although the chamber is warmed to 37°C and the cultures are nourished basally, the chance that this would induce a cellular response cannot be ignored.



For this reason, exposure studies will utilise an NaCl control, which will be used to assess this response, as well as any effects potentially induced by nebulisation of the 0.009% NaCl particle suspension medium. This can be contrasted to an incubator control that will not be placed into the VitroCell chamber, allowing particle-specific effects to be drawn. The method was also used by Drasler *et al.* (2018).

Although the literature on these specific particles is scarce, CB has previously been utilised in VitroCell exposures where it was nebulised in distilled water. The study reported difficulty achieving high enough dose delivery rates, so they were not able to observe IC50 doses in their *in vitro* investigation, though they used exposures in a concentration range of 0 – 13 cm<sup>2</sup>/cm<sup>2</sup>, which, when converted to mass/cm<sup>2</sup>, are higher than the exposures concentrations used here (up to 3.8 µg/mL) (Voss *et al.*, 2020). Drasler *et al.* (2018) used Printex 85 carbon black as a reference material with the VitroCell Cloud and were able to achieve deposited concentrations of 300-1000 ng/cm<sup>2</sup>, which is approximately the range achieved here using single nebulisations; this study does not comment on whether multiple nebulisations were performed to reach higher doses, though here multiple nebulisations were used to achieve higher depositions required (especially when achieving 3100 ng/cm<sup>2</sup>). They point out however that the CB exposure may occur occupationally at 14 mg/m<sup>2</sup> (4-times higher than the threshold limit value of 3.5 mg/m<sup>2</sup>) within CB manufacturing plants (Zhang *et al.*, 2014). Based on alveolar mass retention modelling, this could equate representative exposures required deposition concentrations of 1000 ng/cm<sup>2</sup> (acute) to 700,000 ng/cm<sup>2</sup> (lifetime), the latter of which is completely unachievable using this exposure system.

The 1649b and 2583 were initially tested with the Aerogen nebuliser. However, it was found that there were no changes in QCM deposition as the suspension concentration was changed. Further, SEM imaging of TEM grids revealed no particle deposition. Given the size difference of carbon black (65 nm average diameter) compared to the 1649b, which were 200-10,000 nm (NIST, 2023) and 2583, which can range beyond 50 nm (based on SEM imaging). This significant disparity in sizing could be why a larger mesh nebuliser was required to aerosolise the NIST particle suspensions effectively. To date, no studies have aerosolised these SRMs. Most VitroCell aerosol exposures have utilised engineered nanoparticles; however, some studies have looked at realistic ambient particles. He *et al.* (2013), for example, were able to nebulise UFPs

collected from samples near Schiphol Airport and were able to achieve up to 2.07  $\mu\text{g}/\text{cm}^2$  deposition in a single nebulisation (400  $\mu\text{L}$  of 1000  $\mu\text{g}/\text{mL}$  feed suspension).

#### 4.4.2 Nitrogen Dioxide Exposure Chamber

In the past, much of the work focusing on the toxicity of  $\text{NO}_2$  exposure has taken place within *in vivo* models. Exposure to *in vitro* systems poses a different challenge as several other factors, besides the  $\text{NO}_2$  concentration, must be controlled. Here, an  $\text{NO}_2$  exposure chamber has been developed, allowing the  $\text{O}_2$  concentration,  $\text{CO}_2$  concentration, temperature, and relative humidity to be maintained at levels comparable to a standard tissue culture incubator.

Early *in vitro*  $\text{NO}_2$  exposures have used chambers where the  $\text{NO}_2$  concentration can be controlled to achieve their exposures (Halliwell et al., 1992; Kelly & Tetley, 1997), though the specifics of the exposure systems are not reported in detail. Ayyagari et al. (2007) exposed *in vitro* conducting airway cells to  $\text{NO}_2$  by adapting a tissue culture incubator to have an  $\text{NO}_2$  inlet.  $\text{NO}_2$  was directly measured inside the incubator, and after the cells were placed into the incubator, the  $\text{NO}_2$  concentration could be slowly increased up to 45 ppm to provide high-dose acute exposures.

Tsukue et al. (2010) took a much more direct approach when exposing A549 to  $\text{NO}_2$ . They adapted a Cultex® system to attach directly to the exhaust of a diesel engine, which could be fitted with a muffler, particle filter or muffler with added  $\text{NO}_2$  to allow high PM low  $\text{NO}_2$ , low PM high  $\text{NO}_2$  or high PM high  $\text{NO}_2$  exposures, respectively. The emissions were diluted utilising a dilution tunnel using background air, allowing realistic exposures to be achieved. Although this is a relevant exposure system, the potential effects of confounding pollutants such as  $\text{SO}_2$  and formaldehyde cannot be removed, and  $\text{NO}_2$ -specific effects would be more challenging to decipher. However, this is interesting as it is one of the few studies that directly contrasts PM and  $\text{NO}_2$  exposure *in vitro*.

A study examined the effect  $\text{NO}_2$  in a manner similar to what will be performed in this work through the use of an exposure chamber. *In vitro* cultures of macrophages exposed to  $\text{NO}_2$  in a ‘special’ exposure chamber which maintains 5%  $\text{CO}_2$  enriched with a constant flow of gaseous pollutant using early adoption of ALI culturing methods. It was found that *in vitro* models could be cultured in  $\text{NO}_2$  conditions (0.2

ppm) for 24 hrs to display oxidative and pro-inflammatory effects (Wallaert & Voisin, 1992).

The WHO 2021 Air Quality Guidelines state a maximal annual average of 10  $\mu\text{g}/\text{m}^3$  or a daily average of 25  $\mu\text{g}/\text{m}^3$  for  $\text{NO}_2$  exposure limits. The utilised  $\text{NO}_2$  exposure concentrations used within this work were 1, 2.5 and 5 ppm (1960, 4900, 9800  $\mu\text{g}/\text{m}^3$ ). Though these concentrations are higher than those stated in the WHO guidelines, they were chosen initially to reflect a long-term exposure at lower, realistic human exposure conditions, to allow mechanistic toxicological effects to be observed within acute exposure durations. Further, the concentrations could encompass higher concentrations of indoor  $\text{NO}_2$  exposure, which can reach 2500  $\mu\text{g}/\text{m}^3$  (WHO, 2010).

It was noted that there were greater fluctuations in the  $\text{NO}_2$  exposure chamber concentration overnight. This could be due to a variety of factors including changes in lab gas concentrations and temperature. Further, the laboratory was unattended, therefore was unable to be monitored and adjusted if needed. However, it is unlikely the system would facilitate the large spikes in variance observed, and it more likely interference with the sensor as opposed to an  $\text{NO}_2$  concentration change.

## 4.5 Summary and Outlook

*Table 4.4 Key conclusions and findings from Chapter 4.*

<b>Chapter Conclusions</b>	<ul style="list-style-type: none"><li>▪ It is shown that CB, 1649b or 2583 can be effectively nebulised and aerosolised using the VitroCell® Cloud system, allowing PM exposures of <i>in vitro</i> cultures at the ALI.</li><li>▪ A novel NO<sub>2</sub> exposure system has been developed and characterised to allow <i>in vitro</i> models to be exposed at the ALI to user-defined NO<sub>2</sub> concentrations.</li></ul>
<b>Project Impact</b>	<b>The VitroCell® Cloud and NO<sub>2</sub> exposure systems can be used in tandem to expose the advanced alveolar barrier models (developed in Chapter 3) to PM and NO<sub>2</sub> simultaneously.</b>

This chapter has demonstrated that CB, 1649b and 2583 are able to be nebulised using a VitroCell® Cloud system, which will allow aerosol exposures to *in vitro* lung models. Morphological examination of the deposited fraction of each PM sample revealed that the particles are within the respirable size range, meaning that the alveolar region of the lung is likely the target of toxicity. Furthermore, it was shown that realistic PM depositions were achieved using this exposure method, allowing these exposures to resemble human exposures accurately.

Alongside the characterisation of PM exposures, the NO<sub>2</sub> exposure system, which was planned to be used in combination with the VitroCell® Cloud, was developed and characterised. Through the adaption of a Coy hypoxia chamber, it has been shown that the NO<sub>2</sub> concentration within the chamber can be accurately maintained up to 5 ppm. Further, reaching these NO<sub>2</sub> concentrations has been shown not to alter other parameters necessary for effective cell growth, such as temperature, humidity, O<sub>2</sub> and CO<sub>2</sub> concentrations.

The subsequent chapters aim to combine the approaches characterised within this chapter and the advanced alveolar triple cell co-culture described in Chapter 3 to perform highly relevant PM and NO<sub>2</sub> co-exposures. This would be done by initially depositing a desired deposited concentration of PM sample onto the alveolar models and then incubating them within a known NO<sub>2</sub> concentration.

## **Chapter 5: Exposure of Advanced *In Vitro* Models to Particulate Matter**

---

A special thanks to Prof. Ulla Birgitte Vogel from the National Research Centre for the Working Environment, Denmark, as well as Dr Joakim Pagels and Dr Vilhelm Malmborg from Lund University, Sweden, for kindly providing the diesel emission particles used within this chapter.

## 5.1 Introduction

Within Chapter 3, an anatomically relevant alveolar triple cell co-culture was developed; subsequently, in Chapter 4, methods of aerosol exposure to PM were characterised. This chapter now intends to combine these two approaches to conduct PM exposure studies that are highly pertinent to human exposures within an *in vitro* system. This will include assessing the response to a range of PM types, including CB, 1649b, 2583 (standard samples), as well as a range of DEPs (fresh samples). Given that the toxicological outcomes are known to vary in response to PM types or PM originating from differing sources (COMEAP, 2022), it is of interest to compare a range of PM samples within the same experimental system, which may shed further information on specific PM effects.

Further, by assessing the PM-induced effect in a range of mono and co-cultures, cell-specific effects or interactions can be deduced. This would allow an increased understanding of the biological responses underpinning PM-induced toxicity, as well as how the triple cell co-culture functions at a system level.

Historically, CB has been used extensively in particle and nanotoxicology, both *in vitro* and *in vivo*. Oxidative stress, inflammatory and genotoxic responses have all been associated with CB exposure (Di Ianni et al., 2022). Within *in vitro* studies, CB was shown to increase ROS production in A549 and THP-1 cells (Danielsen et al., 2011) and increased DNA strand breaks and micronucleus frequency in A549 monocultures (Mroz et al., 2008; Totsuka et al., 2009). These exposures took place under submerged conditions, which have previously been discussed to elicit responses different from those of ALI conditions.

Comparatively, the toxicological information available regarding 1649b is scarcer, whilst 2583 is completely lacking. When examining evidence for 1649 in general (*i.e.* 1649a or 1649b), there is evidence that it could alter epigenetic modification within THP-1 cells (Cao et al., 2021), could increase susceptibility to respiratory infections (Sawyer et al., 2009) and induce genotoxicity (Karlsson et al., 2004). However, no studies examine this standardised ambient PM sample using ALI systems within co-culture models. *In vivo*, urban dust exposure has shown a cytotoxic response and decreased respiratory burst in rat lung macrophages (Breznan et al., 2013; Nadeau et al., 1996).

There are no studies which directly implicate 2583 with toxic outcomes. However, there are several studies which have examined the chemical properties of the dust, which is found to contain various heavy metals, including lead, mercury, arsenic, cadmium and chromium (NIST, 2016), as well as polybrominated diphenyl ethers (Stapleton et al., 2006). Since humans spend 90% of their time indoors, increased focus is required on the indoor environment inhalation exposure hazard.

Data generated in this chapter will be analysed, interpreted, and put into context with other literature (epidemiological, *in vitro*, and *in vivo*) to deduce an inhalation hazard for each PM. Further, co-culture combinations will allow for a mechanistic understanding of which cell(s) may be more or less susceptible to deleterious effects than others. In addition, it will give an understanding of the effects of PM as an individual component prior to co-exposure with NO<sub>2</sub>, allowing a co-exposure effect to be deduced in subsequent chapters.

#### **5.1.1 Aims and Objectives**

This chapter intends to combine the approaches developed and characterised in Chapter 3 and Chapter 4 to:

1. Expose alveolar mono-, co- and triple cell cultures to a range of PM samples.
2. Assess cell growth, viability, barrier function and pro-inflammatory response of these models following PM exposure.

## 5.2 Materials and Methods

### 5.2.1 Experimental Design

The alveolar triple cell co-culture has been previously described in Chapter 3, and methods of particle exposure characterised in Chapter 4. This chapter intends to combine these approaches through:

1. Culturing the triple cell model, or co-/monocultures of epithelial cells and/or dTHP-1 cells (**Figure 5.1**).
2. Taking the cultures to the ALI after 72 hours
3. Exposing the alveolar models at the ALI using the VitroCell® Cloud (or qALI for DEP exposures) whilst utilising relevant positive and negative controls.
4. After 24 hours of exposure to PM samples, toxicological endpoints are assessed, including cell number and viability, barrier function, pro-inflammatory response, and morphology (**Figure 5.2**).

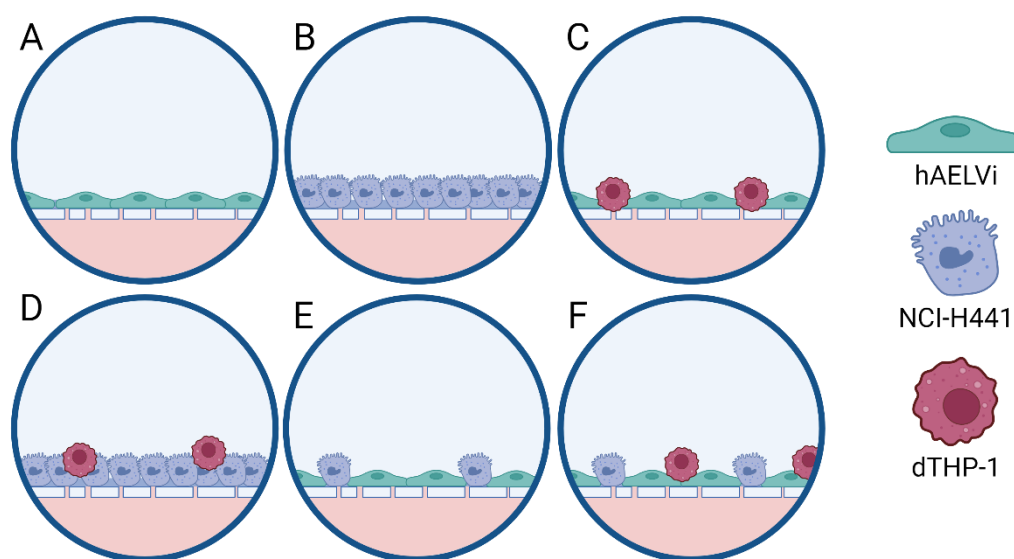


**Figure 5.1** *In vitro* models used within this chapter: (A) hAELVi monoculture, (B) NCI-H441 monoculture, (C) hAELVi + dTHP-1 co-culture, (D) NCI-H441 + dTHP-1 co-culture, (E) hAELVi\_NCI-H441 co-culture and (F) triple cell co-culture. Cultures will be grown at the ALI on transwell inserts. The densities of each cell type are shown on Table 5.1.



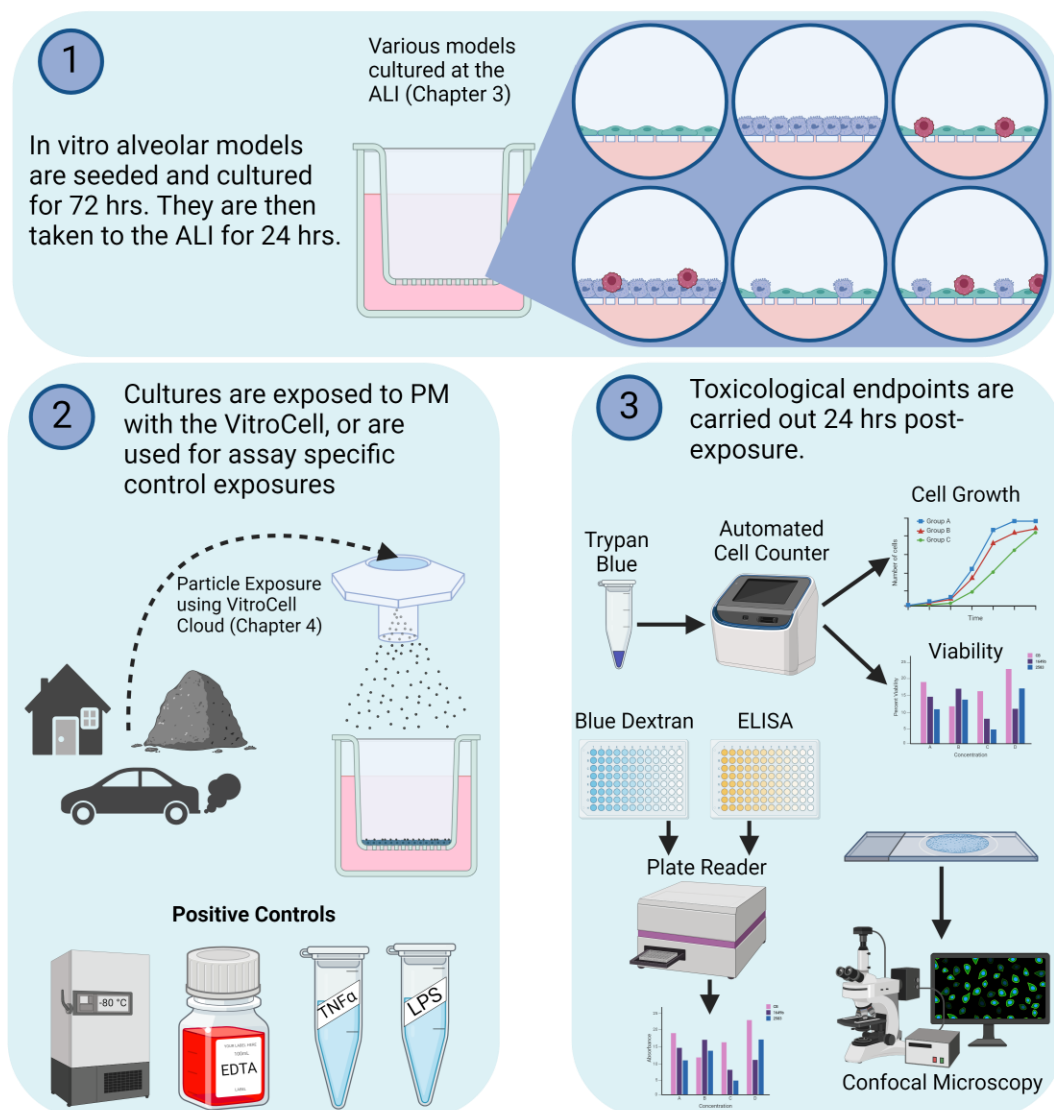


**Figure 5.2** Proposed exposure plan for PM exposure to various in vitro models. Cell cultures are seeded (1) before being exposed to PM, or an assay specific positive control (2) and various toxicological endpoints are assayed (3)

## 5.2.2 Chemical and Reagents

The chemicals and reagents used are described in Chapter 2, Section 2.1.

## 5.2.3 Cell Culture

Refer to Chapter 2 Section 2.2 for the detailed methodology of culturing and passaging techniques of hAELVi, NCI-H441 and (d)THP-1 cells. Refer to Chapter 3 for information regarding the alveolar triple cell co-culture.

Toxicological exposures within this chapter use specific mono/co/triple cultures (Figure 5.1). Table 5.1 outlines parameters adhered to during the seeding and culturing of these models within the transwell inserts.

#### 5.2.4 Exposure of *In Vitro* Models to PM Samples

Suspensions of CB, 1649b or 2583 were prepared as described in Section 4.2.2.1 before being diluted to final concentration.

After cells were cultured at the ALI for 24 hours, they were exposed to CB, 1649b or 2583 using the VitroCell Cloud. Based on the deposition characteristics explored in

*Table 5.1 Seeding densities and media used within various in vitro models.*

		hAELVi Monoculture	NCI-H441 Monoculture	hAELVi_NCI-H441	hAELVi_dTHP-1	NCI-H441_dTHP-1	Triple Cell Co-culture
0 hrs	hAELVi	$2.5 \times 10^5$	0	$4.5 \times 10^5$	$2.5 \times 10^5$	0	$4.5 \times 10^5$
	NCI-H441	0	$2.5 \times 10^5$	$5 \times 10^4$	0	$2.5 \times 10^5$	$5 \times 10^4$
72 hrs	dTHP-1	0	0	0	$3 \times 10^5$	$3 \times 10^5$	$3 \times 10^5$
Cell Culture Media		huAEC	RPMI 1640	50/50	huAEC	RPMI 1640	50/50

Chapter 4, depositions of 390, 780 and 3100 ng/cm<sup>2</sup> were targeted for *in vitro* exposures (as discussed in in Section 4.2.2). It might have been necessary for numerous nebulisations to be performed before the targeted deposition was reached. Therefore, an equal number of NaCl control nebulisations were performed as per the number of times it took to reach the highest exposure concentration to assess any effect of time duration within the VitroCell® Cloud or the exposure to NaCl spiked water.

DEP exposures were undertaken using the qALI method. Particles were suspended in sterile water and diluted to 16.4, 32.8 and 1.304 µg/mL concentrations. These were comparable to the VitroCell® Cloud concentrations used, calculated based on the surface area of a transwell insert. A qALI method was chosen for these exposures due to the small total mass of particles available.

### **5.2.5 Cell Count and Viability**

Methods for counting cells and assessing viability are described in Chapter 2, Section 2.3.

### **5.2.6 Blue Dextran**

Methods for blue dextran barrier integrity analysis are described in Chapter 2, Section 2.6.1.

### **5.2.7 Pro-Inflammatory Response**

Methods for measuring pro-inflammatory response are described in Chapter 2, Section 2.7.

### **5.2.8 Immunocytochemistry and Confocal Microscopy**

General principles of sample fixation and storage, immunocytochemistry and confocal microscopy are described in Chapter 2, Section 2.5.

### **5.2.9 Data and Statistical Analysis**

Exposures were performed at least 3 times on biological replicates at least 2 passages apart. Statistical analysis and data visualisation were performed using GraphPad Prism Version 10.1.2. One-way ANOVAs were performed on the exposure data, utilising a Tukey post hoc multiple comparison test. Any changes in statistical analysis methodology is outlined in the relevant figure legend. Significance is shown compared to the incubator or NaCl control exposures, where a  $p$ -value less than 0.05 was considered statistically significant. Positive controls were not included in the multiple comparison tests.

## 5.3 Results

Within this Chapter, a scheme of the cellular model to which the data is pertinent is shown at the beginning of each relevant section. This is to aid the reader in following the data sets for each cell system and particle exposure.

### 5.3.1 hAELVi Monoculture Exposure to Printex® 90, Urban Dust and Indoor Dust

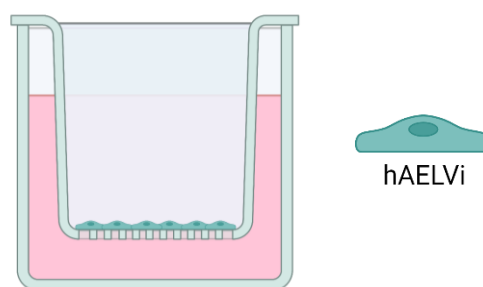


Figure 5.3 Schematic of hAELVi monoculture used in Section 5.3.1.

#### 5.3.1.1 Printex® 90 Carbon Black

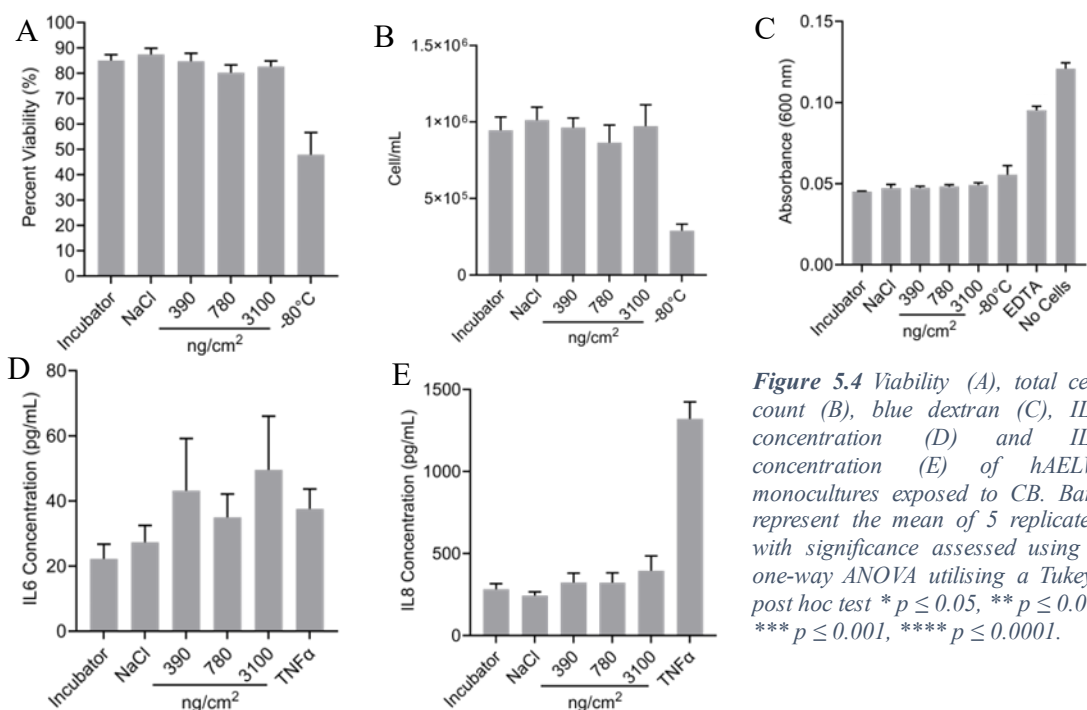
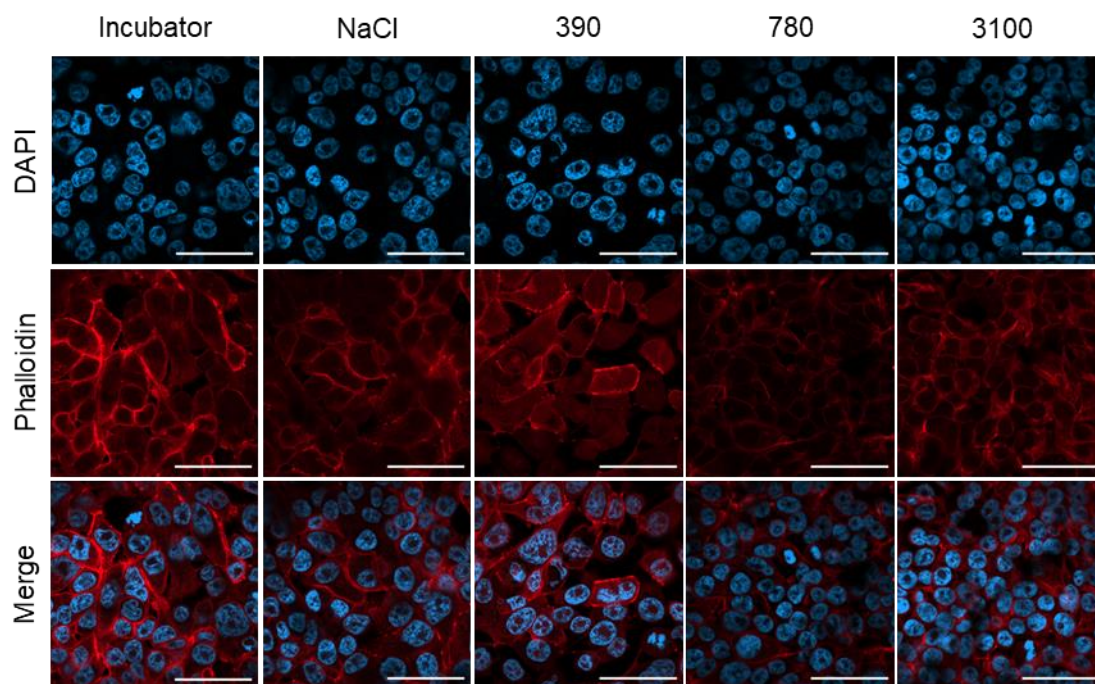


Figure 5.4 Viability (A), total cell count (B), blue dextran (C), IL6 concentration (D) and IL8 concentration (E) of hAELVi monocultures exposed to CB. Bars represent the mean of 5 replicates with significance assessed using a one-way ANOVA utilising a Tukeys post hoc test \*  $p \leq 0.05$ , \*\*  $p \leq 0.01$ , \*\*\*  $p \leq 0.001$ , \*\*\*\*  $p \leq 0.0001$ .

After exposure to CB for 24 hours, viability and total cell count of hAELVi cells were unchanged (Figure 5.3). Viability and total cell count, however, were markedly reduced when cells were exposed to an environment of -80°C for 30 minutes (positive control) before trypan blue counting (Figure 5.4). Further, CB did not alter membrane permeability, as shown by blue dextran absorbance. hAELVi cells treated with EDTA or wells without any cells (positive controls) showed a notable decreases in barrier



**Figure 5.5** Confocal microscopy images of hAELVi monocultures exposed to CB. The nucleus (blue/DAPI), and cytoskeleton (red/phalloidin) are shown. Scale bar = 50  $\mu\text{m}$ .

function. All other exposures yielded absorbances comparable to the incubator control, and the huAEC media which had not been exposed to blue dextran. hAELVi exposed to CB released slightly higher levels of IL6 and IL8 than incubator controls. Only hAELVi monocultures exposed to the TNF $\alpha$  positive control caused a increase in IL8 release, indicating these cells are sensitive and can induce a pro-inflammatory response. This, therefore, would suggest that CB cannot act through pro-inflammatory mechanisms within this cell type.

Phalloidin staining reveals that hAELVi cells may be smaller and rounder following the higher 780 and 3100 ng/cm<sup>2</sup> CB exposures (**Figure 5.5**).

#### 5.3.1.2 SRM 1649b Urban Dust

After exposure to 1649b for 24 hours, the viability of hAELVi cells was not significantly altered ( $p > 0.05$ ), with the total cell number also remaining unchanged. The barrier function was not significantly altered by 1649b exposures ( $p > 0.05$ ) (**Figure 5.6**). Exposure to 1649b did not cause a significant alteration in IL6 or IL8 release at any 1649b concentration ( $p > 0.05$ ). Positive controls of -80  $^{\circ}\text{C}$  treatment caused a large decrease in viability and cell count, and EDTA treatment significantly increased barrier permeability. Treatment with TNF $\alpha$  caused significant increase in and IL8 release.

No alterations to cellular morphology were evident following 1649b exposure to the hAELVi cells after 24 hours (**Figure 5.7**).

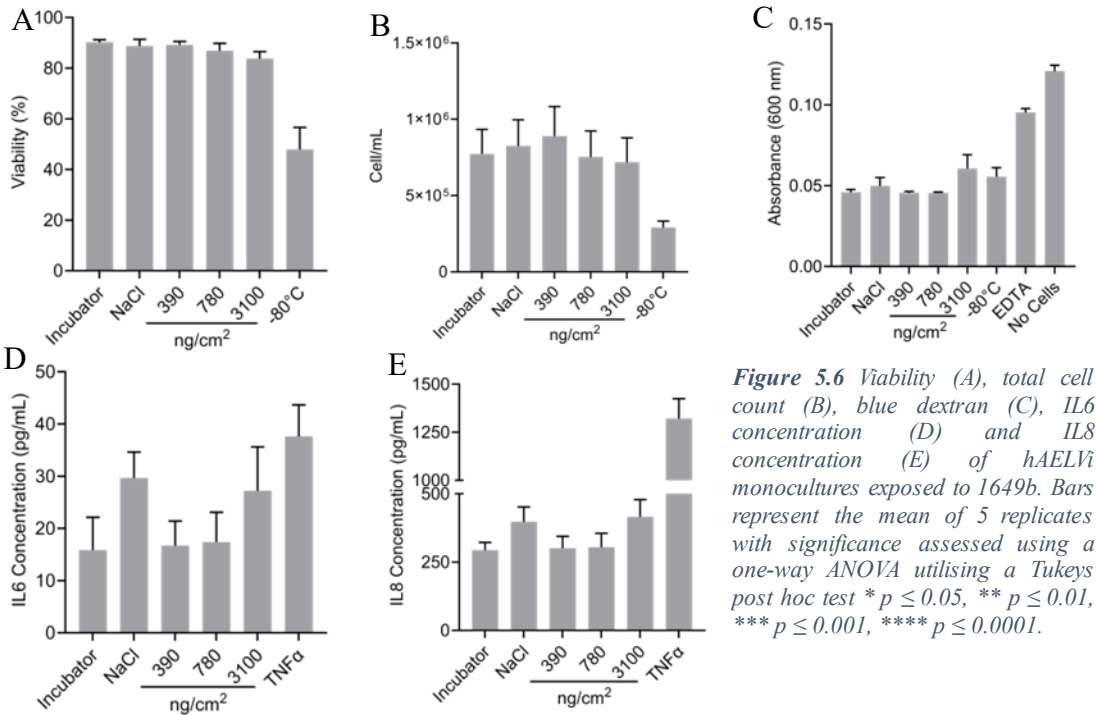


**Figure 5.6** Viability (A), total cell count (B), blue dextran (C), IL6 concentration (D) and IL8 concentration (E) of hAELVi monocultures exposed to 1649b. Bars represent the mean of 5 replicates with significance assessed using a one-way ANOVA utilising a Tukeys post hoc test \*  $p \leq 0.05$ , \*\*  $p \leq 0.01$ , \*\*\*  $p \leq 0.001$ , \*\*\*\*  $p \leq 0.0001$ .

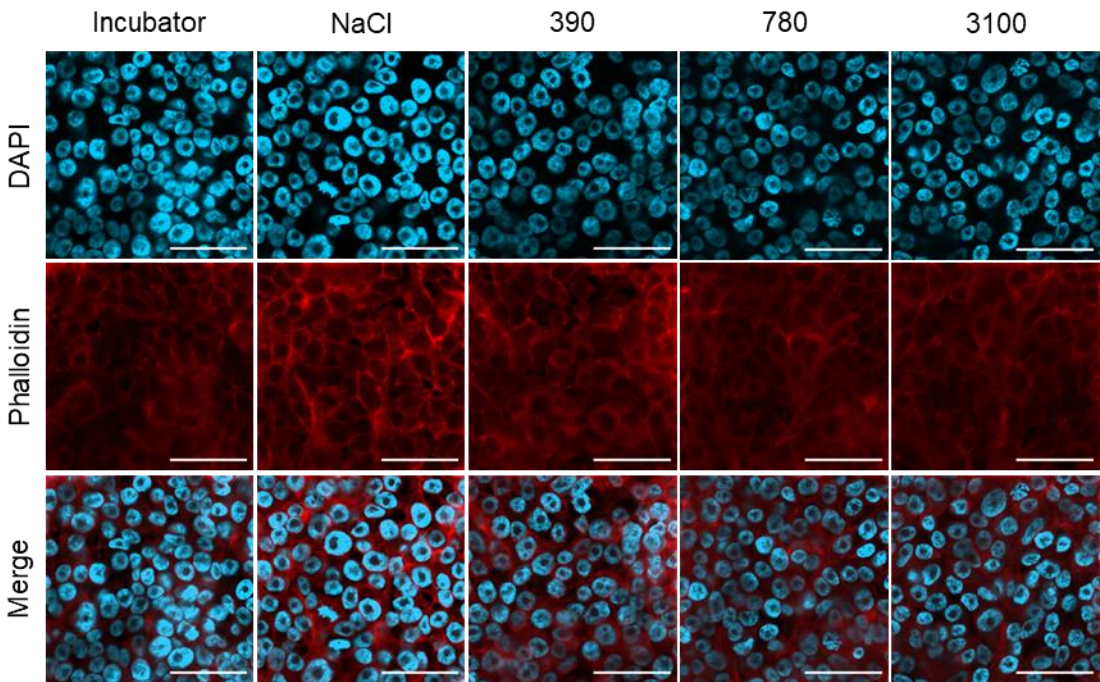
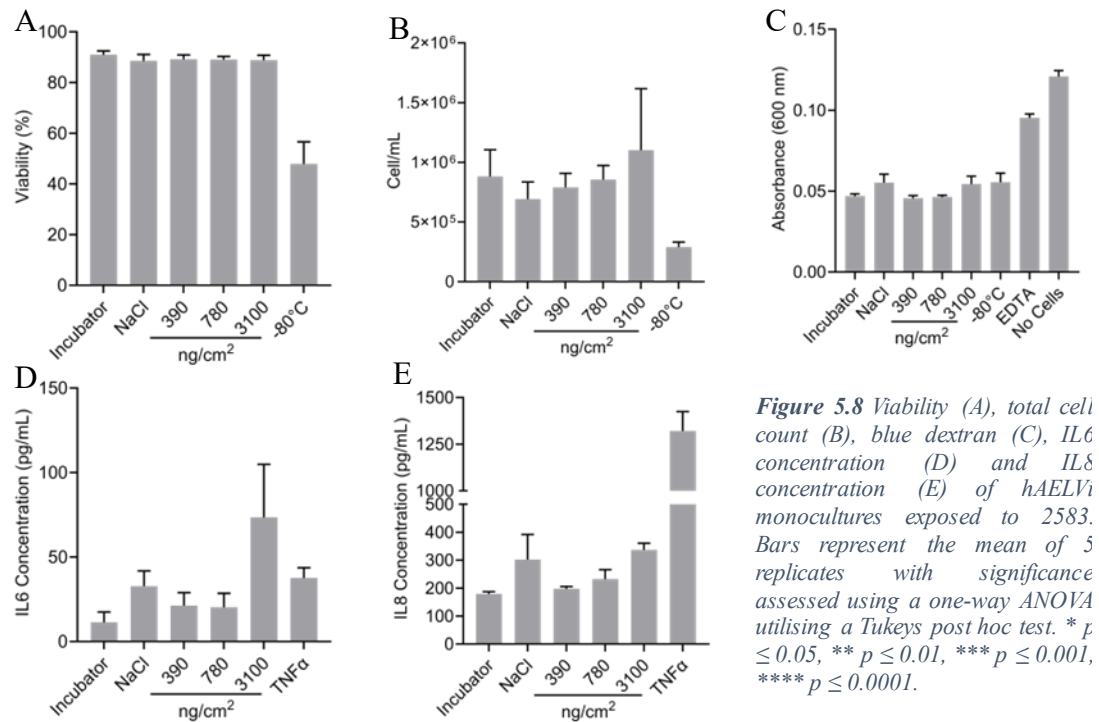


**Figure 5.7** Confocal microscopy images of hAELVi monocultures exposed to 1649b. The nucleus (blue/DAPI) and cytoskeleton (red/phalloidin) are shown. Scale bar = 50 μm.

### 5.3.1.3 SRM 2583 Indoor Dust

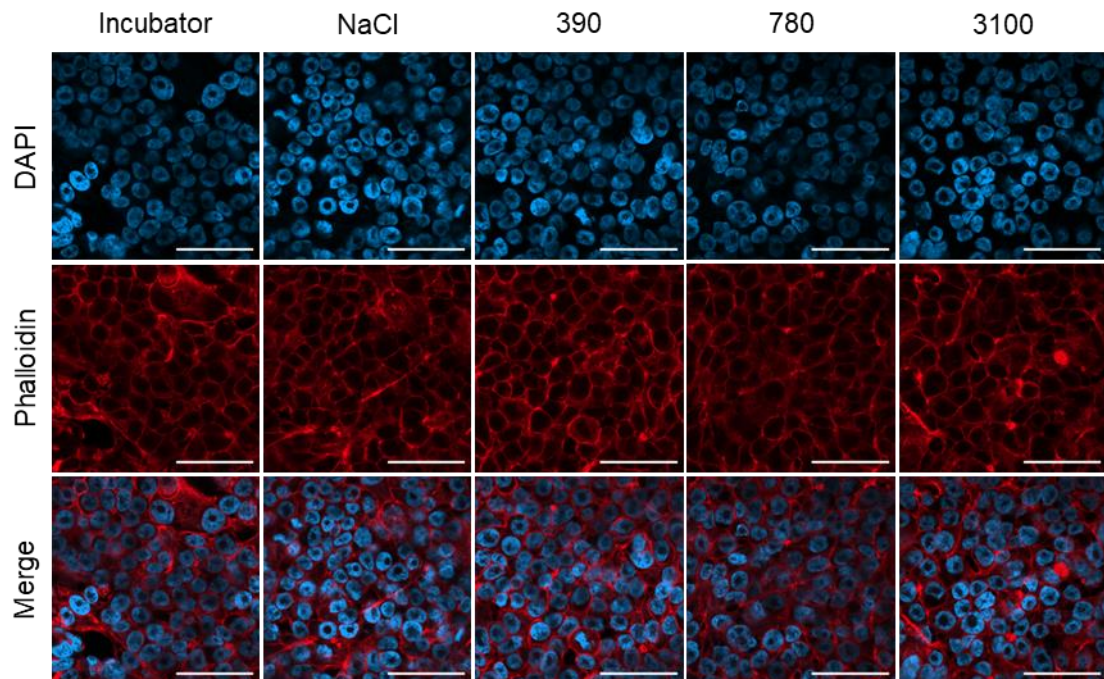
Exposing hAELVi to 2583 for 24 hours resulted in no cell viability or total cell count alterations. Further, 2583 did not alter the barrier function ( $p > 0.05$ ). When hAELVi





**Figure 5.8** Viability (A), total cell count (B), blue dextran (C), IL6 concentration (D) and IL8 concentration (E) of hAELVi monocultures exposed to 2583. Bars represent the mean of 5 replicates with significance assessed using a one-way ANOVA utilising a Tukeys post hoc test. \*  $p \leq 0.05$ , \*\*  $p \leq 0.01$ , \*\*\*  $p \leq 0.001$ , \*\*\*\*  $p \leq 0.0001$ .

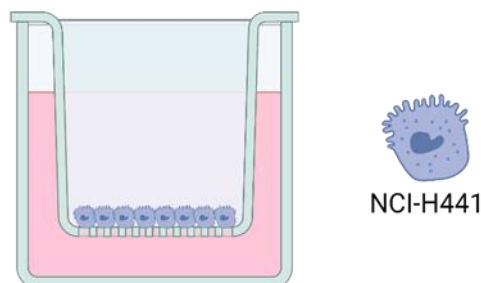
cells were exposed to an environment at  $-80^{\circ}\text{C}$ , viability and cell count were significantly reduced, however. hAELVi cells treated with EDTA also had barrier functions that were significantly reduced (**Figure 5.8**). Indoor dust exposure induced an increase in IL6 release, trending towards significance ( $p = 0.0739$  against incubator control following  $3100 \text{ ng/cm}^2$  exposure) but not IL8.



**Figure 5.9** Confocal microscopy images of hAELVi monocultures exposed to 2583. The nucleus (blue/DAPI) and cytoskeleton (red/phalloidin) are shown. Scale bar =  $50 \mu\text{m}$ .

hAELVi cells here show intense peripheral staining for f-actin. Exposure to NIST 2583 does not appear to alter hAELVi morphology however (**Figure 5.9**).

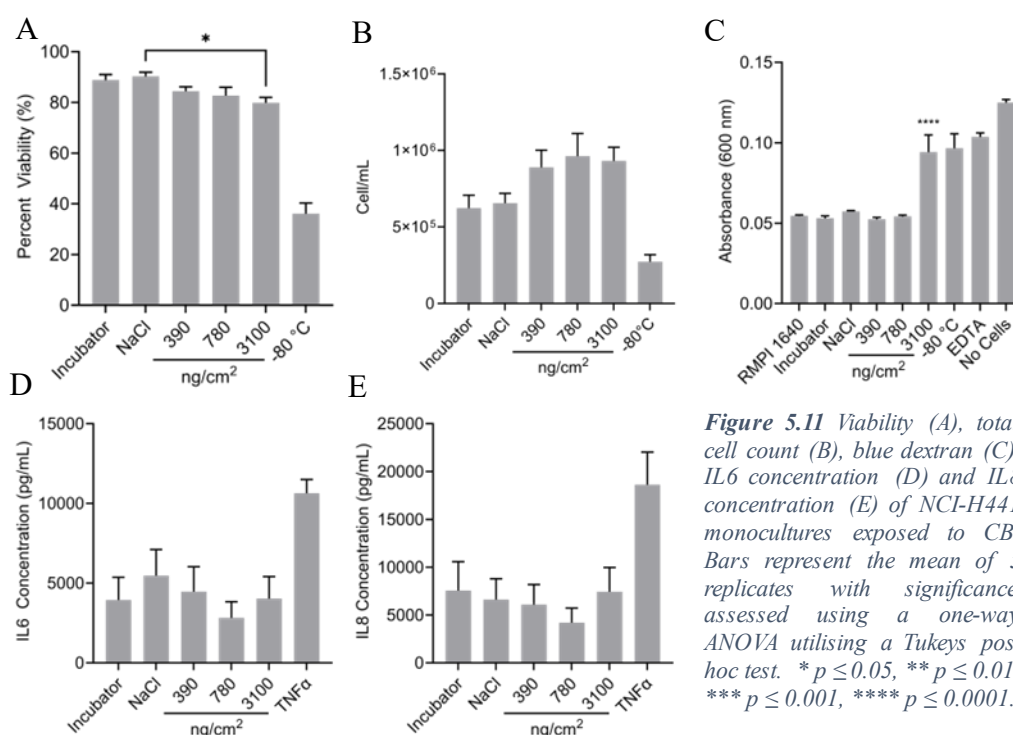
### 5.3.2 NCI-H441 Monoculture Exposure to Printex® 90, 1649b and 2583



*Figure 5.10 Schematic of NCI-H441 monoculture used in Section 5.3.1.*

#### 5.3.2.1 Printex® 90 Carbon Black

When exposed to CB for 24 hours, NCI-H441 cells (**Figure 5.10**) showed a dose-dependent decrease in viability reaching significance at 3100 ng/cm<sup>2</sup> exposed wells ( $p < 0.05$ ). CB did not induce any change in cell count following exposure. CB exposure caused a significant increase in membrane permeability at 3100 ng/cm<sup>2</sup> ( $p \leq 0.0001$  against the incubator and NaCl controls), although it was not significantly altered at 390 or 780 ng/cm<sup>2</sup> (**Figure 5.11**). CB at 3100 ng/cm<sup>2</sup> saw permeability similar to the positive controls of -80 °C and EDTA-treated wells (approx. 0.1 compared to 0.05 for the incubator control, respectively). Wells lacking cells had an absorbance of 0.125.





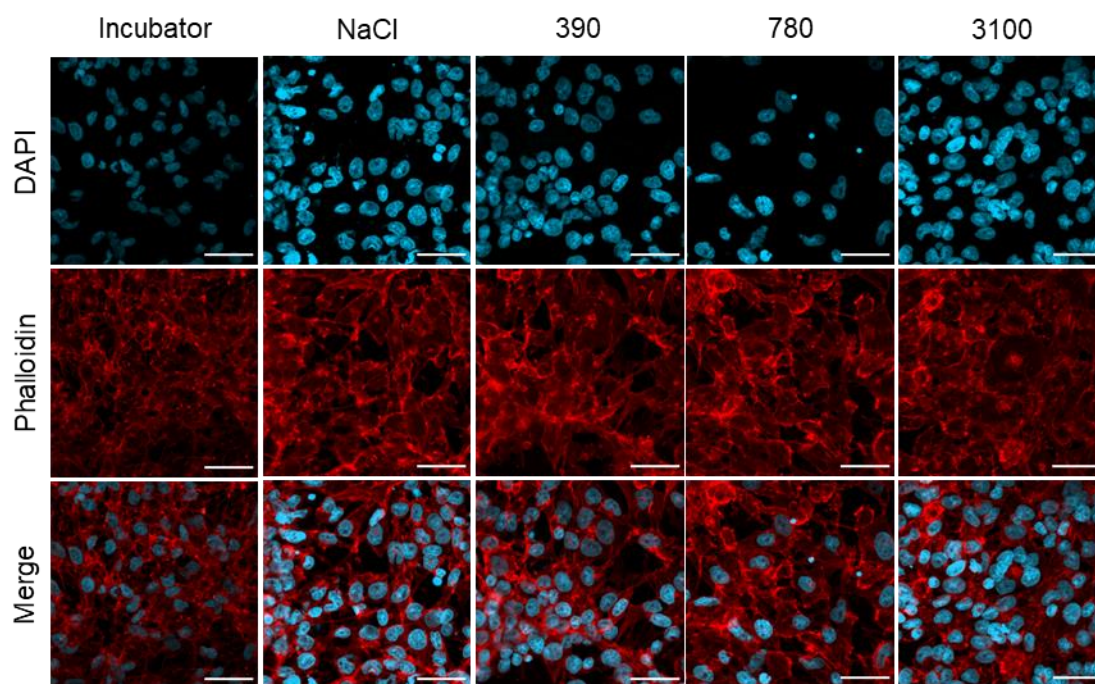


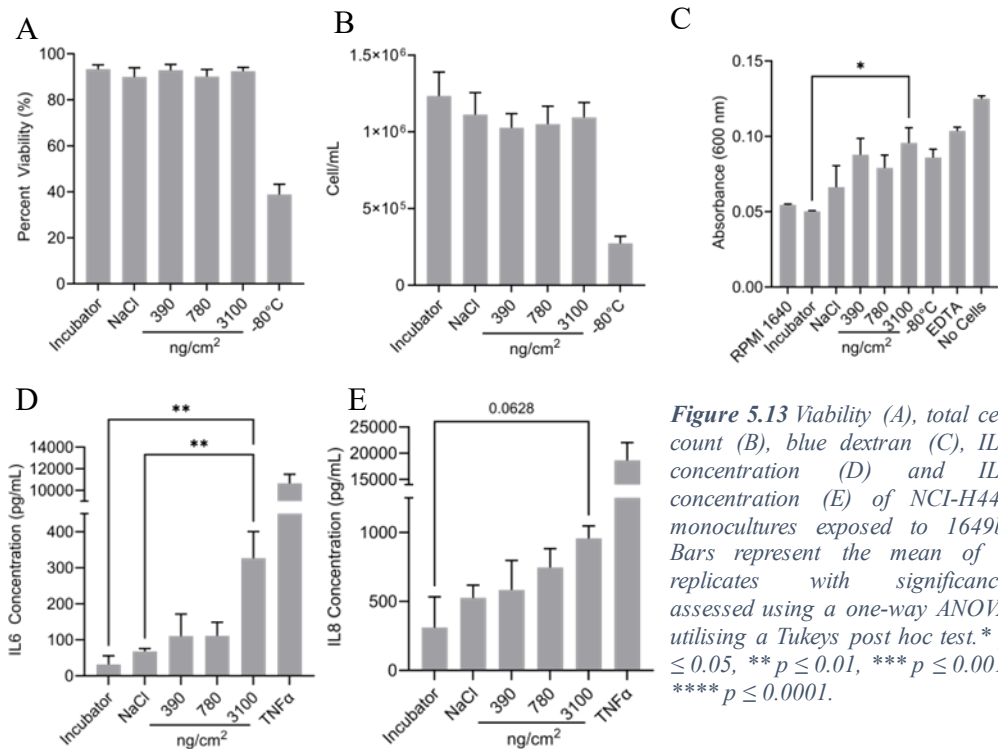
**Figure 5.12** Confocal microscopy images of NCI-H441 monocultures exposed to CB. The nucleus (blue/DAPI) and cytoskeleton (red/phalloidin). Scale bar = 50  $\mu$ m.

When NCI-H441 were exposed to CB, IL6 and IL8 release was not altered and remained at approximately 3000-4000 pg/mL and 5000-7500 pg/mL, respectively. When NCI-H441 were exposed to the TNF $\alpha$  positive control, both pro-inflammatory mediators were increased following 24-hour exposure.

NCI-H441 appears disorganised in morphology, as shown by the phalloidin staining, which has many spiculae, though, there is little effect in morphology resulting from CB exposure (**Figure 5.12**).

### 5.3.2.2 SRM 1649b Urban Dust

When NCI-H441 monocultures were exposed to 1649b for 24 hours, trypan blue exclusion assay revealed no significant change in cell viability or total cell count, except when the cultures were incubated at -80  $^{\circ}$ C for 30 minutes, which saw decreases in both viability and total cell count (**Figure 5.13**). NCI-H441 barrier function was decreased by all concentrations of 1649b, reaching significance when exposed to 3100 ng/cm<sup>2</sup> ( $p < 0.05$ ). When cultures were treated with EDTA, a substantial decrease in barrier function was observed. Further, 1649b exposure was associated with a dose-dependent increase in both IL6 and IL8 release from the NCI-H441 monocultures, reaching significance following 3100 ng/cm<sup>2</sup> exposure for IL6 release against the incubator and NaCl control ( $p < 0.01$ ) and approaching significance for IL8 release



against the incubator control ( $p = 0.0628$ ). TNF $\alpha$  caused a large increase in the release of both pro-inflammatory mediators.

Confocal imaging of NCI-H441 exposed to 1649b showed a typical disorganised arrangement of NCI-H441 with nuclei homogenously spread across the insert about 10-20  $\mu\text{m}$  in width. Phalloidin staining seems to be strongest at the cell borders, though

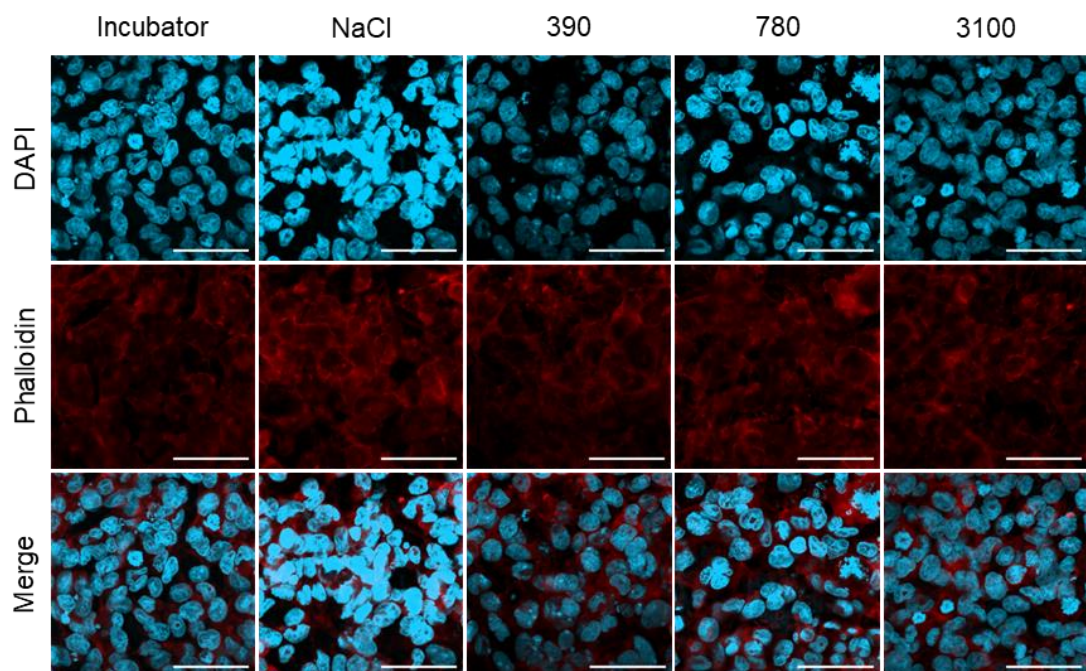
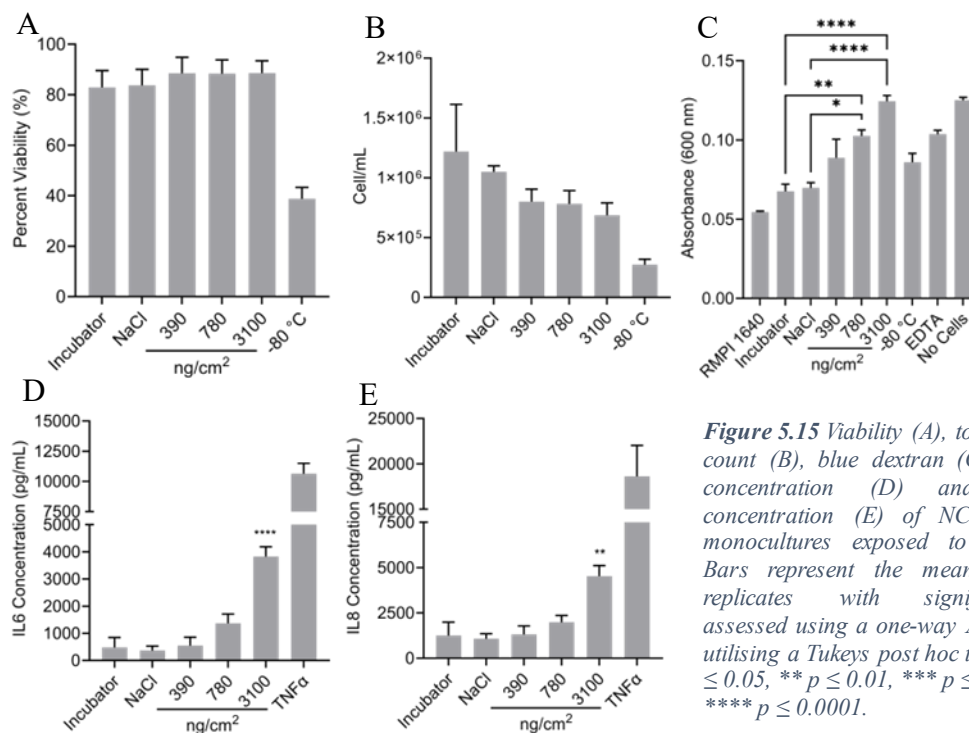


Figure 5.14 Confocal microscopy images of NCI-H441 monocultures exposed to 1649b. The nucleus (blue/DAPI) and cytoskeleton (red/phalloidin) are shown. Scale bar = 50  $\mu\text{m}$ .

no detectable change in morphology is evident upon 1649b exposure compared to controls (**Figure 5.14**).

### 5.3.2.3 SRM 2583 Indoor Dust



**Figure 5.15** Viability (A), total cell count (B), blue dextran (C), IL6 concentration (D) and IL8 concentration (E) of NCI-H441 monocultures exposed to 2583. Bars represent the mean of 5 replicates with significance assessed using a one-way ANOVA utilising a Tukeys post hoc test. \*  $p \leq 0.05$ , \*\*  $p \leq 0.01$ , \*\*\*  $p \leq 0.001$ , \*\*\*\*  $p \leq 0.0001$ .

NCI-H441 did not show any change in their level of viability or cell count following 2583 exposure, which typically remained in the 80-90% range ( $p > 0.05$ ) (**Figure 5.15**). There was a significant increase in barrier permeability at 780 and 3100 ng/cm<sup>2</sup> of 2583 compared to the incubator and NaCl control ( $p \leq 0.05$ ). Reading the absorbance of RPMI 1640 alone showed a decrease compared to the negative control, suggesting a degree of leakiness of the barrier membrane even in non-exposed cultures. IL6 and IL8 showed increase in their release following 2583 exposure, reaching significance at 3100 ng/cm<sup>2</sup> of 2583 ( $p \leq 0.0001$  and  $p \leq 0.01$  for IL6 and IL8 respectively).

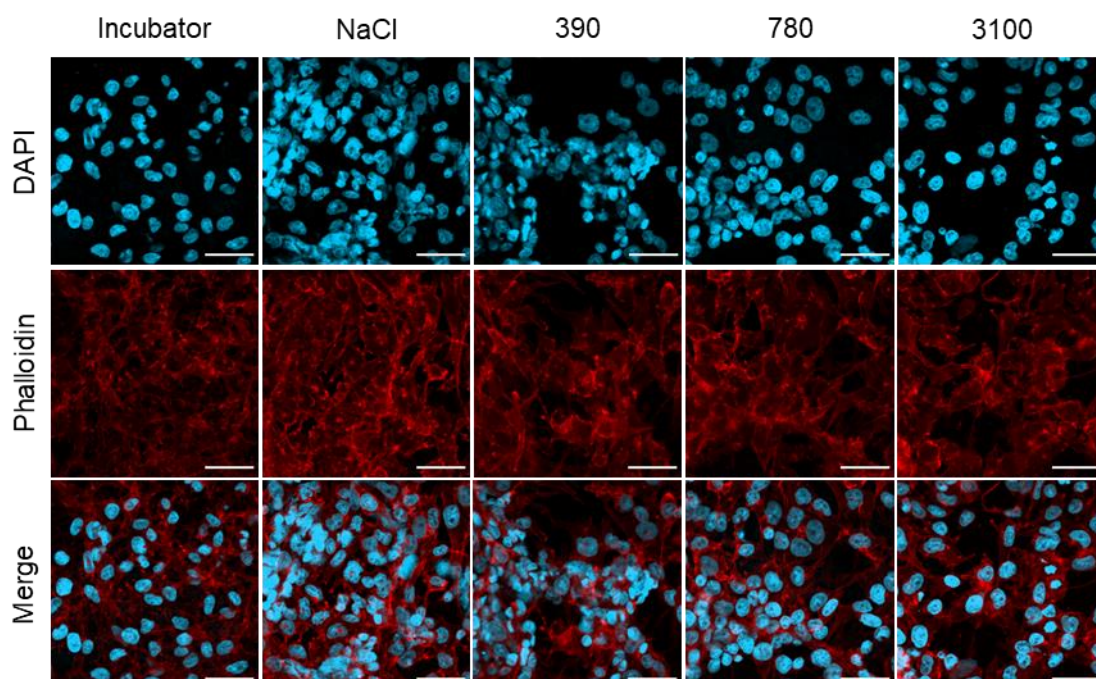


**Figure 5.16** Confocal microscopy images of NCI-H441 monocultures exposed to 2583. The nucleus (blue/DAPI) and cytoskeleton (red/phalloidin) are shown. Scale bar = 50  $\mu$ m.

Like CB and 1649b exposure, the NCI-H441 cells appear to show membrane projections, growing in random directions and overlapping. Exposure to 2583 again appears to alter the NCI-H441 cell size, which are bigger/spread out. There are more gaps within the monolayer at all exposure concentrations, perhaps aligning with the blue dextran data (**Figure 5.16**).



### 5.3.3 hAELVi & NCI-H441 Co-Culture Exposure to Printex® 90, 1649b and 2583

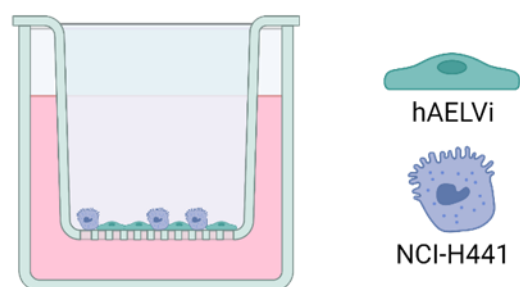
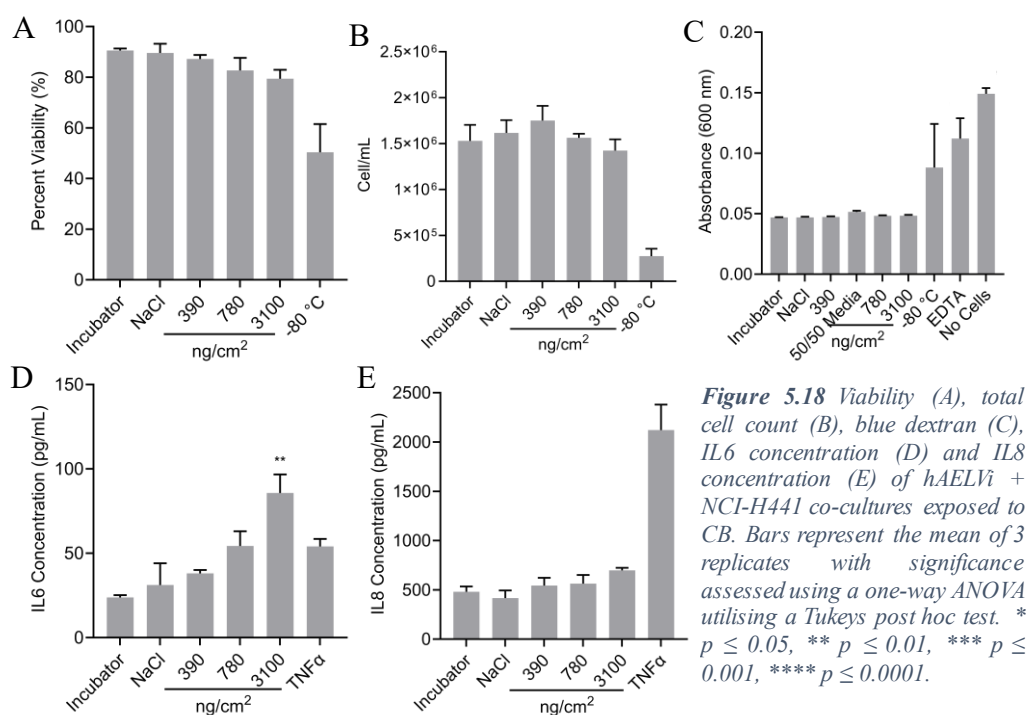
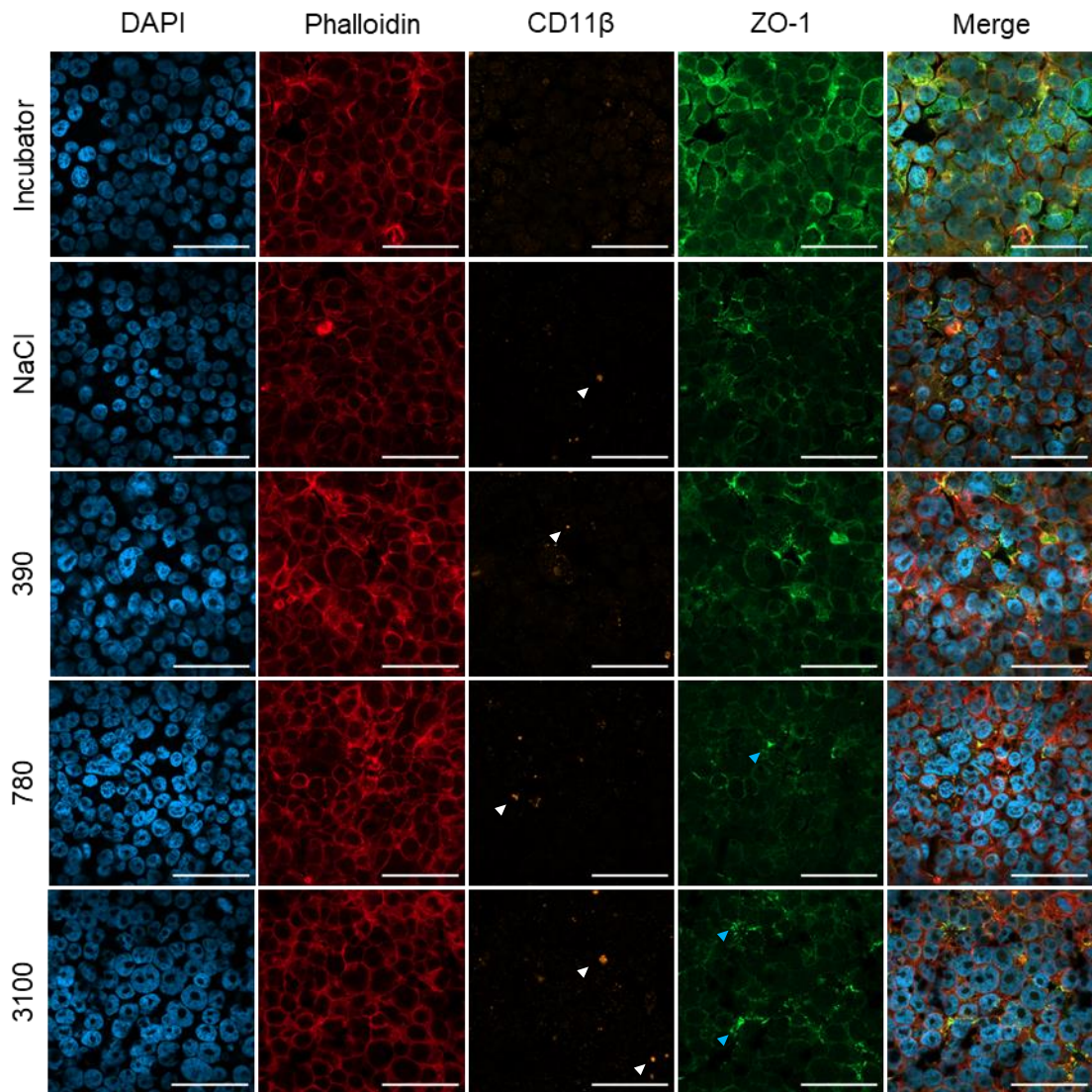


Figure 5.17 Schematic of hAELVi + NCI-H441 monoculture used in Section 5.3.3.

#### 5.3.3.1 Printex® 90 Carbon Black

Moving into the first of the co-culture exposures where hAELVi & NCI-H441 co-cultures (Figure 5.17) were exposed to CB, there was no changes in cell viability, cell count, nor barrier integrity (with the exception of the assay specific positive controls) (Figure 5.18). IL6 concentration within the supernatant was increased in a dose-dependent manner when exposed to CB, reaching significance at 3100 ng/cm<sup>2</sup>





**Figure 5.19** Confocal microscopy images of hAELVI + NCI-H441 co-cultures exposed to CB. The nucleus (blue/DAPI), cytoskeleton (red/phalloidin), CD11 $\beta$  (orange) and ZO-1 (green) are shown. White arrow heads = CD11 $\beta$  clumps. Blue arrow heads show areas of dense ZO-1 staining. Scale bar = 50  $\mu$ m.

exposure concentrations (exceeding the TNF $\alpha$  positive control) ( $p \leq 0.01$  compared to the incubator and NaCl controls). These effects were not observed when assaying IL8 concentration.

Confocal imaging of hAELVi + NCI-H441 co-cultures shows an organised, tight monolayer of cells with phalloidin staining most intense at the periphery of the cells, which does not change when exposed to CB. CD11 $\beta$ , a marker of macrophages, is seen to be dispersed over the entire monolayer. After exposure to CB, CD11 $\beta$  becomes more clustered and intense in small areas. ZO-1, a tight junction protein, is localised mainly to the cell membranes, though there is a high abundance of ZO-1 within the cytoplasm. After CB, ZO-1 staining becomes more vesicular with a degree of non-uniformity compared to the incubator control (white arrowheads). This is especially evident at

3100 ng/cm<sup>2</sup> (blue arrowheads). In the CB-exposed images, especially 3100 ng/cm<sup>2</sup>, there are dark areas within the image (**Figure 5.19**).

### 5.3.3.2 SRM 1649b Urban Dust

After exposure to 1649b, co-cultures of hAELVi + NCI-H441 showed no alterations in viability or cell count ( $p > 0.05$ ) (unless treated with positive control -80 °C exposure) (**Figure 5.20**). Cell counts for NaCl and 1649b exposures were largely reduced compared to incubator control. This may be a factor of a high cell count for incubator control (rather than the NaCl and CB being low *per se*); this is evident when comparing total cell counts of hAELVi + NCI-H441 exposed to other PMs. Other than the -80 °C and ETDA positive controls, which saw significant elevations in barrier permeability, there was no change in barrier function mediated by 1649b. Similarly, except for the TNF $\alpha$  positive control, there were no significant changes in IL6 and IL8 release when treated with 1649b.

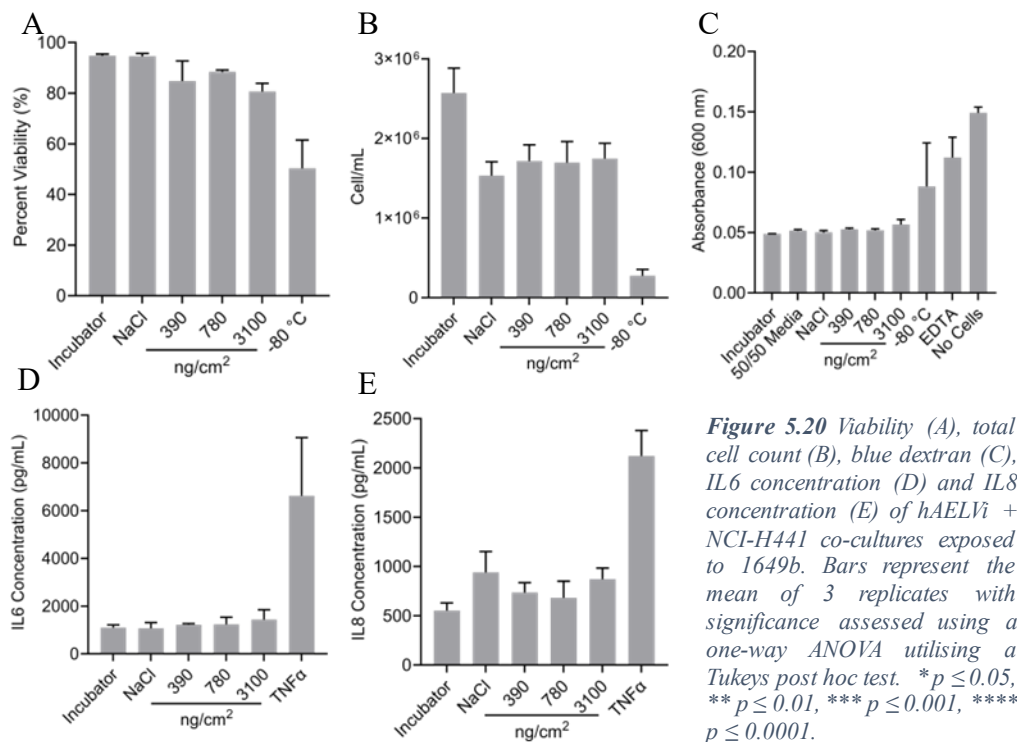


**Figure 5.20** Viability (A), total cell count (B), blue dextran (C), IL6 concentration (D) and IL8 concentration (E) of hAELVi + NCI-H441 co-cultures exposed to 1649b. Bars represent the mean of 3 replicates with significance assessed using a one-way ANOVA utilising a Tukeys post hoc test. \*  $p \leq 0.05$ , \*\*  $p \leq 0.01$ , \*\*\*  $p \leq 0.001$ , \*\*\*\*  $p \leq 0.0001$ .

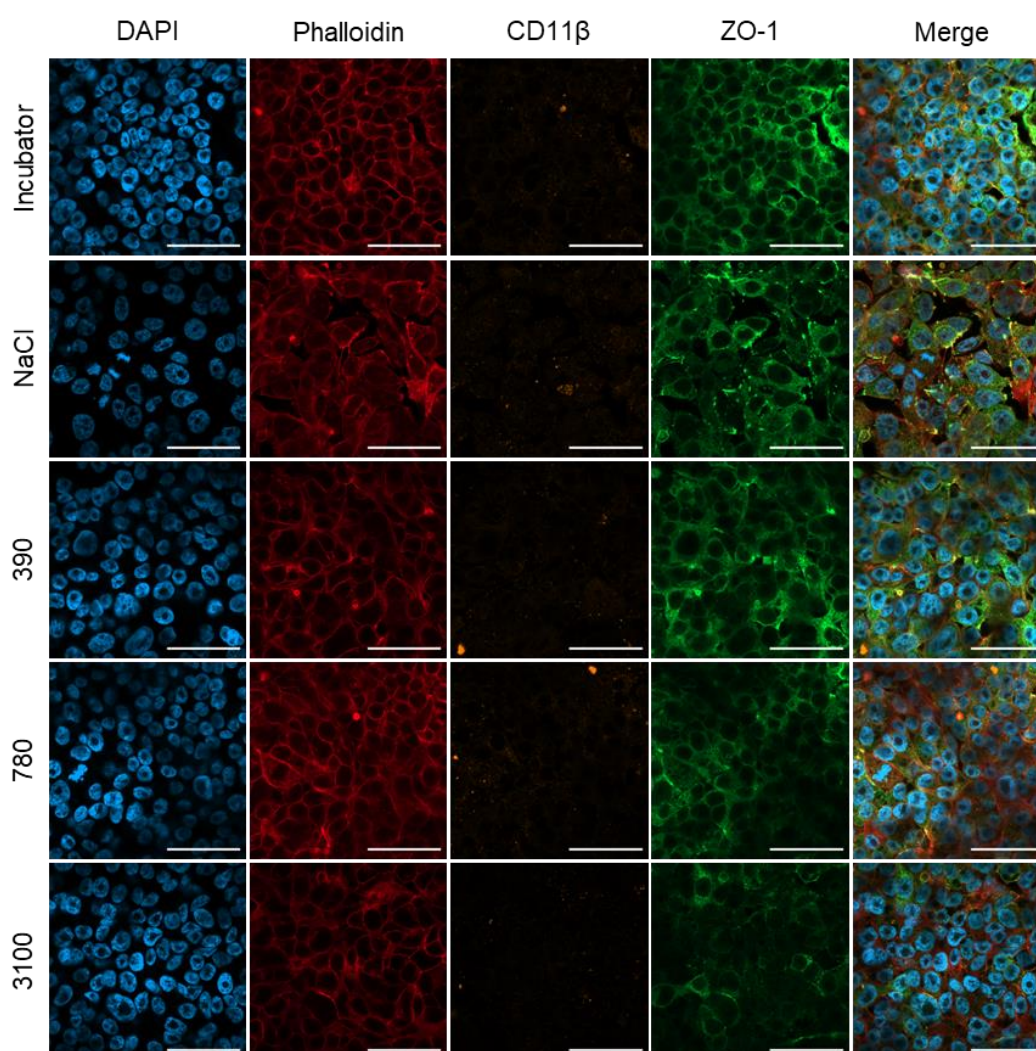


**Figure 5.21** Confocal microscopy images of hAELVi + NCI-H441 co-cultures exposed to 1649b. The nucleus (blue/DAPI), cytoskeleton (red/phalloidin), CD11 $\beta$  (orange) and ZO-1 (green) are shown. Scale bar = 50  $\mu$ m.

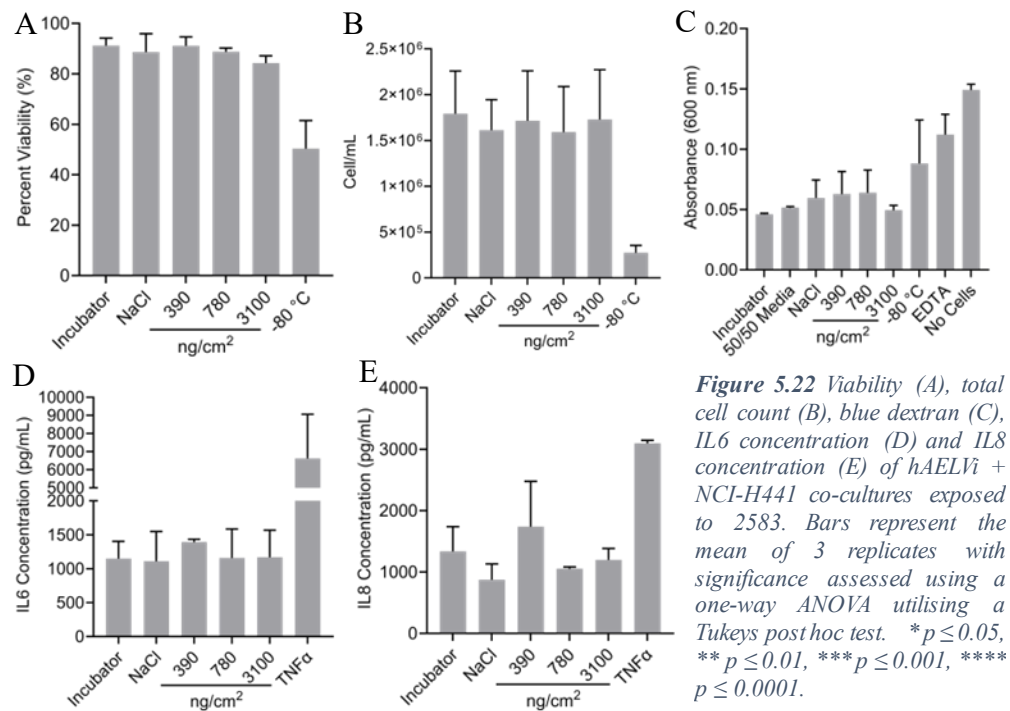
Though there was no change in membrane permeability shown by blue dextran, ZO-1 analysis through confocal imaging showed alterations in morphology and localisation when hAELVi + NCI-H441 co-cultures were exposed to 3100 ng/cm<sup>2</sup> of 1649b compared to all other exposures, which appeared less intense and less localised to the cell periphery. There was an increase in heterogeneity of ZO-1 between individual cells at the 3100 ng/cm<sup>2</sup> ZO-1 staining, some showing vigorous intensity at the cell membrane and some showing vesicular formation throughout the cytoplasm. Neither cytoskeleton nor nuclear morphology were altered following 1649b exposure (**Figure 5.21**).



### 5.3.3.3 SRM 2583 Indoor Dust

Except for assay-specific positive controls, there were no significant alterations in cell viability, total cell count, barrier function, IL6 release or IL8 release upon 2583 exposure in hAELVi + NCI-H441 co-cultures (**Figure 5.22**).

Similarly, there was little change in the morphology of hAELVi + NCI-H441 co-cultures after 2583 exposure shown through little change in ZO-1, CD11b or cytoskeleton staining (**Figure 5.23**).



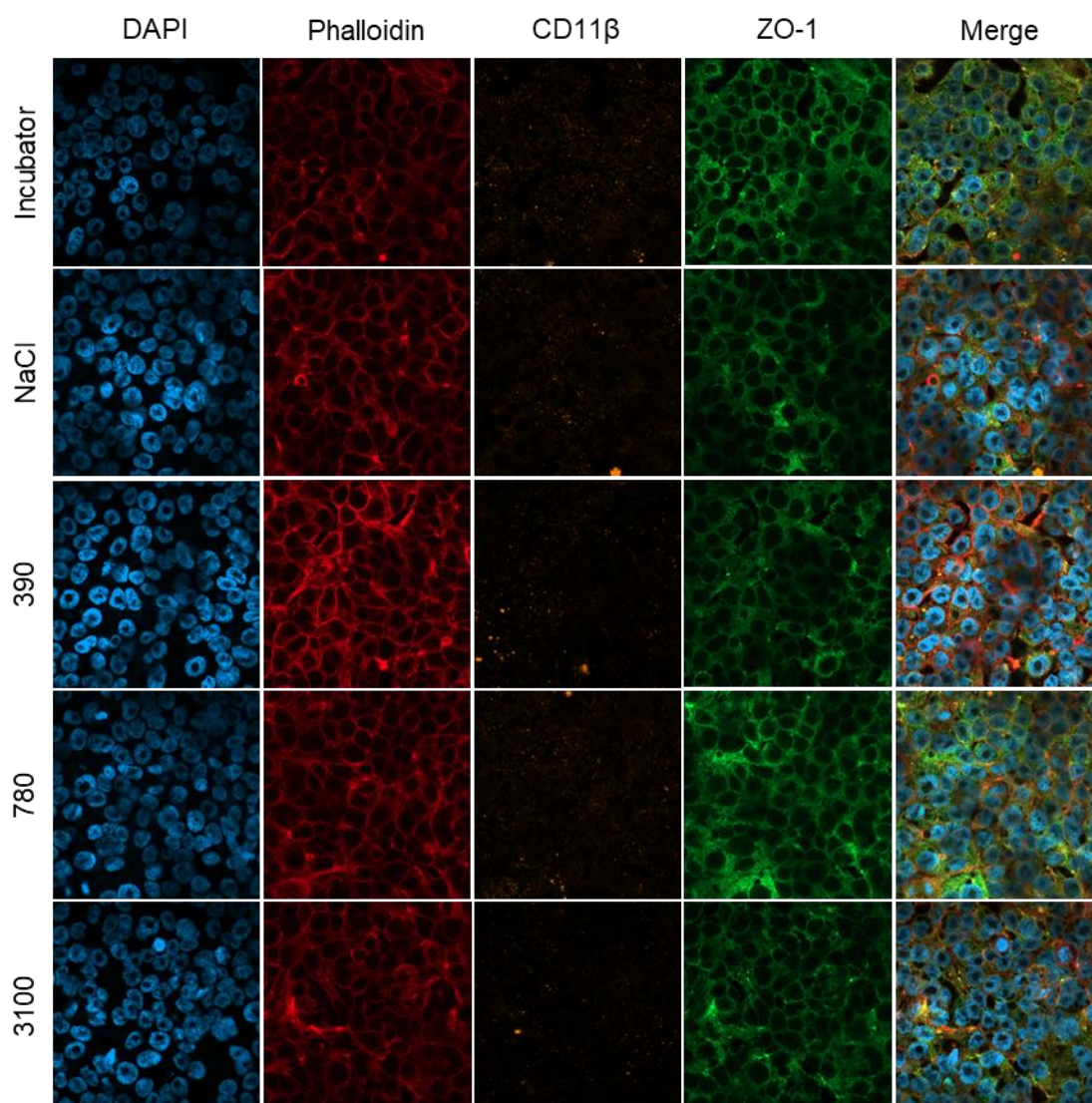


**Figure 5.23** Confocal microscopy images of hAELVi + NCI-H441 co-cultures exposed to 2583. The nucleus (blue/DAPI), cytoskeleton (red/phalloidin), CD11 $\beta$  (orange) and ZO-1 (green) are shown. Scale bar = 50  $\mu$ m.

### 5.3.4 hAELVi & dTHP-1 Co-Culture Exposure to Printex® 90, 1649b and 2583

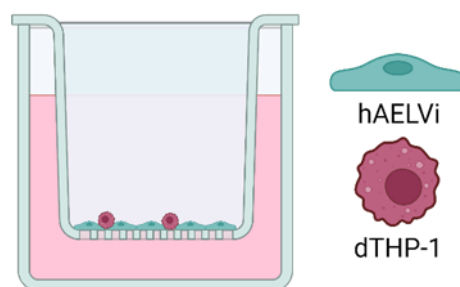
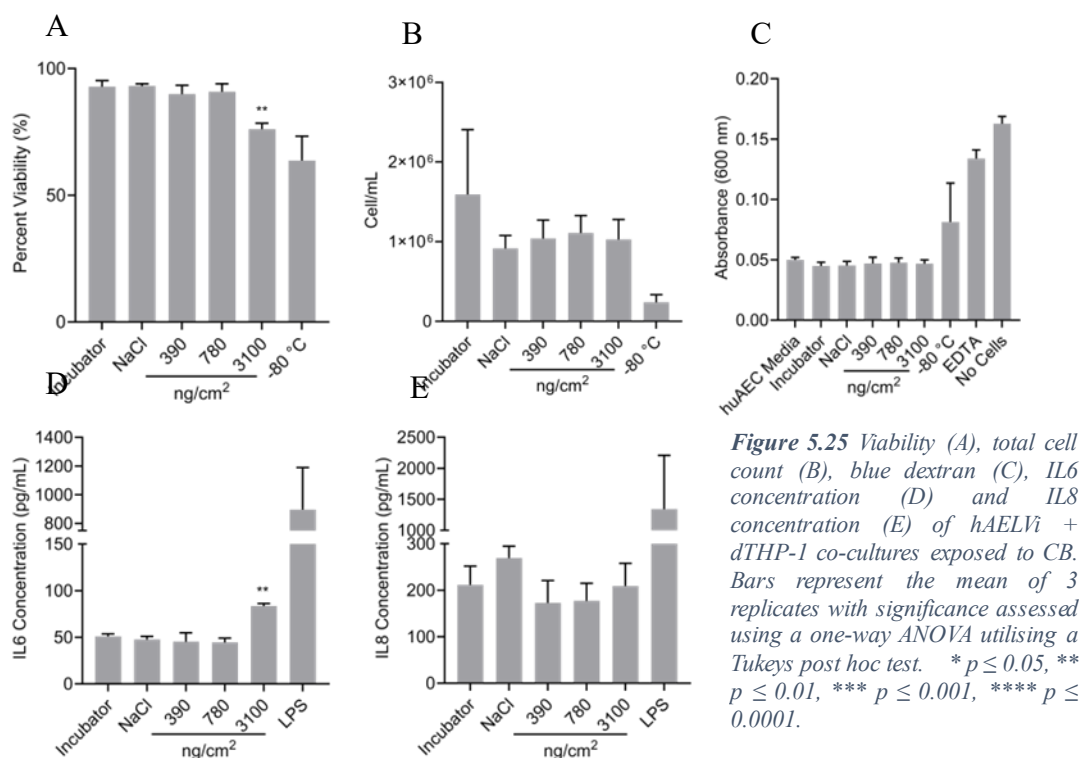


Figure 5.24 Schematic of hAELVi + dTHP-1 co-culture used in Section 5.3.4.

#### 5.3.4.1 Printex® 90 Carbon Black

Upon exposure of hAELVi + dTHP-1 co-cultures (**Figure 5.24**) to CB for 24 hours, there was a significant drop in viability at the 3100 ng/cm<sup>2</sup> exposure ( $p \leq 0.01$  compared to the incubator and NaCl controls) (**Figure 5.25**), though there was no alteration in total cell count or barrier function (except for -80 °C and EDTA positive controls). IL6 release was induced significantly at 3100 ng/cm<sup>2</sup> ( $p \leq 0.01$  compared to the incubator and NaCl controls), though CB did not alter IL8 release.



Morphological analysis reveals that the monolayer becomes looser following CB exposure, with gaps between cells evident (white arrowheads), though, this is less clear at 3100 ng/cm<sup>2</sup>. There are no clear changes in the intensity or localisation of CD11 $\beta$  or ZO-1 staining following CB exposure (**Figure 5.26**).

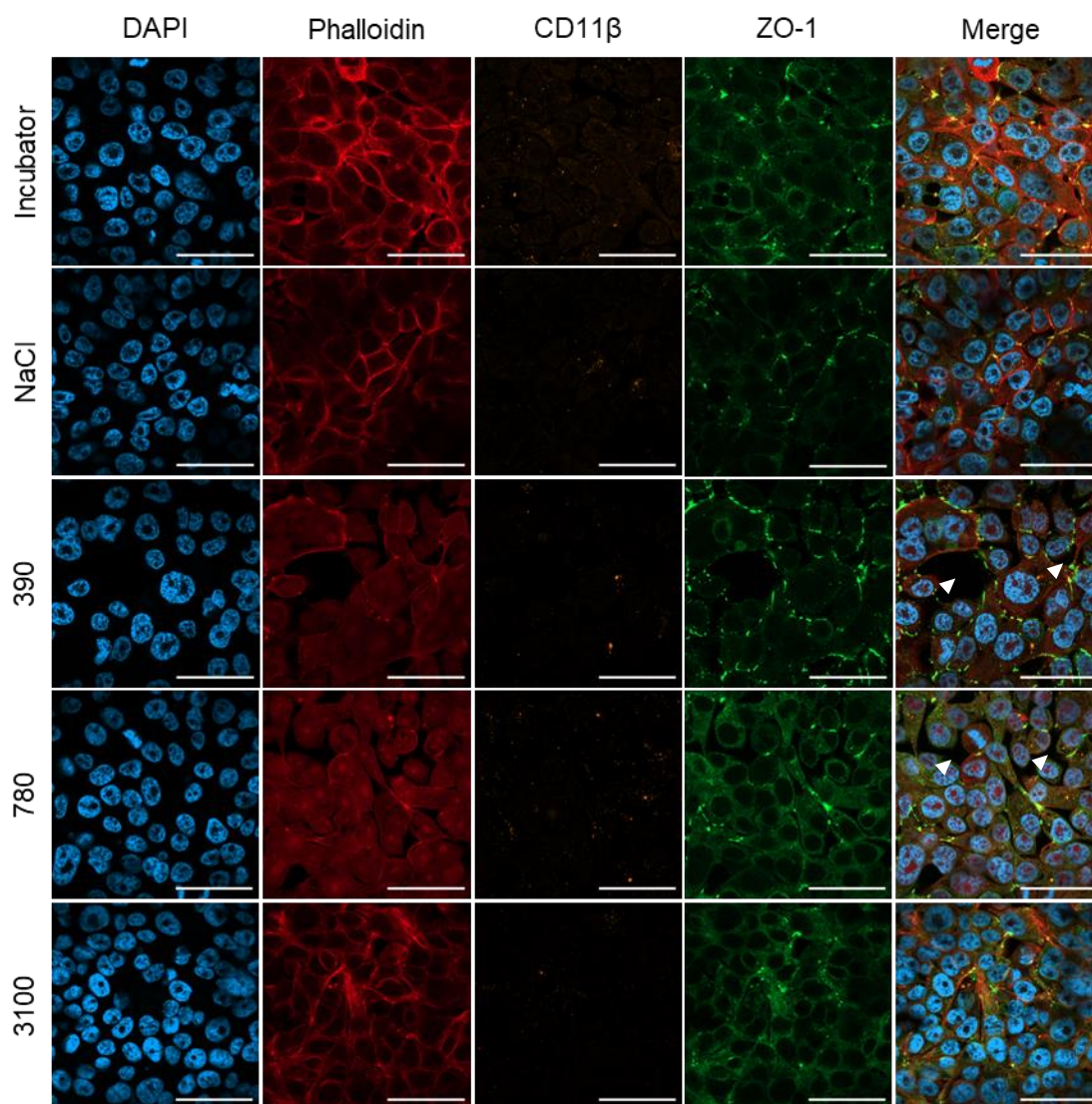


**Figure 5.26** Confocal microscopy images of hAELVI + dTHP-1 co-cultures exposed to CB. The nucleus (blue/DAPI), cytoskeleton (red/phalloidin), CD11 $\beta$  (orange) and ZO-1 (green) are shown. White arrowheads show gaps in the cell monolayer. Scale bar = 50  $\mu$ m.

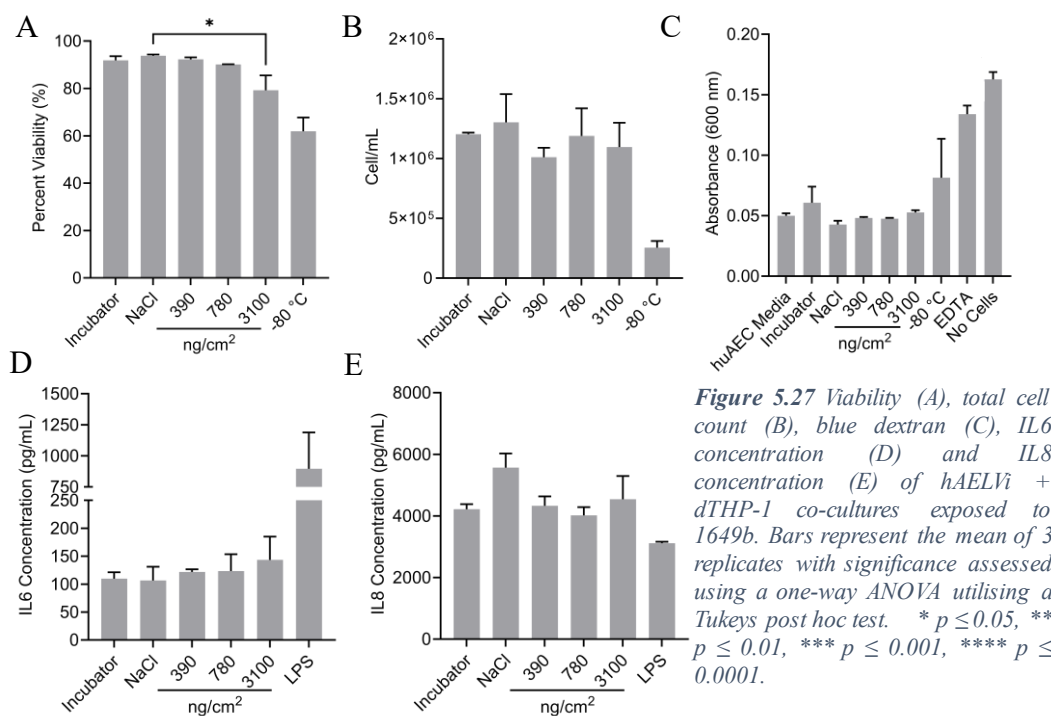
#### 5.3.4.2 SRM 1649b Urban Dust

When hAELVi + dTHP-1 co-cultures were exposed to 1649b there was no cytotoxic effect observed except at 3100 ng/cm<sup>2</sup> which saw a significantly lower viability compared to the NaCl control ( $p < 0.05$ ). Urban dust also had no effect on barrier properties at any of the concentrations used.



Further, the pro-inflammatory response was not altered when hAELVi + dTHP-1 co-cultures were exposed to 1649b (**Figure 5.27**).

Morphological examination reveals that exposed cells appear larger than non-exposed, especially at the highest concentration of 1649b. The cytoskeleton staining appears to become more intense at the periphery of the cells upon exposure. ZO-1 staining moved more peripherally with 1649b exposure, forming intensely stained areas (white arrow heads) compared to the control, where ZO-1 can be seen throughout the cell (**Figure 5.28**).



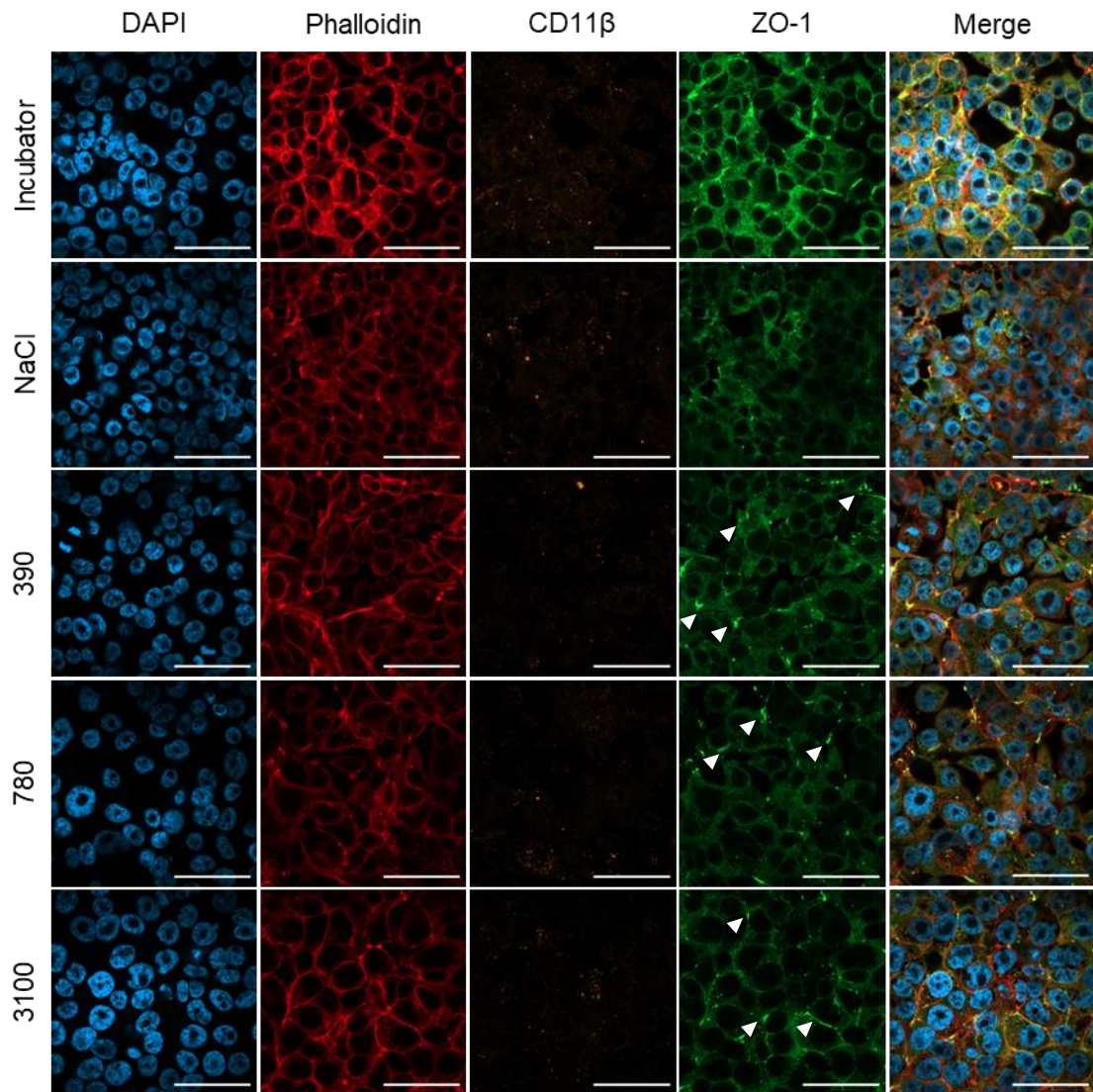


**Figure 5.28** Confocal microscopy images of hAELVi + dTHP-1 co-cultures exposed to 1649b. The nucleus (blue/DAPI), cytoskeleton (red/phalloidin), CD11 $\beta$  (orange) and ZO-1 (green) are shown. White arrow heads show areas of intense membrane ZO-1 staining. Scale bar = 50  $\mu$ m.

### 5.3.4.3 SRM 2583 Indoor Dust

When hAELVi + dTHP-1 co-cultures were exposed to 2583, there was no change in cell viability or cell count. Further, there were no significant changes to the barrier integrity or the release of IL6 and IL8 (**Figure 5.29**).

Exposure of hAELVi + dTHP-1 co-cultures to 2583 shows typical pericellular phalloidin fluorescence, which does not change following exposure. Similarly, CD11 $\beta$  and ZO-1 do not change in localisation following exposure (**Figure 5.30**).

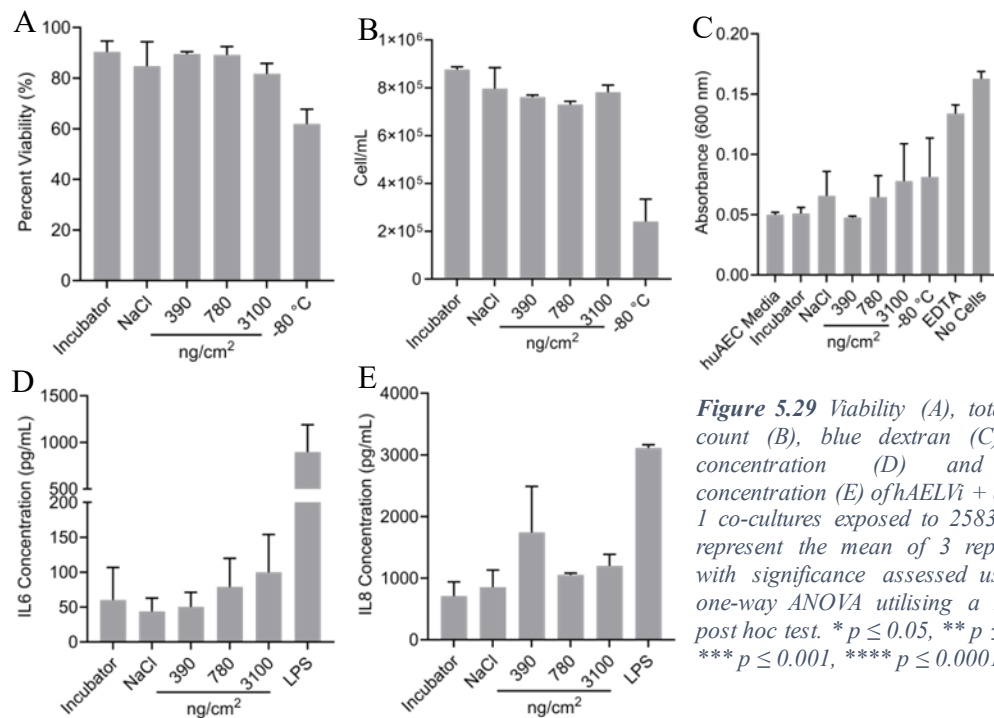


**Figure 5.29** Viability (A), total cell count (B), blue dextran (C), IL6 concentration (D) and IL8 concentration (E) of hAELVi + dTHP-1 co-cultures exposed to 2583. Bars represent the mean of 3 replicates with significance assessed using a one-way ANOVA utilising a Tukeys post hoc test. \*  $p \leq 0.05$ , \*\*  $p \leq 0.01$ , \*\*\*  $p \leq 0.001$ , \*\*\*\*  $p \leq 0.0001$ .

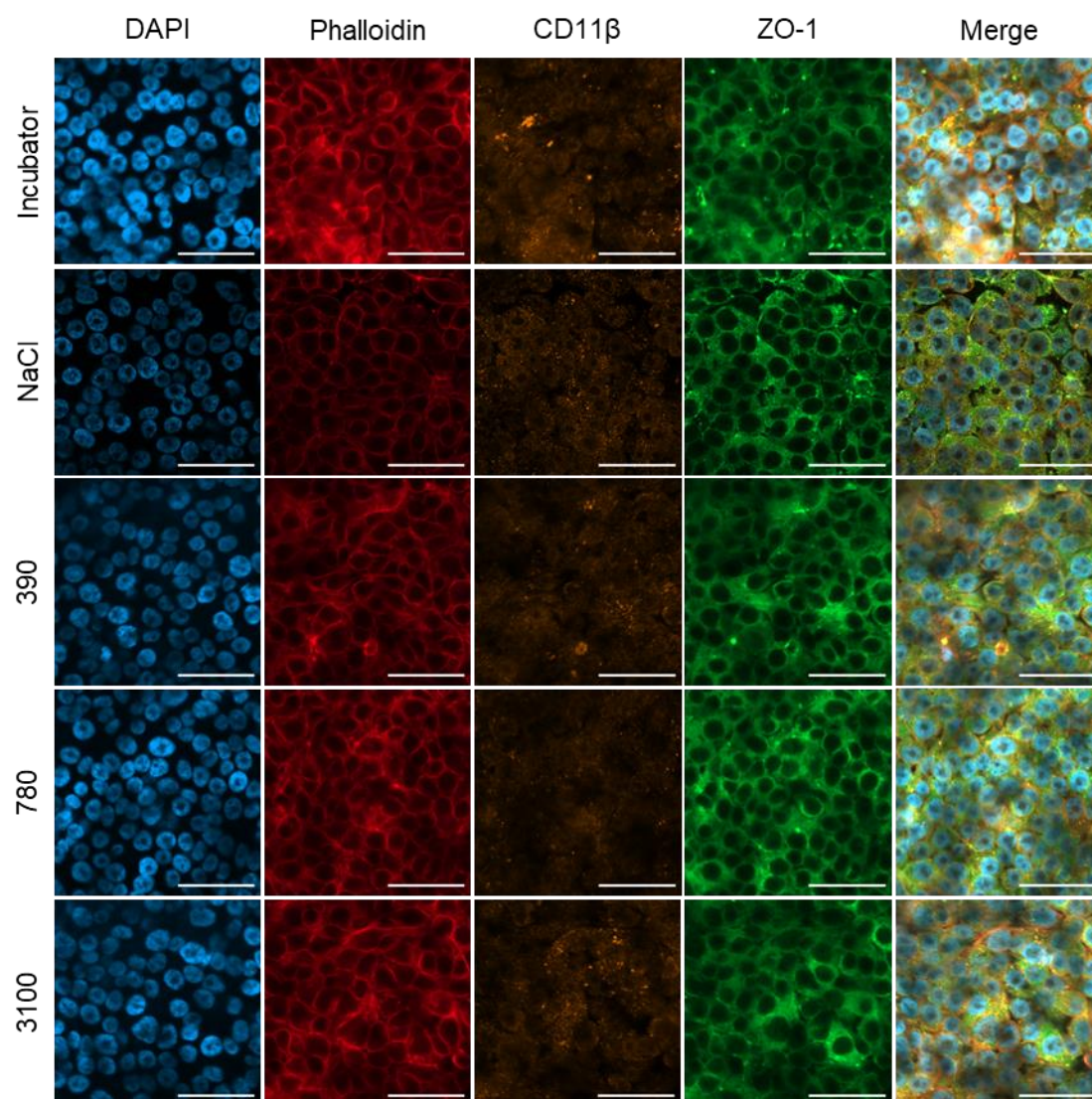


**Figure 5.30** Confocal microscopy images of hAELVi + dTHP-1 co-cultures exposed to 2583. The nucleus (blue/DAPI), cytoskeleton (red/phalloidin), CD11 $\beta$  (orange) and ZO-1 (green) are shown. Scale bar = 50  $\mu$ m.



### 5.3.5 NCI-H441 & dTHP-1 Co-Culture Exposure to Printex® 90, 1649b and 2583

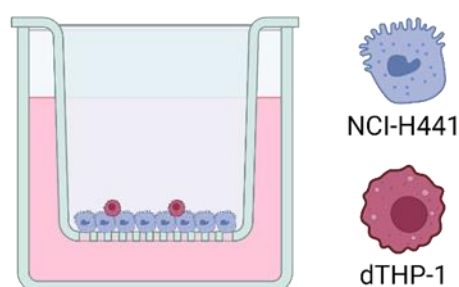
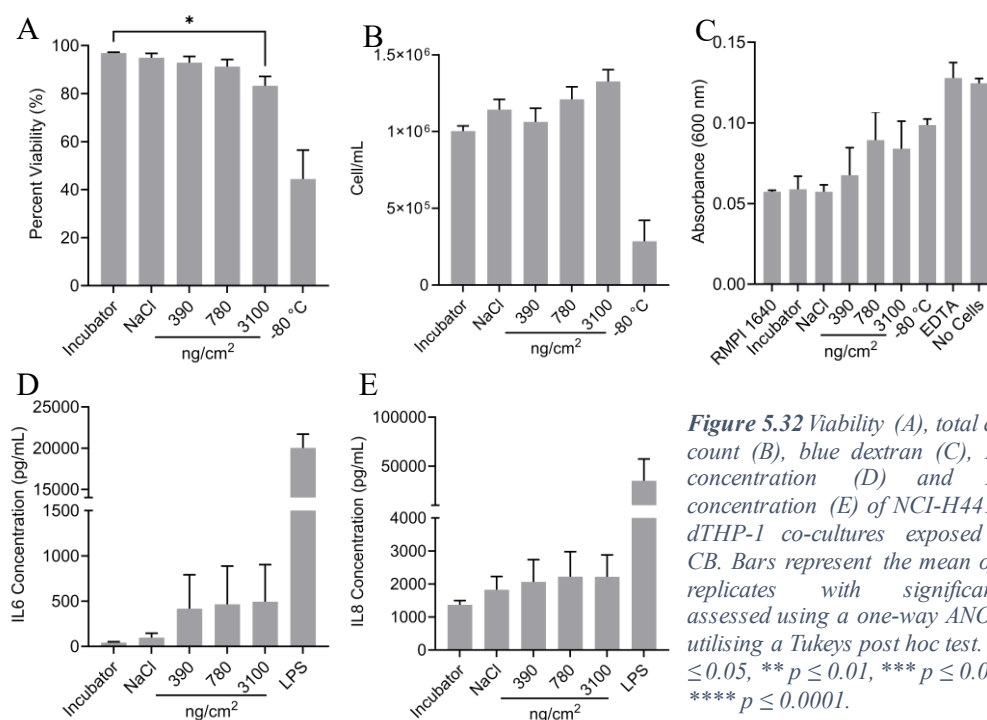


Figure 5.31 Schematic of NCI-H441 + dTHP-1 co-culture used in Section 5.3.5.

#### 5.3.5.1 Printex® 90 Carbon Black

Exposure of CB to NCI-H441 + dTHP-1 co-cultures (**Figure 5.31**) resulted in a dose-dependent decrease in cell viability, reaching significance in the 3100 ng/cm<sup>2</sup> exposed cells ( $p < 0.05$ , compared to the incubator control). Neither the total cell count, nor the barrier integrity were significantly altered by CB exposure ( $p > 0.05$ ) (**Figure 5.32**). This co-culture did not alter its release of IL6 or IL8 after CB exposure (except when treated with LPS).



Intracellular cytoskeletal staining is observed to be more homogenous within CB exposed wells, compared to control cultures which possess cytoskeleton staining at the periphery of the cells. CB exposure results in little change to ZO-1 and CD11β

staining. Dark spots are visible at 3100 ng/cm<sup>2</sup>, which is likely due to the presence of CB on the membrane, impeding the passage of light (**Figure 5.33**).

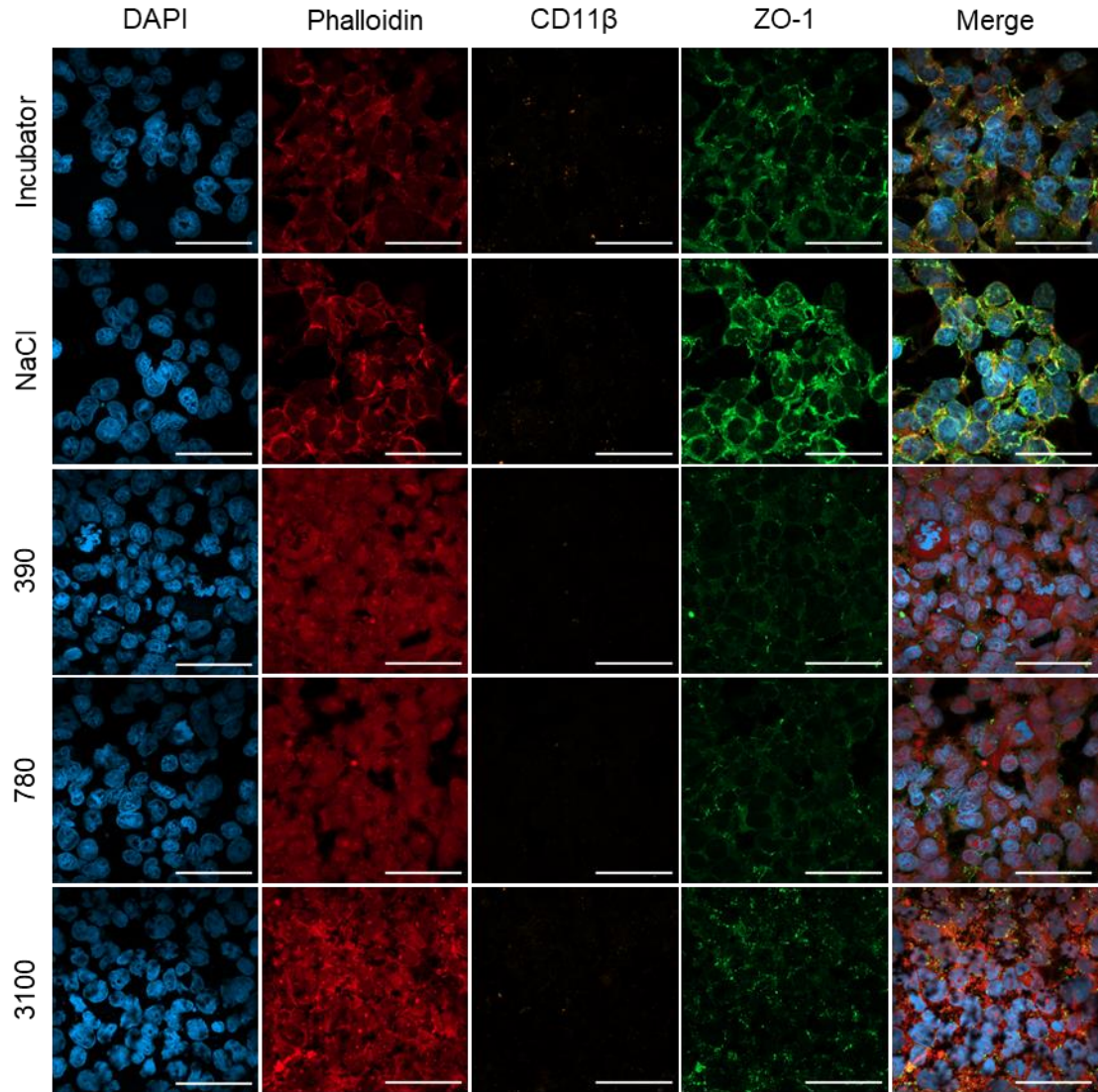


**Figure 5.33** Confocal microscopy images of NCI-H441 + dTHP-1 co-cultures exposed to CB. The nucleus (blue/DAPI), cytoskeleton (red/phalloidin), CD11 $\beta$  (orange) and ZO-1 (green) are shown. Scale bar = 50  $\mu$ m.

### 5.3.5.2 SRM 1649b Urban Dust

Exposing NCI-H441 + dTHP-1 co-cultures to 1649b did not alter cell viability or cell count ( $p > 0.05$ ) (**Figure 5.34**). Urban dust exposure was also not associated with a change in barrier function or IL6/IL8 release ( $p > 0.05$ ).

Morphological examination shows that the cytoskeleton is altered after 1649b exposure in NCI-H441 + dTHP-1 co-cultures, with the shape of the cells altered in the highest exposure concentration. There are no apparent differences in CD11 $\beta$  and ZO-1 localisation following exposure (**Figure 5.35**).

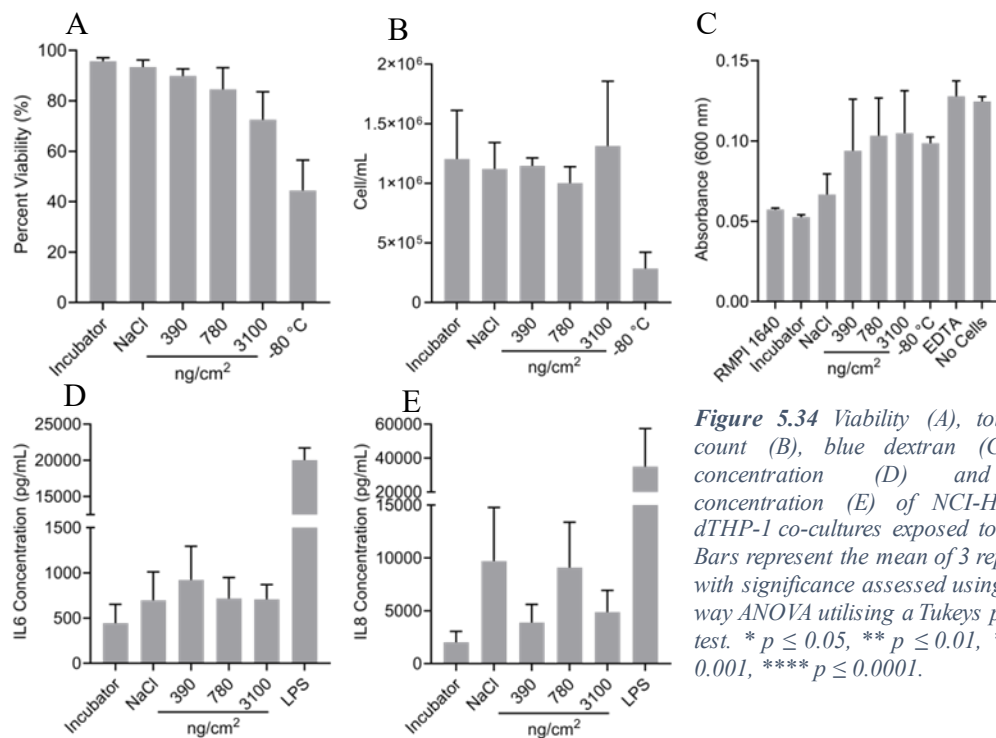


**Figure 5.34** Viability (A), total cell count (B), blue dextran (C), IL6 concentration (D) and IL8 concentration (E) of NCI-H441 + dTHP-1 co-cultures exposed to 1649b. Bars represent the mean of 3 replicates with significance assessed using a one-way ANOVA utilising a Tukeys post hoc test. \*  $p \leq 0.05$ , \*\*  $p \leq 0.01$ , \*\*\*  $p \leq 0.001$ , \*\*\*\*  $p \leq 0.0001$ .

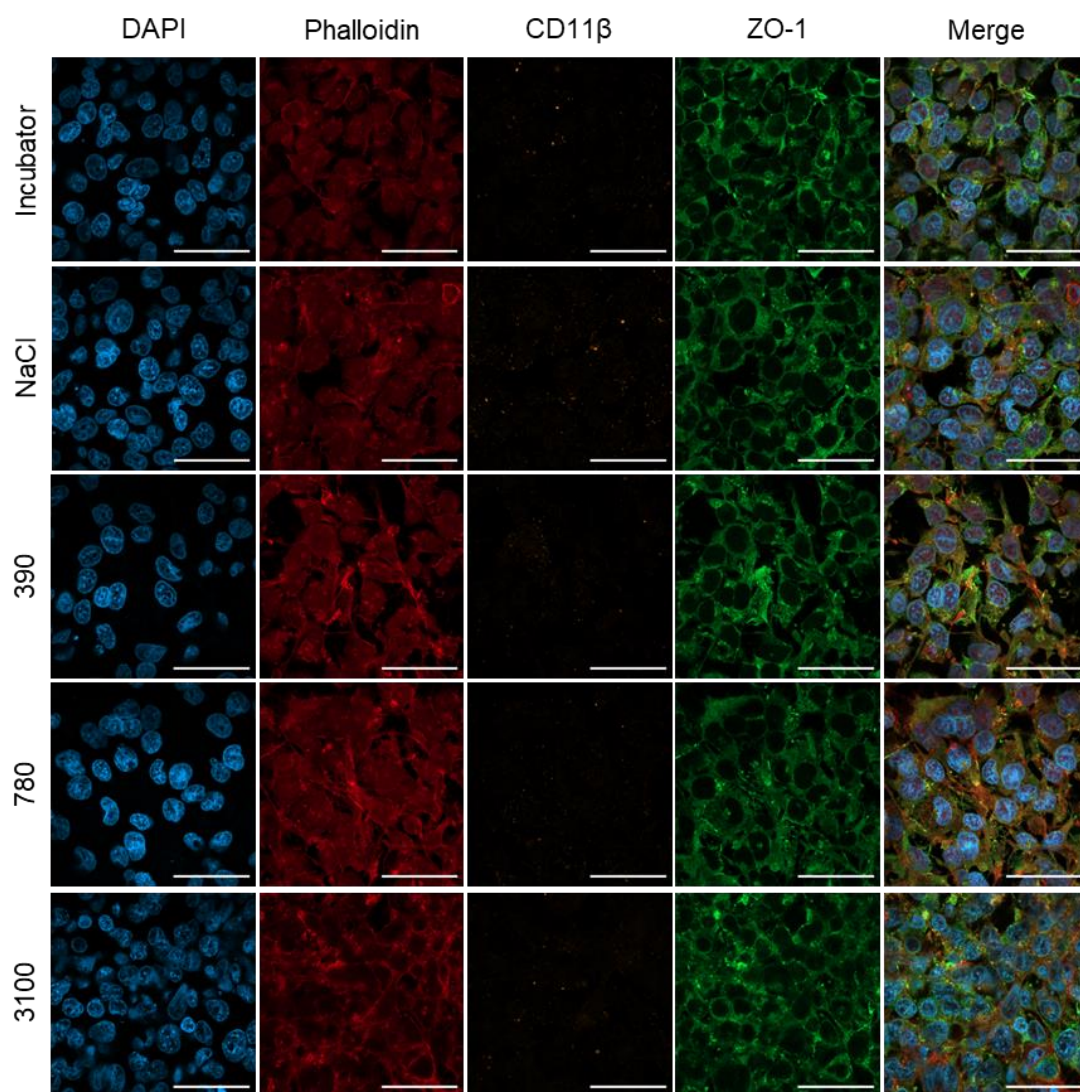


**Figure 5.35** Confocal microscopy images of NCI-H441 + dTHP-1 co-cultures exposed to 1649b. The nucleus (blue/DAPI), cytoskeleton (red/phalloidin), CD11 $\beta$  (orange) and ZO-1 (green) are shown. Scale bar = 50  $\mu$ m.

### 5.3.5.3 SRM 2583 Indoor Dust

When exposed to 2583, NCI-H441 + dTHP-1 co-cultures viability trended towards a significant decrease at 3100 ng/cm<sup>2</sup> ( $p < 0.1$ ). Total cell count was not different across the exposure concentration and shows no trends (**Figure 5.36**). Barrier function shows a dose-dependent permeability increase, reaching significance at 3100 ng/cm<sup>2</sup> ( $p \leq 0.001$ ). Indoor dust also did not trigger a pro-inflammatory response shown by no significance change in IL6 and IL8 release into the media ( $p > 0.05$ ).

Confocal imaging of the NCI-H441 + dTHP-1 co-culture exposed to 2583 shows little change in the shape of the cells following exposure. There is no apparent change in the ZO-1 or CD11 $\beta$  localisation (**Figure 5.37**).

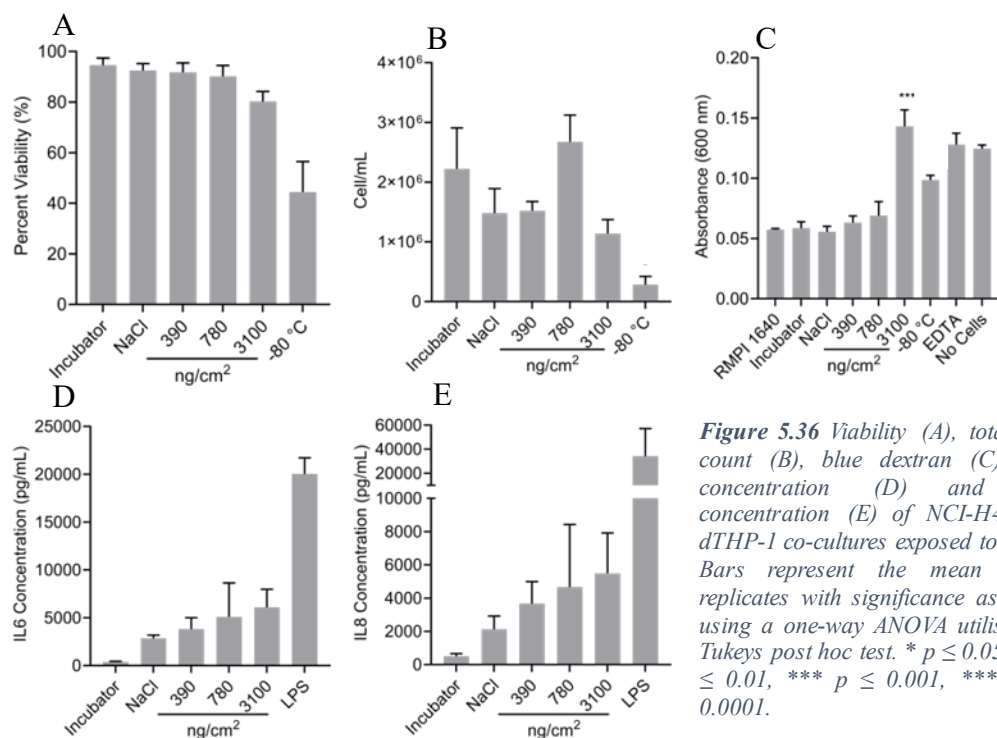


**Figure 5.36** Viability (A), total cell count (B), blue dextran (C), IL6 concentration (D) and IL8 concentration (E) of NCI-H441 + dTHP-1 co-cultures exposed to 2583. Bars represent the mean of 3 replicates with significance assessed using a one-way ANOVA utilising a Tukeys post hoc test. \*  $p \leq 0.05$ , \*\*  $p \leq 0.01$ , \*\*\*  $p \leq 0.001$ , \*\*\*\*  $p \leq 0.0001$ .



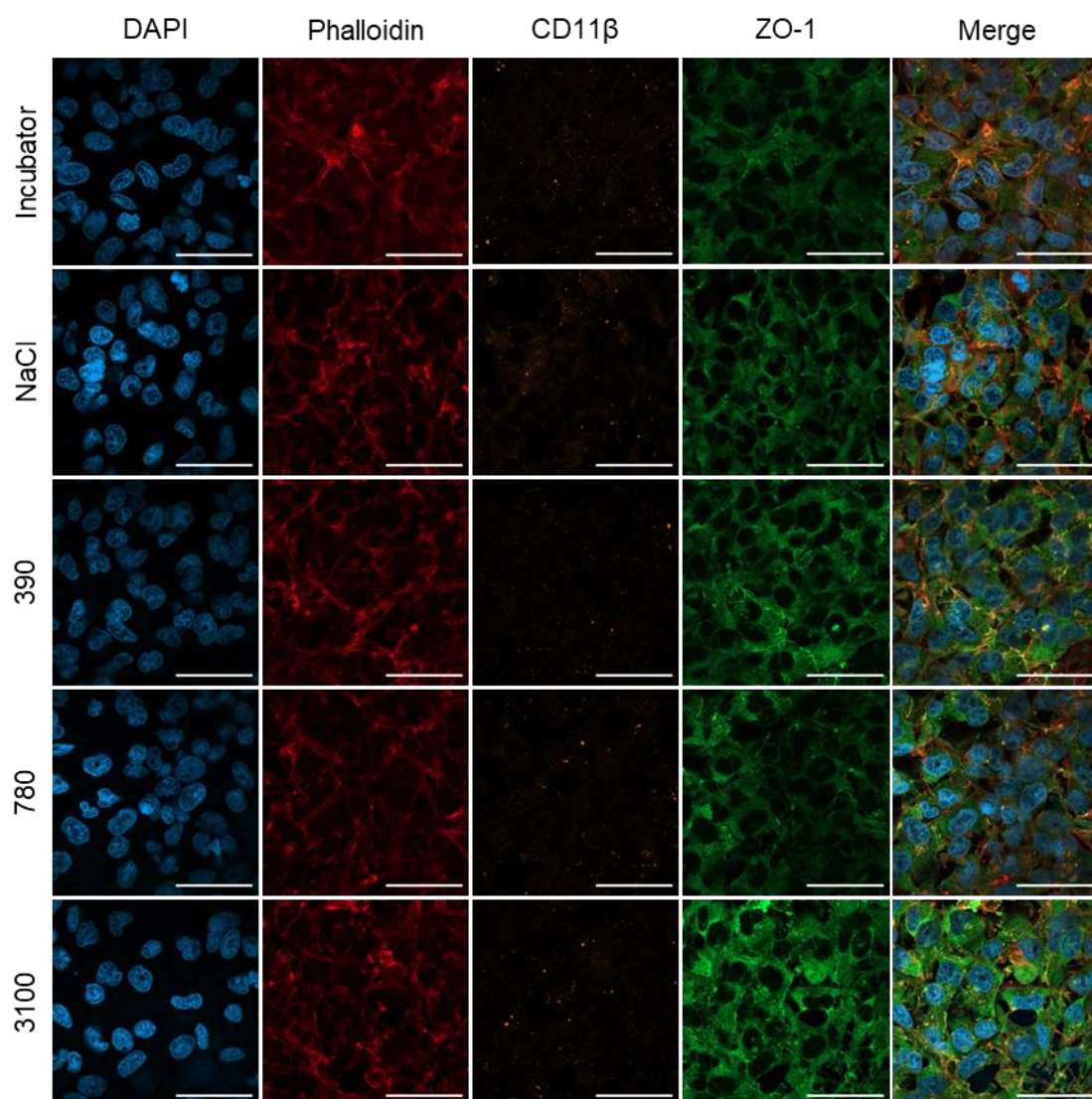


**Figure 5.37** Confocal microscopy images of NCI-H441 + dTHP-1 co-cultures exposed to 2583. The nucleus (blue/DAPI), cytoskeleton (red/phalloidin), CD11 $\beta$  (orange) and ZO-1 (green) are shown. Scale bar = 50  $\mu$ m.

### 5.3.6 Triple Cell Co-Culture Exposure to Printex® 90, 1649b and 2583

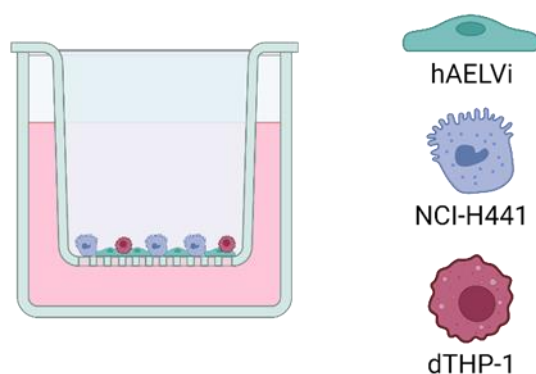


Figure 5.38 Schematic of the triple cell co-culture used in Section 5.3.6.

#### 5.3.6.1 Printex® 90 Carbon Black

Carbon black exposure caused a decrease in viability within the alveolar triple cell co-culture, approaching significance at the highest CB concentration ( $p = 0.61$ ) (Figure 5.38). CB exposure did not alter total cell count or membrane permeability. There was a no significant changes in IL6 and IL8 release in the triple cell co-culture following CB exposure ( $p > 0.05$ ) (Figure 5.39).

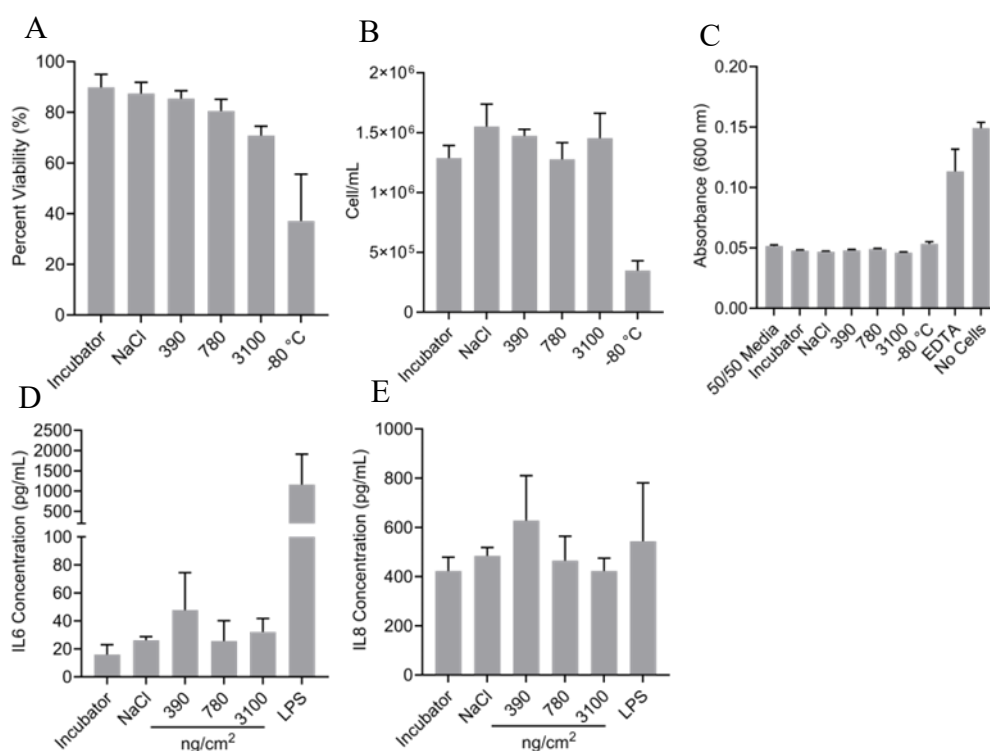
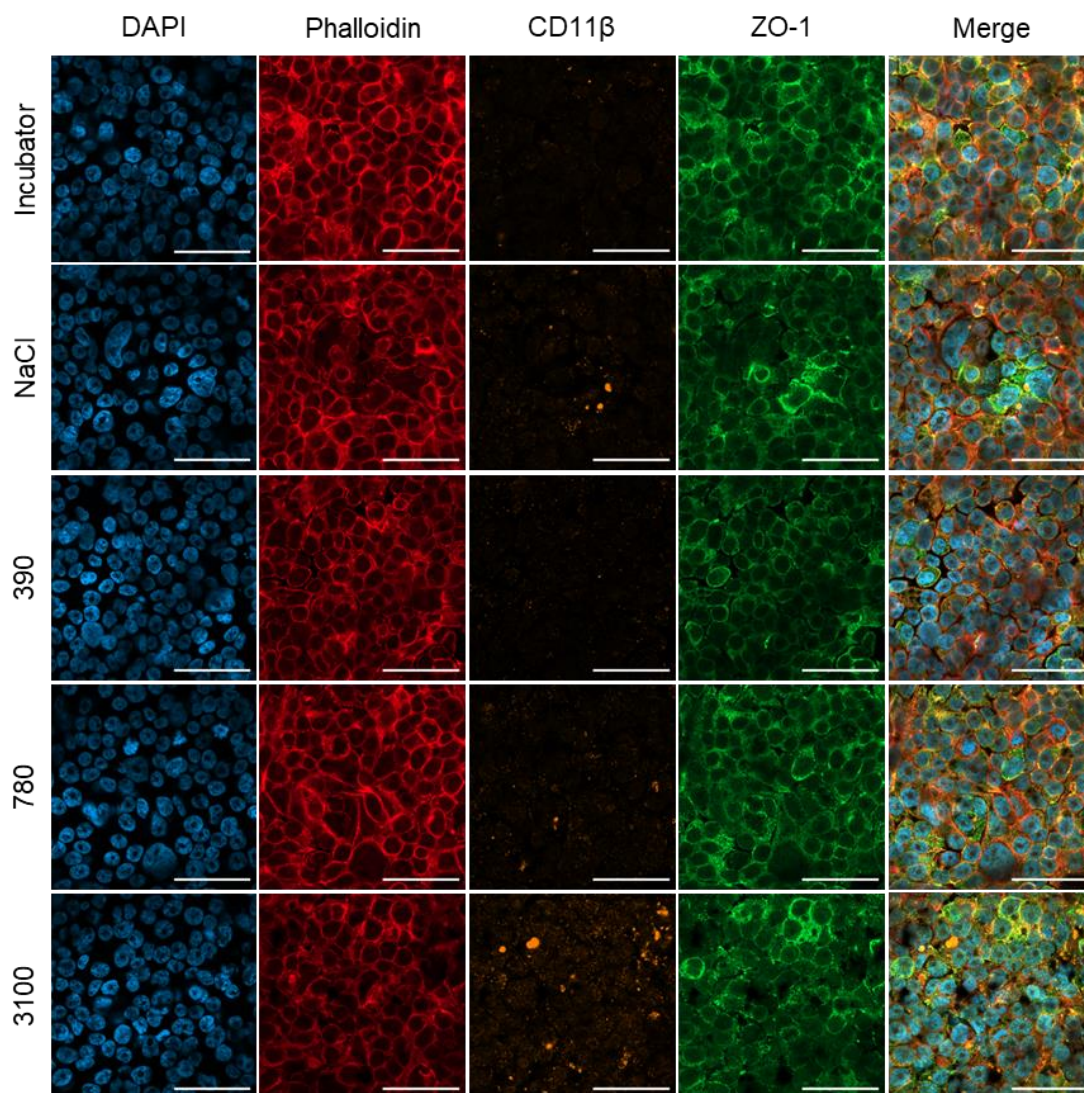


Figure 5.39 Viability (A), total cell count (B), blue dextran (C), IL6 concentration (D) and IL8 concentration (E) of the triple cell co-culture exposed to CB. Bars represent the mean of 3 replicates with significance assessed using a one-way ANOVA utilising a Tukeys post hoc test. \*  $p \leq 0.05$ , \*\*  $p \leq 0.01$ , \*\*\*  $p \leq 0.001$ , \*\*\*\*  $p \leq 0.0001$ .

There were no apparent morphological changes following CB exposure in the triple cell co-culture. However, CD11 $\beta$  staining became stronger with increased CB concentration (**Figure 5.40**).



**Figure 5.40** Confocal microscopy images of the triple cell co-culture exposed to CB. The nucleus (blue/DAPI), cytoskeleton (red/phalloidin), CD11 $\beta$  (orange) and ZO-1 (green) are shown. Scale bar = 50  $\mu$ m.

### 5.3.6.2 SRM 1649b Urban Dust

Urban dust caused a dose-dependent decrease in viability within the triple cell co-culture, reaching significance in the 3100 ng/cm<sup>2</sup> exposure ( $p < 0.05$  vs NaCl exposure) without altering the total cell count or the barrier integrity. Exposure to 1649b did not significantly alter IL6 or IL8 release ( $p > 0.05$ ) (**Figure 5.41**).



Cells were evenly distributed across the membrane, as shown through the confocal images, with cytoskeleton staining strongest at the membranes of the cells, which did not change with 1649b exposure. CD11 $\beta$  shows denser areas of strong staining in the higher exposure concentrations compared to unexposed (white arrow heads). ZO-1 shows increase fluorescent intensity at the membrane in the exposed cells compared to unexposed (**Figure 5.42**).

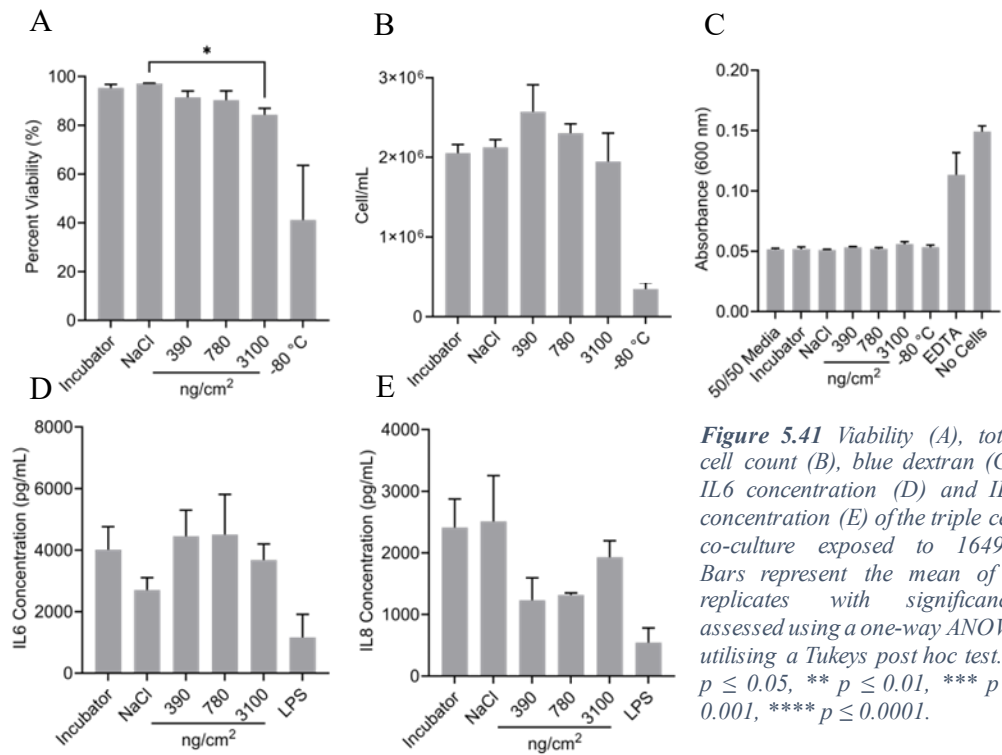


**Figure 5.41** Viability (A), total cell count (B), blue dextran (C), IL6 concentration (D) and IL8 concentration (E) of the triple cell co-culture exposed to 1649b. Bars represent the mean of 3 replicates with significance assessed using a one-way ANOVA utilising a Tukeys post hoc test. \*  $p \leq 0.05$ , \*\*  $p \leq 0.01$ , \*\*\*  $p \leq 0.001$ , \*\*\*\*  $p \leq 0.0001$ .

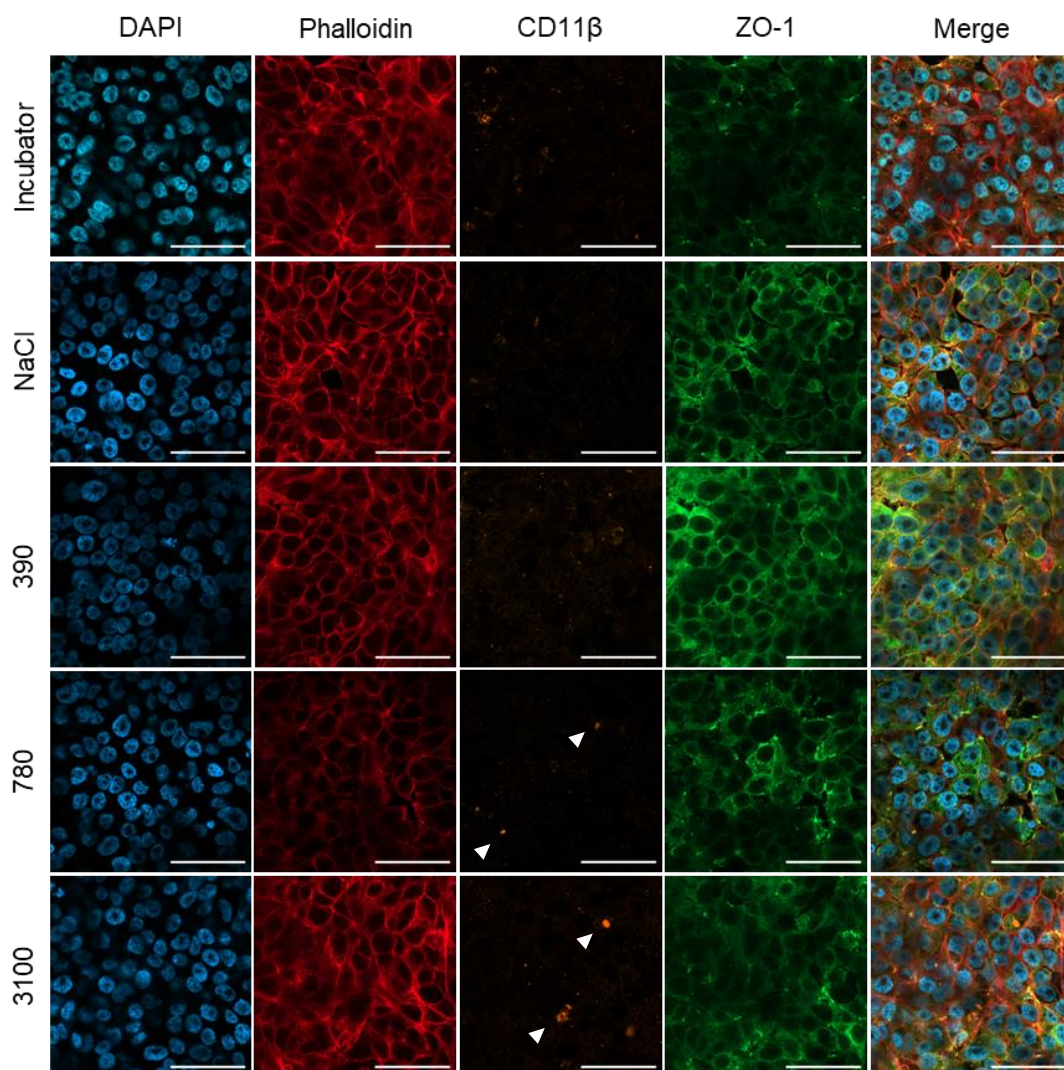


**Figure 5.42** Confocal microscopy images of the triple cell co-culture exposed to 1649b. The nucleus (blue/DAPI), cytoskeleton (red/phalloidin), CD11 $\beta$  (orange) and ZO-1 (green) are shown. White arrow heads show dense sections of CD11 $\beta$  staining. Scale bar = 50  $\mu$ m.

### 5.3.6.3 SRM 2583 Indoor Dust

Indoor dust exposure did not alter viability, cell count, barrier function or IL6/8 release at any 2583 concentration used ( $p > 0.05$ ) (**Figure 5.43**).

Exposure to 2583 seemed to alter the structure of the actin cytoskeleton at 3100 ng/cm<sup>2</sup>, which shows filaments across the entirety of the cell, compared to negative control, which shows phalloidin staining mainly at the cell membranes. Although CD11 $\beta$  staining does not change in terms of localisation, it gets fainter with higher 2583 concentrations. There are no changes in ZO-1 localisation across the exposure concentrations (**Figure 5.44**).

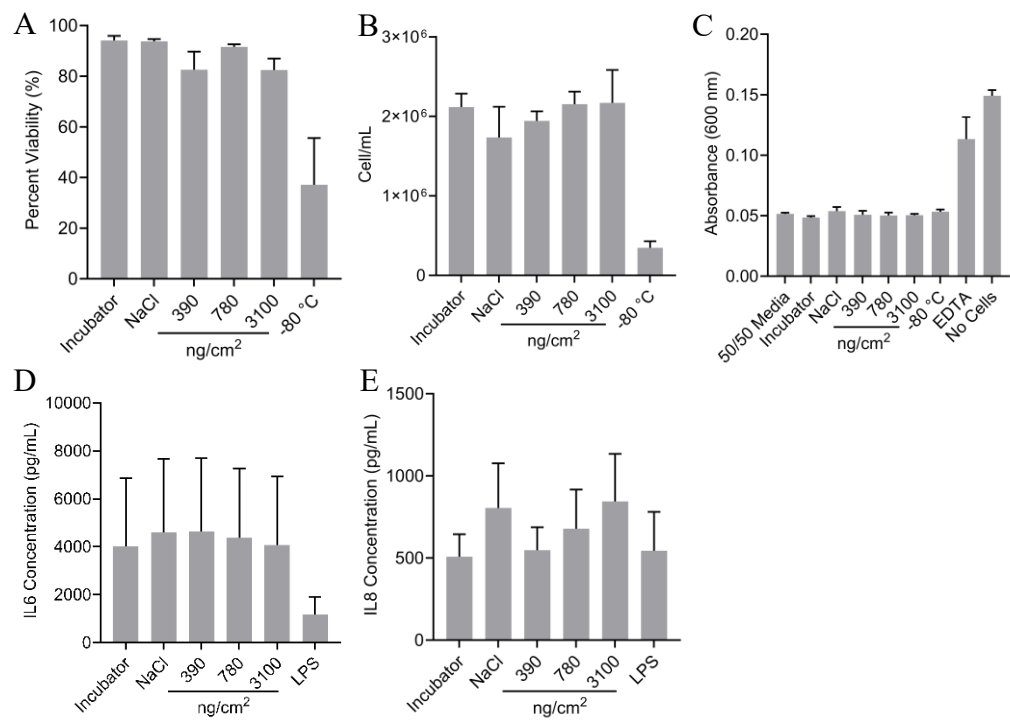


**Figure 5.43** Viability (A), total cell count (B), blue dextran (C), IL6 concentration (D) and IL8 concentration (E) of the triple cell co-culture exposed to 2583. Bars represent the mean of 3 replicates with significance assessed using a one-way ANOVA utilising a Tukeys post hoc test. \*  $p \leq 0.05$ , \*\*  $p \leq 0.01$ , \*\*\*  $p \leq 0.001$ , \*\*\*\*  $p \leq 0.0001$ .

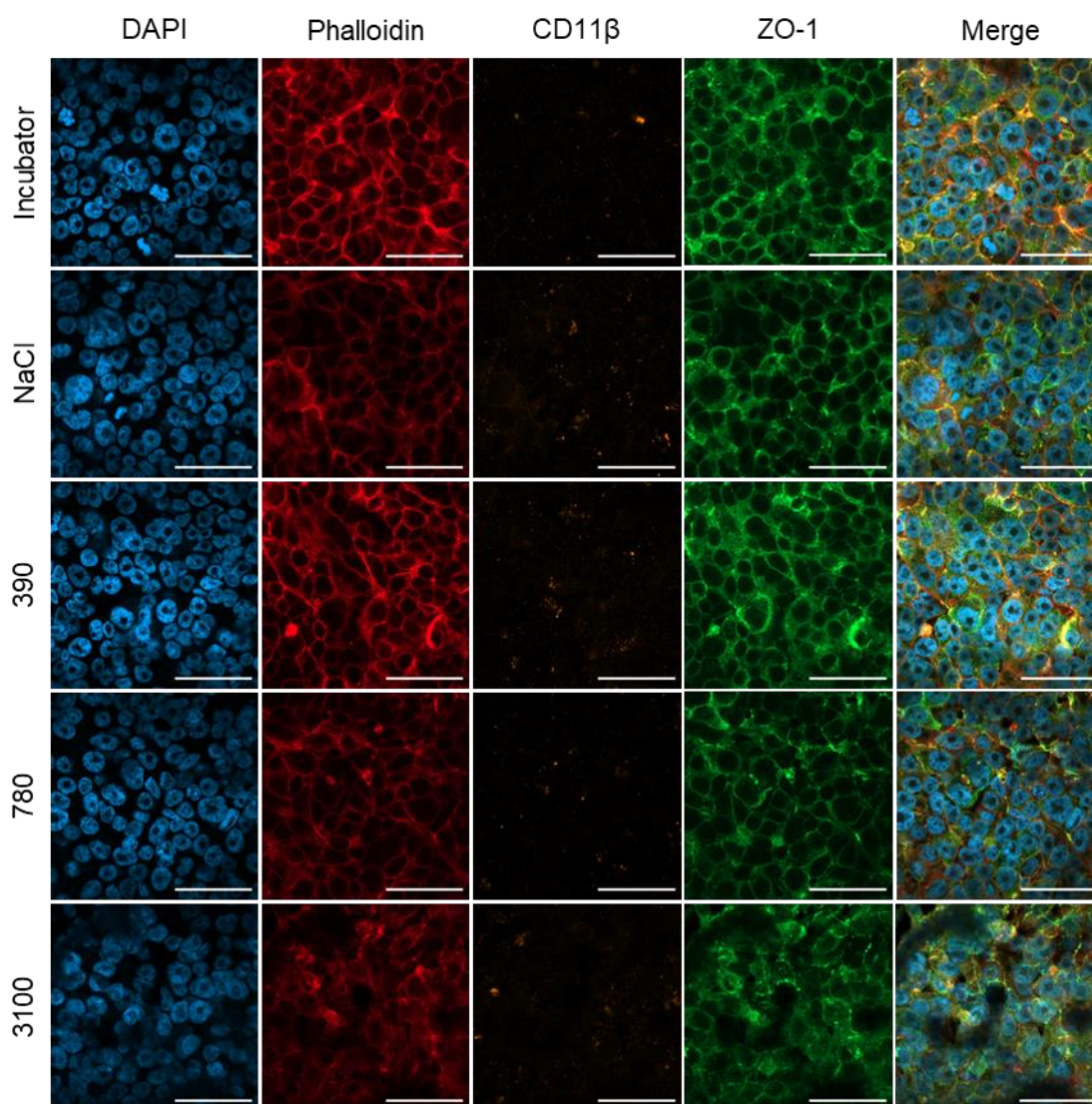


**Figure 5.44** Confocal microscopy images of the triple cell co-culture exposed to 2583. The nucleus (blue/DAPI), cytoskeleton (red/phalloidin), CD11 $\beta$  (orange) and ZO-1 (green) are shown. Scale bar = 50  $\mu$ m

### 5.3.7 Triple Cell Co-Culture Exposure to Diesel Emission Particles

The work so far has examined standardised particles; however, assessing the toxicology of some fresh samples pertinent to NO<sub>2</sub> co-exposure would be of interest. DEPs captured from an engine using varying air intake oxygen percentages were exposed *via* qALI (**Figure 4.1**) to the triple cell co-culture (**Figure 5.38**). The oxygen intake percentages were 9.8, 13 and 17%, and were exposed at concentrations of 16.4, 32.8 and 130.4  $\mu$ g/mL. These exposure concentrations align with the VitroCell® Cloud deposited concentrations of 390, 780 and 3100 ng/cm<sup>2</sup>, respectively, through calculating particle mass across a 0.9 cm<sup>2</sup> transwell insert and aligning with a 21.7  $\mu$ L qALI exposure volume.



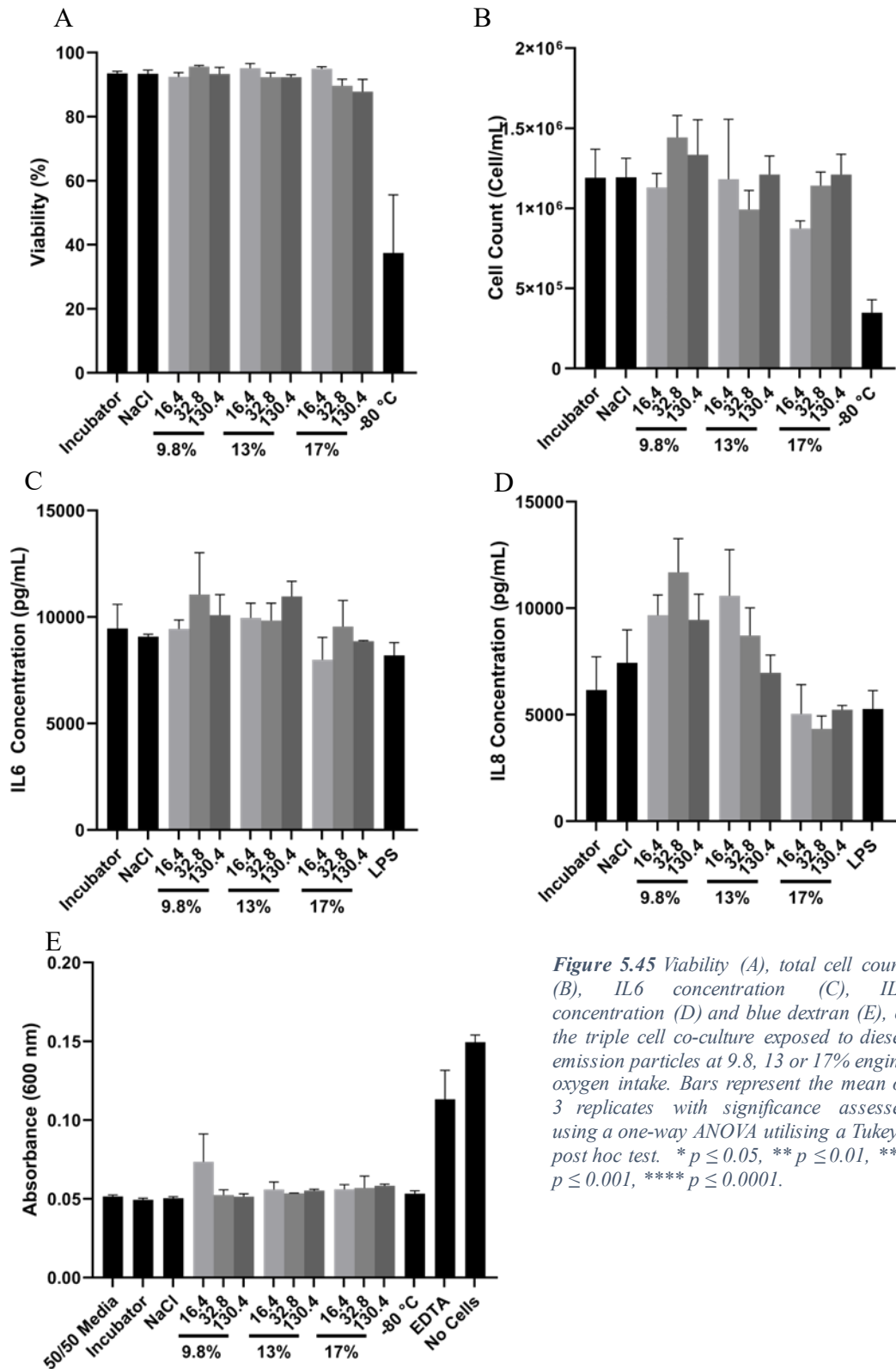


**Figure 5.45** Viability (A), total cell count (B), IL6 concentration (C), IL8 concentration (D) and blue dextran (E), of the triple cell co-culture exposed to diesel emission particles at 9.8, 13 or 17% engine oxygen intake. Bars represent the mean of 3 replicates with significance assessed using a one-way ANOVA utilising a Tukeys post hoc test. \*  $p \leq 0.05$ , \*\*  $p \leq 0.01$ , \*\*\*  $p \leq 0.001$ , \*\*\*\*  $p \leq 0.0001$ .

None of the DEP particles impacted cell viability ( $p > 0.05$ ). DEP exposure at any oxygen intake percentage also did not impact cell count, IL6 release or IL8 release within this model. The barrier function of the triple cell co-culture was not altered through any DEP exposure (**Figure 5.45**).

The triple cell co-culture exposure to DEPs did not dramatically alter the cell morphology, although phalloidin staining may show that cells are rounder compared to the incubator control. CD11 $\beta$  nor ZO-1 immunostaining were altered by DEP exposures (**Figure 5.46**, continues across subsequent pages).

Given the large number of comparisons made across alveolar models and PM types within this chapter, the main effects have been summarised in **Table 5.2**.

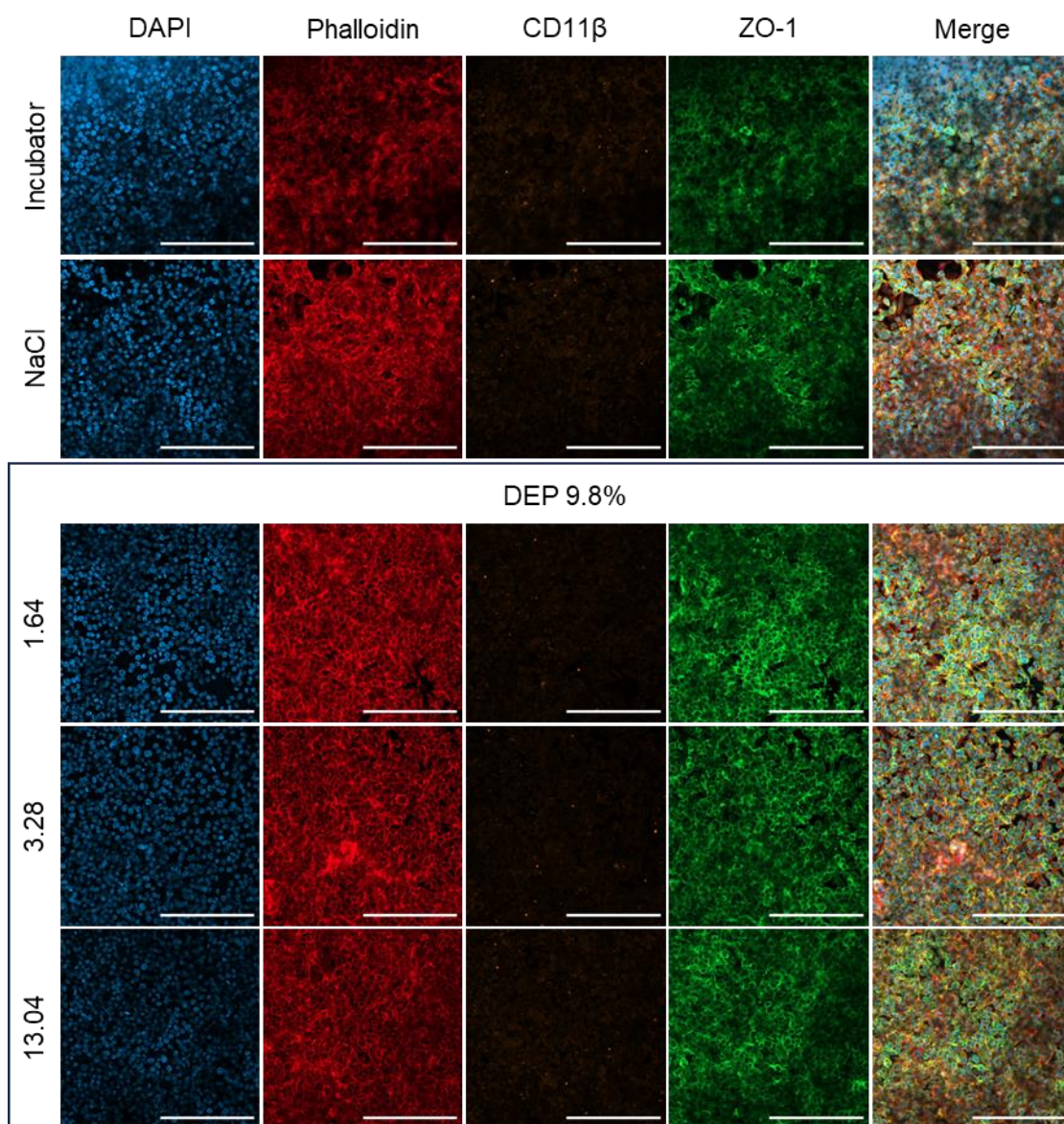


**Figure 5.46a** Confocal microscopy images of the triple cell co-culture exposed to diesel emission particles at 9.8, 13 or 17% engine oxygen intake . The nucleus (blue/DAPI), cytoskeleton (red/phalloidin), CD11 $\beta$  (orange) and ZO-1 (green) are shown. Scale bar = 200  $\mu$ m



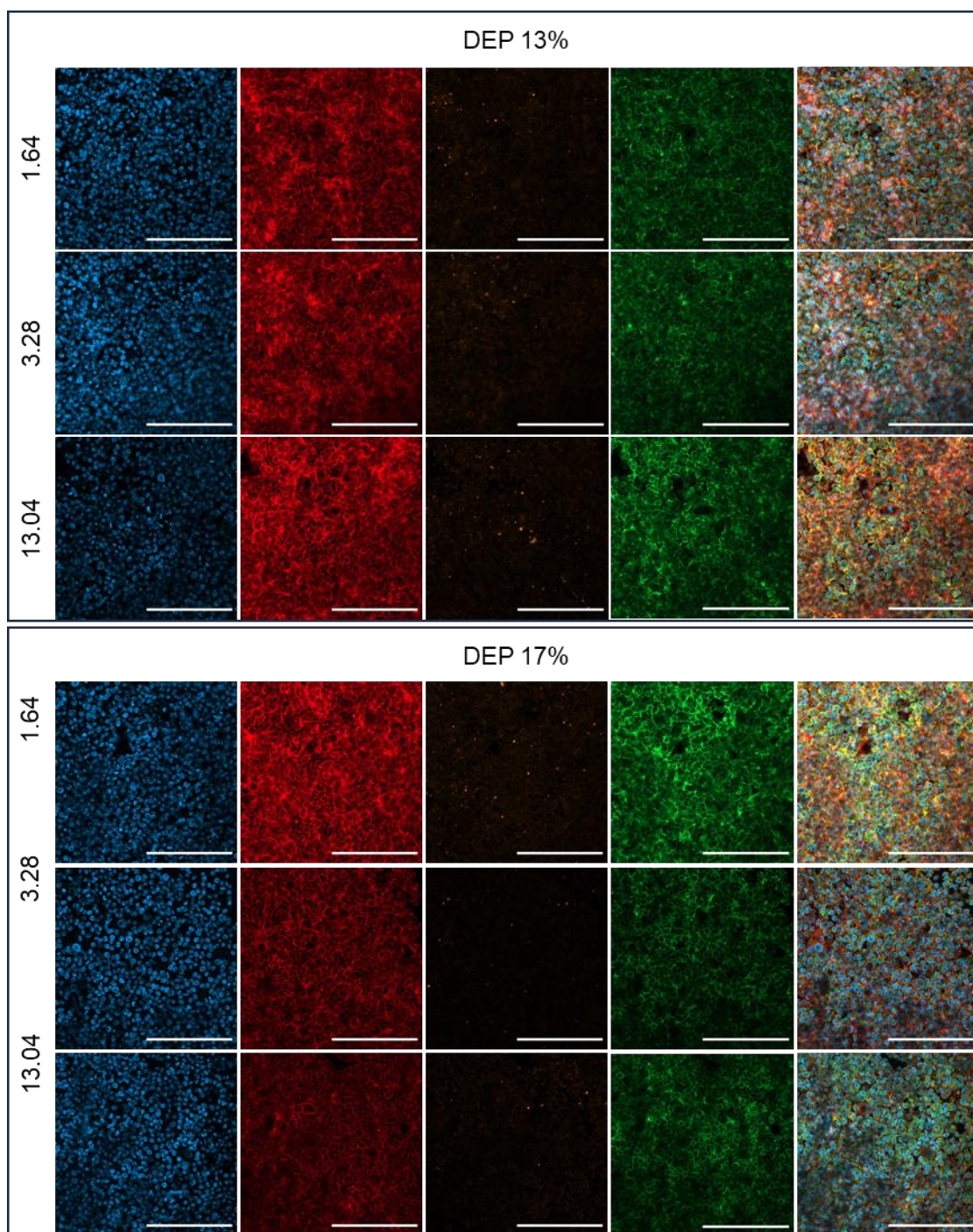


**Figure 5.46b** Confocal microscopy images of the triple cell co-culture exposed to diesel emission particles at 9.8, 13 or 17% engine oxygen intake . The nucleus (blue/DAPI), cytoskeleton (red/phalloidin), CD11 $\beta$  (orange) and ZO-1 (green) are shown. Scale bar = 200  $\mu$ m



*Table 5.2 Main effects observed with differing alveolar models following exposure to CB, 1649b, 2583 and DEPs.*

		<b>Viability</b>	<b>Barrier Function</b>	<b>IL6</b>	<b>IL8</b>
<b>hAELVi</b>	<b>CB</b>	No change	No change	No change	No change
	<b>1649b</b>	No change	No change	No change	No change
	<b>2583</b>	No change	No change	Increase	No change
<b>NCL-H441</b>	<b>CB</b>	Decrease	Decrease	No change	No change
	<b>1649b</b>	No change	Decrease	Increase	Increase
	<b>2583</b>	No change	Decrease	Increase	Increase
<b>hAELVi + NCL-H441</b>	<b>CB</b>	No change	No change	Increase	Increase
	<b>1649b</b>	No change	No change	No change	No change
	<b>2583</b>	No change	No change	No change	No change
<b>hAELVi + dTHP-1</b>	<b>CB</b>	Decrease	No change	Increase	No change
	<b>1649b</b>	Decrease	No change	No change	No change
	<b>2583</b>	No change	No change	No change	No change
<b>NCL-H441 + dTHP-1</b>	<b>CB</b>	Decrease	No change	No change	No change
	<b>1649b</b>	No change	No change	No change	No change
	<b>2583</b>	Decrease	Decrease	No change	No change
<b>Triple Cell Co- Culture</b>	<b>CB</b>	Decrease	No change	No change	No change
	<b>1649b</b>	Decrease	No change	Increase	Decrease
	<b>2583</b>	No change	No change	No change	No change
	<b>DEP 9.8%</b>	No change	No change	No change	No change
	<b>DEP 13%</b>	No change	No change	No change	No change
	<b>DEP 17%</b>	No change	No change	No change	No change
			No change		
			Approaching significant change ( <i>p</i> is between 0.05 and 0.1)		
			Statistically Significant Change ( <i>p</i> is less than 0.05)		

## 5.4 Discussion

This chapter aimed to assess the toxicological response to a range of cell models, namely, monocultures, co-cultures, and triple cell co-culture (described in Chapter 3), to a range of standardised and fresh realistic PM samples. Printex® 90 was used as a model particle of PM and has been widely used to draw interlaboratory comparisons. Indoor and urban PM samples were also used to represent realistic exposure conditions. To maintain this theme of realism, cultures were exposed at the ALI using the VitroCell® Cloud as previously described (Chapter 4). Endpoint assessment entailed viability, cell count, barrier integrity, pro-inflammatory response, and morphology (specifically tight junctions through ZO-1, macrophages through CD11 $\beta$ ). Outcomes from PM exposures were compared to negative controls or assay-specific positive controls.

### 5.4.1 Monoculture Exposures

Initially, epithelial monocultures were utilised to understand the base-level toxicity of these particles within each cell type, which might give information on how these cells might modulate the response of the other when in co-culture. hAELVi and NCI-H441 were used as models of ATI and ATII, respectively.

Neither hAELVi nor NCI-H441 were significantly affected by CB, 1649b or 2583 in terms of their cell count or viability (except hAELVi cells which where the viability was significantly reduced by CB). The cytotoxic response to CB has not been explicitly assessed within hAELVi or NCI-H441 previously, though there are varied responses to CB using other epithelial cell lines. Using submerged exposure methods, 20  $\mu\text{g}/\text{cm}^2$  CB was found to increase lactate dehydrogenase (LDH) abundance within the supernatant of Caco-2 cells (colon cells) (Gerloff et al., 2009). LDH is an enzyme present within cells that can be measured to indicate cell barrier integrity and therefore used as a measure of cell viability (Bahadar et al., 2016). Bengtson *et al.* (2016) also did not observe cytotoxicity in Caco-2 cells after CB exposure.

When exposed to 80  $\mu\text{g}/\text{cm}^2$ , however, LDH was not increased compared to a negative control, with the study citing that this is potentially due to the absorptive capacity of CB, preventing LDH detection. Specifically looking at alveolar epithelial cells, CB did not alter cell viability or cell count in A549 cells exposed for 6 or 24 hours at

concentrations of 2.8, 11.4 or 45.7  $\mu\text{g}/\text{cm}^2$  (submerged conditions), which aligns with the results observed here. Cell cycle analysis reveal that CB exposure (100  $\mu\text{g}/\text{mL}$ ) causes significant cell cycle blockage at G<sub>2</sub> in A549 (An et al., 2008). Whilst this could be an indication of genotoxicity (CB is a recognised carcinogen, and genotoxicity has been reviewed previously (Di Ianni et al., 2022)), it could also be a reason why NCI-H441 and hAELVi treated with CB were not observed to proliferate compared to the controls. A minor cytotoxic effect was observed within hAELVi cells but less so by NCI-H441 in response to exposure to 1649b. Previously, 1649a (the previous version of the 1649 SRM) has induced toxicity in murine embryonic fibroblasts with an IC<sub>50</sub> of 3  $\mu\text{g}/\text{mL}$ , perhaps mediated through oxidative stress or genotoxic mechanisms (Dumax-Vorzet et al., 2015).

Further, COX-2 is upregulated and oxidative stress is increased in human bronchial epithelial cells (HBECS) in response to 1649b exposure (submerged, 300  $\mu\text{g}/\text{cm}^2$ ) which could induce cytotoxicity (Wang et al., 2017). Any cytotoxic effects observed within this work were mild, with all viabilities above 80% and significance not reached during the particle exposures. Significance was reached when cells were cultured at -80°C for 30 minutes, reducing viability to below 50% and reducing the total cells counted. Though it was understandable how this exposure would have reduced the viability, it is less clear how it would impact cell count so substantially in such a transient period. One reason for this could be that the cells are being lysed due to the generation of ice crystals, and the cell fragments are too small to be counted by the automated cell counter.

The barrier integrity of NCI-H441 was significantly altered by CB, 1649b and 2583. However, the hAELVi barrier was not altered by exposure. Given each cell types' physiological role in the healthy human lung, these results are understandable. ATI cells, covering 95% of the alveolar area, the squamous cells possess tight junctions to form an impermeable physical barrier, reducing the risk of fluid leak into the alveolar space and translocation of inhaled xenobiotics into the bloodstream. Covering only 5% of the alveolar area, the cuboidal ATII cells are responsible for the secretion of surfactant, the maturation into ATI cells and play an immunomodulatory role. Considering the distinct differences in the physiology and histology, especially with regards to cell shape, the presence of tight junctions in ATI, and the ratio of each cell type within the human anatomy, it is clear that ATII may not possess the defences to

maintain a tight barrier when challenged with particle exposures. Cells cultured at -80 °C or those treated with EDTA were used as a positive control and caused a predictable decrease in barrier function, almost to the levels of the underlying transwell membrane barrier function (shown as the 'no cells' bar). On the other end of the spectrum, the absorbance of media incubated without the presence of blue dextran was also recorded to understand what the background absorbance would be, which was similar to negative control cultures.

Perhaps the change in barrier function is secondary to another primary effect within the cells. For example, here it has been shown that NCI-H441 mount a much larger pro-inflammatory response to 1649b and 2583 compared to hAELVi cells. Urban dust was also able to trigger a pro-inflammatory response in HBECs exposed at 300 µg/cm<sup>2</sup> in submerged conditions, shown through transcriptomic analysis highlighting increases in IL1β, IL6, IL8 and MMP9 (Wang et al., 2017). In contrast to the standardised dust samples, CB has little effect on the pro-inflammatory response. Given here that the presence of IL6 and IL8 were measured directly within the supernatant, it was speculated that the adsorptive capacity of CB was sequestering the molecules of interest, preventing their detection; however, similar results were observed in A549 when assessing IL8 production through mRNA expression. IL8 expression remained unchanged in submerged conditions, even using exposure concentrations of 160 µg/mL (Di Ianni et al., 2021). Perhaps CB can induce toxicity through another mechanism, as others have shown CB can act through an oxidative stress-mediated mechanism (Danielsen et al., 2011; Gerloff et al., 2009).

To examine the pro-inflammatory data from a different perspective, although PM exposure exerted more of an effect within the NCI-H441 cells than the hAELVi, there is also a difference at the baseline level. The presence of pro-inflammatory cytokines within negative controls of hAELVi is approximately 10-20 and 200-300 pg/mL of IL6 and IL8, respectively. These are elevated into the thousands of picograms per mL in supernatant from NCI-H441. This reflects the immunomodulatory role ATII exerts in healthy physiology (Kasper & Barth, 2017). TNFα was used as a positive control for assessing pro-inflammatory response but was seen to be more potent inducing IL6 and IL8 release in NCI-H441 cells compared to hAELVi (of which IL6 was not released as readily as expected). TNFα will bind to TNFα receptors on the surface of epithelial cells, signalling intracellularly through MAPK and NFκB to induce expression of IL6

and IL8 (Webster & Vucic, 2020). The reason why hAELVi would express IL8 more than IL6 is unclear, though hAELVi is a polyclonal cell line, which could explain this as cells may harbour populations that express specific genes more than others.

#### 5.4.2 Co-Culture Exposures

There are several instances of alveolar co-culture models being used within PM exposure studies previously, often using epithelial cells (commonly A549 cells) with dTHP-1 cells, though the specific co-cultures used within this work have not been commonly explored elsewhere.

Brookes *et al.* (2021) are currently the only other research group to publish their investigations using a hAELVi and NCI-H441 co-culture, finding that TEER was higher in hAELVi and hAELVi + NCI-H441 co-culture (mixed in a 50/50 ratio), peaking at approximately  $1000 \Omega \cdot \text{cm}^2$  compared to NCI-H441 monoculture which peaked at approximately  $100 \Omega \cdot \text{cm}^2$ . This trend is also followed within the exposures with CB, 1649b and 2583. Co-cultures comprising the majority of hAELVi cells (*i.e.*, hAELVi + NCI-H441 and hAELVi + dTHP-1) form a less permeable barrier that is more resistant to becoming permeable upon being challenged with PM. When NCI-H441 are the major constituent of a co-culture (NCI-H441 + dTHP-1), particles cause a significant impairment to barrier function, perhaps an additive effect to the already comparatively reduced function here. Brookes *et al.* (2021) also show that hAELVi + NCI-H441 monocultures possess ZO-1 at the cell membranes, as is shown in this work, though they do not comment on how this may be altered when exposed to PM. Here, changes in ZO-1 have been shown in all co-cultures when exposed to PM, including reduced fluorescence at the membrane and an overall disruption of morphology. Within rat alveolar cells, exposure to PM<sub>10</sub> and DEPs has been shown to reduce co-localisation between ZO-1 and occludin (another tight junction protein) (Caraballo *et al.*, 2011) and in mice lungs, exposure to incense smoke was associated with reduced ZO-1 expression and staining (Yamamoto *et al.*, 2021), whilst cigarette smoke caused ZO-1 to become fragmented and reduced in human endothelial cells (Schweitzer *et al.*, 2011). Though the intracellular mechanisms underpinning this change in ZO-1 localisation have been proven, ZO proteins are regulated by inflammatory mediators, such that ZO-1 levels are significantly lower in asthma patients than in non-asthma patients (de Boer *et al.*, 2008). IL6 and IL8, shown to be upregulated by

CB/1649b/2583, as well as TNF $\alpha$ , IL1 $\beta$ , IL9, IL22 and IL33, are able to regulate ZO proteins mediated by NF $\kappa$ B signalling (Yu et al., 2023), perhaps indicating a mechanism behind the alterations observed.

In general, co-cultures containing NCI-H441 cells have a higher baseline release of IL6 and IL8, perhaps due to ATEC cells' physiological immunomodulatory functions, compared to the hAELVi + dTHP-1 co-culture. Interestingly, hAELVi cells, which mounted more of a pro-inflammatory response to carbon black than either 1649b or 2583 in monoculture studies, continue this trend within hAELVi + NCI-H441 co-cultures. However, the presence of macrophages with the hAELVi cells seems to attenuate this CB response and instead promotes more of a pro-inflammatory response to 1649b and 2583. It would indicate that different PM types may trigger responses from some cell types but not others. When traditionally considering alveolar inflammation, one might consider AMs the primary cell with the potential to initiate an inflammatory response, given it is well known that AMs signal through TLRs to release IL1 $\alpha$ , IL1 $\beta$  and TNF $\alpha$  (Nicod, 2005), though the potential inflammatory signalling role of the epithelial cells is less explored.

This does not explain why the presence of dTHP-1 with hAELVi attenuated the pro-inflammatory response to CB compared to a hAELVi monoculture. However, AMs can modulate inflammation by releasing TNF $\alpha$  and IL1 inhibitors as soluble TNF $\alpha$  receptors or IL1 receptor agonists (Galve-de Rochemonteix et al., 1996). Further, through the release of IL10, AMs may downregulate their own production of TNF $\alpha$  and TNF $\beta$  (Nicod et al., 1995). If CB can draw off this mechanism within the models used here, it could attenuate downstream signalling, causing the changes observed between monoculture and a dTHP-1-containing co-culture.

The only research to date which investigates a hAELVi + dTHP-1 co-culture is from Kletting *et al.* (2018). It was found that the presence of dTHP-1 cells did not alter the barrier function in ALI conditions; however, it has been found that viability was significantly altered between hAELVi monoculture and hAELVi + dTHP-1 co-culture when exposed to starch nanoparticles, but not silver nanoparticles, further suggesting that different cells have particle specific interactions. In this study by Kletting and colleagues, starch and silver nanoparticles were considered to reduce the barrier formation of hAELVi monoculture and hAELVi + dTHP-1 co-cultures, whereas work

within the present study did not see this effect when using PM samples. This could be due to the method of measuring barrier function, where blue dextran was used here compared to TEER, or due to the differences in particles used eliciting different effects. It is also shown that when co-cultures of hAELVi + dTHP-1 were exposed to starch nanoparticles, uptake was seen only within the macrophages and not the hAELVi cells, whereas uptake of starch nanoparticles within hAELVi cells is seen when cells are in monoculture. This difference in uptake ability may again explain the differences observed between monoculture and co-culture. The co-culture used by Kletting *et al.* uses a mixture of small airway epithelial cell culture medium and RMPI, citing that RMPI would increase TEER and reduce permeability. However, the mechanisms underpinning this have not been explored. The polyclonal nature of hAELVi is an essential characteristic to consider, meaning that, through the use of different types of cell culture medium, specific sub-populations of cells may be selected for/against, potentially causing a phenotypic change from the original culture (Carius et al., 2023). The 50/50 media used in the hAELVi + NCI-H441 culture may cause changes compared to the 100% huAEC media used in the hAELVi + dTHP-1 co-culture.

Given that these media types are only used after seeding into transwell inserts (standard culturing and passaging of hAELVi used huAEC media), the changes only occur over 96 hours, and phenotypic drift would not be allowed to be established over a prolonged culture period. However, this does not exclude any change whatsoever. To fully assess the change, a global approach could be taken, such as transcriptomics of hAELVi grown in 50/50 media compared to huAEC to assess differences and how this may impact the observed toxic response.

Cell lines of A549 have also been used in conjunction with macrophage-like cells and assessed for inhalation toxicity. Here, it is shown that CB, 1649b and 2583 caused a cytotoxic response within NCI-H441 + dTHP-1 co-cultures whilst also reducing barrier function and inducing a pro-inflammatory response. Meldrum *et al.* (2022) examined similar A549 + AM co-cultures used here, using either NCI-H441 or A549 in conjunction with dTHP-1 (although they used different densities of each cell type) to assess toxicity to quartz or titanium oxide nanoparticles at different exposure durations used repeated exposure. They found there to be no change in pro-inflammatory response between NCI-H441 monocultures and NCI-H441 + dTHP-1 co-cultures, with suggestions that NCI-H441 cells may not be sensitive to all nanoparticles. Here, we

show that NCI-H441 cells indeed can mount a pro-inflammatory response to realistic air pollution samples. Meldrum *et al.* did find that A549 are more sensitive to the engineered nanoparticles used in their study, perhaps a result of A549 cells' relative genetic instability (Alidousty *et al.*, 2018). Co-cultures incorporating the A549 cell line, therefore, become the focus of their study. Indeed, A549 + dTHP-1 co-cultures are the focus of many exposure studies, such as Friesen *et al.* (2022), which find that  $\alpha$ -quartz particles were capable of inducing cytotoxicity in submerged but not ALI condition. Though they could induce IL8 release in monoculture, but more so co-culture models. This again exemplifies the requirement for realistic *in vitro* models and exposure conditions. It also highlights the importance of the assessment of cell-cell communication and how this may affect the observed response. It is likely that when a xenobiotic agent stimulates dTHP-1, they can secrete TNF $\alpha$ , which binds to the TNF $\alpha$  receptor on the surface of epithelial cells. This in turn could cause an increase in release of pro-inflammatory mediators, specifically IL8 (Friesen *et al.*, 2022; O'Hara *et al.*, 2009). This mechanism was explored in Chapter 3, where it was observed that stimulation of the triple cell co-culture with LPS caused a minor increase in TNF $\alpha$  but a significant increase in IL8 only when all 3 cell types were present. Removal of either the epithelial cells or the dTHP-1 dramatically reduced IL8 levels upon an inflammatory challenge. A similar effect was shown in BEAS-2B + dTHP-1 co-cultures exposed to fly ash (Diabaté *et al.*, 2008). This could work both ways; however, macrophages possess IL6 receptors on their plasma membrane (Wolf *et al.*, 2014), so when IL6 is secreted by epithelial cells, it may become sequestered by binding to the IL6 receptor on dTHP-1 cells. This could reduce its availability within supernatant and reduce the detection *via* ELISA; however, this could also induce signalling through STAT3 and MAPK (Rincon & Irvin, 2012), known to be involved with cellular proliferation and potentially tumorigenesis (Guo *et al.*, 2020; Zhou & Chen, 2021).

Co-culture models could be made more realistic to human exposures using a fluid flow system. Indeed, Meldrum *et al.* (2022) have further developed their A549 + dTHP-1 co-culture by implemented within a device that allows basal media to “flow”, driving realism towards a normal physiological lung. It was found that titanium dioxide and quartz nanoparticle exposures taking place under flow conditions altered cytotoxicity, barrier integrity and pro-inflammatory response compared to static conditions. This



offers further routes on how the models used here could be further developed and potentially how these developments may induce different, and maybe more relevant responses.

### **5.4.3 Triple Culture Exposures**

When the triple cell co-culture was exposed to air pollutant particles, a dose-dependent decrease in cell viability was observed for 1649b, 2583, but most notably, CB. This could be because CB has been shown to induce oxidative stress (an aspect that will be a focus of Chapter 6). Within A549 cells, CB can induce maximal ROS levels after 3 hours (this is particle size dependent), which is also associated with the induction of cytotoxicity (Ryu et al., 2023). As discussed in Chapter 1, a high abundance of ROS within cells is associated with cell damage, namely, lipid peroxidation and damage to DNA and proteins. This could, in turn, lead to cytotoxicity and explain the lower viabilities observed in triple cell co-cultures in carbon black compared to 1649b and 2583. It is likely, however, that the latter 2 PM samples contain an element of black carbon, considering the methods by which the samples were generated. Urban dust is likely to encompass black carbon from traffic or industrial emissions, whereas indoor dust could contain black carbon from fireplaces, cooking, or cigarette smoke. Indeed, within the SEM imaging shown in Chapter 4, the heterogeneous samples appear to contain particles that at least morphologically look similar to the carbon black images, perhaps explaining some of the overlapping effects.

Upon being challenged by CB, 1649b, or 2583, the barrier integrity of the triple cell co-culture remained unchanged. There are a number of reasons why this might be; however, the most likely reason is that hAELVi cells are the predominant cell type within the model. Given that these cells are characterised to form tight junctions with a high TEER, plus the tight barrier role these cells play within a physiological setting, it is clear that the model would be more resistant to barrier function dysfunction. Furthermore, this model contains the highest number of cells out of any of the models discussed within this section (Table 5.1). More cells may mean there is more of a physical barrier for blue dextran crossing the transwell membrane. Further, given the exposure concentrations are the same between models, there are less particles per cell, which could further influence the observed toxicological effects.

The triple cell co-culture appears less capable of forming a pro-inflammatory response compared to the co-/monoculture counterparts. It was often the case that maximal IL6/IL8 release was shown at the lowest exposure concentrations, whereas the higher concentrations and LPS positive control comparatively reduced IL6/IL8 detection. Initially, the lack of response to LPS exposure was puzzling, given that the other co-/monocultures were sensitive to this treatment. This could be due to the nature of the basal LPS exposure and the heightened seeding density of the co-culture, which does not allow the interaction through perfusion of LPS through the transwell insert to act apically. This could be assessed through a qALI LPS exposure of the triple cell co-culture. Additionally, due to the complexity of the model and the potential interaction of the dTHP-1 and epithelial cells, there could be a pro-inflammatory mechanism at play, that is, releasing IL6/IL8 at a background level that is masking delicate changes in pro-inflammatory response.

Similarly to the co-cultures, triple cell co-cultures exposed to CB, 1649b and 2583 had differences in ZO-1 localisation, potentially due to an inflammatory response. CD11 $\beta$  is shown to be reduced in fluorescence following exposure to 1649b and 2583. CD11 $\beta$  is vital in the phagocytic process within AMs, and CD11 $\beta$  expression has been found to be reduced by PM<sub>10</sub> and PM<sub>2.5</sub> but not UFPs (Becker *et al.*, 2003). The change here could, therefore, indicate a reduced defensive phagocytic capacity of dTHP-1 to these PM samples, which are larger than CB and do not induce this same effect.

Although these specific cells have not been used in a triple-cell co-culture model previously, other three or four cell models have been utilised within exposure studies. Costa *et al.* (2019), for example, investigated a triple culture containing NCI-H441 and dTHP-1 cells on the apical surface of transwell inserts and then endothelial cells (HPMEC-ST1.6R) on the basal side of the membrane, utilising the model to assess translocation of nanoparticles across the air-blood barrier, finding that the presence of endothelial cells could increase the TEER of the model compared to a purely apical model. When stimulated with LPS, however, showing that the dTHP-1 and endothelial cells were the primary cells involved in a pro-inflammatory response. In a similar model, Kasper *et al.* (2017) used A549 or NCI-H441 cells, dTHP-1 cells and endothelial cells (ISO-HAS-1). THP-1 ones were utilised in both an M1 and an M2 phenotype, finding that M1 may act as a model of inflammatory lung disease. Developing these co-culture models further, Klein *et al.* (2013) investigated a tetra-

culture comprising A549, dTHP-1, endothelial (EA.hy 926) and mast (HMC-1) cells. In tetra-culture, these cells showed reduced ROS production to any of the monocultures when treated with an oxidative stress inducer. When the model was exposed to silicone dioxide nanoparticles *via* aerosol exposure, uptake was only observed in the dTHP-1. It was also found that submerged conditions significantly increased IL8 secretion of the model. All the data goes to show that the cells used within the model modulate the toxic response.

## 5.5 Summary and Outlook

*Table 5.3 Key conclusions and findings from Chapter 5.*

<b>Chapter Conclusions</b>	<ul style="list-style-type: none"><li>▪ CB, 1649b and 2583 have been found to induce a pro-inflammatory response in mono and co-cultures.</li><li>▪ NCI-H441 cells are particularly prone to reductions in barrier function following exposure.</li><li>▪ All cell types exhibited a loss in viability following PM exposure.</li><li>▪ Co-culturing cells influenced the observed toxic responses, therefore implying a degree of cell-cell communication, which can affect mechanistic toxicology.</li></ul>
<b>Project Impact</b>	<b>The mono/co-cultures used within this work are sensitive to PM-only exposures. Future work will assess how NO<sub>2</sub> co-exposure with the CB, 1649b, 2583 and DEPs may alter this response.</b>

Within this chapter, the outcomes of Chapter 3 and Chapter 4 have been combined in a method that has allowed a relevant triple cell co-culture, as well as a combination of co-cultures, to be exposed to CB, 1649b and 2583 at the ALI *via* aerosol exposure (and DEPs *via* qALI). Using assay-specific positive controls and negative controls, changes to cell growth, viability, barrier function, and pro-inflammatory response have been assessed. It has been found that type 2-like NCI-H441 cells are more susceptible to barrier function loss compared to the type 1-like hAELVi. All cell types were subject to a cytotoxic response in some part, although this was often particle-specific, with CB inducing the greatest effect. The pro-inflammatory response varied between the cultures. It is clear that some cell types are affected by some PM samples more than others; for example, the NCI-H441 cells are highly affected in a pro-inflammatory respect by 2583. However, the co-culturing of cells modulated the measured pro-inflammatory mediator levels. Whether this is due to a difference in response levels, a difference in cell-to-cell communication, or the sequestering of mediators released by one cell type by another cell type is not clear.

It must be noted that there are a large number of statistical comparisons made throughout this chapter which could lead to the discovery of false positive statistical significance. The study is therefore limited by the number of replicates, and would benefit from more repeats of each exposure to increase statistical power.

As we advance, these models will be utilised within co-exposure studies using these particles in a co-exposure scenario with NO<sub>2</sub> (outlined in Chapter 4). The overarching goal would be to utilise the anatomically relevant co-culture model within these studies. However, given the cell-specific effects that have been observed here, it would be pertinent to investigate NO<sub>2</sub> cell-specific interactions prior to the use of the triple culture model.

To conclude, cell-specific effects of PM samples have been measured when exposing at the ALI. Co-exposures of different cells alter the effect observed in the respective monoculture. The mechanisms underlying these responses, however, require further focus.

## **Chapter 6: Co-exposure of Advanced *In Vitro* Models to Nitrogen Dioxide and Particulate Matter**

---

Many thanks to Katie Marchant from the *In Vitro* Toxicology Group at Swansea University for her work in the identification of effective housekeeper genes used during the PCR presented in this chapter.

A special thanks to Prof. Ulla Birgitte Vogel from the National Research Centre for the Working Environment, Denmark, as well as Dr Joakim Pagels and Dr Vilhelm Malmborg from Lund University, Sweden, for kindly providing the diesel emission particles used within this chapter.

## 6.1 Introduction

The particle-only exposures undertaken within Chapter 5 have given an understanding of the toxic responses elicited by advanced *in vitro* models using an aerosol exposure system. Though single pollutant exposures can be helpful in gaining an understanding of pollutant-specific effects, this is not how humans are typically exposed to air pollutants. As explained in Chapter 1, air pollution is a complex mixture of many different pollutants of PM and gases (among other constituents, explained in Chapter 1), meaning numerous types of air pollutants can be inhaled at once in a single breath. To date, little work has been carried out to examine whether these pollutants are able to act in an additive/synergistic manner to cause an augmented response or whether pollutants can interact with each other to modify the toxic response.

### 6.1.1 NO<sub>2</sub> and PM co-exposure parameters

Work within this chapter specifically examines the effects of PM and NO<sub>2</sub> co-exposure, an initial aim of the project outlined in chapter 1 and a research gap identified by COMEAP (COMEAP, 2018). Ambient concentrations of NO<sub>2</sub> and PM are often found to be proportional, such that exposure to one pollutant is usually accompanied by exposure to the other. This is due to the emission sources of these pollutants, such as vehicles within urban environments or gas heating/stoves within indoor environments. As such, PM samples have been selected to represent this, and were characterised in Chapter 4. CB has been used as a surrogate model particle of PM, whereas 1649b and 2583 have been selected to represent exposures occurring within both the ambient urban and indoor environments, respectively. Furthermore, work within the chapter includes particles provided by Prof. Ulla Birgitte Vogel (National Research Centre for the Working Environment, Denmark), namely, diesel emission particle (DEPs) samples from engines with varying oxygen intake percentages (9.8%, 13% and 17%). These were used as diesel engines are known to emit both DEPs and NO<sub>2</sub> concomitantly.

The overarching aims of these exposures, therefore, were to mimic real-life exposures within different environments relevant to human health. To further increase the relevance, PM concentrations have been selected based on realistic human occupational exposure levels (Søs Poulsen et al., 2013). The NO<sub>2</sub> concentrations used

have been variable. The NO<sub>2</sub> exposure system has been devised to allow gas exposures at levels expected within the ambient air; however, indoor NO<sub>2</sub> exposure levels are less well-defined. A wide range of indoor NO<sub>2</sub> concentrations have been reported (The World Health Organization, 2010), from 10 – 2500 µg/m<sup>3</sup> (approx. 5.3 ppb – 1.33 ppm) depending on activity level. Given that this was the first instance in which this system has been used, and the mechanisms of toxicity may be obscure and/or low magnitude, as well as the acuter nature of the exposure (24 hr), a larger concentration was utilised to allow practical toxic assessment.

### **6.1.2 Aims and Objectives**

This chapter has several goals; initially, the toxicity induced by NO<sub>2</sub> without the presence of PM was established in order to understand which mechanisms could be altered during co-exposure. Following this, NO<sub>2</sub> was exposed in conjunction with relevant PM samples. The use of *in vitro* models cultured at the ALI was pertinent here to ensure that the gaseous pollutant could directly contact the cell culture system (*i.e.* a submerged culture would potentially only induce indirect cellular effects due to NO<sub>2</sub> interacting directly with the cell culture media), which was described in Chapter 3. The characteristics and toxicology of the PM samples discussed in Chapters 4 and 5, respectively, were also essential to advise the direction of the study. This chapter, therefore, aims to combine all this knowledge, intending to:

1. Assess NO<sub>2</sub> toxicology in limited single pollution exposures as short exposure durations (4 hr).
2. Examine a dose-response relationship between NO<sub>2</sub> and NCI-H441 or hAELVi monocultures, as well as the triple cell co-culture exposed to 1, 2.5 and 5 ppm NO<sub>2</sub> for 24 hours.
3. Based on the findings of single pollutant NO<sub>2</sub> exposure, assess NO<sub>2</sub> and PM co-exposure using methods and concentrations relevant to human exposure.
4. Assess cell growth, viability, barrier function, pro-inflammatory response, and glutathione concentration following exposure.
5. Analyse data in the context of relevant positive and negative controls and compare them to previously published data.



It is hypothesised that co-exposure will modulate the response compared to single pollutant exposure of either pollutant.

## 6.2 Materials and Methods

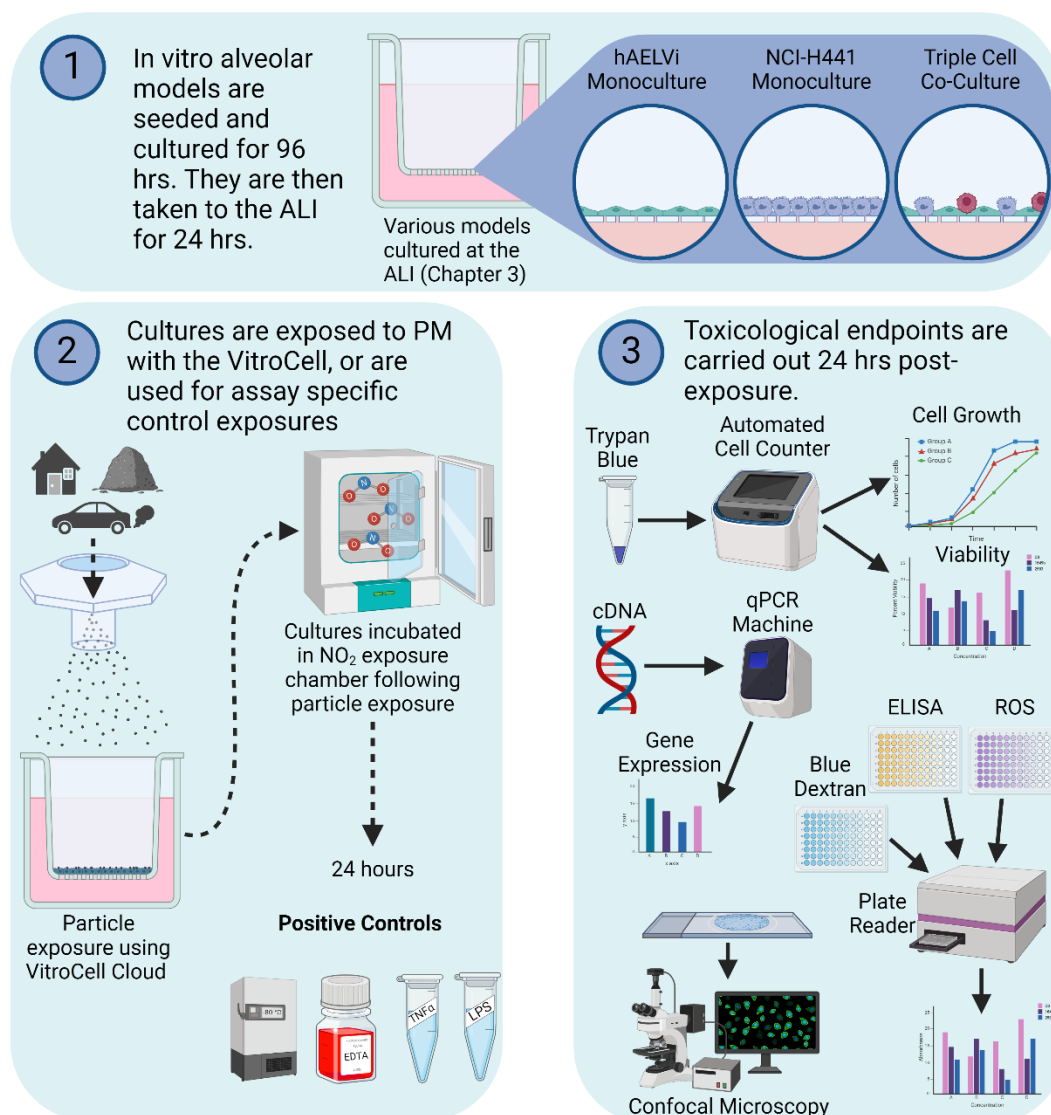


**Figure 6.1** Proposed exposure plan for NO<sub>2</sub> ± PM exposure to various in vitro models. Cell cultures are seeded (1) before being exposed to PM, before being incubated in an NO<sub>2</sub> environment (or not) (2) and various toxicological endpoints are assayed.

### 6.2.1 Experimental Design

Though there is limited toxicological information associated with inhalation exposure to PM or NO<sub>2</sub>, the outcomes following the co-exposure of the two pollutants are mainly unknown. The systems previously outlined (Chapter 4) allow exposure to PM and NO<sub>2</sub> concomitantly, allowing synergistic, additive, or reducing effects to be determined. **Figure 6.1** outlines the experimental design to be used within the chapter:

1. Various *in vitro* models were used within this chapter, specifically, hAELVi or NCI-H441 monocultures or the alveolar triple cell co-culture.

2. The cultures were exposed to PM *via* VitroCell® Cloud exposure before being incubated within the NO<sub>2</sub> exposure chamber for 24 hours. Initial NO<sub>2</sub> exposures took place without the initial PM exposure and were for 4-hour exposure durations. Also, a NO<sub>2</sub> dose response was performed at concentrations of 1, 2.5 and 5 ppm without prior exposure to PM.
3. A number of toxicological endpoints were undertaken following exposure. Specifically, cells were assessed for cell growth and viability *via* trypan blue exclusion assay, and blue dextran assay was used to assess barrier integrity. The supernatants were collected and used in pro-inflammatory cytokine/chemokine ELISAs, and oxidative stress was assayed through glutathione quantification on cell lysates. Finally, morphological examination was carried out through confocal laser scanning microscopy.

### **6.2.2 Chemicals and Reagents**

The chemicals and reagents used are described in Chapter 2, Section 2.1.

### **6.2.3 Cell Culture**

Refer to Chapter 2, Section 2.2 for the detailed methodology for culturing and passaging techniques of hAELVi, NCI-H441 and (d)THP-1 cells. Refer to Chapter 3 for information regarding the alveolar triple cell co-culture.

Toxicological exposures within this chapter use specific mono/triple cell co-cultures (**Figure 5.1**). Table 5.1 outlines parameters that were adhered to during seeding and culturing these models within the transwell inserts.

### **6.2.4 Impact of Geography on Cell Cultures and their exposure to pollutants**

Cell culture seeding into transwell inserts was undertaken at Swansea University. However, the NO<sub>2</sub> exposure chamber was located at the Radiation, Chemical and Environmental Hazards Directorate (RCE), UK Health Security Agency. Therefore, between seeding and exposure, seeded transwell inserts were required to be transported between sites. Inserts were transported under submerged conditions within a pre-sterilised polystyrene box packed with packaging air bags/bubble wrap to ensure plates stayed upright. Once cultures arrived at RCE, cultures were taken to the ALI, and exposures could commence 24 hours later. Endpoint assessments that were required to

be performed immediately following exposure (trypan blue exclusion assay and blue dextran) were carried out at RCE. Supernatants for ELISA and lysates (PCR and glutathione quantification) were collected in RCE and frozen before being transported to Swansea University in ice for processing within a polystyrene box. Fixed wells were stored at RCE at 4°C and were transported for processing on ice within a polystyrene box.

Prior to commencing this work, it was ensured that the travel time would not impact the toxicological endpoints. Data pertaining to this was presented and discussed in Section 4.3.6.

### **6.2.5 Exposure of *In Vitro* Models to Nitrogen Dioxide**

*In vitro* models were grown and cultured according to Chapter 3, and cultures were taken to the ALI 72 hours post-seeding and cultured at the ALI 24 hours prior to exposure to NO<sub>2</sub>.

Initial experimentation utilised an NCI-H441 monoculture, which was used in an acute 4-hour exposure at 5 ppm. Endpoints were then analysed immediately following being removed from the NO<sub>2</sub> exposure chamber.

Following this, monocultures of NCI-H441 or hAELVi cells, as well as the alveolar triple cell co-culture, were exposed to NO<sub>2</sub> in a dose range at concentrations of 1, 2.5 and 5 ppm over 24 hours with toxicological endpoints undertaken immediately following removal from the NO<sub>2</sub> chamber. Given that there is only one NO<sub>2</sub> exposure chamber, exposures were required to be staggered over 3 days, with each concentration taking place on a single day. To account for this, cell culture seeding was staggered to reflect this, and each exposure had its respective negative control that a relative change could be calculated.

### **6.2.6 Exposure of *In Vitro* Models to PM and/or Nitrogen Dioxide**

#### **6.2.6.1 Carbon Black, Urban Dust and Indoor Dust Co-Exposure with Nitrogen Dioxide**

*In vitro* models were grown and cultured according to Section 5.2.3. Cultures were taken to the ALI at 72 hours post-seeding and cultured at the ALI for 24 hours prior to

particle exposure. Exposure to CB, 1649b and 2583 was carried out as in Section 5.2.4; however, utilised a VitroCell® Cloud 6 (as opposed to a VitroCell® Cloud 12, deposition comparisons using CB shown in Appendix 2). Deposited concentrations of particles were targeted at 780 ng/cm<sup>2</sup> as this is the concentration where responses were subtle in PM only exposure, allowing additive/synergistic effects with NO<sub>2</sub> to be identified. Following exposure to PM samples, cultures were placed within the NO<sub>2</sub> exposure chamber at a concentration of 2.5 ppm (as this was the concentration at which the highest effect was observed in the dose-response (**Figure 6.4**, **Figure 6.6**, and **Figure 6.8**)). Following 24-hour incubation in NO<sub>2</sub>, cultures were used immediately in toxicological endpoint assessment.

#### **6.2.6.2 Diesel Emission Particle Co-Exposure with Nitrogen Dioxide**

*In vitro* models were grown and cultured according to Section 5.2.3. Cultures were taken to the ALI at 72 hours post-seeding and cultured at the ALI for 24 hours prior to particle exposure. Due to the minimal mass available, cell cultures were exposed to DEPs through qALI exposure methods, as described in Section 5.2.4.

Following exposure to PM samples, cultures were placed within the NO<sub>2</sub> exposure chamber at a concentration of 2.5 ppm (as this was the concentration at which the highest effect was observed in the dose-response (**Figure 6.4**, **Figure 6.6** and **Figure 6.8**)). Following 24-hour incubation in NO<sub>2</sub>, cultures were used immediately in toxicological endpoint assessment.

#### **6.2.7 Cell Count and Viability**

Methods for counting cells and assessing viability are described in Chapter 2, Section 2.3.

#### **6.2.8 Blue Dextran**

Methods for blue dextran barrier integrity analysis are described in Chapter 2, Section 2.6.1.

#### **6.2.9 Pro-Inflammatory Response**

Methods for measuring pro-inflammatory response are described in Chapter 2, Section 2.7.

## 6.2.10 Oxidative Stress

### 6.2.10.1 Glutathione Quantification

Following 24-hour exposure to NO<sub>2</sub>, the cells on transwell inserts were harvested by removing all cell culture media, washing the insert with PBS, and then incubating in trypsin-EDTA (500 µL per well) for 15 minutes. Cells were confirmed to have detached *via* light microscopy before suspensions were washed down in 500 uL cell culture media, transferred to a 1.5 mL centrifuge tube, and centrifuged at 340 RCF for 5 minutes. The supernatant was then discarded, and cells were washed with 500 uL 4°C PBS and again centrifuged at 340 RCF for 5 minutes. The supernatant was removed, and cells were resuspended in ice-cold mammalian lysis buffer (diluted from 5x to 1x prior to use using MilliQ water) and homogenized by pipetting. The samples were then centrifuged at 17,000 RCF for 15 minutes at 4°C. The supernatant was transferred to a new microcentrifuge tube and stored at -80°C until required for use.

**Table 6.1** BSA concentrations used to create the standard curve within the DC protein quantification assay.

#	Concentration (mg/mL)	Volume of BSA Stock (10mg/mL)	Volume of Lysis Buffer (µL)
1	0	0	20
2	0.25	0.5	19.5
3	0.5	1	19
4	0.75	1.5	18.5
5	1	2	18
6	1.5	3	17
7	2	4	16
8	2.5	5	15
9	3	6	14
10	3.5	7	13
11	4	8	12
12	4.5	9	11
13	5	10	10
14	7.5	15	5
15	10	20	0

Prior to running the GSH assay, it was essential to quantify the total protein within each sample so that any alterations in GSH concentration could be put into the context of the total protein yield. This was performed *via* the DC (detergent compatible) protein assay (Bio-Rad). Given that the protein content of samples would be unknown, a broad standard curve was created (**Table 6.1**) using BSA diluted in 1x mammalian lysis buffer ranging from 0-10 mg/mL. To perform the assay, working reagent A' was

created by adding 20  $\mu\text{L}$  reagent S per 1 mL of reagent A (2 mL created total; therefore, 40  $\mu\text{L}$  reagent S was added to 1 mL reagent A). Within a 96-well plate, 5  $\mu\text{L}$  of sample or standard was added to each well in duplicate, followed by 25  $\mu\text{L}$  of reagent A'. Then, 200  $\mu\text{L}$  of reagent B was added to each well and mixed by pipetting, avoiding the generation of bubbles. The plate was left for 15 minutes to allow the blue colour to develop, the intensity of which is dictated by the protein content. The absorbance at 750 nm of the plate was then read using a FLUOstar Omega plate reader. The protein concentration for each sample is shown in **Figure 6.8** calculated through comparison with a standard curve.

The protein samples to be used in the GSH assay could contain enzymes that would interfere with the assay. Therefore, it was necessary to deproteinise the samples prior to use. This was done using a Deproteinization Sample Preparation Kit. Trichloroacetic acid solution (TCA) (15  $\mu\text{L}$ ) was added to 100  $\mu\text{L}$  of the sample within a 0.5 mL centrifuge tube and mixed by pipetting. This causes the proteins within the sample to precipitate out. The samples were left on ice for 15 minutes to allow the reaction to take place before the samples were centrifuged at 12,000 RCF for 5 minutes. The supernatant from the samples containing GSH was then transferred to another tube. The added TCA reduced the pH of the sample, and there could be leftover TCA present. Therefore, 10  $\mu\text{L}$  of neutralisation buffer (supplied with the kit) was used to neutralise this. The samples were left for 5 minutes with the cap off to allow the reaction to take place and generated  $\text{CO}_2$  to be released.

GSH concentration within the samples was quantified using a GSH/GSSG Ratio Detection Assay Kit. Standards were prepared by first preparing the top standard (10  $\mu\text{M}$ ) by adding 5  $\mu\text{L}$  to 495  $\mu\text{L}$  of assay buffer (provided in the kit). The standards were then serially diluted down to a concentration of 0.1563  $\mu\text{M}$ . GSH assay mixture (GAM) was prepared by adding 100  $\mu\text{L}$  of 100X thiol green stock solution to 10 mL of assay buffer. In duplicate, 50  $\mu\text{L}$  of standards or samples were added to a black, clear flat bottom 96-well plate, followed by 50  $\mu\text{L}$  GAM. This was then incubated at room temperature, protected from light, for 60 minutes. Fluorescence was then measured at Ex/Em 490/520 nm.

To analyse this data, the duplicate readings were averaged, and the mean of the blank was subtracted from each value before the GSH concentration within the samples was determined through comparison with a standard curve. This concentration required correction due to dilution that occurred during the deproteinization step. Therefore, the calculation below was used to determine a 0.8% correction.

$$\% \text{ original concentration} = \frac{\text{initial sample volume}}{(\text{initial sample volume} + \text{TCA volume} + \text{NaHCO}_3 \text{ volume})} \times 100$$

$$\% \text{ original concentration} = \frac{100}{(100 + 15 + 10)} \times 100$$

$$\% \text{ original concentration} = 80$$

By dividing the GSH concentration by the total protein concentration (earlier determined by DC assay), a comparable concentration was calculated.

### 6.2.11 Immunocytochemistry and Confocal Microscopy

General principles of sample fixation and storage, immunocytochemistry and confocal microscopy are described in Chapter 2, Section 2.5.

### 6.2.12 Quantitative Polymerase Chain Reaction

Quantitative polymerase chain reaction (qPCR) allows the quantification of the expression of a specific gene of interest following PM/NO<sub>2</sub> exposure. Gene expression can be quantified by converting transcribed DNA (*i.e.*, mRNA) from cell lysate into copy DNA (cDNA) *via* reverse transcription. The thermal cycler will melt open the cDNA into two single strands, which will bind the primer of the gene of interest, allowing DNA polymerase to bind and the incorporation of complementary nucleotides. SYBR green will then bind to all newly synthesised DNA complexes and fluoresce. The intensity of this fluorescence is then detected by the qPCR machine, quantifying the degree of gene expression in the sample. (Ponchel et al., 2003).

#### 6.2.12.1 RNA Extraction

RNA was extracted from cultures post-exposure using the RNeasy® Mini Kit (containing RNeasy Mini Spin Columns, RLT Lysis Buffer, Buffer RW1, and RPE Buffer) in conjunction with QIAshredder columns. To harvest enough RNA, lysates from three wells of each biological replicate were pooled before RNA extraction.



To obtain cell lysates, from which RNA could be extracted, media was first removed from the transwell insert, and both sides of the insert membrane were washed with PBS three times. After the final PBS wash, 200  $\mu$ L of RLT lysis buffer was added to the apical membrane of the transwell insert and homogenised by pipetting. Lysates were then able to be stored in this state at  $-80^{\circ}\text{C}$ .

To extract RNA from the cell lysates, lysates were added directly to a QIAshredder column within a 2 ml collection tube and centrifuged at 8000 RCF for 2 minutes. This homogenised the cell lysate, aids in the removal of genomic DNA and improves RNA yield. A volume of ethanol equal to the lysate volume used (600  $\mu$ L) was then added to each lysate sample and mixed well using a pipette. The lysate was transferred to an RNeasy spin column within a new 2 ml collection tube. The column was then centrifuged for 15 seconds at 8000 RCF. Flow-through was discarded. The max volume of the RNeasy spin columns was 700  $\mu$ L; therefore, this step was repeated using the same spin column until all the lysate was used. Flow-through was discarded before 700  $\mu$ L of Buffer RW1 was added to the RNeasy spin column and was centrifuged within a 2 mL collection tube for 15 seconds at 8000 RCF. Flow-through was again discarded. Next, 500  $\mu$ L Buffer RPE was added to each spin column, centrifuged for 15 seconds at 8000 RCF and flow-through discarded. Again, 500  $\mu$ L Buffer RPE was added to each spin column. However, this time, it was centrifuged for 2 minutes at 8000 RCF and flow-through discarded. The spin columns were then transferred to a new collection tube and centrifuged for 1 minute at 8000 RCF. This was to ensure that there was no residual liquid on the membrane of the spin column. If there was, the columns were recentrifuged in a new collection tube. The RNeasy spin columns were then placed into a new 1.5 mL collection tube, and 30  $\mu$ L of nuclease-free water was added directly to the filter membrane of the column. This was centrifuged for 1 minute at 8000 RCF to elute RNA.

Extracted RNA was assessed for quality and yield using a NanoPhotometer® NP80. The photometer was set to detect RNA and blanked using 1  $\mu$ L of RNase-free water before 1  $\mu$ L of each RNA sample was used to assess RNA quality (ensuring the 260/280 and 360/230 ratios were above 1.7) and the RNA concentration.

### 6.2.12.2 cDNA Synthesis

The iScript gDNA Clear cDNA Synthesis Kit was used to synthesise cDNA from the RNA samples and was performed as per manufacturer instructions. Firstly, a DNase master mix was created, as shown in **Table 6.2**, with a total of 2  $\mu\text{L}$  being made per reaction.

*Table 6.2 DNase Master Mix Constituents*

Reagent	Volume (per reaction) $\mu\text{L}$
iScript DNase	0.5
iScript DNase Buffer	1.5
Total	2

The reaction mixture was then made up as in **Table 6.3**. RNA (1000 ng) was added, the volume of which was calculated by dividing 1000 over the RNA concentration in  $\text{ng}/\mu\text{L}$ , which gave the number of microlitres required. The mixture was then made up to 16  $\mu\text{L}$  using RNase-free water.

*Table 6.3 Constituents of the reaction mixture for the first thermal cycler run for cDNA synthesis.*

Reagent	Volume ( $\mu\text{L}$ )
DNase Master Mix	2
RNA (1000 ng)	$\frac{1000}{\text{RNA Concentration (ng}/\mu\text{L})}$
Water	Variable
<b>Total</b>	<b>16</b>

The reaction mixture was thoroughly mixed and centrifuged with a mini centrifuge to remove bubbles. The reaction mixtures were placed into a T100 Thermal Cycler under the conditions shown in **Table 6.5**. The thermal cycler finished on an infinite  $4^{\circ}\text{C}$  hold to reduce RNA/cDNA degradation.

*Table 6.4 DNase reaction thermal cycler protocol.*

Step	Temperature ( $^{\circ}\text{C}$ )	Time (min)
DNase Digestion	25	5
DNase Inactivation	75	5
Hold	4	Infinite

After this, 4  $\mu\text{L}$  of iScript reverse transcriptase supermix was added to each reaction. An extra reaction was also performed per batch, which received 4  $\mu\text{L}$  of iScript no-RT control supermix (NRT control) as a genomic material contamination control. The reaction mixture was thoroughly mixed and centrifuged with a mini centrifuge to

remove bubbles. The tubes were then placed within the thermal cycler and run under the protocol within **Table 6.4**.

*Table 6.5 cDNA synthesis reaction thermal cycler protocol*

Step	Temperature (°C)	Time (min)
Priming	24	3
Reverse Transcription	46	20
Reverse Transcription Inactivation	95	1
Hold	4	Infinite

The cDNA was then diluted to a concentration of 10 ng/μL with 80 μL of nuclease-free water, aliquoted to avoid freeze-thaw degradation and stored at -80°C.

Control DNA was generated as above, using unexposed NCI-H441 monocultures, hAELVi monocultures, or triple cell co-cultures and was used within the standard wells of the qPCR plate. The control DNA used aligned with the cultures from which the cDNA samples were extracted.

### 6.2.12.3 Primer validation

*Table 6.6 Sequences of primers used in this work.*

Primer	Sequence
SOD1 Forward	5' CTCACTCTCAGGAGACCATTC 3'
SOD1 Reverse	5' CCACAAGCCAAACGACTTCCAG 3'
HPRT1 Forward	5' ACTGAACGTCTTGCTCGAGA 3'
HPRT1 Reverse	5' TGATGTAATCCAGCAGGTCA 3'
GAPDH Forward	5' CCACATGGCCTCCAAGGAGTAAGAC 3'
GAPDH Reverse	5' AGGAGGGGAGATTTCAGTGTGGTGGG 3'

SOD1, HPRT1 and GAPDH primers (primer sequences are shown in **Table 6.6**) were validated. NCI-H441 control DNA was diluted to 1:10, 1:100 and 1:1000 (log 0, log -1 and log -2, respectively) in nuclease-free water. A SYBR Green supermix was made according to **Table 6.7**, using the primers of interest, SsoAdvanced Universal SYBR® Green Supermix and nuclease-free water.

*Table 6.7 Constituents of the SYBR Green supermix*

Reagent	Volume (μL)
Supermix 2x	10
Forward Primer	1
Reverse Primer	1
Water	7
cDNA	1
<b>Total</b>	<b>20</b>

Within 96 well, non-skirted, low-profile PCR plates, 19  $\mu$ L of SYBR green supermix was added to each of the required wells before 1  $\mu$ L of cDNA was added. The NRT control cDNA and a no template control (NTC) were also utilised, where the cDNA was replaced with nuclease-free water, allowing contamination to be identified. This was conducted in duplicate. The plates were then sealed using a microseal 'B' plate seal and centrifuged for 3 minutes at 3705 RCF. The PCR plates were then put into a CFX Connect Real-Time System qPCR Machine. The thermal cycling protocol is as follows: polymerase is activated, and DNA is denatured by heating to 95°C for 30 seconds and then held at 95°C for another 10 seconds. The temperature is reduced to the required annealing temperature (here, a temperature gradient was used in the primer validation) for 30 seconds. This cycle of 10 seconds at 95°C and 30 seconds at the annealing temperature is repeated for 40 cycles before a melt curve is generated by increasing the temperature from 65 to 95°C in 0.5°C increments every 5 seconds. This melt curve allows the identification of primer dimer formation.

Various temperature gradients were used in the annealing step to validate each primer based on its melt temperature. Primers were checked which temperatures aligned with an efficiency of between 90 and 110%, with an  $R^2 > 0.97$  (in line with MIQE

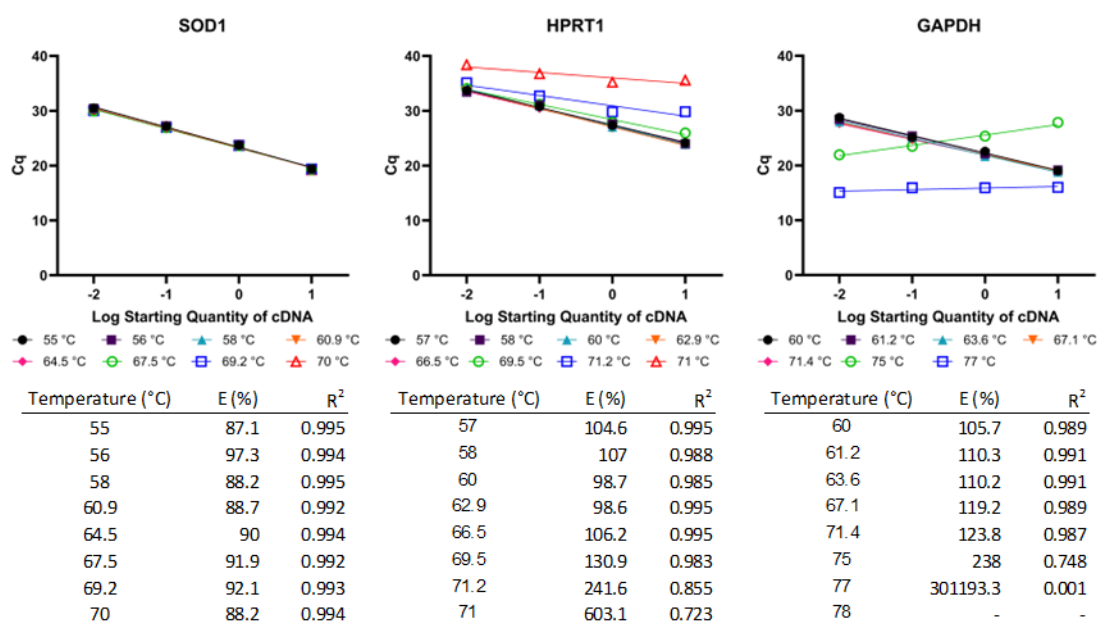


**Figure 6.2** Primer validation data for SOD1, HPRT1 and GAPDH primers (sequences are shown in Table 2.8). untreated cDNA from NCI-H441 grown at ALI were used for primer validation, and each primer had a unique temperature range based of the primer melt temperature. For each primer and temperature efficiency (E) and the R<sup>2</sup> value are shown. There was an attempt to validate GAPDH at 78°C, however the reaction was not functional at this temperature and did not give a value. The C<sub>q</sub> is the cycle number at which the fluorescence first rises above the threshold.

guidelines). Based on the primer validation data, a temperature of 63°C was chosen for the follow-up qPCR analysis (**Figure 6.2**).

#### **6.2.12.4 qPCR**

As in Section 6.2.12.2, SYBR green supermix was created and added to a 96-well PCR plate. qPCR was run to assess the impact of NO<sub>2</sub> on SOD1 expression, using GAPDH and HPRT1 as reference genes. Reference genes B2M and TBP were unable to be validated in these cell lines, therefore the study utilised 2 housekeeper genes (in line with MIQE guidelines).

For each PCR plate, primer standard curves were created using control cDNA. This control cDNA came from untreated cultures of the same cell culture of the sample cDNA to be used. Control cDNA was used within a standard curve undiluted, and at concentrations of 1:10, 1:100 and 1000 diluted in nuclease-free water. Sample cDNA of interest was used neat. Again, an NRT and NTC were utilised to detect contamination. Each condition was conducted in technical triplicate. The plates were then sealed using a microseal 'B' plate seal and centrifuged for 3 minutes at 3705 RCF. The PCR plates were put into a CFX Connect Real-Time System qPCR Machine and run *via* the following protocol: polymerase is activated, and DNA is denatured by heating to 95°C for 30 seconds and then held at 95°C for another 10 seconds. The temperature is reduced to the required annealing temperature (here, a temperature gradient was used in the primer validation) for 30 seconds. This cycle of 10 seconds at 95°C and 30 seconds at the annealing temperature is repeated for 40 cycles before a melt curve is generated by increasing the temperature from 0.6 to 95°C in 0.5°C increments every 5 seconds.

Relative gene expression was calculated using the  $2^{-\Delta\Delta C_t}$  method. The was performed the CFX Maestro software. Gene expression data was then input into GraphPad Prism for statistical analysis.

#### **6.2.13 Data and Statistical Analysis**

Exposures were performed a minimum of 3 times on biological replicates at least 2 passages apart. Statistical analysis and data visualisation were performed using GraphPad Prism Version 10.1.2. One-way ANOVAs were performed on the exposure

data, utilising a Tukey post hoc multiple comparison test (unless otherwise stated in the figure legend). Significance is shown compared to the incubator control exposures.

Relative gene expression was calculated using a GeneStudy within the CFX Maestro software. Gene expression data was input into GraphPad Prism (Version 10.1.1) for statistical analysis.

## 6.3 Results

### 6.3.1 NCI-H441 Response to Nitrogen Dioxide Exposure

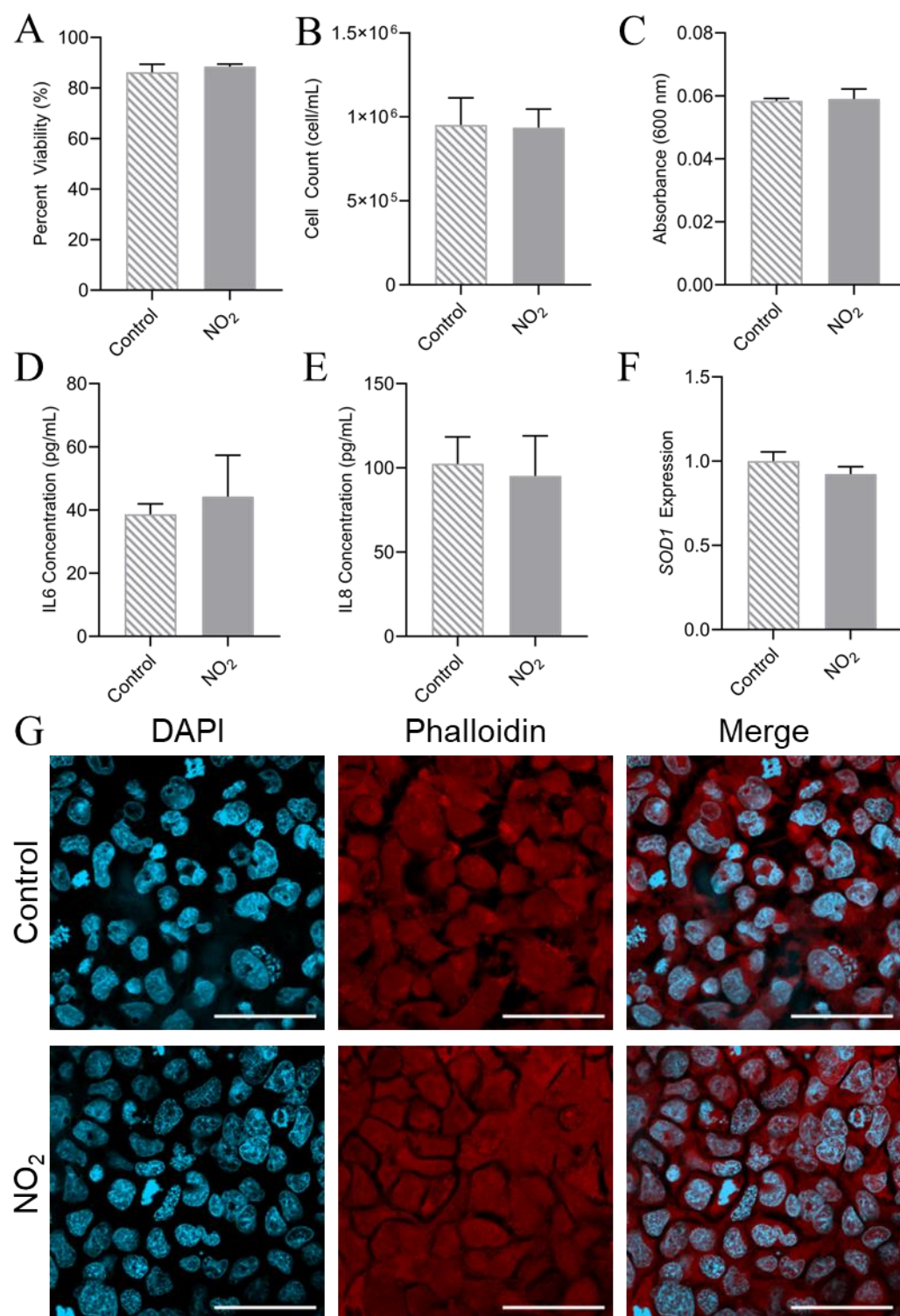


**Figure 6.3** A) Viability, B) total cell count, C) barrier integrity, D) IL6 concentration, E) IL8 concentration and F) SOD1 expression of NCI-H441 monocultures exposed to  $\text{NO}_2$  (5 ppm) for 4 hours. Toxicological analysis was undertaken 4 hours after the end of exposure. Bars represent the mean of 3 replicates with significance assessed using an unpaired *t* test. G) shows confocal imaging of these cultures staining for nucleus (blue) and cytoskeleton (red). 630x magnification, scale bar = 50  $\mu\text{m}$ . Data was assessed for

Preliminary studies investigated an acute, high concentration (5 ppm) of NO<sub>2</sub>. The exposure lasted 4 hours, and an endpoint assessment was conducted 4 hours post-exposure (based on Mirowsky et al. 2016), as the highest oxidative stress effect within human bronchial epithelial cells was reported at this time point. This exposure utilised a monoculture of NCI-H441 cells.

The acute NO<sub>2</sub> exposure did not significantly alter viability, which was above 80% for both exposed and control ( $p > 0.05$ ). The total cell count, membrane permeability, pro-inflammatory state or *SOD1* expression were also unchanged by NO<sub>2</sub> exposure ( $p > 0.05$ ). Confocal imaging revealed, however, that there are morphological changes in NCI-H441 exposed to NO<sub>2</sub>, where the cells appear more spread-out and mosaic in appearance compared to the incubator control cells (**Figure 6.3**).

Given the little quantitative effect observed in this initial study, a dose range of NO<sub>2</sub> was utilised at concentrations of 1, 2.5 and 5 ppm for a prolonged 24-hour exposure, with toxic assessment undertaken immediately following exposure (**Figure 6.4**). Here,

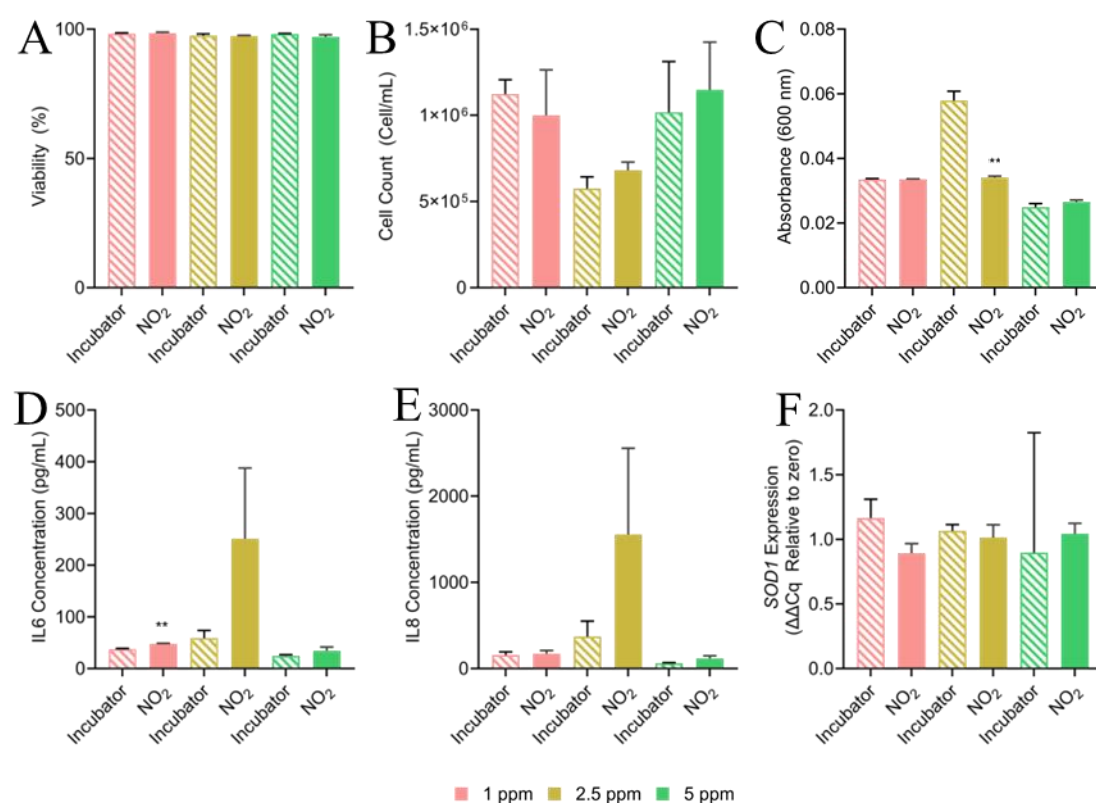


**Figure 6.4** A) Viability, B) total cell count, C) barrier integrity, D) IL6 concentration, E) IL8 concentration and F) SOD1 expression of NCI-H441 monocultures exposed to either 1, 2.5 or 5 ppm NO<sub>2</sub> for 24 hours. Toxicological analysis was undertaken immediately post-exposure. Each NO<sub>2</sub> exposure concentration were undertaken at different point in time so have a respective incubator control. Bars represent the mean of 3 replicates with significance assessed using unpaired *t* tests to compare NO<sub>2</sub> exposures to relevant control exposures. \*  $p \leq 0.05$ , \*\*  $p \leq 0.01$ , \*\*\*  $p \leq 0.001$ , \*\*\*\*  $p \leq 0.0001$ .



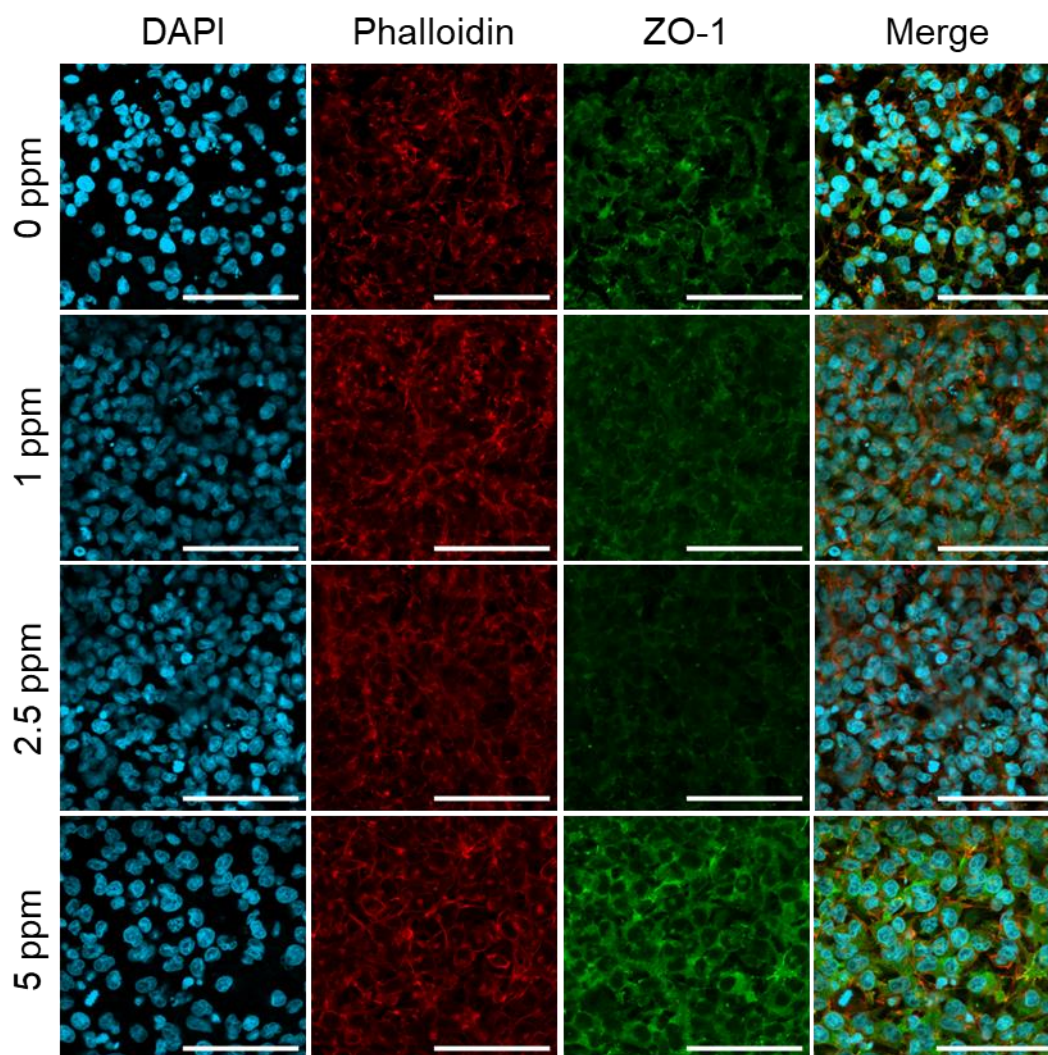


**Figure 6.5** Morphological analysis of NCI-H441 monocultures exposed to either 1, 2.5 or 5 ppm NO<sub>2</sub> for 24 hours. Cells were fixed immediately post-exposure. Fluorescence shows nucleus (blue), cytoskeleton (red) and ZO-1/tight junctions (green). 400x magnification, scale bar = 100  $\mu$ m.

it was found that although there were no changes in viability or total cell count at any concentration ( $p > 0.05$ ), however, there was a significant increase in barrier function at the 2.5 ppm exposure concentration ( $p < 0.01$ ), though, a high negative control absorbance cannot be rule out due to the increased absorbance compared to controls of other exposure concentrations. Further, the NCI-H441 cultures released significantly more IL6 at 1 ppm NO<sub>2</sub> ( $p < 0.01$ ), though IL8 release and *SOD1* expression were unchanged ( $p > 0.05$ ). Confocal imaging reveals morphological changes in the cell shape, which is especially visible with phalloidin stain, which shows rounding of the cell as the NO<sub>2</sub> concentration increases. Further, ZO-1 localisation changes as a response to NO<sub>2</sub> exposure, where the unexposed cells show areas of high and low ZO-1 staining, and exposed NCI-H441 appears to possess ZO-1 evenly distributed throughout the cell (**Figure 6.5**).

### 6.3.2 hAELVi Response to Nitrogen Dioxide Exposure

Given that ATI are responsible for gas exchange within an *in vivo* system, it was hypothesized that the hAELVi cells could be more impacted by NO<sub>2</sub> exposure than NCI-H441 cells. Therefore, these cells were also utilised in a dose-finding study using concentrations of 1, 2.5 and 5 ppm for 24 hours, with toxic assessment undertaken immediately following exposure (**Figure 6.6**). NO<sub>2</sub> exposure did not alter cell viability or total cell count at any concentration ( $p > 0.05$ ). NO<sub>2</sub> exposure caused an increase in IL8 presence within the supernatant (at 2.5 ppm –  $p < 0.05$ ). NO<sub>2</sub> exposure did not alter barrier function, nor did it alter IL6 release or SOD1 expression ( $p > 0.05$ ).

Confocal imaging of hAELVi cells exposed to NO<sub>2</sub> reveals that phalloidin staining, which is usually peripheral in these cells, becomes more intense as the concentration of NO<sub>2</sub> increases. Also, ZO-1 staining intensity increases with NO<sub>2</sub> and becomes less evenly distributed, with areas of higher fluorescence (especially visible at 1 ppm) (**Figure 6.7**).

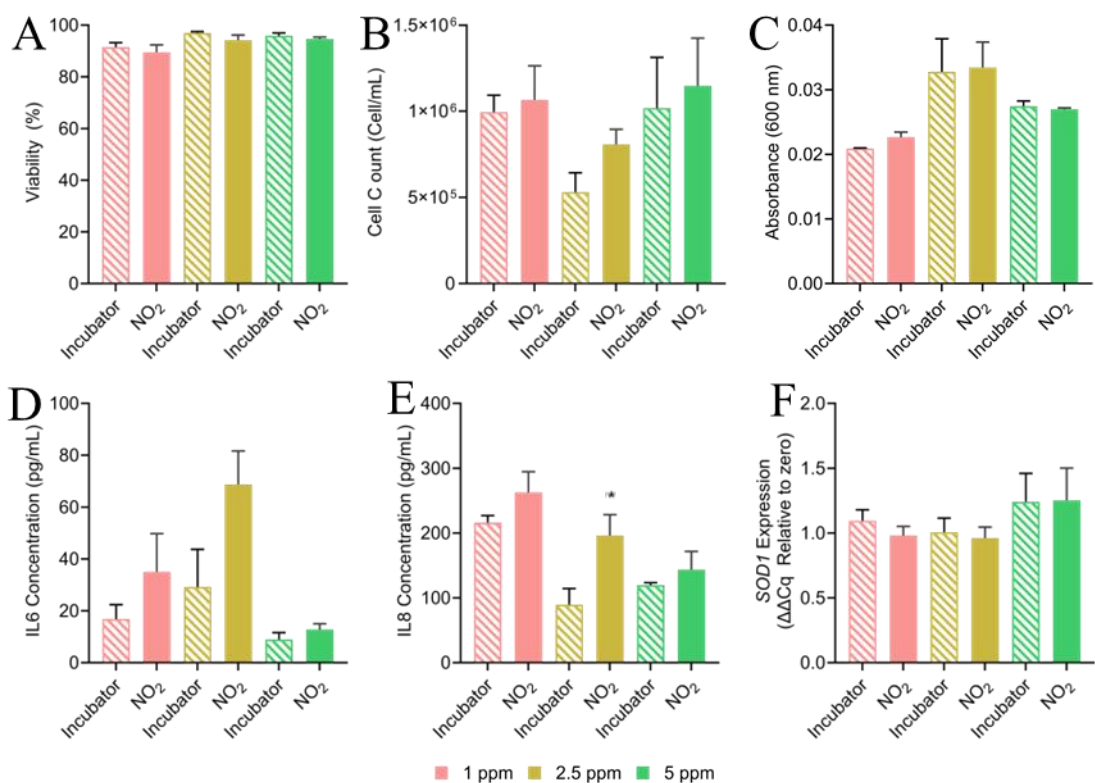


**Figure 6.6** A) Viability, B) total cell count, C) barrier integrity, D) IL6 concentration, E) IL8 concentration and F) SOD1 expression of hAELVi monocultures exposed to either 1, 2.5 or 5 ppm NO<sub>2</sub> for 24 hours. Toxicological analysis was undertaken immediately post-exposure. Each NO<sub>2</sub> exposure concentration were undertaken at different point in time so have a respective incubator control. Bars represent the mean of 3 replicates with significance assessed using unpaired *t* tests to compare NO<sub>2</sub> exposures to relevant control exposures. \*  $p \leq 0.05$ , \*\*  $p \leq 0.01$ , \*\*\*  $p \leq 0.001$ , \*\*\*\*  $p \leq 0.0001$ .

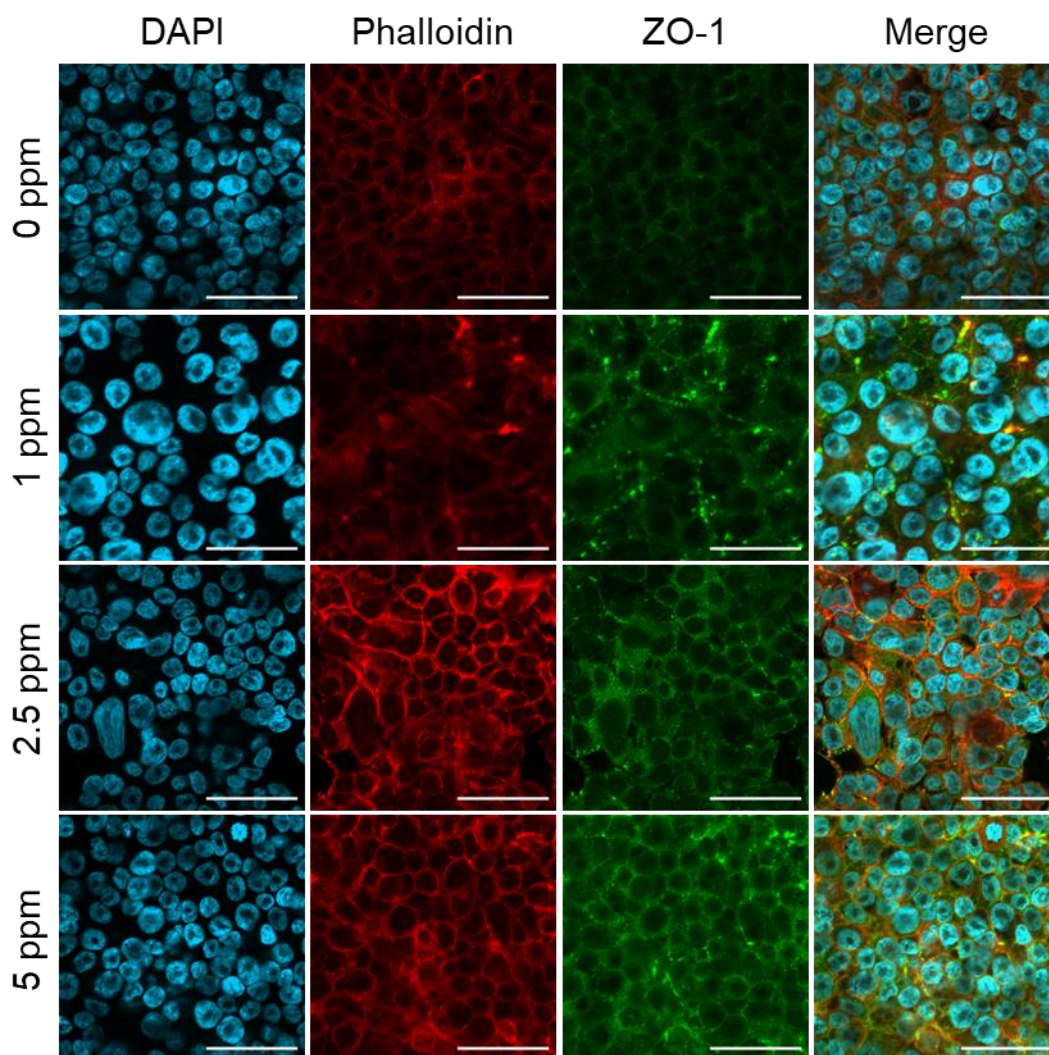


**Figure 6.7** Morphological analysis of hAELVi monocultures exposed to either 1, 2.5 or 5 ppm NO<sub>2</sub> for 24 hours. Cells were fixed immediately post-exposure. Fluorescence shows nucleus (blue), cytoskeleton (red) and ZO-1/tight junctions (green). 400x magnification, scale bar = 100  $\mu$ m.

### 6.3.3 Alveolar Triple Cell Co-Culture Response to Nitrogen Dioxide Exposure

The triple cell co-culture (detailed in Chapter 3) was utilised within the same exposure set-up, using NO<sub>2</sub> concentrations of 1, 2.5 and 5 ppm for 24-hour exposures. Using this model, viability and total cell count remained unchanged following NO<sub>2</sub> exposure ( $p > 0.05$ ) (**Figure 6.8**). Barrier function was observed to become stronger following NO<sub>2</sub> exposure at all concentrations, though this was not dose-dependent and significance was only reached at 2.5 ppm ( $p < 0.01$ ). In contrast to what was observed



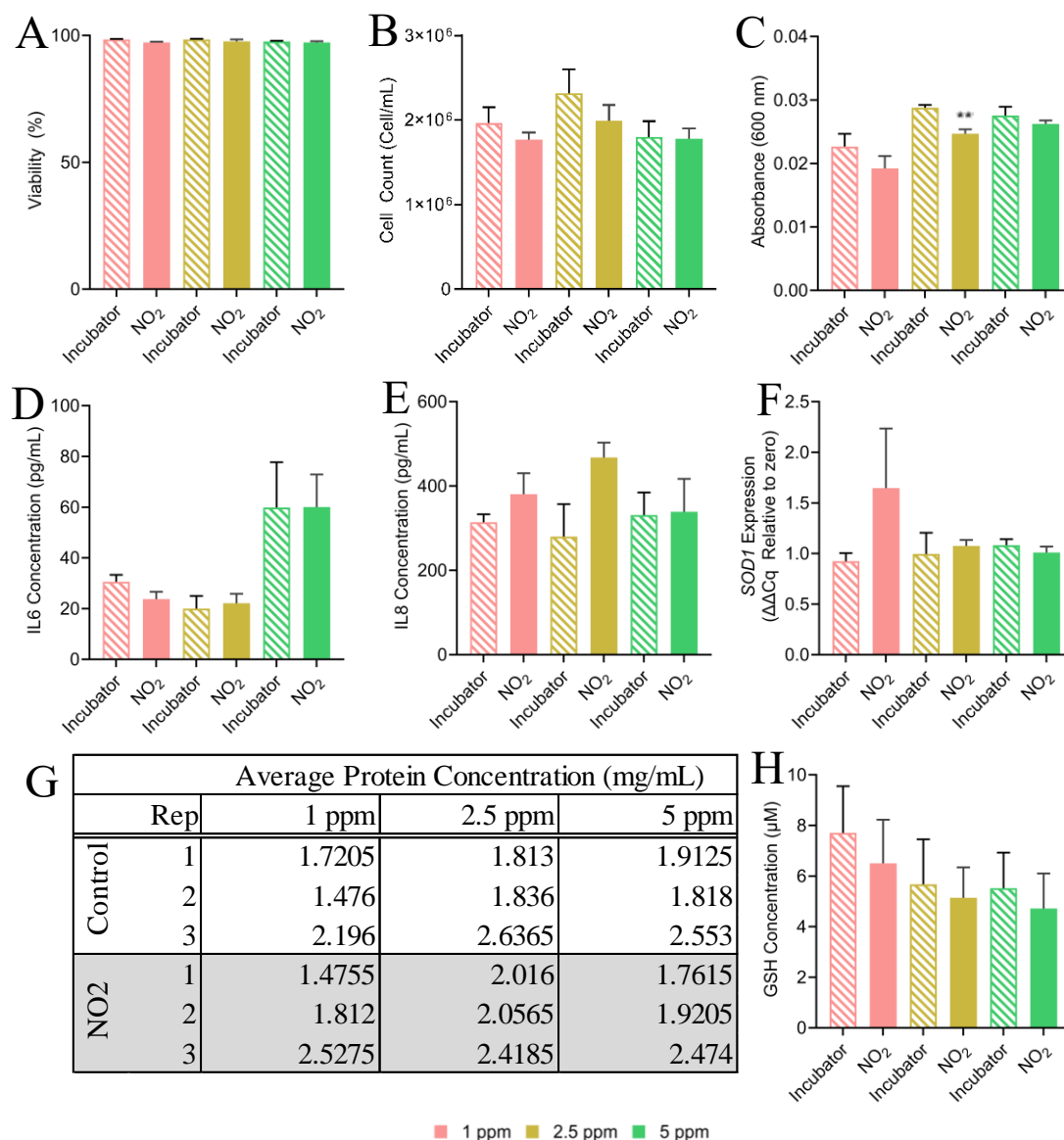


**Figure 6.8** A) Viability, B) total cell count, C) barrier integrity, D) IL6 concentration, E) IL8 concentration, F) SOD1 expression, G) protein concentration and H) GSH concentration (standardised against the protein concentration) of alveolar triple cell co-cultures exposed to either 1, 2.5 or 5 ppm NO<sub>2</sub> for 24 hours. Toxicological analysis was undertaken immediately post-exposure. Each NO<sub>2</sub> exposure concentration were undertaken at different point in time so have a respective incubator control. Bars represent the mean of 3 replicates with significance assessed using unpaired *t* tests to compare NO<sub>2</sub> exposures to relevant control exposures. \* *p* ≤ 0.05, \*\* *p* ≤ 0.01, \*\*\* *p* ≤ 0.001, \*\*\*\* *p* ≤ 0.0001.

in the same experimental set-up using monocultures of either NCI-H441 or hAELVi cells, the triple cell co-culture did not augment its release of IL6 following NO<sub>2</sub> exposure, though IL8 was increased approaching significance at 2.5 ppm (*p* < 0.1). SOD1 expression and GSH concentration were not altered by NO<sub>2</sub> exposure (*p* > 0.05).

NO<sub>2</sub> exposure does not clearly impact cell morphology shown by the phalloidin staining. Neither CD11 $\beta$  nor ZO-1 staining appear to be altered by NO<sub>2</sub> exposure (Figure 6.9).

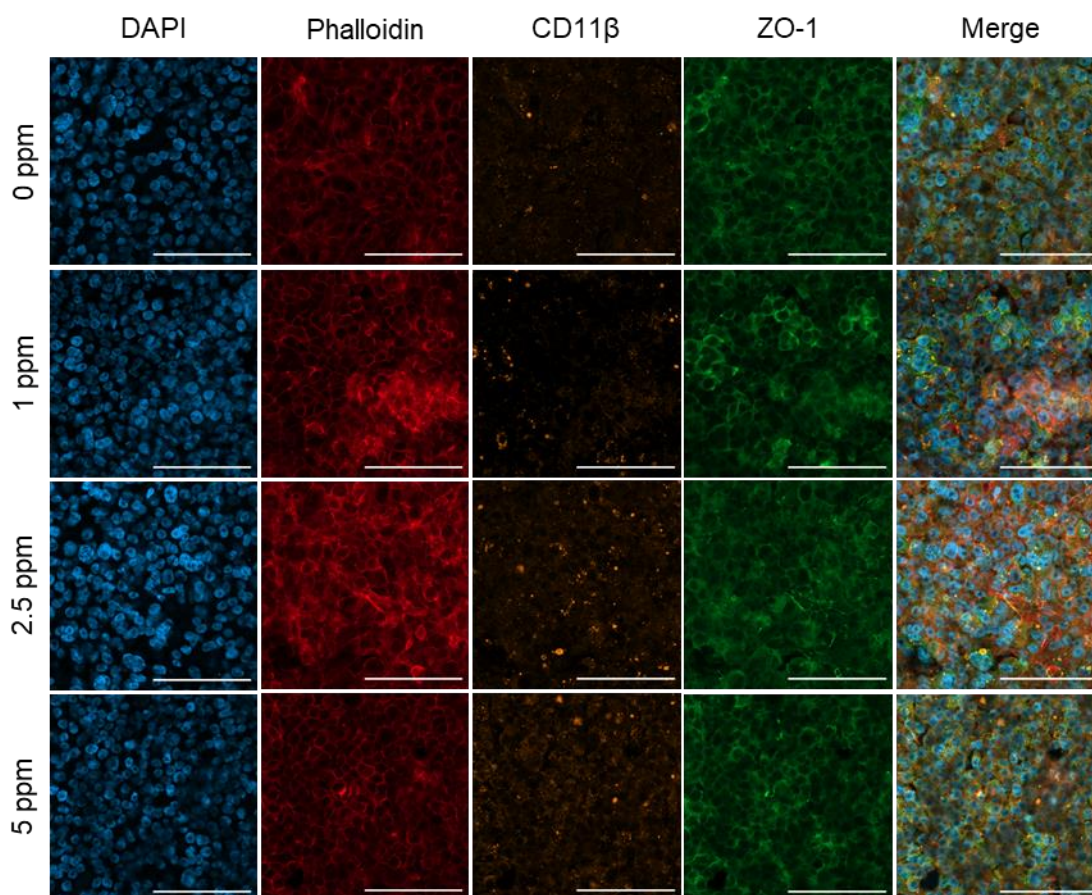


**Figure 6.9** Morphological analysis of triple cell co-cultures exposed to either 1, 2.5 or 5 ppm NO<sub>2</sub> for 24 hours. Cells were fixed immediately post-exposure. Fluorescence shows nucleus (blue), cytoskeleton (red) and ZO-/tight junctions (green). 400x magnification, scale bar = 100  $\mu$ m.

#### 6.3.4 Assessing for Interaction Between Nitrogen Dioxide and Negative Particle Controls

Prior to combining NO<sub>2</sub> and VitroCell® exposures, the assessment of exposure of cells to a non-particle containing aerosol (NaCl spiked H<sub>2</sub>O) was conducted to assess for any interactions that may occur as NO<sub>2</sub> is known to react with NaCl within the air (or aerosol) to form nitrosyl chloride (Schroeder & Urone, 1974). NCI-H441 monocultures were then exposed to NaCl spiked saline at a 0.009% (NaCl) or 0.0009%

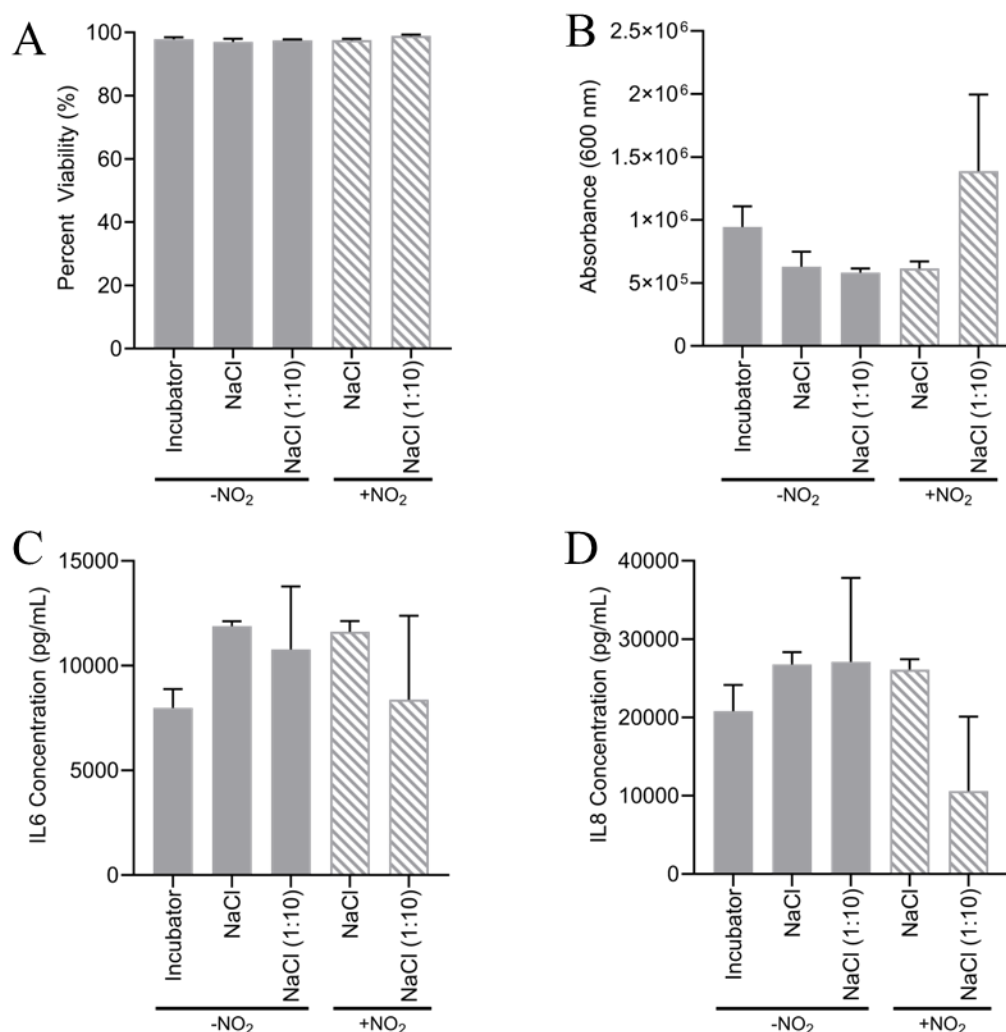


**Figure 6.10** A) Viability, B) total cell count, C) barrier integrity, D) IL6 concentration and E) IL8 concentration of alveolar NCI-H441 monolayers exposed to either NaCl at 0.009%, or 0.0009% (1:10) via VitroCell® Cloud, then either incubated in 5 ppm NO<sub>2</sub> or not for 24 hours. Toxicological analysis was undertaken immediately post-exposure. Bars represent the mean of 3 replicates with significance assessed using a one-way ANOVA utilising a Dunnetts post hoc test (compared to the incubator control). \*  $p \leq 0.05$ , \*\*  $p \leq 0.01$ , \*\*\*  $p \leq 0.001$ , \*\*\*\*  $p \leq 0.0001$ .

(NaCl 1:10) concentration and then assessed with and without NaCl exposure. There were no alterations in viability in any exposures compared to the incubator control, with viability remaining above 90% in all cases. Monolayer barrier function was seen unchanged with NaCl, NaCl 1:10 and NaCl + NO<sub>2</sub>. The pro-inflammatory response was unchanged in all exposures too, shown through similar levels of IL6 and IL8 ( $p > 0.05$ ) (Figure 6.10).

### 6.3.5 NCI-H441 Co-Exposure to Printex® 90 and Nitrogen Dioxide

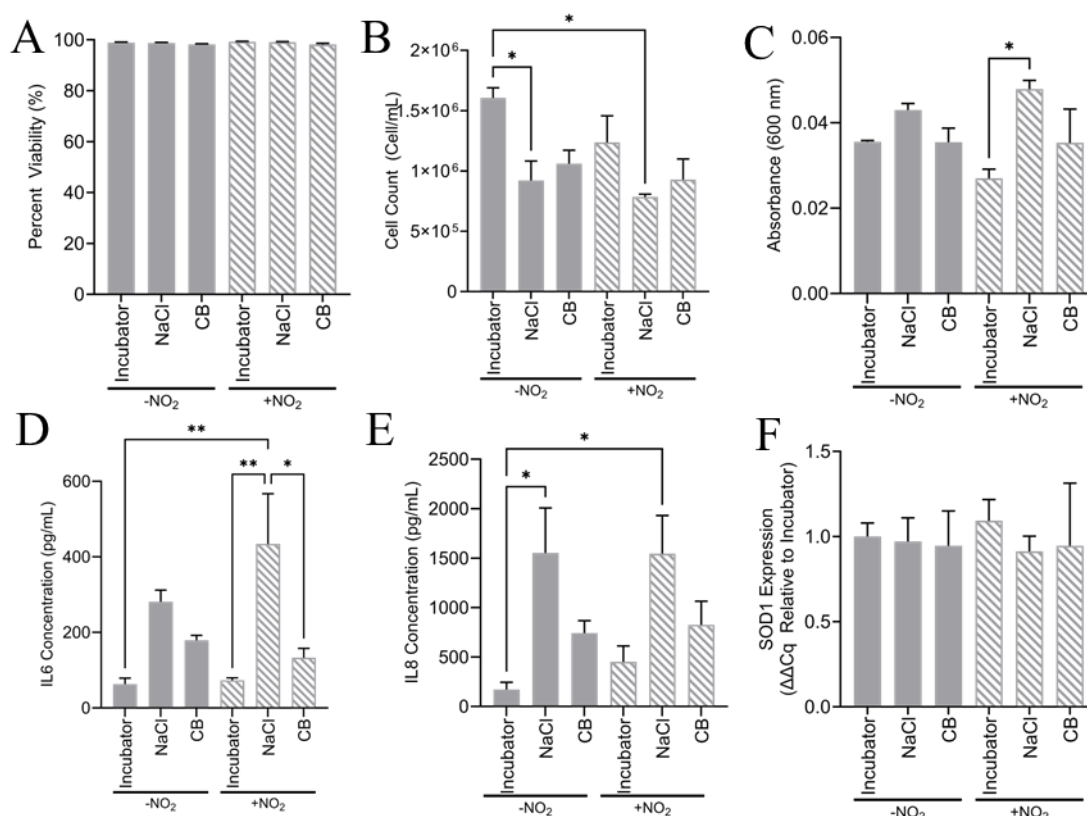


**Figure 6.11** A) Viability, B) total cell count, C) barrier integrity, D) IL6 concentration, E) IL8 concentration and F) SOD1 expression of alveolar NCI-H441 monocultures exposed to either CB (780 ng/cm²) then either incubated in 5 ppm NO₂, or not, for 24 hours. Toxicological analysis was undertaken immediately post-exposure. Bars represent the mean of 3 replicates with significance assessed using a one-way ANOVA utilising a Tukeys post hoc test. \*  $p \leq 0.05$ , \*\*  $p \leq 0.01$ , \*\*\*  $p \leq 0.001$ , \*\*\*\*  $p \leq 0.0001$ .

Initial co-exposure studies utilised an NCI-H441 monoculture, which was exposed to either NO₂ (5 ppm), CB (780 ng/cm²) or both pollutants in co-exposure. None of the exposure conditions significantly altered viability ( $p > 0.05$ ). The incubator control had significantly more cells than the NaCl and NaCl + NO₂ controls however ( $p < 0.05$ ) (**Figure 6.11**). When assessing the barrier function of NCI-H441 cells exposed to CB ± NO₂, it was interesting to find that the NaCl + NO₂ exposure had a reduction in barrier function ( $p < 0.05$ ). When assessing the pro-inflammatory response to CB ± NO₂ exposures, the results were varied. The NaCl exposure control induced maximal IL6 release, with this effect augmented when NaCl was co-exposed with NO₂ ( $p < 0.05$ ) CB exposure with or without NO₂ did not significantly alter IL6 or IL8 release ( $p > 0.05$ ). NO₂ only exposure did not alter IL6 release ( $p > 0.05$ ), which remained at a baseline level comparable to the incubator control. IL8 release showed similar findings to that of IL6, with maximal IL8 release occurring when NCI-H441 cells were exposed to NaCl in the presence of or without NO₂ ( $p < 0.0001$ ). CB did not induced



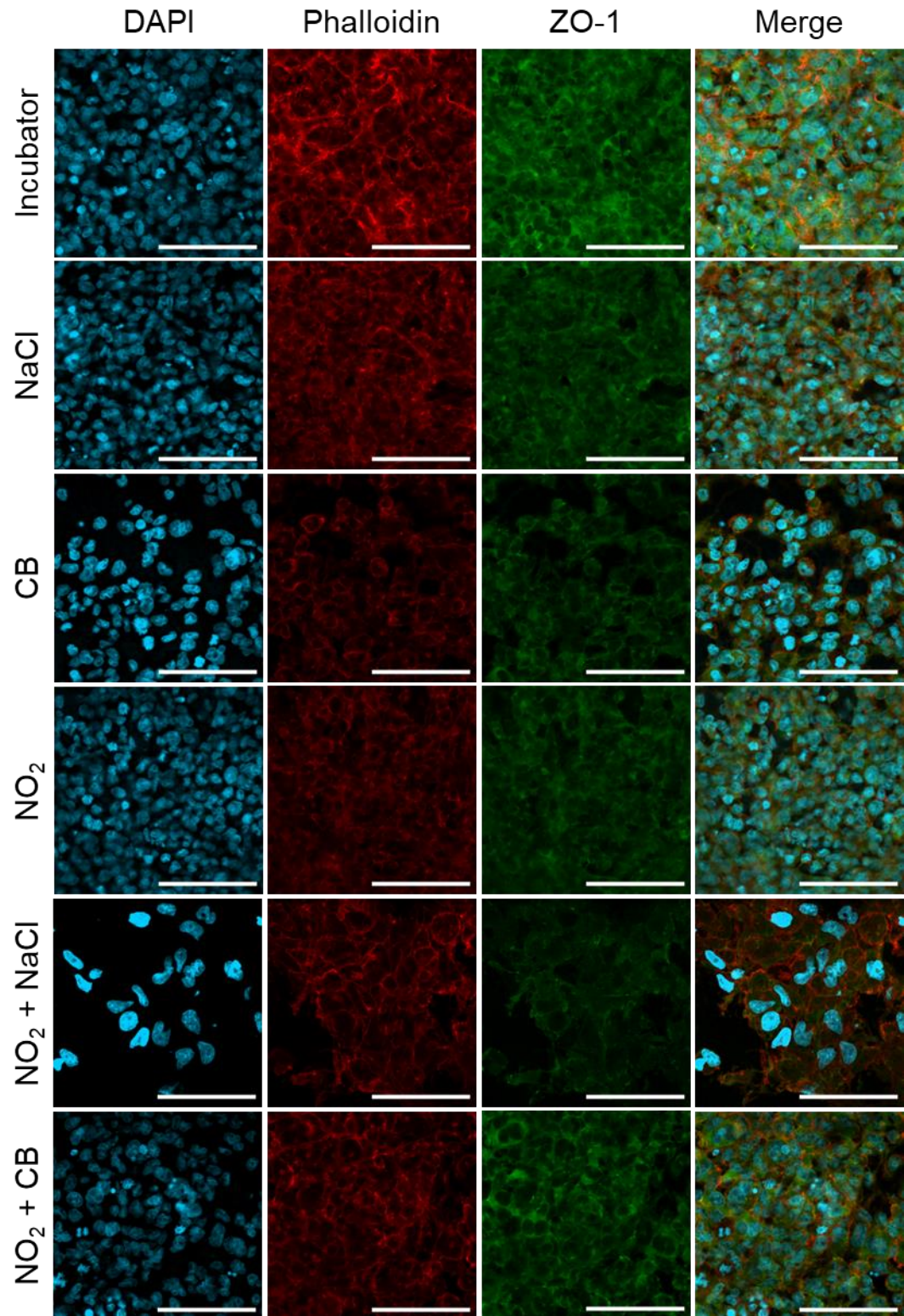


**Figure 6.12** Morphological analysis of NCI-H441 monocultures exposed to 780 ng/cm<sup>2</sup> CB  $\pm$  NO<sub>2</sub> at 5 ppm. Cells were fixed immediately post-exposure. Fluorescence shows nucleus (blue), cytoskeleton (red) and ZO-1/tight junctions (green). 400x magnification, scale bar = 100  $\mu$ m.

a significant release of IL8. RT-qPCR analysis reveals that *SOD1* expression is not significantly ( $p > 0.05$ ) altered by NO<sub>2</sub>  $\pm$  CB exposure.



Staining NCI-H441 for nuclei, cytoskeleton, and ZO-1 showed similar findings to those in the NO<sub>2</sub> dose-response within NCI-H441 cells, where those cells that were exposed to NO<sub>2</sub> appear more organised and rounder in appearance shown through the phalloidin staining, compared to the incubator and NaCl controls which appear more disorganised and less rounded. Cultures exposed to CB seem to have more gaps between cells, disrupting the monolayer compared to the control, though this is especially noticeable in the NaCl + NO<sub>2</sub> exposed cells (**Figure 6.12**).

### 6.3.6 Triple Cell Co-Culture Co-Exposure to Printex® 90 and Nitrogen Dioxide

A similar approach of CB ± NO<sub>2</sub> within the triple cell co-culture, using 780 ng/cm<sup>2</sup> of CB. However, this time, NO<sub>2</sub> was used at a concentration of 2.5 ppm, as this is the concentration where the highest effects were seen in the NO<sub>2</sub> dose response (**Figure 6.13**). CB is seen to induce significant cytotoxicity in single and co-pollutant exposures ( $p < 0.05$ ) with NO<sub>2</sub>, though there seems to be no synergistic or additive influence of NO<sub>2</sub>. Neither NaCl nor NO<sub>2</sub> induced cytotoxicity and had viabilities comparable to that of the incubator control ( $p > 0.05$ ). The total cell count were unchanged throughout the exposures ( $p < 0.05$ ). The exposures did not alter barrier function in any instance

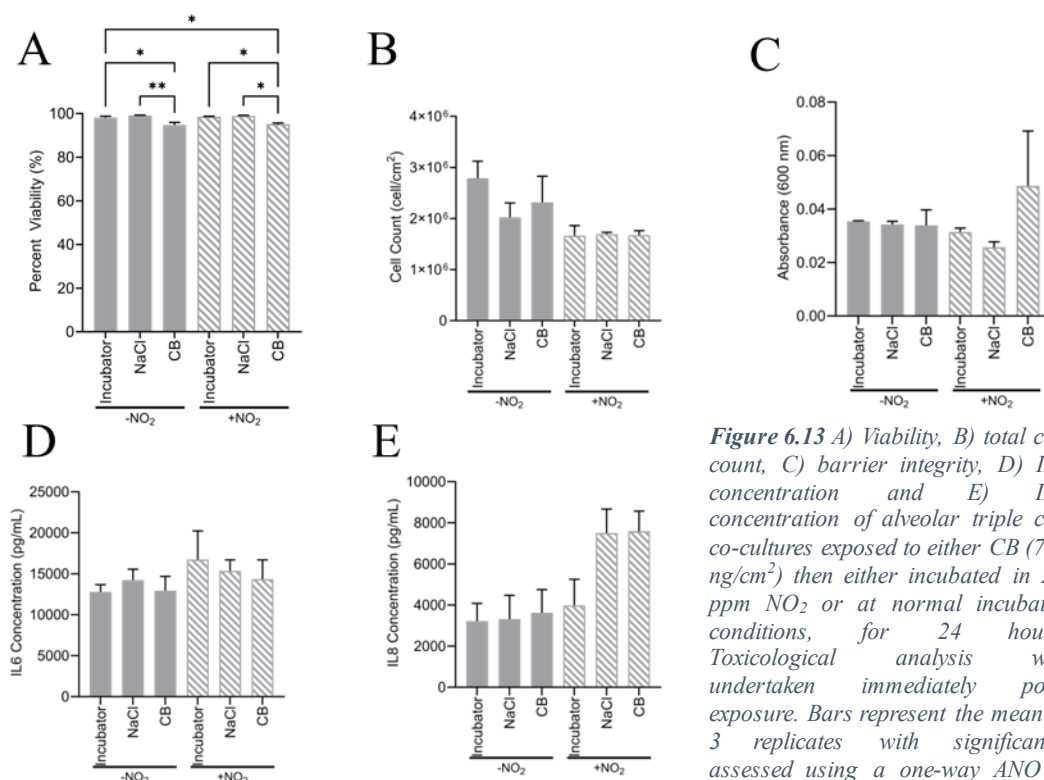


**Figure 6.13** A) Viability, B) total cell count, C) barrier integrity, D) IL6 concentration and E) IL8 concentration of alveolar triple cell co-cultures exposed to either CB (780 ng/cm<sup>2</sup>) then either incubated in 2.5 ppm NO<sub>2</sub> or at normal incubator conditions, for 24 hours. Toxicological analysis was undertaken immediately post-exposure. Bars represent the mean of 3 replicates with significance assessed using a one-way ANOVA utilising a Tukeys post hoc test. \*  $p \leq 0.05$ , \*\*  $p \leq 0.01$ , \*\*\*  $p \leq 0.001$ , \*\*\*\*  $p \leq 0.0001$ .

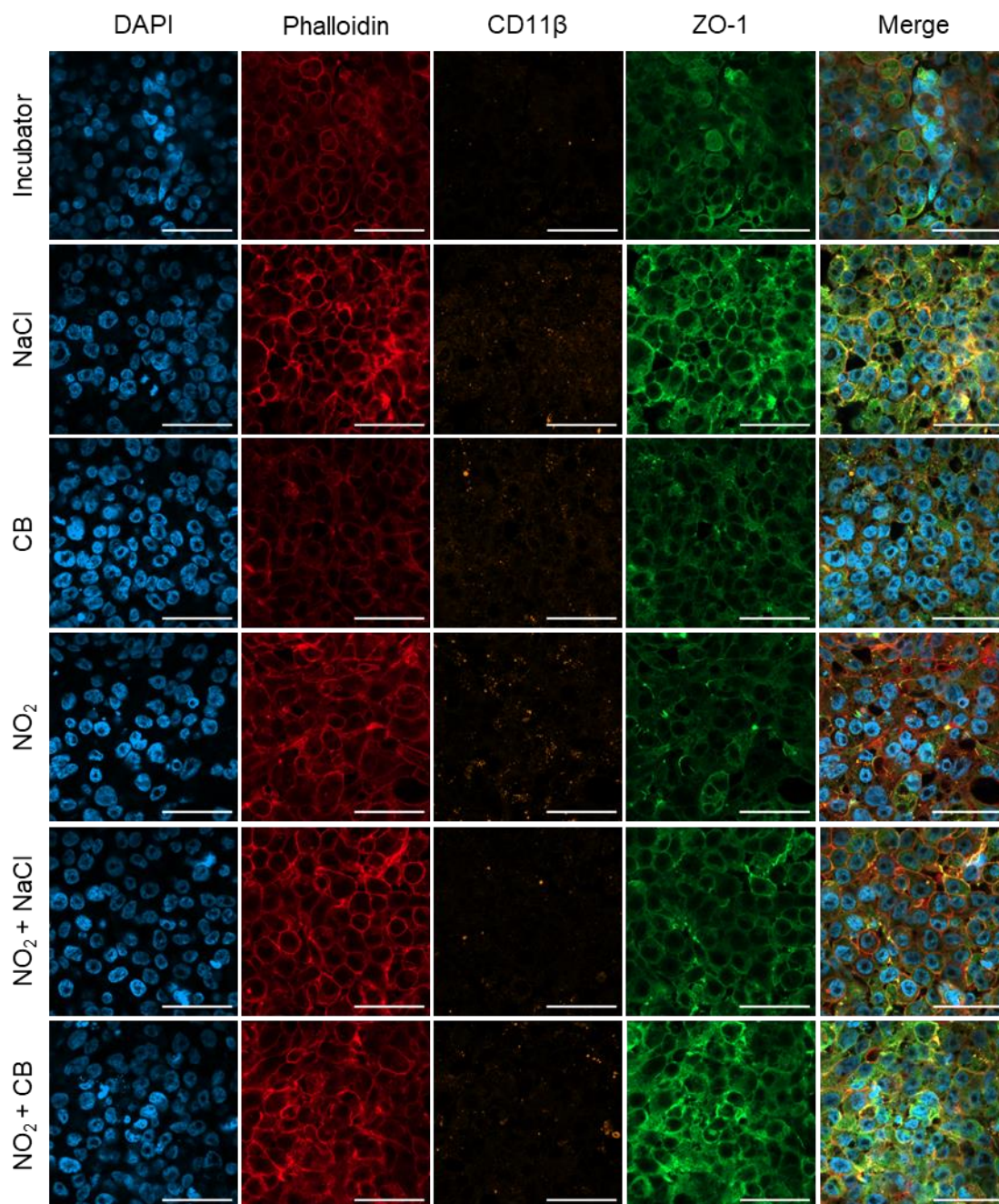


**Figure 6.14** Morphological analysis of triple cell co-cultures exposed to  $780 \text{ ng/cm}^2 \text{ CB} \pm \text{NO}_2$  at 2.5 ppm. Cells were fixed immediately post-exposure. Fluorescence shows nucleus (blue), cytoskeleton (red), CD11 $\beta$  (orange) and ZO-1/tight junctions (green). 400x magnification, scale bar =  $100 \mu\text{m}$ .

( $p > 0.05$ ). In terms of pro-inflammatory response, single pollutant exposures without  $\text{NO}_2$  did not induce a response. When cultures were exposed to  $\text{NO}_2$ , regardless of co-exposure with CB, IL6 and IL8 release were unchanged.

Confocal imagery reveals that the culture monolayer stays confluent following all exposures; however, the cytoskeleton becomes disorganised following CB exposures ( $\pm \text{NO}_2$ ) compared to control exposures where cytoskeleton staining is mainly localised to the cell periphery. Minimal CD11 $\beta$  staining is observed in the incubator control. All

other exposures show stronger staining with more CD11 $\beta$  positive vesicular-like structures, with these structures appearing larger in the NO<sub>2</sub>-exposed cultures. ZO-1 is mainly localised to the plasma membrane of the cells, with some intracellular staining present in the form of vesicular-like structures. Following CB and all NO<sub>2</sub> exposures, ZO-1 is not notably altered (**Figure 6.14**).

### **6.3.7 Triple Cell Co-Culture Co-Exposure to Indoor/Urban Dust and Nitrogen Dioxide**

Given that CB is used as a surrogate model particle of PM, there was a desire to assess co-exposure of NO<sub>2</sub> with particles in which co-exposure would occur in ambient air. Therefore, the relevant triple cell co-culture was co-exposed with NO<sub>2</sub> and 1649b or 2583. Indoor dust was found to reduce cell viability, though this only reached significance when co-exposed with NO<sub>2</sub> ( $p < 0.05$ ) (**Figure 6.15**). Urban dust did not significantly alter viability in single-pollutant exposures, nor when co-exposed with NO<sub>2</sub> (though, is approaching significance compared to the NO<sub>2</sub> single-pollutant exposure  $p < 0.1$ ). Cell count was seen to be significantly increased ( $p < 0.05$ ) in the NaCl only exposure with all other exposures showed cell counts similar to those of the incubator control. NO<sub>2</sub> exposures, regardless of co-exposure, caused an increase in barrier function, though, there was no indication of any modulation by PM co-exposure ( $p < 0.05$ ).

IL6 and IL8 release were not altered by NO<sub>2</sub> exposure with or without the presence of 1649b or 2583 ( $p > 0.05$ ).

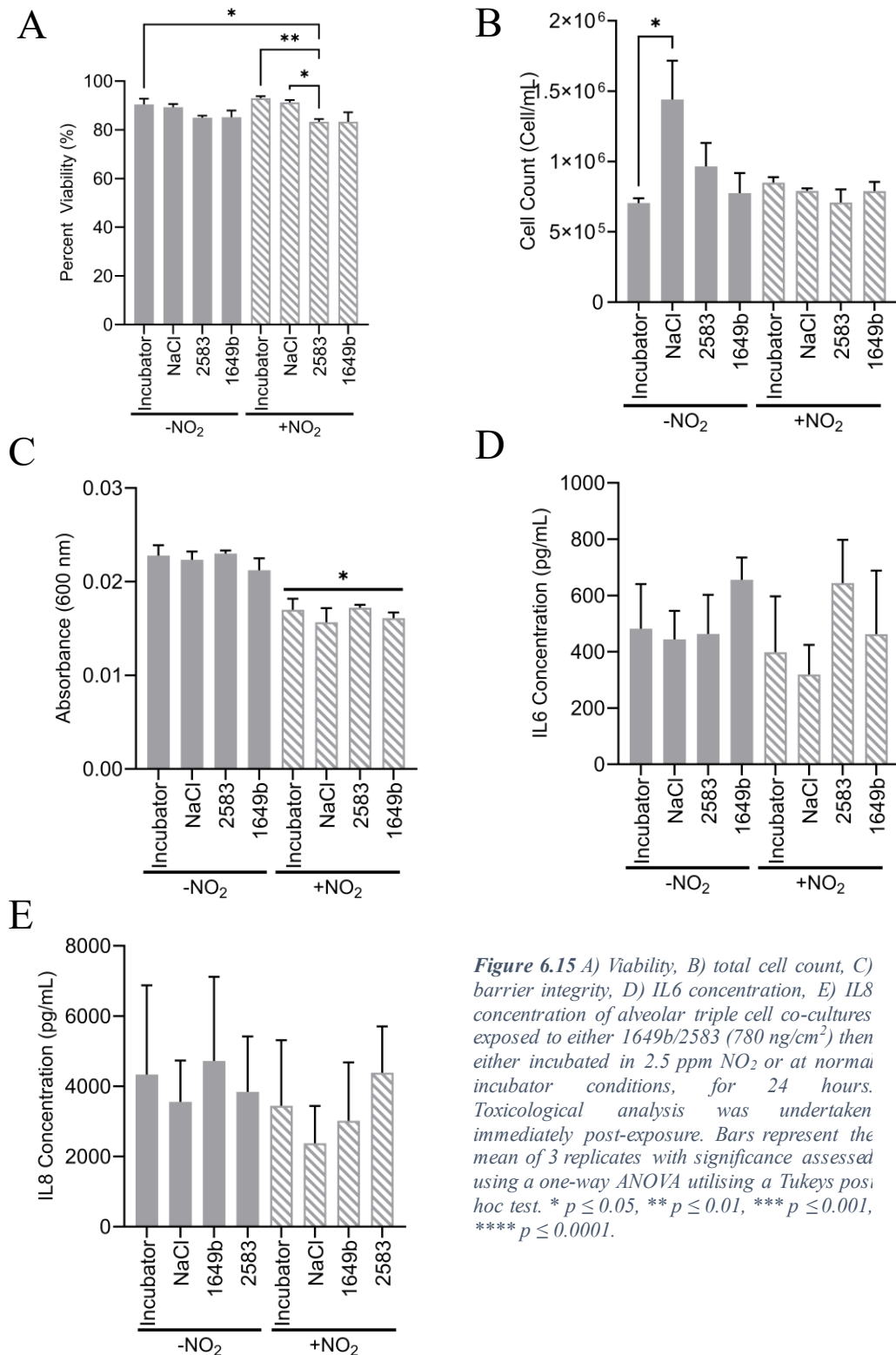


**Figure 6.15** A) Viability, B) total cell count, C) barrier integrity, D) IL6 concentration, E) IL8 concentration of alveolar triple cell co-cultures exposed to either 1649b/2583 (780 ng/cm<sup>2</sup>) then either incubated in 2.5 ppm NO<sub>2</sub> or at normal incubator conditions, for 24 hours. Toxicological analysis was undertaken immediately post-exposure. Bars represent the mean of 3 replicates with significance assessed using a one-way ANOVA utilising a Tukeys post hoc test. \*  $p \leq 0.05$ , \*\*  $p \leq 0.01$ , \*\*\*  $p \leq 0.001$ , \*\*\*\*  $p \leq 0.0001$ .

Neither 1649b and 2583 were found to alter ZO-1 localisation. NO<sub>2</sub> exposure, however, slightly reduced the appearance of vesicular CD11 $\beta$  in this instance however (Figure 6.16).



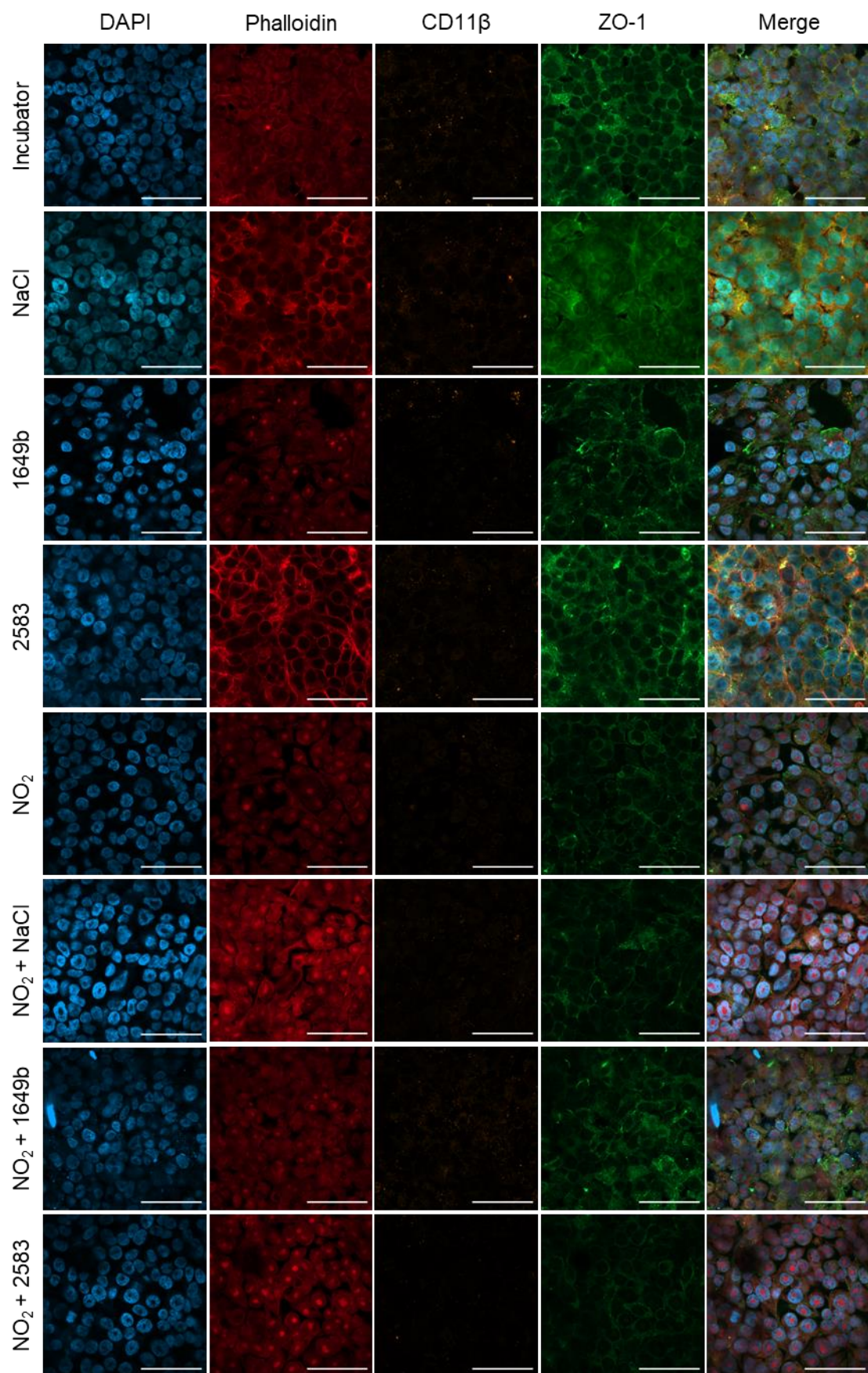


**Figure 6.16** Morphological analysis of triple cell co-cultures exposed to 780 ng/cm<sup>2</sup> 1649b/2583  $\pm$  NO<sub>2</sub> at 2.5 ppm. Cells were fixed immediately post-exposure. Fluorescence shows nucleus (blue), cytoskeleton (red), CD11 $\beta$  (orange), and ZO-/tight junctions (green). 400x magnification, scale bar = 100  $\mu$ m.

### 6.3.8 Triple Cell Co-Culture Co-Exposure to Diesel Emission Particles and Nitrogen Dioxide

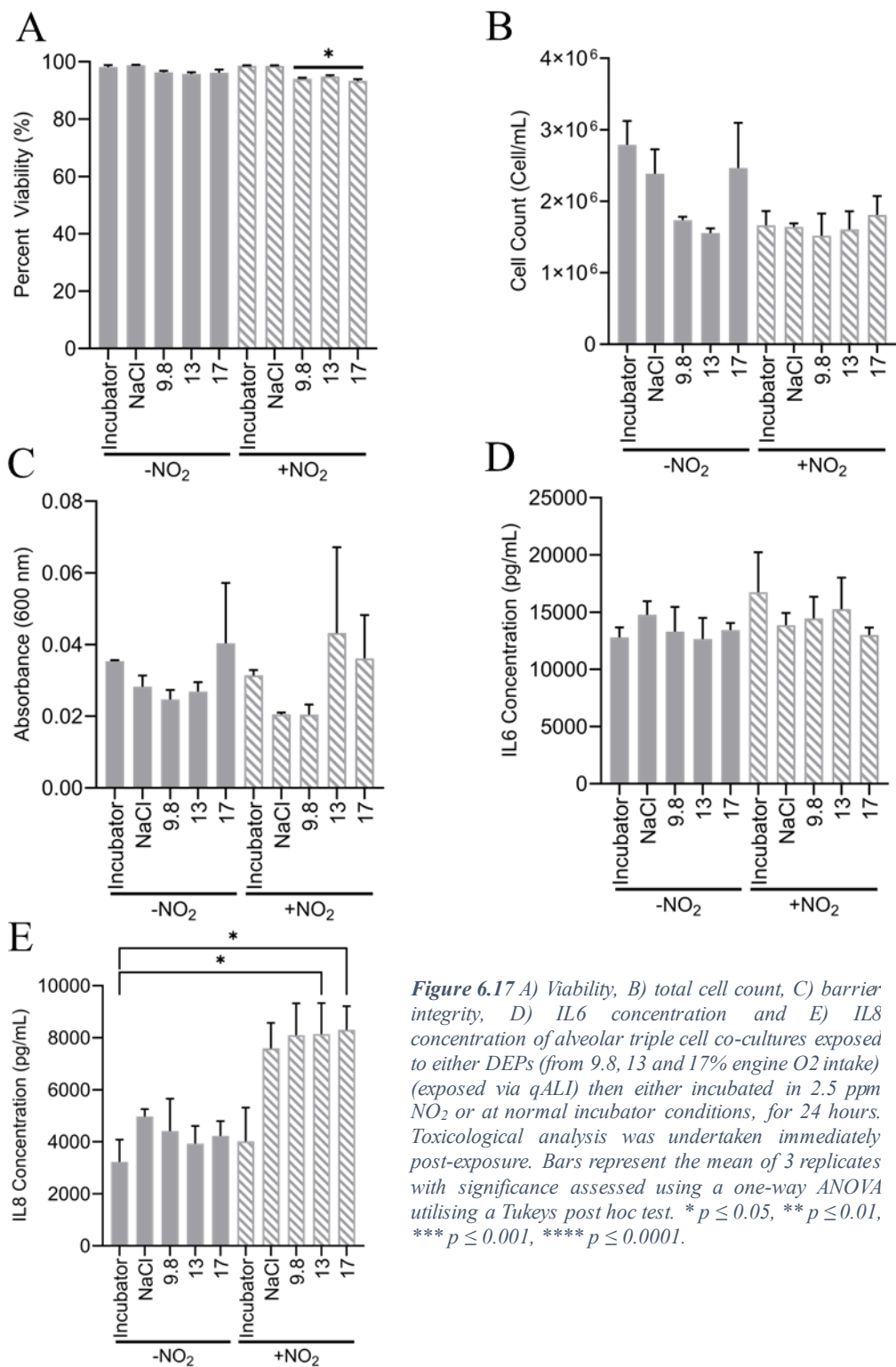


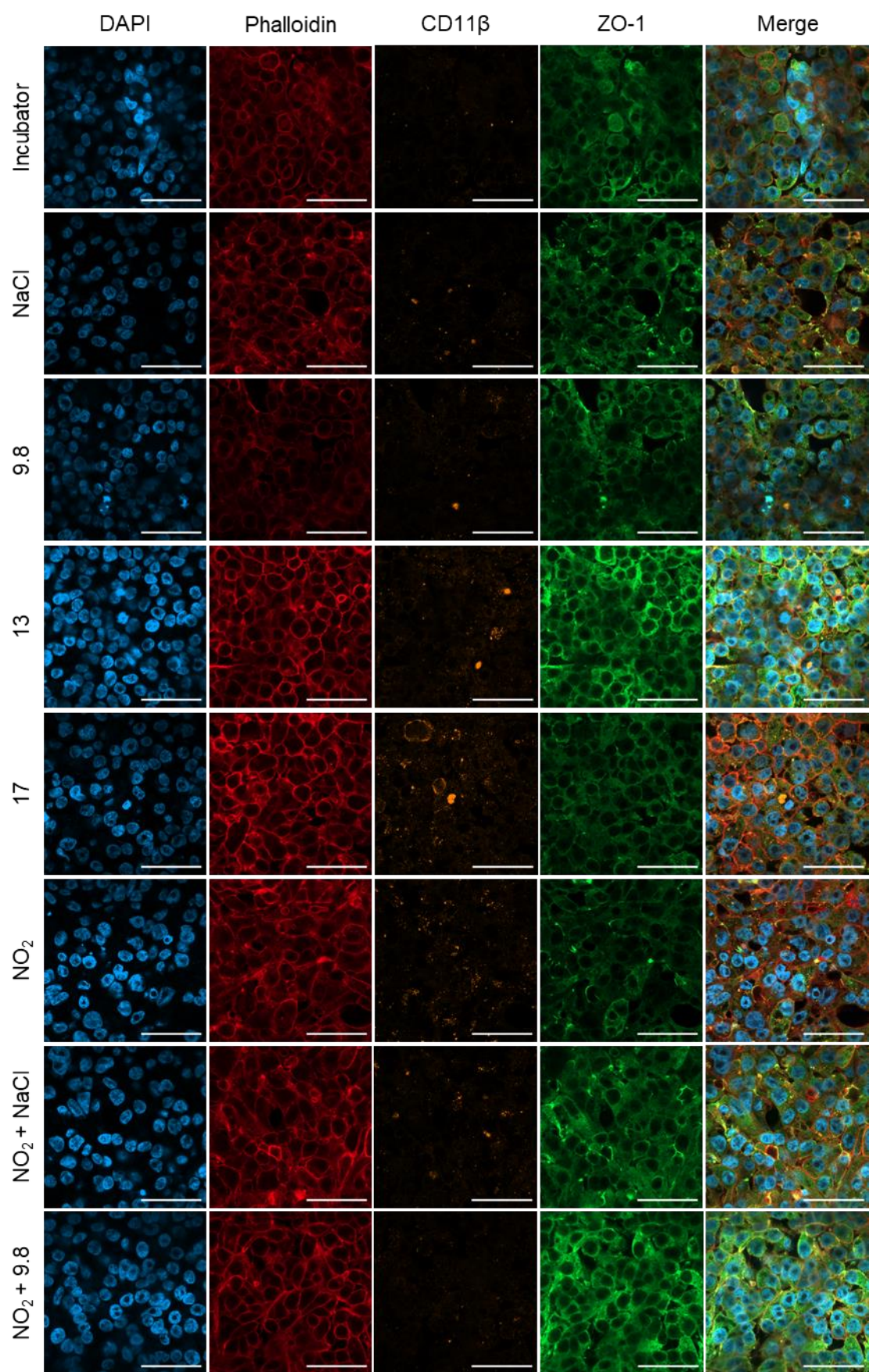
**Figure 6.17** A) Viability, B) total cell count, C) barrier integrity, D) IL6 concentration and E) IL8 concentration of alveolar triple cell co-cultures exposed to either DEPs (from 9.8, 13 and 17% engine O<sub>2</sub> intake) (exposed via qALI) then either incubated in 2.5 ppm NO<sub>2</sub> or at normal incubator conditions, for 24 hours. Toxicological analysis was undertaken immediately post-exposure. Bars represent the mean of 3 replicates with significance assessed using a one-way ANOVA utilising a Tukeys post hoc test. \*  $p \leq 0.05$ , \*\*  $p \leq 0.01$ , \*\*\*  $p \leq 0.001$ , \*\*\*\*  $p \leq 0.0001$ .

Given the limited mass of DEPs available, exposures of the triple culture with DEPs took place at the qALI prior to incubation with or without NO<sub>2</sub>. DEPs were found to significantly reduce viability compared to the incubator and NaCl controls, as well as NO<sub>2</sub> alone or NO<sub>2</sub> + NaCl ( $p < 0.05$ ). Cell counts between the exposures were not significantly different (**Figure 6.17**). Barrier function was also not significantly altered by DEP ± NO<sub>2</sub> exposure. NO<sub>2</sub> exposure did not significantly alter IL6 release ( $p > 0.05$ ). IL8 release, on the other hand, was significantly increased following NO<sub>2</sub> co-exposure with DEP 13% and 17% (compared to the incubator control –  $p < 0.05$ ) through, were not significantly different to the NaCl control –  $p > 0.05$ ).

Following NO<sub>2</sub> exposure, regardless of co-exposure, the cytoskeleton shows morphological changes to the cell within the triple cell co-culture, which appear larger and more irregular in shape, compared to the non-NO<sub>2</sub> exposed cells which appear more circular. Further, phalloidin staining is observed more across the entirety of the cell following all NO<sub>2</sub> exposures compared to non-NO<sub>2</sub> exposures, which have phalloidin staining mainly localised at the cell boundaries. All exposures increased the staining intensity of CD11β, which also formed large vesicular structures following both DEP and NO<sub>2</sub> exposure (**Figure 6.18**).

Given that many made in this data chapter, as with Chapter 5, the main effects of NO<sub>2</sub> exposure, and PM/NO<sub>2</sub> co-exposure have been outlined in Table 6.8 and 6.9, respectively.







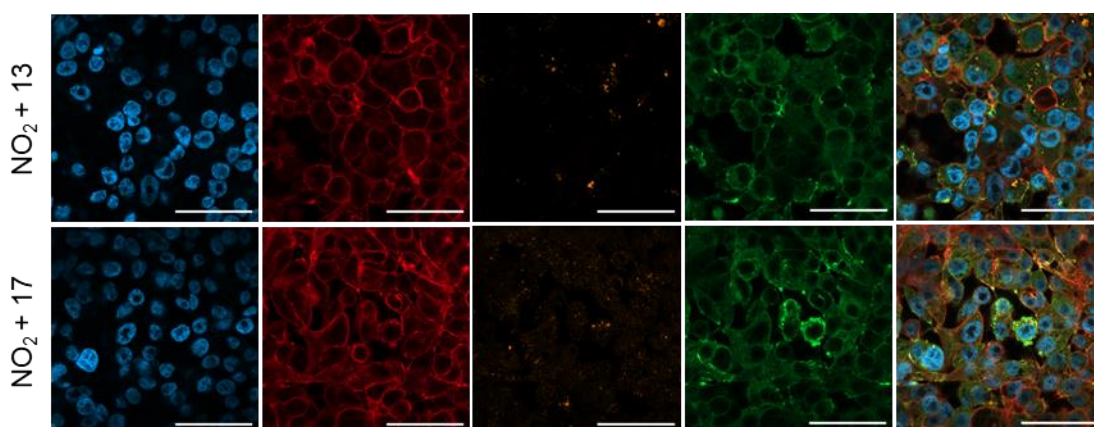


**Figure 6.18** (and previous page) Morphological analysis of triple cell co-cultures exposed to 780 ng/cm<sup>2</sup> DEPs (from 9.8, 13 and 17% engine O<sub>2</sub> intake) (exposed via qALI) ± NO<sub>2</sub> at 2.5 ppm. Cells were fixed immediately post-exposure. Fluorescence shows nucleus (blue), cytoskeleton (red), CD11β (orange) and ZO/tight junctions (green). 400x magnification, scale bar = 100 μm.

**Table 6.8** Summary of the main effects observed following NO<sub>2</sub> exposure within hAELVi cells, NCI-H441 cells or the alveolar triple cell co-culture.

	NO <sub>2</sub> Exposure		Viability	Barrier Function	IL6	IL8	SOD1
	ppm	Hours					
hAELVi	1	24	No change	No change	No change	No change	No change
	2.5	24	No change	No change	Increase	No change	No change
	5	24	No change	No change	No change	No change	No change
NCI-H441	1	24	No change	No change	Increase	No change	No change
	2.5	24	No change	Increase	No change	No change	No change
	5	4	No change	No change	No change	No change	No change
	5	24	No change	No change	No change	No change	No change
Triple Cell Co-Culture	1	24	No change	No change	No change	No change	No change
	2.5	24	No change	Increase	No change	Increase	No change
	5	24	No change	No change	No change	Increase	No change
				No change			
				Approaching significant change (p is between 0.05 and 0.1)			
				Statistically Significant Change			

**Table 6.9** Summary of the main effects observed on the triple cell co-culture following co-exposures of PM samples: CB, 1649, 2583 or DEPs with NO<sub>2</sub>.

PM	NO <sub>2</sub>	Viability	Barrier Function	IL6	IL8
CB	0 ppm	Decrease	No change	No change	No change
	2.5 ppm	Decrease	No change	No change	No change
1649b	0 ppm	No change	No change	No change	No change
	2.5 ppm	No change	Increase	No change	No change
2583	0 ppm	No change	No change	No change	No change
	2.5 ppm	No change	Increase	No change	No change
DEP 9.8%	0 ppm	Decrease	No change	No change	No change
	2.5 ppm	Decrease	No change	No change	No change
DEP 13%	0 ppm	Decrease	No change	No change	No change
	2.5 ppm	Decrease	No change	No change	No change
DEP 17%	0 ppm	Decrease	No change	No change	No change
	2.5 ppm	Decrease	No change	No change	No change
			No change		
			Approaching significant change (p is between 0.05 and 0.1)		
			Statistically Significant Change		

## 6.4 Discussion

This chapter aimed to compare toxicity induced by exposure to PM, NO<sub>2</sub>, or a combination of the two pollutants. The PM samples used were first CB, used as a model PM particle, and then more realistic PM particles, including 1649b, 2583, and DEPs. In each case, exposures were performed both as a single pollutant and multi-pollutant exposures to allow assessment of any additive, synergistic and contradictory effects. All exposures occurred at the ALI, with viability, cell number, barrier integrity, pro-inflammatory response, and oxidative stress assessments.

### 6.4.1 Effects of Nitrogen Dioxide Exposure on NCI-H441 and hAELVi Monocultures and the Triple Cell Co-Culture

At the time of experimentation, there were no studies that had examined NO<sub>2</sub> exposure within these cells; therefore, a limited set of preliminary studies were performed within NCI-H441 monocultures to assess the toxic response following an acute (4 hr), high concentration (5 ppm) exposure. There were no changes in cell count, viability, barrier function or pro-inflammatory response 4 hours following exposure. The timings of this exposure were based on Mirowsky *et al.* (2016), which found the maximal oxidative stress effect 4 hours post NO<sub>2</sub> exposure within human bronchial epithelial cells. Although oxidative stress was not directly measured here, the association between oxidative stress, cytotoxicity, and inflammation is understood. The lack of change following exposure could be explained by differences in cell type first. The relatively long double time of 58 hours in NCI-H441 cells (ATCC, 2024a) could explain why there are no changes in cell number or viability (especially if cell death is triggered through cell cycle arrest (Barnum & O'Connell, 2014) over such a short duration. If cell death were to occur, then the mechanism of cell death could influence the rate at which effects would be observed. Apoptosis, for example, can take up to 24 hours (Saraste, 1999) to occur, whereas necrosis is more of a rapid response, though this is typically associated with a complementing inflammatory response (Khalid & Azimpouran, 2023), which was absent here. Along a similar theme, the lack of change in viability could be that the mechanisms by which NO<sub>2</sub> may exert a toxic response did not have time to take effect. For example, if cell death was going to be caused by a pro-inflammatory stimulus, then the time scales examined may not have given sufficient time for these processes to occur and signal.

When this exposure was extended to 24 hours, however, in NCI-H441 cells, there were still no changes in viability or cell count in the NO<sub>2</sub> exposed compared to the negative control treated cells. However, a pro-inflammatory effect was observed, especially at 2.5 ppm concentration. This effect was also exhibited when hAELVi cells, or the triple cell co-culture where 2.5 ppm exposures induced the greatest pro-inflammatory effect. Many studies have previously implicated oxidative stress in response to NO<sub>2</sub> exposure, such as Mirowsky *et al.* (2016) that found an increased expression of *HMOX1* at 4 hours post 2 hour-long exposure to NO<sub>2</sub> at 1, 2, 3 and 5 ppm, as well as a host of other genes involved in oxidative stress shown through PCR array. *In vivo* studies have further shown this effect, with increased transcription of *HMOX1*, as well as *MT1G* and *NOS2*, which encode metallothionein, which has shown antioxidative capabilities to be able to scavenge hydroxyl radicals (Ruttkey-Nedecky *et al.*, 2013) and inducible nitric oxide synthase, which can promote oxidative stress, respectively (Justo & Suemoto, 2022). Analysis of *SOD1* expression here, however, was unable to replicate this finding, where NO<sub>2</sub> did not cause an effect at any concentration. If NO<sub>2</sub> exposure were to increase ROS production, it may, therefore, be expected that *SOD1* was upregulated to maintain REDOX balance through the catalysing the conversion of superoxide radicals into oxygen and hydrogen peroxide (Eleutherio *et al.*, 2021). Within cells however, radicals are continuously generated at a baseline level during cellular respiration, therefore *SOD1* is constitutively expressed. Due to this high baseline level of SOD1, it is considered not as easy to induce as the other superoxide dismutase enzymes (SOD2 and SOD3) and perhaps another target would be more sensitive.

To directly assess oxidative stress, triple cell co-cultures exposed to 1, 2.5 or 5 ppm NO<sub>2</sub> were quantified for their GSH content. All 3 concentrations were found to reduce GSH levels non-significantly, though there was no evidence of a dose-dependent effect. GSH is an oxygen radical scavenging molecule, where sequestering of ROS will convert GSH to its oxidised form, GSSG. A reduction in GSH is, therefore, an indication of an oxidative effect (Nuhu *et al.*, 2020; Zitka *et al.*, 2012). Paradoxically, Kelly *et al.* (1996) reported an increase in GSH within bronchial lavage of humans exposed to 2 ppm NO<sub>2</sub> for 1.5 or 4 hours (though no changes in GSSG). However, this could have been caused by GSH leakage (due to cell damage) or increased synthesis, and export of GSH, given that other markers indicated increased oxidative stress

(decreased uric acid and ascorbic acid). Conversely, a time dependant loss in GSH was observed in human *ex vivo* BAL cells following 4 hours of exposure to 50, 150, 400 and 1000 ppb NO<sub>2</sub>, dropping approximately 25% over the exposure duration, though, again, the rate of loss was less than ascorbic and uric acid. Differences in the antioxidant composition of the respiratory lining fluid appeared to influence the response, therefore suggesting that an individual's risk to NO<sub>2</sub> may differ as antioxidants within the lining fluid increased. The data indicate that NO<sub>2</sub> may induce a toxic response through oxidative stress effects, which in turn has been shown to play a role in epithelial cell apoptosis (Waghray et al., 2005), macrophage polarisation (and subsequent inflammation) (Duffield et al., 2005) and is associated with the onset of asthma, COPD and lung cancer (Rogers & Cismowski, 2018), all of which have been linked with NO<sub>2</sub> through epidemiological studies (Anenberg et al., 2022; Hamra Ghassan et al., 2015; Zhang et al., 2018). Epithelial damage associated with oxidative stress could also potentially lead to pulmonary fibrosis (Otoupalova et al., 2020). Indeed, NO<sub>2</sub> exposure has been associated with idiopathic pulmonary fibrosis incidence, progression, and mortality within epidemiological studies (Conti et al., 2018; Yoon et al., 2021; Yoon et al., 2023).

The pathogenesis of asthma, COPD, lung cancer and pulmonary fibrosis are multifaceted. Chronic inflammation has been associated, for example, with the development of lung fibrosis (Heukels et al., 2019), and the relationship between oxidative stress and inflammation is clear. Within NCI-H441 and hAELVi monocultures, as well as the triple cell co-culture, NO<sub>2</sub> was able to induce a pro-inflammatory response shown by an upregulation of IL6 and IL8. Inhaled pathogens, pollutants and allergens can induce an inflammatory response to a variety of mechanisms. When directly interacting with epithelial cells, for example, TLRs will recognise PAMPs, which will signal through myeloid differentiation primary response gene 88 (MyD88) or TIR-domain-containing adapter-inducing interferon- $\beta$  (TRIF) to increase translocation of transcription factor NF $\kappa$ B to the nucleus. Once there, this will increase the expression of genes encoding pro-inflammatory proteins such as IL6, IL8 and TNF $\alpha$  (Grippi et al., 2015). Macrophages, on the other hand, express a range of PRRs to assist in the inflammatory response, though they are in a quiescent state under 'normal' conditions to limit damage to surrounding epithelial cells, though they are able to become activated in response to inhaled pollutants (Grippi et al., 2015).

Though the exact mechanism by which NO<sub>2</sub> triggers a pro-inflammatory response is unknown, there are a few proposed mechanisms of action. Firstly, the pro-inflammatory is a downstream response from another effect; for example, the increase in IL6 and IL8 could be secondary to an oxidative stress effect as oxidative stress has been shown to increase TNF $\alpha$  and IL6 previously (Prabhakar, 2013). Secondly, NO<sub>2</sub> may interact with cells directly. NO<sub>2</sub> cytotoxicity was observed specifically with epithelial cells in the log phase or those near a wound created in *in vitro* cultures, suggesting that dividing cells may present surface molecules that could be sensitive to oxidative modification by NO<sub>2</sub> (Persinger et al., 2001). However, confluent cultures were used, and cytotoxicity was not observed in the present work. Finally, NO<sub>2</sub> is a soluble compound with the ability to dissolve in water to form nitric acid and nitric oxide (Tan & Piri, 2013), the prior of which has been shown to cause pulmonary inflammation (Meaden et al., 2019).

NO<sub>2</sub> exposure did not significantly alter barrier function in any of the *in vitro* lung models used, though an increase in barrier function was shown after exposure within the triple culture, and 2.5 ppm increased NCI-H441 monoculture function. Data from Chapter 5 would suggest that the barrier function of hAELVi cells, or cultures majority comprised of hAELVi, are not easily disrupted (at least by particles). However, NCI-H441 cultures were more easily altered. Within rats, NO<sub>2</sub> exposure was shown to be associated with a transformation of type 2 alveolar epithelial cells into type 1 alveolar epithelial cells. Notably, the type 2 cell “flattens out” before becoming type 1 (Evans et al., 1975). This may align with the fluorescent images captured of NCI-H441 following NO<sub>2</sub> exposure, which appeared to spread out and become rounder in a dose dependant manner following exposure, potentially indicative of a transformation to a type 1 phenotype.

Furthermore, NCI-H441 exposed to 5 ppm NO<sub>2</sub> for 24 hours expressed higher levels of tight junction protein ZO-1, which is typically associated with increased barrier function and type 1 alveolar cells (Kuehn et al., 2016). This could also explain the mild increase in barrier function observed in the triple cell co-culture exposed to NO<sub>2</sub>. The minority NCI-H441 population could undergo morphological change to improve the already tight barrier further.

In addition, confocal imaging of the CD11 $\beta$  within the triple cell culture shows a change in localisation following NO<sub>2</sub> exposure. Specifically, greater fluorescence is observed following exposure with the presence of areas of high fluorescence, particularly in the 2.5 ppm exposure. CD11 $\beta$  has been proposed as a target to show the inflammatory state of alveolar macrophages (Duan et al., 2016). Further, exposure to cigarette smoke and asbestos has been shown to increase subpopulations of CD11 $\beta$  positive alveolar macrophages (Cass et al., 2021; Joshi et al., 2019) driven by IL1 $\alpha$ . The induction of these cell types was associated with a reduction in fibrogenesis, a reduction in  $\alpha$ -smooth muscle actin and reduced matrix metalloproteinase 9 activity (which contributes to epithelial to mesenchymal transition), perhaps indicating a protective role of these cells.

#### **6.4.2 Co-exposure of NCI-H441 Monoculture and Triple Cell Co-Culture to Nitrogen Dioxide and Carbon Black**

When taking the NO<sub>2</sub> exposures forward to be used in combination with the VitroCell® Cloud PM exposures, it was first necessary to check for interactions that may occur at a baseline level between the NaCl-containing aerosol and the NO<sub>2</sub>. NCI-H441 monocultures were exposed to NaCl spiked saline *via* aerosol exposure at 0.009% (the NaCl concentration used in PM exposures) or 0.0009%  $\pm$  NO<sub>2</sub>. Exposure to NaCl  $\pm$  NO<sub>2</sub> did not alter viability, although it did increase barrier function compared to the incubator untreated control. The reasons why NO<sub>2</sub> could cause this effect have already been discussed; however, it is not clear why NaCl might induce this effect, especially given that exposures conducted using the Cloud 12 at Swansea University did not cause this change. Perhaps the barrier function is being lost slightly during the travel period to RCE, which is then altered by the NaCl exposure. Indeed, NaCl has been shown to affect the barrier properties of the alveoli. However, this was in the case of hypertonic NaCl concentrations, causing a loss of tight junctions (Högman et al., 2002). Alternatively, something could be altered in the cell culture media during travel, such as a reduction in liquid volume due to evaporation owed to being outside of a humidified incubator. When the inserts are then placed within the VitroCell Cloud12 chamber, this could be replenished. However, the media was changed as soon as the cultures arrived at RCE to minimise these changes.

Exposure to  $\text{NaCl} \pm \text{NO}_2$  was associated with an increase in IL6 and IL8. Again, the reasons for this are not clear. It is known that  $\text{NO}_2$  and  $\text{NaCl}$  can react to form nitrosyl chloride (Last & Warren, 1987), an inhalable toxin that can react with water to form hydrochloric acid (National Center for Biotechnology Information, 2024). Indeed, *in vivo* inhalation exposure to  $\text{NO}_2 \pm \text{NaCl}$  found a synergistic effect of the two, leading to increased collagen production and lung permeability (Last & Warren, 1987). The concentrations of  $\text{NaCl}$  used within the present work are approximately 8-fold higher than the  $1 \text{ mg/m}^3$  used by Last and Warren (based on nebulising a  $200 \text{ }\mu\text{L}$  of a  $0.009\%$   $\text{NaCl}$  solution into a  $0.022 \text{ m}^3$  chamber). However, work here did not mix  $\text{NaCl}$  and  $\text{NO}_2$  in aerosol, and only once the  $\text{NaCl}$  had deposited on the cell models. Nitrosyl chloride is a nitrosylating agent and could induce cell and DNA damage, potentially leading to an inflammatory response (Arroyo & Carmichael, 1997).

Having an understanding of the baseline response between the exposure systems, NCI-H441 cells or the triple cell co-culture were implemented with  $\text{NO}_2 \pm \text{PM}$  studies, where initially CB was used as a model PM particle. Neither  $\text{NO}_2$ , CB, nor a combination of the two significantly altered viability in the NCI-H441 monoculture, though minor reductions were observed following CB exposure. CB exposure, however, caused a significant decrease in viability compared to the incubator control, though there appeared to be no synergist or additive effect with  $\text{NO}_2$ . This aligns with previous studies on single pollutant exposures.

All exposures within the NCI-H441 resulted in a decrease in total cell count compared to the incubator control. This was associated with a reduction in barrier function in  $\text{NaCl}$  and  $\text{NaCl} + \text{NO}_2$  exposed cells, potentially mediated through the mechanisms described previously. There was an increase in barrier function in  $\text{NO}_2$ -only exposure, which could be a factor in the potential type 2 to type 1 phenotypic change previously reported (Evans et al., 1975). There was more significant variability in barrier function when the NCI-H441 monocultures were exposed to CB, both with and without  $\text{NO}_2$ . However, the average remained similar to that of the incubator control. Triple cell co-cultures exhibited a significant loss in barrier function only when CB and  $\text{NO}_2$  were co-exposed, perhaps indicating a synergistic effect targeting the hAELVi or dTHP-1 cells. Co-exposure within NCI-H441 monocultures resulted in impaired barrier function compared to the  $\text{NO}_2$ -only exposure, perhaps suggesting that barrier function changes are a result of particle exposures as opposed to  $\text{NO}_2$  exposures. Indeed, carbon

nanoparticles have been shown to reduce TEER and increase dextran permeability in 16HBE14o- bronchial cells exposed at ALI using a VitroCell® Cloud system (Stermann et al., 2022).

Further aligning with the findings shown here, NO<sub>2</sub> (400 ppb) was found to not alter the barrier properties of human bronchial epithelial cells from non-asthmatic individuals. However, cells from donors with asthma have a significant decrease in barrier function (Bayram et al., 2002). The data suggest that perhaps the individual with underlying health effects may be predisposed to the NO<sub>2</sub> effect. Given that PM can exacerbate pre-existing pulmonary conditions, this may indicate a route for synergistic toxicity between NO<sub>2</sub> and PM.

Following CB ± NO<sub>2</sub> exposure, both IL6 and IL8 release show a similar trend between the two pro-inflammatory mediators. The pro-inflammatory response to NO<sub>2</sub> was only observed in the dose-response data for both the NCI-H441 monoculture and triple cell co-culture. Carbon black produced a pro-inflammatory effect in the NCI-H441 monocultures but not the triple cell co-culture; however, co-exposure of both pollutants did not increase IL6 or IL8 release beyond the level that carbon black was able to induce, perhaps suggesting that CB is a more potent driver of inflammation than NO<sub>2</sub> (at the concentrations used), and do not interact in an additive manner. Within the triple cell co-culture, only IL8 release was significantly increased during co-exposure. This could indicate that there is an interaction occurring between NO<sub>2</sub> and CB that is targeting the hAELVi or dTHP-1 cells. Within Chapter 3, it is shown that the triple cell co-culture can react to different stimuli depending on the presence of activated dTHP-1, leading to a subsequent IL8 release (likely from the epithelial cells). Although alveolar macrophages are well known for their ability to mount a pro-inflammatory response, their role as a regulator of the inflammatory state is often not discussed. Alveolar macrophages possess the ability to reduce inflammatory state through a number of mechanisms, such as the phagocytosis of apoptotic cells, stopping the release of pro-inflammatory and toxic content whilst also releasing anti-inflammatory factors (Allard et al., 2018). Within *in vivo* studies, this mechanism has been shown to be disrupted by NO<sub>2</sub> exposure, where rat BALF contained less NO and augmented lymph node cell proliferation following NO<sub>2</sub> exposure (Koike et al., 2001). It is plausible that a similar effect is taking place within the triple cell co-culture, where



dTHP-1 cells are providing an anti-inflammatory role, which is being switched off by NO<sub>2</sub>, allowing a CB-induced pro-inflammatory effect.

NO<sub>2</sub> ± CB did not significantly alter *SOD1* expression within NCI-H441 monocultures. Carbon nanoparticles were found to cause no alterations in *SOD1* expression within 16HBE14o- cells (Stermann et al., 2022), and in fact, rats intratracheally instilled with PM<sub>2.5</sub> samples had reduced activity and protein levels, though, showed increased ROS levels (Niu et al., 2022), potentially through disruption of Nrf2 expression.

Confocal imaging again revealed that NCI-H441 cells spread out and rounded following NO<sub>2</sub> exposure regardless of co-exposure with CB or NaCl. CB exposure, regardless of co-exposure with NO<sub>2</sub>, caused an inconsistent monolayer, with apparent gaps between cells, which are potentially an effect of the CB. However, the blue dextran data does not support the idea that this is causing a measurable effect in terms of the barrier function. This could be associated with some clumping of ZO-1 at the membrane observed in CB-exposed cells, which appears to increase with NO<sub>2</sub> co-exposure.

In comparison to the NCI-H441 morphological examination, triple cell co-cultures appear to express f-actin and ZO-1 at the plasma membranes. Changes that may have resulted in the increased barrier permeability in response to NO<sub>2</sub> + CB co-exposure are not directly evident. However, there is an alteration in phalloidin stain localisation following co-exposure. Using a high dose of 200 µg/cm<sup>2</sup>, changes in *TUBA1C* (encoding tubulin alpha 1c, a cytoskeleton protein) were noted, perhaps indicating remodelling of the cytoskeleton is taking place, which could explain the changes in actin localisation seen here. Given the vast roles the cytoskeleton plays through structural, signalling and cellular trafficking, it is difficult to work out precisely the mechanisms at play here (Ispanixtlahuatl-Meráz et al., 2018).

#### **6.4.3 Co-exposure of the Triple Cell Co-Culture to Nitrogen Dioxide and Urban/Indoor Dust (SRM 1649b & SRM 2583)**

Both 1649b and 2583 were able to reduce viability, though significance was only reached once PM was co-exposed with NO<sub>2</sub>. It is difficult to determine the exact mechanisms underpinning the cause of an increased effect. However, perhaps this

could be related again to the reduced anti-inflammatory effect of NO<sub>2</sub> on macrophages, allowing an enhanced pro-inflammatory response, which in turn could lead to cytotoxicity, as has previously been demonstrated in alveolar epithelial cells (Muroya et al., 2012). There is no significant difference in viability between cultures exposed to 1649b or 2583 without NO<sub>2</sub> compared to with NO<sub>2</sub>; however, further repetitions or investigation into cell death markers may be required to determine whether there is indeed an additive/synergistic effect here or whether the significance results observed are random variation only.

As was observed within the triple cell co-culture NO<sub>2</sub> dose finding investigation, there is an increase in barrier function following NO<sub>2</sub> exposure. However, there did not appear to be an effect induced by 1649b or 2583, corroborating with the findings of Chapter 5. It would therefore appear that within the time frame studies, 1649b/2583 do not play a role in the barrier function of this triple cell co-culture. Again, it is possible that the augmented barrier function could be a result of morphological changes to the NCI-H441 cells within the co-culture, though cell type-specific tracking would be required to confirm this.

1649b and 2583 were found to possess the ability to drive a pro-inflammatory response (as was shown in Chapter 3). However, there was no evidence that NO<sub>2</sub> was able to act synergistically or additively. Given the heterogeneity of the PM samples used here compared to CB, it is possible that a number of different mechanisms could drive inflammation. CB, for example, could be driving a pro-inflammatory response secondary to cellular oxidative stress (Niechoda et al., 2023). In contrast, the NIST particles could contain black carbon nanoparticles acting through a similar mechanism, as well as allergens or endotoxins that could be directly stimulating TLRs on the cell membranes to drive a pro-inflammatory response that could potentially evade anti-inflammatory mechanisms of the macrophages, or perhaps directly stimulate dTHP-1 cells themselves. It has already been shown that the triple cell co-culture mounts a pro-inflammatory response to an inflammatory stimulus of LPS found on bacterial membranes. However, the lung can also mount pro-inflammatory responses to other allergens such as house dust mites, pollen and fungal spores (Byrne et al., 2013; Deng et al., 2019; Furlong-Silva & Cook, 2022). It is highly likely that these PM samples contain allergens in some respect due to the nature of their collection. Within nasal epithelial cells, however, co-exposure of house dust mite allergen and NO<sub>2</sub> caused a

synergistic pro-inflammatory effect where IL6 and IL8 release was observed beyond the level of NO<sub>2</sub> or house dust mite allergen single pollutant exposure (Koehler et al., 2016). Further, NO<sub>2</sub> has been shown to be able to act with molecules on the surface of PM or with PM themselves to produce nitrate, which could further cause toxicity and would be more likely to occur with these heterogeneous PM samples (Gu et al., 2017).

Within BEAS-2b bronchial cells, urban particulate matter was able to induce transcription of tight junction proteins, including ZO-1, associating this change with alterations in barrier function and subsequent inflammation (Park et al., 2023). Morphological examination reveals localisation changes to ZO-1 after urban dust exposure, with denser plasma membrane staining, perhaps indicative of a protective effect. Interestingly, this effect is not as apparent with NO<sub>2</sub> co-exposure, which suggests a loss of this effect.

It appears that CB has more of a synergistic effect with NO<sub>2</sub> than either 1649b or 2583; however, the potential synergistic cytotoxic effect between NO<sub>2</sub> and 1649b/2583 requires further focus. Through assessment of other cytotoxic endpoints, such as lactate dehydrogenase release or MTT assay, further relationships could be concluded. Further, a dose-finding study of the two pollutants together may shed further light on any potential relationship between the pollutants.

#### **6.4.4 Co-exposure of Triple Cell Co-Culture to Nitrogen Dioxide and Diesel Emission Particles**

In a very similar manner to the 1649b and 2583 ± NO<sub>2</sub> co-exposures, DEPs reduced triple cell co-culture viability, though significance was only reached after co-exposure with NO<sub>2</sub>. This was also associated with an increase in IL8 (but not IL6) release in co-exposures, but not PM or NO<sub>2</sub>. This could be an indication that DEPs and NO<sub>2</sub> could act synergistically to induce specific effects. Wooding *et al.* (2019) exposed human subjects to diesel exhaust emissions with particles or after particle depletion with an endotoxin allergen challenge. It was found that particle-depleted NO<sub>2</sub> + allergen caused a more significant inflammatory response and a reduction in lung function compared to when particles were present. This shows that particles and NO<sub>2</sub> are able to act as a mechanism to modulate pro-inflammatory response, again, perhaps through the disruption of macrophage antioxidant effects. The effects observed here are similar to those that occurred when CB was co-exposed with NO<sub>2</sub>, where an increase in IL8

but not IL6 release occurs. This could be due to the time frame (24 hrs) in which the cultures are exposed. The innate immune response is rapid, so perhaps the maximal pro-inflammatory response has been missed. Further, IL6 has been shown to possess an intrinsic negative feedback mechanism through interaction with STAT3 to reduce its own expression (Verboogen et al., 2019). Further, within murine models, exposure to an inflammatory stimulus showed IL6 release into BALF occurred in waves, peaking in the first 3 days post-exposure, then from days 8-10 (Kobayashi et al., 2015).

The DEPs used here have been directly implicated within inhalation exposure studies using C57BL/6 mice exposed *via* intratracheal instillation. All three DEP types possessed the ability to induce an inflammatory response shown through neutrophil influx after 1 day, and an acute phase response shown through increases in Saa3 mRNA. Further, on day 28 post-exposure, the induction of DNA strand breaks, in line with the production of ROS, was shown (Bendtsen et al., 2020). The generation of ROS, although not directly measured here, could be a factor in the cytotoxicity shown here. It has previously been shown that higher oxygen intakes increase the ROS formation potential of these particles (Gren et al., 2020), which perhaps aligns with this viability data, which shows the greatest cytotoxic effect when DEP 17% is exposed in co-exposure with NO<sub>2</sub>. Given the potential oxidative stress effect NO<sub>2</sub> could impart, this may be an additive effect.

Karthikeyan *et al.* (2013) attempted to investigate the effects of complete diesel emissions inhalation in rats from a Cummins ISM heavy-duty diesel engine, with and without a diesel particle filter. Emissions without the filter had an NO<sub>2</sub> concentration of 4 ppm and particles at 169 µg/m<sup>3</sup> ( $3.2 \times 10^5$  particles/cm<sup>3</sup>, the mode particle size being 60-70 nm). The addition of the filter increased NO<sub>2</sub> concentration to 16 ppm and reduced particle concentration to 2 µg/m<sup>3</sup> (however, particle count was increased to  $4.4 \times 10^5$  particles/cm<sup>3</sup>, and particle size was significantly lower at 7-8 nm). However, the exposure to emissions from the engine lacking the filter increased markers of inflammation, such as lung neutrophilia, increased BAL protein content, and expression of MT2A, IL6 and PTGS2 within lung tissue. A more significant inflammatory response was observed when a particle filter was present by 2- to 4-fold. This, therefore, could be an NO<sub>2</sub> effect given that NO<sub>2</sub> concentration was 4-fold higher in this exposure than the non-particle filter exposure. This aligns with the data shown within the chapter, suggesting an inflammatory role of NO<sub>2</sub>, though a dose-dependent

interaction was not able to be determined within the present work. It is important to note, however, that the particle filter increased the proportion of ultrafine particles, which could have had an effect, as well as other gases such as CO and SO<sub>2</sub>. The presence of the particle filter also increased markers of oxidative stress, such as HO-1 and iNOS, suggesting an NO<sub>2</sub>-directed effect that has been noted here previously. Some markers of inflammation and oxidative stress, such as IL1 $\beta$  and TNF $\alpha$ , as well as SOD2 and GSTA1, were not correlated with NO<sub>2</sub> concentration but were upregulated by the presence of a particle filter. This could perhaps suggest a separate role of the ultrafine particle fraction, which could work in conjunction with NO<sub>2</sub> to elicit augmented toxic responses.

It is important to note, however, that during this study, the NaCl + NO<sub>2</sub> exposure also had high IL8 levels, though slightly lower than the DEP + NO<sub>2</sub> exposures. Therefore, the potential of an NaCl/NO<sub>2</sub> interaction cannot be ruled out.

The triple cell co-culture exhibits no apparent morphological changes following exposure to DEP  $\pm$  NO<sub>2</sub>. However, co-exposed cultures (regardless of DEP oxygen intake percentage) appear to have a loss of clearly defined cell border shown through phalloidin staining, with what appears to be some cytoskeleton remodelling having taken place. Although it is difficult to attribute this to any one reason, oxidative stress, which has been attributed to both NO<sub>2</sub> and DEP exposure, has been shown to cause this change within actin structures (Valdivia et al., 2015).

DEP 17% appeared to increase barrier permeability slightly, although there was an evident lack of change in the ZO-1 localisation shown through immunofluorescent staining. NO<sub>2</sub> co-exposure did not appear to alter this effect. Standardised DEPs from NIST (SRM 2975) have been shown to reduce TEER and increase barrier permeability within 16HBE14o- human bronchial epithelial cells within submerged conditions. Additionally, DEPs decreased tricellulin abundance within these cells, a tight junction-associated MARVEL protein (Smyth et al., 2020). SRM 2975 was also found to reduce occludin expression in 16HBE14o- cells and reduce TEER; however, co-culturing these epithelial cells with monocyte-derived macrophages and monocyte-derived dendritic cells attenuated this TEER reduction (Lehmann et al., 2009). This change in TEER response perhaps indicates a requirement for exposures to be conducted within

the context of the surrounding cells and tissue, as this could modulate toxicological outcomes.

## 6.5 Summary and Outlook

*Table 6.10 Key conclusions and findings from Chapter 7.*

<b>Chapter Conclusions</b>	<ul style="list-style-type: none"> <li>▪ NO<sub>2</sub> induced a pro-inflammatory effect within alveolar cells. This was especially evident at 2.5 ppm.</li> <li>▪ NO<sub>2</sub> was able to confer a morphological change within the alveolar models, although the mechanism underpinning this requires elucidation.</li> <li>▪ Co-exposure of PM with NO<sub>2</sub> generally increased cytotoxicity compared to either single pollutant exposures.</li> <li>▪ Co-exposure of NO<sub>2</sub> and PM may amplify the pro-inflammatory response, although confounding effects between NO<sub>2</sub> and NaCl (used as a nebulisation exposure control) require further focus.</li> </ul>
<b>Project Impact</b>	<p><b>A method of simultaneously exposing <i>in vitro</i> models to PM and NO<sub>2</sub> has been proven. Co-exposure to NO<sub>2</sub> and PM has been shown to alter the toxic response compared to either pollutant type as a single pollutant. However, further work is required to elucidate the mechanisms underpinning these changes.</b></p>

Exposure of alveolar models to NO<sub>2</sub> as a single pollutant exposure was shown not to impact the viability of the cells, although 2.5 ppm NO<sub>2</sub> was shown to induce a maximal pro-inflammatory response (compared to 1 or 5 ppm). Furthermore, NO<sub>2</sub> appeared to alter the morphology of the cultures. This was especially noticeable within the NCI-H441 cells, perhaps suggestive of a transition to an ATI-like phenotype, which could also explain the increased barrier function that was noted.

Although PM exposures were generally found to induce a slight decrease in cell viability, co-exposing PM with NO<sub>2</sub> was found to amplify this effect, often to the point of statistical significance. Furthermore, pro-inflammatory response was also amplified following PM + NO<sub>2</sub> co-exposures, compared to either as a single pollutant exposure. However, it was noted that there is likely an interaction occurring between NO<sub>2</sub> and NaCl that could potentially contribute to this pro-inflammatory increase.

The data within this chapter indeed indicated that NO<sub>2</sub> and PM are able to act independently, and have the potential to act additively/synergistically to influence toxicity, although, the exact routes of toxicity appear to be governed by the type of PM used. Further work is required to elucidate the mechanisms underpinning these changes.

## **Chapter 7: Transcriptomic Response to Nitrogen Dioxide and Particulate Matter Co-exposure**

---

Many thanks to Dr Martin Leonard for assisting in the data analysis of the RNA sequencing data.

A special thanks to Prof. Ulla Birgitte Vogel from the National Research Centre for the Working Environment, Denmark, as well as Dr. Joakim Pagels and Dr. Vilhelm Malmberg from Lund University, Sweden, for kindly providing the diesel emission particles used within this chapter.



## 7.1 Introduction

Within Chapter 6, there appears to be some effect of  $\text{NO}_2 \pm \text{PM}$  co-exposure, although it was not possible to identify an exact mechanism of action underpinning any potential toxicity. Therefore, in an attempt to distinguish some pathways that might be altered by either or both pollutant types, a global approach was taken. This may prove effective in confirming the effect mechanisms observed in previous chapters, as well as allowing further assessment for other toxicological responses that may occur and that have thus far been untested. Transcriptomic methods, such as RNA sequencing (RNA-Seq), allow quantitative assessment of gene expression, alternative splicing, and allele-specific expression (Kukurba & Montgomery, 2015).

Pioneering experimentation into gene expression often utilised qPCR or northern blots (Ginzinger, 2002; Josefsen & Nielsen, 2011), though this requires a known gene of interest. RNA-Seq allows the entire transcriptome to be quantified through next-generation sequencing of cDNA created from RNA harvested from cells of interest (**Figure 7.1**). This then allows previously unconsidered genes to be assayed. The RNA-Seq process follows three main steps: preparing an RNA-Seq library, sequencing, and data analysis.

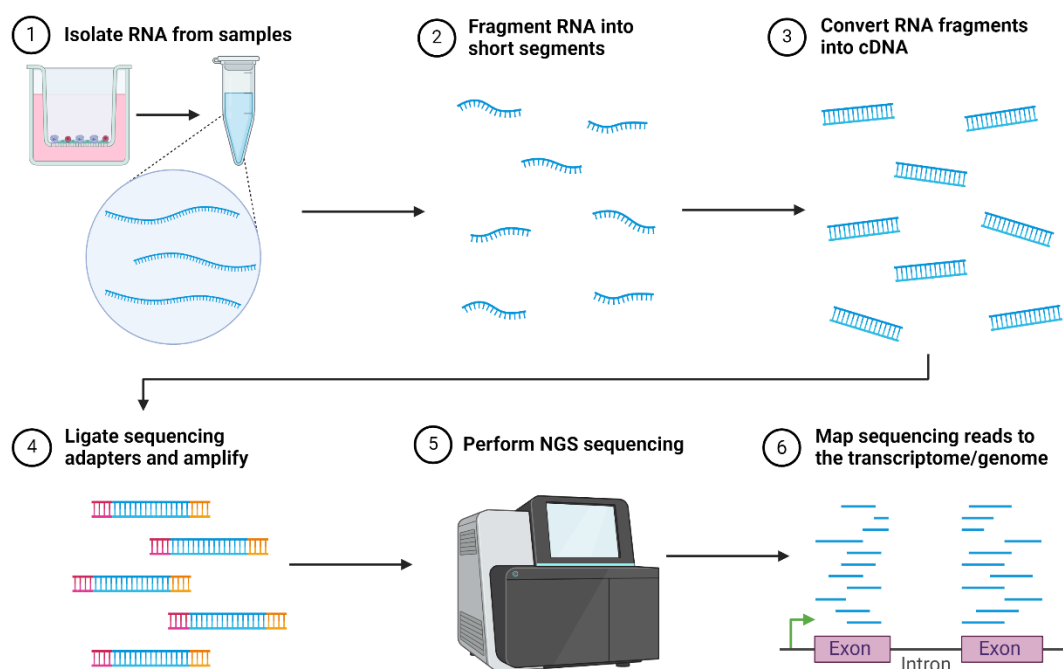


*Figure 7.1 Schematic of RNA-Seq methodology.*

Generally, RNA is isolated from the test samples before being broken into smaller fragments, allowing compatibility with short-read sequencers. RNA fragments are then converted to double-stranded DNA using reverse transcriptase and DNA polymerase. Each DNA sample is then barcoded using sequence adapters. This means that numerous samples can be sequenced simultaneously, and sample-specific genes can be extracted within the analysis step. PCR can then be used to amplify the fragments containing these sequence adapters. The concentration and fragment length are then checked for compatibility with the sequencer prior to sequencing. The samples are then sequenced through next-generation sequencing (NGS) techniques.

Through the use of the barcode, the output is demultiplexed. The output sequence can then be fragmented and aligned with a location on a chromosome by comparing it to a fragmented genome (from the species of interest). Fragmentation of the sequence allows alignment with a location in the genome, even if it contains a mutated sequence or an error has occurred during sequencing. By assessing the corresponding sequence locations and aligning them with known gene locations, a read count for each gene can be generated. The data can then be normalised to control for sample differences in read efficiency prior to data analysis.

This method of toxicogenomic testing could prove more efficient than traditional toxicological testing, which is time-consuming and often focuses on single endpoint analysis. As such, toxicogenomics has been heralded as a ‘new era’ in toxicology (Aardema & MacGregor, 2002), with transcriptomics predicted to have a significant impact within the field. RNA-Seq, with its extensive dynamic range (therefore possessing the ability to detect both low and high expression levels), allows genome-wide transcriptomic sequencing, which can then be used to deduce mechanisms of action of various toxins, drugs, and biologics. Within this work, RNA-Seq could provide quantitative data that could elucidate either PM or NO<sub>2</sub>-specific effects within the triple cell co-culture whilst also identifying how their effects could be modulated through co-exposure. Further, given that this is a global analysis, it allows insight into the entire transcriptome, which may further allow for the elucidation of the mechanisms.

#### **7.1.1 Aims and Objectives**

Here, RNA-Seq will be utilised to:

1. Further elucidate mechanisms underpinning potential toxicity of NO<sub>2</sub> exposure within the triple cell co-culture.
2. Contrast the RNA-Seq findings with NO<sub>2</sub> co-exposure using either 2583 or DEP (17% engine oxygen intake).

## **7.2 Methods**

### **7.2.1 Triple Cell Co-Culture Protocol**

Refer to Chapter 3 for a detailed characterisation of the triple cell co-culture.

### **7.2.2 Indoor Dust/Diesel Emission Particle and Nitrogen Dioxide Exposures**

Refer to Chapter 6, Section 6.2 for details on the exposure protocol.

### **7.2.3 RNA Sequencing Analysis**

#### **7.2.4 RNA Extraction**

RNA was extracted from relevant samples according to the protocol described in Section 6.2.12.1. For each exposure, RNA was extracted from biological triplicates. RNA was pooled from three 12-well transwell inserts for each replicate. In addition to RNA quality and yield assessment a NanoPhotometer® NP80 (IMPLEN GmbH, Germany), RNA quality was also determined using a 2100 Bioanalyzer Instrument (Agilent, USA). RNA samples were checked that they had an RNA integrity number (RIN) of 8 or greater. Subsequent RNA-Seq steps were undertaken in conjunction with BGI Genomics (Hong Kong).

#### **7.2.5 Library Preparation and Next-Generation Sequencing**

RNA samples with an RIN of 8 or greater were used for TruSeq™ library preparation following the manufacturer protocol (Illumina, San Diego, USA). Briefly, 200 ng of RNA is purified through polyadenine selection using oligo-dT attached microbeads. mRNA is then fragmented using divalent cations before being copied into first strand cDNA using reverse transcriptase. Second-strand cDNA is then generated using DNA polymerase I and RNase H. cDNA fragments undergo end repair through the addition of a single 'A' base and ligation with the adapters before the samples are amplified through PCR. Sequencing was carried out using the 150PE sequencing method on the Illumina HiSeq™ 2000 platform (BGI, Hong Kong).

### 7.2.6 Data Analysis

Raw sequence data was processed to remove adaptor sequences, and low-quality reads. Up to 40 million clean reads per sample were annotated to the human GRCh38 reference genome, and counts were processed for relative gene expression using CLC Genomics browser software (CLCBIO, Aarhus, Denmark). Statistically significant differences in gene expression were considered using FDR q-values of  $< 0.05$ .

RStudio (version 4.3.0) was used to make volcano plots of differentially expressed genes. Genes with an FDR q-value of  $< 0.05$  and a  $\log_2$  fold change of more than 1.5 on either side of 0 were considered as differentially expressed genes (DEGs). DEGs were visualised using various online platforms and software including DiVenn 2.0 (Sun et al., 2019), Heatmapper (Babicki et al., 2016), STRING (version 12.0) (Szklarczyk et al., 2019), DAVID (Huang et al., 2009; Sherman et al., 2022), Cytoscape (version 3.10.1) and GraphPad Prism (version 10.1.2).

## 7.3 Results

### 7.3.1 Transcriptomic Changes Following Co-Exposure of Indoor Dust or Diesel Emission Particles with Nitrogen Dioxide

All expressed genes were initially visualised within volcano plots to give an indication of the number of DEGs for each exposure (**Figure 7.2**). It was initially observed that

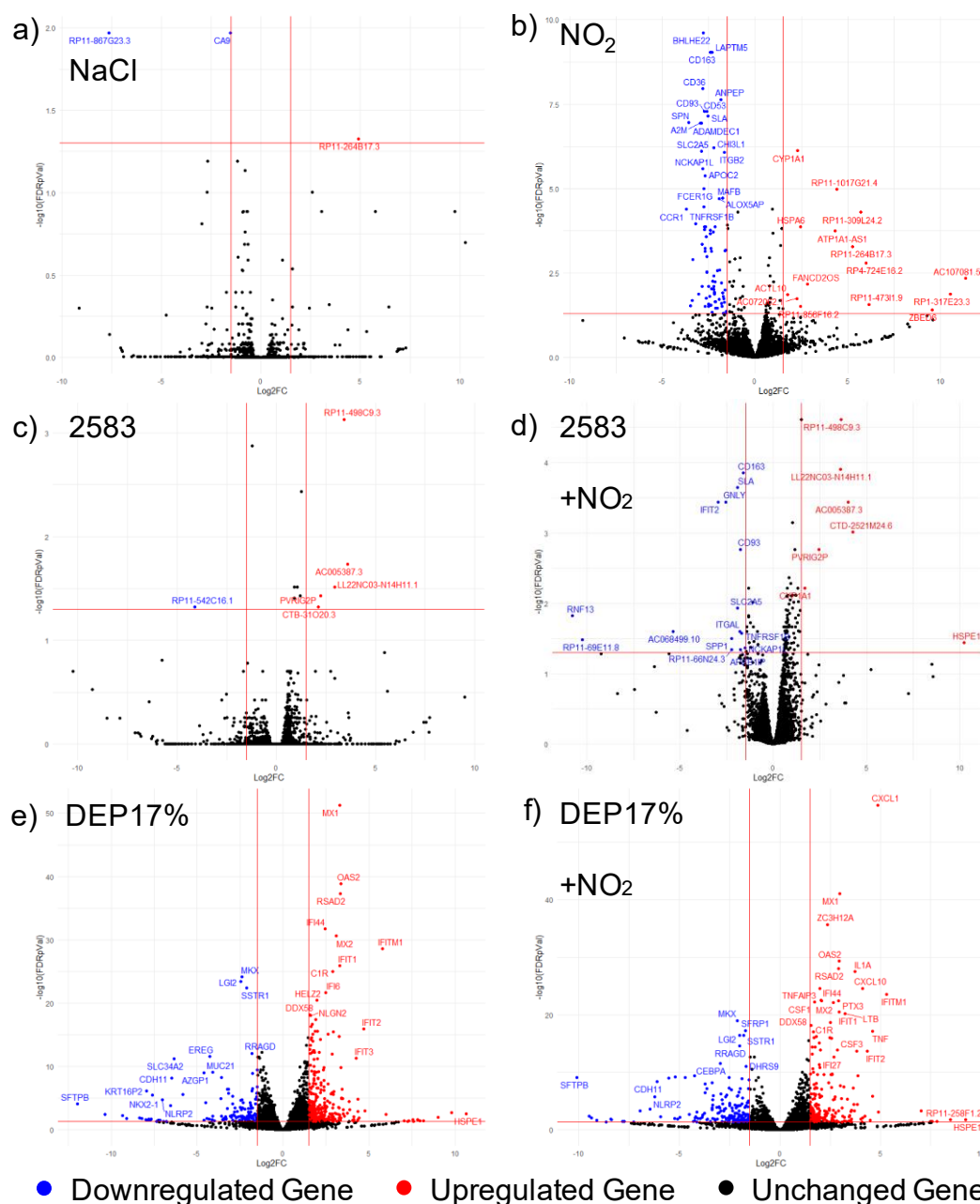


**Figure 7.2** Volcano plots of gene expression changes after triple cell co-culture exposure to (A) NaCl, (B) NO<sub>2</sub>, (C) 2583, (D) 2583 + NO<sub>2</sub>, (E) DEP 17% or (F) DEP 17% + NO<sub>2</sub>. Log<sub>2</sub> fold-changes are shown against the incubator control for the NaCl and NO<sub>2</sub> exposure, or against NaCl for all other exposures. Down or upregulated DEGs are shown as blue or red points, respectively, with red lines showing DEG cutoff values of a 1.5 Log<sub>2</sub> fold-change either side of zero, and a -log<sub>10</sub> p-value of above 1.3 (95% confidence interval). Genes that are not differentially expressed are black. Genes that are highly differentially expressed are labelled with the gene name with a cut off on labelling based on label overlaps.

there were only minor transcriptomic differences following NaCl control exposure compared to the incubator control (3 DEGs) (**Figure 7.2a**).

NO<sub>2</sub> exposure at 5 ppm, on the other hand, resulted in far more DEGs, with the majority resulting from downregulation when compared to the incubator control. There were several upregulated genes, too, including RP11 long non-coding RNAs. This does not mean that there is no physiological effect, as long non-coding RNAs have been shown to play a role in cell differentiation and cancer, for example (Y. Lin et al., 2021) (**Figure 7.2b**). Exposure to 2583 (780 ng/cm<sup>2</sup>) resulted in 6 DEGs, 5 of which were upregulated, although co-exposure with 2583 with NO<sub>2</sub> resulted in an increased number of DEGs (**Figure 7.2c-d**). Co-exposure of 2583 and NO<sub>2</sub> did not increase the number of DEGs, however, when compared to NO<sub>2</sub> as a single exposure. Exposure to DEPs (32.8 µg/mL) resulted in the highest number of DEGs; this number was further increased following DEP and NO<sub>2</sub> co-exposure. Expression changes of PM exposure triple cell co-cultures are shown against the NaCl control (**Figure 7.2e-f**).

To further elucidate the differential transcriptomics of the triple cell co-culture when treated with PM and NO<sub>2</sub>, gene expression was analysed between co-exposures compared to the respective single pollutant exposure (**Figure 7.3**). Co-exposure of 2583 and NO<sub>2</sub> resulted in only 1 DEG compared to 2583 single pollutant exposure. This was a downregulation of interferon-induced protein with tetratricopeptide repeats 2 (IFIT2) expression (**Figure 7.3a**). Co-exposure of DEP and NO<sub>2</sub>, however, resulted

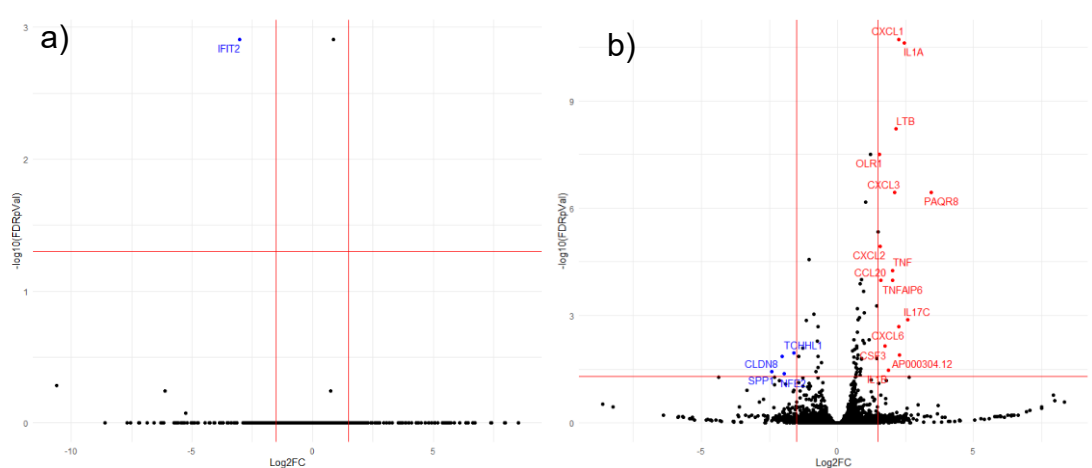


**Figure 7.3** Volcano plots of gene expression changes after triple cell co-culture exposure to (A) 2583 + NO<sub>2</sub> co-exposure against 2583 single pollutant exposure and (B) DEP 17% + NO<sub>2</sub> co-exposure against DEP 17% single pollutant exposure. Log<sub>2</sub> fold-changes are shown against the incubator control for the NaCl and NO<sub>2</sub> exposure, or against NaCl for all other exposures. Down or upregulated DEGs are shown as blue or red points, respectively, with red lines showing DEG cutoff values of a 1.5 Log<sub>2</sub> fold-change either side of zero, and a  $-\log_{10}$  p-value of above 1.3 (95% confidence interval). Genes that are not differentially expressed are black. Genes that are highly differentially expressed are labelled with the gene name with a cut off on labelling based on label overlaps.

in 19 DEGs compared to DEP exposure alone. Of these, 15 were upregulated, and 4 were downregulated. The upregulated genes include several CXC chemokine family members and pro-inflammatory mediators, including IL1 $\alpha$ , IL1 $\beta$  and TNF $\alpha$  (Figure 7.3b).

**Table 7.1** Number of DEGs resulting from each exposure using thresholds of a Log<sub>2</sub>fold change of 1.5 and a p-value of  $\leq 0.05$ .

Exposure	Compared Against	Upregulated	Downregulated	Total
NaCl	Incubator	1	2	3
NO <sub>2</sub>	Incubator	15	79	94
2583	NaCl	1	5	6
2583 + NO <sub>2</sub>	NaCl	7	15	22
DEP17%	NaCl	330	138	468
DEP17% + NO <sub>2</sub>	NaCl	224	176	400
2583 + NO <sub>2</sub>	2583	0	1	1
DEP17% + NO <sub>2</sub>	DEP	15	4	19

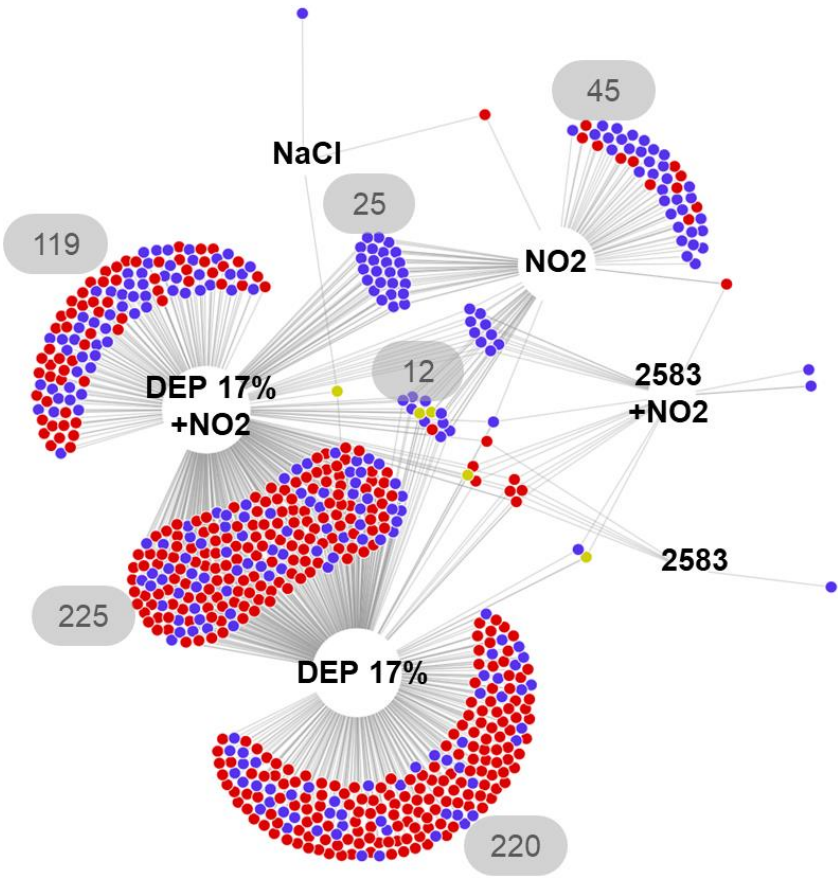


**Figure 7.4** Number of overlapping or different DEGs for each exposure. Numbers show the number of DEGs if there was over 10 DEGs for a given DEG cluster. Red points show upregulated DEGs whereas blue show downregulated DEGs. Yellow points indicate that the DEG was up or down regulated depending on the exposure.



DEGs for each (co-)exposure were investigated through DiVenn (**Figure 7.4**), where it was again shown that DEP-exposed cultures harboured the most genes possessing differential expression. Co-exposure of DEPs with NO<sub>2</sub> appears to differentially express 225 of the same genes as DEP-only exposure, as well as 119 different genes. DEP-only exposure possesses 220 DEGs that are not altered within the DEP and NO<sub>2</sub> co-exposure.

Of the limited DEGs resulting from 2583 exposure, all but 1 appear as DEGs in other exposure groups. There are 4 upregulated DEGs shared between 2583 exposure and 2583 and NO<sub>2</sub> co-exposure cultures, suggesting similar cellular responses between these groups, perhaps driven solely by 2583.

NO<sub>2</sub> exposure resulted in 45 DEGs that were not altered by any other exposure, although 47 of the downregulated genes were also downregulated by DEP and NO<sub>2</sub> co-exposure, and 10 of the downregulated genes were also downregulated by 2583 and NO<sub>2</sub> co-exposure. DEP exposure and DEP and NO<sub>2</sub> co-exposure resulted in 12 DEGs that were altered by NO<sub>2</sub> exposure, perhaps indicating some common response pathways between the two pollutants. However, the sheer number of different DEGs between exposure groups would suggest mainly differential routes of toxicity.

Of the 3 DEGs resulting from NaCl exposure, 1 is shared with NO<sub>2</sub> exposure, 1 is shared with DEP exposure (although the direction of the fold change is different), and 1 is unseen elsewhere.

### **7.3.2 Enriched Processes Following Exposure to DEP and Nitrogen Dioxide Co-Exposure**

Given the limited DEGs resulting from 2583 or 2583 + NO<sub>2</sub> exposure, pathway analysis was not possible. Therefore, the following analysis focuses only on the NO<sub>2</sub>, DEP and DEP + NO<sub>2</sub> exposures.

DEGs from these exposures were run through STRING analysis to gain a better understanding of which mechanisms could be at play underpinning the differences in gene expression highlighted previously. This will also give a greater understanding of the biological responses that could underpin toxicity induced by these air pollutants at a population level. To achieve this, DEGs were input into the STRING database to assess for known protein-protein interactions and align DEGs with enriched gene

ontology (GO) terms. Protein-protein interactions were only acknowledged if reaching a high confidence threshold and were then clustered by k-means clustering.

NO<sub>2</sub> exposure resulted in a single cluster that could be aligned with the GO term of ‘neutrophil activation involved in immune response’ (**Figure 7.5****Figure 7.5**). This could align with the pro-inflammatory changes observed in the previous chapter. Although other clusters were present for NO<sub>2</sub> single pollutant exposure, they were not expansive enough to align with individual biological process GO terms. A small cluster containing MMP2 and MMP9, however, must be noted here as there is evidence that these two proteases can work in tandem to drive lung fibrosis (Bormann et al., 2022).

When all DEGs resulting from NO<sub>2</sub> exposure were aligned with GO terms, there are particularly numerous enrichments in biological process GO terms associated with inflammatory response, such as ‘positive regulation of macrophage fusion.’ and ‘positive regulation of phagocytosis, engulfment’. The most highly enriched biological process GO term was ‘negative regulation of autophagic cell death’. There is also particular enrichment in the cellular component GO term for “integrin alphaL-beta2 complex” and “integrin alphaX-beta2 complex”, as well as molecular function GO terms “cytokine binding” and “immune receptor activity”. These could further highlight an inflammatory aspect of NO<sub>2</sub> exposure (**Figure 7.6**).

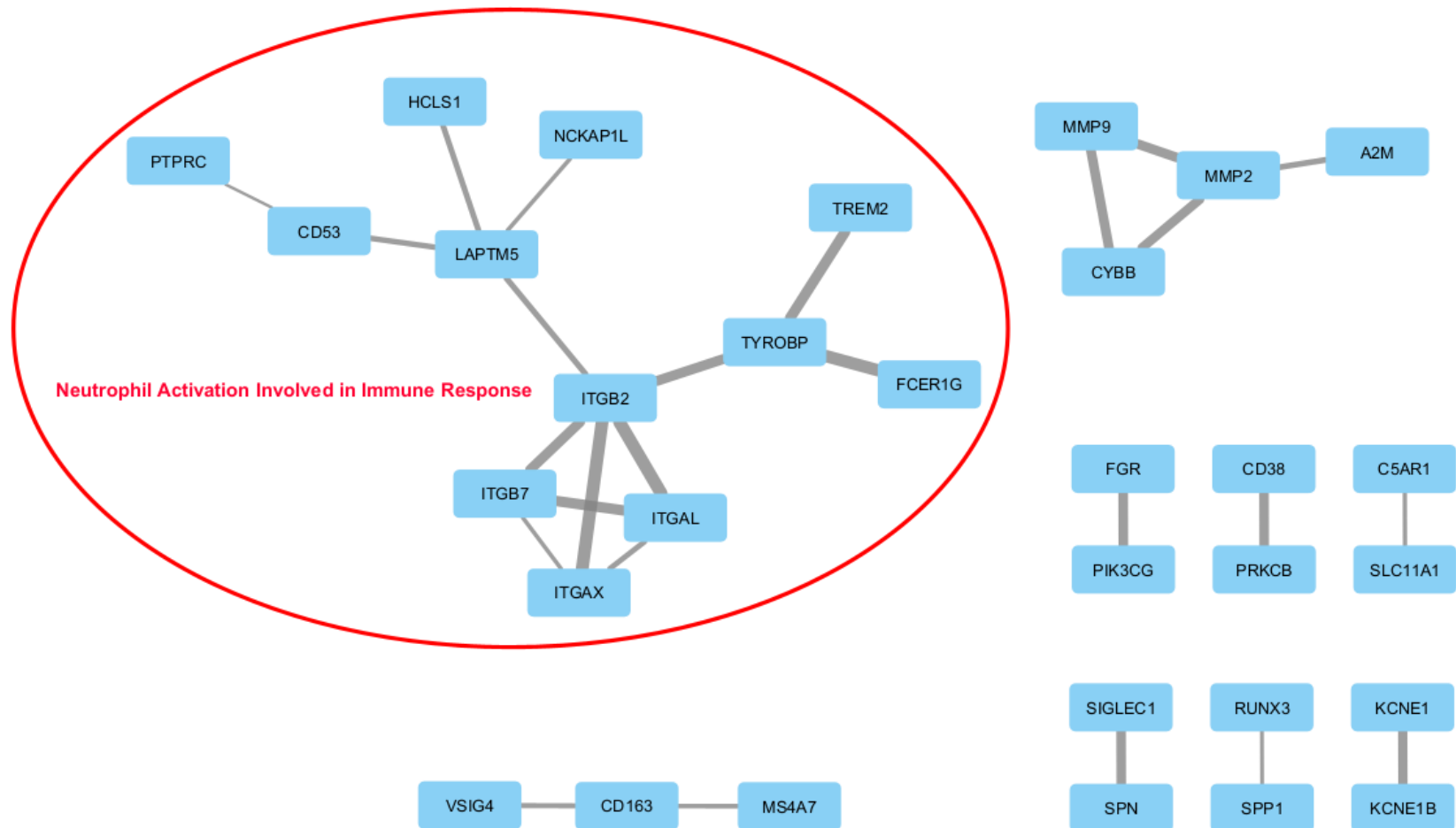


**Figure 7.5** STRING analysis of DEGs resulting from NO<sub>2</sub> exposure (against incubator control). STRING database was used to elucidate known and predicted protein-protein interactions. Textmining was turned off, and interactions with a high confidence (0.700) are shown. Proteins without any interactions are hidden. Interactions are clustered through k-means clustering. Linkage thickness indicates 'combined' score of the interaction considering gene fusion, homology, co-expression, experimentally determined interaction and database annotation.

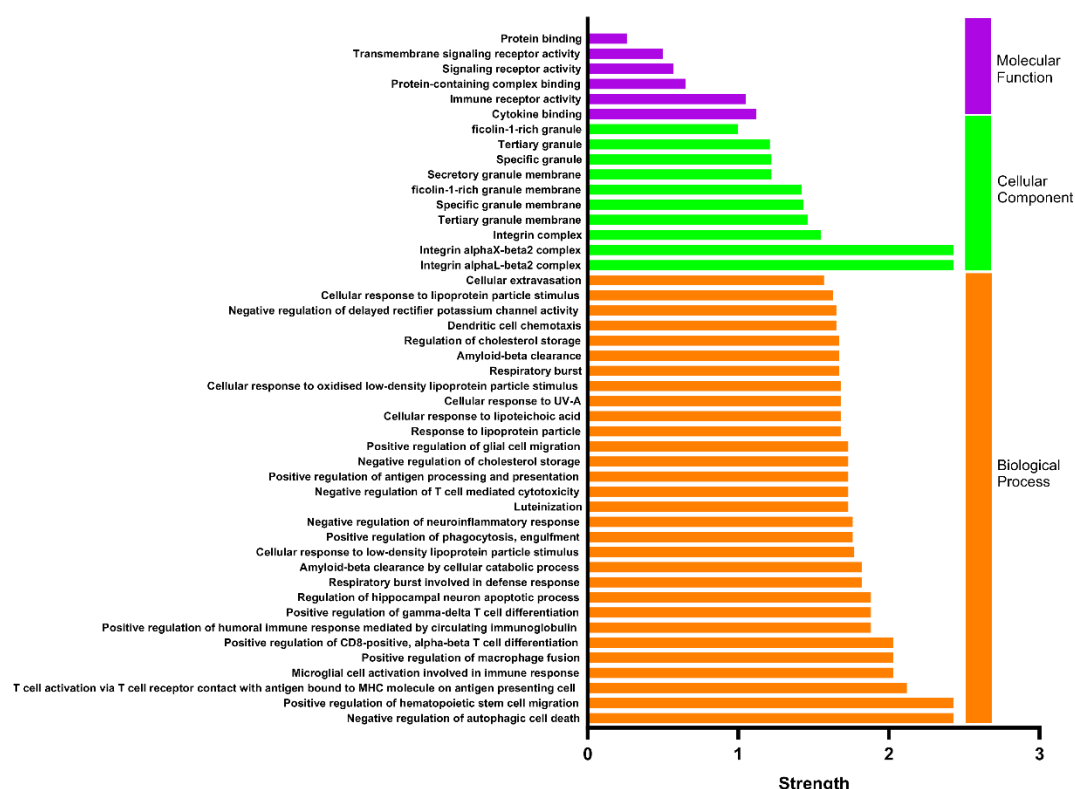


**Figure 7.6** GO terms for Biological Processes, Cellular Component and Molecular Function (top 30, 10 and 10 terms, respectively, shown for each class based off the strength) shown for NO<sub>2</sub> exposure (compared to incubator control). GO term strength is a measure that describes how large the enrichment effect is. This is generated by comparing the number of proteins in the network that are annotated for a certain GO term, compared to what would be expected to be annotated in a random network of proteins of the same size.

STRING analysis of DEP exposure-induced DEGs resulted in 3 annotated clusters. There is a cluster of 26 proteins that are highly linked with ‘interleukin-27 mediated signalling pathway’. IL27 is a cytokine that may be able to stimulate T cells to induce a pro- or anti-inflammatory effect (Yoshida & Hunter, 2015). Other annotated clusters include a network of guanylate binding proteins (GBPs), CXC chemokines and C-C motif chemokines associated with ‘regulation of cell chemotaxis’, and a cluster around fibroblast growth factor 1 (FGF1) associated with ‘positive regulation of phosphatidylinositol 3-kinase signalling’ (**Figure 7.7**), DEGs from DEP exposure were most highly associated with the biological process GO term of ‘positive regulation of extracellular matrix constituent secretion’ (**Figure 7.8**). Like NO<sub>2</sub> exposure, inflammatory process-related GO terms were enriched, such as ‘positive regulation of MHC class 1 biosynthetic process’, ‘regulation of interleukin-18 production’ and ‘response to interferon-alpha’. There was enrichment of cellular

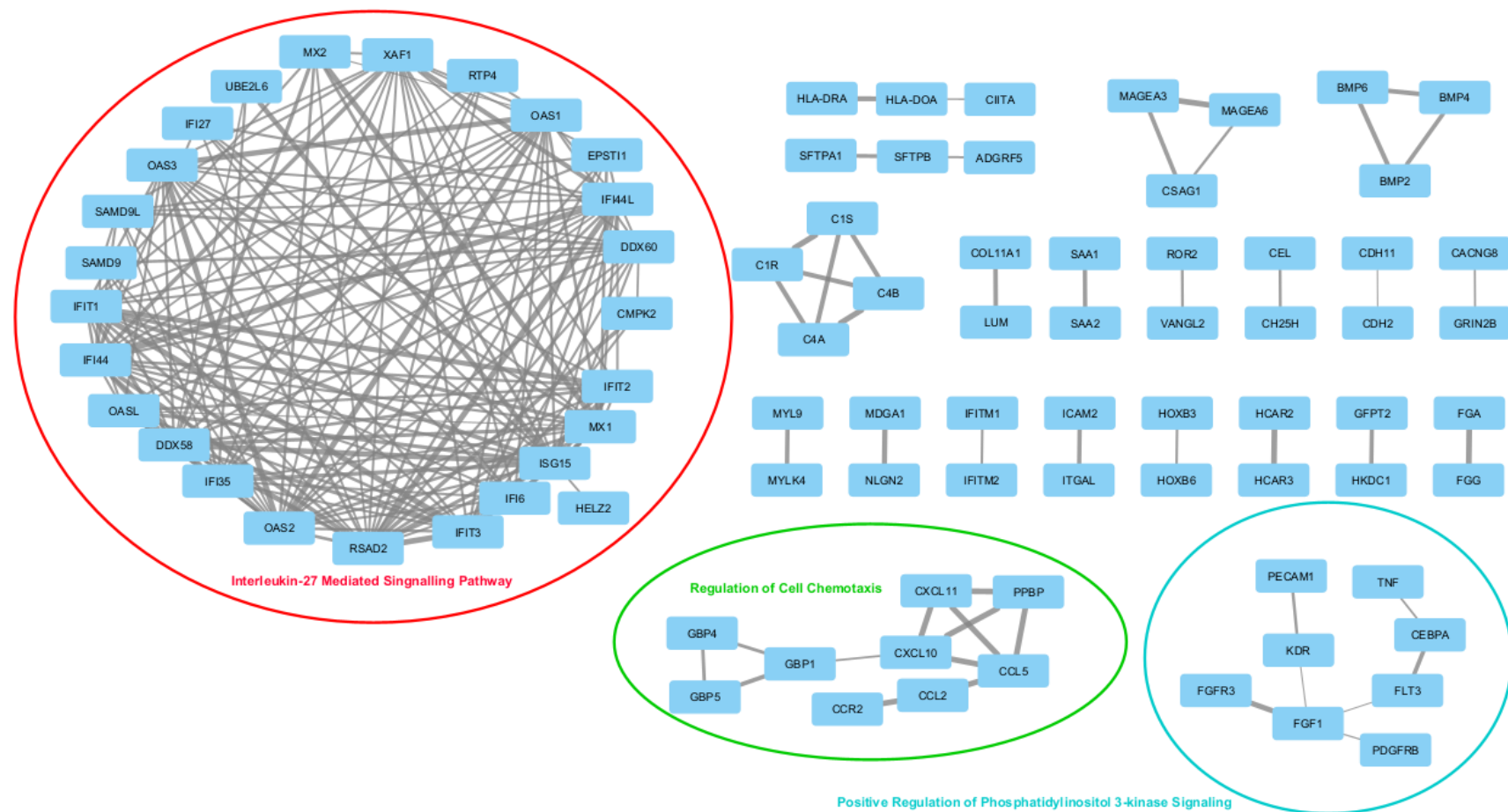


**Figure 7.7** STRING analysis of DEGs resulting from DEP exposure (against NaCl control). STRING database was used to elucidate known and predicted protein-protein interactions. Textmining was turned off, and interactions with a high confidence (0.700) are shown. Proteins without any interactions are hidden. Interactions are clustered through k-means clustering. Linkage thickness indicates 'combined' score of the interaction taking into account gene fusion, homology, co-expression, experimentally determined interaction and database annotation.

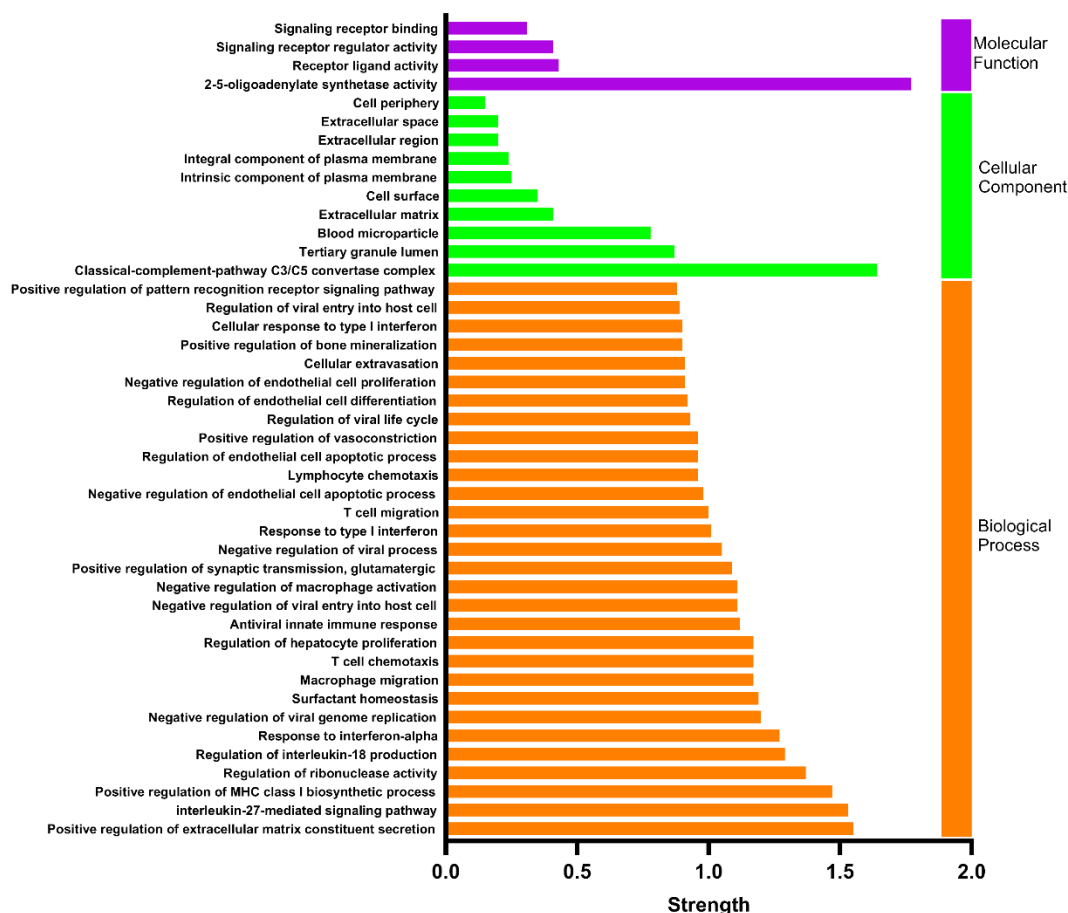


**Figure 7.8** GO terms for Biological Processes, Cellular Component and Molecular Function (top 30, 10 and 10 terms, respectively, shown for each class based off the strength) shown for DEP 17% exposure (compared to NaCl control). GO term strength is a measure that describes how large the enrichment effect is. This is generated by comparing the number of proteins in the network that are annotated for a certain GO term, compared to what would be expected to be annotated in a random network of proteins of the same size.

component and molecular function GO terms ‘classical-complement-pathway C3/C5 convertase complex’ and ‘2-5-oligoadenylate synthetase activity’, both of which are associated with an inflammatory response.

Through co-exposure of DEPs with NO<sub>2</sub>, again like NO<sub>2</sub> single pollutant exposure, there was enrichment in a network related to the ‘interleukin-27 mediated signalling pathway’ (**Figure 7.9**). There is another cluster that incorporates many of the GBPs and chemokines from the ‘regulation of cell chemotaxis’ shown in DEP only exposure.

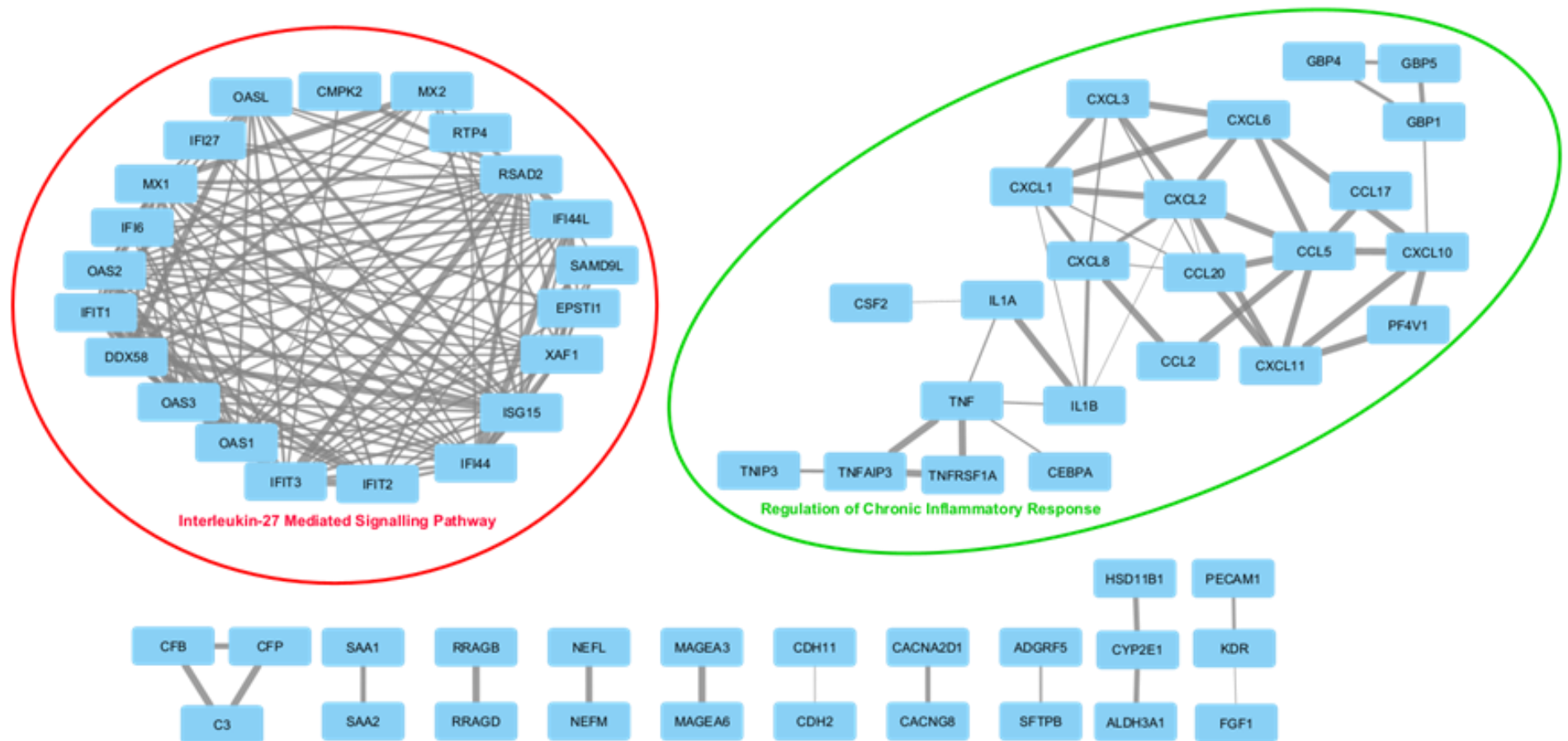


**Figure 7.9** STRING analysis of DEGs resulting from DEP + NO<sub>2</sub> co-exposure (against NaCl control). STRING database was used to elucidate known and predicted protein-protein interactions. Textmining was turned off, and interactions with a high confidence (0.700) are shown. Proteins without any interactions are hidden. Interactions are clustered through k-means clustering. Linkage thickness indicates 'combined' score of the interaction taking into account gene fusion, homology, co-expression, experimentally determined interaction and database annotation.

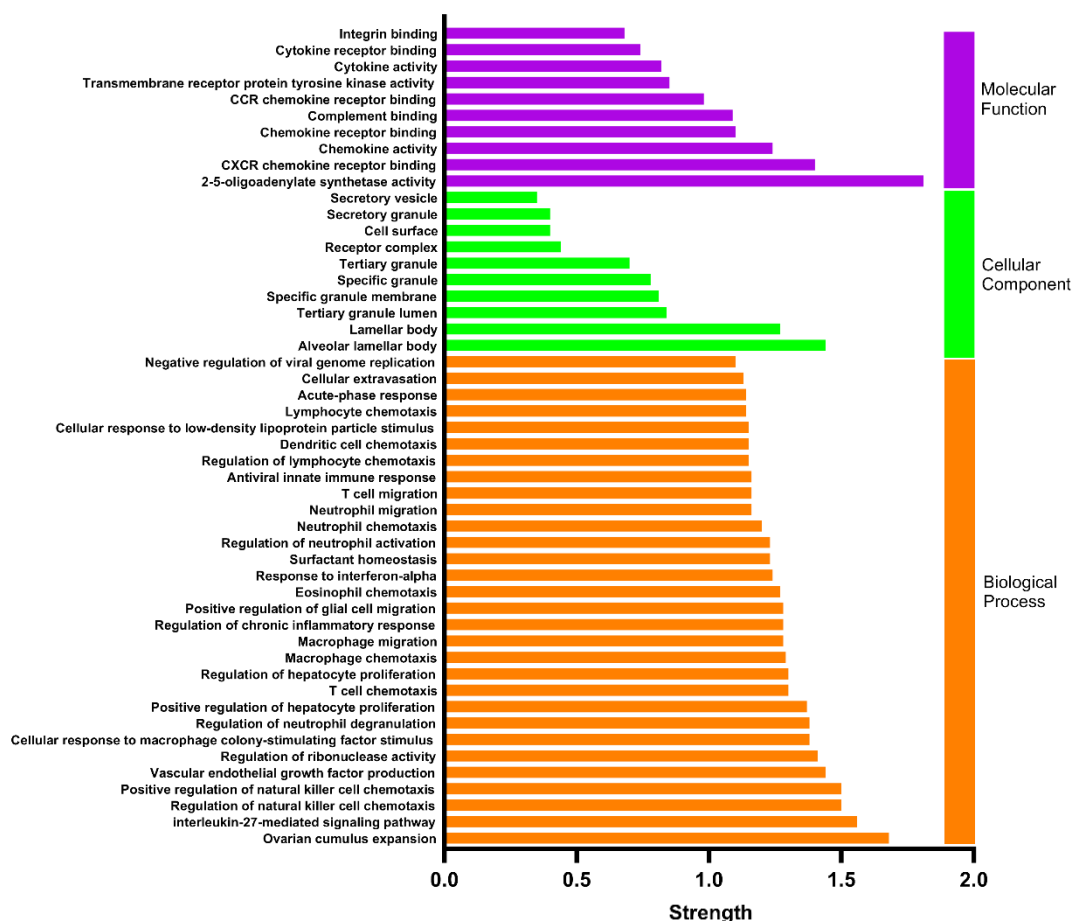


**Figure 7.10** GO terms for Biological Processes, Cellular Component and Molecular Function (top 30, 10 and 16 terms, respectively, shown for each class based off the strength) shown for DEP 17% + NO<sub>2</sub> co-exposure (compared to NaCl exposure). GO term strength is a measure that describes how large the enrichment effect is. This is generated by comparing the number of proteins in the network that are annotated for a certain GO term, compared to what would be expected to be annotated in a random network of proteins of the same size.

However, within NO<sub>2</sub> + DEP exposure, there are a number of pro-inflammatory cytokines enriched that are not enriched in the DEP-only exposure, such as IL1 $\alpha$ , IL1 $\beta$  and TNF $\alpha$ . Given that this response seems to be beyond a solely chemotactic response, this cluster has been aligned with the GO term of ‘regulation of chronic inflammatory response’.

Investigation of GO terms that are enriched when accounting for all DEGs associated with NO<sub>2</sub> + DEP exposure highlights that ‘ovarian cumulus expansion’ is the most enriched biological process. Although this GO term is not especially relevant to inhalation toxicology, it could perhaps be an indicator of broader biological processes such as cellular proliferation and differentiation. Again, numerous GO terms are associated with inflammatory response, especially chemotaxis and immune cell



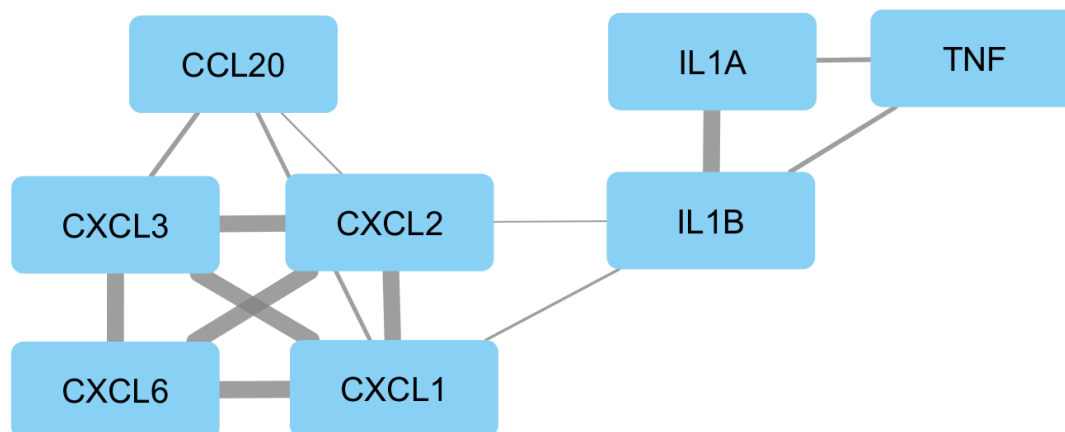


**Figure 7.12** STRING analysis of DEGs resulting from DEP + NO<sub>2</sub> co-exposure (against DEP single pollutant exposure). STRING database was used to elucidate known and predicted protein-protein interactions. Textmining was turned off, and interactions with a high confidence (0.700) are shown. Proteins without any interactions are hidden. Interactions are clustered through k-means clustering. Linkage thickness indicates 'combined' score of the interaction taking into account gene fusion, homology, co-expression, experimentally determined interaction and database annotation.

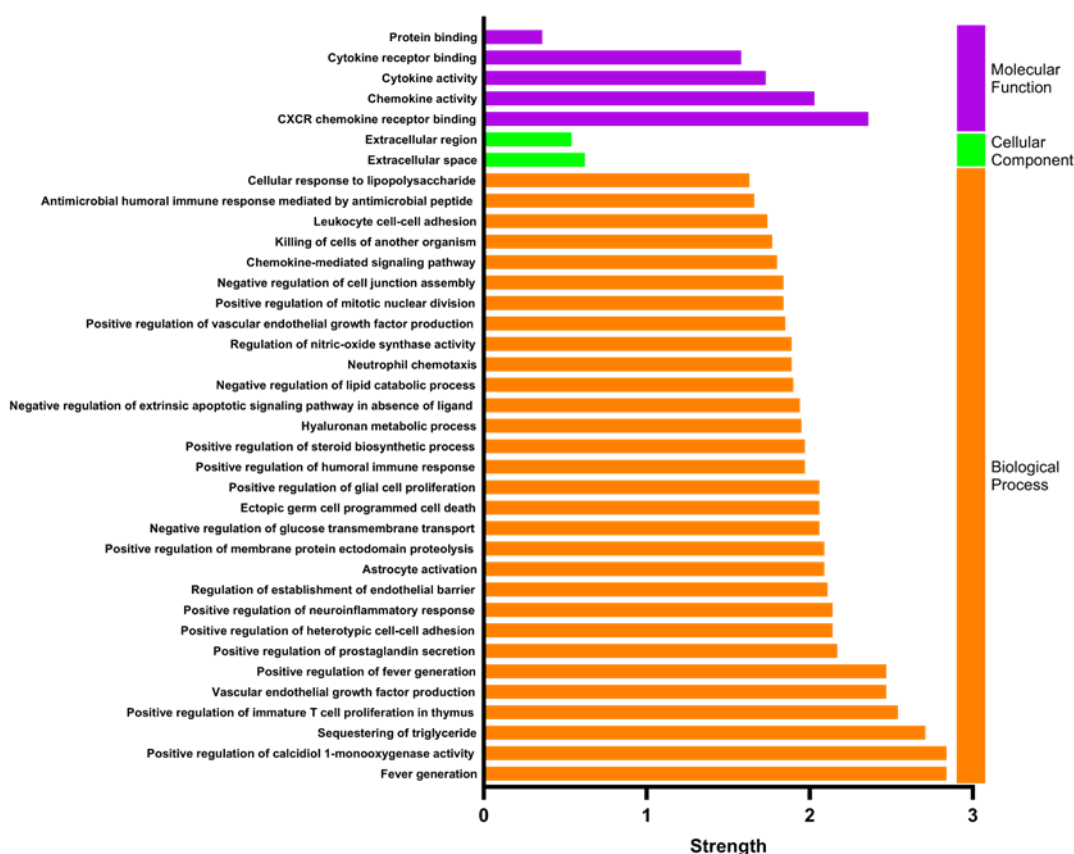


**Figure 7.11** GO terms for Biological Processes, Cellular Component and Molecular Function (top 30, 10 and 10 terms, respectively, shown for each class based off the strength) shown for DEP 17% + NO<sub>2</sub> co-exposure (compared to DEP 17% single pollutant exposure). GO term strength is a measure that describes how large the enrichment effect is. This is generated by comparing the number of proteins in the network that are annotated for a certain GO term, compared to what would be expected to be annotated in a random network of proteins of the same size.

translocation/migration (**Figure 7.10**). '2-5-oligoadenylate synthetase activity' is the most enriched molecular function GO term, with 'alveolar lamellar body' the highest

enriched cellular component GO term.

There are clearly alterations in transcriptomics between DEP single pollutant exposures and DEP + NO<sub>2</sub> co-exposures. Therefore, DEGs between DEP + NO<sub>2</sub> vs. DEP-only exposure were analysed through STRING to deduce potential changes that could be induced through NO<sub>2</sub> exposure with PM (**Figure 7.12**). One cluster is enriched within these DEGs, containing several CXC chemokines as well as cytokines IL1 $\alpha$ , IL1 $\beta$  and TNF $\alpha$ . This highlights an inflammatory change that NO<sub>2</sub> could induce. Indeed, when examining GO terms associated with DEP + NO<sub>2</sub> co-exposure compared to DEP exposure, numerous factors are involved with inflammatory response and chemotaxis (**Figure 7.11**).

### **7.3.3 Single Gene Analysis of Indoor Dust, DEP and Nitrogen Dioxide Exposures**

Although the analysis thus far has considered the RNA-Seq data in the forms of groups, clusters and GO terms, these analyses have not given insight into whether the DEGs are up or downregulated and how this could, therefore, infer biological response. To further address the mechanisms underpinning potential toxicity induced by PM and/or NO<sub>2</sub>, several genes highlighted within Section 7.3.2 have been analysed as singular components, allowing the direction of enrichment to be analysed. These gene expressions are shown as transcripts per million (TPM). Significance is shown against the the relative control (NO<sub>2</sub> against the incubator control or DEP/2583/DEP+NO<sub>2</sub>/2583+NO<sub>2</sub> against the NaCl control) unless otherwise shown on the respective graphs.

### 7.3.3.1 Chemokine Expression

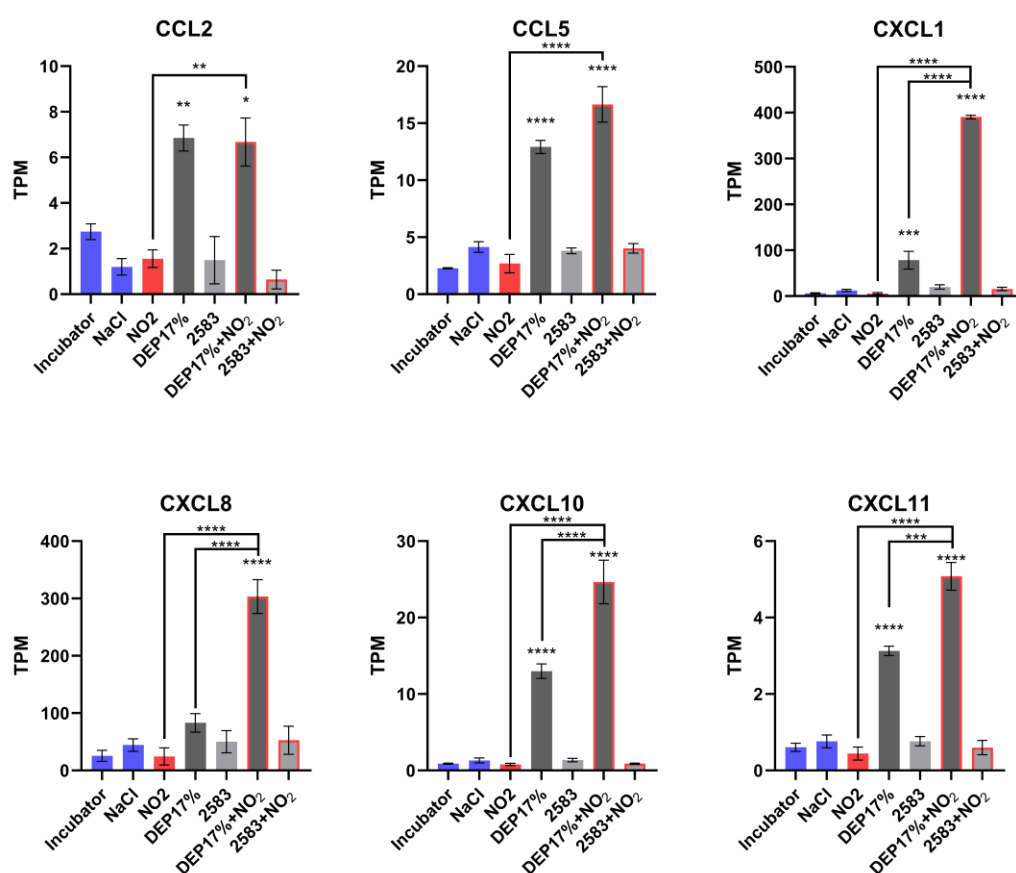


**Figure 7.13** Gene expression of chemokines following exposure to DEP 17% or 2583  $\pm$  NO<sub>2</sub>. Expression is shown as transcripts per million and error bars show the SEM. Significance shown through FDR p-values \*  $p \leq 0.05$ , \*\*  $p \leq 0.01$ , \*\*\*  $p \leq 0.001$ , \*\*\*\*  $p \leq 0.0001$ .

Chemokine expression has been highlighted as significantly altered by DEP and DEP + NO<sub>2</sub> exposure. Therefore, single gene analysis has been undertaken to deduce the direction and magnitude of enrichment (**Figure 7.13**). Initially, it is seen that chemokine expression is not significantly altered by NO<sub>2</sub> as a single pollutant, 2583 or 2583 + NO<sub>2</sub>. DEP is, however, found to significantly increase expression of CCL2, CCL5, CXCL1, CXCL10 and CXCL11, but not CXCL8. Co-exposure of DEP with NO<sub>2</sub> appears to amplify this response, where CXCL1, CXCL8, CXCL10 and CXCL11 significantly increase compared to DEP-only exposure. CCL5 levels increase in DEP + NO<sub>2</sub> exposure compared to DEP-only exposure, but significance is not reached, whereas CCL2 expression is similar between the two groups. This indicates that at the time-point measures, DEPs were able to induce the expression of chemokines, and the NO<sub>2</sub> was able to modulate this activity further.

### 7.3.3.2 Guanylate Binding Protein Expression

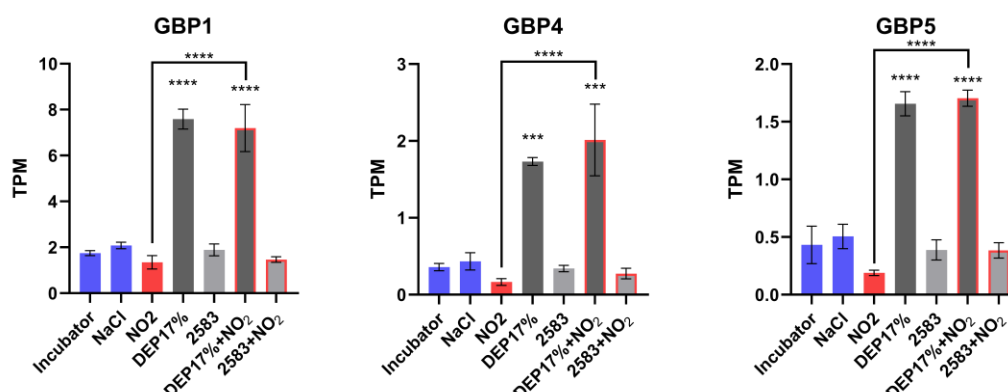


**Figure 7.14** Gene expression of guanylate binding protein following exposure to DEP 17% or 2583  $\pm$  NO<sub>2</sub>. Expression is shown as transcripts per million and error bars show the SEM. Significance shown through FDR *p*-values \*  $p \leq 0.05$ , \*\*  $p \leq 0.01$ , \*\*\*  $p \leq 0.001$ , \*\*\*\*  $p \leq 0.0001$ .

Guanylate binding proteins (GBPs) are interferon-inducible GTPases which play a role in innate immunity and antibacterial defence (Tretina et al., 2019) and were highlighted as enriched genes within the STRING analysis. Analysis of the RPKM of GBP1, GBP4 and GBP5 reveals an upregulation following DEP exposure, though this did not seem to be adjusted within the NO<sub>2</sub> co-exposures. Interestingly, NO<sub>2</sub> as a single pollutant appears to non-significantly decrease GBP1/4/5 expression following exposure (**Figure 7.14**).

### 7.3.3.3 Cytokine Expression

Pro-inflammatory cytokine (and related protein) function was altered by DEP and NO<sub>2</sub> exposures. Although DEP exposure non-significantly increased the expression of IL1 $\alpha$ , IL1 $\beta$ , IL6, IL17c and TNF $\alpha$ , co-exposure with NO<sub>2</sub> further amplified this response so that significance was reached (**Figure 7.15**). NO<sub>2</sub> on its own did not augment IL1 $\alpha$ , IL1 $\beta$ , IL6 or TNF $\alpha$  expression, although IL10 receptor subunit- $\alpha$  (IL10R $\alpha$ ) was significantly downregulated by NO<sub>2</sub> exposure. NO<sub>2</sub> co-exposure with

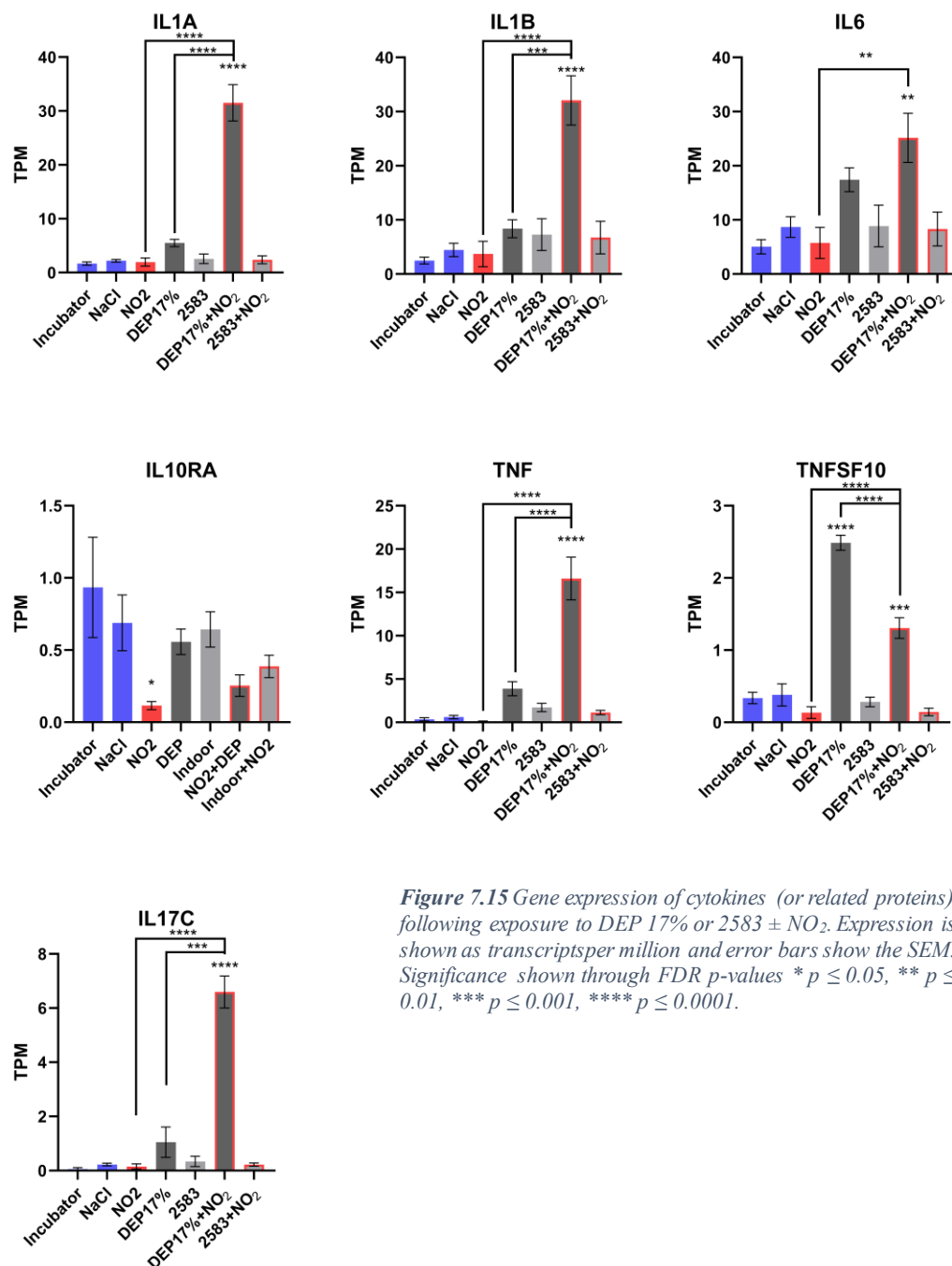


**Figure 7.15** Gene expression of cytokines (or related proteins) following exposure to DEP 17% or 2583  $\pm$  NO<sub>2</sub>. Expression is shown as transcripts per million and error bars show the SEM. Significance shown through FDR  $p$ -values \*  $p \leq 0.05$ , \*\*  $p \leq 0.01$ , \*\*\*  $p \leq 0.001$ , \*\*\*\*  $p \leq 0.0001$ .

DEP or 2583 also non-significantly reduced IL10R $\alpha$  expression. Additionally, DEP and DEP + NO<sub>2</sub> exposures increased the expression of TNF superfamily member 10 (TNFSF10/TRAIL). However, DEP + NO<sub>2</sub> exposure had significantly decreased TRAIL expression compared to DEP exposure alone.

### 7.3.3.4 Inflammatory Gene Expression

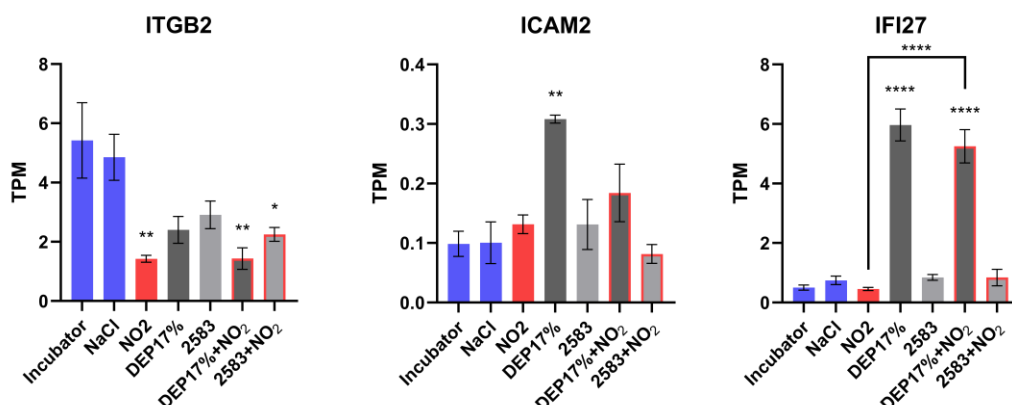


**Figure 7.16** Gene expression of inflammatory related proteins following exposure to DEP 17% or 2583  $\pm$  NO<sub>2</sub>. Expression is shown as transcripts per million and error bars show the SEM. Significance shown through FDR *p*-values \* *p*  $\leq$  0.05, \*\* *p*  $\leq$  0.01, \*\*\* *p*  $\leq$  0.001, \*\*\*\* *p*  $\leq$  0.0001.

These exposures also altered other inflammatory-related genes. Integrin Subunit Beta 2 (ITGB2), for example, is a surface protein involved in inflammation through lymphocyte homing, cell adhesion and cell surface-mediated signal transduction (Liu et al., 2023). Here, NO<sub>2</sub> was found to reduce ITGB2 expression significantly, regardless of co-exposure. DEP and 2583 alone reduced ITGB2 compared to the controls, but these effects were non-significant (**Figure 7.16**).

Intercellular Adhesion Molecule 2 (ICAM2) is required for neutrophil transmigration into the lung and is shown here to be upregulated by DEP exposure. NO<sub>2</sub>, 2583, 2583 + NO<sub>2</sub> and DEP + NO<sub>2</sub> slightly but non-significantly increase ICAM2 expression (**Figure 7.16**).

Interferon Alpha Inducible Protein 27 (IFI27) can act as a pro-apoptotic factor, increasing TNF $\alpha$  and TRAIL-induced apoptosis, as well as playing a role in viral defence (Villamayor et al., 2023). DEP increased IFI27 expression; however, co-exposure with NO<sub>2</sub> did not further modulate expression (**Figure 7.16**).

### 7.3.3.5 Oxidative Stress Gene Expression

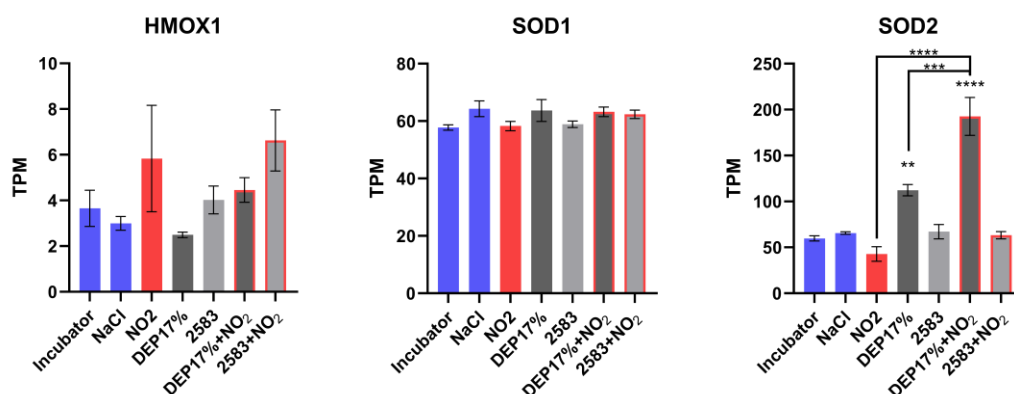


**Figure 7.17** Gene expression oxidative stress related proteins following exposure to DEP 17% or 2583  $\pm$  NO<sub>2</sub>. Expression is shown as transcripts per million and error bars show the SEM. Significance shown through FDR *p*-values \* *p*  $\leq$  0.05, \*\* *p*  $\leq$  0.01, \*\*\* *p*  $\leq$  0.001, \*\*\*\* *p*  $\leq$  0.0001.

It has previously been shown that NO<sub>2</sub> might be able to induce toxicity through an oxidative mechanism. RNA-Seq data concedes the qPCR data from Chapter 6, showing no changes in SOD1 expression following exposure (**Figure 7.17**). However, NO<sub>2</sub> did induce a non-significant increase in haem oxygenase 1 (HMOX1), an enzyme responsible for the breakdown of the oxidant haem and is known to have a defensive role against oxidant and inflammatory-related stresses within the lung (Villamayor et al., 2023). DEP enriches SOD2, on the other hand, compared to the control. Co-exposure to DEP and NO<sub>2</sub>, however, is shown to increase SOD2 significantly more than DEP exposure alone.

### 7.3.3.6 Surfactant Protein Expression

As previously mentioned, surfactant proteins are vital to ensuring effective lung function by reducing alveolar surface tension, as well as playing a role in innate and adaptive immunity (Nayak et al., 2012).

It was shown that all exposures reduced surfactant protein (SFTP) A1, although significance was only reached after DEP and DEP + NO<sub>2</sub> exposure, where SFTPA1 expression was almost reduced to zero. A similar trend was observed with SFTPB, where expression was reduced to zero by DEP and DEP + NO<sub>2</sub> exposure (**Figure 7.18**). These exposures did not alter SFTPD expression, and SFTPC was not expressed at all by this model (data not shown).

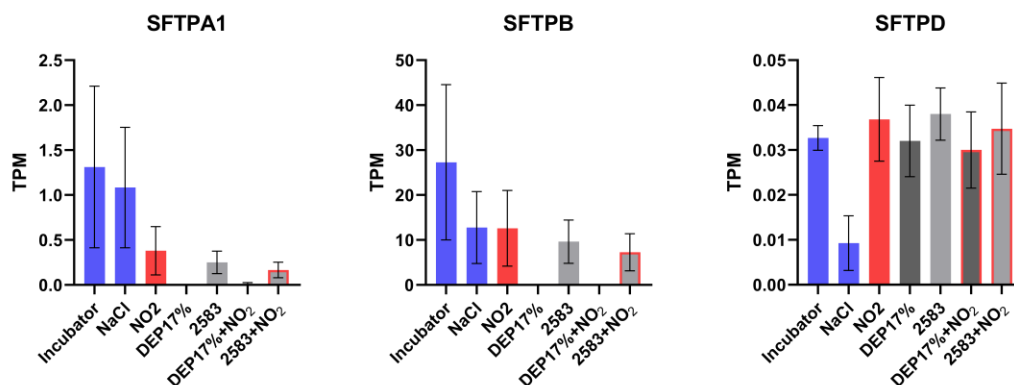


**Figure 7.18** Gene expression surfactant proteins following exposure to DEP 17% or 2583  $\pm$  NO<sub>2</sub>. Expression is shown as transcripts per million and error bars show the SEM. Significance shown through FDR p-values \*  $p \leq 0.05$ , \*\*  $p \leq 0.01$ , \*\*\*  $p \leq 0.001$ , \*\*\*\*  $p \leq 0.0001$ .

### 7.3.3.7 Expression of Other Differentially Expressed Genes

Mucins protect epithelial surfaces from physical, chemical, or biological harm. Mucin 21 (MUC21) expression could infer an anti-apoptotic effect on cells (Tian et al., 2022). Here, all exposures resulted in a decrease in MUC21 expression, although DEP exposure ( $\pm$  NO<sub>2</sub>) decreased expression to the point of statistical significance (**Figure 7.19**).

Solute carrier family 11 member 1 (SLC11A1) is a protein found on the membrane of phagosomes, which are involved in antibacterial activity (Ding et al., 2014). SLC11A1 appears to be significantly downregulated by NO<sub>2</sub> exposure, although it is less so impacted by DEP or 2583 exposure (**Figure 7.19**).

Matrix metalloproteinase 9 (MMP9) is an enzyme that is involved in the activation of TGF- $\beta$  and is involved in lung regeneration and repair following lung injury (Bormann et al., 2022). MMP9 is reduced by NO<sub>2</sub> exposure, as well as 2583, although not to a statistically significant extent (**Figure 7.19**).

As mentioned in Chapter 1, CYP1A1 is an enzyme involved in the detoxification of many toxins (Mescher & Haarmann-Stemmann, 2018). NO<sub>2</sub> here is shown to significantly increase CYP1A1 expression, although co-exposure with DEP or 2582 also increases its expression, significance is not reached (**Figure 7.19**).



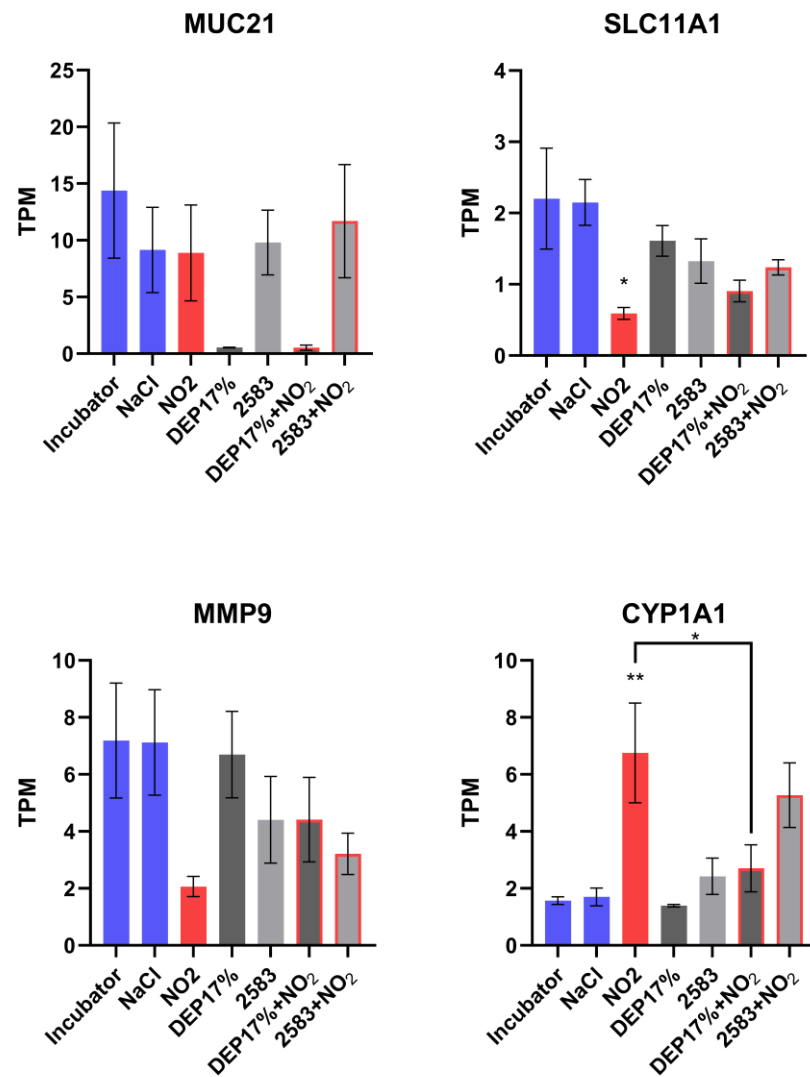


**Figure 7.19** Gene expression MUC 21, SLC11A1, MMP9 and CYP1A1 following exposure to DEP 17% or 2583  $\pm$  NO<sub>2</sub>. Expression is shown as transcripts per million and error bars show the SEM. Significance shown through FDR *p*-values \*  $p \leq 0.05$ , \*\*  $p \leq 0.01$ , \*\*\*  $p \leq 0.001$ , \*\*\*\*  $p \leq 0.0001$ .

## 7.4 Discussion

When first considering the number of DEGs for each exposure, it is shown that there are minimally altered genes resulting from NaCl exposure. Specifically, RP11-867G23.3 and CA9 are downregulated, and RP11-264B17.3 is upregulated. Although there is little information present regarding the cellular function of RP11-867G23.3, RP11-264B17.3 could have a role in cell death (Cheng et al., 2023). However, further studies are required to elucidate this. It is doubtful that RP11-264B17.3 would have a significant effect on cell death as previous chapters have shown no cytotoxic effect of NaCl exposure, and there is no other alteration in cell death-related genes such as BAX or Bcl-2. CA9 encodes carbonic anhydrase 9, which is a cell surface glycoprotein that catalyses the hydration of CO<sub>2</sub> to bicarbonate and hydrogen ions (Pastorekova & Gillies, 2019). It is involved in acid-base balance, and it could, therefore, be postulated that additional NaCl could alter this balance within the cell culture media, thus changing the expression of CA9.

It is interesting that there were no differentially expressed genes associated with an inflammatory response in the NaCl control exposed cultures compared to the incubator, given that often an IL6 and/or IL8 response was seen following NaCl exposure. Perhaps the expression of pro-inflammatory proteins had attenuated by the time of RNA extraction, but the proteins remained present in the supernatant explaining their detection *via* ELISA.

As will be discussed throughout this following section, there are areas in which the findings of this work contrast with findings of the work of others. Although the NO<sub>2</sub> concentrations used within this work are generally higher than ambient NO<sub>2</sub> levels, they are often lower than those that have been used previously within *in vitro* and *in vivo* toxicological studies. This should be a consideration when making a comparison of findings. Further, the PM exposure concentration used has been chosen as it is within a human exposure relevant range, which is often lower than PM concentrations used within toxicological studies. Therefore, given the acute duration of exposure, it may be considered that the responses within this work would be more modest.

### 7.4.1 Inflammation

Regardless, compared to PM or NO<sub>2</sub> exposure, NaCl resulted in far fewer DEGs. NO<sub>2</sub> exposure resulted in a downregulation of many genes whilst simultaneously upregulating numerous genes. Given the number of DEGs for this exposure, it was initially valuable to examine effects in terms of GO terms to gain a better understanding of broadly which mechanisms might be altered. Consistent with previous literature, inflammatory processes appeared to be enriched following NO<sub>2</sub> exposure, with a particular network of genes around the protein integrin subunit beta 2 (ITGB2), which exhibits reduced expression. Beta 2-integrins are mainly expressed by myeloid cells so that they can be present within the dTHP-1 cells.

Interestingly, ITGB2 has been shown to inhibit macrophage activation and cytokine production upon activation of TLRs by LPS, therefore showing an anti-inflammatory function (Fagerholm et al., 2019). Indeed, beta-2 integrin signalling has been shown to act in an anti-inflammatory manner *in vitro* and *in vivo*, inducing IL10 expression, which is a suppressor of cytokine production (Wang et al., 2010). Therefore, in this instance, it would be expected that a reduction in ITGB2 would result in a loss of this anti-inflammatory effect and a potential increase in pro-inflammatory outputs. Examining IL10 shows explicitly that this culture is minimally expressing IL10 (at least at the time point observed). However, there is a significant reduction in IL10 receptor (IL10R) expression following NO<sub>2</sub> exposure. Upon binding to IL10R, IL10 will induce the transactivation of anti-inflammatory genes through STAT3 signalling. Anti-inflammatory proteins, such as suppressors of cytokine signalling 3 (SOCS3), can then inhibit PRR-induced expression of pro-inflammatory factors (Shouval et al., 2014). Here, the associated reduction or increase in anti- and pro-inflammatory proteins, respectively, is not observed, perhaps due to the lack of a direct pro-inflammatory stimulus or a lack of IL10 transcription. Regardless, within *in vivo* or human conditions, the reduction in IL10R expression, and thus the reduced signalling through this receptor-mediated pathway, could contribute to an increased risk of pulmonary fibrosis. Nakagome *et al.* (2006) have shown that bleomycin-induced pulmonary fibrosis in mice could be suppressed through the intravenous delivery of IL10 plasmids. Given that NO<sub>2</sub> has been shown to progress pulmonary fibrosis and increase mortality risk in patients possessing pulmonary fibrosis, this could perhaps

suggest a mechanism underpinning this NO<sub>2</sub> effect (Yoon et al., 2021; Yoon et al., 2023).

MMP2 and MMP9 are found to be downregulated by NO<sub>2</sub> within this model. This is contradictory to previous work that has found that *in vivo* exposure to diesel emissions increased MMP9 expression (Lund et al., 2009) (here, NO<sub>2</sub> and DEP exposure did not enrich MMP9 either). Although this is paradoxical, there is a potential mechanism at play here. NO has been found to reduce the expression of MMP2 within endothelial cells (Chen & Wang, 2004) (MMP2 is often co-expressed with MMP9 (Buttacavoli et al., 2021)). Further, exposure of NHBE bronchial epithelial cells with NO<sub>2</sub> was found to increase NO levels, likely through both enzymatic and non-enzymatic interactions. Nitric oxide synthases (NOSs), as part of healthy physiology, convert L-arginine to NO. NOS inhibitors were shown to reduce NO at later time points during NO<sub>2</sub> exposure in NHBE cells; however, they did not interrupt an initial NO increase, which could be a result of NO<sub>2</sub> absorption into the cell culture media or the cells themselves (Ayyagari et al., 2004). Therefore, NO<sub>2</sub> exposure could directly increase NO concentrations, which could subsequently reduce MMP transcription.

Given that the cell culture media is in direct contact with the NO<sub>2</sub>, this could form an interaction that would not occur within an *in vivo* system, therefore inducing this contradictory effect. This is further suggested, given that there was no increase in the transcription of NOSs within NO<sub>2</sub>-exposed cells. Regardless, the known role that MMP2/9 plays in tissue remodelling could also explain the differences in cellular morphology observed following NO<sub>2</sub> exposure in Chapter 6.

Far fewer genes are enriched following 2583 exposure compared to DEP or NO<sub>2</sub> exposures, namely, upregulations of PVRIG2P, CTB-31O20.3, AC005387.3, RP11-498C9.3 and LL22NCO3-N14H11.1, and a downregulation of RP11-542C16.1. PVRIG2P is a pseudogene and is non-functional, whilst the others appear to be non-well-researched long non-coding RNAs. Co-exposure of 2583 with NO<sub>2</sub> resulted in more DEGs and more DEGs likely to have an impact on biological processes. These DEGs were significantly enriched for “T cell activation *via* T cell receptor contact with antigen bound to MHC molecule on antigen-presenting cell”, as shown through DAVID bioinformatics, as well as “inflammatory response” and “phagocytosis”. This is interesting as 2583 appears to show a pro-inflammatory response at the protein level

(Chapter 5 and Chapter 6), yet this is not seen in the transcriptomics. Co-exposing 2583 with NO<sub>2</sub>, however, differentially expresses pro-inflammatory-related gene expression. Integrin subunit alpha L (ITGAL) appears to contribute to all these effects, although it is similarly expressed within NO<sub>2</sub> only and 2583 + NO<sub>2</sub> exposures and likely is not a factor induced by 2583 alone. In fact, the only DEG between 2583 and 2583 + NO<sub>2</sub> exposure is Interferon Induced Protein with Tetratricopeptide Repeats 2 (IFIT2). IFIT2 is an antiviral gene that binds to mRNA to enhance the transcription of antiviral and innate immunity proteins by reducing ribosomal pausing. The influenza virus, however, possesses the ability to hijack this process and utilise IFIT2 to enhance the transcription of its own mRNA (Tran et al., 2020). Here, a reduction in IFIT2 expression was observed following NO<sub>2</sub> + 2583 exposure, which could potentially mean that these cells are more prone to viral attack due to their reduced ability to translate antiviral mRNA; alternatively, that the cells are protecting themselves from viral attack through reducing IFIT2 levels, reducing the ability for viruses to lever a cells' own mechanisms against itself.

Compared to 2583, DEPs result in a far higher number of DEGs. This is perhaps exemplary of the COMEAP differential toxicity statement, highlighting that PM is not all equal and possesses different toxic capabilities. DEGs relating to DEP exposure appear to signal broadly through a pro-inflammatory mediated manner, showing a high degree of chemokine and pro-inflammatory mediator expression. Previous work within A549 cells has associated DEP exposure with IL1 $\beta$  release, as was observed here (Tsukue et al., 2010). Although contradictory to this work, other studies have indicated that DEPs can suppress TNF $\alpha$  release from AMs (Amakawa et al., 2003), whilst others have shown that conditioned media from DEP-exposed macrophages was able to stimulate cytokine release in endothelial cells through a TNF $\alpha$  dependant mechanism (Shaw et al., 2011).

Firstly, this indicates the importance of a cell system-based approach, where different cell types can interact to induce differential toxic outcomes. Secondly, this adds context to the findings found here. To add more context, within BEAS-2B cells, transcriptomic data has shown a DEP-driven increase in CCL5 and CXCL10, also shown here (Totlandsdal et al., 2010). Many of these studies, however, also show a significant increase in IL6 and IL8 following DEP exposure that was not replicated here and not observed within the direct protein measurements (Chapter 5). Within the

present work, an increase in IL6 and IL8 expression following DEP exposure would have been expected, given the enrichment of other pro-inflammatory genes. However, it is possible that given that these data represent a snapshot in time, IL6 and IL8 had not yet been transactivated, and perhaps given extra time, IL6 and IL8 enrichment could have been shown, though, it is expected that IL6 and/or IL8 release would have been observed within this timeframe based on previous studies (Meldrum, Evans, et al., 2022). This appears to be cell type/co-culture dependent however, which could also explain why little effect was shown here. Alternatively, it could be that this model required additional stimulus to induce IL6 and IL8 transactivation upon DEP exposure.

Indeed, co-exposure of DEPs with NO<sub>2</sub> appears to induce this response, showing significant increases in IL6 and CXCL8 expression compared to DEP or NO<sub>2</sub> exposure alone. This could be due to the heightened expression of other genes related to the pro-inflammatory cascade, such as CCL5, CXCL1, CXCL10, IL1 $\alpha$ , IL1 $\beta$  and TNF $\alpha$  compared to single pollutant exposures, that could have driven IL6 and IL8 to be transcribed at augmented levels. Although it is not initially clear why NO<sub>2</sub> could induce this amplified effect, it could be due to the synergistic activity of the two pollutants, where NO<sub>2</sub> could be inhibiting the cells' anti-inflammatory systems through an IL10/IL10R mediated manner. Meanwhile, DEP induces a pro-inflammatory response that intrinsic anti-inflammatory mechanisms can no longer counter. STRING and GO analysis of DEGs between NO<sub>2</sub> and PM highlight chemotactic and pro-inflammatory effects with enrichment for the KEGG pathway 'TNF Signalling Pathway' (**Figure 7.20**). It could be postulated that TNF $\alpha$  is a trigger in the observed response, as a TNF $\alpha$

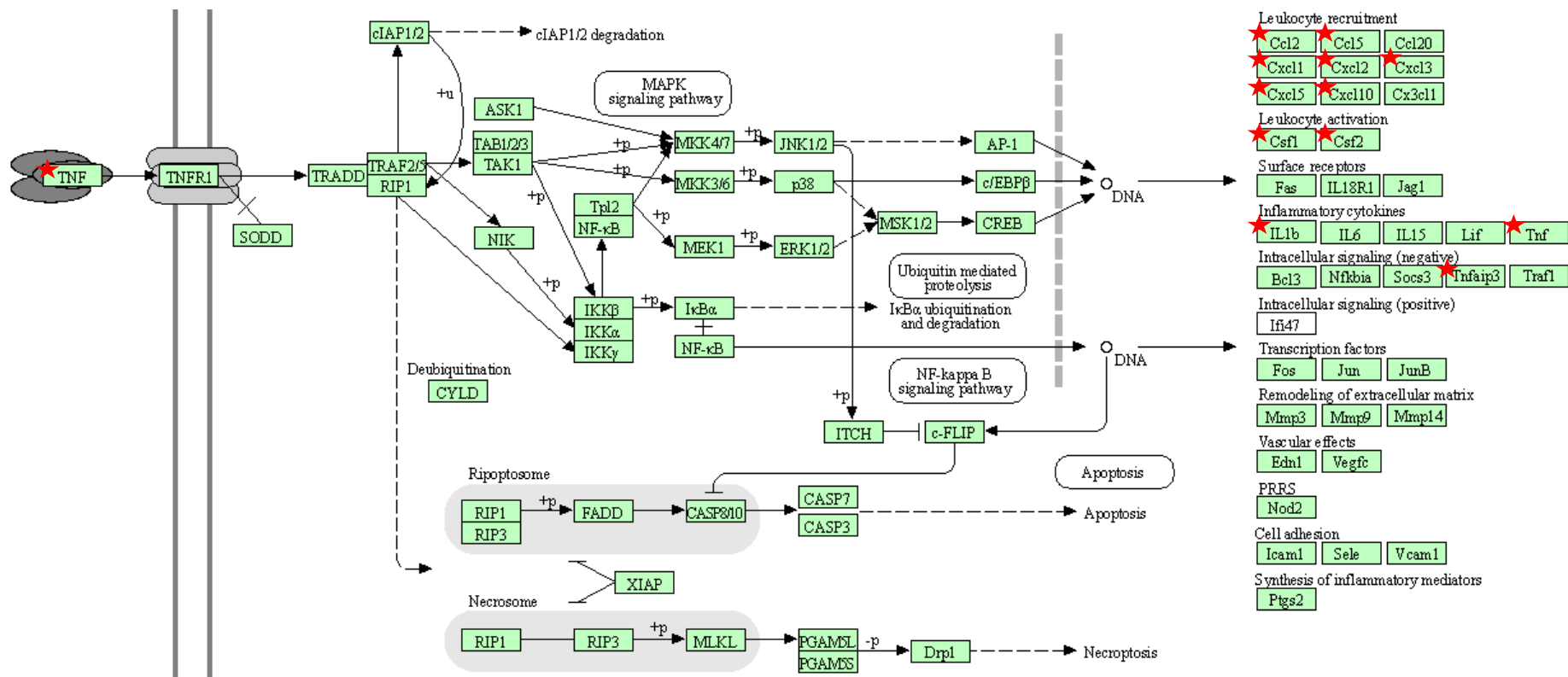


**Figure 7.20** TNF signalling pathway. Red stars indicate DEGs following NO<sub>2</sub> and DEP 17% co-exposure. Figure from <https://david.ncifcrf.gov/>.

response has been shown previously in this model (Chapter 3). IL10 has shown to be an inhibitor of TNF $\alpha$  within alveolar macrophages (Armstrong et al., 1996), and therefore further explains the observed results.

Airway inflammation has been associated with the onset of airway diseases such as COPD and asthma (Angelis et al., 2014; Murdoch & Lloyd, 2010), and therefore, this could provide a mechanism by which NO<sub>2</sub> + PM co-exposure, especially in terms of traffic-related air pollutions (given the effects observed with DEPs), could induce an effect on public health.

Another route in which these pollutants could have triggered a pro-inflammatory effect is through the cytokine IL17C. IL17C has first been shown to be a driver of neutrophilic inflammation and tissue destruction in mice exposed to the *Haemophilus influenzae* and cigarette smoke and upregulated by *Mycoplasma pneumoniae* and *Staphylococcus aureus* or exposure to IL1 $\beta$  or TNF $\alpha$  (Ramirez-Carrozzi et al., 2011; Vella et al., 2021) (**Figure 7.21**). IL17C is expressed in a TLR-dependent manner and is often considered epithelial cell-derived cytokine, with the ability for autocrine signalling through binding to IL17 receptor A and E heterodimers to induce antimicrobial peptide production (Ramirez-Carrozzi et al., 2011). Further, IL17C levels have been shown to be elevated within advanced COPD patients, compared to moderate COPD, perhaps indicating a mechanism of air pollution-induced/exacerbated COPD (Vella et al., 2021). The link between COPD, lung cancer and IL17C has been suggested, with it being predicted that IL17C can induce neutrophilia of the tumour microenvironment, inducing inflammation and tumour proliferation. Indeed, IL17C has been associated with worse non-small cell lung cancer prognosis (Jungnickel et al., 2017).

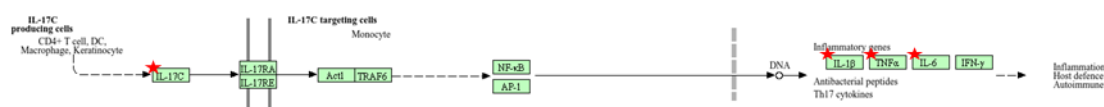


**Figure 7.21** IL17C transduction pathway. Red stars indicate DEGs following NO<sub>2</sub> + DEP co-exposure. Figure from <https://david.ncifcrf.gov/>.

## 7.4.2 Oxidative Stress

As discussed, there is a clear trend that NO<sub>2</sub> is driving an effect that enhances the pro-inflammatory response of DEPs. IL10/IL17C signalling has already been proposed as a mechanism by which this could occur. However, non-inflammatory processes such



as oxidative stress should also be considered. Within previous chapters, there were no effects observed on *SOD1* expression following NO<sub>2</sub> exposure ± PM. However, it was speculated that SOD2 could be another viable target to assess oxidative stress. The RNA-Seq shows that the DEPs, but not NO<sub>2</sub> or 2583, induce SOD2 expression. However, this is significantly increased again upon co-exposure of DEP and NO<sub>2</sub>, implying a synergistic effect here. Perhaps NO<sub>2</sub> and DEP are driving oxidative stress through different mechanisms inducing this effect. There is an increase in HMOX1 expression following NO<sub>2</sub> exposure, though this is not replicated in the DEP + NO<sub>2</sub> co-exposure (it is increased by 2583 + NO<sub>2</sub> exposure, however). Within bronchial epithelial cells, 5 ppm NO<sub>2</sub> has been shown to increase HMOX1 expression (Mirowsky et al., 2016). Although Karthikeyan *et al.* (2013) were not able to attribute, NO<sub>2</sub> concentration increases with SOD2 expression within rat models when exposed to diesel emission through a particle filter, attributing changes in SOD2 expression to unfiltered UFPs. This also aligns with the findings here, where SOD2 is expressed following DEP exposure. This could perhaps indicate that the two pollutants are independently causing oxidative stress through separate mechanisms, which are then converging to induce an amplified response. Further, given that oxidative stress can lead to inflammation (Hussain et al., 2016), this could provide a mechanism by which augmented chemo/cytokine expression is induced by DEP + NO<sub>2</sub> co-exposure.

However, the ability of the inflammatory oxidative relationship to act in both directions must be acknowledged, and it is just as possible that increases in SOD2 could be a response to an increased pro-inflammatory state.

### **7.4.3 Metabolism and Detoxification**

On this note, NO<sub>2</sub>, but not PM, exposure increased CYP1A1 transcription. This is contradictory to other evidence finding that NO<sub>2</sub> may induce a reduction in CYP1A1 transcription (Karthikeyan et al., 2013). Others have found that complete diesel exhaust emissions increase CYP1A1 transcription within human subjects (Friberg et al., 2023). Regardless, within the triple cell co-culture, the CYP1A1 increase could be indicative of detoxification processes taking place in response to NO<sub>2</sub> exposure, which could again drive either oxidative stress or inflammation or both (Stading et al., 2020; Tian et al., 2020). What is not clear, however, is that this CYP1A1 increase is not mirrored in the NO<sub>2</sub> + PM co-exposures, being only minorly increased. Assessing

CYP1A1 at a protein level could provide further clarification on this. This could be done through a Western blot of lysed cells following exposure. Alternatively, fluorescent techniques such as immunocytochemistry and confocal microscopy on fixed cultures or kits such as the Promega P450-Glo™ on live cells could be used to quantify CYP1A1. Performing such techniques at various time points following exposure may shed light on whether, for example, PM might be causing an early spike in CYP1A1, which subsequently is not measured after 24 hours. Also, it must be noted that the NO<sub>2</sub> concentration used here is relatively high compared to PM (in the context of human exposures).

#### **7.4.4 Surfactant Proteins**

DEPs have been shown here to align with previous data, showing a reduction of surfactant proteins following DEP exposure (Cienciewicki et al., 2007; Ryu et al., 2020; Wu et al., 2022). However, it is seen that NO<sub>2</sub> and 2583 have a similar effect on SFTPA1 and SFTPC, although not to the magnitude that DEPs do. Given that the defence properties of SFTPA1 and surface tension properties of SFTPC (Devendra & Spragg, 2002) could, therefore, be diminished with pollutant exposure, it is clear how this could influence the onset of pulmonary disease. Furthermore, the reduction of SFTPA1 by DEP may allow further toxicity from other pollutants as the intrinsic defence mechanisms of SFTPA1 could be reduced. Therefore, a synergistic activity between pollutants that could cause inflammation and oxidative stress changes was observed. This emphasises the need to focus further on the effect of inhaled pollutants on the surfactant layer.

## 7.5 Summary and Outlook

*Table 7.2 Summary of key findings and conclusions from Chapter 7.*

<b>Chapter Conclusions</b>	<ul style="list-style-type: none"> <li>▪ RNA-Seq analysis revealed DEP exposure resulted in more DEGs than 2583 exposure.</li> <li>▪ NO<sub>2</sub>-only exposure increased the number of DEGs resulting from DEP and 2583 exposure.</li> <li>▪ NO<sub>2</sub> + DEP exposures increased amplified the transcription of pro-inflammatory-related genes, perhaps driven by an NO<sub>2</sub>-induced reduction in IL10 signalling.</li> <li>▪ These exposures also altered genes involved with oxidative stress, surfactant and metabolism.</li> </ul>
<b>Project Impact</b>	<p><b>RNA-Seq has shed light on a potential mechanism that could confer an amplified inflammatory response following NO<sub>2</sub> + DEP exposure (compared to respective single pollutant exposures). This information could explain the association between air pollution exposure and related morbidities. However, this effect appeared to be context-dependent, with the type of PM and method of exposure showing to have an effect.</b></p>

Through RNA-Seq analysis, DEGs resulting from NO<sub>2</sub>, 2583 and DEP exposure have been identified. Firstly, within the triple cell culture, it was noted that NO<sub>2</sub> and DEP resulted in a far more significant transcriptomic change compared to 2583. Pathways and processes related to inflammatory response and chemotaxis were commonly upregulated between NO<sub>2</sub> and DEP exposures. Upon closer inspection of specific genes and the magnitude of expression differences, it appears that co-exposure to NO<sub>2</sub> and DEP amplifies the pro-inflammatory response induced by DEP-only exposure. It is speculated that this could be a result of a NO<sub>2</sub>-driven reduction in IL10-mediated anti-inflammatory signalling. Furthermore, NO<sub>2</sub> and DEP appear to act through an IL17C-mediated mechanism, perhaps amplifying the inflammatory state and could be indicative of pulmonary morbidities.

Given the alterations in oxidative stress and detoxification-related genes resulting from NO<sub>2</sub> exposure, it is hypothesised that these processes could further contribute to the pro-inflammatory response shown to be significantly altered between DEP exposure and DEP + NO<sub>2</sub> co-exposure.

It is important to note, however, that these data represent a single snapshot in time, and to further understand the mechanisms underpinning these toxicological responses, it

may be pertinent first to examine transcriptomics over earlier and later periods. This could further elucidate which mechanisms could be activated, leading to the transcription changes observed. Furthermore, a dose-response study of NO<sub>2</sub> or DEPs implemented within the RNA-Seq analysis could allow the identification of concentration-dependent effects, which could provide further evidence to support suggested mechanisms of action. Finally, assessing these changes at a protein level through ELISAs or Western blots could further distinguish the underlying signalling pathways causing the observed changes, primarily through assessing the phosphorylation status of signalling proteins. Identification of protein-protein interactions could then be examined through proximity ligation assays, which would reaffirm whether suggested signalling pathways are indeed occurring following exposure.

## Chapter 8: Discussion

---

## 8.1 Summary of Introduction and Aims

Air pollution exposure is responsible for 9 million premature deaths annually worldwide (Fuller et al., 2022), and as such, guidelines and policies to reduce exposure risk are continually being developed and implemented (World Health Organization, 2021). However, there is difficulty when establishing pollutant reduction strategies due to the heterogeneous nature of air pollution, with the potential for each aspect to possess individual, specific effects on human health, which may then act synergistically when an individual is exposed to a pollutant mixture. Two pollutants, PM and NO<sub>2</sub>, are often found to be proportional within the ambient air, and as such, it is difficult to disentangle the effects of either pollutant singularly from the epidemiological evidence (COMEAP, 2015, 2018). Given that both pollutants have been linked to morbidity and mortality (Fuller et al., 2022), there is a requirement to assess which pollutant drives hazardous effects or whether both possess the capabilities to induce a toxic response and are able to modulate this effect in a synergistic or additive manner when co-exposure occurs. This project, therefore, intends to compare the effects of both pollutants, both individually and within co-exposure within the same experimental system to elucidate the toxic effects.

## 8.2 Summary Development of the Alveolar Triple Cell Co-Culture

To address this call to research, the project took an *in vitro* approach, which would allow controlled exposure to PM, NO<sub>2</sub> or PM + NO<sub>2</sub> at defined, realistic concentrations. However, there was a requirement initially to develop a relevant and well-characterised *in vitro* model. Given that the alveolar epithelial barrier is a primary point of toxicity, this was replicated using hAELVi, NCI-H441 and dTHP-1 cells as models for ATI, ATII and AMs, respectively. Although the NCI-H441 and dTHP-1 cells have been characterised previously (Mitchell, 2022; Risby, 2022), hAELVi cells were initially characterised here according to GIVIMP (OECD, 2018) guidelines, finding that the cells were effectively grown at the ALI and could form a tight monolayer.

Subsequently, a triple cell-co-culture was developed using these three cell types. The ATI to ATII ratio targeted for this culture (at the time of exposure) was 13-16:1 (Crapo et al., 1982). CellTracker™ analysis revealed that a 16.44:1 seeding ratio was achieved

using the hAELVi and NCI-H441 co-culture. Next, the model was characterised, again through CellTracker™ analysis, to have 1.13 dTHP-1 cells per  $18 \times 10^3 \mu\text{m}^2$ , near the anatomically relevant targeted cell density of 1 AM per  $18 \times 10^3 \mu\text{m}^2$  (Stone et al., 1992). The model was further shown to possess a tight barrier function, the ability to react to a pro-inflammatory stimulus, and the ability to be cultured at the ALI. These characteristics are vital for a model that intends to resemble the alveolar barrier (Barnes, 2004; Crapo et al., 1982).

### **8.3 Summary of the Characterisation of Particulate Matter and Nitrogen Dioxide Exposure Methods**

The exposure methods used within this can be split into PM exposures and NO<sub>2</sub> exposures, which were discussed in Chapter 4.

*In vitro* models were exposed to PM using a VitroCell® Cloud 12 system, which allows a particle suspension to be nebulised, forming an aerosol that will deposit onto the transwell insert membranes. Three particle types were used with this system: CB, 1649b and 2583, representing exposures occurring both indoors and outdoors. Although CB has been used with a Cloud system previously, prior research would suggest this is the first time 1649b or 2583 have been used within this system. For this reason, it was important to understand the deposited mass of each particle prior to exposing cells. CB, 1649b and 2583 were nebulised at a concentration of 50-1000, 250-2000 and 250-2000  $\mu\text{g/mL}$  respectively, finding a deposition range of 151-450, 524-846, 350-1114  $\text{ng/cm}^2$ , respectively. These deposition ranges are broadly similar to what has been published previously using similar particles within aerosol exposure systems (Drasler et al., 2018; He et al., 2020). Further, these particles are within a range that would allow *in vivo* relevant exposure concentrations (Søs Poulsen et al., 2013), and as such, targeted exposure concentrations of 390, 780 and 3100  $\text{ng/cm}^2$  were utilised. SEM imaging also revealed that the deposited fraction of these PM samples was in the size range of 5  $\mu\text{m}$  or less, broadly within the respirable particle size range (Wippich et al., 2020), making the alveolar models described in Chapter 3 highly relevant to the investigation of toxicity induced by these particles.

As this aerosol exposure technique is a transient process that will deposit particles which remain *in situ* for the exposure duration, it allows the *in vitro* cultures to be physically moved whilst maintaining the PM exposure at the ALI. Therefore, it allows

cells to be incubated in varying conditions. Here, the NO<sub>2</sub> concentration in which the cells were to be cultured was altered. This was done through the development of an NO<sub>2</sub> exposure chamber, which allowed the internal gas concentrations to be controlled and maintained. Initial testing found that NO<sub>2</sub> concentrations were possible up to 5 ppm whilst maintaining cell culture-relevant O<sub>2</sub>, CO<sub>2</sub> and humidification conditions. This represents a potential new method for *in vitro* air pollution co-exposure assessment.

#### **8.4 Summary of Effects of Particulate Matter Exposure**

Chapter 5 combined the approaches described in Chapter 3 and Chapter 4 to expose an anatomically relevant alveolar model to PM within realistic conditions. This would allow a baseline understanding of the effects caused by each PM type and an understanding of how cells within the triple cell co-culture respond to these PM types.

Generally, the viability of monocultures was not impacted by CB, 1649b or 2583, whereas co-cultures seemed to display an augmented cytotoxic effect, perhaps indicative of a communicative role between differing cell types. This could be through a pro-inflammatory signal, which was generally observed to be exaggerated in the co-cultures, especially those containing dTHP-1 cells. Vis *et al.* (2020) reviewed co-culture systems and explained that cell types can interact not only directly through surface receptors but also through signalling molecules released into the cell culture media. The heightened relevance of a co-culture system compared to traditionally used monocultures may, therefore, highlight a response that is more transferable to *in vivo* or human exposures, which is exemplified here. Of note, the triple cell co-culture appeared to possess the greatest cytotoxic effect, perhaps indicating a synergistic role of all 3 cell types.

Chapter 5 also showed that each CB, 1649b and 2583 possess the ability to induce a pro-inflammatory effect within the cultures used here, although NCI-H441 cells seem to be most sensitive (compared to the hAELVi cells) when exposed to 1649b and 2583. hAELVi cells, on the other hand, appeared to respond in a pro-inflammatory manner more to CB. This trend was also observed in the hAELVi & NCI-H441 co-culture, likely due to the predominance of hAELVi cells within the model. Although the addition of dTHP-1 cells did not appear to amplify the release of IL6 and IL8 compared to the unexposed cultures, baseline levels of IL6 and IL8 often appeared to be higher,



perhaps indicating that dTHP-1 cells are releasing mediators that are inducing a background pro-inflammatory effect from the epithelial cells. Indeed, it has been shown that dTHP-1 can release factors such as  $\text{TNF}\alpha$  and  $\text{IL1}\beta$ , which could induce a pro-inflammatory response from epithelial cells once released into the cell culture media. Therefore, in terms of pro-inflammatory response, not only is it shown that each cell type possesses different abilities to produce a pro-inflammatory response, but also the cell type response is dependent on the type of particle being exposed.

NCI-H441 cells (or NCI-H441 & dTHP-1 co-cultures) were particularly prone to diminished barrier function following PM exposure, whereas hAELVi cells, or cultures comprising the majority hAELVi cells, were more resistant to barrier function impairment. Though it is challenging to define a molecular mechanism that underpins this difference, it could partially be due to the difference in physiological role between ATI and ATII cells. ATI and ATII possess different tight junction proteins, specifically claudins (Wittekindt, 2017), which could confer differences in permeability. Further, pro-inflammatory cytokines, which are often shown to be released at a higher level in NCI-H441 cells, can reduce barrier function (Capaldo & Nusrat, 2009), which may further contribute to this effect.

Overall, the PM exposure studies tended to coincide with previously published literature, with cultures showing pro-inflammatory responses when challenged with PM, similar to is observed in *in vivo*, controlled human exposure and epidemiological studies (Di Ianni et al., 2022; Environmental Protection Agency, 2019; Huang & Ghio, 2009). Though, the inflammatory effects of DEPs shown by Bendtsen *et al.* (2020) were not mirrored, which could be due to the relatively low dosage used, or the acute duration of exposure in an *in vitro* system.

## **8.5 Summary of the Effects of Particle Matter and Nitrogen Dioxide (Co-) Exposure in Alveolar Models**

Having gained an understanding of the effects of PM exposures within the alveolar models, attention was then focused on the response to  $\text{NO}_2$  single pollutant exposures, allowing a direct comparison between the two pollutant types.

$\text{NO}_2$  was found not to impair viability or barrier function in the same manner as PM exposures could, even whilst utilising a relatively high exposure concentration of 5

ppm for 24 hours. Given that human exposures would occur at a lower concentration for prolonged periods/repeated exposures over the years, it warrants further investigation into the chronic effects of NO<sub>2</sub> exposure and whether this would alter the responses observed. NO<sub>2</sub> was found to be able to act through a pro-inflammatory mechanism, however, especially at 2.5 ppm. Oxidative stress and an upregulation of CYP1A1 were observed following NO<sub>2</sub> exposure, which could be speculated to induce this pro-inflammatory effect. Indeed, NO<sub>2</sub> has been previously shown to induce oxidative stress within airway epithelial cells *in vitro* (Mirowsky et al., 2016), although a minor effect was only shown here through analysis of GSH concentration and no changes in *SOD1* expression were observed. Again, this could be due to the acute nature of the exposures.

However, there was an evident alteration in morphology for both NCI-H441 and hAELVi cells exposed to NO<sub>2</sub>. NCI-H441 cells clearly spread out, whereas hAELVi cells appear to become rounder. Previous work has shown a phenotypic change of ATII cells into an ATI-like phenotype (Evans et al., 1975), which could underpin this change and explain why triple cell co-cultures exposed to NO<sub>2</sub> exhibited stronger barrier

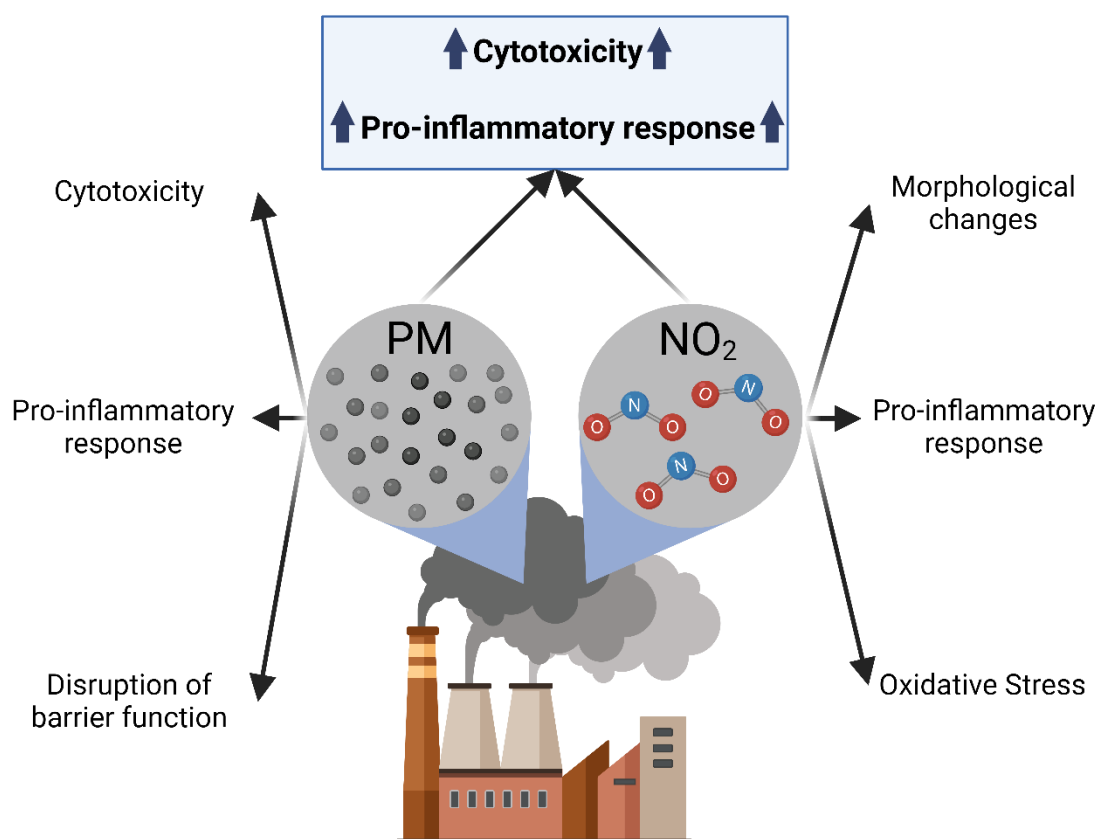


**Figure 8.1** Toxicological effects caused by either PM or NO<sub>2</sub> within the alveolar models used in this work. Co-exposure of PM and NO<sub>2</sub> appeared to increase cytotoxicity and pro-inflammatory cytokine release.

function. If this is indeed the case, within *in vivo* and human settings, there could be a loss of ATII function, *i.e.*, surfactant secretion, ATI progenitor cells and anti-inflammatory peptide release, which could confer pathology and/or increase susceptibility to other xenobiotic exposures.

As with the PM exposures, the toxicological outcome of NO<sub>2</sub> co-exposed with PM was highly dependent on the PM sample used. A common theme, however, was that the PM-associated decrease in viability was amplified when co-exposed with NO<sub>2</sub> (**Figure 8.1**). This was especially obvious when PM samples used were 1649b, 2583 or DEPs compared to CB, perhaps suggesting an increased effect of real-life PM samples compared to pristine samples.

The change in viability could potentially be due to the pro-inflammatory effect NO<sub>2</sub> could have on dTHP-1 cells, having a knock-on cytotoxic effect. Higher levels of pro-inflammatory cytokines were observed following exposure to PM or NO<sub>2</sub>, which were often increased in co-exposure conditions, further demonstrated by RNA-Seq. It is clear, therefore, that both NO<sub>2</sub> and PM can act in a pro-inflammatory manner (**Figure 8.3**). Whether NO<sub>2</sub> directly induced a pro-inflammatory response or this is secondary to an oxidative stress effect, which has also been demonstrated here, remains unclear, though, the mechanisms identified here have been put into the context of previously published mechanisms in **Figure 8.3**. However, it could indicate a synergistic effect that could explain why these pollutants exacerbate immune/inflammatory diseases such as asthma and COPD.

Further, there appeared to be synergistic activity that induced pro-inflammatory mediator release when NO<sub>2</sub> was co-exposed with CB, 2583 and DEPs. Indeed, this was demonstrated through RNA-Seq which was discussed in Chapter 7. Co-exposure of DEP and NO<sub>2</sub> amplified the expression of pro-inflammatory genes such as IL1 $\alpha$ , IL1 $\beta$ , TNF $\alpha$ , IL6 and IL17C. This finding is interesting as chronic inflammation has been associated with airway diseases such as COPD and asthma (Angelis et al., 2014; Murdoch & Lloyd, 2010). It also could indicate susceptibility to a range of other conditions, such as respiratory tract infections and exacerbated allergic responses (Panzner et al., 2015; Sethi, 2010). An NO<sub>2</sub>-induced reduction in IL10 signalling may drive this increase in the pro-inflammatory state. NO<sub>2</sub> appears to reduce IL10R expression, which could mitigate anti-inflammatory responses (but not increase pro-

inflammatory responses directly). This, combined with a pro-inflammatory agent (DEPs in this case), could cause an amplification of the inflammatory effect. This mechanism of action could first be elucidated by using an inhibitor of IL10R, or by knocking out IL10/IL10R to assess whether this can amplify a pro-inflammatory response from DEP. This could allow the direct impact of NO<sub>2</sub> on IL10 signalling can be determined.

Given the varied gene expression resulting from these exposures, findings could be used to generate an adverse outcome pathway (AOP) for air pollution exposure at the alveolar level. However, the data here might suggest that the AOP would need to be more specific, given the confounding findings between 2583 and DEP exposure. Perhaps co-exposures of DEPs and NO<sub>2</sub> could advise a traffic-related air pollution exposure AOP. However, further analysis into other confounding pollutants, such as CO and non-exhaust traffic-related PM, would be required, as well as the consideration that longer-term/chronic exposures may alter the responses.

Throughout this work, a range of PM samples have been used. Further work is required to deduce which physical and/or chemical properties can be drivers of certain toxicological responses. Tables 4.1 and 9.1 outline the known physical and chemical characteristics of the particles used within this work, though, they are so widely different it is difficult to pinpoint exact causes of specific toxicological mechanisms. The urban dust for example has a much higher lead content than the indoor dust, but also higher cadmium. It is likely that either of these characteristics will not only impart a direct effect onto the cells it contacts, but also how it potentially reacts with other confounding pollutants (*i.e.* NO<sub>2</sub>). It would be of use that if within future toxicological work investigating PM, that there is a minimum requirement for particle characterisation. This could allow meta-analyses to be conducted to deduce structure-function relationships.

It must be noted that at times there were inconsistencies between data chapters. For example, indoor dust was shown in Chapter 5 to increase pro-inflammatory response, whereas this was not shown in Chapter 6 (during NO<sub>2</sub> co-exposure) or by RNA-seq. This is potentially due to working with three cells at one time (in the triple culture), potentially increasing the risk of passage to passage variation. Further, three replicates was often used in this work. Given the high variance observed, increasing the number

of replicates to five (or more) could allow further identification of potential toxicological mechanisms through increased statistical power.

Overall, the findings of this work were inconsistent with similar work. As outlined within COMEAPs 2018 NO<sub>2</sub> report, epidemiological studies would suggest a role for NO<sub>2</sub> and/or PM in respiratory effects. It has been shown here that both PM and NO<sub>2</sub> could potentially possess the ability to induce toxic effects as singular entities. However, RNA-Seq also outlines mechanisms by which these pollutants could act synergistically.

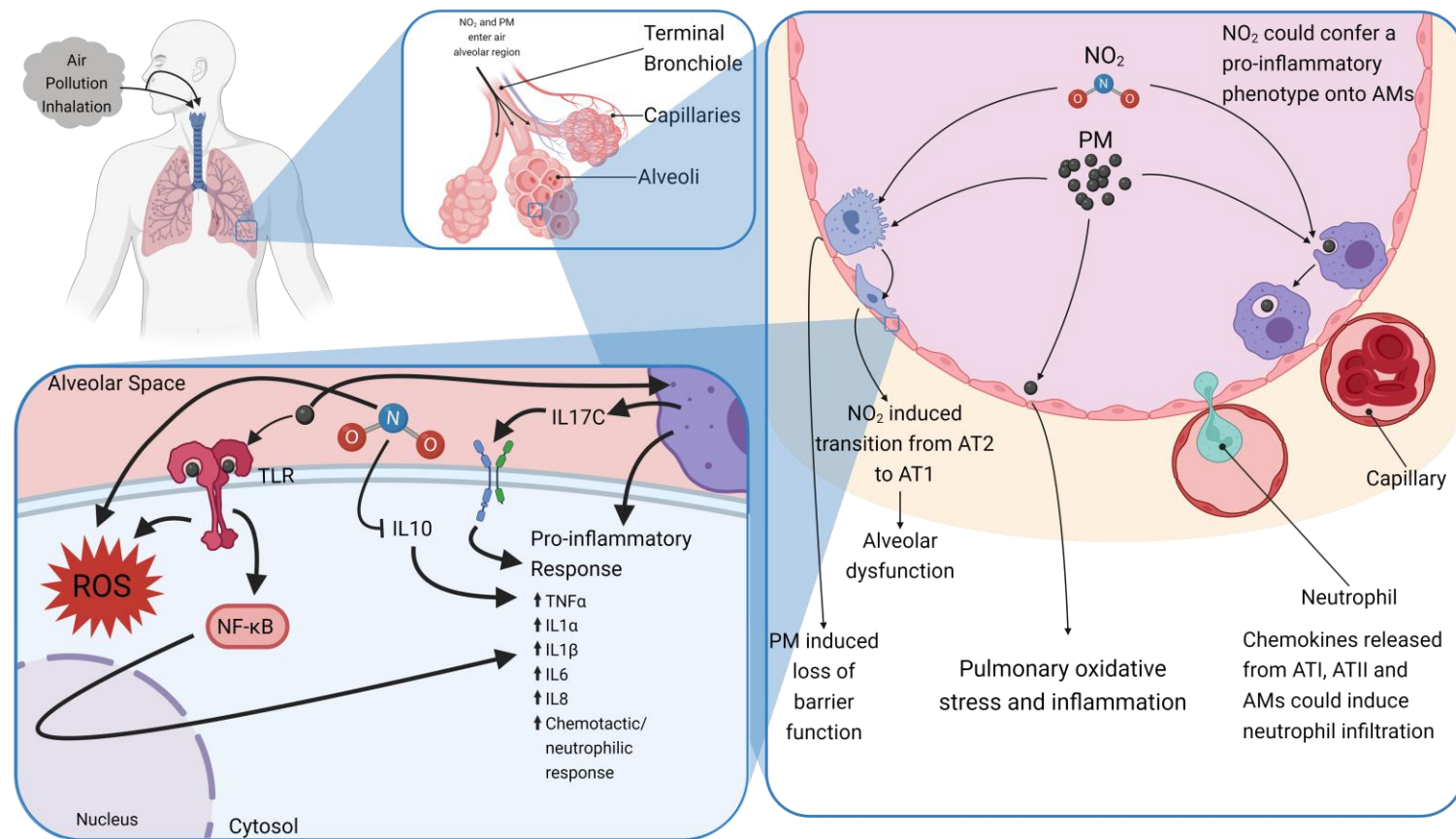


**Figure 8.2** Possible routes of toxicity caused by PM and NO<sub>2</sub> co-exposure implicated within this work. (1) Pollutants can penetrate the lung to the level of the alveoli. (2) At a cellular level, PM can reduce ATII barrier function whereas NO<sub>2</sub> causes morphological changes to ATII, maybe to an ATI phenotype. Both pollutants possess the ability to induce a pro-inflammatory response within epithelial cells, perhaps exacerbated by an interaction between NO<sub>2</sub> and AMs. (3) At a singular cell level, PM could be acting on extracellular receptors, such as TLR4, to induce a pro-inflammatory response and oxidative stress, or causing oxidative stress directly. PM may also induce the release of IL17C on macrophages, triggering a pro-inflammatory response from epithelial cells in a paracrine manner. This could in turn lead to cytotoxicity. This could be additive with the effects of NO<sub>2</sub> on AMs and epithelial cells which have shown to increase IL6 and IL8 release. NO<sub>2</sub> may also inhibit anti-inflammatory signalling through IL10, which may go on to induce a pro-inflammatory phenotype

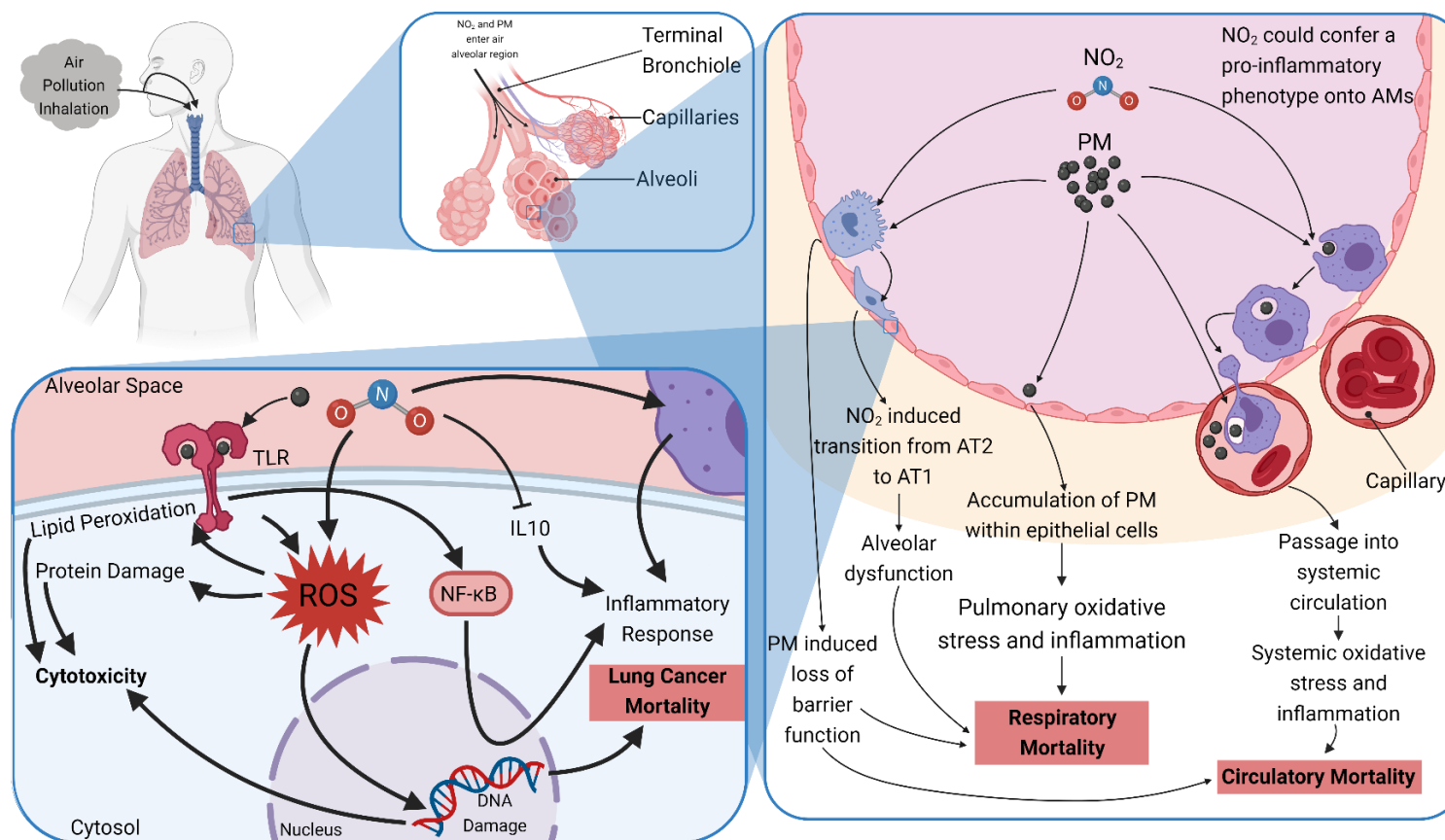


**Figure 8.3** Possible routes of toxicity caused by PM and NO<sub>2</sub> co-exposure implicated within this work, put into the context with published literature. (1) Pollutants can penetrate the lung to the level of the alveoli. (2) At a cellular level, PM can reduce AII barrier function whereas NO<sub>2</sub> causes morphological changes to AII, maybe to an ATI phenotype. Both pollutants possess the ability to induce oxidative stress and a pro-inflammatory response within epithelial cells, perhaps exacerbated by an interaction between NO<sub>2</sub> and AMs. This could lead to respiratory morbidities and mortalities, as well, the pro-inflammatory mediators could have a response at a systemic level. This could be increased by translocation of PM directly to the bloodstream, perhaps increased due to the loss of AII barrier function. (3) At a singular cell level, PM could be acting on extracellular receptors, such as TLR4, to induce a pro-inflammatory response and oxidative stress, or causing oxidative stress directly. This could in turn lead to cell damage and cytotoxicity. This could be additive with the effects of NO<sub>2</sub> on AMs and epithelial cells which have shown to increase IL6 and IL8 release. NO<sub>2</sub> may also inhibit anti-inflammatory signalling through IL10, which may go on to induce a pro-inflammatory phenotype. Further, generated ROS could induce DNA damage, potentially explaining the increase in lung cancers reported in the literature in response to NO<sub>2</sub> and PM exposure.

## 8.6 Conclusion

Overall, it appears that there may be some overlap in the toxicological mechanisms induced by PM and NO<sub>2</sub> and potentially possess the ability to act in an additive and synergistic manner, though, there is a requirement to examine these mechanisms in closer detail. Further, there may be mandate to examine the effects of many realistic co-exposures, such as PM and O<sub>3</sub> or SO<sub>2</sub>.

The implications of this work are varied. Firstly, the research conducted here provides an initial platform for other researchers to build off when investigating the effects of NO<sub>2</sub> and PM co-exposure through the identification of some potential pathways of single-pollutant and multi-pollutant toxicity. The RNA-Seq data is especially useful for the identification of novel mechanisms. Further, the exposure methodology and *in vitro* approaches taken within this work could be taken into future research investigating other inhaled xenobiotics (such as other ambient PM samples, or occupational PM within the VitroCell® Cloud, or the NO<sub>2</sub> chamber could be adapted to expose other gaseous pollutants), or as a means to test the efficacy of inhaled therapies. As such, it is foreseeable that this work could be valuable to the wider public health field. The exposure approaches developed could also be utilised in chronic exposure studies, which could perhaps advise benefits to air quality policies, although, it would initially be required that the exposure approaches could be scaled to a human exposure level.

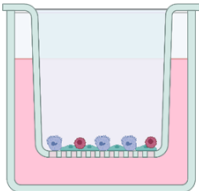
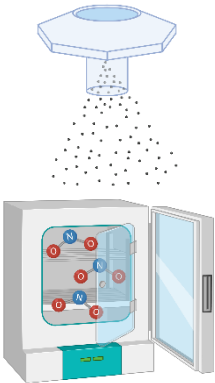
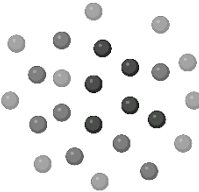
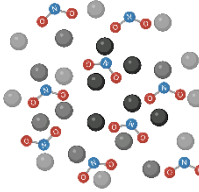
This thesis aimed first to develop an anatomically relevant triple cell co-culture system that could be implemented within PM and NO<sub>2</sub> co-exposure studies. Overall, this study concludes:

1. hAELVi, NCI-H441, and dTHP-1 cells can be co-cultured at the ALI to provide a sensitive *in vitro* model of the alveolar epithelial barrier. This model was cultured at anatomically relevant cell coverage/number ratios, forming a tight barrier that was sensitive to pro-inflammatory stimuli.
2. The triple cell co-culture could be implemented within the aerosol PM and NO<sub>2</sub> exposure systems using the VitroCell® Cloud and a modified hypoxia chamber, respectively. This would allow realistic exposure to both pollutants in tandem, allowing the research question to be addressed.



3. Exposure to relevant PM samples resulted in varying responses from each cell type and different co-culture models. Briefly, NCI-H441 cells were prone to barrier dysfunction, whereas all cell types possessed the ability to mount a pro-inflammatory response and induce cytotoxicity. Some PM samples were able to induce a pro-inflammatory effect more than others. For example, indoor dust was more pro-inflammatory than carbon black.
4. NO<sub>2</sub> appears to induce toxicity in all cell types through a pro-inflammatory mechanism, perhaps relating to oxidative stress.
5. Co-exposure of PM with NO<sub>2</sub> was often found to augment cytotoxicity and pro-inflammatory response from the triple cell co-culture, although this was dependent on the PM samples used.
6. RNA-Seq confirmed point 5, suggesting that NO<sub>2</sub> may reduce triple cell-co-culture anti-inflammatory capabilities and increase susceptibility to pro-inflammatory response.

## 8.7 Future Perspectives

 <p><b>In Vitro Alveolar Model</b></p>	<ol style="list-style-type: none"> <li>1. Compare the toxicological response of this system to primary cells and commercially available models such as EpiAlveolar™ from MatTek.</li> <li>2. Assess the potential for the alveolar triple cell co-culture to be cultured for longer durations to allow chronic exposures and whether this alters the relative cell densities.</li> <li>3. Assess the viability of dTHP-1 cells in long-term culture.</li> <li>4. Expand this co-culture to contain more cell types, such as endothelial or fibroblast cells on the basal transwell surface.</li> <li>5. Expanding on the above point, this model could be implicated within a dynamic flow system with circulating dendritic cells.</li> <li>6. Assess the ability of the model to produce a surfactant layer <i>via</i> fluorescent staining or transmission electron microscopy.</li> </ol>
 <p><b>Exposure Methods</b></p>	<ol style="list-style-type: none"> <li>1. Consider a chronic NO<sub>2</sub> and PM exposure approach, using repeated exposures to simulate day-to-day human exposures or long-term low-concentration NO<sub>2</sub> exposures.</li> <li>2. Assess the feasibility of using a system to deliver PM and NO<sub>2</sub> simultaneously, such as the Cultex® system.</li> <li>3. Investigate methods for ageing PM samples within NO<sub>2</sub> environments to understand if this can then influence toxicity.</li> <li>4. Assess morphological differences between PM exposed via VitroCell® Cloud, and a dry powder exposure system such as the VitroCell® PowderX.</li> </ol>
 <p><b>PM Exposure</b></p>	<ol style="list-style-type: none"> <li>1. Consider approaches to characterise what properties of PM can drive a toxic effect, whether they are PM size/shape, chemical composition, endotoxin content, etc.</li> <li>2. Assess toxicological changes in response to relevant PM co-exposures, such as 2583 and house dust mites, for example.</li> </ol>
 <p><b>PM and NO<sub>2</sub> Co-exposure</b></p>	<ol style="list-style-type: none"> <li>1. Elucidate the proposed mechanisms of toxicity identified through the RNA-Seq analysis at a protein level, through ELISAs and Western blots, for example.</li> <li>2. Assess the ability of NO<sub>2</sub> to induce a further range of cellular responses, such as genotoxicity, given the links made between NO<sub>2</sub> and lung cancer in epidemiological studies.</li> <li>3. Assess transcriptional changes in ATH exposed to NO<sub>2</sub> to assess for ATI-like transition.</li> <li>4. Consider temporal responses and that changes may occur early during exposure (especially since PM is exposed initially), and that perhaps earlier analysis could reveal additional mechanisms of toxicity.</li> </ol>

## Chapter 9: Appendices

---

## 9.1 Appendix 1

The published chemical properties of the particulate matter samples used within this work, namely, Printex® 90 CB, NIST SRM 1649b Urban Dust, NIST SRM 2583 Indoor Dust, and DEPs from engines using 9.8, 13 and 17% oxygen intake percentages are described in **Table 9.1**.

*Table 9.1 Pre-published Chemical Properties for CB, 1349b, 2583, and DEP 9.8, 13 and 17%.*

	Printex 90	NIST Urban Dust (1649b)	NIST Trace Elements in Indoor Dust (2583)	Diesel Emission Particles (9.7%)	Diesel Emission Particles (13%)	Diesel Emission Particles (17%)
Extracted elemental mass fractions (µg/g)						
V				14	6	ND
Cr			80 ± 22	8	7	52
Mn				92	53	ND
Fe				220	137	2115
Co				2	1	88
Ni				15	6	118
Cu				2.349	629	13160
Ga				1	1	1
As			7.0 ± 1.6	ND	ND	ND
Se				2	0	ND
Rb				2	1	1
Sr				99	54	41
Ag				0	0	0
Cd		26.10 ± 0.28	7.3 ± 3.7	ND	ND	ND
In				0	0	0
Cs				0	0	0
Ba				15	10	9
Hg		1.80 ± 0.04	1.56 ± 0.19	0	0	0
Ti				0	0	0
Pb		12864 ± 62	85.9 ± 7.2	ND	ND	ND
Bi				0	0	0
U				ND	0	ND
PAH Content						
Native PAH (µg/g)						
naphthalene		0.946 ± 0.086		4.4	136.8	6.8
biphenyl		0.182 ± 0.020		5	67.7	2.7
acenaphthylene		0.193 ± 0.023		16.2	96.9	2.8
acenaphthene		0.197 ± 0.040		1	17	2

fluorene		0.223 ± 0.035	17.5	44.8	2.9
phenanthrene	0.018	4.03 ± 0.06	423.7	236.9	44.7
anthracene		0.410 ± 0.004	60.9	17.8	3.3
fluoranthene	0.0185	6.24 ± 0.0	1677	141.4	162.2
pyrene		4.98 ± 0.14	2381.6	182.8	223.2
retene		0.238 ± 0.011	9.1	271.8	166.1
benzo(a)anthracene	0.0038	2.11 ± 0.05	1378.15	5.5	15.2
chrysene	0.0118	3.045 ± 0.028	2609.2	9.3	52.8
benzo(b)fluoranthene		6.18 ± 0.18	4158.16	207.6	40.7
benzo(k)fluoranthene		1.702 ± 0.049	1094	887.6	59
benzo(a)pyrene		2.47 ± 0.24	3739.3	61.3	32.8
perylene	0.0221	0.614 ± 0.011	638.3	14.5	10
indeno(1,2,3-c,d)pyrene		2.89 ± 0.16	2072.1	2.3	8.7
dibenzo(a,h)anthracene		0.294 ± 0.002	40.2	27.2	7.1
benzo(g,h,i)perylene		3.97 ± 0.04	2608.5	31.6	14.3
coronene		3.16 ± 0.05	752.3	7.6	0.5
benzo(c)phenanthrene		0.460 ± 0.013			
triphenylene		1.324 ± 0.004			
benzo(j)fluoranthene		1.725 ± 0.043			
benzo(e)pyrene		2.974 ± 0.053			
dibenz(a,j)anthracene		0.305 ± 0.027			
benzo(b)chrysene		0.339 ± 0.043			
picene		0.399 ± 0.022			
dibenzo(b,k)fluoranthene		0.670 ± 0.053			
dibenzo(a,e)pyrene		0.567 ± 0.025			
4H-Cyclopenta[def]phenanthrene		0.255 ± 0.023			
Benzo[ghi]fluoranthene		0.901 ± 0.015			
Benzo[a]fluoranthene		0.386 ± 0.027			
Cyclopenta[cd]pyrene		0.343 ± 0.012			
Dibenz[a,c]anthracene		0.204 ± 0.016			
Benzo[c]chrysene		0.084 ± 0.001			
Dibenz[a,h + a,c]anthracene					
Benzo[e]pyrene					
<b>Total Native PAH</b>	<b>0.0742</b>	<b>55.01</b>	<b>23686.3</b>	<b>2468.7</b>	<b>857.6</b>
<b>Alkyl-PAH (µg/g)</b>					
2-methylnaphthalene		0.904 ± 0.011	<LOD	150.3	2.8
1-methylnaphthalene			1.4	106.5	2.5
2,3-dimethylnaphthalene			3.8	51.8	7.3

2,3,5-trimethylnaphthalene		0.2	14.7	2.1
1-methylfluorene		0.4	11.1	3.3
4-methylphenanthrene		8.5	16.9	7.1
3-methylphenanthrene	0.555 ± 0.031	11	14.1	7.8
1-methylphenanthrene	0.335 ± 0.061	11.5	16.6	<LOD
1-methylantracene		17.6	16.6	6.9
2-phenylnaphthalene		83.1	25.5	6.3
1-methylfluoranthene	0.114 ± 0.015	41.8	23.7	6.9
1-methylpyrene	0.363 ± 0.005	166.8	34.7	23.3
2-methylchrysene	0.354 ± 0.006	54.4	0.4	1.2
3-methylfluoranthene	0.328 ± 0.031			
9-Methylphenanthrene	0.437 ± 0.044			
6-Methylchrysene	0.160 ± 0.003			
2-Methylphenanthrene	0.896 ± 0.047			
1,7-Dimethylphenanthrene	0.216 ± 0.024			
3-Methylchrysene	0.232 ± 0.002			
2-Methylpyrene	0.527 ± 0.014			
4-Methylpyrene	0.239 ± 0.014			
8-Methylfluoranthene	0.233 ± 0.006			
1,2-Dimethylphenanthrene				
1,6-, 1,7-, 2,5-, and 2,9-Dimethylphenanthrene				
1,8-Dimethylphenanthrene				
2,6-Dimethylphenanthrene				
2,7-Dimethylphenanthrene				
3,6-Dimethylphenanthrene				
1-, 3-, and 7-Methylfluoranthene				
3-Methylfluoranthene	0.328 ± 0.031			
<b>Total Alkyl-PAH</b>	<b>6.221</b>	<b>400.4</b>	<b>482.9</b>	<b>77.2</b>
<b>Dibenzothiophenes (DBT) (µg/g)</b>				
dibenzothiophene	0.193 ± 0.002	44.1	52.3	99.7
2-methyldibenzothiophene		1.1	4.8	13.1
1-methyldibenzothiophene		0.4	12.4	6.6
4-methyldibenzothiophene		0.2	1	1.2
2,8-dimethyldibenzothiophene		0.5	5.9	4

2,4,7-trimethyldibenzothiophene		0.5	1.9	3.3
<b>Total DBT</b>	<b>0.193</b>	<b>46.8</b>	<b>78.2</b>	<b>127.8</b>
<b>Nitro-PAH (µg/g)</b>				
1-Nitronaphthalene		0.1	1.6	0.1
2-Nitronaphthalene		0.3	11.9	0.8
5-nitro acenaphthalene		1.3	<LOD	2
2-Nitrofluorene		0.1	0	0
9-Nitroanthracene		0.6	0	0
9-Nitrophenanthrene	1.77 ± 0.07 (µg/kg)	0.7	0	0
4-Nitropyrene		9.4	0	0.3
3-Nitrofluoranthene	4.67 ± 0.35 (µg/kg)	9.2	0	<LOD
1-Nitropyrene	74.8 ± 1.9 (µg/kg)	2.4	0.1	4
2-Nitropyrene	10.9 ± 0.1 (µg/kg)	88.6	0.2	0.2
7-Nitrobenz[a]anthracene	24.4 ± 0.4 (µg/kg)	7	6.4	<LOD
6-Nitrochrysene	3.60 ± 0.21 (µg/kg)	0.2	<LOD	<LOD
3-Nitrobenzanthrone		0.3	0.1	0.2
6-Nitrobenzo[a]pyrene		10.4	0.8	0.8
3-Nitrophenanthrene	21.8 ± 1.2 (µg/kg)			
2-Nitrofluoranthene	304 ± 25 (µg/kg)			
1,3-Dinitropyrene				
1,6-Dinitropyrene				
1,8-Dinitropyrene				
8-Nitrofluoranthene				
<b>Total Nitro-PAHs</b>	<b>445.94 (µg/kg)</b>	<b>130.5</b>	<b>21.2</b>	<b>8.4</b>
<b>Oxy-PAH (µg/g)</b>				
Napthalene-1-aldehyde		17.7	246.9	11.9
2-Naphthaldehyde		67.6	1005.5	104
p-Fluorenone		136	168.3	49.7
9,10 Anthraquinone		146.6	10.5	31.9
1,4 Anthraquinone		25.2	6.5	1.3
Phenanthrene-9-aldehyde		50.3	0.5	2.8
Benzanthrone		1475.6	1.3	21.6
Benz[a]anthracene-7,12-dione		201.3	0.1	0.8
<b>Total Oxy-PAH</b>		<b>2488.3</b>	<b>1452.3</b>	<b>314.3</b>
<b>PCB Congeners (µg/kg)</b>				

PCB 49 (2,2',4,5'-Tetrachlorobiphenyl)	9.1 ± 1.7
PCB 52 (2,2',5,5'-Tetrachlorobiphenyl)	24.3 ± 6.1
PCB 101 (2,2',4,5,5'-Pentachlorobiphenyl)	56.4 ± 5.2
PCB 105 (2,3,3',4,4'-Pentachlorobiphenyl)	10.0 ± 1.0
PCB 110 (2,3,3',4',6-Pentachlorobiphenyl)	33.7 ± 5.0
PCB 149 (2,2',3,4',5',6-Hexachlorobiphenyl)	79.4 ± 3.2
PCB 151 (2,2',3,5,5',6-Hexachlorobiphenyl)	33.4 ± 3.6
PCB 153 (2,2',4,4',5,5'-Hexachlorobiphenyl)	76.6 ± 0.4
PCB 163 (2,3,3',4',5,6-Hexachlorobiphenyl)	22.2 ± 0.3
PCB 183 (2,2',3,4,4',5',6-Heptachlorobiphenyl)	17.2 ± 1.5
PCB 187 (2,2',3,4',5,5',6-Heptachlorobiphenyl)	39.3 ± 2.8
PCB 194 (2,2',3,3',4,4',5,5'-Octachlorobiphenyl)	28.5 ± 2.8
PCB 206 (2,2',3,3',4,4',5,5',6-Nonachlorobiphenyl)	17.0 ± 2.1
<b>Total PCB Congeners</b>	<b>447.1</b>
<b>Selected Chlorinated Pesticides (µg/kg)</b>	
trans-Chlordane (γ-Chlordane)	51.9 ± 9.0
trans-Nonachlor	33.7 ± 6.1
4,4'-DDE	50.7 ± 0.4
4,4'-DDD	37.7 ± 3.1
<b>Total Chlorinated Pesticides</b>	<b>174</b>



## 9.2 Appendix 2

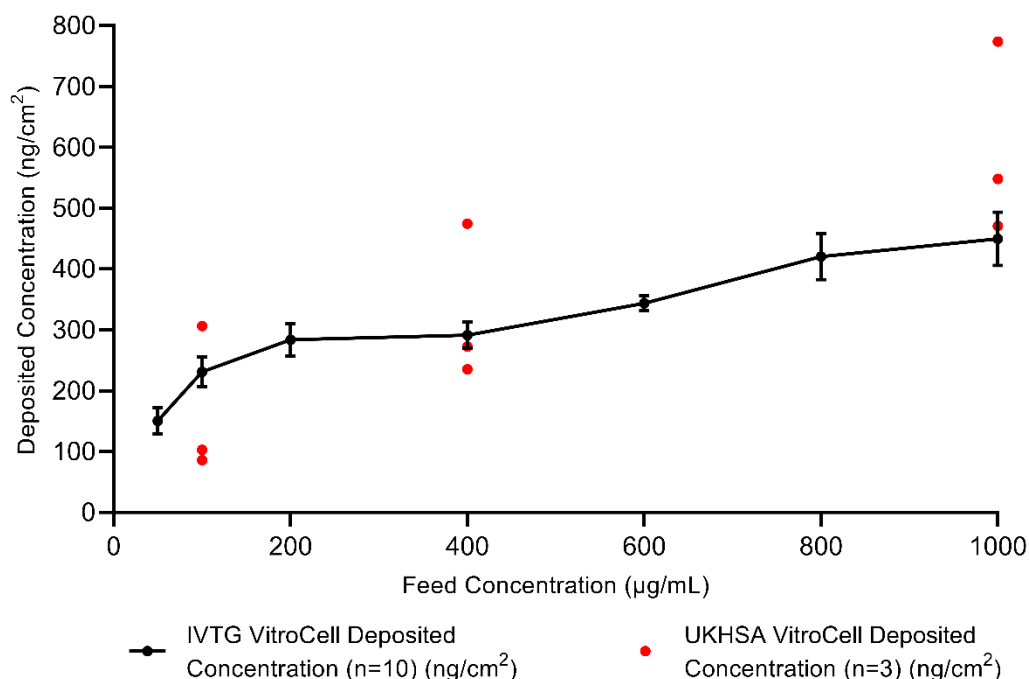


**Figure 9.1** VitroCell® Cloud systems within Swansea University (IVTG) and RCE (UKHSA) were compared using CB to model deposition. The black points and line show an n=10 deposition curve using the IVTG Cloud ( $\pm$  SEM). The red points then show 3 replicated using 100, 400 and 1000  $\mu$ mL carbon black within the UKHSA system to assess comparable depositions.

The VitroCell® Cloud within the *In Vitro* Toxicology Group (IVTG) (Swansea University) and at UKHSAs Radiation and Chemical Hazards Directorate (RCE) were produced for different transwell insert sizes. The IVTG system is a Cloud 12, suitable for 12 well insert sizes. The UKHSA Cloud, on the other hand, is a Cloud 6, that has the capability of accommodating 6 well insert sizes, though it can accommodate 12 well inserts using plastic adapter rings.

Prior to initial exposure, CB was used to assess that the deposition achieved within each system was comparable, allowing accurate exposures within each system. It is shown that the UKHSA Cloud system shows depositions resembling the IVTG Cloud system (**Figure 9.1**).

### 9.3 Appendix 3

Transcriptomic analysis was conducted according to the exposure methodology outlined in Chapter 6, and the RNA-Sequencing analysis is discussed in Chapter 7. The resulting DEGs from NO<sub>2</sub>, 2583, DEP (17%), NO<sub>2</sub> + 2583 and NO<sub>2</sub> + DEP (17%) are shown in **Table 9.2**. Further, comparisons drawn between DEP only and DEP + NO<sub>2</sub> co-exposure, as well as 2583 and 2583 + NO<sub>2</sub> co-exposure, are also shown. Genes were considered differentially expressed if they possessed a Log<sub>2</sub> fold change beyond 1.5 on either side of zero and a *p*-value below 0.05.

*Table 9.2 DEGs from NO<sub>2</sub>, 2583, DEP (17%), NO<sub>2</sub> + 2583 and NO<sub>2</sub> + DEP (17%).*

Name	Log <sub>2</sub> fold change	FDR p-value	ENSEMBL IDs	Synonyms	Description
<b><i>NO<sub>2</sub> against Incubator</i></b>					
A2M	-2.9634588	1.2E-07	<a href="#">ENSG00000175899</a>	A2MD CPAMD5 FWP007 S863-7	alpha-2-macroglobulin
AC072062.1	2.2526389	0.01831	<a href="#">ENSG00000229267</a>		small nucleolar RNA host gene 31
AC107081.5	11.374341	0.0045	<a href="#">ENSG00000236498</a>	None	None
ACTL10	1.772004	0.01376	<a href="#">ENSG00000182584</a>	None	None
ADAMDEC1	-2.8844382	1.2E-07	<a href="#">ENSG00000134028</a>	M12.219	ADAM like decysin 1
ALOX5AP	-1.9577409	2E-05	<a href="#">ENSG00000132965</a>	FLAP	arachidonate 5-lipoxygenase activating protein
ANPEP	-1.8343224	2.3E-08	<a href="#">ENSG00000166825</a>	AP-M AP-N APN CD13 GP150 LAP1 P150 PEPN hAPN	alanyl aminopeptidase, membrane
APBB1IP	-2.2422549	0.008	<a href="#">ENSG00000077420</a>	INAG1 PREL1 RARP1 RIAM	amyloid beta precursor protein binding family B member 1 interacting protein
APOC2	-2.6909694	4.2E-06	<a href="#">ENSG00000234906</a>	APO-CII APOC-II	apolipoprotein C2
ARHGEF25	-2.5252058	0.03064	<a href="#">ENSG00000240771</a>	GEFT p63RhoGEF	Rho guanine nucleotide exchange factor 25
ATP1A1-AS1	4.3109031	0.00018	<a href="#">ENSG00000203865</a>	ATP1A1OS C1orf203	ATP1A1 antisense RNA 1
BHLHE22	-2.7931738	2.4E-10	<a href="#">ENSG00000180828</a>	BHLHB5 Beta3 Beta3a CAGL85 TNRC20	basic helix-loop-helix family member e22
C5AR1	-1.6919095	0.01854	<a href="#">ENSG00000197405</a>	C5A C5AR C5R1 CD88	complement C5a receptor 1
CCR1	-3.7081842	4.1E-05	<a href="#">ENSG00000163823</a>	CD191 CKR-1 CKR1 CMKBR1 HM145 MIP1aR SCYAR1	C-C motif chemokine receptor 1

CCR2	-2.6485983	0.01731	<a href="#">ENSG00000121807</a>	CC-CKR-2 CCR-2 CCR2A CCR2B CD192 CKR2 CKR2A CKR2B CMKBR2 MCP-1-R	C-C motif chemokine receptor 2
CD163	-2.4016291	9.2E-10	<a href="#">ENSG00000177575</a>	M130 MM130 SCAR1	CD163 molecule
CD209	-3.5012422	0.02989	<a href="#">ENSG00000090659</a>	CDSIGN CLEC4L DC-SIGN DC-SIGN1 hDC-SIGN	CD209 molecule
CD36	-2.8179948	1.1E-08	<a href="#">ENSG00000135218</a>	BDPLT10 CHDS7 FAT GP3B GP4 GPIV PASIV SCARB3	CD36 molecule
CD38	-1.5617133	0.04354	<a href="#">ENSG00000004468</a>	ADPRC1 cADPR1	CD38 molecule
CD53	-2.6061944	5.2E-08	<a href="#">ENSG00000143119</a>	MOX44 TSPAN25	CD53 molecule
CD93	-2.7407995	5.2E-08	<a href="#">ENSG00000125810</a>	C1QR1 C1qRP CDw93 ECSM3 MXRA4 dJ737E23.1	CD93 molecule
CEBPA	-1.5807883	0.00066	<a href="#">ENSG00000245848</a>	C/EBP-alpha CEBP	CCAAT enhancer binding protein alpha
CES1	-2.125354	0.03434	<a href="#">ENSG00000198848</a>	ACAT CE-1 CEH CES2 HMSE HMSE1 PCE-1 REH SES1 TGH hCE-1	carboxylesterase 1
CHI3L1	-2.2267204	6.2E-07	<a href="#">ENSG00000133048</a>	ASRT7 CGP-39 GP-39 GP39 HC-gp39 HCGP-3P YK-40 YKL-40 YKL40 YYL-40 hCGP-39	chitinase 3 like 1
CMPK2	-2.2005344	0.01314	<a href="#">ENSG00000134326</a>	NDK TMPK2 TYKi UMP-CMPK2	cytidine/uridine monophosphate kinase 2
CNR1	-1.7543926	0.01249	<a href="#">ENSG00000118432</a>	CANN6 CB-R CB1 CB1A CB1K5 CB1R CNR	cannabinoid receptor 1
COL8A2	-1.7361955	0.01571	<a href="#">ENSG00000171812</a>	FECD FECD1 PPCD PPCD2	collagen type VIII alpha 2 chain
CSF3R	-2.7132464	0.03043	<a href="#">ENSG00000119535</a>	CD114 GCSFR SCN7	colony stimulating factor 3 receptor
CYBB	-2.3595284	0.00072	<a href="#">ENSG00000165168</a>	AMCBX2 CGD CGDX GP91-1 GP91-PHOX GP91PHOX IMD34 NOX2 p91-PHOX	cytochrome b-245 beta chain
CYP1A1	2.3024496	7.6E-07	<a href="#">ENSG00000140465</a>	AHH AHRR CP11 CYP1 CYPIA1 P1-450 P450-C P450DX	cytochrome P450 family 1 subfamily A member 1
DDIT4L	-2.454681	0.01572	<a href="#">ENSG00000145358</a>	REDD2 Rtp801L	DNA damage inducible transcript 4 like
DOK2	-2.3273513	0.04577	<a href="#">ENSG00000147443</a>	p56DOK p56dok-2	docking protein 2
FANCD2OS	2.8406628	0.00687	<a href="#">ENSG00000163705</a>	C3orf24	FANCD2 opposite strand
FCER1G	-2.7508031	1E-05	<a href="#">ENSG00000158869</a>	FCRG	Fc epsilon receptor Ig
FCGR2A	-2.2323425	0.0097	<a href="#">ENSG00000143226</a>	CD32 CD32A CDw32 FCG2 FCGR2 FCGR2A1 FcGR FcgammaRIIa IGFR2	Fc gamma receptor IIa
FGR	-2.2024559	0.01156	<a href="#">ENSG00000000938</a>	SRC2 c-fgr c-src2 p55-Fgr p55c-fgr p58-Fgr p58c-fgr	FGR proto-oncogene, Src family tyrosine kinase
GAS7	-1.9386138	0.01934	<a href="#">ENSG00000007237</a>		growth arrest specific 7
GNLY	-2.6570772	0.00013	<a href="#">ENSG00000115523</a>	D2S69E LAG-2 LAG2 NKG5 TLA519	granulysin
GPRIN3	-3.4025331	0.02052	<a href="#">ENSG00000185477</a>	GRIN3	GPRIN family member 3
HCLS1	-1.7328133	0.04889	<a href="#">ENSG00000180353</a>	CTTNL HS1 lckBP1 p75	hematopoietic cell-specific Lyn substrate 1

HSPA6	2.4400923	0.00014	<a href="#">ENSG00000173110</a>		heat shock protein family A (Hsp70) member 6
IL10RA	-2.7292306	0.00013	<a href="#">ENSG00000110324</a>	CD210 CD210a CDW210A HIL-10R IL-10R1 IL10R	interleukin 10 receptor subunit alpha
IRF8	-2.0326279	0.03479	<a href="#">ENSG00000140968</a>	H-ICSBP ICSBP ICSBP1 IMD32A IMD32B IRF-8	interferon regulatory factor 8
ITGAL	-2.4062813	0.00022	<a href="#">ENSG00000005844</a>	CD11A LFA-1 LFA1A	integrin subunit alpha L
ITGAX	-1.8023964	0.00623	<a href="#">ENSG00000140678</a>	CD11C SLEB6	integrin subunit alpha X
ITGB2	-1.6734702	8.5E-07	<a href="#">ENSG00000160255</a>	CD18 LAD LCAMB LFA-1 MAC-1 MF17 MFI7	integrin subunit beta 2
ITGB7	-2.148503	0.00013	<a href="#">ENSG00000139626</a>		integrin subunit beta 7
KCNE1	-2.3999694	0.0006	<a href="#">ENSG00000180509</a>	ISK JLNS JLNS2 LQT2/5 LQT5 MinK	potassium voltage-gated channel subfamily E regulatory subunit 1
KCNE1B	-2.5142904	0.0259	<a href="#">ENSG00000276289</a>	KCNE1B	potassium voltage-gated channel subfamily E regulatory subunit 1B
KLHL6	-2.394639	0.02802	<a href="#">ENSG00000172578</a>		kelch like family member 6
LAIR1	-2.688075	0.0006	<a href="#">ENSG00000167613</a>	CD305 LAIR-1	leukocyte associated immunoglobulin like receptor 1
LAPTM5	-2.3103353	9.2E-10	<a href="#">ENSG00000162511</a>	CLAST6	lysosomal protein transmembrane 5
LRRC37A17P	-2.022002	0.00265	<a href="#">ENSG00000263142</a>	LRRC37A5	leucine rich repeat containing 37 member A17, pseudogene
MAFB	-1.7630509	1.9E-05	<a href="#">ENSG00000204103</a>	DURS3 KRML MCTO	MAF bZIP transcription factor B
MMP2	-2.6465073	0.00027	<a href="#">ENSG00000087245</a>	CLG4 CLG4A MMP-2 MMP-II MONA TBE-1	matrix metalloproteinase 2
MMP9	-1.5686783	0.04841	<a href="#">ENSG00000100985</a>	CLG4B GELB MANDP2 MMP-9	matrix metalloproteinase 9
MS4A7	-2.8499947	0.008	<a href="#">ENSG00000166927</a>	4SPAN2 CD20L4 CFFM4 MS4A8	membrane spanning 4-domains A7
MYO1F	-2.2580658	0.00019	<a href="#">ENSG00000142347</a>		myosin IF
NCKAP1L	-2.8231918	2.6E-06	<a href="#">ENSG00000123338</a>	HEM1 IMD72	NCK associated protein 1 like
P2RY8	-2.8643954	0.00044	<a href="#">ENSG00000182162</a>	P2Y8	P2Y receptor family member 8
PIK3CG	-2.1572649	0.02216	<a href="#">ENSG00000105851</a>	IMD97 PI3CG PI3K PI3Kgamma PIK3p110gamma p120-PI3K	phosphatidylinositol-4,5-bisphosphate 3-kinase catalytic subunit gamma
PLEK	-2.5057943	0.00786	<a href="#">ENSG00000115956</a>	P47 PLEK1	pleckstrin
PRKCB	-3.063809	0.01311	<a href="#">ENSG00000166501</a>	PKC-beta PKCB PKCbeta PRKCB1 PRKCB2	protein kinase C beta
PTPN7	-1.8113513	0.02519	<a href="#">ENSG00000143851</a>	BPTP-4 HEPTP LC-PTP LPTP PTPNI	protein tyrosine phosphatase non-receptor type 7
PTPRC	-2.6216915	0.00294	<a href="#">ENSG00000081237</a>	B220 CD45 CD45R GP180 IMD105 L-CA LCA LY5 T200	protein tyrosine phosphatase receptor type C
RCBTB2	-1.6157203	0.01015	<a href="#">ENSG00000136161</a>	CHC1L RLG	RCC1 and BTB domain containing protein 2
RCSD1	-2.3414673	0.00923	<a href="#">ENSG00000198771</a>	CAPZIP MK2S4	RCSD domain containing 1
RP11-1017G21.4	4.4086443	1E-05	<a href="#">ENSG00000258959</a>	None	None

RP11-21C4.1	-3.360387	0.00126	<a href="#">ENSG00000254102</a>		BHLHE22 antisense RNA 1
RP11-246K15.1	-2.6039302	0.00102	<a href="#">ENSG00000253821</a>	None	None
RP11-264B17.3	5.264002	0.00052	<a href="#">ENSG00000261067</a>	None	None
RP11-301G19.1	-2.6923522	0.00072	<a href="#">ENSG00000227706</a>	None	None
RP11-309L24.2	5.717734	5.1E-05	<a href="#">ENSG00000242902</a>		FLNC antisense RNA 1
RP11-473I1.9	6.1414234	0.0269	<a href="#">ENSG00000263244</a>	None	None
RP11-856F16.2	2.4564983	0.03105	<a href="#">ENSG00000256469</a>	None	None
RP1-317E23.3	10.544808	0.01311	<a href="#">ENSG00000228172</a>	None	None
RP3-414A15.2	-2.1459139	0.02263	<a href="#">ENSG00000258695</a>	None	None
RP4-724E16.2	6.0065454	0.00161	<a href="#">ENSG00000197670</a>	None	None
RUNX3	-1.9231906	0.00261	<a href="#">ENSG00000206333</a>	AML2 CBFA3 PEBP2aC	RUNX family transcription factor 3
SASH3	-2.4207829	0.00017	<a href="#">ENSG00000122122</a>	753P9 CXorf9 HACS2 IMD102 SH3D6C SLY	SAM and SH3 domain containing 3
SIGLEC1	-2.2373666	0.00387	<a href="#">ENSG00000088827</a>	CD169 SIGLEC-1 SN	sialic acid binding Ig like lectin 1
SLA	-2.5495492	7.1E-08	<a href="#">ENSG00000155926</a>	SLA1 SLAP	Src like adaptor
SLAMF8	-2.3018794	0.00546	<a href="#">ENSG00000158714</a>	BLAME CD353 SBB142	SLAM family member 8
SLC11A1	-1.6396015	0.0007	<a href="#">ENSG00000182800</a>	LSH NRAMP NRAMP1	solute carrier family 11 member 1
SLC2A5	-2.9044548	7.8E-07	<a href="#">ENSG00000142583</a>	GLUT-5 GLUT5	solute carrier family 2 member 5
SLC8A1	-1.6664419	0.02324	<a href="#">ENSG00000183023</a>	NCX1	solute carrier family 8 member A1
SPN	-3.5849882	1.1E-07	<a href="#">ENSG00000197471</a>	CD43 GALGP GPL115 LEU-22 LSN	sialophorin
SPP1	-3.1923271	0.00011	<a href="#">ENSG00000118785</a>	BNSP BSPI ETA-1 OPN	secreted phosphoprotein 1
TCTEX1D1	-2.156797	0.00575	<a href="#">ENSG00000152760</a>	TCTEX1D1	dynein light chain Tctex-type family member 5
TNFRSF1B	-2.7594017	3.5E-05	<a href="#">ENSG00000281373</a>	CD120b TBPII TNF-R-II TNF-R75 TNFBR TNFR1B TNFR2 TNFR80 p75 p75TNFR	TNF receptor superfamily member 1B
TREM2	-1.7870559	0.03105	<a href="#">ENSG00000095970</a>	PLOSL2 TREM-2 Trem2a Trem2b Trem2c	triggering receptor expressed on myeloid cells 2
TYROBP	-2.6187198	0.00302	<a href="#">ENSG00000011600</a>	DAP12 KARAP PLOSL PLOSL1	transmembrane immune signaling adaptor TYROBP
VSIG4	-2.7413221	0.00017	<a href="#">ENSG00000155659</a>	CRIg Z39IG	V-set and immunoglobulin domain containing 4
ZBED6	9.5604851	0.03872	<a href="#">ENSG00000257315</a>	MGR	zinc finger BED-type containing 6

### DEP 17% against NaCl

ABCB11	-1.8613098	0.00522	<a href="#">ENSG00000073734</a>	ABC16 BRIC2 BSEP PFIC-2 PFIC2 PGY4 SPGP	ATP binding cassette subfamily B member 11
--------	------------	---------	---------------------------------	-----------------------------------------	--------------------------------------------

AC002310.7	2.6551491	0.00945	<a href="#">ENSG00000239791</a>	None	None
AC005387.3	3.8501774	3.5E-05	<a href="#">ENSG00000268938</a>	None	None
AC007040.11	2.5944871	0.02379	<a href="#">ENSG00000258881</a>	None	None
AC007193.8	4.1072873	0.00867	<a href="#">ENSG00000269151</a>	None	None
AC068499.10	2.3803563	0.00513	<a href="#">ENSG00000268650</a>		uncharacterized LOC102725254
AC079779.4	-2.4505602	0.0437	<a href="#">ENSG00000228643</a>	None	None
AC114803.3	2.43913	0.04127	<a href="#">ENSG00000230432</a>	None	None
ACSBG1	-2.3872747	0.01419	<a href="#">ENSG00000103740</a>	BG BG1 BGM GR-LACS LPD	acyl-CoA synthetase bubblegum family member 1
ADAMTS3	1.5372826	0.0157	<a href="#">ENSG00000156140</a>	ADAMTS-4 HKLLS3	ADAM metalloproteinase with thrombospondin type 1 motif 3
ADCYAP1	2.0808017	0.04458	<a href="#">ENSG00000141433</a>	PACAP	adenylate cyclase activating polypeptide 1
ADGRE1	1.8624245	0.00392	<a href="#">ENSG00000174837</a>	EMR1 TM7LN3	adhesion G protein-coupled receptor E1
ADGRF5	-2.6720913	0.0012	<a href="#">ENSG00000069122</a>	GPR116 KPG_001	adhesion G protein-coupled receptor F5
AE000658.22	2.135743	0.02357	<a href="#">ENSG00000257096</a>	None	None
AGMAT	-1.5702911	0.04897	<a href="#">ENSG00000116771</a>		agmatinase
AGT	1.5231825	0.00049	<a href="#">ENSG00000135744</a>	ANHU SERPINA8 hFLT1	angiotensinogen
AL157871.2	3.4963027	0.00069	<a href="#">ENSG00000259052</a>	None	None
ALDH4A1	1.8905278	2.1E-05	<a href="#">ENSG00000159423</a>	ALDH4 P5CD P5CDh	aldehyde dehydrogenase 4 family member A1
ALMS1-IT1	-3.0687152	0.0074	<a href="#">ENSG00000230002</a>		ALMS1 intronic transcript 1
AMOT	1.5238927	5.2E-05	<a href="#">ENSG00000126016</a>		angiomin
ANGPT1	2.1346724	0.00012	<a href="#">ENSG00000154188</a>	AGP1 AGPT AGPT-1 ANG1 HAE5	angiopoietin 1
ANO2	4.1098347	0.02678	<a href="#">ENSG00000047617</a>	C12orf3 TMEM16B	anoctamin 2
ANO3	2.4414265	0.0003	<a href="#">ENSG00000134343</a>	C11orf25 DYT23 DYT24 GENX-3947 TMEM16C	anoctamin 3
APLN	1.8580112	0.00113	<a href="#">ENSG00000171388</a>	APEL XNPEP2	apelin
APOBEC3F	1.5852513	0.00048	<a href="#">ENSG00000128394</a>	A3F ARP8 BK150C2.4.MRNA KA6	apolipoprotein B mRNA editing enzyme catalytic subunit 3F
APOL1	1.7195515	1.1E-14	<a href="#">ENSG00000100342</a>	APO-L APOL APOL-I FSGS4	apolipoprotein L1
APOL3	1.6224153	0.00053	<a href="#">ENSG00000128284</a>	APOLIII CG121 CG12_1 apoL-III	apolipoprotein L3
AQP3	2.2112021	4.6E-07	<a href="#">ENSG00000165272</a>	AQP-3 GIL	aquaporin 3 (Gill blood group)
ARHGAP9	-1.9625756	0.00506	<a href="#">ENSG00000123329</a>	10C RGL1	Rho GTPase activating protein 9
ARSI	1.9084774	2.6E-06	<a href="#">ENSG00000183876</a>	ASI SPG66	arylsulfatase family member I
ATOX8	2.4901079	0.00041	<a href="#">ENSG00000168874</a>	HATH6 bHLHa21	atonal bHLH transcription factor 8

ATP8B3	1.5627466	0.00525	<a href="#">ENSG00000130270</a>	ATPIK	ATPase phospholipid transporting 8B3
AXIN2	1.795338	0.01379	<a href="#">ENSG00000168646</a>	AXIL ODCRCS	axin 2
AZGP1	-4.5989223	1E-09	<a href="#">ENSG00000160862</a>	ZA2G ZAG	alpha-2-glycoprotein 1, zinc-binding
B3GNT6	-8.3418974	0.01245	<a href="#">ENSG00000198488</a>	B3Gn-T6 BGnT-6 beta-1,3-Gn-T6 beta3Gn-T6	UDP-GlcNAc:betaGal beta-1,3-N-acetylglucosaminyltransferase 6
B4GALNT1	1.6427609	2E-06	<a href="#">ENSG00000135454</a>	GALGT GALNACT GalNAc-T SPG26	beta-1,4-N-acetyl-galactosaminyltransferase 1
BAGE2	1.7552949	0.00381	<a href="#">ENSG00000187172</a>	None	None
BATF2	1.6135935	0.00445	<a href="#">ENSG00000168062</a>	SARI	basic leucine zipper ATF-like transcription factor 2
BMP2	-1.535068	1.6E-06	<a href="#">ENSG00000125845</a>	BDA2 BMP2A SSFSC SSFSC1	bone morphogenetic protein 2
BMP4	1.5121443	0.00225	<a href="#">ENSG00000125378</a>	BMP2B BMP2B1 MCOPS6 OFC11 ZYME	bone morphogenetic protein 4
BMP6	-1.5005884	1.5E-06	<a href="#">ENSG00000153162</a>	IO VGR VGR1	bone morphogenetic protein 6
BVES-AS1	-2.0291003	0.00553	<a href="#">ENSG00000203808</a>	C6orf112 bA99L11.2	BVES antisense RNA 1
C11orf86	2.2457123	0.02597	<a href="#">ENSG00000173237</a>	FACI	chromosome 11 open reading frame 86
C14orf132	3.4423108	3.8E-07	<a href="#">ENSG00000227051</a>	C14orf88	chromosome 14 open reading frame 132
C1QL1	1.8137686	6.6E-05	<a href="#">ENSG00000131094</a>	C1QRF C1QTNF14 CRF CTRP14	complement C1q like 1
C1QL4	1.9300269	0.00883	<a href="#">ENSG00000186897</a>	C1QTNF11 CTRP11	complement C1q like 4
C1QTNF2	1.7225153	0.01358	<a href="#">ENSG00000145861</a>	CTRP2 zacrp2	C1q and TNF related 2
C1R	2.8839988	1E-25	<a href="#">ENSG00000159403</a>	EDS8 EDSPD1	complement C1r
C1S	1.620191	5.2E-15	<a href="#">ENSG00000182326</a>	EDSPD2	complement C1s
C2CD4C	1.9310267	0.00059	<a href="#">ENSG00000183186</a>	FAM148C KIAA1957 NLF3	C2 calcium dependent domain containing 4C
C3AR1	1.5154723	0.03808	<a href="#">ENSG00000171860</a>	AZ3B C3AR HNFAG09	complement C3a receptor 1
C4A	2.04905	2.4E-07	<a href="#">ENSG00000244731</a>	C4 C4A2 C4A3 C4A4 C4A6 C4AD C4S CO4 CPAMD2 RG	complement C4A (Chido/Rodgers blood group)
C4B	2.0586879	0.00024	<a href="#">ENSG00000224389</a>	C4B1 C4B12 C4B2 C4B3 C4B5 C4BD C4B_2 C4F CH CO4 CPAMD3	complement C4B (Chido/Rodgers blood group)
C6orf15	-2.9847495	0.01097	<a href="#">ENSG00000204542</a>	STG	chromosome 6 open reading frame 15
C8orf88	1.9217717	0.00464	<a href="#">ENSG00000253250</a>		chromosome 8 open reading frame 88
CACNG8	1.5406528	0.00011	<a href="#">ENSG00000142408</a>		calcium voltage-gated channel auxiliary subunit gamma 8
CAMK2N2	4.3676228	1.6E-05	<a href="#">ENSG00000163888</a>	CAM-KIIN CAMKIIN	calcium/calmodulin dependent protein kinase II inhibitor 2

CBFA2T3	-1.8378409	0.00932	<a href="#">ENSG00000129993</a>	ETO2 MTG16 MTGR2 RUNX1T3 ZMYND4	CBFA2/RUNX1 partner transcriptional co-repressor 3
CCDC152	2.3906497	0.02299	<a href="#">ENSG00000198865</a>	CH5400	coiled-coil domain containing 152
CCDC8	1.646818	0.00476	<a href="#">ENSG00000169515</a>	3M3 PPP1R20 p90	coiled-coil domain containing 8
CCL2	2.4617799	0.00046	<a href="#">ENSG00000108691</a>	GDCF-2 HC11 HSMCR30 MCAF MCP-1 MCP1 SCYA2 SMC-CF	C-C motif chemokine ligand 2
CCL5	1.5895675	2.1E-07	<a href="#">ENSG00000271503</a>	D17S136E RANTES SCYA5 SIS-delta SISd TCP228 eoCP	C-C motif chemokine ligand 5
CCNB2P1	-2.8432457	0.00565	<a href="#">ENSG00000214998</a>		cyclin B2 pseudogene 1
CCR2	-2.994937	0.00602	<a href="#">ENSG00000121807</a>	CC-CKR-2 CCR-2 CCR2A CCR2B CD192 CKR2 CKR2A CKR2B CMKBR2 MCP-1-R	C-C motif chemokine receptor 2
CD200	1.5287365	0.0207	<a href="#">ENSG00000091972</a>	MOX1 MOX2 MRC OX-2	CD200 molecule
CD33	1.5639344	0.00044	<a href="#">ENSG00000105383</a>	SIGLEC-3 SIGLEC3 p67	CD33 molecule
CDH11	-6.4759503	6.8E-09	<a href="#">ENSG00000140937</a>	CAD11 CDHOB ESWS OB OSF-4 TBHS2	cadherin 11
CDH2	1.6404687	1.3E-06	<a href="#">ENSG00000170558</a>	ACOGS ADHD8 ARVD14 CD325 CDHN CDw325 NCAD	cadherin 2
CEACAM5	-4.4176252	0.01849	<a href="#">ENSG00000105388</a>	CD66e CEA	CEA cell adhesion molecule 5
CEBPA	-1.5955962	7.9E-05	<a href="#">ENSG00000245848</a>	C/EBP-alpha CEBP	CCAAT enhancer binding protein alpha
CEL	1.7913938	0.00029	<a href="#">ENSG00000170835</a>	BAL BSDL BSSL CELL CEase FAP FAPP LIPA MODY8	carboxyl ester lipase
CFAP206	2.0370387	0.03577	<a href="#">ENSG00000272514</a>	C6orf165 dJ382I10.1	cilia and flagella associated protein 206
CFB	2.0638964	0.0008	<a href="#">ENSG00000243649</a>	AHUS4 ARMD14 BF BFD CFAB CFBD FB FBI12 GBG H2-Bf PBF2	complement factor B
CH17-140K24.2	3.7451165	0.00244	<a href="#">ENSG00000280029</a>	None	None
CH25H	2.8693674	0.02999	<a href="#">ENSG00000138135</a>	C25H	cholesterol 25-hydroxylase
CH507-513H4.4	4.1305414	0.04476	<a href="#">ENSG00000280614</a>	None	None
CH507-513H4.6	4.3234117	0.038	<a href="#">ENSG00000280800</a>	None	None
CHI3L2	2.2042287	9.9E-08	<a href="#">ENSG00000064886</a>	CHIL2 YKL-39 YKL39	chitinase 3 like 2
CHN1	1.7225058	1.5E-07	<a href="#">ENSG00000128656</a>	ARHGAP2 CHN DURS2 NC RHOGAP2	chimerin 1
CHST6	1.6249842	3.1E-07	<a href="#">ENSG00000183196</a>	C-GlcNAc6ST GST4-beta MCDC1 glcNAc6ST-5 gn6st-5 hCGn6ST	carbohydrate sulfotransferase 6
CIITA	2.408166	0.00013	<a href="#">ENSG00000179583</a>	C2TA CIITAIV MHC2TA NLRA	class II major histocompatibility complex transactivator
CLCA2	1.6811427	3.3E-05	<a href="#">ENSG00000137975</a>	CACC CACC3 CLCRG2 CaCC-3	chloride channel accessory 2



CMPK2	2.3991553	1.6E-10	<a href="#">ENSG00000134326</a>	NDK TMPK2 TYKi UMP-CMPK2	cytidine/uridine monophosphate kinase 2
CNTN5	2.931689	0.04888	<a href="#">ENSG00000149972</a>	HNB-2s NB-2	contactin 5
COL11A1	1.6995333	0.0129	<a href="#">ENSG00000060718</a>	CO11A1 COLL6 DFNA37 STL2	collagen type XI alpha 1 chain
COPZ2	1.5600702	0.01568	<a href="#">ENSG00000005243</a>	zeta2-COP	COPI coat complex subunit zeta 2
CRABP2	-2.0173502	0.00043	<a href="#">ENSG00000143320</a>	CRABP-II RBP6	cellular retinoic acid binding protein 2
CRIP2	1.5759866	0.00019	<a href="#">ENSG00000182809</a>	CRIP CRP2 ESP1	cysteine rich protein 2
CRNDE	1.7037893	0.00016	<a href="#">ENSG00000245694</a>		uncharacterized LOC101927480
CSAG1	1.7323616	0.00022	<a href="#">ENSG00000198930</a>	CSAGE CT24.1	chondrosarcoma associated gene 1
CSDC2	1.7943601	0.00237	<a href="#">ENSG00000172346</a>	PIPPIN dJ347H13.2	cold shock domain containing C2
CSF3	2.0786181	0.00038	<a href="#">ENSG00000108342</a>	C17orf33 CSF3OS GCSF	colony stimulating factor 3
CTA-384D8.35	1.524693	3.5E-05	<a href="#">ENSG00000272666</a>	None	None
CTAGE11P	-2.1989703	0.02998	<a href="#">ENSG00000214249</a>		CTAGE family member 11, pseudogene
CTB-129P6.4	-7.6854423	0.01915	<a href="#">ENSG00000267282</a>	None	None
CTC-512J12.4	1.6344071	0.0277	<a href="#">ENSG00000267188</a>	None	None
CTC-558O2.2	2.3519861	0.02411	<a href="#">ENSG00000254192</a>	None	None
CTD-2196E14.9	9.807521	0.00185	<a href="#">ENSG00000260482</a>	None	None
CTD-2263F21.1	2.0095568	0.02044	<a href="#">ENSG00000251257</a>		uncharacterized LOC124900964
CTD-2376I4.2	1.7124775	0.03498	<a href="#">ENSG00000272081</a>	None	None
CTD-2521M24.6	3.2467714	0.00396	<a href="#">ENSG00000269481</a>	None	None
CTD-2554C21.2	-7.2631517	0.03339	<a href="#">ENSG00000267640</a>	None	None
CTNNA3	-2.4008186	0.02922	<a href="#">ENSG00000183230</a>	ARVD13 VR22	catenin alpha 3
CXADRP3	4.3661747	0.00125	<a href="#">ENSG00000265766</a>		CXADR pseudogene 3
CXCL1	2.6123932	8.4E-16	<a href="#">ENSG00000163739</a>	FSP GRO1 GROa MGSA MGSA-a NAP-3 SCYB1	C-X-C motif chemokine ligand 1
CXCL10	3.2582205	1.9E-15	<a href="#">ENSG00000169245</a>	C7 IFI10 INP10 IP-10 SCYB10 crg-2 gIP-10 mob-1	C-X-C motif chemokine ligand 10
CXCL11	1.9909733	5.9E-06	<a href="#">ENSG00000169248</a>	H174 I-TAC IP-9 IP9 SCYB11 SCYB9B b-R1	C-X-C motif chemokine ligand 11
CYP4B1	1.8121453	0.00862	<a href="#">ENSG00000142973</a>	CYP1VB1 P-450HP	cytochrome P450 family 4 subfamily B member 1
DAPK2	1.9125196	5.7E-08	<a href="#">ENSG00000035664</a>	DRP-1 DRP1	death associated protein kinase 2
DCAF8L2	1.7335634	0.00785	<a href="#">ENSG00000189186</a>	WDR42C	DDB1 and CUL4 associated factor 8 like 2
DDX58	1.5523264	7E-19	<a href="#">ENSG00000107201</a>	DDX58 RIG-I RIG1 RLR-1 SGMRT2	RNA sensor RIG-I
DDX60	1.6918456	2.2E-17	<a href="#">ENSG00000137628</a>		DEAD/H-box helicase 60

DIO2	2.8198333	0.00423	<a href="#">ENSG00000211448</a>	5DII D2 DIOII SELENOY SeIY TXDI2	iodothyronine deiodinase 2
DISP2	1.6560861	0.00019	<a href="#">ENSG00000140323</a>	C15orf36 DISPB HsT16908 LINC00594	dispatched RND transporter family member 2
DLX4	2.2384692	0.00311	<a href="#">ENSG00000108813</a>	BP1 DLX7 DLX8 DLX9 OFC15	distal-less homeobox 4
DPF3	1.6650167	0.02475	<a href="#">ENSG00000205683</a>	BAF45C CERD4 SMARCG3	double PHD fingers 3
DPYS	-3.9799279	0.03918	<a href="#">ENSG00000147647</a>	DHP DHPase	dihydropyrimidinase
EMP3	1.8129387	9E-11	<a href="#">ENSG00000142227</a>	YMP	epithelial membrane protein 3 (MAM blood group)
EPHA5	2.0628274	0.0095	<a href="#">ENSG00000145242</a>	CEK7 EHK-1 EHK1 EK7 HEK7 TYRO4	EPH receptor A5
EPHX3	-2.5029571	0.0003	<a href="#">ENSG00000105131</a>	ABHD9 EH3	epoxide hydrolase 3
EPSTI1	1.7101337	3.5E-05	<a href="#">ENSG00000133106</a>	BRESI1	epithelial stromal interaction 1
EREG	-4.2604555	2.5E-12	<a href="#">ENSG00000124882</a>	EPR ER Ep	epiregulin
ESM1	-3.6020868	1.2E-05	<a href="#">ENSG00000164283</a>	endocan	endothelial cell specific molecule 1
ESRRAP2	2.1419826	0.0434	<a href="#">ENSG00000235438</a>		uncharacterized LOC105370105
ESX1	2.379436	1.5E-08	<a href="#">ENSG00000123576</a>	ESX1L ESXR1	ESX homeobox 1
EVI2A	7.5491251	0.02612	<a href="#">ENSG00000126860</a>	EVDA EVI-2A EVI2	ecotropic viral integration site 2A
FAM133A	1.5166904	0.00047	<a href="#">ENSG00000179083</a>	CT115	family with sequence similarity 133 member A
FAM20A	1.9230208	0.00974	<a href="#">ENSG00000108950</a>	AI1G AIGFS FP2747	FAM20A golgi associated secretory pathway pseudokinase
FAM222A	-1.5151841	1.7E-07	<a href="#">ENSG00000139438</a>	C12orf34	family with sequence similarity 222 member A
FBLN5	2.8144369	0.01067	<a href="#">ENSG00000140092</a>	ADCL2 ARCL1A ARMD3 CMT1H DANCE EVEC FIBL-5 HNARMD UP50	fibulin 5
FGA	4.4155648	0.01355	<a href="#">ENSG00000171560</a>	Fib2	fibrinogen alpha chain
FGF1	1.5154765	0.0012	<a href="#">ENSG00000113578</a>	AFGF ECGF ECGF-beta ECGFA ECGFB FGF-1 FGF-alpha FGFA GLIO703 HBGF-1 HBGF1	fibroblast growth factor 1
FGFR3	1.9565169	0.00075	<a href="#">ENSG00000068078</a>	ACH CD333 CEK2 HSFGFR3EX JTK4	fibroblast growth factor receptor 3
FGG	2.4468464	0.00147	<a href="#">ENSG00000171557</a>		fibrinogen gamma chain
FIBIN	2.7388375	5.6E-05	<a href="#">ENSG00000176971</a>		fin bud initiation factor homolog
FKBP11	-3.1670649	3.8E-07	<a href="#">ENSG00000134285</a>	FKBP19	FKBP prolyl isomerase 11
FLG	3.4705006	1.2E-05	<a href="#">ENSG00000143631</a>	ATOD2 FLG-1 FLG1	filaggrin
FLT3	-2.7415121	0.0148	<a href="#">ENSG00000122025</a>	CD135 FLK-2 FLK2 STK1	fms related receptor tyrosine kinase 3
FOXL1	1.6665826	0.0059	<a href="#">ENSG00000176678</a>	FKH6 FKHL11 FREAC7 OTSC11	forkhead box L1
FSD1	1.7391406	9.7E-05	<a href="#">ENSG00000105255</a>	GLFND MIR1	fibronectin type III and SPRY domain containing 1
FSIP2-AS1	-2.8951864	0.0433	<a href="#">ENSG00000231646</a>		FSIP2 antisense RNA 1

FZD2	1.5184668	5.3E-08	<a href="#">ENSG00000180340</a>	Fz2 OMOD2 fz-2 fzE2 hFz2	frizzled class receptor 2
GAL3ST4	1.6261732	0.0027	<a href="#">ENSG00000197093</a>	GAL3ST-4	galactose-3-O-sulfotransferase 4
GBP1	1.8216195	5.5E-13	<a href="#">ENSG00000117228</a>	hGBP1	guanylate binding protein 1
GBP4	1.9339727	9.6E-06	<a href="#">ENSG00000162654</a>	Mpa2	guanylate binding protein 4
GBP5	1.6556421	0.00033	<a href="#">ENSG00000154451</a>	GBP-5	guanylate binding protein 5
GCNA	-2.348724	0.00034	<a href="#">ENSG00000147174</a>	ACRC NAAR1 SPGFX4	germ cell nuclear acidic peptidase
GFPT2	1.7874474	1.5E-08	<a href="#">ENSG00000131459</a>	GFAT GFAT2	glutamine-fructose-6-phosphate transaminase 2
GLIPR1L1	1.7535011	0.01949	<a href="#">ENSG00000173401</a>	ALKN2972 PRO7434	GLIPR1 like 1
GLYATL1P2	2.8472797	0.00347	<a href="#">ENSG00000254717</a>		glycine-N-acyltransferase like 1 pseudogene 2
GOLGA8M_1	-3.4539236	0.02119	<a href="#">ENSG00000188626</a>		golgin A8 family member M
GPR158	1.884313	0.00075	<a href="#">ENSG00000151025</a>	mGlyR	G protein-coupled receptor 158
GPR162	1.6444986	4E-05	<a href="#">ENSG00000250510</a>	A-2 GRCA	G protein-coupled receptor 162
GRIN2B	-1.604732	1.6E-05	<a href="#">ENSG00000273079</a>	DEE27 EIEE27 GluN2B MRD6 NMDAR2B NR2B NR3 hNR3	glutamate ionotropic receptor NMDA type subunit 2B
GSDMD	1.6124764	7E-11	<a href="#">ENSG00000104518</a>	DF5L DFNA5L FKSG10 GSDMDC1	gasdermin D
HAGLR	-3.2266972	0.00045	<a href="#">ENSG00000224189</a>	HOXD-AS1 MIR7704HG Mdgt STEEL	HOXD antisense growth-associated long non-coding RNA
HBE1	1.5250071	7.4E-05	<a href="#">ENSG00000213931</a>	HBE	hemoglobin subunit epsilon 1
HCAR2	1.8263256	3.9E-05	<a href="#">ENSG00000182782</a>	GPR109A HCA2 HM74a HM74b NIACR1 PUMAG Puma-g	hydroxycarboxylic acid receptor 2
HCAR3	1.9486424	5.9E-06	<a href="#">ENSG00000255398</a>	GPR109B HCA3 HM74 PUMAG Puma-g	hydroxycarboxylic acid receptor 3
HELZ2	1.9767724	3.9E-21	<a href="#">ENSG00000130589</a>	PDIP-1 PRIC285	helicase with zinc finger 2
HEPHL1	1.5362527	9.7E-07	<a href="#">ENSG00000181333</a>	HJDD ZP	hephaestin like 1
HHIPL2	2.9241485	2.7E-06	<a href="#">ENSG00000143512</a>	KIAA1822L	HHIP like 2
HIST2H2BD	3.1120806	0.00275	<a href="#">ENSG00000220323</a>	H2B/o H2B/s H2BFO HIST2H2BD	H2B clustered histone 19, pseudogene
HKDC1	3.0288867	0.02107	<a href="#">ENSG00000156510</a>	RP92	hexokinase domain containing 1
HLA-DOA	1.6660945	0.01512	<a href="#">ENSG00000204252</a>	HLA-DNA HLA-DZA HLADZ	major histocompatibility complex, class II, DO alpha
HLA-DRA	2.318316	0.00041	<a href="#">ENSG00000204287</a>	HLA-DRA1	major histocompatibility complex, class II, DR alpha
HLA-K	-2.3155543	5.4E-05	<a href="#">ENSG00000230795</a>	HLA-70 HLA70 HLAK	major histocompatibility complex, class I, K (pseudogene)
HMSD	1.5285218	0.0251	<a href="#">ENSG00000221887</a>	ACC-6 ACC6 C18orf53 HMSD-v	histocompatibility minor serpin domain containing
HOGA1	3.0137952	0.00257	<a href="#">ENSG00000241935</a>	C10orf65 DHDPS2 DHDPSL HP3 NPL2	4-hydroxy-2-oxoglutarate aldolase 1

HOXA4	1.5954974	0.03088	<a href="#">ENSG00000197576</a>	HOX1 HOX1D	homeobox A4
HOXB2	2.5075771	0.00021	<a href="#">ENSG00000173917</a>	HOX2 HOX2H Hox-2.8 K8	homeobox B2
HOXB3	2.1760477	0.00306	<a href="#">ENSG00000120093</a>	HOX2 HOX2G Hox-2.7	homeobox B3
HOXB6	2.4037882	1.1E-05	<a href="#">ENSG00000108511</a>	HOX2 HOX2B HU-2 Hox-2.2	homeobox B6
HOXB-AS1	1.8576471	0.01124	<a href="#">ENSG00000230148</a>	HOXB3OS	HOXB cluster antisense RNA 1
HPGD	-6.798552	0.04989	<a href="#">ENSG00000164120</a>	15-PGDH PGDH PGDH1 PHOAR1 SDR36C1	15-hydroxyprostaglandin dehydrogenase
HR	2.2150338	0.00061	<a href="#">ENSG00000168453</a>	ALUNC AU HSA277165 HYPT4 MUHH MUHH1	HR lysine demethylase and nuclear receptor corepressor
HSD11B1	-3.3678666	0.01246	<a href="#">ENSG00000117594</a>	11-DH 11-beta-HSD1 CORTRD2 HDL HSD11 HSD11B HSD11L SDR26C1	hydroxysteroid 11-beta dehydrogenase 1
HSPA6	-2.4658498	2.1E-05	<a href="#">ENSG00000173110</a>		heat shock protein family A (Hsp70) member 6
HSPB3	3.3070871	0.00464	<a href="#">ENSG00000169271</a>	DHMN2C HMN2C HMND4 HSPL27	heat shock protein family B (small) member 3
HSPE1	10.65525	0.00284	<a href="#">ENSG00000115541</a>	CPN10 EPF GROES HSP10	heat shock protein family E (Hsp10) member 1
ICAM2	1.5484249	0.03253	<a href="#">ENSG00000108622</a>	CD102	intercellular adhesion molecule 2
IFI27	2.941988	3.3E-16	<a href="#">ENSG00000165949</a>	FAM14D ISG12 ISG12A P27	interferon alpha inducible protein 27
IFI35	1.6716244	5E-10	<a href="#">ENSG00000068079</a>	IFP35	interferon induced protein 35
IFI44	2.4448417	2E-32	<a href="#">ENSG00000137965</a>	MTAP44 TLDC5 p44	interferon induced protein 44
IFI44L	2.8565333	1.1E-12	<a href="#">ENSG00000137959</a>	C1orf29 GS3686 TLDC5B	interferon induced protein 44 like
IFI6	2.4718321	2.2E-22	<a href="#">ENSG00000126709</a>	6-16 FAM14C G1P3 IFI-6-16 IFI616	interferon alpha inducible protein 6
IFIT1	3.2931483	1.4E-26	<a href="#">ENSG00000185745</a>	C56 G10P1 IFI-56 IFI-56K IFI56 IFIT-1 IFNAI1 ISG56 P56 RNM561	interferon induced protein with tetratricopeptide repeats 1
IFIT2	4.6856197	1.2E-16	<a href="#">ENSG00000119922</a>	G10P2 GARG-39 IFI-54 IFI-54K IFI54 IFIT-2 ISG-54 ISG-54K ISG54 P54 cig42	interferon induced protein with tetratricopeptide repeats 2
IFIT3	4.2398817	5E-12	<a href="#">ENSG00000119917</a>	CIG-49 GARG-49 IFI60 IFIT4 IRG2 ISG60 P60 RIG-G cig41	interferon induced protein with tetratricopeptide repeats 3
IFITM1	5.7945876	2.4E-29	<a href="#">ENSG00000185885</a>	9-27 CD225 DSPA2a IFI17 LEU13	interferon induced transmembrane protein 1
IFITM2	1.7870301	3.1E-13	<a href="#">ENSG00000185201</a>	1-8D DSPA2c	interferon induced transmembrane protein 2
IFNL1	2.4948239	0.02791	<a href="#">ENSG00000182393</a>	IL-29 IL29	interferon lambda 1
IGFBP2	1.8839476	0.00042	<a href="#">ENSG00000115457</a>	IBP2 IGF-BP53	insulin like growth factor binding protein 2
IGFBP5	-2.9446122	0.03187	<a href="#">ENSG00000115461</a>	IBP5	insulin like growth factor binding protein 5
IGFBP7-AS1	2.2048818	0.02195	<a href="#">ENSG00000245067</a>		IGFBP7 antisense RNA 1

IKZF3	-1.9642453	0.00264	<a href="#">ENSG00000161405</a>	AIO AIOLOS IMD84 ZNFN1A3	IKAROS family zinc finger 3
IL21R-AS1	1.7200805	9.6E-05	<a href="#">ENSG00000259954</a>		IL21R antisense RNA 1
ILDR2	1.7102524	0.00046	<a href="#">ENSG00000143195</a>	C1orf32 dJ782G3.1	immunoglobulin like domain containing receptor 2
IP6K3	2.7306141	5E-05	<a href="#">ENSG00000161896</a>	IHPK3 INSP6K3	inositol hexakisphosphate kinase 3
IRF8	-2.8069513	0.00034	<a href="#">ENSG00000140968</a>	H-ICSBP ICSBP ICSBP1 IMD32A IMD32B IRF-8	interferon regulatory factor 8
ISG15	1.8181283	1.6E-09	<a href="#">ENSG00000187608</a>	G1P2 IFI15 IMD38 IP17 UCRP hUCRP	ISG15 ubiquitin like modifier
ITGAL	-1.8751853	0.00166	<a href="#">ENSG00000005844</a>	CD11A LFA-1 LFA1A	integrin subunit alpha L
KB-1572G7.2	7.5877961	0.04755	<a href="#">ENSG00000273000</a>	None	None
KB-1592A4.15	2.4089522	0.04748	<a href="#">ENSG00000197210</a>	None	None
KB-1732A1.1	1.699639	0.00192	<a href="#">ENSG00000253669</a>	None	None
KCNB1	2.3340928	0.00832	<a href="#">ENSG00000158445</a>	DEE26 DRK1 Kv2.1	potassium voltage-gated channel subfamily B member 1
KCNC3	-2.2617427	0.01611	<a href="#">ENSG00000131398</a>	KSHIID KV3.3 SCA13	potassium voltage-gated channel subfamily C member 3
KCNE4	3.3217376	0.02891	<a href="#">ENSG00000152049</a>	MIRP3	potassium voltage-gated channel subfamily E regulatory subunit 4
KCNIP3	1.7723609	2.2E-06	<a href="#">ENSG00000115041</a>	CSEN DREAM KCHIP3	potassium voltage-gated channel interacting protein 3
KDR	-3.1677801	1.9E-06	<a href="#">ENSG00000128052</a>	CD309 FLK1 VEGFR VEGFR2	kinase insert domain receptor
KRT16P2	-7.9530275	7.5E-07	<a href="#">ENSG00000227300</a>	None	None
KRT34	-1.6529215	0.00502	<a href="#">ENSG00000131737</a>	HA4 Ha-4 K34 KRTHA4 hHa4	keratin 34
LA16c-13E4.3	-6.9448771	0.04928	<a href="#">ENSG00000236235</a>	None	None
LA16c-60D12.2	-4.0758766	0.00716	<a href="#">ENSG00000279442</a>	None	None
LAMA4	1.5533201	0.0002	<a href="#">ENSG00000112769</a>	CMD1JJ LAMA3 LAMA4*-1	laminin subunit alpha 4
LAMC2	-1.5069535	3.8E-10	<a href="#">ENSG00000058085</a>	B2T BM600 CSF EBR2 EBR2A JEB3A JEB3B LAMB2T LAMNB2	laminin subunit gamma 2
LAMP3	1.9550288	8.9E-10	<a href="#">ENSG00000078081</a>	CD208 DC-LAMP DCLAMP LAMP LAMP-3 TSC403	lysosomal associated membrane protein 3
LARGE1	1.6467199	0.00285	<a href="#">ENSG00000133424</a>	LARGE MDC1D MDDGA6 MDDGB6	LARGE xylosyl- and glucuronyltransferase 1
LDLRAD1	1.8219883	0.02339	<a href="#">ENSG00000203985</a>		low density lipoprotein receptor class A domain containing 1
LGI2	-2.4615827	3.6E-24	<a href="#">ENSG00000153012</a>	LGIL2	leucine rich repeat LGI family member 2
LHX6	-1.5230576	6.2E-06	<a href="#">ENSG00000106852</a>	LHX6.1 hLHX6	LIM homeobox 6

LIMS2	1.8394094	0.01191	<a href="#">ENSG00000072163</a>	LGMD2W MDRCMTT PINCH-2 PINCH2	LIM zinc finger domain containing 2
LINC00431	-2.2568889	0.01201	<a href="#">ENSG00000225760</a>	None	None
LINC00839	2.843291	1.3E-06	<a href="#">ENSG00000185904</a>		long intergenic non-protein coding RNA 839
LINC01098	1.5845055	0.01157	<a href="#">ENSG00000231171</a>		long intergenic non-protein coding RNA 1098
LINC01234	1.9917507	0.00054	<a href="#">ENSG00000249550</a>	LCAL84 MBOP onco-lncRNA-32	long intergenic non-protein coding RNA 1234
LINC01270	1.6758758	0.00707	<a href="#">ENSG00000203999</a>		long intergenic non-protein coding RNA 1270
LINC01293	-2.5785741	0.0437	<a href="#">ENSG00000230836</a>	None	None
LINC01405	2.3172335	0.02357	<a href="#">ENSG00000185847</a>		long intergenic non-protein coding RNA 1405
LINC01419	3.2628132	0.02491	<a href="#">ENSG00000253898</a>	LVCAT7 PRLH1 TCONS_00014497	long intergenic non-protein coding RNA 1419
LINC01482	1.9360348	0.0369	<a href="#">ENSG00000267659</a>		long intergenic non-protein coding RNA 1482
LINC01687	1.776775	0.00386	<a href="#">ENSG00000233215</a>		long intergenic non-protein coding RNA 1687
LINC02159	2.4480883	0.01994	<a href="#">ENSG00000253417</a>		long intergenic non-protein coding RNA 2159
LL22NC03-N14H11.1	3.414543	1.1E-05	<a href="#">ENSG00000272872</a>	None	None
LL22NC03-N64E9.1	-1.8987067	4.8E-05	<a href="#">ENSG00000271127</a>	None	None
LLfos-48D6.2	-2.3667092	0.00686	<a href="#">ENSG00000273734</a>	None	None
LPCAT3	-7.796353	0.02207	<a href="#">ENSG00000111684</a>	C3F LPCAT LPLAT12 LPSAT MBOAT5 OACT5 nessy	lysophosphatidylcholine acyltransferase 3
LRP4	1.5039672	0.00565	<a href="#">ENSG00000134569</a>	CLSS CMS17 LRP-4 LRP10 MEGF7 SOST2	LDL receptor related protein 4
LRRC17	3.8965836	0.00067	<a href="#">ENSG00000128606</a>	P37NB	leucine rich repeat containing 17
LRRC4C	2.1873148	1.5E-06	<a href="#">ENSG00000148948</a>	NGL-1 NGL1	leucine rich repeat containing 4C
LTF	2.9183956	0.00798	<a href="#">ENSG00000012223</a>	GIG12 HEL110 HLF2 LF	lactotransferrin
LUM	-3.563199	0.00716	<a href="#">ENSG00000139329</a>	LDC SLRR2D	lumican
LYNX1_3	1.6666298	0.00846	<a href="#">ENSG00000180155</a>		Ly6/neurotoxin 1
MAGEA11	1.9635362	2.7E-07	<a href="#">ENSG00000185247</a>	CT1.11 MAGE-11 MAGE11 MAGEA-11	MAGE family member A11
MAGEA3	2.0689535	7.3E-10	<a href="#">ENSG00000221867</a>	CT1.3 HIP8 HYPD MAGE3 MAGEA6	MAGE family member A3
MAGEA6	1.8373616	6.7E-10	<a href="#">ENSG00000197172</a>	CT1.6 MAGE-3b MAGE3B MAGE6	MAGE family member A6
MAPK8IP2	1.7609624	0.00712	<a href="#">ENSG00000263503</a>	None	None
MARK2P16	2.2439948	0.02152	<a href="#">ENSG00000270670</a>	None	None

MATN2	1.6543996	0.00014	<a href="#">ENSG00000132561</a>		matrilin 2
MDGA1	2.4327674	0.00512	<a href="#">ENSG00000112139</a>	GPIM MAMDC3	MAM domain containing glycosylphosphatidylinositol anchor 1
MEIS3	1.7827793	0.00113	<a href="#">ENSG00000105419</a>	MRG2	Meis homeobox 3
MFAP5	-1.7745523	3.3E-07	<a href="#">ENSG00000197614</a>	AAT9 MAGP-2 MAGP2 MFAP-5 MP25	microfibril associated protein 5
MGAT5B	1.6414361	0.00511	<a href="#">ENSG00000167889</a>	GnT-IX GnT-VB	alpha-1,6-mannosylglycoprotein 6-beta-N-acetylglucosaminyltransferase B
MGC32805	1.8374045	0.01219	<a href="#">ENSG00000250328</a>		uncharacterized LOC153163
MIR3681HG	3.3302262	0.01559	<a href="#">ENSG00000224184</a>		MIR3681 host gene
MKX	-2.4039578	6.7E-25	<a href="#">ENSG00000150051</a>	C10orf48 IFRX IRXL1	mohawk homeobox
MKX-AS1	-2.7416217	0.01263	<a href="#">ENSG00000230500</a>	None	None
MUC21	-4.106391	8.5E-10	<a href="#">ENSG00000204544</a>	C6orf205 KMQK697 MUC-21	mucin 21, cell surface associated
MX1	3.2951813	5.2E-52	<a href="#">ENSG00000157601</a>	IFI-78K IFI78 MX MxA lncMX1-215	MX dynamin like GTPase 1
MX2	3.0982193	2.6E-31	<a href="#">ENSG00000183486</a>	MXB	MX dynamin like GTPase 2
MXRA5	2.786343	2.2E-06	<a href="#">ENSG00000101825</a>		matrix remodeling associated 5
MYEOV	-2.9274302	4.7E-06	<a href="#">ENSG00000172927</a>	OCIM	myeloma overexpressed
MYL9	1.9946482	5.9E-12	<a href="#">ENSG00000101335</a>	LC20 MLC-2C MLC2 MMIHS4 MRLC1 MYRL2	myosin light chain 9
MYLK4	1.8985974	0.02783	<a href="#">ENSG00000145949</a>	SgK085	myosin light chain kinase family member 4
NAALADL2-AS2	-2.407801	0.00057	<a href="#">ENSG00000226779</a>	None	None
NAPSA	-9.0852302	0.01587	<a href="#">ENSG00000131400</a>	KAP Kdap NAP1 NAPA SNAPA	napsin A aspartic peptidase
NECAB1	1.6790641	0.00711	<a href="#">ENSG00000123119</a>	EFCBP1 STIP-1	N-terminal EF-hand calcium binding protein 1
NEFL	2.0292272	6.3E-09	<a href="#">ENSG00000277586</a>	CMT1F CMT2E CMTDIG NF-L NF68 NFL PPP1R110	neurofilament light chain
NEURL3	1.8381674	0.02902	<a href="#">ENSG00000163121</a>	LINCR RNFI32	neuralized E3 ubiquitin protein ligase 3
NFE2	2.0597333	0.00213	<a href="#">ENSG00000123405</a>	NF-E2 p45	nuclear factor, erythroid 2
NKX2-1	-7.6117008	3.5E-06	<a href="#">ENSG00000136352</a>	BCH BHC NK-2 NKX2.1 NKX2A NMTC1 T/EBP TEBP TITF1 TTF-1 TTF1	NK2 homeobox 1
NLGN2	1.6104364	9.9E-19	<a href="#">ENSG00000169992</a>		neuroligin 2
NLRP12	-4.1194144	0.03914	<a href="#">ENSG00000142405</a>	CLR19.3 FCAS2 NALP12 PAN6 PYPAF7 RNO RNO2	NLR family pyrin domain containing 12
NLRP2	-7.0230195	1.9E-05	<a href="#">ENSG00000225556</a>	CLR19.9 NALP2 NBS1 OZEMA18 PAN1 PYPAF2	NLR family pyrin domain containing 2
NRSN2	1.6946516	5.6E-13	<a href="#">ENSG00000125841</a>	C20orf98 dJ1103G7.6	neurensin 2

OAS1	2.3564535	3.8E-10	<a href="#">ENSG00000089127</a>	E18/E16 IFI-4 IMD100 OIAS OIASI	2'-5'-oligoadenylate synthetase 1
OAS2	3.3543965	1.5E-39	<a href="#">ENSG00000111335</a>		2'-5'-oligoadenylate synthetase 2
OAS3	2.0447177	8.7E-09	<a href="#">ENSG00000111331</a>	p100 p100OAS	2'-5'-oligoadenylate synthetase 3
OASL	2.1859714	5.2E-15	<a href="#">ENSG00000135114</a>	OASL1 OASLd TRIP-14 TRIP14 p59-OASL p59OASL	2'-5'-oligoadenylate synthetase like
OCIAD1-AS1	-7.7133897	0.02342	<a href="#">ENSG00000248256</a>		OCIAD1 antisense RNA 1
OGDHL	1.6812913	0.0004	<a href="#">ENSG00000197444</a>	YOBELN	oxoglutarate dehydrogenase L
ORM1	1.8778305	0.00292	<a href="#">ENSG00000229314</a>	A1AG1 AGP-A AGP1 HEL-S-153w ORM	orosomucoid 1
P2RY8	-1.9952017	0.00491	<a href="#">ENSG00000182162</a>	P2Y8	P2Y receptor family member 8
PAGE1	7.2611886	0.0499	<a href="#">ENSG00000068985</a>	AL5 CT16.3 GAGE-9 GAGEB1 PAGE-1	PAGE family member 1
PALM	2.2072643	0.00469	<a href="#">ENSG00000099864</a>	PALM1	paralemmin
PALM3	2.0639142	0.03046	<a href="#">ENSG00000187867</a>		paralemmin 3
PAQR8	-3.5779518	5.2E-09	<a href="#">ENSG00000170915</a>	C6orf33 LMPB1 MPRB	progesterone and adipoQ receptor family member 8
PARP10	1.5848112	4.8E-14	<a href="#">ENSG00000178685</a>	ARTD10	poly(ADP-ribose) polymerase family member 10
PCDH9	1.6287908	0.0017	<a href="#">ENSG00000184226</a>		protocadherin 9
PCDHB5	2.6984497	0.02543	<a href="#">ENSG00000113209</a>	PCDH-BETA5	protocadherin beta 5
PCDHB8	1.9702739	0.02052	<a href="#">ENSG00000120322</a>	PCDH-BETA8 PCDH3I	protocadherin beta 8
PCDHGA8	7.9719139	0.03637	<a href="#">ENSG00000253767</a>	PCDH-GAMMA-A8	protocadherin gamma subfamily A, 8
PDGFRB	1.824412	0.00015	<a href="#">ENSG00000113721</a>	CD140B IBGC4 IMF1 JTK12 KOGS PDGFR PDGFR-1 PDGFR1 PENTT	platelet derived growth factor receptor beta
PDZK1IP1	1.8396018	2.2E-09	<a href="#">ENSG00000162366</a>	DD96 MAP17 SPAP	PDZK1 interacting protein 1
PECAM1	-1.5100291	0.0057	<a href="#">ENSG00000261371</a>	CD31 CD31/EndoCAM PECA1 PECAM-1 endoCAM	platelet and endothelial cell adhesion molecule 1
PENK	-2.9835292	0.0053	<a href="#">ENSG00000181195</a>	PE PENK-A	proenkephalin
PIK3CG	-2.407367	0.00062	<a href="#">ENSG00000105851</a>	IMD97 PI3CG PI3K PI3Kgamma PIK3p110gamma p120-PI3K	phosphatidylinositol-4,5-bisphosphate 3-kinase catalytic subunit gamma
PLEKHA4	2.223145	3.7E-08	<a href="#">ENSG00000105559</a>	PEPP1	pleckstrin homology domain containing A4
PLEKHD1	-2.905407	0.00476	<a href="#">ENSG00000175985</a>	UPF0639	pleckstrin homology and coiled-coil domain containing D1
PLIN5	1.6051829	0.03608	<a href="#">ENSG00000214456</a>	LSDA5 LSDP5 MLDP OXPAT	perilipin 5
PLPPR5	-2.5949342	0.00938	<a href="#">ENSG00000117598</a>	LPPR5 PAP2 PAP2D PRG5	phospholipid phosphatase related 5
PODNL1	2.4752129	0.00128	<a href="#">ENSG00000132000</a>	SLRR5B	podocan like 1



PPBP	-2.0508426	0.03047	<a href="#">ENSG00000163736</a>	B-TG1 Beta-TG CTAP-III CTAP3 CTAPIII CXCL7 LA-PF4 LDGF MDGF NAP-2 PBP SCYB7 TC1 TC2 TGB TGB1 THBGB THBGB1	pro-platelet basic protein
PPP4R3CP	1.6254948	0.00519	<a href="#">ENSG00000224960</a>	FLFL3P PPP4R3CP SMEK3P smk1	protein phosphatase 4 regulatory subunit 3C
PRAL	3.3580191	1.4E-10	<a href="#">ENSG00000279296</a>	None	None
PRDM9	1.6734735	0.00035	<a href="#">ENSG00000164256</a>	KMT8B MEISETZ MSBP3 PFM6 ZNF899	PR/SET domain 9
PRH1-PRR4	-8.2230553	0.01795	<a href="#">ENSG00000275778</a>	PRH1	PRH1-PRR4 readthrough
PRKCB	-1.942297	0.00753	<a href="#">ENSG00000166501</a>	PKC-beta PKCB PKCbeta PRKCB1 PRKCB2	protein kinase C beta
PRR4	1.5660558	0.00085	<a href="#">ENSG00000111215</a>	LPRP PROL4	proline rich 4
PSG1	2.2679917	0.00033	<a href="#">ENSG00000231924</a>	B1G1 CD66f DHFRP2 FL-NCA-1/2 PBG1 PS-beta-C/D PS-beta-G-1 PSBG-1 PSBG1 PSG95 PSGGA PSGIIA SP1	pregnancy specific beta-1-glycoprotein 1
PSMB8-AS1	4.3525882	0.02539	<a href="#">ENSG00000204261</a>	TAP1-AS1 TAPSAR1	PSMB8 antisense RNA 1 (head to head)
PTGS2	-1.7901542	0.00033	<a href="#">ENSG00000073756</a>	COX-2 COX2 GRIPGHS PGG/HS PGHS-2 PHS-2 hCox-2	prostaglandin-endoperoxide synthase 2
PTN	2.869317	0.01966	<a href="#">ENSG00000105894</a>	HARP HB-GAM HBBM HBGF-8 HBGF8 HBNF HBNF-1 NEGF1 OSF-1	pleiotrophin
PTPMT1	-7.3546696	0.04604	<a href="#">ENSG00000110536</a>	DUSP23 MOSP PLIP PNAS-129	protein tyrosine phosphatase mitochondrial 1
PTPN7	-1.5685125	0.01075	<a href="#">ENSG00000143851</a>	BPTP-4 HEPTP LC-PTP LPTP PTPNI	protein tyrosine phosphatase non-receptor type 7
PTPRN	3.2365216	0.00028	<a href="#">ENSG00000054356</a>	IA-2 IA-2/PTP IA2 ICA512 R-PTP-N	protein tyrosine phosphatase receptor type N
PTX3	1.7737385	4.3E-08	<a href="#">ENSG00000163661</a>	TNFAIP5 TSG-14	pentraxin 3
PVRIG2P	2.003943	0.00229	<a href="#">ENSG00000235333</a>	None	None
RAET1E	-3.3162034	0.01835	<a href="#">ENSG00000164520</a>	LETAL N2DL-4 NKG2DL4 RAET1E2 RL-4 ULBP4 bA350J20.7	retinoic acid early transcript 1E
RARRES3	1.8591683	0.00273	<a href="#">ENSG00000133321</a>	HRASLS4 HRSL4 PLA1/2-3 PLAAT-4 RARRES3 RIG1 TIG3	phospholipase A and acyltransferase 4
RASD1	-2.4670161	0.00711	<a href="#">ENSG00000108551</a>	AGS1 DEXRAS1 MGC:26290	ras related dexamethasone induced 1
RBM20	3.3765088	0.01471	<a href="#">ENSG00000203867</a>		RNA binding motif protein 20
RBPM52	1.873222	0.00114	<a href="#">ENSG00000166831</a>		RNA binding protein, mRNA processing factor 2
REEP2	1.8042798	9E-09	<a href="#">ENSG00000132563</a>	C5orf19 SGC32445 SPG72 SPG72A SPG72B Yip2d	receptor accessory protein 2
RGAG1	2.3916521	1.6E-07	<a href="#">ENSG00000243978</a>	MAR9 MART9 RGAG1 SIRH10	retrotransposon Gag like 9
RGCC	-1.8928841	0.00045	<a href="#">ENSG00000102760</a>	C13orf15 RGC-32 RGC32 bA157L14.2	regulator of cell cycle
RNF182	1.7252334	0.00046	<a href="#">ENSG00000180537</a>		ring finger protein 182
RNF212	-2.539693	0.03042	<a href="#">ENSG00000178222</a>	SPGF62 ZHP3	ring finger protein 212

ROR2	2.2541609	0.00034	<a href="#">ENSG00000169071</a>	BDB BDB1 NTRKR2	receptor tyrosine kinase like orphan receptor 2
RP11-1024P17.1	2.9747883	0.01553	<a href="#">ENSG00000261468</a>	None	None
RP11-104H15.7	2.4045125	0.0061	<a href="#">ENSG00000262880</a>	None	None
RP11-114H23.1	-1.9881701	0.01397	<a href="#">ENSG00000258077</a>	None	None
RP11-136I14.5	-3.4541243	0.0157	<a href="#">ENSG00000255689</a>	None	None
RP11-1399P15.1	2.665004	0.01448	<a href="#">ENSG00000273445</a>	None	None
RP11-142E9.1	3.2816731	0.01322	<a href="#">ENSG00000276672</a>	None	None
RP11-146F11.5	-2.067142	0.0072	<a href="#">ENSG00000260167</a>	None	None
RP11-148B18.4	2.0808625	0.01839	<a href="#">ENSG00000236098</a>	None	None
RP11-155D18.12	-9.351442	0.00632	<a href="#">ENSG00000272762</a>	None	None
RP11-16K12.1	1.678369	0.03502	<a href="#">ENSG00000177699</a>		uncharacterized LOC100129540
RP11-174O3.3	-3.3011959	0.02218	<a href="#">ENSG00000240661</a>	None	None
RP11-180D21.3	3.141859	0.04904	<a href="#">ENSG00000224943</a>	None	None
RP11-246K15.1	-1.549706	0.02364	<a href="#">ENSG00000253821</a>	None	None
RP11-258F1.2	7.8229798	0.02338	<a href="#">ENSG00000279428</a>	None	None
RP11-260M19.2	7.0601741	0.03793	<a href="#">ENSG00000258913</a>	C14orf144	long intergenic non-protein coding RNA 2691
RP11-263K19.4	1.5405722	0.00043	<a href="#">ENSG00000231064</a>		THBS3 antisense RNA 1
RP11-278A23.1	2.4480695	0.02169	<a href="#">ENSG00000226180</a>		uncharacterized LOC100129215
RP11-292D4.1	-2.0914861	0.01272	<a href="#">ENSG00000248346</a>	None	None
RP11-329E24.6	2.8873101	0.0004	<a href="#">ENSG00000231937</a>	None	None
RP11-366M4.11	1.7439021	0.03072	<a href="#">ENSG00000248632</a>	None	None
RP11-374M1.2	1.7598218	0.03491	<a href="#">ENSG00000231527</a>	FAM27A FAM27A1 FAM27A3 bA7G23.5	family with sequence similarity 27 member C
RP1-138A5.3	2.289944	0.00707	<a href="#">ENSG00000282914</a>	None	None
RP1-138B7.6	-4.1178393	0.02743	<a href="#">ENSG00000277611</a>	None	None
RP11-395N3.2	-2.6933787	0.01035	<a href="#">ENSG00000272622</a>	None	None
RP11-400N13.2	-3.2438747	4.2E-07	<a href="#">ENSG00000228437</a>	None	None

RP11-407N17.5	2.0987794	0.02397	<a href="#">ENSG00000258940</a>		MIA2 antisense RNA 1
RP11-462G12.1	2.5485576	0.02043	<a href="#">ENSG00000262185</a>		long intergenic non-protein coding RNA 2861
RP11-469A15.2	-1.871562	0.00012	<a href="#">ENSG00000230623</a>	None	None
RP11-473I1.9	4.7571418	0.00106	<a href="#">ENSG00000263244</a>	None	None
RP11-498C9.3	2.940851	0.00011	<a href="#">ENSG00000262413</a>	None	None
RP11-4N23.1	-1.5697511	0.04852	<a href="#">ENSG00000256306</a>	None	None
RP11-521C20.3	2.6787324	0.0265	<a href="#">ENSG00000259409</a>	None	None
RP11-54F2.1	1.5195972	2.1E-05	<a href="#">ENSG00000251196</a>	None	None
RP11-54O7.17	1.7955061	9.2E-05	<a href="#">ENSG00000272512</a>	None	None
RP11-550P17.5	2.8473232	0.00334	<a href="#">ENSG00000228560</a>	None	None
RP11-586K2.1	4.052035	0.03269	<a href="#">ENSG00000253553</a>	None	None
RP11-61K9.3	1.5299842	0.00065	<a href="#">ENSG00000275964</a>	None	None
RP11-638I8.1	-3.5133836	0.02762	<a href="#">ENSG00000283247</a>		coiled-coil domain containing 201
RP11-644F5.10	7.3142523	0.04163	<a href="#">ENSG00000258311</a>	None	None
RP11-667K14.4	-7.9695966	0.026	<a href="#">ENSG00000262533</a>	None	None
RP11-686D22.3	-4.2999088	0.02235	<a href="#">ENSG00000267648</a>	None	None
RP11-69E11.8	-10.351627	0.0034	<a href="#">ENSG00000228060</a>	None	None
RP11-732A19.2	-3.3601473	0.01371	<a href="#">ENSG00000254641</a>	None	None
RP11-734I18.1	1.799902	0.03295	<a href="#">ENSG00000251129</a>	None	None
RP11-793H13.10	2.1614822	0.04439	<a href="#">ENSG00000267281</a>		ATF7-NPFF readthrough
RP11-81H3.2	1.9502309	0.00292	<a href="#">ENSG00000251138</a>		long intergenic non-protein coding RNA 2882
RP11-867G23.3	5.988818	0.00349	<a href="#">ENSG00000245156</a>	None	None
RP11-93B14.6	-3.3443462	0.00954	<a href="#">ENSG00000167046</a>	None	None
RP11-967K21.1	2.7229229	0.00332	<a href="#">ENSG00000247934</a>	None	None
RP1-283E3.4	9.0118956	0.0102	<a href="#">ENSG00000227775</a>	None	None
RP13-631K18.3	-1.7498357	0.01701	<a href="#">ENSG00000254991</a>	None	None
RP13-631K18.5	-1.5871109	0.038	<a href="#">ENSG00000255400</a>		long intergenic non-protein coding RNA 2989
RP3-340N1.2	-6.5339834	0.00017	<a href="#">ENSG00000227066</a>		uncharacterized LOC117779438

RP3-402G11.26	1.6707015	0.03072	<a href="#">ENSG00000273253</a>		TRABD antisense RNA 1
RP4-608O15.3	1.5765708	0.02483	<a href="#">ENSG00000276911</a>	None	None
RP4-635E18.9	2.4178661	5.6E-05	<a href="#">ENSG00000277726</a>	None	None
RP4-798A10.7	1.8628778	0.01766	<a href="#">ENSG00000261135</a>	None	None
RPL12P14	2.4483614	0.0405	<a href="#">ENSG00000224321</a>	None	None
RPSAP52	-2.0085339	0.00156	<a href="#">ENSG00000241749</a>	RPSA_17_1251	ribosomal protein SA pseudogene 52
RRAGD	-1.79862	8.5E-13	<a href="#">ENSG0000025039</a>	HOMG7 RAGD bA11D8.2.1	Ras related GTP binding D
RSAD2	3.3325513	5.1E-38	<a href="#">ENSG00000134321</a>	SAND cig33 cig5 vig1	radical S-adenosyl methionine domain containing 2
RTP4	2.5521948	0.00026	<a href="#">ENSG00000136514</a>	IFRG28 Z3CXXC4	receptor transporter protein 4
RXRG	3.5802278	0.00735	<a href="#">ENSG00000143171</a>	NR2B3 RXR-gamma RXRC RXRgamma	retinoid X receptor gamma
S1PR3	1.5813945	0.00043	<a href="#">ENSG00000213694</a>	C9orf108 C9orf47 EDG-3 EDG3 LPB3 S1P3 bA791O21.3	sphingosine-1-phosphate receptor 3
SAA1	1.9969731	2.5E-16	<a href="#">ENSG00000173432</a>	PIG4 SAA SAA2 TP53I4	serum amyloid A1
SAA2	2.1086122	5.5E-13	<a href="#">ENSG00000134339</a>	SAA SAA1	serum amyloid A2
SAA2-SAA4	1.6647748	2.9E-15	<a href="#">ENSG00000255071</a>		SAA2-SAA4 readthrough
SAMD9	1.6084271	8.5E-13	<a href="#">ENSG00000205413</a>	C7orf5 DRIF1 M7MLS2 MIRAGE NFTC OEF1 OEF2	sterile alpha motif domain containing 9
SAMD9L	1.8331316	8.6E-10	<a href="#">ENSG00000177409</a>	ATXPC C7DELq C7orf6 DEL7q DRIF2 M7MLS1 MLSM7 SCA49 UEF1	sterile alpha motif domain containing 9 like
SASH3	-1.6455092	0.00502	<a href="#">ENSG00000122122</a>	753P9 CXorf9 HACS2 IMD102 SH3D6C SLY	SAM and SH3 domain containing 3
SCG2	2.1553294	0.02938	<a href="#">ENSG00000171951</a>	CHGC EM66 SN SgII	secretogranin II
SCN1B	1.5771251	0.00019	<a href="#">ENSG00000105711</a>	ATFB13 BRGDA5 DEE52 EIEE52 GEFSP1	sodium voltage-gated channel beta subunit 1
SDHD_2	-1.8174548	0.01513	<a href="#">ENSG00000255292</a>	None	None
SELENOP	1.7539968	0.01849	<a href="#">ENSG00000250722</a>	SELP SEPP SEPP1 SeP	selenoprotein P
SEMA6B	1.5748303	1.9E-13	<a href="#">ENSG00000167680</a>	EPM11 SEM-SEMA-Y SEM-SEMA-Z SEMA-VIB SEMAN semaZ	semaphorin 6B
SFTA2	-1.9325156	0.0405	<a href="#">ENSG00000196260</a>	GSGL541 SFTPG SP-G UNQ541	surfactant associated 2
SFTA3_1	-7.3538394	0.04923	<a href="#">ENSG00000257520</a>	NANCI PAHRF SFTPH SP-H SPH	surfactant associated 3
SFTPA1	-7.7958036	0.02651	<a href="#">ENSG00000122852</a>	COLEC4 ILD1 PSAP PSP-A PSPA SFTP1 SFTPA1B SP-A SP-A1 SPA SPA1	surfactant protein A1
SFTPB	-11.954906	8E-05	<a href="#">ENSG00000168878</a>	PSP-B SFTB3 SFTP3 SMDP1 SP-B	surfactant protein B
SGO1-AS1	1.6753907	0.01124	<a href="#">ENSG00000231304</a>	SGOL1-AS1	SGO1 antisense RNA 1
SLC15A3	1.6882512	0.00396	<a href="#">ENSG00000110446</a>	OCTP PHT2 PTR3 hPHT2	solute carrier family 15 member 3
SLC22A17	1.6944416	0.04997	<a href="#">ENSG00000092096</a>	24p3R BOCT BOIT NGALR NGALR2 NGALR3 hBOIT	solute carrier family 22 member 17
SLC2A14	1.7189397	0.00254	<a href="#">ENSG00000173262</a>	GLUT14 SLC2A3P3	solute carrier family 2 member 14

SLC30A2	1.7772337	0.03901	<a href="#">ENSG00000158014</a>	PP12488 TNZD ZNT2 ZnT-2	solute carrier family 30 member 2
SLC34A2	-6.350776	6E-12	<a href="#">ENSG00000157765</a>	NAPI-3B NAPI-IIb NPTIIb NaPi2b PULAM	solute carrier family 34 member 2
SLC9A2	-1.5455751	1.6E-05	<a href="#">ENSG00000115616</a>	NHE2	solute carrier family 9 member A2
SLCO4A1-AS1	-2.3731218	1.7E-05	<a href="#">ENSG00000232803</a>		SLCO4A1 antisense RNA 1
SLITRK1	2.132519	0.00895	<a href="#">ENSG00000178235</a>	LRRC12 TTM	SLIT and NTRK like family member 1
SLX1B	-7.8629607	0.03175	<a href="#">ENSG00000181625</a>	GIYD2	SLX1 homolog B, structure-specific endonuclease subunit
SMTNL2	1.6189679	0.0482	<a href="#">ENSG00000188176</a>		smoothelin like 2
SOX2	-4.6178882	0.02863	<a href="#">ENSG00000181449</a>	ANOP3 MCOPS3	SRY-box transcription factor 2
SPECC1L-ADORA2A	8.1744841	0.04166	<a href="#">ENSG00000258555</a>		SPECC1L-ADORA2A readthrough (NMD candidate)
SPOCK2	-1.6317507	0.00319	<a href="#">ENSG00000107742</a>	testican-2	SPARC (osteonectin), cwcv and kazal like domains proteoglycan 2
SPRR2D	-2.371793	0.00664	<a href="#">ENSG00000163216</a>		small proline rich protein 2D
SPRR3	-3.075471	0.00748	<a href="#">ENSG00000163209</a>		small proline rich protein 3
SRRM3	2.3758144	6E-07	<a href="#">ENSG00000177679</a>		serine/arginine repetitive matrix 3
SSTR1	-2.1037974	4E-23	<a href="#">ENSG00000139874</a>	SRIF-2 SS-1-R SS1-R SS1R SST1	somatostatin receptor 1
STAC2	3.4084849	1.1E-05	<a href="#">ENSG00000141750</a>	24b2 24b2/STAC2	SH3 and cysteine rich domain 2
SUCLA2-AS1	-1.7250132	0.00559	<a href="#">ENSG00000227848</a>	None	None
SULF1	1.5875265	0.0036	<a href="#">ENSG00000137573</a>	SULF-1	sulfatase 1
SUSD3	-1.8887915	0.00015	<a href="#">ENSG00000157303</a>		sushi domain containing 3
SV2A	1.9145315	3.8E-18	<a href="#">ENSG00000159164</a>	SLC22B1 SV2	synaptic vesicle glycoprotein 2A
SYT11	1.7935419	0.01399	<a href="#">ENSG00000132718</a>	SYT12 sytXI	synaptotagmin 11
TBXA2R	1.9605743	0.02026	<a href="#">ENSG00000006638</a>	BDPLT13 TXA2-R	thromboxane A2 receptor
TCN1	-1.6929905	0.03013	<a href="#">ENSG00000134827</a>	HC TC-1 TC1 TCI	transcobalamin 1
TDRD1	-4.4976702	4.8E-05	<a href="#">ENSG00000095627</a>	CT41.1	tudor domain containing 1
TESPA1	2.4250516	0.00128	<a href="#">ENSG00000135426</a>	HSPC257 ITPRID3 KIAA0748	thymocyte expressed, positive selection associated 1
TGFBR3	1.5033951	0.00616	<a href="#">ENSG00000069702</a>	BGCAN betaglycan	transforming growth factor beta receptor 3
TM4SF18	-7.1571837	0.0346	<a href="#">ENSG00000163762</a>	L6D	transmembrane 4 L six family member 18
TMEM185API	1.8949324	0.04493	<a href="#">ENSG00000235254</a>	None	None
TMEM255B	2.2360413	0.00173	<a href="#">ENSG00000184497</a>	FAM70B	transmembrane protein 255B
TMEM45B	-2.2094192	0.00053	<a href="#">ENSG00000151715</a>		transmembrane protein 45B
TMPRSS2	-2.9193615	9E-05	<a href="#">ENSG00000184012</a>	PRSS10	transmembrane serine protease 2

TNF	2.5750693	3E-05	<a href="#">ENSG00000232810</a>	DIF TNF-alpha TNFA TNFSF2 TNLG1F	tumor necrosis factor
TNFSF10	2.6345563	6.3E-08	<a href="#">ENSG00000121858</a>	APO2L Apo-2L CD253 TANCR TL2 TNLG6A TRAIL	TNF superfamily member 10
TNIP3	2.2924802	0.0003	<a href="#">ENSG00000050730</a>	ABIN-3 LIND	TNFAIP3 interacting protein 3
TNS2	1.7790291	3.4E-13	<a href="#">ENSG00000111077</a>	C1-TEN C1TEN TENC1	tensin 2
TP53INP2	1.5055537	3.1E-05	<a href="#">ENSG00000078804</a>	C20orf110 DOR PIG-U PIGU PINH dJ1181N3.1	tumor protein p53 inducible nuclear protein 2
TPI1P2	1.8220274	0.00633	<a href="#">ENSG00000230359</a>		triosephosphate isomerase 1 pseudogene 2
TRANK1	1.7467537	8E-16	<a href="#">ENSG00000168016</a>	LBA1	tetratricopeptide repeat and ankyrin repeat containing 1
TRIM61	1.8706889	0.00161	<a href="#">ENSG00000183439</a>	RNF35	tripartite motif containing 61
TTLL11-IT1	-5.8290488	2.7E-06	<a href="#">ENSG00000237548</a>	None	None
TXLNB	3.5187564	0.00337	<a href="#">ENSG00000164440</a>	C6orf198 LST001 MDP77 dJ522B19.2	taxilin beta
UBBP4	3.2615306	0.00039	<a href="#">ENSG00000263563</a>	None	None
UBE2L6	1.8770208	2.8E-16	<a href="#">ENSG00000156587</a>	RIG-B UBCH8	ubiquitin conjugating enzyme E2 L6
UBXN10	-3.4602386	0.02612	<a href="#">ENSG00000162543</a>	UBXD3	UBX domain protein 10
UPK3B	1.5867477	0.0008	<a href="#">ENSG00000243566</a>	P35 UP3B UPIIB	uroplakin 3B
VANGL2	1.8039922	7.5E-12	<a href="#">ENSG00000162738</a>	LPP1 LTAP STB1 STBM STBM1	VANGL planar cell polarity protein 2
VASH2	-1.7757521	1.4E-09	<a href="#">ENSG00000143494</a>		vasohibin 2
VENTXP3	1.7614467	0.04393	<a href="#">ENSG00000257364</a>	None	None
VGF	1.6541885	4.4E-05	<a href="#">ENSG00000128564</a>	SCG7 SgVII	VGF nerve growth factor inducible
XAF1	2.9622574	1E-06	<a href="#">ENSG00000132530</a>	BIRC4BP HSXIAPAF1 XIAPAF1	XIAP associated factor 1
XAGE1A	-2.8334715	0.00168	<a href="#">ENSG00000204379</a>	CT12.1 CT12.1A CT12.1B CTP9 GAGED2 XAGE-1 XAGE1 XAGE1B	X antigen family member 1A
YPEL1	2.3554556	0.01372	<a href="#">ENSG00000100027</a>	FKSG3	yippee like 1
ZBED6CL	1.8849246	0.02018	<a href="#">ENSG00000188707</a>	None	None
ZC3H12A	1.6326449	5.1E-17	<a href="#">ENSG00000163874</a>	MCPIP MCPIP-1 MCPIP1 Reg1 dJ423B22.1	zinc finger CCCH-type containing 12A
ZFP37	2.8719593	0.03986	<a href="#">ENSG00000136866</a>	ZNF906 zfp-37	ZFP37 zinc finger protein
ZNF540	-1.6478378	0.03817	<a href="#">ENSG00000171817</a>	Nbla10512	zinc finger protein 540
ZPLD1	-1.797301	7.7E-07	<a href="#">ENSG00000170044</a>		zona pellucida like domain containing 1
<b>2583 vs NaCl</b>					
AC005387.3	3.6038785	0.01832	<a href="#">ENSG00000268938</a>	Novel transcript, antisense to FKBP8 NONHSAG025135.2 HSALNG0124637 Lnc-KXD1-3	Novel transcript, antisense to FKBP8

CTB-31O20.3	2.1051562	0.04782	<a href="#">ENSG00000267007</a>	Novel transcript, antisense to REXO1 NONHSAG024391.2 Lnc-ONECUT3-3 HSALNG0123081	Novel transcript, antisense to REXO1
LL22NC03-N14H11.1	2.9297642	0.03065	<a href="#">ENSG00000272872</a>	Novel transcript, sense intronic to novel transcript HSALNG0133778 Lnc-POTEH-6	Novel transcript, sense intronic to novel transcript
PVRIG2P	2.2243274	0.03697	<a href="#">ENSG00000235333</a>	PVRIG2P	PVR related immunoglobulin domain containing 2, pseudogene
RP11-498C9.3	3.4229439	0.00074	<a href="#">ENSG00000262413</a>	RP11-498C9.3	Novel transcript, antisense ARHGDI A
RP11-542C16.1	-4.1251734	0.04761	<a href="#">ENSG00000263171</a>	RP11-542C16.1	H3K27ac-H3K4me1 HESC Enhancer GRCh37_chr17:7258543-7259069

<i>DEP+NO2 against NaCl</i>					
A2M	-2.155576	6.8E-05	<a href="#">ENSG00000175899</a>	A2MD CPAMD5 FWP007 S863-7	alpha-2-macroglobulin
AC005387.3	3.8501713	4.2E-05	<a href="#">ENSG00000268938</a>	None	None
AC007193.8	4.0329903	0.0144	<a href="#">ENSG00000269151</a>	None	None
AC114730.8	1.847887	0.01064	<a href="#">ENSG00000215692</a>	None	None
AC114803.3	2.5705192	0.03932	<a href="#">ENSG00000230432</a>	None	None
AC159540.1	3.5747528	0.04835	<a href="#">ENSG00000230606</a>	None	None
ACSBG1	-2.2107564	0.03048	<a href="#">ENSG00000103740</a>	BG BG1 BGM GR-LACS LPD	acyl-CoA synthetase bubblegum family member 1
ADAMTS3	1.5150817	0.0248	<a href="#">ENSG00000156140</a>	ADAMTS-4 HKLLS3	ADAM metalloproteinase with thrombospondin type 1 motif 3
ADAMTS9	1.5173754	0.01947	<a href="#">ENSG00000163638</a>		ADAM metalloproteinase with thrombospondin type 1 motif 9
ADGRF5	-2.9342995	0.00054	<a href="#">ENSG00000069122</a>	GPR116 KPG_001	adhesion G protein-coupled receptor F5
ADORA3	-3.2187126	0.02127	<a href="#">ENSG00000282608</a>	A3AR	adenosine A3 receptor
AGMAT	-1.7403538	0.03772	<a href="#">ENSG00000116771</a>		agmatinase
AIM2	-2.5105452	0.02136	<a href="#">ENSG00000163568</a>	PYHIN4	absent in melanoma 2
AL157871.2	3.1201306	0.00475	<a href="#">ENSG00000259052</a>	None	None
ALOX5AP	-1.6377105	7.2E-05	<a href="#">ENSG00000132965</a>	FLAP	arachidonate 5-lipoxygenase activating protein
ANGPT1	1.6558317	0.00787	<a href="#">ENSG00000154188</a>	AGP1 AGPT AGPT-1 ANG1 HAE5	angiopoietin 1
ANKRD7	2.0266394	0.03224	<a href="#">ENSG00000106013</a>	TSA806	ankyrin repeat domain 7

ANO2	4.0764761	0.04015	<a href="#">ENSG00000047617</a>	C12orf3 TMEM16B	anoctamin 2
ANO3	1.8789543	0.01435	<a href="#">ENSG00000134343</a>	C11orf25 DYT23 DYT24 GENX-3947 TMEM16C	anoctamin 3
APBB1IP	-2.3507467	0.00053	<a href="#">ENSG00000077420</a>	INAG1 PREL1 RARP1 RIAM	amyloid beta precursor protein binding family B member 1 interacting protein
APLN	1.9777219	0.00055	<a href="#">ENSG00000171388</a>	APEL XNPEP2	apelin
APOC2	-2.6855194	1.9E-06	<a href="#">ENSG00000234906</a>	APO-CII APOC-II	apolipoprotein C2
AQP3	1.6229509	0.00097	<a href="#">ENSG00000165272</a>	AQP-3 GIL	aquaporin 3 (Gill blood group)
ARHGAP9	-1.5866302	0.02912	<a href="#">ENSG00000123329</a>	10C RGL1	Rho GTPase activating protein 9
ARSI	1.5889571	0.00027	<a href="#">ENSG00000183876</a>	ASI SPG66	arylsulfatase family member I
AXIN2	1.762257	0.02261	<a href="#">ENSG00000168646</a>	AXIL ODCRCS	axin 2
AZGP1	-4.6885612	8.9E-10	<a href="#">ENSG00000160862</a>	ZA2G ZAG	alpha-2-glycoprotein 1, zinc-binding
B3GNT6	-8.3498977	0.01846	<a href="#">ENSG00000198488</a>	B3Gn-T6 BGnT-6 beta-1,3-Gn-T6 beta3Gn-T6	UDP-GlcNAc:betaGal beta-1,3-N-acetylglucosaminyltransferase 6
B4GALNT1	1.5377675	1.5E-05	<a href="#">ENSG00000135454</a>	GALGT GALNACT GalNAc-T SPG26	beta-1,4-N-acetyl-galactosaminyltransferase 1
BACH1-IT1	1.8313437	0.04328	<a href="#">ENSG00000248476</a>	None	None
BHLHE22	-2.0087052	3E-07	<a href="#">ENSG00000180828</a>	BHLHB5 Beta3 Beta3a CAGL85 TNRC20	basic helix-loop-helix family member e22
C14orf132	3.6355589	5.7E-08	<a href="#">ENSG00000227051</a>	C14orf88	chromosome 14 open reading frame 132
C1orf147	1.6616919	0.00037	<a href="#">ENSG00000162888</a>	C1orf147	IKBKE antisense RNA 1
C1R	2.509934	2.4E-19	<a href="#">ENSG00000159403</a>	EDS8 EDSPD1	complement C1r
C6orf15	-3.3409869	0.01182	<a href="#">ENSG00000204542</a>	STG	chromosome 6 open reading frame 15
C6orf223	-1.9672782	6.8E-05	<a href="#">ENSG00000181577</a>	C6orf223	long intergenic non-protein coding RNA 3040
C8orf46	1.5543885	0.00539	<a href="#">ENSG00000169085</a>	C8orf46	vexin
C8orf88	1.5460294	0.04995	<a href="#">ENSG00000253250</a>		chromosome 8 open reading frame 88
CACNA2D1	2.0849653	0.0089	<a href="#">ENSG00000153956</a>	CACNA2 CACNL2A CCHL2A DEE110 LINC01112 lncRNA-N3	calcium voltage-gated channel auxiliary subunit alpha2delta 1
CACNG8	1.5120116	0.00021	<a href="#">ENSG00000142408</a>		calcium voltage-gated channel auxiliary subunit gamma 8
CAMK2N2	3.7101964	0.00058	<a href="#">ENSG00000163888</a>	CAM-KIIN CAMKIIN	calcium/calmodulin dependent protein kinase II inhibitor 2
CCDC144NL-AS1	-3.8208977	0.00277	<a href="#">ENSG00000233098</a>		CCDC144NL antisense RNA 1
CCDC157	1.7875533	0.04798	<a href="#">ENSG00000187860</a>		coiled-coil domain containing 157



CCDC188	1.9193992	0.03468	<a href="#">ENSG00000234409</a>		coiled-coil domain containing 188
CCDC8	1.8066701	0.00196	<a href="#">ENSG00000169515</a>	3M3 PPP1R20 p90	coiled-coil domain containing 8
CCL2	2.3575938	0.00129	<a href="#">ENSG00000108691</a>	GDCF-2 HC11 HSMCR30 MCAF MCP-1 MCP1 SCYA2 SMC-CF	C-C motif chemokine ligand 2
CCL3	1.9934358	0.01011	<a href="#">ENSG00000277632</a>	G0S19-1 LD78 LD78ALPHA MIP-1-alpha MIP1A SCI SCYA3	C-C motif chemokine ligand 3
CCL3L3	2.605635	0.00878	<a href="#">ENSG00000276085</a>	464.2 D17S1718 G0S19-2 LD78 LD78BETA SCYA3L SCYA3L1	C-C motif chemokine ligand 3 like 3
CCL4	4.1098752	0.00782	<a href="#">ENSG00000275302</a>	ACT2 AT744.1 G-26 HC21 LAG-1 LAG1 MIP-1-beta MIP1B MIP1B1 SCYA2 SCYA4	C-C motif chemokine ligand 4
CCL4L2	4.4803382	0.02314	<a href="#">ENSG00000276070</a>	AT744.2 CCL4L SCYA4L SCYQ4L2	C-C motif chemokine ligand 4 like 2
CCL5	1.8801188	2.3E-10	<a href="#">ENSG00000271503</a>	D17S136E RANTES SCYA5 SIS-delta SISd TCP228 eoCP	C-C motif chemokine ligand 5
CCNB2P1	-2.0696915	0.02487	<a href="#">ENSG00000214998</a>		cyclin B2 pseudogene 1
CCR1	-3.0234417	9.3E-05	<a href="#">ENSG00000163823</a>	CD191 CKR-1 CKR1 CMKBR1 HM145 MIP1aR SCYAR1	C-C motif chemokine receptor 1
CCR2	-4.9464901	0.00768	<a href="#">ENSG00000121807</a>	CC-CKR-2 CCR-2 CCR2A CCR2B CD192 CKR2 CKR2A CKR2B CMKBR2 MCP-1-R	C-C motif chemokine receptor 2
CD163	-1.5702089	8.7E-06	<a href="#">ENSG00000177575</a>	M130 MM130 SCAR11	CD163 molecule
CD36	-2.4049972	1.1E-07	<a href="#">ENSG00000135218</a>	BDPLT10 CHDS7 FAT GP3B GP4 GPIV PASIV SCARB3	CD36 molecule
CD52	-3.0601102	0.00138	<a href="#">ENSG00000169442</a>	CDW52 EDDM5 HE5	CD52 molecule
CD53	-1.7431541	0.00013	<a href="#">ENSG00000143119</a>	MOX44 TSPAN25	CD53 molecule
CD93	-2.1200521	1.5E-06	<a href="#">ENSG00000125810</a>	C1QR1 C1qRP CDw93 ECSM3 MXRA4 dJ737E23.1	CD93 molecule
CDH11	-6.0994703	4.2E-09	<a href="#">ENSG00000140937</a>	CAD11 CDHOB ESWS OB OSF-4 TBHS2	cadherin 11
CDH2	1.686403	6.2E-07	<a href="#">ENSG00000170558</a>	ACOGS ADHD8 ARVD14 CD325 CDHN CDw325 NCAD	cadherin 2
CEACAM5	-2.7302032	0.04619	<a href="#">ENSG00000105388</a>	CD66e CEA	CEA cell adhesion molecule 5
CEBPA	-2.960396	2.8E-12	<a href="#">ENSG00000245848</a>	C/EBP-alpha CEBP	CCAAT enhancer binding protein alpha
CES1	-2.1029882	0.01319	<a href="#">ENSG00000198848</a>	ACAT CE-1 CEH CES2 HMSE HMSE1 PCE-1 REH SES1 TGH hCE-1	carboxylesterase 1
CFB	1.9658526	0.00227	<a href="#">ENSG00000243649</a>	AHUS4 ARMD14 BF BFD CFAB CFBD FB FBI12 GBG H2-Bf PBF2	complement factor B
CFP	-2.837071	0.00687	<a href="#">ENSG00000126759</a>	BFD PFC PFD PROPERDIN	complement factor properdin
CHI3L1	-2.5049873	7.4E-10	<a href="#">ENSG00000133048</a>	ASRT7 CGP-39 GP-39 GP39 HC-gp39 HCGP-3P YK-40 YKL-40 YKL40 YYL-40 hCGP-39	chitinase 3 like 1
CHI3L2	1.8278934	3.2E-05	<a href="#">ENSG00000064886</a>	CHIL2 YKL-39 YKL39	chitinase 3 like 2
CHN1	1.7787476	4.9E-08	<a href="#">ENSG00000128656</a>	ARHGAP2 CHN DURS2 NC RHOGAP2	chimerin 1

CLDN11	1.7471701	1.1E-06	<a href="#">ENSG00000013297</a>	HLD22 OSP OTM	claudin 11
CMB9-22P13.1	-1.5376771	2.1E-09	<a href="#">ENSG00000173727</a>	None	None
CMPK2	2.0744298	9.7E-08	<a href="#">ENSG00000134326</a>	NDK TMPK2 TYKi UMP-CMPK2	cytidine/uridine monophosphate kinase 2
CNTN5	3.5538607	0.01379	<a href="#">ENSG00000149972</a>	HNB-2s NB-2	contactin 5
COL23A1	-2.2159665	0.00135	<a href="#">ENSG00000050767</a>		collagen type XXIII alpha 1 chain
COL8A1	1.612482	4.7E-15	<a href="#">ENSG00000144810</a>	C3orf7	collagen type VIII alpha 1 chain
COPZ2	1.5695056	0.02042	<a href="#">ENSG00000005243</a>	zeta2-COP	COPI coat complex subunit zeta 2
CRABP2	-2.1734659	0.00015	<a href="#">ENSG00000143320</a>	CRABP-II RBP6	cellular retinoic acid binding protein 2
CRNDE	1.5316344	0.00138	<a href="#">ENSG00000245694</a>		uncharacterized LOC101927480
CSAG1	1.536304	0.00236	<a href="#">ENSG00000198930</a>	CSAGE CT24.1	chondrosarcoma associated gene 1
CSDC2	1.7177319	0.00574	<a href="#">ENSG00000172346</a>	PIPPIN dJ347H13.2	cold shock domain containing C2
CSF1	1.7269533	6.4E-23	<a href="#">ENSG00000184371</a>	CSF-1 MCSF PG-M-CSF	colony stimulating factor 1
CSF2	2.1689549	0.00876	<a href="#">ENSG00000164400</a>	CSF GMCSF	colony stimulating factor 2
CSF3	3.8271454	2E-14	<a href="#">ENSG00000108342</a>	C17orf33 CSF3OS GCSF	colony stimulating factor 3
CTB-31O20.3	1.8908193	0.0047	<a href="#">ENSG00000267007</a>	None	None
CTD-2196E14.9	7.4961068	0.03774	<a href="#">ENSG00000260482</a>	None	None
CTD-2369P2.8	1.7903812	7.3E-07	<a href="#">ENSG00000267607</a>	ICR LncRNA-ECM	ICAM4 antisense RNA 1
CTD-2521M24.6	3.2022112	0.00662	<a href="#">ENSG00000269481</a>	None	None
CTD-2554C21.2	-7.2711183	0.04912	<a href="#">ENSG00000267640</a>	None	None
CXADRP3	3.2847621	0.03953	<a href="#">ENSG00000265766</a>		CXADR pseudogene 3
CXCL1	4.8580256	3.4E-57	<a href="#">ENSG00000163739</a>	FSP GRO1 GROa MGSA MGSA-a NAP-3 SCYB1	C-X-C motif chemokine ligand 1
CXCL10	4.101956	2.5E-25	<a href="#">ENSG00000169245</a>	C7 IFI10 INP10 IP-10 SCYB10 crg-2 gIP-10 mob-1	C-X-C motif chemokine ligand 10
CXCL11	2.6107852	2.1E-10	<a href="#">ENSG00000169248</a>	H174 I-TAC IP-9 IP9 SCYB11 SCYB9B b-R1	C-X-C motif chemokine ligand 11
CXCL2	2.4827433	1.1E-16	<a href="#">ENSG00000081041</a>	CINC-2a GRO2 GROb MGSA-b MIP-2a MIP2 MIP2A SCYB2	C-X-C motif chemokine ligand 2
CXCL3	2.8542998	1.3E-14	<a href="#">ENSG00000163734</a>	CINC-2b GRO3 GROg MIP-2b MIP2B SCYB3	C-X-C motif chemokine ligand 3
CXCL6	3.0682685	4.1E-06	<a href="#">ENSG00000124875</a>	CKA-3 GCP-2 GCP2 SCYB6	C-X-C motif chemokine ligand 6
CXCL8	2.6603656	6.8E-06	<a href="#">ENSG00000169429</a>	GCP-1 GCP1 IL8 LECT LUCT LYNAP MDNCF MONAP NAF NAP-1 NAP1 SCYB8	C-X-C motif chemokine ligand 8
CYTH4	-2.0354776	0.00237	<a href="#">ENSG00000100055</a>	CYT4 DJ63G5.1 PSCD4 cytohesin-4	cytohesin 4
DCAF8L2	1.7993573	0.00741	<a href="#">ENSG00000189186</a>	WDR42C	DDB1 and CUL4 associated factor 8 like 2
DCSTAMP	-3.5869802	0.01278	<a href="#">ENSG00000164935</a>	FIND TM7SF4 hDC-STAMP	dendrocyte expressed seven transmembrane protein

DDX58	1.5459724	7.9E-19	<a href="#">ENSG00000107201</a>	DDX58 RIG-I RIG1 RLR-1 SGMRT2	RNA sensor RIG-I
DHRS9	-1.6729164	9.4E-12	<a href="#">ENSG00000073737</a>	3-alpha-HSD 3ALPHA-HSD RDH-TBE RDH15 RDHL RDHTBE RETSR8 SDR9C4 hRoDH-E2	dehydrogenase/reductase 9
DOK2	-2.3515941	0.00856	<a href="#">ENSG00000147443</a>	p56DOK p56dok-2	docking protein 2
DPF3	1.6869863	0.03089	<a href="#">ENSG00000205683</a>	BAF45C CERD4 SMARCG3	double PHD fingers 3
EPHA5	2.3145922	0.00349	<a href="#">ENSG00000145242</a>	CEK7 EHK-1 EHK1 EK7 HEK7 TYRO4	EPH receptor A5
EPHB3	-1.906371	0.00486	<a href="#">ENSG00000182580</a>	EK2 ETK2 HEK2 TYRO6	EPH receptor B3
EREG	-3.3595895	6.1E-09	<a href="#">ENSG00000124882</a>	EPR ER Ep	epiregulin
ESM1	-2.1590124	0.02234	<a href="#">ENSG00000164283</a>	endocan	endothelial cell specific molecule 1
ESRRAP2	2.3251572	0.03224	<a href="#">ENSG00000235438</a>		uncharacterized LOC105370105
ESX1	2.4386853	6.1E-09	<a href="#">ENSG00000123576</a>	ESX1L ESXR1	ESX homeobox 1
FBLN5	3.5457396	0.00066	<a href="#">ENSG00000140092</a>	ADCL2 ARCL1A ARMD3 CMT1H DANCE EVEC FIBL-5 HNARMD UP50	fibulin 5
FCER1G	-1.7542906	0.00167	<a href="#">ENSG00000158869</a>	FCRG	Fc epsilon receptor Ig
FGF1	1.7801143	7.8E-05	<a href="#">ENSG00000113578</a>	AFGF ECGF ECGF-beta ECGFA ECGFB FGF-1 FGF-alpha FGFA GLIO703 HBGF-1 HBGF1	fibroblast growth factor 1
FGFR3	1.8942335	0.00174	<a href="#">ENSG00000068078</a>	ACH CD333 CEK2 HSFGFR3EX JTK4	fibroblast growth factor receptor 3
FIBIN	1.8307994	0.02774	<a href="#">ENSG00000176971</a>		fin bud initiation factor homolog
FKBP11	-2.015074	0.00397	<a href="#">ENSG00000134285</a>	FKBP19	FKBP prolyl isomerase 11
FLG	2.9227476	0.00058	<a href="#">ENSG00000143631</a>	ATOD2 FLG-1 FLG1	filaggrin
FLRT3	-1.6853767	6.3E-05	<a href="#">ENSG00000125848</a>	HH21	fibronectin leucine rich transmembrane protein 3
FOXJ1	1.6276174	0.01064	<a href="#">ENSG00000176678</a>	FKH6 FKHL11 FREAC7 OTSC11	forkhead box L1
FSD1	1.5536953	0.00104	<a href="#">ENSG00000105255</a>	GLFND MIR1	fibronectin type III and SPRY domain containing 1
GBP1	1.6687969	9.5E-11	<a href="#">ENSG00000117228</a>	hGBP1	guanylate binding protein 1
GBP4	2.0720922	1.5E-06	<a href="#">ENSG00000162654</a>	Mpa2	guanylate binding protein 4
GBP5	1.616466	0.00066	<a href="#">ENSG00000154451</a>	GBP-5	guanylate binding protein 5
GCNA	-2.1537541	0.00136	<a href="#">ENSG00000147174</a>	ACRC NAAR1 SPGFX4	germ cell nuclear acidic peptidase
GFPT2	1.8146762	9.5E-09	<a href="#">ENSG00000131459</a>	GFAT GFAT2	glutamine-fructose-6-phosphate transaminase 2
GIPC3	-2.0708871	0.01816	<a href="#">ENSG00000179855</a>	C19orf64 DFNB15 DFNB72 DFNB95	GIPC PDZ domain containing family member 3
GLIPR1L1	2.0138267	0.00675	<a href="#">ENSG00000173401</a>	ALKN2972 PRO7434	GLIPR1 like 1
GLULP4	-1.9033256	0.02425	<a href="#">ENSG00000178723</a>	GLULP	glutamate-ammonia ligase pseudogene 4
GNLY	-2.475783	2.7E-05	<a href="#">ENSG00000115523</a>	D2S69E LAG-2 LAG2 NKG5 TLA519	granulysin

GRIN2B	-1.5987461	2.1E-05	<a href="#">ENSG00000273079</a>	DEE27 EIEE27 GluN2B MRD6 NMDAR2B NR2B NR3 hNR3	glutamate ionotropic receptor NMDA type subunit 2B
HAGLR	-3.0169451	0.00107	<a href="#">ENSG00000224189</a>	HOXD-AS1 MIR7704HG Mdgt STEEL	HOXD antisense growth-associated long non-coding RNA
HCAR2	1.8070748	6.2E-05	<a href="#">ENSG00000182782</a>	GPR109A HCA2 HM74a HM74b NIACR1 PUMAG Puma-g	hydroxycarboxylic acid receptor 2
HCAR3	2.5297592	2.5E-10	<a href="#">ENSG00000255398</a>	GPR109B HCA3 HM74 PUMAG Puma-g	hydroxycarboxylic acid receptor 3
HELZ2	1.6090101	7.4E-14	<a href="#">ENSG00000130589</a>	PDIP-1 PRIC285	helicase with zinc finger 2
HHIPL2	2.3087794	0.0009	<a href="#">ENSG00000143512</a>	KIAA1822L	HHIP like 2
HIST1H2BG	-1.7919698	0.03784	<a href="#">ENSG00000273802</a>	H2B.1A H2B/a H2BC10 H2BC4 H2BC6 H2BC7 H2BFA HIST1H2BG dJ221C16.8	H2B clustered histone 8
HIST2H2BD	2.6455063	0.02194	<a href="#">ENSG00000220323</a>	H2B/o H2B/s H2BFO HIST2H2BD	H2B clustered histone 19, pseudogene
HLA-K	-1.6988541	0.00454	<a href="#">ENSG00000230795</a>	HLA-70 HLA70 HLAK	major histocompatibility complex, class I, K (pseudogene)
HMSD	1.7665676	0.00906	<a href="#">ENSG00000221887</a>	ACC-6 ACC6 C18orf53 HSMD-v	histocompatibility minor serpin domain containing
HOGA1	2.336902	0.04328	<a href="#">ENSG00000241935</a>	C10orf65 DHDPS2 DHDPSL HP3 NPL2	4-hydroxy-2-oxoglutarate aldolase 1
HOPX	-1.8692813	3.2E-05	<a href="#">ENSG00000171476</a>	CAMEO HOD HOP LAGY NECC1 OB1 SMAP31 TOTO	HOP homeobox
HOXB2	2.4570532	0.00041	<a href="#">ENSG00000173917</a>	HOX2 HOX2H Hox-2.8 K8	homeobox B2
HOXB6	1.9576615	0.00114	<a href="#">ENSG00000108511</a>	HOX2 HOX2B HU-2 Hox-2.2	homeobox B6
HPGD	-3.2484908	0.01463	<a href="#">ENSG00000164120</a>	15-PGDH PGDH PGDH1 PHOAR1 SDR36C1	15-hydroxyprostaglandin dehydrogenase
HSPA6	-1.8688333	0.00329	<a href="#">ENSG00000173110</a>		heat shock protein family A (Hsp70) member 6
HSPB3	3.4668341	0.00371	<a href="#">ENSG00000169271</a>	DHMN2C HMN2C HMND4 HSPL27	heat shock protein family B (small) member 3
HSPE1	9.2251651	0.01785	<a href="#">ENSG00000115541</a>	CPN10 EPF GROES HSP10	heat shock protein family E (Hsp10) member 1
IFI27	2.6781569	2.4E-13	<a href="#">ENSG00000165949</a>	FAM14D ISG12 ISG12A P27	interferon alpha inducible protein 27
IFI44	2.0788913	3.8E-23	<a href="#">ENSG00000137965</a>	MTAP44 TLDC5 p44	interferon induced protein 44
IFI44L	2.593975	2.3E-10	<a href="#">ENSG00000137959</a>	C1orf29 GS3686 TLDC5B	interferon induced protein 44 like
IFI6	2.006342	1.3E-14	<a href="#">ENSG00000126709</a>	6-16 FAM14C G1P3 IFI-6-16 IFI616	interferon alpha inducible protein 6
IFIT1	2.9430057	3.5E-21	<a href="#">ENSG00000185745</a>	C56 G10P1 IFI-56 IFI-56K IFI56 IFIT-1 IFNAI1 ISG56 P56 RNM561	interferon induced protein with tetratricopeptide repeats 1
IFIT2	4.3489903	2.1E-14	<a href="#">ENSG00000119922</a>	G10P2 GARG-39 IFI-54 IFI-54K IFI54 IFIT-2 ISG-54 ISG-54K ISG54 P54 cig42	interferon induced protein with tetratricopeptide repeats 2
IFIT3	3.8926112	4.6E-10	<a href="#">ENSG00000119917</a>	CIG-49 GARG-49 IFI60 IFIT4 IRG2 ISG60 P60 RIG-G cig41	interferon induced protein with tetratricopeptide repeats 3

IFITM1	5.2976084	2.6E-24	<a href="#">ENSG00000185885</a>	9-27 CD225 DSPA2a IFI17 LEU13	interferon induced transmembrane protein 1
IFNL1	3.5605788	0.00045	<a href="#">ENSG00000182393</a>	IL-29 IL29	interferon lambda 1
IGFBP2	1.7057789	0.00284	<a href="#">ENSG00000115457</a>	IBP2 IGF-BP53	insulin like growth factor binding protein 2
IL10RA	-1.5535883	0.02504	<a href="#">ENSG00000110324</a>	CD210 CD210a CDW210A HIL-10R IL-10R1 IL10R	interleukin 10 receptor subunit alpha
IL17C	4.6198196	1.7E-06	<a href="#">ENSG00000124391</a>	CX2 IL-17C	interleukin 17C
IL1A	3.7205453	3.1E-28	<a href="#">ENSG00000115008</a>	IL-1A IL1 IL1-ALPHA IL1F1	interleukin 1 alpha
IL1B	2.7461254	1.9E-06	<a href="#">ENSG00000125538</a>	IL-1 IL1-BETA IL1F2 IL1beta	interleukin 1 beta
IL4I1	1.6050848	0.00018	<a href="#">ENSG00000104951</a>	FIG1 LAAO LAO hIL4I1	interleukin 4 induced 1
IRF8	-2.7879403	0.00051	<a href="#">ENSG00000140968</a>	H-ICSBP ICSBP ICSBP1 IMD32A IMD32B IRF-8	interferon regulatory factor 8
ISG15	1.5016763	2.1E-06	<a href="#">ENSG00000187608</a>	G1P2 IFI15 IMD38 IP17 UCRP hUCRP	ISG15 ubiquitin like modifier
ITGAL	-2.8785934	5.9E-06	<a href="#">ENSG00000005844</a>	CD11A LFA-1 LFA1A	integrin subunit alpha L
ITGB2	-1.8795951	1.3E-09	<a href="#">ENSG00000160255</a>	CD18 LAD LCAMB LFA-1 MAC-1 MF17 MFI7	integrin subunit beta 2
ITGB7	-2.0903041	8.3E-05	<a href="#">ENSG00000139626</a>		integrin subunit beta 7
KCNC3	-3.7430433	0.00125	<a href="#">ENSG00000131398</a>	KSHIID KV3.3 SCA13	potassium voltage-gated channel subfamily C member 3
KCNE1	-2.0261891	0.00059	<a href="#">ENSG00000180509</a>	ISK JLNS JLNS2 LQT2/5 LQT5 MinK	potassium voltage-gated channel subfamily E regulatory subunit 1
KCNE1B	-2.4822087	0.00372	<a href="#">ENSG00000276289</a>	KCNE1B	potassium voltage-gated channel subfamily E regulatory subunit 1B
KCNIP3	1.5115869	0.00016	<a href="#">ENSG00000115041</a>	CSEN DREAM KCHIP3	potassium voltage-gated channel interacting protein 3
KCTD14	1.5934232	0.00369	<a href="#">ENSG00000151364</a>		potassium channel tetramerization domain containing 14
KDR	-3.2915758	1.1E-06	<a href="#">ENSG00000128052</a>	CD309 FLK1 VEGFR VEGFR2	kinase insert domain receptor
KLHL6	-2.4553706	0.00736	<a href="#">ENSG00000172578</a>		kelch like family member 6
KRT16P2	-5.5103719	1E-09	<a href="#">ENSG00000227300</a>	None	None
KRT6B	1.6411861	2.4E-11	<a href="#">ENSG00000185479</a>	CK-6B CK6B K6B KRTL1 PC2 PC4	keratin 6B
KRT81	1.818972	5.9E-17	<a href="#">ENSG00000205426</a>	HB1 Hb-1 K81 KRTHB1 MLN137 ghHkb1 hHAKB2-1	keratin 81
LA16c-13E4.3	-5.0732262	0.01451	<a href="#">ENSG00000236235</a>	None	None
LA16c-60D12.2	-4.0616431	0.01057	<a href="#">ENSG00000279442</a>	None	None
LAIR1	-2.6792448	0.0002	<a href="#">ENSG00000167613</a>	CD305 LAIR-1	leukocyte associated immunoglobulin like receptor 1
LAMP3	1.7914033	4.5E-08	<a href="#">ENSG00000078081</a>	CD208 DC-LAMP DCLAMP LAMP LAMP-3 TSC403	lysosomal associated membrane protein 3

LARGE1	1.6854043	0.00305	<a href="#">ENSG00000133424</a>	LARGE MDC1D MDDGA6 MDDGB6	LARGE xylosyl- and glucuronyltransferase 1
LGI2	-1.9806725	4.2E-17	<a href="#">ENSG00000153012</a>	LGIL2	leucine rich repeat LGI family member 2
LIMS2	1.6307326	0.04711	<a href="#">ENSG00000072163</a>	LGMD2W MDRCMTT PINCH-2 PINCH2	LIM zinc finger domain containing 2
LINC00839	2.7287539	5.2E-06	<a href="#">ENSG00000185904</a>		long intergenic non-protein coding RNA 839
LINC00900	-2.5977943	0.04924	<a href="#">ENSG00000246100</a>	None	None
LINC01098	1.5156757	0.02445	<a href="#">ENSG00000231171</a>		long intergenic non-protein coding RNA 1098
LINC01111	1.694304	0.04253	<a href="#">ENSG00000254300</a>		long intergenic non-protein coding RNA 1111
LINC01207	-2.2610406	0.0039	<a href="#">ENSG00000248771</a>	LINC01207 h.EPR	small integral membrane protein 31
LINC01234	1.7861695	0.00394	<a href="#">ENSG00000249550</a>	LCAL84 MBOP onco-lncRNA-32	long intergenic non-protein coding RNA 1234
LINC01405	2.3373343	0.03055	<a href="#">ENSG00000185847</a>		long intergenic non-protein coding RNA 1405
LINC01687	1.5151868	0.02802	<a href="#">ENSG00000233215</a>		long intergenic non-protein coding RNA 1687
LL22NC03-N14H11.1	3.0808529	0.00015	<a href="#">ENSG00000272872</a>	None	None
LL22NC03-N64E9.1	-2.5138156	5.1E-08	<a href="#">ENSG00000271127</a>	None	None
LLfos-48D6.2	-2.3429855	0.01057	<a href="#">ENSG00000273734</a>	None	None
LOX	1.5158299	8E-05	<a href="#">ENSG00000113083</a>	AAT10	lysyl oxidase
LPCAT3	-7.8043668	0.03265	<a href="#">ENSG00000111684</a>	C3F LPCAT LPLAT12 LPSAT MBOAT5 OACT5 nessy	lysophosphatidylcholine acyltransferase 3
LRRC17	3.4382961	0.00566	<a href="#">ENSG00000128606</a>	P37NB	leucine rich repeat containing 17
LRRC4C	1.93379	5.4E-05	<a href="#">ENSG00000148948</a>	NGL-1 NGL1	leucine rich repeat containing 4C
LTB	3.2406193	5.9E-21	<a href="#">ENSG00000227507</a>	TNFC TNFSF3 TNLG1C p33	lymphotoxin beta
LYNX1_3	1.6598688	0.01231	<a href="#">ENSG00000180155</a>		Ly6/neurotoxin 1
LYZ	-2.6338675	0.01121	<a href="#">ENSG00000090382</a>	LYZF1 LZM	lysozyme
MAGEA11	1.5347159	0.00024	<a href="#">ENSG00000185247</a>	CT1.11 MAGE-11 MAGE11 MAGEA-11	MAGE family member A11
MAGEA3	1.6298538	5.3E-06	<a href="#">ENSG00000221867</a>	CT1.3 HIP8 HYPD MAGE3 MAGEA6	MAGE family member A3
MARK2P16	2.6384335	0.00573	<a href="#">ENSG00000270670</a>	None	None
MCEMP1	-3.4385834	0.03279	<a href="#">ENSG00000183019</a>	C19orf59	mast cell expressed membrane protein 1
MERTK	-1.6842324	0.02789	<a href="#">ENSG00000153208</a>	MER RP38 Tyro12 c-Eyk c-mer	MER proto-oncogene, tyrosine kinase

MGAT5B	1.5314326	0.01492	<a href="#">ENSG00000167889</a>	GnT-IX GnT-VB	alpha-1,6-mannosylglycoprotein 6-beta-N-acetylglucosaminyltransferase B
MIR3142HG	2.4234188	0.04409	<a href="#">ENSG00000253522</a>		MIR3142 host gene
MKX	-2.0975507	1.1E-19	<a href="#">ENSG00000150051</a>	C10orf48 IFRX IRXL1	mohawk homeobox
MKX-AS1	-3.0965467	0.01397	<a href="#">ENSG00000230500</a>	None	None
MSC	2.4431928	0.00019	<a href="#">ENSG00000178860</a>	ABF-1 ABF1 MYOR bHLHa22	musculin
MT1A	-1.5763291	0.00195	<a href="#">ENSG00000205362</a>	MT-1A MT-1A MT1 MT1S MTC	metallothionein 1A
MTCO1P12	1.5573285	0.00079	<a href="#">ENSG00000237973</a>		MT-CO1 pseudogene 12
MUC21	-4.2284429	4E-10	<a href="#">ENSG00000204544</a>	C6orf205 KMQK697 MUC-21	mucin 21, cell surface associated
MX1	2.9645486	8.6E-42	<a href="#">ENSG00000157601</a>	IFI-78K IFI78 MX MxA IncMX1-215	MX dynamin like GTPase 1
MX2	2.6622311	7.1E-23	<a href="#">ENSG00000183486</a>	MXB	MX dynamin like GTPase 2
MYEOV	-3.6216754	6.5E-08	<a href="#">ENSG00000172927</a>	OCIM	myeloma overexpressed
MYH14	-2.4755979	0.01208	<a href="#">ENSG00000105357</a>	DFNA4 DFNA4A FP17425 MHC16 MYH17 NMHC-II-C PNMHH myosin	myosin heavy chain 14
MYL9	1.7108275	1.2E-08	<a href="#">ENSG00000101335</a>	LC20 MLC-2C MLC2 MMIHS4 MRLC1 MYRL2	myosin light chain 9
MYO16	-1.5906579	0.0318	<a href="#">ENSG00000041515</a>	MYAP3 MYR8 Myo16b NYAP3 PPP1R107	myosin XVI
MYO1F	-2.0479173	5.7E-05	<a href="#">ENSG00000142347</a>		myosin IF
MYO7A	-1.8175355	0.03291	<a href="#">ENSG00000137474</a>	DFNA11 DFNB2 MYOVIIA MYU7A NSRD2 USH1B	myosin VIIA
NAALADL2-AS2	-1.6427687	0.01958	<a href="#">ENSG00000226779</a>	None	None
NAPSA	-9.0934585	0.02309	<a href="#">ENSG00000131400</a>	KAP Kdap NAP1 NAPA SNAPA	napsin A aspartic peptidase
NCF4	-2.0421266	0.04409	<a href="#">ENSG00000100365</a>	CGD3 NCF P40PHOX SH3PXD4	neutrophil cytosolic factor 4
NCKAP1L	-1.6848701	0.00277	<a href="#">ENSG00000123338</a>	HEM1 IMD72	NCK associated protein 1 like
NCOA7	1.6929962	9.2E-17	<a href="#">ENSG00000111912</a>	ERAP140 ESNA1 NCOA7-AS Nb1a00052 Nb1a10993 TLDC4 dJ187J11.3	nuclear receptor coactivator 7
NECAB1	1.9225343	0.00168	<a href="#">ENSG00000123119</a>	EFCBP1 STIP-1	N-terminal EF-hand calcium binding protein 1
NEFL	2.1835512	2.7E-10	<a href="#">ENSG00000277586</a>	CMT1F CMT2E CMTDIG NF-L NF68 NFL PPP1R110	neurofilament light chain
NEURL3	2.6722865	0.00039	<a href="#">ENSG00000163121</a>	LINCR RNFI32	neuralized E3 ubiquitin protein ligase 3
NFKBIZ	1.667472	9.8E-18	<a href="#">ENSG00000144802</a>	I-kappa-B-zeta IKBZ INAP IkappaB-zeta MAIL ikB-zeta ikappaBzeta	NFKB inhibitor zeta
NKX2-1	-9.4763576	0.00425	<a href="#">ENSG00000136352</a>	BCH BHC NK-2 NKX2.1 NKX2A NMTC1 T/EBP TEBP TITF1 TTF-1 TTF1	NK2 homeobox 1
NLGN1	1.621118	0.01843	<a href="#">ENSG00000169760</a>	NL1 NLG1	neuroligin 1

NLRP2	-6.2188091	1.9E-06	<a href="#">ENSG00000022556</a>	CLR19.9 NALP2 NBS1 OZEMA18 PAN1 PYPAF2	NLR family pyrin domain containing 2
NRSN2	1.5326057	2.1E-10	<a href="#">ENSG00000125841</a>	C20orf98 dJ1103G7.6	neurensin 2
NUDT10	1.8088752	0.02194	<a href="#">ENSG00000122824</a>	APS2 DIPP3-alpha DIPP3a	nudix hydrolase 10
OAS1	1.9466414	8.1E-07	<a href="#">ENSG00000089127</a>	E18/E16 IFI-4 IMD100 OIAS OIASI	2'-5'-oligoadenylate synthetase 1
OAS2	2.9433992	4.7E-30	<a href="#">ENSG00000111335</a>		2'-5'-oligoadenylate synthetase 2
OAS3	1.7182169	3.9E-06	<a href="#">ENSG00000111331</a>	p100 p100OAS	2'-5'-oligoadenylate synthetase 3
OASL	1.9683092	4.5E-12	<a href="#">ENSG00000135114</a>	OASL1 OASLd TRIP-14 TRIP14 p59-OASL p59OASL	2'-5'-oligoadenylate synthetase like
OCIAD1-AS1	-7.7213799	0.03468	<a href="#">ENSG00000248256</a>		OCIAD1 antisense RNA 1
ORM1	1.8391737	0.00542	<a href="#">ENSG00000229314</a>	A1AG1 AGP-A AGP1 HEL-S-153w ORM	orosomucoid 1
P2RY8	-3.3225632	5.3E-05	<a href="#">ENSG00000182162</a>	P2Y8	P2Y receptor family member 8
PALM3	2.0475572	0.04561	<a href="#">ENSG00000187867</a>		paralemmin 3
PARVG	-2.8738793	0.00403	<a href="#">ENSG00000138964</a>		parvin gamma
PCBP3	1.6583217	0.01057	<a href="#">ENSG00000183570</a>	ALPHA-CP3 PCBP3-OT1 PCBP3OT	poly(rC) binding protein 3
PDE1B	-1.91796	0.01496	<a href="#">ENSG00000123360</a>	HEL-S-79p PDE1B1 PDES1B	phosphodiesterase 1B
PDGFRB	1.684707	0.00088	<a href="#">ENSG00000113721</a>	CD140B IBGC4 IMF1 JTK12 KOGS PDGFR PDGFR-1 PDGFR1 PENTT	platelet derived growth factor receptor beta
PDZK1IP1	1.59555	5.9E-07	<a href="#">ENSG00000162366</a>	DD96 MAP17 SPAP	PDZK1 interacting protein 1
PECAM1	-2.6222653	1E-06	<a href="#">ENSG00000261371</a>	CD31 CD31/EndoCAM PECA1 PECAM-1 endoCAM	platelet and endothelial cell adhesion molecule 1
PENK	-3.8459728	0.00638	<a href="#">ENSG00000181195</a>	PE PENK-A	proenkephalin
PIK3CG	-3.1327935	0.00012	<a href="#">ENSG00000105851</a>	IMD97 PI3CG PI3K PI3Kgamma PIK3p110gamma p120-PI3K	phosphatidylinositol-4,5-bisphosphate 3-kinase catalytic subunit gamma
PIP	-2.5436094	0.04927	<a href="#">ENSG00000159763</a>	BRST-2 GCDFP-15 GCDFP15 GPIP4	prolactin induced protein
PLEKHA4	1.6389049	0.00028	<a href="#">ENSG00000105559</a>	PEPP1	pleckstrin homology domain containing A4
PLEKHD1	-2.4901974	0.01546	<a href="#">ENSG00000175985</a>	UPF0639	pleckstrin homology and coiled-coil domain containing D1
PLPPR5	-1.9345627	0.0443	<a href="#">ENSG00000117598</a>	LPPR5 PAP2 PAP2D PRG5	phospholipid phosphatase related 5
PPP1R35	-8.6234461	0.04214	<a href="#">ENSG00000160813</a>	C7orf47	protein phosphatase 1 regulatory subunit 35
PRAL	3.0078274	2.4E-08	<a href="#">ENSG00000279296</a>	None	None
PRAM1	-2.3906351	0.00374	<a href="#">ENSG00000133246</a>	PML-RAR PRAM-1	PML-RARA regulated adaptor molecule 1
PRAME	-2.9769148	0.00016	<a href="#">ENSG00000185686</a>	CT130 MAPE OIP-4 OIP4	PRAME nuclear receptor transcriptional regulator
PRKCB	-3.3669681	0.00017	<a href="#">ENSG00000166501</a>	PKC-beta PKCB PKCbeta PRKCB1 PRKCB2	protein kinase C beta



PSG1	2.2311373	0.00056	<a href="#">ENSG00000231924</a>	B1G1 CD66f DHFRP2 FL-NCA-1/2 PBG1 PS-beta-C/D PS-beta-G-1 PSBG-1 PSBG1 PSG95 PSGGA PSGIIA SP1	pregnancy specific beta-1-glycoprotein 1
PTN	2.8354981	0.03029	<a href="#">ENSG00000105894</a>	HARP HB-GAM HBBM HBGF-8 HBGF8 HBNF HBNF-1 NEGF1 OSF-1	pleiotrophin
PTPN7	-2.3717689	0.00015	<a href="#">ENSG00000143851</a>	BPTP-4 HEPTP LC-PTP LPTP PTPNI	protein tyrosine phosphatase non-receptor type 7
PTPRN	2.7196888	0.00559	<a href="#">ENSG00000054356</a>	IA-2 IA-2/PTP IA2 ICA512 R-PTP-N	protein tyrosine phosphatase receptor type N
PTX3	2.9334144	3.8E-23	<a href="#">ENSG00000163661</a>	TNFAIP5 TSG-14	pentraxin 3
PVRIG2P	1.9036526	0.00617	<a href="#">ENSG00000235333</a>	None	None
RAET1E	-6.9376773	0.00056	<a href="#">ENSG00000164520</a>	LETAL N2DL-4 NKG2DL4 RAET1E2 RL-4 ULBP4 bA350J20.7	retinoic acid early transcript 1E
RASD1	-2.758271	0.00512	<a href="#">ENSG00000108551</a>	AGS1 DEXRAS1 MGC:26290	ras related dexamethasone induced 1
RBM20	3.0952159	0.04262	<a href="#">ENSG00000203867</a>		RNA binding motif protein 20
RBPM52	1.6362935	0.00943	<a href="#">ENSG00000166831</a>		RNA binding protein, mRNA processing factor 2
RCS1D1	-1.8883458	0.01882	<a href="#">ENSG00000198771</a>	CAPZIP MK2S4	RCS1D domain containing 1
RDH5	-4.115452	0.04209	<a href="#">ENSG00000135437</a>	9cRDH HSD17B9 RDH1 SDR9C5	retinol dehydrogenase 5
REEP2	1.7215652	6.7E-08	<a href="#">ENSG00000132563</a>	C5orf19 SGC32445 SPG72 SPG72A SPG72B Yip2d	receptor accessory protein 2
RGAG1	1.8683059	0.0002	<a href="#">ENSG00000243978</a>	MAR9 MART9 RGAG1 SIRH10	retrotransposon Gag like 9
RGCC	-2.2347353	5.4E-05	<a href="#">ENSG00000102760</a>	C13orf15 RGC-32 RGC32 bA157L14.2	regulator of cell cycle
RNASE2	-2.6665923	0.01265	<a href="#">ENSG00000169385</a>	EDN RAF3 RNS2	ribonuclease A family member 2
RNF212	-3.9434519	0.01209	<a href="#">ENSG00000178222</a>	SPGF62 ZHP3	ring finger protein 212
ROR2	1.8441452	0.00919	<a href="#">ENSG00000169071</a>	BDB BDB1 NTRKR2	receptor tyrosine kinase like orphan receptor 2
RP11-1024P17.1	2.7775302	0.03874	<a href="#">ENSG00000261468</a>	None	None
RP11-104H15.7	2.2553263	0.01646	<a href="#">ENSG00000262880</a>	None	None
RP11-1105O14.1	-2.5714111	0.0097	<a href="#">ENSG00000253270</a>	None	None
RP11-114H23.1	-2.0508335	0.01575	<a href="#">ENSG00000258077</a>	None	None
RP11-136I14.5	-4.2263768	0.02744	<a href="#">ENSG00000255689</a>	None	None
RP11-142E9.1	2.9118066	0.04846	<a href="#">ENSG00000276672</a>	None	None
RP11-155D18.12	-9.3595891	0.00962	<a href="#">ENSG00000272762</a>	None	None
RP11-174O3.3	-5.2336506	0.01225	<a href="#">ENSG00000240661</a>	None	None
RP11-180D21.3	4.2184452	0.00465	<a href="#">ENSG00000224943</a>	None	None

RP11-214O1.2	1.6950657	0.0135	<a href="#">ENSG00000266709</a>		uncharacterized protein MGC12916
RP11-221J22.2	-1.6814912	0.02335	<a href="#">ENSG00000241280</a>	None	None
RP11-246K15.1	-2.8497873	3.2E-05	<a href="#">ENSG00000253821</a>	None	None
RP11-258F1.2	8.481536	0.01616	<a href="#">ENSG00000279428</a>	None	None
RP11-260M19.2	7.5592603	0.03207	<a href="#">ENSG00000258913</a>	C14orf144	long intergenic non-protein coding RNA 2691
RP11-278A23.1	2.5593156	0.0203	<a href="#">ENSG00000226180</a>		uncharacterized LOC100129215
RP11-292D4.1	-2.2539467	0.01296	<a href="#">ENSG00000248346</a>	None	None
RP11-301G19.1	-1.6049509	0.01744	<a href="#">ENSG00000227706</a>	None	None
RP11-301M17.1	2.0436872	0.04214	<a href="#">ENSG00000227700</a>	None	None
RP11-326C3.2	-1.5478173	6.9E-08	<a href="#">ENSG00000255026</a>	None	None
RP11-329E24.6	2.6083995	0.00297	<a href="#">ENSG00000231937</a>	None	None
RP11-335I12.2	2.1745879	0.02137	<a href="#">ENSG00000256072</a>	None	None
RP11-374M1.2	1.9242903	0.02359	<a href="#">ENSG00000231527</a>	FAM27A FAM27A1 FAM27A3 bA7G23.5	family with sequence similarity 27 member C
RP11-400N13.2	-3.7009404	1E-08	<a href="#">ENSG00000228437</a>	None	None
RP11-432I5.2	-1.8622866	0.0088	<a href="#">ENSG00000260593</a>	None	None
RP11-467L19.16	1.6474123	0.01503	<a href="#">ENSG00000278626</a>	None	None
RP11-469A15.2	-1.5278118	0.00388	<a href="#">ENSG00000230623</a>	None	None
RP11-473I1.9	4.9096912	0.00088	<a href="#">ENSG00000263244</a>	None	None
RP11-47I22.2	-2.00057	0.02918	<a href="#">ENSG00000250548</a>		long intergenic non-protein coding RNA 1303
RP11-498C9.3	3.3527725	5.4E-06	<a href="#">ENSG00000262413</a>	None	None
RP11-4N23.4	-1.8583509	3.2E-06	<a href="#">ENSG00000277935</a>	None	None
RP11-54F2.1	1.8375603	5.9E-08	<a href="#">ENSG00000251196</a>	None	None
RP11-54O7.17	1.6821629	0.00044	<a href="#">ENSG00000272512</a>	None	None
RP11-550P17.5	3.6760044	4.3E-05	<a href="#">ENSG00000228560</a>	None	None
RP11-58O9.2	1.7554975	5.4E-05	<a href="#">ENSG00000279806</a>	None	None
RP11-618G20.1	1.7987696	0.03539	<a href="#">ENSG00000258964</a>	None	None
RP11-638I8.1	-4.2898423	0.03872	<a href="#">ENSG00000283247</a>		coiled-coil domain containing 201
RP11-644F5.10	7.806754	0.03704	<a href="#">ENSG00000258311</a>	None	None

RP11-81H3.2	1.7619099	0.01317	<a href="#">ENSG00000251138</a>		long intergenic non-protein coding RNA 2882
RP11-867G23.3	7.0129639	0.00047	<a href="#">ENSG00000245156</a>	None	None
RP11-872D17.8	1.5725634	0.01277	<a href="#">ENSG00000254979</a>	None	None
RP11-93B14.6	-4.2126986	0.00816	<a href="#">ENSG00000167046</a>	None	None
RP3-340N1.2	-8.3985286	0.01541	<a href="#">ENSG00000227066</a>		uncharacterized LOC117779438
RP3-402G11.26	2.2461403	0.00215	<a href="#">ENSG00000273253</a>		TRABD antisense RNA 1
RP4-608O15.3	1.5156949	0.04657	<a href="#">ENSG00000276911</a>	None	None
RP4-635E18.9	1.9342406	0.00388	<a href="#">ENSG00000277726</a>	None	None
RP5-1120P11.1	-1.5844947	9.3E-05	<a href="#">ENSG00000237686</a>	DATOC-1	stem cell inhibitory RNA transcript
RP5-943J3.2	1.5155583	0.03083	<a href="#">ENSG00000272931</a>	None	None
RPL32P29	-2.875184	0.03784	<a href="#">ENSG00000244270</a>	RPL32_8_1362	ribosomal protein L32 pseudogene 29
RPSAP52	-1.5313319	0.02466	<a href="#">ENSG00000241749</a>	RPSA_17_1251	ribosomal protein SA pseudogene 52
RRAGD	-1.9986538	2.7E-15	<a href="#">ENSG0000025039</a>	HOMG7 RAGD bA11D8.2.1	Ras related GTP binding D
RSAD2	2.9234287	9.5E-29	<a href="#">ENSG00000134321</a>	SAND cig33 cig5 vig1	radical S-adenosyl methionine domain containing 2
RXRG	3.2242172	0.02867	<a href="#">ENSG00000143171</a>	NR2B3 RXR-gamma RXRC RXRgamma	retinoid X receptor gamma
S1PR3	1.999745	2.1E-06	<a href="#">ENSG00000213694</a>	C9orf108 C9orf47 EDG-3 EDG3 LPB3 S1P3 bA791O21.3	sphingosine-1-phosphate receptor 3
SAA1	1.9604461	7.6E-16	<a href="#">ENSG00000173432</a>	PIG4 SAA SAA2 TP5314	serum amyloid A1
SAA2	1.9880691	1.7E-11	<a href="#">ENSG00000134339</a>	SAA SAA1	serum amyloid A2
SAA2-SAA4	2.0404514	2.7E-23	<a href="#">ENSG00000255071</a>		SAA2-SAA4 readthrough
SASH3	-2.4921801	4.9E-05	<a href="#">ENSG00000122122</a>	753P9 CXorf9 HACS2 IMD102 SH3D6C SLY	SAM and SH3 domain containing 3
SCN3A	2.7668022	0.03596	<a href="#">ENSG00000153253</a>	DEE62 EIEE62 FFEVF4 NAC3 Nav1.3	sodium voltage-gated channel alpha subunit 3
SFRP1	-1.6901215	5.3E-18	<a href="#">ENSG00000104332</a>	FRP FRP-1 FRP1 FrzA SARP2	secreted frizzled related protein 1
SFTA2	-2.0751436	0.04239	<a href="#">ENSG00000196260</a>	GSGL541 SFTPG SP-G UNQ541	surfactant associated 2
SFTPA1	-5.9245727	0.00558	<a href="#">ENSG00000122852</a>	COLEC4 ILD1 PSAP PSP-A PSPA SFTP1 SFTPA1B SP-A SP-A1 SPA SPA1	surfactant protein A1
SFTPA2	-3.611028	0.01621	<a href="#">ENSG00000185303</a>	COLEC5 ILD2 PSAP PSP-A PSPA SFTP1 SFTPA2B SP-2A SP-A SPA2 SPAII	surfactant protein A2
SFTPB	-10.072505	8E-10	<a href="#">ENSG00000168878</a>	PSP-B SFTB3 SFTP3 SMDP1 SP-B	surfactant protein B
SGO1-AS1	1.6975647	0.01371	<a href="#">ENSG00000231304</a>	SGOL1-AS1	SGO1 antisense RNA 1
SIGLEC11	-2.5263769	0.03795	<a href="#">ENSG00000161640</a>		sialic acid binding Ig like lectin 11
SLA	-2.0669178	1.3E-06	<a href="#">ENSG00000155926</a>	SLA1 SLAP	Src like adaptor

SLC22A31	-1.6197914	0.03858	<a href="#">ENSG00000259803</a>		solute carrier family 22 member 31
SLC2A5	-2.9258537	5.6E-07	<a href="#">ENSG00000142583</a>	GLUT-5 GLUT5	solute carrier family 2 member 5
SLC34A2	-5.2036751	6.7E-10	<a href="#">ENSG00000157765</a>	NAPI-3B NAPI-IIb NPTIb NaPi2b PULAM	solute carrier family 34 member 2
SLC40A1	-4.1132669	0.00076	<a href="#">ENSG00000138449</a>	FPN FPN1 HFE4 IREG1 MST079 MSTP079 MTP1 SLC11A3	solute carrier family 40 member 1
SLC5A2	1.6816058	0.02467	<a href="#">ENSG00000140675</a>	SGLT2	solute carrier family 5 member 2
SLITRK1	2.1802061	0.00997	<a href="#">ENSG00000178235</a>	LRRC12 TTM	SLIT and NTRK like family member 1
SPDYE6	-1.5867958	0.02377	<a href="#">ENSG00000260097</a>		speedy/RINGO cell cycle regulator family member E6
SPI1	-1.8361878	0.01316	<a href="#">ENSG00000066336</a>	AGM10 OF PU.1 SFPI1 SPI-1 SPI-A	Spi-1 proto-oncogene
SPN	-2.4847222	6.8E-05	<a href="#">ENSG00000197471</a>	CD43 GALGP GPL115 LEU-22 LSN	sialophorin
SPOCK2	-1.5562319	0.00712	<a href="#">ENSG00000107742</a>	testican-2	SPARC (osteonectin), cwcv and kazal like domains proteoglycan 2
SPP1	-3.7120895	3.4E-07	<a href="#">ENSG00000118785</a>	BNSP BSPI ETA-1 OPN	secreted phosphoprotein 1
SPRR3	-2.3014584	0.03528	<a href="#">ENSG00000163209</a>		small proline rich protein 3
SRRM3	1.9228316	0.00022	<a href="#">ENSG00000177679</a>		serine/arginine repetitive matrix 3
SS18L2	-4.1731494	0.00579	<a href="#">ENSG00000008324</a>	KIAA-iso	SS18 like 2
SSTR1	-1.7996634	4.2E-17	<a href="#">ENSG00000139874</a>	SRIF-2 SS-1-R SS1-R SS1R SST1	somatostatin receptor 1
ST18	-1.6131172	2.2E-05	<a href="#">ENSG00000147488</a>	NZF-3 NZF3 ZC2H2C3 ZC2HC10 ZNF387	ST18 C2H2C-type zinc finger transcription factor
STAC2	2.7677049	0.00111	<a href="#">ENSG00000141750</a>	24b2 24b2/STAC2	SH3 and cysteine rich domain 2
SV2A	1.7493325	4.7E-15	<a href="#">ENSG00000159164</a>	SLC22B1 SV2	synaptic vesicle glycoprotein 2A
SYNGR3	1.5079232	0.00315	<a href="#">ENSG00000127561</a>		synaptogyrin 3
TCTEX1D1	-1.8253793	0.00113	<a href="#">ENSG00000152760</a>	TCTEX1D1	dynein light chain Tctex-type family member 5
TDRD1	-6.4433329	0.00028	<a href="#">ENSG00000095627</a>	CT41.1	tudor domain containing 1
TENM1	1.9213214	0.01277	<a href="#">ENSG00000009694</a>	ODZ1 ODZ3 TEN-M1 TEN1 TNM TNM1 ten-1	teneurin transmembrane protein 1
TESPA1	1.8225668	0.04128	<a href="#">ENSG00000135426</a>	HSPC257 ITPRID3 KIAA0748	thymocyte expressed, positive selection associated 1
THSD7A	-2.6214578	0.01183	<a href="#">ENSG00000005108</a>		thrombospondin type 1 domain containing 7A
TM4SF18	-4.4869695	0.00208	<a href="#">ENSG00000163762</a>	L6D	transmembrane 4 L six family member 18
TMEM255A	-2.0264136	0.04132	<a href="#">ENSG00000125355</a>	FAM70A	transmembrane protein 255A
TMEM255B	1.7004731	0.04409	<a href="#">ENSG00000184497</a>	FAM70B	transmembrane protein 255B
TMEM45B	-2.0052181	0.00283	<a href="#">ENSG00000151715</a>		transmembrane protein 45B
TMPRSS2	-2.745454	0.00027	<a href="#">ENSG00000184012</a>	PRSS10	transmembrane serine protease 2
TNF	4.5935386	6.8E-18	<a href="#">ENSG00000232810</a>	DIF TNF-alpha TNFA TNFSF2 TNLG1F	tumor necrosis factor
TNFAIP2	2.5848044	1.3E-16	<a href="#">ENSG00000185215</a>	B94 EXOC3L3	TNF alpha induced protein 2

TNFAIP3	1.9880368	2.5E-25	<a href="#">ENSG00000118503</a>	A20 AIFBL1 AISBL OTUD7C TNFA1P2	TNF alpha induced protein 3
TNFAIP6	2.5830676	4E-08	<a href="#">ENSG00000123610</a>	TSG-6 TSG6	TNF alpha induced protein 6
TNFRSF1B	-1.5217329	0.01171	<a href="#">ENSG00000028137</a>	CD120b TBPII TNF-R-II TNF-R75 TNFBR TNFR1B TNFR2 TNFR80 p75 p75TNFR	TNF receptor superfamily member 1B
TNFSF10	1.629542	0.00488	<a href="#">ENSG00000121858</a>	APO2L Apo-2L CD253 TANCR TL2 TNLG6A TRAIL	TNF superfamily member 10
TNIP3	3.1864467	3.3E-08	<a href="#">ENSG00000050730</a>	ABIN-3 LIND	TNFAIP3 interacting protein 3
TRIM61	1.6461073	0.01089	<a href="#">ENSG00000183439</a>	RNF35	tripartite motif containing 61
TTLL11-IT1	-3.3276897	5.6E-06	<a href="#">ENSG00000237548</a>	None	None
TYROBP	-2.0637588	0.00766	<a href="#">ENSG00000011600</a>	DAP12 KARAP PLOS PLOSL1	transmembrane immune signaling adaptor TYROBP
UBD	1.8056913	6.8E-05	<a href="#">ENSG00000213886</a>	FAT10 GABBR1 UBD-3	ubiquitin D
UBXN10	-3.4391754	0.03837	<a href="#">ENSG00000162543</a>	UBXD3	UBX domain protein 10
UGT1A1	2.7837582	0.0014	<a href="#">ENSG00000241635</a>	BILIQT1 GNT1 HUG-BR1 UDPGT UGT1 UGT1A	UDP glucuronosyltransferase family 1 member A1
UPK3BP1	3.4521639	0.02558	<a href="#">ENSG00000242435</a>		uroplakin 3B pseudogene 1
VAV1	-1.6426322	0.00236	<a href="#">ENSG00000141968</a>	VAV	vav guanine nucleotide exchange factor 1
VSIG4	-1.7925795	0.01183	<a href="#">ENSG00000155659</a>	CRIg Z39IG	V-set and immunoglobulin domain containing 4
WSCD1	1.9417358	0.00573	<a href="#">ENSG00000179314</a>		WSC domain containing 1
WTIP	1.6200663	0.00736	<a href="#">ENSG00000142279</a>		WT1 interacting protein
XAF1	2.2964557	0.00061	<a href="#">ENSG00000132530</a>	BIRC4BP HSXIAPAF1 XIAPAF1	XIAP associated factor 1
XAGE1A	-3.3710072	0.00033	<a href="#">ENSG00000204379</a>	CT12.1 CT12.1A CT12.1B CTP9 GAGED2 XAGE-1 XAGE1 XAGE1B	X antigen family member 1A
XYLT1	-2.4970839	0.00387	<a href="#">ENSG00000103489</a>	DBQD2 PXYLT1 XT-I XT1 XTI XYLT1 xy1T-I	xylosyltransferase 1
ZBED6CL	2.2398356	0.00538	<a href="#">ENSG00000188707</a>	None	None
ZC3H12A	2.3576659	2E-36	<a href="#">ENSG00000163874</a>	MCPIP MCPIP-1 MCPIP1 Reg1 dJ423B22.1	zinc finger CCCH-type containing 12A
ZIC2	-2.3151775	0.04262	<a href="#">ENSG00000043355</a>	HPE5	Zic family member 2
ZNF157	-1.6008336	0.03151	<a href="#">ENSG00000147117</a>	HZF22	zinc finger protein 157
ZPLD1	-1.9608305	7.3E-08	<a href="#">ENSG00000170044</a>		zona pellucida like domain containing 1

### 2583+NO<sub>2</sub> against NaCl

AC005387.3	4.0006692	0.00036	<a href="#">ENSG00000268938</a>	None	None
AC068499.10	-5.3909098	0.02513	<a href="#">ENSG00000268650</a>		uncharacterized LOC102725254

APBB1IP	-1.7802296	0.04597	<a href="#">ENSG00000077420</a>	INAG1 PREL1 RARP1 RIAM	amyloid beta precursor protein binding family B member 1 interacting protein
CD163	-1.6264365	0.00014	<a href="#">ENSG00000177575</a>	M130 MM130 SCAR1	CD163 molecule
CD93	-1.7648249	0.00171	<a href="#">ENSG00000125810</a>	C1QR1 C1qRP CDw93 ECSM3 MXRA4 dJ737E23.1	CD93 molecule
CTD-2521M24.6	4.2528297	0.00097	<a href="#">ENSG00000269481</a>	None	None
CYP1A1	1.675839	0.00609	<a href="#">ENSG00000140465</a>	AHH AHRR CP11 CYP1 CYPIA1 P1-450 P450-C P450DX	cytochrome P450 family 1 subfamily A member 1
GNLY	-2.5554754	0.00036	<a href="#">ENSG00000115523</a>	D2S69E LAG-2 LAG2 NKG5 TLA519	granulysin
HSPE1	10.237195	0.03639	<a href="#">ENSG00000115541</a>	CPN10 EPF GROES HSP10	heat shock protein family E (Hsp10) member 1
IFIT2	-2.9548084	0.00036	<a href="#">ENSG00000119922</a>	G10P2 GARG-39 IFI-54 IFI-54K IFI54 IFIT-2 ISG-54 ISG-54K ISG54 P54 cig42	interferon induced protein with tetratricopeptide repeats 2
ITGAL	-1.8007734	0.02513	<a href="#">ENSG00000005844</a>	CD11A LFA-1 LFA1A	integrin subunit alpha L
LL22NC03-N14H11.1	3.5924691	0.00013	<a href="#">ENSG00000272872</a>	None	None
NCKAP1L	-1.5331973	0.04277	<a href="#">ENSG00000123338</a>	HEM1 IMD72	NCK associated protein 1 like
PVRIG2P	2.4296399	0.00171	<a href="#">ENSG00000235333</a>	None	None
RNF13	-10.796393	0.01497	<a href="#">ENSG00000082996</a>	DEE73 EIEE73 RZF	ring finger protein 13
RP11-498C9.3	3.6377172	2.4E-05	<a href="#">ENSG00000262413</a>	None	None
RP11-66N24.3	-2.2317904	0.04597	<a href="#">ENSG00000258727</a>		AP1G2 antisense RNA 1
RP11-69E11.8	-10.25342	0.03283	<a href="#">ENSG00000228060</a>	None	None
SLA	-1.9360709	0.00023	<a href="#">ENSG00000155926</a>	SLA1 SLAP	Src like adaptor
SLC2A5	-1.9286437	0.01176	<a href="#">ENSG00000142583</a>	GLUT-5 GLUT5	solute carrier family 2 member 5
SPP1	-2.2415463	0.03189	<a href="#">ENSG00000118785</a>	BNSP BSPI ETA-1 OPN	secreted phosphoprotein 1
TNFRSF1B	-1.7113588	0.02656	<a href="#">ENSG00000028137</a>	CD120b TBPII TNF-R-II TNF-R75 TNFBR TNFR1B TNFR2 TNFR80 p75 p75TNFR	TNF receptor superfamily member 1B

<i>DEP+NO<sub>2</sub> against DEP</i>					
TCHHL1	-1.6117065	0.0109	<a href="#">ENSG00000182898</a>	S100A17 THHL1	trichohyalin like 1
IL1A	2.4409669	2.4E-11	<a href="#">ENSG00000115008</a>	IL-1A IL1 IL1-ALPHA IL1F1	interleukin 1 alpha
IL1B	1.8759324	0.0336	<a href="#">ENSG00000125538</a>	IL-1 IL1-BETA IL1F2 IL1beta	interleukin 1 beta
TNFAIP6	2.0340507	0.0001	<a href="#">ENSG00000123610</a>	TSG-6 TSG6	TNF alpha induced protein 6
CCL20	1.5919781	0.0001	<a href="#">ENSG00000115009</a>	CKb4 Exodus LARC MIP-3-alpha MIP-3a MIP3A SCYA20 ST38	C-C motif chemokine ligand 20
CXCL6	2.2482884	0.00206	<a href="#">ENSG00000124875</a>	CKA-3 GCP-2 GCP2 SCYB6	C-X-C motif chemokine ligand 6

CXCL1	2.2456325	1.9E-11	<a href="#">ENSG00000163739</a>	FSP GRO1 GROa MGSA MGSA-a NAP-3 SCYB1	C-X-C motif chemokine ligand 1
CXCL3	2.0999408	3.6E-07	<a href="#">ENSG00000163734</a>	CINC-2b GRO3 GROg MIP-2b MIP2B SCYB3	C-X-C motif chemokine ligand 3
CXCL2	1.5684257	1.1E-05	<a href="#">ENSG00000081041</a>	CINC-2a GRO2 GROb MGSA-b MIP-2a MIP2 MIP2A SCYB2	C-X-C motif chemokine ligand 2
SPP1	-2.4227636	0.03657	<a href="#">ENSG00000118785</a>	BNSP BSPI ETA-1 OPN	secreted phosphoprotein 1
TNF	2.0184693	5.4E-05	<a href="#">ENSG00000232810</a>	DIF TNF-alpha TNFA TNFSF2 TNLG1F	tumor necrosis factor
LTB	2.1547182	6.1E-09	<a href="#">ENSG00000227507</a>	TNFC TNFSF3 TNLG1C p33	lymphotoxin beta
PAQR8	3.4483554	3.6E-07	<a href="#">ENSG00000170915</a>	C6orf33 LMPB1 MPRB	progesterone and adipoQ receptor family member 8
OLR1	1.5513784	3.1E-08	<a href="#">ENSG00000173391</a>	CLEC8A LOX1 LOXIN SCARE1 SLOX1	oxidized low density lipoprotein receptor 1
NFE2	-1.9689896	0.04274	<a href="#">ENSG00000123405</a>	NF-E2 p45	nuclear factor, erythroid 2
IL17C	2.5699045	0.00132	<a href="#">ENSG00000124391</a>	CX2 IL-17C	interleukin 17C
CSF3	1.7485272	0.00721	<a href="#">ENSG00000108342</a>	C17orf33 CSF3OS GCSF	colony stimulating factor 3
CLDN8	-2.0364163	0.01366	<a href="#">ENSG00000156284</a>	HEL-S-79	claudin 8
AP000304.12	2.2676006	0.01245	<a href="#">ENSG00000249209</a>	None	None

### 2583+NO<sub>2</sub> against 2583

IFIT2	-3.0284334	0.00123	<a href="#">ENSG00000119922</a>	G10P2 GARG-39 IFI-54 IFI-54K IFI54 IFIT-2 ISG-54 ISG-54K ISG54 P54 cig42	interferon induced protein with tetratricopeptide repeats 2
-------	------------	---------	---------------------------------	--------------------------------------------------------------------------	-------------------------------------------------------------

## Chapter 10: References

---

- Aalapathi, S., Ganapathy, S., Manapuram, S., Anumolu, G., & Prakya, B. M. (2014). Toxicity and bio-accumulation of inhaled cerium oxide nanoparticles in CD1 mice. *Nanotoxicology*, 8(7), 786-798. <https://doi.org/10.3109/17435390.2013.829877>
- Aardema, M. J., & MacGregor, J. T. (2002). Toxicology and genetic toxicology in the new era of “toxicogenomics”: impact of “-omics” technologies. *Mutation Research/Fundamental and Molecular Mechanisms of Mutagenesis*, 499(1), 13-25. [https://doi.org/https://doi.org/10.1016/S0027-5107\(01\)00292-5](https://doi.org/https://doi.org/10.1016/S0027-5107(01)00292-5)
- Abbas, I., Garçon, G., Saint-Georges, F., Billet, S., Verdin, A., Gosset, P.,...Shirali, P. (2010). Occurrence of molecular abnormalities of cell cycle in L132 cells after in vitro short-term exposure to air pollution PM2.5. *Chemico-Biological Interactions*, 188(3), 558-565. <https://doi.org/https://doi.org/10.1016/j.cbi.2010.09.014>
- Ackermann, J. A., Hofheinz, K., Zaiss, M. M., & Krönke, G. (2017). The double-edged role of 12/15-lipoxygenase during inflammation and immunity. *Biochimica et Biophysica Acta. Molecular and Cell Biology of Lipids*, 1862(4), 371-381. <https://doi.org/10.1016/j.bbalip.2016.07.014>
- Ackermann-Liebrich, U., Leuenberger, P., Schwartz, J., Schindler, C., Monn, C., Bolognini, G.,...Zemp, E. (1997). Lung function and long term exposure to air pollutants in Switzerland. Study on Air Pollution and Lung Diseases in Adults (SAPALDIA) Team. *American Journal of Respiratory and Critical Care Medicine*, 155(1), 122-129. <https://doi.org/10.1164/ajrccm.155.1.9001300>
- Alessandri, A. L., Sousa, L. P., Lucas, C. D., Rossi, A. G., Pinho, V., & Teixeira, M. M. (2013). Resolution of inflammation: mechanisms and opportunity for drug development.



- Pharmacology and Therapeutics*, 139(2), 189-212.  
<https://doi.org/10.1016/j.pharmthera.2013.04.006>
- Alexis, N. E., Lay, J. C., Zeman, K., Bennett, W. E., Peden, D. B., Soukup, J. M.,...Becker, S. (2006). Biological material on inhaled coarse fraction particulate matter activates airway phagocytes in vivo in healthy volunteers. *Journal of Allergy and Clinical Immunology*, 117(6), 1396-1403.  
<https://doi.org/10.1016/j.jaci.2006.02.030>
- Alidousty, C., Baar, T., Martelotto, L. G., Heydt, C., Wagener, S., Fassunke, J.,...Schultheis, A. M. (2018). Genetic instability and recurrent MYC amplification in ALK-translocated NSCLC: a central role of TP53 mutations. *The Journal of Pathology*, 246(1), 67-76.  
<https://doi.org/https://doi.org/10.1002/path.5110>
- Allard, B., Panariti, A., & Martin, J. G. (2018). Alveolar Macrophages in the Resolution of Inflammation, Tissue Repair, and Tolerance to Infection [Mini Review]. *Frontiers in Immunology*, 9.
- Allen, J. L., Liu, X., Pelkowski, S., Palmer, B., Conrad, K., Oberdörster, G.,...Cory-Slechta, D. A. (2014). Early postnatal exposure to ultrafine particulate matter air pollution: persistent ventriculomegaly, neurochemical disruption, and glial activation preferentially in male mice. *Environmental Health Perspectives*, 122(9), 939-945.  
<https://doi.org/10.1289/ehp.1307984>
- Allen, J. L., Liu, X., Weston, D., Prince, L., Oberdörster, G., Finkelstein, J. N.,...Cory-Slechta, D. A. (2014). Developmental exposure to concentrated ambient ultrafine particulate matter air pollution in mice results in persistent and sex-dependent behavioral neurotoxicity and glial activation. *Toxicological Sciences*, 140(1), 160-178.  
<https://doi.org/10.1093/toxsci/kfu059>
- Amakawa, K., Terashima, T., Matsuzaki, T., Matsumaru, A., Sagai, M., & Yamaguchi, K. (2003). SUPPRESSIVE EFFECTS OF DIESEL EXHAUST PARTICLES ON CYTOKINE RELEASE FROM HUMAN AND MURINE ALVEOLAR MACROPHAGES. *Experimental Lung*

- Research*, 29(3), 149-164.  
<https://doi.org/10.1080/01902140303770>
- Amann, M., Cofala, J., Klimot, Z., Nagl, C., & Schieder, W. (2018). Measures to Address Air Pollution from Small Combustion Sources. In: International Institute for Applied Systems Analysis (IIASA); Laxenburg, Austria.
- Ambroz, A., Vlkova, V., Rossner, P., Rossnerova, A., Svecova, V., Milcova, A.,...Sram, R. J. (2016). Impact of air pollution on oxidative DNA damage and lipid peroxidation in mothers and their newborns. *International Journal of Hygiene and Environmental Health*, 219(6), 545-556.  
<https://doi.org/10.1016/j.ijheh.2016.05.010>
- Amor, S., Puentes, F., Baker, D., & van der Valk, P. (2010). Inflammation in neurodegenerative diseases. *Immunology*, 129(2), 154-169. <https://doi.org/10.1111/j.1365-2567.2009.03225.x>
- An, J. L., Wang, Y. S., Li, X., Sun, Y., & Shen, S. H. (2008). Relationship between surface UV radiation and air pollution in Beijing. *Huan jing ke xue= Huanjing kexue*, 29(4), 1053-1058.
- Anbari, K., Khaniabadi, Y. O., Sicard, P., Naqvi, H. R., & Rashidi, R. (2022). Increased tropospheric ozone levels as a public health issue during COVID-19 lockdown and estimation the related pulmonary diseases. *Atmospheric Pollution Research*, 13(12), 101600.  
<https://doi.org/https://doi.org/10.1016/j.apr.2022.101600>
- Anenberg, S. C., Moheggh, A., Goldberg, D. L., Kerr, G. H., Brauer, M., Burkart, K.,...Lamsal, L. (2022). Long-term trends in urban NO<sub>2</sub> concentrations and associated paediatric asthma incidence: estimates from global datasets. *The Lancet Planetary Health*, 6(1), e49-e58. [https://doi.org/10.1016/S2542-5196\(21\)00255-2](https://doi.org/10.1016/S2542-5196(21)00255-2)
- Angelis, N., Porpodis, K., Zarogoulidis, P., Spyratos, D., Kioumis, I., Papaiwannou, A.,...Zarogoulidis, K. (2014). Airway inflammation in chronic obstructive pulmonary disease. *Journal of Thoracic Disease; Vol 6, Supplement 1 (March 24, 2014): Journal of Thoracic Disease*

*(Cardiothoracic diseases closely related from diagnosis to treatment).*

ANSES. (2019). *Health effects according to components, sources and particle size impact on air pollution of the technologies and composition of the motor vehicle fleet operating in France.*

Armstrong, L., Jordan, N., & Millar, A. (1996). Interleukin 10 (IL-10) regulation of tumour necrosis factor alpha (TNF-alpha) from human alveolar macrophages and peripheral blood monocytes. *Thorax*, 51(2), 143. <https://doi.org/10.1136/thx.51.2.143>

Arredouani, M. S., Yang, Z., Imrich, A., Ning, Y., Qin, G., & Kobzik, L. (2006). The macrophage scavenger receptor SR-AI/II and lung defense against pneumococci and particles. *American Journal of Respiratory Cell and Molecular Biology*, 35(4), 474-478. <https://doi.org/10.1165/rcmb.2006-0128OC>

Arroyo, C., & Carmichael, A. (1997). Role of cytokine and nitric oxide in the inflammatory response produced by sulfur mustard (HD) [10.1039/A702508D]. *Journal of the Chemical Society, Perkin Transactions 2*(12), 2495-2500. <https://doi.org/10.1039/A702508D>

ATCC. (2024a). *NCI-H441 [H441]*. Retrieved 05 February 2024 from <https://www.atcc.org/products/htb-174>

ATCC. (2024b). *THP-1*. Retrieved 4 February 2024 from <https://www.atcc.org/products/tib-202>

Atkinson, R. W., Anderson, H. R., Sunyer, J., Ayres, J., Baccini, M., Vonk, J. M.,...Katsouyanni, K. (2001). Acute effects of particulate air pollution on respiratory admissions: results from APHEA 2 project. Air Pollution and Health: a European Approach. *American Journal of Respiratory and Critical Care Medicine*, 164(10 Pt 1), 1860-1866. <https://doi.org/10.1164/ajrccm.164.10.2010138>

Avelar-Freitas, B. A., Almeida, V. G., Pinto, M. C. X., Mourão, F. A. G., Massensini, A. R., Martins-Filho, O. A.,...Brito-Melo, G. E. A. (2014). Trypan blue exclusion assay by flow cytometry. *Brazilian journal of medical and biological*

- research, 47(4), 307-315. <https://doi.org/10.1590/1414-431X20143437>
- Ayres, J., G. (1997). Trends in air quality in the UK. *Allergy*, 52, 7-13.
- Ayyagari, V. N., Januszkiewicz, A., & Nath, J. (2004). Pro-inflammatory responses of human bronchial epithelial cells to acute nitrogen dioxide exposure. *Toxicology*, 197(2), 148-163.  
<https://doi.org/https://doi.org/10.1016/j.tox.2003.12.017>
- Ayyagari, V. N., Januszkiewicz, A., & Nath, J. (2007). Effects of Nitrogen Dioxide on the Expression of Intercellular Adhesion Molecule-1, Neutrophil Adhesion, and Cytotoxicity: Studies in Human Bronchial Epithelial Cells. *Inhalation Toxicology*, 19(2), 181-194.  
<https://doi.org/10.1080/08958370601052121>
- Baan, R., Straif, K., Grosse, Y., Secretan, B., El Ghissassi, F., & Coglianò, V. (2006). Carcinogenicity of carbon black, titanium dioxide, and talc. *The Lancet Oncology*, 7(4), 295-296. [https://doi.org/10.1016/S1470-2045\(06\)70651-9](https://doi.org/10.1016/S1470-2045(06)70651-9)
- Babicki, S., Arndt, D., Marcu, A., Liang, Y., Grant, J. R., Maciejewski, A., & Wishart, D. S. (2016). Heatmapper: web-enabled heat mapping for all. *Nucleic Acids Research*, 44(W1), W147-W153. <https://doi.org/10.1093/nar/gkw419>
- Baglòle, C. J., Ray, D. M., Bernstein, S. H., Feldon, S. E., Smith, T. J., Sime, P. J., & Phipps, R. P. (2006). More than structural cells, fibroblasts create and orchestrate the tumor microenvironment. *Immunological Investigations*, 35(3-4), 297-325. <https://doi.org/10.1080/08820130600754960>
- Bahadar, H., Maqbool, F., Niaz, K., & Abdollahi, M. (2016). Toxicity of Nanoparticles and an Overview of Current Experimental Models. *Iran Biomed J*, 20(1), 1-11. <https://doi.org/10.7508/ibj.2016.01.001>
- Bals, R., Wang, X., Zasloff, M., & Wilson, J. M. (1998). The peptide antibiotic LL-37/hCAP-18 is expressed in epithelia of the human lung where it has broad antimicrobial activity at the airway surface. *Proceedings of the National Academy*

- of Sciences of the United States of America*, 95(16), 9541-9546. <https://doi.org/10.1073/pnas.95.16.9541>
- Bannuscher, A., Schmid, O., Drasler, B., Rohrbasser, A., Braakhuis, H. M., Meldrum, K.,...Rothen-Rutishauser, B. (2022). An inter-laboratory effort to harmonize the cell-delivered in vitro dose of aerosolized materials. *NanoImpact*, 28, 100439. <https://doi.org/https://doi.org/10.1016/j.impact.2022.100439>
- Bargner, W. R., & Garrett, W. D. (1970). Surface Active Organic Material in the Marine Atmosphere. *Journal of Geophysical Research*, 75(24), 5.
- Barnes, P. J. (2004). Alveolar Macrophages as Orchestrators of COPD. *COPD: Journal of Chronic Obstructive Pulmonary Disease*, 1(1), 59-70. <https://doi.org/10.1081/COPD-120028701>
- Barnum, K. J., & O'Connell, M. J. (2014). Cell cycle regulation by checkpoints. *Methods Mol Biol*, 1170, 29-40. [https://doi.org/10.1007/978-1-4939-0888-2\\_2](https://doi.org/10.1007/978-1-4939-0888-2_2)
- Bateman, D. N. (2012). Carbon monoxide. *Medicine*, 40(3), 115-116. <https://doi.org/10.1016/j.mpmed.2011.12.003>
- Bauer, H., Kasper-Giebl, A., Zibuschka, F., Hitzenberger, R., Kraus, G. F., & Puxbaum, H. (2002). Determination of the carbon content of airborne fungal spores. *Analytical Chemistry*, 74(1), 91-95. <https://doi.org/10.1021/ac010331>+
- Bauer, R. N., Müller, L., Brighton, L. E., Duncan, K. E., & Jaspers, I. (2014). Interaction with Epithelial Cells Modifies Airway Macrophage Response to Ozone. *American Journal of Respiratory Cell and Molecular Biology*, 52(3), 285-294. <https://doi.org/10.1165/rcmb.2014-0035OC>
- Bayram, H., Rusznak, C., Khair, O. A., Sapsford, R. J., & Abdelaziz, M. M. (2002). Effect of ozone and nitrogen dioxide on the permeability of bronchial epithelial cell cultures of non-asthmatic and asthmatic subjects. *Clinical & Experimental Allergy*, 32(9), 1285-1292.

<https://doi.org/https://doi.org/10.1046/j.1365-2745.2002.01435.x>

- Beamer, C. A., & Holian, A. (2005). Scavenger receptor class A type I/II (CD204) null mice fail to develop fibrosis following silica exposure. *American Journal of Physiology. Lung Cellular and Molecular Physiology*, 289(2), L186-195. <https://doi.org/10.1152/ajplung.00474.2004>
- Beck-Speier, I., Dayal, N., Karg, E., Maier, K. L., Schumann, G., Schulz, H.,...Heyder, J. (2005). Oxidative stress and lipid mediators induced in alveolar macrophages by ultrafine particles. *Free Radical Biology and Medicine*, 38(8), 1080-1092. <https://doi.org/https://doi.org/10.1016/j.freeradbiomed.2005.01.004>
- Becker, S., Dailey, L., Soukup, J. M., Silbajoris, R., & Devlin, R. B. (2005). TLR-2 is involved in airway epithelial cell response to air pollution particles. *Toxicology and Applied Pharmacology*, 203(1), 45-52. <https://doi.org/10.1016/j.taap.2004.07.007>
- Becker, S., & Soukup, J. (2003). Coarse(PM 2.5-10 ), Fine(PM 2.5 ), and Ultrafine Air Pollution Particles Induce/Increase Immune Costimulatory Receptors on Human Blood-Derived Monocytes but not on Alveolar Macrophages. *Journal of Toxicology and Environmental Health, Part A*, 66(9), 847-859. <https://doi.org/10.1080/15287390306381>
- Becker, S., Soukup, J. M., Sioutas, C., & Cassee, F. R. (2003). RESPONSE OF HUMAN ALVEOLAR MACROPHAGES TO ULTRAFINE, FINE, AND COARSE URBAN AIR POLLUTION PARTICLES. *Experimental Lung Research*, 29(1), 29-44. <https://doi.org/10.1080/01902140303762>
- Beelen, R., Raaschou-Nielsen, O., Stafoggia, M., Andersen, Z. J., Weinmayr, G., Hoffmann, B.,...Hoek, G. (2014). Effects of long-term exposure to air pollution on natural-cause mortality: an analysis of 22 European cohorts within the multicentre ESCAPE project. *The Lancet*, 383(9919), 785-795. [https://doi.org/10.1016/S0140-6736\(13\)62158-3](https://doi.org/10.1016/S0140-6736(13)62158-3)



- Behera, S. N., Sharma, M., Aneja, V. P., & Balasubramanian, R. (2013). Ammonia in the atmosphere: a review on emission sources, atmospheric chemistry and deposition on terrestrial bodies. *Environmental Science and Pollution Research*, 20(11), 8092-8131. <https://doi.org/10.1007/s11356-013-2051-9>
- Bell, M. L., & Davis, D. L. (2001). Reassessment of the lethal London fog of 1952: novel indicators of acute and chronic consequences of acute exposure to air pollution. *Environmental Health Perspective*, 109 Suppl 3, 389-394. <https://doi.org/10.1289/ehp.01109s3389>
- Bendtsen, K. M., Gren, L., Malmborg, V. B., Shukla, P. C., Tunér, M., Essig, Y. J.,...Vogel, U. B. (2020). Particle characterization and toxicity in C57BL/6 mice following instillation of five different diesel exhaust particles designed to differ in physicochemical properties. *Particle and Fibre Toxicology*, 17(1), 38. <https://doi.org/10.1186/s12989-020-00369-9>
- Bengtson, S., Kling, K., Madsen, A. M., Noergaard, A. W., Jacobsen, N. R., Clausen, P. A.,...Vogel, U. (2016). No cytotoxicity or genotoxicity of graphene and graphene oxide in murine lung epithelial FE1 cells in vitro. *Environmental and Molecular Mutagenesis*, 57(6), 469-482. <https://doi.org/https://doi.org/10.1002/em.22017>
- Bhatnagar, A. (2017). Environmental Determinants of Cardiovascular Disease. *Circulation Research*, 121(2), 162-180. <https://doi.org/10.1161/CIRCRESAHA.117.306458>
- Bhattacharya, J., & Westphalen, K. (2016). Macrophage-epithelial interactions in pulmonary alveoli. *Seminars in Immunopathology*, 38(4), 461-469. <https://doi.org/10.1007/s00281-016-0569-x>
- Bhattacharya, K., Mukherjee, S. P., Gallud, A., Burkert, S. C., Bistarelli, S., Bellucci, S.,...Fadeel, B. (2016). Biological interactions of carbon-based nanomaterials: From coronation to degradation. *Nanomedicine*:

- Nanotechnology, Biology and Medicine*, 12(2), 333-351.  
<https://doi.org/https://doi.org/10.1016/j.nano.2015.11.011>
- Blank, F., Rothen-Rutishauser, B., & Gehr, P. (2007). Dendritic Cells and Macrophages Form a Transepithelial Network against Foreign Particulate Antigens. *American Journal of Respiratory Cell and Molecular Biology*, 36(6), 669-677.  
<https://doi.org/10.1165/rcmb.2006-0234OC>
- Bleecker, M. L. (2015). Chapter 12 - Carbon monoxide intoxication. In M. Lotti & M. L. Bleecker (Eds.), *Handbook of Clinical Neurology* (Vol. 131, pp. 191-203). Elsevier. <https://doi.org/https://doi.org/10.1016/B978-0-444-62627-1.00024-X>
- Blomberg, A., Krishna, M. T., Bocchino, V., Biscione, G. L., Shute, J. K., Kelly, F. J.,...Sandström, T. (1997). The Inflammatory Effects of 2 ppm NO<sub>2</sub> on the Airways of Healthy Subjects. *American Journal of Respiratory and Critical Care Medicine*, 156(2), 418-424.  
<https://doi.org/10.1164/ajrccm.156.2.9612042>
- Bormann, T., Maus, R., Stolper, J., Tort Tarrés, M., Brandenberger, C., Wedekind, D.,...Maus, U. A. (2022). Role of matrix metalloprotease-2 and MMP-9 in experimental lung fibrosis in mice. *Respiratory Research*, 23(1), 180. <https://doi.org/10.1186/s12931-022-02105-7>
- Bosson, J. A., Mudway, I. S., & Sandström, T. (2019). Traffic-related Air Pollution, Health, and Allergy: The Role of Nitrogen Dioxide. *American Journal of Respiratory and Critical Care Medicine*, 200(5), 523-524.  
<https://doi.org/10.1164/rccm.201904-0834ED>
- Braun-Fahrländer, C., Vuille, J. C., Sennhauser, F. H., Neu, U., Künzle, T., Grize, L.,...Wüthrich, B. (1997). Respiratory health and long-term exposure to air pollutants in Swiss schoolchildren. SCARPOL Team. Swiss Study on Childhood Allergy and Respiratory Symptoms with Respect to Air Pollution, Climate and Pollen. *American Journal of Respiratory and Critical Care Medicine*, 155(3), 1042-1049. <https://doi.org/10.1164/ajrccm.155.3.9116984>



- Breznan, D., Goegan, P., Chauhan, V., Karthikeyan, S., Kumarathasan, P., Cakmak, S.,...Vincent, R. (2013). Respiratory burst in alveolar macrophages exposed to urban particles is not a predictor of cytotoxicity. *Toxicology in Vitro*, 27(4), 1287-1297.  
<https://doi.org/https://doi.org/10.1016/j.tiv.2013.02.014>
- Brook, R. D., Franklin, B., Cascio, W., Hong, Y., Howard, G., Lipsett, M.,...Association, E. P. o. P. a. P. S. o. t. A. H. (2004). Air pollution and cardiovascular disease: a statement for healthcare professionals from the Expert Panel on Population and Prevention Science of the American Heart Association. *Circulation*, 109(21), 2655-2671.  
<https://doi.org/10.1161/01.CIR.0000128587.30041.C8>
- Brookes, O., Boland, S., Lai Kuen, R., Miremont, D., Movassat, J., & Baeza-Squiban, A. (2021). Co-culture of type I and type II pneumocytes as a model of alveolar epithelium. *PLOS ONE*, 16(9), e0248798.  
<https://doi.org/10.1371/journal.pone.0248798>
- Brooks, E. R., & Wallingford, J. B. (2014). Multiciliated cells. *Current Biology*, 24(19), R973-982.  
<https://doi.org/10.1016/j.cub.2014.08.047>
- Brown, D. M., Donaldson, K., Borm, P. J., Schins, R. P., Dehnhardt, M., Gilmour, P.,...Stone, V. (2004). Calcium and ROS-mediated activation of transcription factors and TNF-alpha cytokine gene expression in macrophages exposed to ultrafine particles. *American Journal of Physiology. Lung Cellular and Molecular Physiology*, 286(2), L344-353.  
<https://doi.org/10.1152/ajplung.00139.2003>
- Brunekreef, B., & Holgate, S. T. (2002). Air pollution and health. *The Lancet*, 360(9341), 1233-1242.  
[https://doi.org/10.1016/S0140-6736\(02\)11274-8](https://doi.org/10.1016/S0140-6736(02)11274-8)
- Brunekreef, B., Strak, M., Chen, J., Andersen, Z., Atkinson, R., Bauwelinck, M.,...Hoek, G. (2021). *Mortality and Morbidity Effects of Long Term Exposure to Low-Level*

*PM2.5, BC, NO2, and O3: An Analysis of European Cohorts in the ELAPSE Project.* H. E. Institute.

- Bucki, R., & Janmey, P. A. (2006). Interaction of the gelsolin-derived antibacterial PBP 10 peptide with lipid bilayers and cell membranes. *Antimicrobial Agents and Chemotherapy*, 50(9), 2932-2940. <https://doi.org/10.1128/AAC.00134-06>
- Bumb, R. R., Crummett, W. B., Cutie, S. S., Gledhill, J. R., Hummel, R. H., Kagel, R. O.,...Woods, J. S. (1980). Trace chemistries of fire: a source of chlorinated dioxins. *Science*, 210(4468), 385-390. <https://doi.org/10.1126/science.6159682>
- Burge, H. A., & Rogers, C. A. (2000). Outdoor allergens. *Environmental Health Perspectives*, 108 Suppl 4, 653-659. <https://doi.org/10.1289/ehp.00108s4653>
- Buttacavoli, M., Di Cara, G., Roz, E., Pucci-Minafra, I., Feo, S., & Cancemi, P. (2021). Integrated Multi-Omics Investigations of Metalloproteinases in Colon Cancer: Focus on MMP2 and MMP9. *International Journal of Molecular Sciences*, 22(22).
- Button, B., Cai, L. H., Ehre, C., Kesimer, M., Hill, D. B., Sheehan, J. K.,...Rubinstein, M. (2012). A periciliary brush promotes the lung health by separating the mucus layer from airway epithelia. *Science*, 337(6097), 937-941. <https://doi.org/10.1126/science.1223012>
- Byrne, A. J., Jones, C. P., Gowers, K., Rankin, S. M., & Lloyd, C. M. (2013). Lung Macrophages Contribute to House Dust Mite Driven Airway Remodeling via HIF-1 $\alpha$ . *PLOS ONE*, 8(7), e69246. <https://doi.org/10.1371/journal.pone.0069246>
- Canning, P., Sorrell, F. J., & Bullock, A. N. (2015). Structural basis of Keap1 interactions with Nrf2. *Free Radical Biology and Medicine*, 88(Pt B), 101-107. <https://doi.org/10.1016/j.freeradbiomed.2015.05.034>
- Cao, X., Lintelmann, J., Padoan, S., Bauer, S., Huber, A., Mudan, A.,...Zimmermann, R. (2021). Adenine derivatization for LC-MS/MS epigenetic DNA modifications studies on monocytic THP-1 cells exposed to reference particulate

- matter. *Analytical Biochemistry*, 618, 114127.  
<https://doi.org/https://doi.org/10.1016/j.ab.2021.114127>
- Capaldo, C. T., & Nusrat, A. (2009). Cytokine regulation of tight junctions. *Biochimica et Biophysica Acta (BBA) - Biomembranes*, 1788(4), 864-871.  
<https://doi.org/https://doi.org/10.1016/j.bbamem.2008.08.027>
- Caraballo, J. C., Yshii, C., Westphal, W., Moninger, T., & Comellas, A. P. (2011). Ambient particulate matter affects occludin distribution and increases alveolar transepithelial electrical conductance. *Respirology*, 16(2), 340-349.  
<https://doi.org/https://doi.org/10.1111/j.1440-1843.2010.01910.x>
- Carey, I. M., Atkinson, R. W., Kent, A. J., van Staa, T., Cook, D. G., & Anderson, H. R. (2013). Mortality associations with long-term exposure to outdoor air pollution in a national English cohort. *American Journal of Respiratory and Critical Care Medicine*, 187(11), 1226-1233.  
<https://doi.org/10.1164/rccm.201210-1758OC>
- Carius, P., Jungmann, A., Bechtel, M., Grißmer, A., Boese, A., Gasparoni, G.,...Lehr, C.-M. (2023). A Monoclonal Human Alveolar Epithelial Cell Line (“Arlo”) with Pronounced Barrier Function for Studying Drug Permeability and Viral Infections. *Advanced Science*, 10(8), 2207301.  
<https://doi.org/https://doi.org/10.1002/advs.202207301>
- Carlsen, H. K., Valdimarsdóttir, U., Briem, H., Dominici, F., Finnbjornsdottir, R. G., Jóhannsson, T.,...Gudnason, T. (2021). Severe volcanic SO<sub>2</sub> exposure and respiratory morbidity in the Icelandic population – a register study. *Environmental Health*, 20(1), 23.  
<https://doi.org/10.1186/s12940-021-00698-y>
- Carslaw, D. C. (2005). Evidence of an increasing NO<sub>2</sub>/NO<sub>x</sub> emissions ratio from road traffic emissions. *Atmospheric Environment*, 39(26), 4793-4802.  
<https://doi.org/https://doi.org/10.1016/j.atmosenv.2005.06.023>

- Cass, S. P., Mekhael, O., Thayaparan, D., McGrath, J. J. C., Revill, S. D., Fantauzzi, M. F.,...Ask, K. (2021). Increased Monocyte-Derived CD11b+ Macrophage Subpopulations Following Cigarette Smoke Exposure Are Associated With Impaired Bleomycin-Induced Tissue Remodelling [Original Research]. *Frontiers in Immunology*, 12.
- Cassee, F. R., Héroux, M.-E., Gerlofs-Nijland, M. E., & Kelly, F. J. (2013). Particulate matter beyond mass: recent health evidence on the role of fractions, chemical constituents and sources of emission. *Inhalation Toxicology*, 25(14), 802-812. <https://doi.org/10.3109/08958378.2013.850127>
- Castell, J. V., Donato, M. T., & Gómez-Lechón, M. J. (2005). Metabolism and bioactivation of toxicants in the lung. The in vitro cellular approach. *Experimental and Toxicologic Pathology*, 57 Suppl 1, 189-204. <https://doi.org/10.1016/j.etp.2005.05.008>
- Catalá, A., & Díaz, M. (2016). Editorial: Impact of Lipid Peroxidation on the Physiology and Pathophysiology of Cell Membranes. *Frontiers in Physiology*, 7, 423. <https://doi.org/10.3389/fphys.2016.00423>
- Cesaroni, G., Forastiere, F., Stafoggia, M., Andersen, Z. J., Badaloni, C., Beelen, R.,...Peters, A. (2014). Long term exposure to ambient air pollution and incidence of acute coronary events: prospective cohort study and meta-analysis in 11 European cohorts from the ESCAPE Project. *The British Medical Journal*, 348, f7412. <https://doi.org/10.1136/bmj.f7412>
- Chao, X., Yi, L., Lan, L. L., Wei, H. Y., & Wei, D. (2020). Long-term PM(2.5) exposure increases the risk of non-small cell lung cancer (NSCLC) progression by enhancing interleukin-17a (IL-17a)-regulated proliferation and metastasis. *Aging (Albany NY)*, 12(12), 11579-11602. <https://doi.org/10.18632/aging.103319>
- Charlson, R. J., Lovelockt, J. E., Andreae, M. O., & Warren, S. G. (1987). Oceanic phytoplankton, atmospheric sulphur, cloud albedo and climate *Nature*, 326, 655 – 661.

- Chen, B. Y., Chan, C. C., Lee, C. T., Cheng, T. J., Huang, W. C., Jhou, J. C.,...Guo, Y. L. (2012). The association of ambient air pollution with airway inflammation in schoolchildren. *American Journal of Epidemiology*, 175(8), 764-774. <https://doi.org/10.1093/aje/kwr380>
- Chen, H., & Wang, D. (2004). Nitric Oxide Inhibits Matrix Metalloproteinase-2 Expression via the Induction of Activating Transcription Factor 3 in Endothelial Cells. *Molecular Pharmacology*, 65(5), 1130. <https://doi.org/10.1124/mol.65.5.1130>
- Chen, S., Zhao, M., Wu, G., Yao, C., & Zhang, J. (2012). Recent Advances in Morphological Cell Image Analysis. *Computational and Mathematical Methods in Medicine*, 2012, 101536. <https://doi.org/10.1155/2012/101536>
- Chen, T.-M., Kuschner, W. G., Gokhale, J., & Shofer, S. (2007). Outdoor Air Pollution: Nitrogen Dioxide, Sulfur Dioxide, and Carbon Monoxide Health Effects. *The American Journal of the Medical Sciences*, 333(4), 249-256. <https://doi.org/10.1097/MAJ.0b013e31803b900f>
- Chen, Y., Shen, G., Huang, Y., Zhang, Y., Han, Y., Wang, R.,...Tao, S. (2016). Household air pollution and personal exposure risk of polycyclic aromatic hydrocarbons among rural residents in Shanxi, China. *Indoor Air*, 26(2), 246-258. <https://doi.org/10.1111/ina.12204>
- Cheng, Y., Xu, L., Wang, J., Cao, X., Chen, D., Zhang, P.,...Qin, L. (2023). Analysis of bulk RNA-seq data from sepsis patients reveals sepsis-associated lncRNAs and targeted cell death-related genes contributing to immune microenvironment regulation [Original Research]. *Frontiers in Immunology*, 14.
- Cherng, T. W., Paffett, M. L., Jackson-Weaver, O., Campen, M. J., Walker, B. R., & Kanagy, N. L. (2011). Mechanisms of diesel-induced endothelial nitric oxide synthase dysfunction in coronary arterioles. *Environmental Health Perspectives*, 119(1), 98-103. <https://doi.org/10.1289/ehp.1002286>

- Cienciewicki, J., Gowdy, K., Krantz, Q. T., Linak, W. P., Brighton, L., Gilmour, M. I., & Jaspers, I. (2007). Diesel Exhaust Enhanced Susceptibility to Influenza Infection is Associated with Decreased Surfactant Protein Expression. *Inhalation Toxicology*, 19(14), 1121-1133. <https://doi.org/10.1080/08958370701665426>
- CMO. (2022). *Chief Medical Officer's Annual Report 2022 Air pollution*.
- COMEAP. (2015). Statement on the Evidence for the Effects of Nitrogen Dioxide on Health. In: Committee on the Medical Effects of Air Pollution.
- COMEAP. (2018). *Associations of long-term average concentrations of nitrogen dioxide with mortality*. Retrieved from <https://www.gov.uk/government/publications/nitrogen-dioxide-effects-on-mortality>
- COMEAP. (2022). *Statement on the differential toxicity of particulate matter according to source or constituents: 2022*. Retrieved 25 January 2024 from <https://www.gov.uk/government/publications/particulate-air-pollution-health-effects-of-exposure/statement-on-the-differential-toxicity-of-particulate-matter-according-to-source-or-constituents-2022>
- Conti, S., Harari, S., Caminati, A., Zanobetti, A., Schwartz, Joel D., Bertazzi, P. A.,...Madotto, F. (2018). The association between air pollution and the incidence of idiopathic pulmonary fibrosis in Northern Italy. *European Respiratory Journal*, 51(1), 1700397. <https://doi.org/10.1183/13993003.00397-2017>
- Costa, A., de Souza Carvalho-Wodarz, C., Seabra, V., Sarmento, B., & Lehr, C.-M. (2019). Triple co-culture of human alveolar epithelium, endothelium and macrophages for studying the interaction of nanocarriers with the air-blood barrier. *Acta Biomaterialia*, 91, 235-247. <https://doi.org/https://doi.org/10.1016/j.actbio.2019.04.037>



- Crapo, J. D., Barry, B. E., Gehr, P., Bachofen, M., & Weibel, E. R. (1982). Cell number and cell characteristics of the normal human lung. *The American Review of Respiratory Disease*, 126(2), 332-337. <https://doi.org/10.1164/arrd.1982.126.2.332>
- Danielsen, P. H., Møller, P., Jensen, K. A., Sharma, A. K., Wallin, H., Bossi, R.,...Loft, S. (2011). Oxidative Stress, DNA Damage, and Inflammation Induced by Ambient Air and Wood Smoke Particulate Matter in Human A549 and THP-1 Cell Lines. *Chemical Research in Toxicology*, 24(2), 168-184. <https://doi.org/10.1021/tx100407m>
- David, E., & Niculescu, V.-C. (2021). Volatile Organic Compounds (VOCs) as Environmental Pollutants: Occurrence and Mitigation Using Nanomaterials. *International Journal of Environmental Research and Public Health*, 18(24).
- de Boer, W. I., Sharma, H. S., Baelemans, S. M. I., Hoogsteden, H. C., Lambrecht, B. N., & Braunstahl, G. J. (2008). Altered expression of epithelial junctional proteins in atopic asthma: possible role in inflammation. *Canadian Journal of Physiology and Pharmacology*, 86(3), 105-112. <https://doi.org/10.1139/Y08-004>
- de Jong, P. M., van Sterkenburg, M. A., Hesselink, S. C., Kempenaar, J. A., Mulder, A. A., Mommaas, A. M.,...Ponc, M. (1994). Ciliogenesis in human bronchial epithelial cells cultured at the air-liquid interface. *American Journal of Respiratory Cell and Molecular Biology*, 10(3), 271-277. <https://doi.org/10.1165/ajrcmb.10.3.8117445>
- de Souza, A. R., Zago, M., Eidelman, D. H., Hamid, Q., & Bagloli, C. J. (2014). Aryl hydrocarbon receptor (AhR) attenuation of subchronic cigarette smoke-induced pulmonary neutrophilia is associated with retention of nuclear RelB and suppression of intercellular adhesion molecule-1 (ICAM-1). *Toxicological Sciences*, 140(1), 204-223. <https://doi.org/10.1093/toxsci/kfu068>

- DEFRA. (2019). *Clean Air Strategy*. Retrieved from <https://www.gov.uk/government/publications/clean-air-strategy-2019>
- DEFRA. (2020). *Air quality: using cleaner fuels for domestic burning. Summary of responses and government response*. <https://www.gov.uk/government/consultations/air-quality-using-cleaner-fuels-for-domestic-burning/outcome/summary-of-responses-and-government-response>
- DEFRA. (2023a). *Air Pollution in the UK 2022*.
- DEFRA. (2023b). Emissions of air pollutants in the UK – Sulphur dioxide (SO<sub>2</sub>). In.
- DEFRA. (2023c). *Ozone (O<sub>3</sub>)*. Retrieved 25 January 2024 from <https://www.gov.uk/government/statistics/air-quality-statistics/concentrations-of-ozone>
- DEFRA. (2024). *Graph of hourly measurements*. Retrieved 25 January 2024 from
- Deng, R., Chen, X., Zhang, Y., Bian, F., Gao, N., Hu, J.,...Li, D.-Q. (2019). Short ragweed pollen promotes M2 macrophage polarization via TSLP/TSLPR/OX40L signaling in allergic inflammation. *Mucosal Immunology*, 12(5), 1141-1149. <https://doi.org/10.1038/s41385-019-0187-8>
- Department for Transport, O. f. L. E. V., Department for Business, Energy & Industrial Strategy, The Rt Hon Alok Sharma MP, and The Rt Hon Grant Shapps MP. (2020). *Government takes historic step towards net-zero with end of sale of new petrol and diesel cars by 2030*.
- Devalia, J. L., Sapsford, R. J., Cundell, D. R., Rusznak, C., Campbell, A. M., & Davies, R. J. (1993). Human bronchial epithelial cell dysfunction following in vitro exposure to nitrogen dioxide. *European Respiratory Journal*, 6(9), 1308.
- Devendra, G., & Spragg, R. G. (2002). Lung surfactant in subacute pulmonary disease. *Respiratory Research*, 3(1), 11. <https://doi.org/10.1186/rr168>
- Di Ianni, E., Erdem, J. S., Møller, P., Sahlgren, N. M., Poulsen, S. S., Knudsen, K. B.,...Jacobsen, N. R. (2021). In vitro-in



- vivo correlations of pulmonary inflammogenicity and genotoxicity of MWCNT. *Particle and Fibre Toxicology*, 18(1), 25. <https://doi.org/10.1186/s12989-021-00413-2>
- Di Ianni, E., Jacobsen, N. R., Vogel, U. B., & Møller, P. (2022). Systematic review on primary and secondary genotoxicity of carbon black nanoparticles in mammalian cells and animals. *Mutation Research/Reviews in Mutation Research*, 790, 108441. <https://doi.org/https://doi.org/10.1016/j.mrrev.2022.108441>
- Diabaté, S., Mühlhopt, S., Paur, H.-R., & Krug, H. F. (2008). The Response of a Co-culture Lung Model to Fine and Ultrafine Particles of Incinerator Fly Ash at the Air–liquid Interface. *Alternatives to Laboratory Animals*, 36(3), 285-298. <https://doi.org/10.1177/026119290803600306>
- Diaz-Sanchez, D., Jyrala, M., Ng, D., Nel, A., & Saxon, A. (2000). In vivo nasal challenge with diesel exhaust particles enhances expression of the CC chemokines rantes, MIP-1alpha, and MCP-3 in humans. *Clinical Immunology*, 97(2), 140-145. <https://doi.org/10.1006/clim.2000.4921>
- Diaz-Sanchez, D., Tsien, A., Fleming, J., & Saxon, A. (1997). Combined diesel exhaust particulate and ragweed allergen challenge markedly enhances human in vivo nasal ragweed-specific IgE and skews cytokine production to a T helper cell 2-type pattern. *Journal of Immunology*, 158(5), 2406-2413.
- Ding, X., Zhang, X., Yang, Y., Ding, Y., Xue, W., Meng, Y.,... Yin, Z. (2014). Polymorphism, Expression of Natural Resistance-associated Macrophage Protein 1 Encoding Gene (NRAMP1) and Its Association with Immune Traits in Pigs. *Asian-Australas J Anim Sci*, 27(8), 1189-1195. <https://doi.org/10.5713/ajas.2014.14017>
- Ding, Y., Weindl, P., Lenz, A.-G., Mayer, P., Krebs, T., & Schmid, O. (2020). Quartz crystal microbalances (QCM) are suitable for real-time dosimetry in nanotoxicological studies using VITROCELL®Cloud cell exposure systems.

- Particle and Fibre Toxicology*, 17(1), 44.  
<https://doi.org/10.1186/s12989-020-00376-w>
- Donaldson, K., Brown, D. M., Mitchell, C., Dineva, M., Beswick, P. H., Gilmour, P., & MacNee, W. (1997). Free radical activity of PM10: iron-mediated generation of hydroxyl radicals. *Environmental Health Perspectives*, 105 Suppl 5, 1285-1289.  
<https://doi.org/10.1289/ehp.97105s51285>
- Douwes, J., Thorne, P., Pearce, N., & Heederik, D. (2003). Bioaerosol health effects and exposure assessment: progress and prospects. *Annals of Occupational Hygiene*, 47(3), 187-200. <https://doi.org/10.1093/annhyg/meg032>
- Drasler, B., Kucki, M., Delhaes, F., Buerki-Thurnherr, T., Vanhecke, D., Korejwo, D.,...Wick, P. (2018). Single exposure to aerosolized graphene oxide and graphene nanoplatelets did not initiate an acute biological response in a 3D human lung model. *Carbon*, 137, 125-135.  
<https://doi.org/https://doi.org/10.1016/j.carbon.2018.05.012>
- Drumm, K., Oettinger, R., Smolarski, R., Bay, M., & Kienast, K. (1998). In vitro study of human alveolar macrophages inflammatory mediator transcriptions and releases induced by soot FR 101, Printex 90, titandioxide and Chrysotile B. *European journal of medical research*, 3(9), 432-438.
- Dröge, W. (2002). Free radicals in the physiological control of cell function. *Physiological Reviews*, 82(1), 47-95.  
<https://doi.org/10.1152/physrev.00018.2001>
- Du, X., Jiang, S., Zeng, X., Zhang, J., Pan, K., Song, L.,...Xie, Y. (2019). Fine particulate matter-induced cardiovascular injury is associated with NLRP3 inflammasome activation in Apo E. *Ecotoxicology and Environmental Safety*, 174, 92-99. <https://doi.org/10.1016/j.ecoenv.2019.02.064>
- Duan, M., Steinfort, D. P., Smallwood, D., Hew, M., Chen, W., Ernst, M.,...Hibbs, M. L. (2016). CD11b immunophenotyping identifies inflammatory profiles in the mouse and human lungs. *Mucosal Immunology*, 9(2), 550-563. <https://doi.org/10.1038/mi.2015.84>

- Duffield, J. S., Forbes, S. J., Constandinou, C. M., Clay, S., Partolina, M., Vuthoori, S.,...Iredale, J. P. (2005). Selective depletion of macrophages reveals distinct, opposing roles during liver injury and repair. *The Journal of Clinical Investigation*, 115(1), 56-65. <https://doi.org/10.1172/JCI22675>
- Dumax-Vorzet, A. F., Tate, M., Walmsley, R., Elder, R. H., & Povey, A. C. (2015). Cytotoxicity and genotoxicity of urban particulate matter in mammalian cells. *Mutagenesis*, 30(5), 621-633. <https://doi.org/10.1093/mutage/gev025>
- Dvorak, A., Tilley, A. E., Shaykhiev, R., Wang, R., & Crystal, R. G. (2011). Do Airway Epithelium Air–Liquid Cultures Represent the In Vivo Airway Epithelium Transcriptome? *American Journal of Respiratory Cell and Molecular Biology*, 44(4), 465-473. <https://doi.org/10.1165/rcmb.2009-0453OC>
- Ebrahimi, H., Aryan, Z., Saeedi Moghaddam, S., Bisignano, C., Rezaei, S., Pishgar, F.,...Naghavi, M. (2021). Global, regional, and national burden of respiratory tract cancers and associated risk factors from 1990 to 2019: a systematic analysis for the Global Burden of Disease Study 2019. *The Lancet Respiratory Medicine*, 9(9), 1030-1049. [https://doi.org/10.1016/S2213-2600\(21\)00164-8](https://doi.org/10.1016/S2213-2600(21)00164-8)
- El-Shimy, W. S., El-Dib, A. S., Nagy, H. M., & Sabry, W. (2014). A study of IL-6, IL-8, and TNF- $\alpha$  as inflammatory markers in COPD patients. *Egyptian Journal of Bronchology*, 8(2), 91-99. <https://doi.org/10.4103/1687-8426.145698>
- Eleutherio, E. C. A., Silva Magalhães, R. S., de Araújo Brasil, A., Monteiro Neto, J. R., & de Holanda Paranhos, L. (2021). SOD1, more than just an antioxidant. *Archives of Biochemistry and Biophysics*, 697, 108701. <https://doi.org/https://doi.org/10.1016/j.abb.2020.108701>
- Environmental Agency. (2023). *State of the environment: health, people and the environment*. Retrieved 25 January 2024 from <https://www.gov.uk/government/publications/state-of-the-environment/state-of-the-environment-health-people-and-the-environment>

- Environmental Protection Agency. (2018). *Volatile Organic Compounds Emissions*. Retrieved 25 January 2024 from <https://cfpub.epa.gov/roe/indicator.cfm?i=23>
- Environmental Protection Agency. (2019). *Integrated Science Assessment (ISA) for Particulate Matter*.
- Environmental Protection Agency. (2023a). *Carbon Monoxide Trends*. Retrieved 25 January 2024 from
- Environmental Protection Agency. (2023b). *Volatile Organic Compounds' Impact on Indoor Air Quality*. Retrieved 25 January 2024 from <https://www.epa.gov/indoor-air-quality-iaq/volatile-organic-compounds-impact-indoor-air-quality>
- EPA. (2016). *Toxicological Review of Ammonia Noncancer Inhalation*.
- Erisman, J. W., & Schaap, M. (2004). The need for ammonia abatement with respect to secondary PM reductions in Europe. *Environmental Pollution*, 129(1), 159-163. <https://doi.org/https://doi.org/10.1016/j.envpol.2003.08.042>
- European Union. (2009). EC 1223/2009 OF THE EUROPEAN PARLIAMENT AND OF THE COUNCIL. In.
- Evans, M. J., Cabral, L. J., Stephens, R. J., & Freeman, G. (1975). Transformation of alveolar Type 2 cells to Type 1 cells following exposure to NO<sub>2</sub>. *Experimental and Molecular Pathology*, 22(1), 142-150. [https://doi.org/https://doi.org/10.1016/0014-4800\(75\)90059-3](https://doi.org/https://doi.org/10.1016/0014-4800(75)90059-3)
- Faber, S. C., & McCullough, S. D. (2018). Through the Looking Glass: In Vitro Models for Inhalation Toxicology and Interindividual Variability in the Airway. *Applied In Vitro Toxicology*, 4(2), 115-128. <https://doi.org/10.1089/aivt.2018.0002>
- Fagerholm, S. C., Guenther, C., Lloret Asens, M., Savinko, T., & Uotila, L. M. (2019). Beta2-Integrins and Interacting Proteins in Leukocyte Trafficking, Immune Suppression, and Immunodeficiency Disease [Mini Review]. *Frontiers in Immunology*, 10.

- Farina, F., Lonati, E., Brambilla, A., Dal Magro, R., Milani, C., Botto, L.,...Bulbarelli, A. (2017). Diesel exhaust particles (DEP) pre-exposure contributes to the anti-oxidant response impairment in hCMEC/D3 during post-oxygen and glucose deprivation damage. *Toxicology Letters*, 274, 1-7.  
[https://doi.org/https://doi.org/10.1016/j.toxlet.2017.04.003](https://doi.org/10.1016/j.toxlet.2017.04.003)
- Faustini, A., Rapp, R., & Forastiere, F. (2014). Nitrogen dioxide and mortality: review and meta-analysis of long-term studies. *European Respiratory Journal*, 44(3), 744.  
<https://doi.org/10.1183/09031936.00114713>
- Fischer, P. H., Marra, M., Ameling, C. B., Hoek, G., Beelen, R., de Hoogh, K.,...Houthuijs, D. (2015). Air Pollution and Mortality in Seven Million Adults: The Dutch Environmental Longitudinal Study (DUELS). *Environmental Health Perspective*, 123(7), 697-704.  
<https://doi.org/10.1289/ehp.1408254>
- Fonken, L. K., Xu, X., Weil, Z. M., Chen, G., Sun, Q., Rajagopalan, S., & Nelson, R. J. (2011). Air pollution impairs cognition, provokes depressive-like behaviors and alters hippocampal cytokine expression and morphology. *Molecular Psychiatry*, 16(10), 987-995, 973.  
<https://doi.org/10.1038/mp.2011.76>
- Frampton, M. W., Boscia, J., Roberts, N. J., Azadniv, M., Torres, A., Cox, C.,...Utell, M. J. (2002). Nitrogen dioxide exposure: effects on airway and blood cells. *American Journal of Physiology-Lung Cellular and Molecular Physiology*, 282(1), L155-L165.  
<https://doi.org/10.1152/ajplung.2002.282.1.L155>
- Freire, C., Ramos, R., Puertas, R., Lopez-Espinosa, M. J., Julvez, J., Aguilera, I.,...Olea, N. (2010). Association of traffic-related air pollution with cognitive development in children. *Journal of Epidemiology and Community Health*, 64(3), 223-228. <https://doi.org/10.1136/jech.2008.084574>
- Friberg, M., Behndig, A. F., Bosson, J. A., Muala, A., Barath, S., Dove, R.,...Pourazar, J. (2023). Human exposure to diesel exhaust induces CYP1A1 expression and AhR activation

- without a coordinated antioxidant response. *Particle and Fibre Toxicology*, 20(1), 47.  
<https://doi.org/10.1186/s12989-023-00559-1>
- Friesen, A., Fritsch-Decker, S., Hufnagel, M., Mülhopt, S., Stapf, D., Hartwig, A., & Weiss, C. (2022). Comparing  $\alpha$ -Quartz-Induced Cytotoxicity and Interleukin-8 Release in Pulmonary Mono- and Co-Cultures Exposed under Submerged and Air-Liquid Interface Conditions. *International Journal of Molecular Sciences*, 23(12).
- Fuller, R., Landrigan, P. J., Balakrishnan, K., Bathan, G., Bose-O'Reilly, S., Brauer, M.,...Yan, C. (2022). Pollution and health: a progress update. *The Lancet Planetary Health*, 6(6), e535-e547. [https://doi.org/10.1016/S2542-5196\(22\)00090-0](https://doi.org/10.1016/S2542-5196(22)00090-0)
- Furlong-Silva, J., & Cook, P. C. (2022). Fungal-mediated lung allergic airway disease: The critical role of macrophages and dendritic cells. *PLOS Pathogens*, 18(7), e1010608.  
<https://doi.org/10.1371/journal.ppat.1010608>
- Gairola, S., Sinha, A., & Kaundal, R. K. (2023). Linking NLRP3 inflammasome and pulmonary fibrosis: mechanistic insights and promising therapeutic avenues. *Inflammopharmacology*. <https://doi.org/10.1007/s10787-023-01389-5>
- Galve-de Rochemonteix, B., Nicod, L. P., & Dayer, J. M. (1996). Tumor necrosis factor soluble receptor 75: the principal receptor form released by human alveolar macrophages and monocytes in the presence of interferon gamma. *American Journal of Respiratory Cell and Molecular Biology*, 14(3), 279-287.  
<https://doi.org/10.1165/ajrcmb.14.3.8845179>
- Garn, H., Siese, A., Stumpf, S., Barth, P. J., Müller, B., & Gerns, D. (2003). Shift Toward an Alternatively Activated Macrophage Response in Lungs of NO<sub>2</sub>-Exposed Rats. *American Journal of Respiratory Cell and Molecular Biology*, 28(3), 386-396.  
<https://doi.org/10.1165/rcmb.4888>



- Garte, S., Gaspari, L., Alexandrie, A.-K., Ambrosone, C., Autrup, H., Autrup, J. L.,...Taioli, E. (2001). Metabolic Gene Polymorphism Frequencies in Control Populations<sup>1</sup>. *Cancer Epidemiology, Biomarkers & Prevention*, 10(12), 1239-1248.
- Gaudino, G., Xue, J., & Yang, H. (2020). How asbestos and other fibers cause mesothelioma. *Translational Lung Cancer Research; Vol 9, Supplement 1 (February 28, 2020): Translational Lung Cancer Research (Mesothelioma: What We know and What We Do Not Know in 2020)*.
- Ge, C., Peters, S., Olsson, A., Portengen, L., Schüz, J., Almansa, J.,...Vermeulen, R. (2020). Diesel Engine Exhaust Exposure, Smoking, and Lung Cancer Subtype Risks. A Pooled Exposure–Response Analysis of 14 Case–Control Studies. *American Journal of Respiratory and Critical Care Medicine*, 202(3), 402-411. <https://doi.org/10.1164/rccm.201911-2101OC>
- Gehring, U., Gruzieva, O., Agius, R. M., Beelen, R., Custovic, A., Cyrus, J.,...Brunekreef, B. (2013). Air pollution exposure and lung function in children: the ESCAPE project. *Environmental Health perspectives*, 121(11-12), 1357-1364. <https://doi.org/10.1289/ehp.1306770>
- Geiser, M. (2010). Update on Macrophage Clearance of Inhaled Micro- and Nanoparticles. *Journal of Aerosol Medicine and Pulmonary Drug Delivery*, 23(4), 207-217. <https://doi.org/10.1089/jamp.2009.0797>
- Gerloff, K., Albrecht, C., Boots, A. W., Förster, I., & Schins, R. P. F. (2009). Cytotoxicity and oxidative DNA damage by nanoparticles in human intestinal Caco-2 cells. *Nanotoxicology*, 3(4), 355-364. <https://doi.org/10.3109/17435390903276933>
- Ghio, A. J., Carraway, M. S., & Madden, M. C. (2012). Composition of air pollution particles and oxidative stress in cells, tissues, and living systems. *Journal of Toxicology and Environmental Health - Part B: Critical Reviews*, 15(1), 1-21. <https://doi.org/10.1080/10937404.2012.632359>

- Ghio, A. J., Soukup, J. M., & Madden, M. C. (2018). The toxicology of air pollution predicts its epidemiology. *Inhalation Toxicology*, 30(9-10), 327-334. <https://doi.org/10.1080/08958378.2018.1530316>
- Ginoux, P., Prospero, J., Gill, T., Hsu, N., & Zhao, M. (2012). Globalscale attribution of anthropogenic and natural dust sources and their emission rates based on modis deep blue aerosol products. *Reviews of Geophysics*, 50, RG3005. <https://doi.org/https://doi.org/10.1029/2012RG000388>
- Ginzinger, D. G. (2002). Gene quantification using real-time quantitative PCR: An emerging technology hits the mainstream. *Experimental Hematology*, 30(6), 503-512. [https://doi.org/https://doi.org/10.1016/S0301-472X\(02\)00806-8](https://doi.org/https://doi.org/10.1016/S0301-472X(02)00806-8)
- Gong, J., Zhu, T., Kipen, H., Wang, G., Hu, M., Guo, Q.,...Zhang, J. (2014). Comparisons of ultrafine and fine particles in their associations with biomarkers reflecting physiological pathways. *Environmental Science & Technology*, 48(9), 5264-5273. <https://doi.org/10.1021/es5006016>
- Gordon, S. B., Bruce, N. G., Grigg, J., Hibberd, P. L., Kurmi, O. P., Lam, K. B.,...Martin, W. J. (2014). Respiratory risks from household air pollution in low and middle income countries. *The Lancet Respiratory Medicine*, 2(10), 823-860. [https://doi.org/10.1016/S2213-2600\(14\)70168-7](https://doi.org/10.1016/S2213-2600(14)70168-7)
- Gordon, S. B., & Read, R. C. (2002). Macrophage defences against respiratory tract infections: The immunology of childhood respiratory infections. *British Medical Bulletin*, 61(1), 45-61. <https://doi.org/10.1093/bmb/61.1.45>
- Goto, Y., Ishii, H., Hogg, J. C., Shih, C. H., Yatera, K., Vincent, R., & van Eeden, S. F. (2004). Particulate matter air pollution stimulates monocyte release from the bone marrow. *American Journal of Respiratory and Critical Care Medicine*, 170(8), 891-897. <https://doi.org/10.1164/rccm.200402-235OC>



- Grashoff, W. F., Sont Jk Fau - Sterk, P. J., Sterk Pj Fau - Hiemstra, P. S., Hiemstra Ps Fau - de Boer, W. I., de Boer Wi Fau - Stolk, J., Stolk J Fau - Han, J.,...van Krieken, J. M. (1997). Chronic obstructive pulmonary disease: role of bronchiolar mast cells and macrophages. *The American Journal of Pathology*, 151(0002-9440 (Print)).
- Greater London Authority. (2022). *70 years since the great London smog*.
- Gren, L., Malmborg, V. B., Jacobsen, N. R., Shukla, P. C., Bendtsen, K. M., Eriksson, A. C.,...Pagels, J. (2020). Effect of Renewable Fuels and Intake O<sub>2</sub> Concentration on Diesel Engine Emission Characteristics and Reactive Oxygen Species (ROS) Formation. *Atmosphere*, 11(6).
- Grippi, M. A., Elias, J. A., Fishman, J. A., Kotloff, R. M., Pack, A. I., Senior, R. M., & Siegel, M. D. (2015). In *Fishman's Pulmonary Diseases and Disorders*, 5e. McGraw-Hill Education.
- Groneberg, D. A., Eynott, P. R., Oates, T., Lim, S., Wu, R., Carlstedt, I.,...Chung, K. F. (2002). Expression of MUC5AC and MUC5B mucins in normal and cystic fibrosis lung. *Respiratory Medicine*, 96(2), 81-86. <https://doi.org/10.1053/rmed.2001.1221>
- Gruber, D. R., Toner, J. J., Miears, H. L., Shernyukov, A. V., Kiryutin, A. S., Lomzov, A. A.,...Smirnov, S. L. (2018). Oxidative damage to epigenetically methylated sites affects DNA stability, dynamics and enzymatic demethylation. *Nucleic Acids Research*, 46(20), 10827-10839. <https://doi.org/10.1093/nar/gky893>
- Gu, Y., Lin, H., Liu, T., Xiao, J., Zeng, W., Li, Z.,...Ma, W. (2017). The Interaction between Ambient PM<sub>10</sub> and NO<sub>2</sub> on Mortality in Guangzhou, China. *International Journal of Environmental Research and Public Health*, 14(11). <https://doi.org/10.3390/ijerph14111381>
- Guo, Y. J., Pan, W. W., Liu, S. B., Shen, Z. F., Xu, Y., & Hu, L. L. (2020). ERK/MAPK signalling pathway and tumorigenesis (Review). *Exp Ther Med*, 19(3), 1997-2007. <https://doi.org/10.3892/etm.2020.8454>

- Gurgueira, S. A., Lawrence, J., Coull, B., Murthy, G. G., & González-Flecha, B. (2002). Rapid increases in the steady-state concentration of reactive oxygen species in the lungs and heart after particulate air pollution inhalation. *Environmental Health Perspectives*, 110(8), 749-755. <https://doi.org/10.1289/ehp.02110749>
- Haberzettl, P., Duffin, R., Krämer, U., Höhr, D., Schins, R. P., Borm, P. J., & Albrecht, C. (2007). Actin plays a crucial role in the phagocytosis and biological response to respirable quartz particles in macrophages. *Archives of Toxicology*, 81(7), 459-470. <https://doi.org/10.1007/s00204-007-0178-5>
- Halliwell, B., Hu, M.-L., Louie, S., Duvall, T. R., Tarkington, B. K., Motchnik, P., & Cross, C. E. (1992). Interaction of nitrogen dioxide with human plasma Antioxidant depletion and oxidative damage. *FEBS Letters*, 313(1), 62-66. [https://doi.org/10.1016/0014-5793\(92\)81185-O](https://doi.org/10.1016/0014-5793(92)81185-O)
- Hamra, G. B., Laden, F., Cohen, A. J., Raaschou-Nielsen, O., Brauer, M., & Loomis, D. (2015). Lung Cancer and Exposure to Nitrogen Dioxide and Traffic: A Systematic Review and Meta-Analysis. *Environmental Health Perspective*, 123(11), 1107-1112. <https://doi.org/10.1289/ehp.1408882>
- Hamra Ghassan, B., Laden, F., Cohen Aaron, J., Raaschou-Nielsen, O., Brauer, M., & Loomis, D. (2015). Lung Cancer and Exposure to Nitrogen Dioxide and Traffic: A Systematic Review and Meta-Analysis. *Environmental Health Perspectives*, 123(11), 1107-1112. <https://doi.org/10.1289/ehp.1408882>
- Hartwig, A. (2010). Mechanisms in cadmium-induced carcinogenicity: recent insights. *Biometals*, 23(5), 951-960. <https://doi.org/10.1007/s10534-010-9330-4>
- Haworth, R., Platt, N., Keshav, S., Hughes, D., Darley, E., Suzuki, H.,...Gordon, S. (1997). The macrophage scavenger receptor type A is expressed by activated macrophages and protects the host against lethal endotoxic

- shock. *Journal of Experimental Medicine*, 186(9), 1431-1439. <https://doi.org/10.1084/jem.186.9.1431>
- He, R.-W., Braakhuis, H. M., Vandebriel, R. J., Staal, Y. C. M., Gremmer, E. R., Fokkens, P. H. B.,...Cassee, F. R. (2021). Optimization of an air-liquid interface in vitro cell co-culture model to estimate the hazard of aerosol exposures. *Journal of Aerosol Science*, 153, 105703. <https://doi.org/https://doi.org/10.1016/j.jaerosci.2020.105703>
- He, R.-W., Gerlofs-Nijland, M. E., Boere, J., Fokkens, P., Leseman, D., Janssen, N. A. H., & Cassee, F. R. (2020). Comparative toxicity of ultrafine particles around a major airport in human bronchial epithelial (Calu-3) cell model at the air–liquid interface. *Toxicology in Vitro*, 68, 104950. <https://doi.org/https://doi.org/10.1016/j.tiv.2020.104950>
- Health and Safety Executive. (2022). *The Cross-Government Group on Gas Safety and Carbon Monoxide Awareness. Annual Report*.
- Heinrich, J., Pitz, M., Bischof, W., Krug, N., & Borm, P. J. A. (2003). Endotoxin in fine (PM<sub>2.5</sub>) and coarse (PM<sub>2.5</sub>–10) particle mass of ambient aerosols. A temporo-spatial analysis. *Atmospheric Environment*, 37(26), 3659-3667.
- Helleday, R., Sandstrom, T., & Stjernberg, N. (1994). Differences in bronchoalveolar cell response to nitrogen dioxide exposure between smokers and nonsmokers. *European Respiratory Journal*, 7(7), 1213.
- Herr, C., Beisswenger, C., Hess, C., Kandler, K., Suttorp, N., Welte, T.,...Group, R. B. f. t. C. S. (2009). Suppression of pulmonary innate host defence in smokers. *Thorax*, 64(2), 144-149. <https://doi.org/10.1136/thx.2008.102681>
- Heukels, P., Moor, C. C., von der Thüsen, J. H., Wijsenbeek, M. S., & Kool, M. (2019). Inflammation and immunity in IPF pathogenesis and treatment. *Respiratory Medicine*, 147, 79-91. <https://doi.org/https://doi.org/10.1016/j.rmed.2018.12.015>
- Hiemstra, P. S., McCray, P. B., & Bals, R. (2015). The innate immune function of airway epithelial cells in inflammatory

- lung disease. *European Respiratory Journal*, 45(4), 1150-1162. <https://doi.org/10.1183/09031936.00141514>
- Hill, W., Lim, E. L., Weeden, C. E., Lee, C., Augustine, M., Chen, K.,...Consortium, T. R. (2023). Lung adenocarcinoma promotion by air pollutants. *Nature*, 616(7955), 159-167. <https://doi.org/10.1038/s41586-023-05874-3>
- Hites, R. A. (2011). Dioxins: an overview and history. *Environmental Science and Toxicology*, 45(1), 16-20. <https://doi.org/10.1021/es1013664>
- Hiura, T. S., Kaszubowski, M. P., Li, N., & Nel, A. E. (1999). Chemicals in diesel exhaust particles generate reactive oxygen radicals and induce apoptosis in macrophages. *The Journal of Immunology*, 163(10), 5582-5591.
- Hoffman, E. A., Frey, B. L., Smith, L. M., & Auble, D. T. (2015). Formaldehyde Crosslinking: A Tool for the Study of Chromatin Complexes\*. *Journal of Biological Chemistry*, 290(44), 26404-26411. <https://doi.org/https://doi.org/10.1074/jbc.R115.651679>
- Hosgood, H. D., Boffetta, P., Greenland, S., Lee, Y. C., McLaughlin, J., Seow, A.,...Lan, Q. (2010). In-home coal and wood use and lung cancer risk: a pooled analysis of the International Lung Cancer Consortium. *Environmental Health Perspectives*, 118(12), 1743-1747. <https://doi.org/10.1289/ehp.1002217>
- Huang, D. W., Sherman, B. T., & Lempicki, R. A. (2009). Systematic and integrative analysis of large gene lists using DAVID bioinformatics resources. *Nature Protocols*, 4(1), 44-57. <https://doi.org/10.1038/nprot.2008.211>
- Huang, Y.-C. T., & Ghio, A. J. (2009). Controlled human exposures to ambient pollutant particles in susceptible populations. *Environmental Health*, 8(1), 33. <https://doi.org/10.1186/1476-069X-8-33>
- Hussain, T., Tan, B., Yin, Y., Blachier, F., Tossou, M. C. B., & Rahu, N. (2016). Oxidative Stress and Inflammation: What Polyphenols Can Do for Us? *Oxidative Medicine and*

- Cellular Longevity*, 2016, 7432797.  
<https://doi.org/10.1155/2016/7432797>
- Hutchinson Emma, J., & Pearson Peter, J. G. (2004). An evaluation of the environmental and health effects of vehicle exhaust catalysts in the UK. *Environmental Health Perspectives*, 112(2), 132-141.  
<https://doi.org/10.1289/ehp.6349>
- Högman, M., Mörk, A. C., & Roomans, G. M. (2002). Hypertonic saline increases tight junction permeability in airway epithelium. *European Respiratory Journal*, 20(6), 1444. <https://doi.org/10.1183/09031936.02.00017202>
- Ichinose, T., & Sagai, M. (1982). Studies on biochemical effects of nitrogen dioxide. III. Changes of the antioxidative protective systems in rat lungs and of lipid peroxidation by chronic exposure. *Toxicology and Applied Pharmacology*, 66(1), 1-8. [https://doi.org/10.1016/0041-008x\(82\)90056-4](https://doi.org/10.1016/0041-008x(82)90056-4)
- International Agency for Research on Cancer. (2024). *IARC Monographs on the Identification of Carcinogenic Hazards to Humans*. Retrieved 08 March 2024 from <https://monographs.iarc.who.int/list-of-classifications/>
- Irgen-Giorgio, S., Yoshida, S., Walling, V., & Chong, S. (2022). Fixation can change the appearance of phase separation in living cells. *eLife*, 11, e79903.  
<https://doi.org/10.7554/eLife.79903>
- Ishii, H., Fujii, T., Hogg, J. C., Hayashi, S., Mukae, H., Vincent, R., & van Eeden, S. F. (2004). Contribution of IL-1 $\beta$  and TNF- $\alpha$  to the initiation of the peripheral lung response to atmospheric particulates (PM10). *American Journal of Physiology-Lung Cellular and Molecular Physiology*, 287(1), L176-L183.  
<https://doi.org/10.1152/ajplung.00290.2003>
- Ispanixtlahuatl-Meráz, O., Schins, R. P. F., & Chirino, Y. I. (2018). Cell type specific cytoskeleton disruption induced by engineered nanoparticles [10.1039/C7EN00704C]. *Environmental Science: Nano*, 5(2), 228-245.  
<https://doi.org/10.1039/C7EN00704C>

- Jackson, P., Hougaard, K. S., Boisen, A. M. Z., Jacobsen, N. R., Jensen, K. A., Møller, P.,...Wallin, H. (2012). Pulmonary exposure to carbon black by inhalation or instillation in pregnant mice: Effects on liver DNA strand breaks in dams and offspring. *Nanotoxicology*, 6(5), 486-500. <https://doi.org/10.3109/17435390.2011.587902>
- Jacobsen, N. R., Møller, P., Cohn, C. A., Loft, S., Vogel, U., & Wallin, H. (2008). Diesel exhaust particles are mutagenic in FE1-Muta™Mouse lung epithelial cells. *Mutation Research/Fundamental and Molecular Mechanisms of Mutagenesis*, 641(1), 54-57. <https://doi.org/https://doi.org/10.1016/j.mrfmmm.2008.03.001>
- Jacobsen, N. R., Saber, A. T., White, P., Møller, P., Pojana, G., Vogel, U.,...Wallin, H. (2007). Increased mutant frequency by carbon black, but not quartz, in the lacZ and cII transgenes of muta™mouse lung epithelial cells. *Environmental and Molecular Mutagenesis*, 48(6), 451-461. <https://doi.org/https://doi.org/10.1002/em.20300>
- Jacquemin, B., Siroux, V., Sanchez, M., Carsin, A. E., Schikowski, T., Adam, M.,...Kauffmann, F. (2015). Ambient air pollution and adult asthma incidence in six European cohorts (ESCAPE). *Environmental Health Perspective*, 123(6), 613-621. <https://doi.org/10.1289/ehp.1408206>
- Jaenicke, R. (2005). Abundance of Cellular Material and Proteins in the Atmosphere. *Science*, 308(5718), 73. <https://doi.org/10.1126/science.1106335>
- Jakubczyk, K., Dec, K., Kałduńska, J., Kawczuga, D., Kochman, J., & Janda, K. (2020). Reactive oxygen species - sources, functions, oxidative damage. *Pol Merkur Lekarski*, 48(284), 124-127.
- Jiang, R., Jones, M. J., Sava, F., Kobor, M. S., & Carlsten, C. (2014). Short-term diesel exhaust inhalation in a controlled human crossover study is associated with changes in DNA methylation of circulating mononuclear cells in asthmatics.



- Particle and Fibre Toxicology*, 11, 71.  
<https://doi.org/10.1186/s12989-014-0071-3>
- Jiang, X. Q., Mei, X. D., & Feng, D. (2016). Air pollution and chronic airway diseases: what should people know and do? *Journal of Thoracic Disease*, 8(1), E31-40.  
<https://doi.org/10.3978/j.issn.2072-1439.2015.11.50>
- Jiménez, L. A., Thompson, J., Brown, D. A., Rahman, I., Antonicelli, F., Duffin, R.,...MacNee, W. (2000). Activation of NF-kappaB by PM(10) occurs via an iron-mediated mechanism in the absence of IkappaB degradation. *Toxicology and Applied Pharmacology*, 166(2), 101-110. <https://doi.org/10.1006/taap.2000.8957>
- Johnson, D. E., O'Keefe, R. A., & Grandis, J. R. (2018). Targeting the IL-6/JAK/STAT3 signalling axis in cancer. *Nature Reviews Clinical Oncology*, 15(4), 234-248.  
<https://doi.org/10.1038/nrclinonc.2018.8>
- Jorres, R., Nowak, D., Grimminger, F., Seeger, W., Oldigs, M., & Magnussen, H. (1995). The effect of 1 ppm nitrogen dioxide on bronchoalveolar lavage cells and inflammatory mediators in normal and asthmatic subjects. *European Respiratory Journal*, 8(3), 416.
- Josefsen, K., & Nielsen, H. (2011). Northern Blotting Analysis. In H. Nielsen (Ed.), *RNA: Methods and Protocols* (pp. 87-105). Humana Press. [https://doi.org/10.1007/978-1-59745-248-9\\_7](https://doi.org/10.1007/978-1-59745-248-9_7)
- Joshi, N., Watanabe, S., Verma, R., Jablonski, R., Chen, C., Cheresh, P.,...V. Misharin, A. (2019). A spatially restricted fibrotic niche in pulmonary fibrosis is sustained by M-CSF/M-CSFR signaling in monocyte-derived alveolar macrophages. *European Respiratory Journal*, 1900646.  
<https://doi.org/10.1183/13993003.00646-2019>
- Juginović, A., Vuković, M., Aranza, I., & Biloš, V. (2021). Health impacts of air pollution exposure from 1990 to 2019 in 43 European countries. *Scientific Reports*, 11(1), 22516.  
<https://doi.org/10.1038/s41598-021-01802-5>
- Jung, E. J., Avliyakov, N. K., Boontheung, P., Loo, J. A., & Nel, A. E. (2007). Pro-oxidative DEP chemicals induce heat

- shock proteins and an unfolding protein response in a bronchial epithelial cell line as determined by DIGE analysis. *Proteomics*, 7(21), 3906-3918. <https://doi.org/10.1002/pmic.200700377>
- Jungnickel, C., Schmidt, L. H., Bittigkoffer, L., Wolf, L., Wolf, A., Ritzmann, F.,...Beisswenger, C. (2017). IL-17C mediates the recruitment of tumor-associated neutrophils and lung tumor growth. *Oncogene*, 36(29), 4182-4190. <https://doi.org/10.1038/onc.2017.28>
- Justo, A. F. O., & Suemoto, C. K. (2022). The modulation of neuroinflammation by inducible nitric oxide synthase. *Journal of Cell Communication and Signaling*, 16(2), 155-158. <https://doi.org/10.1007/s12079-021-00663-x>
- Järup, L. (2003). Hazards of heavy metal contamination. *British Medical Bulletin*, 68, 167-182. <https://doi.org/10.1093/bmb/ldg032>
- Kampa, M., & Castanas, E. (2008). Human health effects of air pollution. *Environmental Pollution*, 151(2), 362-367. <https://doi.org/10.1016/j.envpol.2007.06.012>
- Kampfrath, T., Maiseyeu, A., Ying, Z., Shah, Z., Deiuliis, J. A., Xu, X.,...Rajagopalan, S. (2011). Chronic fine particulate matter exposure induces systemic vascular dysfunction via NADPH oxidase and TLR4 pathways. *Circulation Research*, 108(6), 716-726. <https://doi.org/10.1161/CIRCRESAHA.110.237560>
- Kang, M. I., Kobayashi, A., Wakabayashi, N., Kim, S. G., & Yamamoto, M. (2004). Scaffolding of Keap1 to the actin cytoskeleton controls the function of Nrf2 as key regulator of cytoprotective phase 2 genes. *Proceedings of the National Academy of Sciences of the United States of America*, 101(7), 2046-2051. <https://doi.org/10.1073/pnas.0308347100>
- Kansanen, E., Kuosmanen, S. M., Leinonen, H., & Levonen, A. L. (2013). The Keap1-Nrf2 pathway: Mechanisms of activation and dysregulation in cancer. *Redox Biology*, 1, 45-49. <https://doi.org/10.1016/j.redox.2012.10.001>



- Karagulian, F., Belis, C. A., Dora, C. F. C., Prüss-Ustün, A. M., Bonjour, S., Adair-Rohani, H., & Amann, M. (2015). Contributions to cities' ambient particulate matter (PM): A systematic review of local source contributions at global level. *Atmospheric Environment*, 120, 475–483. <https://doi.org/https://doi.org/10.1016/j.atmosenv.2015.08.087>
- Karanasiou, A., Moreno, N., Moreno, T., Viana, M., de Leeuw, F., & Querol, X. (2012). Health effects from Sahara dust episodes in Europe: literature review and research gaps. *Environment International*, 47, 107-114. <https://doi.org/10.1016/j.envint.2012.06.012>
- Karlsson, H. L., Nygren, J., & Möller, L. (2004). Genotoxicity of airborne particulate matter: the role of cell–particle interaction and of substances with adduct-forming and oxidizing capacity. *Mutation Research/Genetic Toxicology and Environmental Mutagenesis*, 565(1), 1-10. <https://doi.org/https://doi.org/10.1016/j.mrgentox.2004.07.015>
- Karthikeyan, S., Thomson, E. M., Kumarathasan, P., Guénette, J., Rosenblatt, D., Chan, T.,... Vincent, R. (2013). Nitrogen Dioxide and Ultrafine Particles Dominate the Biological Effects of Inhaled Diesel Exhaust Treated by a Catalyzed Diesel Particulate Filter. *Toxicological Sciences*, 135(2), 437-450. <https://doi.org/10.1093/toxsci/kft162>
- Kaspar, J. W., Niture, S. K., & Jaiswal, A. K. (2009). Nrf2:INrf2 (Keap1) signaling in oxidative stress. *Free Radical Biology and Medicine*, 47(9), 1304-1309. <https://doi.org/10.1016/j.freeradbiomed.2009.07.035>
- Kasper, J. Y., Hermanns, M. I., Unger, R. E., & Kirkpatrick, C. J. (2017). A responsive human triple-culture model of the air–blood barrier: incorporation of different macrophage phenotypes. *Journal of Tissue Engineering and Regenerative Medicine*, 11(4), 1285-1297. <https://doi.org/https://doi.org/10.1002/term.2032>
- Kasper, M., & Barth, K. (2017). Potential contribution of alveolar epithelial type I cells to pulmonary fibrosis.

- Bioscience Reports*, 37(6), BSR20171301.  
<https://doi.org/10.1042/BSR20171301>
- Katsouyanni, K. (2003). Ambient air pollution and health. *British Medical Bulletin*, 68, 143-156.  
<https://doi.org/10.1093/bmb/ldg028>
- Katsouyanni, K. (2006). Aphea Project: Air Pollution and Health: A European Approach. *Epidemiology*, 17(6).
- Katsouyanni, K., Schwartz, J., Spix, C., Touloumi, G., Zmirou, D., Zanobetti, A.,...Anderson, H. R. (1996). Short term effects of air pollution on health: a European approach using epidemiologic time series data: the APHEA protocol. *Journal of Epidemiology and Community Health*, 50 Suppl 1, S12-18. [https://doi.org/10.1136/jech.50.suppl\\_1.s12](https://doi.org/10.1136/jech.50.suppl_1.s12)
- Katsouyanni, K., Touloumi, G., Samoli, E., Gryparis, A., Le Tertre, A., Monopolis, Y.,...Schwartz, J. (2001). Confounding and effect modification in the short-term effects of ambient particles on total mortality: results from 29 European cities within the APHEA2 project. *Epidemiology*, 12(5), 521-531.  
<https://doi.org/10.1097/00001648-200109000-00011>
- Kelly, F. J., Blomberg, A., Frew, A., Holgate, S. T., & Sandstrom, T. (1996). Antioxidant kinetics in lung lavage fluid following exposure of humans to nitrogen dioxide. *American Journal of Respiratory and Critical Care Medicine*, 154(6), 1700-1705.  
<https://doi.org/10.1164/ajrccm.154.6.8970358>
- Kelly, F. J., & Tetley, T. D. (1997). Nitrogen dioxide depletes uric acid and ascorbic acid but not glutathione from lung lining fluid. *Biochemical Journal*, 325(1), 95-99.  
<https://doi.org/10.1042/bj3250095>
- Kensler, T. W., Wakabayashi, N., & Biswal, S. (2007). Cell survival responses to environmental stresses via the Keap1 - Nrf2-ARE pathway. *Annual Review of Pharmacology and Toxicology*, 47, 89-116.  
<https://doi.org/10.1146/annurev.pharmtox.46.120604.141046>

- Kerkhof, M., Postma, D. S., Brunekreef, B., Reijmerink, N. E., Wijga, A. H., de Jongste, J. C.,...Koppelman, G. H. (2010). Toll-like receptor 2 and 4 genes influence susceptibility to adverse effects of traffic-related air pollution on childhood asthma. *Thorax*, 65(8), 690-697. <https://doi.org/10.1136/thx.2009.119636>
- Khalid, N., & Azimpouran, M. (2023). *Necrosis* (<https://www.ncbi.nlm.nih.gov/books/NBK557627/>). StatPearls.
- Kim, Y. K., Jung, J. S., Lee, S. H., & Kim, Y. W. (1997). Effects of antioxidants and Ca<sup>2+</sup> in cisplatin-induced cell injury in rabbit renal cortical slices. *Toxicology and Applied Pharmacology*, 146(2), 261-269. <https://doi.org/10.1006/taap.1997.8252>
- Klein, S. G., Serchi, T., Hoffmann, L., Blömeke, B., & Gutleb, A. C. (2013). An improved 3D tetraculture system mimicking the cellular organisation at the alveolar barrier to study the potential toxic effects of particles on the lung. *Particle and Fibre Toxicology*, 10(1), 31. <https://doi.org/10.1186/1743-8977-10-31>
- Kletting, S., Barthold, S., Repnik, U., Griffiths, G., Loretz, B., Schneider-Daum, N.,...Lehr, C. M. (2018). Co-culture of human alveolar epithelial (hAELVi) and macrophage (THP-1) cell lines. *ALTEX*, 35(2), 211-222. <https://doi.org/10.14573/altex.1607191>
- Knudsen, L., & Ochs, M. (2018). The micromechanics of lung alveoli: structure and function of surfactant and tissue components. *Histochemistry and Cell Biology*, 150(6), 661-676. <https://doi.org/10.1007/s00418-018-1747-9>
- Kobayashi, A., Kang, M. I., Watai, Y., Tong, K. I., Shibata, T., Uchida, K., & Yamamoto, M. (2006). Oxidative and electrophilic stresses activate Nrf2 through inhibition of ubiquitination activity of Keap1. *Molecular Cell Biology*, 26(1), 221-229. <https://doi.org/10.1128/MCB.26.1.221-229.2006>
- Kobayashi, M., & Yamamoto, M. (2006). Nrf2-Keap1 regulation of cellular defense mechanisms against electrophiles and

- reactive oxygen species. *Advances in Enzyme Regulation*, 46, 113-140.  
<https://doi.org/10.1016/j.advenzreg.2006.01.007>
- Kobayashi, T., Tanaka, K., Fujita, T., Umezawa, H., Amano, H., Yoshioka, K.,...Kasuya, Y. (2015). Bidirectional role of IL-6 signal in pathogenesis of lung fibrosis. *Respiratory Research*, 16(1), 99. <https://doi.org/10.1186/s12931-015-0261-z>
- Koehler, C., Paulus, M., Ginzkey, C., Hackenberg, S., Scherzad, A., Ickrath, P.,...Kleinsasser, N. (2016). The Proinflammatory Potential of Nitrogen Dioxide and Its Influence on the House Dust Mite Allergen Der p 1. *International Archives of Allergy and Immunology*, 171(1), 27-35. <https://doi.org/10.1159/000450751>
- Koike, E., Kobayashi, T., & Utsunomiya, R. (2001). Effect of exposure to nitrogen dioxide on alveolar macrophage-mediated immunosuppressive activity in rats. *Toxicology Letters*, 121(2), 135-143.  
[https://doi.org/https://doi.org/10.1016/S0378-4274\(01\)00331-9](https://doi.org/https://doi.org/10.1016/S0378-4274(01)00331-9)
- Kondo, T., Tagami, S., Yoshioka, A., Nishimura, M., & Kawakami, Y. (1994). Current smoking of elderly men reduces antioxidants in alveolar macrophages. *American Journal of Respiratory and Critical Care Medicine*, 149(1), 178-182. <https://doi.org/10.1164/ajrccm.149.1.8111579>
- Kong, H., Zhang, Y., Li, Y., Cui, Z., Xia, K., Sun, Y.,...Zhu, Y. (2013). Size-Dependent Cytotoxicity of Nanocarbon Blacks. *International Journal of Molecular Sciences*, 14(11), 22529-22543.
- Kubota, K., Murakami, M., Takenaka, S., Kawai, K., & Kyono, H. (1987). Effects of long-term nitrogen dioxide exposure on rat lung: morphological observations. *Environmental Health Perspective*, 73, 157-169.  
<https://doi.org/10.1289/ehp.8773157>
- Kuehn, A., Kletting, S., de Souza Carvalho-Wodarz, C., Repnik, U., Griffiths, G., Fischer, U.,...Lehr, C. M. (2016). Human alveolar epithelial cells expressing tight junctions to model

- the air-blood barrier. *ALTEX - Alternatives to animal experimentation*, 33(3), 251-260.  
<https://doi.org/10.14573/altex.1511131>
- Kukurba, K. R., & Montgomery, S. B. (2015). RNA Sequencing and Analysis. *Cold Spring Harbor Protocols*, 2015(11), pdb.top084970.
- Kumar, S., Wang, G., Zheng, N., Cheng, W., Ouyang, K., Lin, H.,...Liu, J. (2019). HIMF (Hypoxia-Induced Mitogenic Factor)-IL (Interleukin)-6 Signaling Mediates Cardiomyocyte-Fibroblast Crosstalk to Promote Cardiac Hypertrophy and Fibrosis. *Hypertension*, 73(5), 1058-1070.  
<https://doi.org/10.1161/HYPERTENSIONAHA.118.12267>
- Kwon, H.-S., Ryu, M. H., & Carlsten, C. (2020). Ultrafine particles: unique physicochemical properties relevant to health and disease. *Experimental & Molecular Medicine*, 52(3), 318-328. <https://doi.org/10.1038/s12276-020-0405-1>
- Lanki, T., Hampel, R., Tiittanen, P., Andrich, S., Beelen, R., Brunekreef, B.,...Peters, A. (2015). Air Pollution from Road Traffic and Systemic Inflammation in Adults: A Cross-Sectional Analysis in the European ESCAPE Project. *Environmental Health Perspectives*, 123(8), 785-791. <https://doi.org/10.1289/ehp.1408224>
- Laskin, D. (2006). The Great London Smog. *Weatherwise*, 59(6), 42-45. <https://doi.org/10.3200/WEWI.59.6.42-45>
- Last, J. A., & Warren, D. L. (1987). Synergistic interaction between nitrogen dioxide and respirable aerosols of sulfuric acid or sodium chloride on rat lungs. *Toxicology and Applied Pharmacology*, 90(1), 34-42.  
[https://doi.org/https://doi.org/10.1016/0041-008X\(87\)90303-6](https://doi.org/https://doi.org/10.1016/0041-008X(87)90303-6)
- Lehmann, A. D., Blank, F., Baum, O., Gehr, P., & Rothen-Rutishauser, B. M. (2009). Diesel exhaust particles modulate the tight junction protein occludin in lung cells in

- vitro. *Particle and Fibre Toxicology*, 6(1), 26.  
<https://doi.org/10.1186/1743-8977-6-26>
- Leibrock, L., Wagener, S., Singh, A. V., Laux, P., & Luch, A. (2019). Nanoparticle induced barrier function assessment at liquid–liquid and air–liquid interface in novel human lung epithelia cell lines. *Toxicology Research*, 8(6), 1016-1027. <https://doi.org/10.1039/c9tx00179d>
- Lenz, A.-G., Stoeger, T., Cei, D., Schmidmeir, M., Semren, N., Burgstaller, G.,...Schmid, O. (2014). Efficient Bioactive Delivery of Aerosolized Drugs to Human Pulmonary Epithelial Cells Cultured in Air–Liquid Interface Conditions. *American Journal of Respiratory Cell and Molecular Biology*, 51(4), 526-535.  
<https://doi.org/10.1165/rcmb.2013-0479OC>
- Lenz, A. G., Karg, E., Lentner, B., Dittrich, V., Brandenberger, C., Rothen-Rutishauser, B.,...Schmid, O. (2009). A dose-controlled system for air-liquid interface cell exposure and application to zinc oxide nanoparticles. *Particle and Fibre Toxicology*, 6(1), 32. <https://doi.org/10.1186/1743-8977-6-32>
- Li, D., Firozi, P. F., Wang, L. E., Bosken, C. H., Spitz, M. R., Hong, W. K., & Wei, Q. (2001). Sensitivity to DNA damage induced by benzo(a)pyrene diol epoxide and risk of lung cancer: a case-control analysis. *Cancer Research*, 61(4), 1445-1450.
- Li, R., Navab, K., Hough, G., Daher, N., Zhang, M., Mittelstein, D.,...Hsiai, T. K. (2015). Effect of exposure to atmospheric ultrafine particles on production of free fatty acids and lipid metabolites in the mouse small intestine. *Environmental Health Perspectives*, 123(1), 34-41.  
<https://doi.org/10.1289/ehp.1307036>
- Li, Z., Wu, Y., Chen, H. P., Zhu, C., Dong, L., Wang, Y.,...Chen, Z. H. (2018). MTOR Suppresses Environmental Particle-Induced Inflammatory Response in Macrophages. *Journal of Immunology*, 200(8), 2826-2834.  
<https://doi.org/10.4049/jimmunol.1701471>



- Lin, Shih, H., Jung, C.-R., Wang, C.-M., Chang, Y.-C., Hsieh, C.-Y., & Hwang, B.-F. (2021). Effect of exposure to fine particulate matter during pregnancy and infancy on paediatric allergic rhinitis. *Thorax*, 76(6), 568. <https://doi.org/10.1136/thoraxjnl-2020-215025>
- Lin, C.-H., Wan, C., Liu, W.-S., & Wang, H.-H. (2021). PM2.5 Induces Early Epithelial Mesenchymal Transition in Human Proximal Tubular Epithelial Cells through Activation of IL-6/STAT3 Pathway. *International Journal of Molecular Sciences*, 22(23).
- Lin, Y., Zhang, Y., Xu, L., Long, W., Shan, C., Ding, H.,...Shi, Z. (2021). High expression of an unknown long noncoding RNA RP11-290L1.3 from GDM macrosomia and its effect on preadipocyte differentiation. *Endocrine Connections*, 10(2), 191-204. <https://doi.org/10.1530/EC-20-0584>
- Liu, H., Wang, J., Luo, T., Zhen, Z., Liu, L., Zheng, Y.,...Hu, X. (2023). Correlation between ITGB2 expression and clinical characterization of glioma and the prognostic significance of its methylation in low-grade glioma(LGG) [Original Research]. *Frontiers in Endocrinology*, 13.
- Llewellyn, S. V., Parak, W. J., Hühn, J., Burgum, M. J., Evans, S. J., Chapman, K. E.,...Clift, M. J. D. (2022). Deducing the cellular mechanisms associated with the potential genotoxic impact of gold and silver engineered nanoparticles upon different lung epithelial cell lines in vitro. *Nanotoxicology*, 16(1), 52-72. <https://doi.org/10.1080/17435390.2022.2030823>
- Loane, C., Pilinis, C., Lekkas, T. D., & Politis, M. (2013). Ambient particulate matter and its potential neurological consequences. *Reviews in Neurosciences*, 24(3), 323-335. <https://doi.org/10.1515/revneuro-2013-0001>
- Loboda, A., Damulewicz, M., Pyza, E., Jozkowicz, A., & Dulak, J. (2016). Role of Nrf2/HO-1 system in development, oxidative stress response and diseases: an evolutionarily conserved mechanism. *Cellular and Molecular Life Sciences*, 73(17), 3221-3247. <https://doi.org/10.1007/s00018-016-2223-0>

- Lopez-Castejon, G., & Brough, D. (2011). Understanding the mechanism of IL-1 $\beta$  secretion. *Cytokine & Growth Factor Reviews*, 22(4), 189-195. <https://doi.org/https://doi.org/10.1016/j.cytogfr.2011.10.001>
- Lovera-Leroux, M., Crobeddu, B., Kassis, N., Petit, P. X., Janel, N., Baeza-Squiban, A., & Andreau, K. (2015). The iron component of particulate matter is antiapoptotic: A clue to the development of lung cancer after exposure to atmospheric pollutants? *Biochimie*, 118, 195-206. <https://doi.org/https://doi.org/10.1016/j.biochi.2015.09.030>
- Lund, A. K., Lucero, J., Lucas, S., Madden, M. C., McDonald, J. D., Seagrave, J.-C.,...Campen, M. J. (2009). Vehicular Emissions Induce Vascular MMP-9 Expression and Activity Associated With Endothelin-1–Mediated Pathways. *Arteriosclerosis, Thrombosis, and Vascular Biology*, 29(4), 511-517. <https://doi.org/10.1161/ATVBAHA.108.176107>
- Lundqvist, M., Stigler, J., Elia, G., Lynch, I., Cedervall, T., & Dawson, K. A. (2008). Nanoparticle size and surface properties determine the protein corona with possible implications for biological impacts. *Proceedings of the National Academy of Sciences*, 105(38), 14265-14270. <https://doi.org/10.1073/pnas.0805135105>
- Ma, B., Stepanov, I., & Hecht, S. S. (2019). Recent Studies on DNA Adducts Resulting from Human Exposure to Tobacco Smoke. *Toxics*, 7(1).
- MacIntyre, E. A., Gehring, U., Mölter, A., Fuertes, E., Klümper, C., Krämer, U.,...Heinrich, J. (2014). Air pollution and respiratory infections during early childhood: an analysis of 10 European birth cohorts within the ESCAPE Project. *Environmental Health Perspective*, 122(1), 107-113. <https://doi.org/10.1289/ehp.1306755>
- Mahadevan, B., Luch, A., Atkin, J., Nguyen, T., Sharma, A. K., Amin, S., & Baird, W. M. (2006). Investigation of the genotoxicity of dibenzo[c,p]chrysene in human carcinoma



- MCF-7 cells in culture. *Chemico-Biological Interactions*, 164(3), 181-191.  
<https://doi.org/https://doi.org/10.1016/j.cbi.2006.09.015>
- Mallone, S., Stafoggia, M., Faustini, A., Gobbi, G. P., Marconi, A., & Forastiere, F. (2011). Saharan dust and associations between particulate matter and daily mortality in Rome, Italy. *Environmental Health Perspectives*, 119(10), 1409-1414. <https://doi.org/10.1289/ehp.1003026>
- Manikandan, P., & Nagini, S. (2018). Cytochrome P450 Structure, Function and Clinical Significance: A Review. *Current Drug Targets*, 19(1), 38-54.  
<https://doi.org/10.2174/1389450118666170125144557>
- Manisalidis, I., Stavropoulou, E., Stavropoulos, A., & Bezirtzoglou, E. (2020). Environmental and Health Impacts of Air Pollution: A Review [10.3389/fpubh.2020.00014]. *Frontiers in Public Health*, 8, 14.
- Marc-Malovrh, M., Camlek, L., Škrjat, S., Kern, I., Fležar, M., Dežman, M., & Korošec, P. (2020). Elevated eosinophils, IL5 and IL8 in induced sputum in asthma patients with accelerated FEV1 decline. *Respiratory Medicine*, 162(1532-3064 (Electronic)).
- Martini, F. H., Nath, J. L., & Bartholomew, E. F. (2018). *Fundamentals of Anatomy & Physiology* (Vol. 11). Pearson Education, Inc.
- Mayor of London. (2023). *Inner London Ultra Low Emission Zone - One year Report*.
- McCreanor, J., Cullinan, P., Nieuwenhuijsen, M. J., Stewart-Evans, J., Malliarou, E., Jarup, L.,...Zhang, J. (2007). Respiratory Effects of Exposure to Diesel Traffic in Persons with Asthma. *New England Journal of Medicine*, 357(23), 2348-2358.  
<https://doi.org/10.1056/NEJMoa071535>
- Meaden, C. W., Kashani, J. S., & Vetrano, S. (2019). Pulmonary Edema Occurring after Nitric Acid Exposure. *Case Reports in Emergency Medicine*, 2019, 9303170.  
<https://doi.org/10.1155/2019/9303170>

- Mehta, M., Chen, L. C., Gordon, T., Rom, W., & Tang, M. S. (2008). Particulate matter inhibits DNA repair and enhances mutagenesis. *Mutation Research*, 657(2), 116-121. <https://doi.org/10.1016/j.mrgentox.2008.08.015>
- Meldrum, K., Evans, S. J., Vogel, U., Tran, L., Doak, S. H., & Clift, M. J. D. (2022). The influence of exposure approaches to in vitro lung epithelial barrier models to assess engineered nanomaterial hazard. *Nanotoxicology*, 16(1), 114-134. <https://doi.org/10.1080/17435390.2022.2051627>
- Meldrum, K., Moura, J. A., Doak, S. H., & Clift, M. J. D. (2022). Dynamic Fluid Flow Exacerbates the (Pro-)Inflammatory Effects of Aerosolised Engineered Nanomaterials In Vitro. *Nanomaterials*, 12(19).
- Meldrum, K., Risby, H., Mitchell, S., & Clift, M. J. D. (2020). *PATROLS Standard Operating Procedures (SOP) Guidance Document for macrophage differentiation from THP-1 cells*. Retrieved 13 March 2024 from <https://www.patrols-h2020.eu/publications/sops/index.php>
- Mescher, M., & Haarmann-Stemmann, T. (2018). Modulation of CYP1A1 metabolism: From adverse health effects to chemoprevention and therapeutic options. *Pharmacology & Therapeutics*, 187, 71-87. <https://doi.org/10.1016/j.pharmthera.2018.02.012>
- Mihara, M., Hashizume, M., Yoshida, H., Suzuki, M., & Shiina, M. (2011). IL-6/IL-6 receptor system and its role in physiological and pathological conditions. *Clinical Science*, 122(4), 143-159. <https://doi.org/10.1042/CS20110340>
- Miller, M. R., Raftis, J. B., Langrish, J. P., McLean, S. G., Samutritai, P., Connell, S. P.,...Mills, N. L. (2017). Inhaled Nanoparticles Accumulate at Sites of Vascular Disease. *ACS Nano*, 11(5), 4542-4552. <https://doi.org/10.1021/acsnano.6b08551>
- Mirowsky, J., Hickey, C., Horton, L., Blaustein, M., Galdanes, K., Peltier, R. E.,...Gordon, T. (2013). The effect of particle

- size, location and season on the toxicity of urban and rural particulate matter. *Inhalation Toxicology*, 25(13), 747-757.  
<https://doi.org/10.3109/08958378.2013.846443>
- Mirowsky, J. E., Dailey, L. A., & Devlin, R. B. (2016). Differential expression of pro-inflammatory and oxidative stress mediators induced by nitrogen dioxide and ozone in primary human bronchial epithelial cells. *Inhalation Toxicology*, 28(8), 374-382.  
<https://doi.org/10.1080/08958378.2016.1185199>
- Mitchell, S. (2022). *Investigating the human health implications of e-cigarettes - An in vitro mechanistic toxicology approach* [Swansea University].
- Mittleman, M. A., & Mostofsky, E. (2011). Physical, psychological and chemical triggers of acute cardiovascular events: preventive strategies. *Circulation*, 124(3), 346-354.  
<https://doi.org/10.1161/CIRCULATIONAHA.110.968776>
- Miyabara, Y., Takano, H., Ichinose, T., Lim, H. B., & Sagai, M. (1998). Diesel exhaust enhances allergic airway inflammation and hyperresponsiveness in mice. *American Journal of Respiratory and Critical Care Medicine*, 157(4 Pt 1), 1138-1144.  
<https://doi.org/10.1164/ajrccm.157.4.9708066>
- Moldoveanu, B., Otmishi, P., Jani, P., Walker, J., Sarmiento, X., Guardiola, J.,... Yu, J. (2009). Inflammatory mechanisms in the lung. *Journal of inflammation research*, 2, 1-11.
- Montuschi, P., Barnes, P. J., & Roberts, L. J. (2004). Isoprostanes: markers and mediators of oxidative stress. *Federation of American Societies for Experimental Biology Journal*, 18(15), 1791-1800.  
<https://doi.org/10.1096/fj.04-2330rev>
- Moura, J. A., Meldrum, K., Doak, S. H., & Clift, M. J. D. (2023). Alternative lung cell model systems for toxicology testing strategies: Current knowledge and future outlook. *Seminars in Cell & Developmental Biology*, 147, 70-82.  
<https://doi.org/https://doi.org/10.1016/j.semcdb.2022.12.006>

- Mroz, R., Schins, R., Li, R., L., J., Drost, R., Holownia, A.,...Donaldson, K. (2008). Nanoparticle-driven DNA damage mimics irradiation-related carcinogenesis pathways. *European Respiratory Journal*, 31(2), 241. <https://doi.org/10.1183/09031936.00006707>
- Mumford, J. L., Li, X., Hu, F., Lu, X. B., & Chuang, J. C. (1995). Human exposure and dosimetry of polycyclic aromatic hydrocarbons in urine from Xuan Wei, China with high lung cancer mortality associated with exposure to unvented coal smoke. *Carcinogenesis*, 16(12), 3031-3036. <https://doi.org/10.1093/carcin/16.12.3031>
- Muranaka, M., Suzuki, S., Koizumi, K., Takafuji, S., Miyamoto, T., Ikemori, R., & Tokiwa, H. (1986). Adjuvant activity of diesel-exhaust particulates for the production of IgE antibody in mice. *The Journal of Allergy and Clinical Immunology*, 77(4), 616-623. [https://doi.org/10.1016/0091-6749\(86\)90355-6](https://doi.org/10.1016/0091-6749(86)90355-6)
- Murdoch, J. R., & Lloyd, C. M. (2010). Chronic inflammation and asthma. *Mutation Research/Fundamental and Molecular Mechanisms of Mutagenesis*, 690(1), 24-39. <https://doi.org/https://doi.org/10.1016/j.mrfmmm.2009.09.005>
- Muroya, M., Chang, K., Uchida, K., Bougaki, M., & Yamada, Y. (2012). Analysis of cytotoxicity induced by proinflammatory cytokines in the human alveolar epithelial cell line A549. *Biosci Trends*, 6(2), 70-80.
- Mylona, S. (1996). Sulphur dioxide emissions in Europe 1880–1991 and their effect on sulphur concentrations and depositions. *Tellus B*, 48(5), 662-689. <https://doi.org/https://doi.org/10.1034/j.1600-0889.1996.t01-2-00005.x>
- Müller, Seifart, & Barth. (1998). Effect of air pollutants on the pulmonary surfactant system [<https://doi.org/10.1046/j.1365-2362.1998.00342.x>]. *European Journal of Clinical Investigation*, 28(9), 762-777. <https://doi.org/https://doi.org/10.1046/j.1365-2362.1998.00342.x>

- Münzel, T., Gori, T., Al-Kindi, S., Deanfield, J., Lelieveld, J., Daiber, A., & Rajagopalan, S. (2018). Effects of gaseous and solid constituents of air pollution on endothelial function. *European Heart Journal*, 39(38), 3543-3550. <https://doi.org/10.1093/eurheartj/ehy481>
- Nadeau, D., Vincent, R., Kumarathasan, P., Brook, J., & Dufresne, A. (1996). Cytotoxicity of ambient air particles to rat lung macrophages: Comparison of cellular and functional assays. *Toxicology in Vitro*, 10(2), 161-172. [https://doi.org/https://doi.org/10.1016/0887-2333\(95\)00115-8](https://doi.org/https://doi.org/10.1016/0887-2333(95)00115-8)
- Naeher, L. P., Brauer, M., Lipsett, M., Zelikoff, J. T., Simpson, C. D., Koenig, J. Q., & Smith, K. R. (2007). Woodsmoke health effects: a review. *Inhalation Toxicology*, 19(1), 67-106. <https://doi.org/10.1080/08958370600985875>
- Nakagome, K., Dohi, M., Okunishi, K., Tanaka, R., Miyazaki, J., & Yamamoto, K. (2006). In vivo IL-10 gene delivery attenuates bleomycin induced pulmonary fibrosis by inhibiting the production and activation of TGF- $\beta$  in the lung. *Thorax*, 61(10), 886. <https://doi.org/10.1136/thx.2005.056317>
- Nalayanda, D. D., Puleo, C., Fulton, W. B., Sharpe, L. M., Wang, T.-H., & Abdullah, F. (2009). An open-access microfluidic model for lung-specific functional studies at an air-liquid interface. *Biomedical Microdevices*, 11(5), 1081. <https://doi.org/10.1007/s10544-009-9325-5>
- Nathan, C., & Ding, A. (2010). Nonresolving inflammation. *Cell*, 140(6), 871-882. <https://doi.org/10.1016/j.cell.2010.02.029>
- National Academies of Sciences, E. g., and Medicine, Division, H. a. M., Practice, B. o. P. H. a. P. H., & Update), C. t. R. t. H. E. i. V. V. o. E. t. H. E. B. (2018). Veterans and Agent Orange: Update 11 (2018). In. <https://doi.org/NBK535904>
- National Atmospheric Emissions Inventory. (2021). *About Lead*. Retrieved 25 January 2024 from [https://naei.beis.gov.uk/overview/pollutants?pollutant\\_id=17](https://naei.beis.gov.uk/overview/pollutants?pollutant_id=17)

- National Center for Biotechnology Information. (2024). *PubChem Compound Summary for CID 17601, Nitrosyl chloride*. Retrieved 05 March 2024 from
- Nawrot, T. S., Martens, D. S., Hara, A., Plusquin, M., Vangronsveld, J., Roels, H. A., & Staessen, J. A. (2015). Association of total cancer and lung cancer with environmental exposure to cadmium: the meta-analytical evidence. *Cancer Causes Control*, 26(9), 1281-1288. <https://doi.org/10.1007/s10552-015-0621-5>
- Nayak, A., Dodagatta-Marri, E., Tsolaki, A. G., & Kishore, U. (2012). An Insight into the Diverse Roles of Surfactant Proteins, SP-A and SP-D in Innate and Adaptive Immunity [Review]. *Frontiers in Immunology*, 3.
- Nemmar, A., Al-Salam, S., Zia, S., Marzouqi, F., Al-Dhaheri, A., Subramaniyan, D.,...Kazzam, E. E. (2011). Contrasting actions of diesel exhaust particles on the pulmonary and cardiovascular systems and the effects of thymoquinone. *British Journal of Pharmacology*, 164(7), 1871-1882. <https://doi.org/https://doi.org/10.1111/j.1476-5381.2011.01442.x>
- Nicod, L. P. (2005). Lung defences: an overview. *European Respiratory Review*, 14(95), 45. <https://doi.org/10.1183/09059180.05.00009501>
- Nicod, L. P., el Habre, F., Dayer, J. M., & Boehringer, N. (1995). Interleukin-10 decreases tumor necrosis factor alpha and beta in alloreactions induced by human lung dendritic cells and macrophages. *American Journal of Respiratory Cell and Molecular Biology*, 13(1), 83-90. <https://doi.org/10.1165/ajrcmb.13.1.7598941>
- Niechoda, A., Roslan, J., Maciorowska, K., Roslan, M., Ejsmont, K., & Holownia, A. (2023). Oxidative stress and activation of H2A.X in lung alveolar epithelial cells (A549) by nanoparticulate carbon black. *Respiratory Physiology & Neurobiology*, 316, 104140. <https://doi.org/https://doi.org/10.1016/j.resp.2023.104140>
- NIST. (2016). *Certificate of Analysis SRM 2583 Trace Elements in Indoor Dust (Nominal Mass Fraction of 90 mg/kg Lead)*.



- NIST. (2023). *Standard Reference Material 1649b Urban Dust Certificate of Analysis*.
- Niu, R., Cheng, J., Sun, J., Li, F., Fang, H., Lei, R.,...Li, J. (2022). Alveolar Type II Cell Damage and Nrf2-SOD1 Pathway Downregulation Are Involved in PM2.5-Induced Lung Injury in Rats. *International Journal of Environmental Research and Public Health*, 19(19).
- Nkadi, P. O., Merritt, T. A., & Pillers, D. A. (2009). An overview of pulmonary surfactant in the neonate: genetics, metabolism, and the role of surfactant in health and disease. *Molecular Genetics and Metabolism*, 97(2), 95-101. <https://doi.org/10.1016/j.ymgme.2009.01.015>
- Nuhu, F., Gordon, A., Sturmey, R., Seymour, A.-M., & Bhandari, S. (2020). Measurement of Glutathione as a Tool for Oxidative Stress Studies by High Performance Liquid Chromatography. *Molecules*, 25(18).
- OECD. (2018). Guidance Document on Good In Vitro Method Practices (GIVIMP). In.
- Ogbodo, J. O., Arazu, A. V., Iguh, T. C., Onwodi, N. J., & Ezike, T. C. (2022). Volatile organic compounds: A proinflammatory activator in autoimmune diseases [Review]. *Frontiers in Immunology*, 13.
- Ohtoshi, T., Takizawa, H., Okazaki, H., Kawasaki, S., Takeuchi, N., Ohta, K., & Ito, K. (1998). Diesel exhaust particles stimulate human airway epithelial cells to produce cytokines relevant to airway inflammation in vitro. *Journal of Allergy and Clinical Immunology*, 101(6), 778-785. [https://doi.org/https://doi.org/10.1016/S0091-6749\(98\)70307-0](https://doi.org/https://doi.org/10.1016/S0091-6749(98)70307-0)
- Okado-Matsumoto, A., & Fridovich, I. (2001). Subcellular Distribution of Superoxide Dismutases (SOD) in Rat Liver: Cu,Zn-SOD IN MITOCHONDRIA \*. *Journal of Biological Chemistry*, 276(42), 38388-38393. <https://doi.org/10.1074/jbc.M105395200>
- Orellano, P., Reynoso, J., & Quaranta, N. (2021). Short-term exposure to sulphur dioxide (SO<sub>2</sub>) and all-cause and respiratory mortality: A systematic review and meta-

- analysis. *Environment International*, 150, 106434.  
<https://doi.org/https://doi.org/10.1016/j.envint.2021.106434>
- Otoupalova, E., Smith, S., Cheng, G., & Thannickal, V. J. (2020). Oxidative Stress in Pulmonary Fibrosis. In *Comprehensive Physiology* (pp. 509-547).  
<https://doi.org/https://doi.org/10.1002/cphy.c190017>
- Ottaviano, F. G., Handy, D. E., & Loscalzo, J. (2008). Redox regulation in the extracellular environment. *Circulation Journal*, 72(1), 1-16. <https://doi.org/10.1253/circj.72.1>
- O'Hara, A. M., Bhattacharyya, A., Bai, J., Mifflin, R. C., Ernst, P. B., Mitra, S., & Crowe, S. E. (2009). Tumor necrosis factor (TNF)- $\alpha$ -induced IL-8 expression in gastric epithelial cells: Role of reactive oxygen species and AP endonuclease-1/redox factor (Ref)-1. *Cytokine*, 46(3), 359-369.  
<https://doi.org/https://doi.org/10.1016/j.cyto.2009.03.010>
- Palecanda, A., & Kobzik, L. (2001). Receptors for unopsonized particles: the role of alveolar macrophage scavenger receptors. *Current Molecular Medicine*, 1(5), 589-595.  
<https://doi.org/10.2174/1566524013363384>
- Pan, J., Plant, J. A., Voulvoulis, N., Oates, C. J., & Ihlenfeld, C. (2010). Cadmium levels in Europe: implications for human health. *Environ Geochem Health*, 32(1), 1-12.  
<https://doi.org/10.1007/s10653-009-9273-2>
- Pandya, R. J., Solomon, G., Kinner, A., & Balme, J. R. (2002). Diesel exhaust and asthma: hypotheses and molecular mechanisms of action. *Environmental Health Perspectives*, 110(suppl 1), 103-112.  
<https://doi.org/10.1289/ehp.02110s1103>
- Panzner, P., Malkusová, I., Vachová, M., Liška, M., Brodská, P., Růžicková, O., & Malý, M. (2015). Bronchial inflammation in seasonal allergic rhinitis with or without asthma in relation to natural exposure to pollen allergens [10.1016/j.aller.2013.06.009]. *Allergologia et Immunopathologia*, 43(1), 3-9.  
<https://doi.org/10.1016/j.aller.2013.06.009>



- Park, S.-H., Lee, H.-C., Jeong, H. M., Lee, J.-S., Cha, H.-J., Kim, C. H.,...Song, K. S. (2023). Inhibition of Urban Particulate Matter-Induced Airway Inflammation by RIPK3 through the Regulation of Tight Junction Protein Production. *International Journal of Molecular Sciences*, 24(17).
- Parliament of the United Kingdom. (1956). *Clean Air Act 1956*.
- Pastorekova, S., & Gillies, R. J. (2019). The role of carbonic anhydrase IX in cancer development: links to hypoxia, acidosis, and beyond. *Cancer and Metastasis Reviews*, 38(1), 65-77. <https://doi.org/10.1007/s10555-019-09799-0>
- Patel, B., Gupta, N., & Ahsan, F. (2015). Particle engineering to enhance or lessen particle uptake by alveolar macrophages and to influence the therapeutic outcome. *European Journal of Pharmaceutics and Biopharmaceutics*, 89, 163-174.  
<https://doi.org/https://doi.org/10.1016/j.ejpb.2014.12.001>
- Patrick, L. (2006). Lead Toxicity, a review of the literature. Part I: Exposure, Evaluation, and treatment. *Alternative medicine review*, 11(1).
- Paur, H.-R., Cassee, F. R., Teeguarden, J., Fissan, H., Diabate, S., Aufderheide, M.,...Schmid, O. (2011). In-vitro cell exposure studies for the assessment of nanoparticle toxicity in the lung—A dialog between aerosol science and biology. *Journal of Aerosol Science*, 42(10), 668-692. <https://doi.org/https://doi.org/10.1016/j.jaerosci.2011.06.005>
- Pease, J. E., & Sabroe, I. (2002). The Role of Interleukin-8 and its Receptors in Inflammatory Lung Disease. *American Journal of Respiratory Medicine*, 1(1), 19-25. <https://doi.org/10.1007/BF03257159>
- Peng, R. D., Samoli, E., Pham, L., Dominici, F., Touloumi, G., Ramsay, T.,...Samet, J. M. (2013). Acute effects of ambient ozone on mortality in Europe and North America: results from the APHENA study. *Air Quality, Atmosphere and Health*, 6(2), 445-453. <https://doi.org/10.1007/s11869-012-0180-9>

- Perez, L., Tobias, A., Querol, X., Künzli, N., Pey, J., Alastuey, A.,...Sunyer, J. (2008). Coarse particles from Saharan dust and daily mortality. *Epidemiology*, 19(6), 800-807. <https://doi.org/10.1097/ede.0b013e31818131cf>
- Persinger, R. L., Blay, W. M., Heintz, N. H., Hemenway, D. R., & Janssen-Heininger, Y. M. W. (2001). Nitrogen Dioxide Induces Death in Lung Epithelial Cells in a Density-Dependent Manner. *American Journal of Respiratory Cell and Molecular Biology*, 24(5), 583-590. <https://doi.org/10.1165/ajrcmb.24.5.4340>
- Peters, A., Dockery, D. W., Muller, J. E., & Mittleman, M. A. (2001). Increased particulate air pollution and the triggering of myocardial infarction. *Circulation*, 103(23), 2810-2815. <https://doi.org/10.1161/01.cir.103.23.2810>
- Philip, A. T., & Gerson, B. (1994). Lead Poisoning-Part I: Incidence, Etiology, and Toxicokinetics. *Clinics in Laboratory Medicine*, 14(2), 423-444. [https://doi.org/https://doi.org/10.1016/S0272-2712\(18\)30386-X](https://doi.org/https://doi.org/10.1016/S0272-2712(18)30386-X)
- Platz, J., Beisswenger, C., Dalpke, A., Koczulla, R., Pinkenburg, O., Vogelmeier, C., & Bals, R. (2004). Microbial DNA induces a host defense reaction of human respiratory epithelial cells. *Journal of Immunology*, 173(2), 1219-1223. <https://doi.org/10.4049/jimmunol.173.2.1219>
- Poland, C. A., Duffin, R., Kinloch, I., Maynard, A., Wallace, W. A. H., Seaton, A.,...Donaldson, K. (2008). Carbon nanotubes introduced into the abdominal cavity of mice show asbestos-like pathogenicity in a pilot study. *Nature Nanotechnology*, 3(7), 423-428. <https://doi.org/10.1038/nnano.2008.111>
- Polivka, B. J. (2018). The Great London Smog of 1952. *The American Journal of Nursing*, 118(4), 57-61. <https://doi.org/10.1097/01.NAJ.0000532078.72372.c3>
- Poloniecki, J. D., Atkinson, R. W., de Leon, A. P., & Anderson, H. R. (1997). Daily time series for cardiovascular hospital admissions and previous day's air pollution in London, UK.

- Occupational and Environmental Medicine*, 54(8), 535-540. <https://doi.org/10.1136/oem.54.8.535>
- Polzer, G., Lind, I., Mosbach, M., Schmidt, A., & Seidel, A. (1994). Combined influence of quartz dust, ozone and NO<sub>2</sub> on chemotactic mobility, release of chemotactic factors and other cytokines by macrophages in vitro. *Toxicology Letters*, 72(1), 307-315. [https://doi.org/https://doi.org/10.1016/0378-4274\(94\)90042-6](https://doi.org/https://doi.org/10.1016/0378-4274(94)90042-6)
- Pompella, A., Maellaro, E., Benedetti, A., & Casini, A. F. (2019). Glutathione depletion, lipid peroxidation, and the antecedents of ferroptosis: What about cellular calcium ? *Free Radical Biology and Medicine*, 143, 221-222. <https://doi.org/10.1016/j.freeradbiomed.2019.08.004>
- Ponchel, F., Toomes, C., Bransfield, K., Leong, F. T., Douglas, S. H., Field, S. L.,...Markham, A. F. (2003). Real-time PCR based on SYBR-Green I fluorescence: An alternative to the TaqMan assay for a relative quantification of gene rearrangements, gene amplifications and micro gene deletions. *BMC Biotechnology*, 3(1), 18. <https://doi.org/10.1186/1472-6750-3-18>
- Pope, C. A., Burnett, R. T., Thun, M. J., Calle, E. E., Krewski, D., Ito, K., & Thurston, G. D. (2002). Lung cancer, cardiopulmonary mortality, and long-term exposure to fine particulate air pollution. *Journal of American Medical Association*, 287(9), 1132-1141. <https://doi.org/10.1001/jama.287.9.1132>
- Pope, C. A., Dockery, D. W., Spengler, J. D., & Raizenne, M. E. (1991). Respiratory health and PM<sub>10</sub> pollution. A daily time series analysis. *The American Review of Respiratory Disease*, 144(3 Pt 1), 668-674. [https://doi.org/10.1164/ajrccm/144.3\\_Pt\\_1.668](https://doi.org/10.1164/ajrccm/144.3_Pt_1.668)
- Poschl, U. (2005). Atmospheric Aerosols: Composition, Transformation, Climate and Health Effects. *Angewandte Chemie International Edition*, 44, 7520-7540. <https://doi.org/https://doi.org/10.1002/anie.200501122>

- Prabhakar, O. (2013). Cerebroprotective effect of resveratrol through antioxidant and anti-inflammatory effects in diabetic rats. *Naunyn-Schmiedeberg's Archives of Pharmacology*, 386(8), 705-710. <https://doi.org/10.1007/s00210-013-0871-2>
- Prahalad, A. K., Soukup, J. M., Inmon, J., Willis, R., Ghio, A. J., Becker, S., & Gallagher, J. E. (1999). Ambient air particles: effects on cellular oxidant radical generation in relation to particulate elemental chemistry. *Toxicology and Applied Pharmacology*, 158(2), 81-91. <https://doi.org/10.1006/taap.1999.8701>
- Qin, G., Xia, J., Zhang, Y., Guo, L., Chen, R., & Sang, N. (2018). Ambient fine particulate matter exposure induces reversible cardiac dysfunction and fibrosis in juvenile and older female mice. *Particle and Fibre Toxicology*, 15(1), 27. <https://doi.org/10.1186/s12989-018-0264-2>
- Querol, X., Peya, J., Pandolfia, M., Alastueya, A., Cusacka, M., Péreza, N.,...Kleanthousd, S. (2009). African dust contributions to mean ambient PM10 mass-levels across the Mediterranean Basin. *Atmospheric Environment*, 43(28), 4266-4277. <https://doi.org/https://doi.org/10.1016/j.atmosenv.2009.06.013>
- Raaschou-Nielsen, O., Andersen, Z. J., Beelen, R., Samoli, E., Stafoggia, M., Weinmayr, G.,...Hoek, G. (2013). Air pollution and lung cancer incidence in 17 European cohorts: prospective analyses from the European Study of Cohorts for Air Pollution Effects (ESCAPE). *The Lancet Oncology*, 14(9), 813-822. [https://doi.org/10.1016/S1470-2045\(13\)70279-1](https://doi.org/10.1016/S1470-2045(13)70279-1)
- Ramirez-Carrozzi, V., Sambandam, A., Luis, E., Lin, Z., Jeet, S., Lesch, J.,...Pappu, R. (2011). IL-17C regulates the innate immune function of epithelial cells in an autocrine manner. *Nature Immunology*, 12(12), 1159-1166. <https://doi.org/10.1038/ni.2156>
- Ranft, U., Schikowski, T., Sugiri, D., Krutmann, J., & Krämer, U. (2009). Long-term exposure to traffic-related particulate

- matter impairs cognitive function in the elderly. *Environmental Research*, 109(8), 1004-1011. <https://doi.org/10.1016/j.envres.2009.08.003>
- RCP. (2016). Every breath we take: the lifelong impact of air pollution. Report of a working party. In. London: RCP.
- Rebbeck, T. R. (1997). Molecular epidemiology of the human glutathione S-transferase genotypes GSTM1 and GSTT1 in cancer susceptibility. *Cancer Epidemiology, Biomarkers & Prevention*, 6(9), 733-743.
- Reiss, R., Anderson, E. L., Cross, C. E., Hidy, G., Hoel, D., McClellan, R., & Moolgavkar, S. (2007). Evidence of Health Impacts of Sulfate-and Nitrate-Containing Particles in Ambient Air. *Inhalation Toxicology*, 19(5), 419-449. <https://doi.org/10.1080/08958370601174941>
- Ren, H., Birch, N. P., & Suresh, V. (2016). An Optimised Human Cell Culture Model for Alveolar Epithelial Transport. *PLOS ONE*, 11(10), e0165225. <https://doi.org/10.1371/journal.pone.0165225>
- Riches, D. W. H., & Martin, T. R. (2018). Overview of Innate Lung Immunity and Inflammation. *Methods in Molecular Biology*, 1809, 17-30. [https://doi.org/10.1007/978-1-4939-8570-8\\_2](https://doi.org/10.1007/978-1-4939-8570-8_2)
- Riechelmann, H. (2004). Cellular and molecular mechanisms in environmental and occupational inhalation toxicology. *GMS Current Topics in Otorhinolaryngology - Head and Neck Surgery*, 3, Doc02.
- Rincon, M., & Irvin, C. G. (2012). Role of IL-6 in Asthma and Other Inflammatory Pulmonary Diseases [Review]. *International Journal of Biological Sciences*, 8(9), 1281-1290. <https://doi.org/10.7150/ijbs.4874>
- Risby, H. (2022). *Understanding the Human Health Impacts of Carbon-Based Nanomaterials Under Occupational Exposure Scenarios* [Swansea University].
- Riva, D. R., Magalhães, C. B., Lopes, A. A., Lanças, T., Mauad, T., Malm, O.,...Zin, W. A. (2011). Low dose of fine particulate matter (PM<sub>2.5</sub>) can induce acute oxidative stress, inflammation and pulmonary impairment in healthy

- mice. *Inhalation Toxicology*, 23(5), 257-267.  
<https://doi.org/10.3109/08958378.2011.566290>
- Roca-Barceló, A., Crabbe, H., Ghosh, R., Freni-Sterrantino, A., Fletcher, T., Leonardi, G.,...Piel, F. B. (2020). Temporal trends and demographic risk factors for hospital admissions due to carbon monoxide poisoning in England. *Preventive Medicine*, 136, 106104.  
<https://doi.org/https://doi.org/10.1016/j.ypmed.2020.106104>
- Rogers, L. K., & Cismowski, M. J. (2018). Oxidative stress in the lung – The essential paradox. *Current Opinion in Toxicology*, 7, 37-43.  
<https://doi.org/https://doi.org/10.1016/j.cotox.2017.09.001>
- Rose, M. C., & Voynow, J. A. (2006). Respiratory tract mucin genes and mucin glycoproteins in health and disease. *Physiological Reviews*, 86(1), 245-278.  
<https://doi.org/10.1152/physrev.00010.2005>
- Ruttkay-Nedecky, B., Nejdí, L., Gumulec, J., Zitka, O., Masarik, M., Eckschlager, T.,...Kizek, R. (2013). The Role of Metallothionein in Oxidative Stress. *International Journal of Molecular Sciences*, 14(3), 6044-6066.
- Ryu, M., Lau, K., Wooding, D., Fan, S., D. Sin, D., & Carlsten, C. (2020). Particle depletion of diesel exhaust restores allergen-induced lung-protective surfactant protein D in human lungs. *Thorax*, 75(8), 640.  
<https://doi.org/10.1136/thoraxjnl-2020-214561>
- Ryu, Y., Roh, S., & Joung, Y. S. (2023). Assessing the cytotoxicity of aerosolized carbon black and benzo[a]pyrene with controlled physical and chemical properties on human lung epithelial cells. *Scientific Reports*, 13(1), 9358. <https://doi.org/10.1038/s41598-023-35586-7>
- Saber, A. T., Bornholdt, J., Dybdahl, M., Sharma, A. K., Loft, S., Vogel, U., & Wallin, H. (2005). Tumor necrosis factor is not required for particle-induced genotoxicity and pulmonary inflammation. *Archives of Toxicology*, 79(3), 177-182. <https://doi.org/10.1007/s00204-004-0613-9>



- Saber, A. T., Jensen, K. A., Jacobsen, N. R., Birkedal, R., Mikkelsen, L., Møller, P.,...Vogel, U. (2012). Inflammatory and genotoxic effects of nanoparticles designed for inclusion in paints and lacquers. *Nanotoxicology*, 6(5), 453-471. <https://doi.org/10.3109/17435390.2011.587900>
- Sagai, M., Ichinose, T., & Kubota, K. (1984). Studies on the biochemical effects of nitrogen dioxide. IV. Relation between the change of lipid peroxidation and the antioxidative protective system in rat lungs upon life span exposure to low levels of NO<sub>2</sub>. *Toxicol Appl Pharmacol*, 73(3), 444-456. [https://doi.org/10.1016/0041-008x\(84\)90097-8](https://doi.org/10.1016/0041-008x(84)90097-8)
- Sakamoto, N., Hayashi, S., Gosselink, J., Ishii, H., Ishimatsu, Y., Mukae, H.,...van Eeden, S. F. (2007). Calcium dependent and independent cytokine synthesis by air pollution particle-exposed human bronchial epithelial cells. *Toxicology and Applied Pharmacology*, 225(2), 134-141. <https://doi.org/10.1016/j.taap.2007.07.006>
- Salomon, J. J., Muchitsch, V. E., Gausterer, J. C., Schwagerus, E., Huwer, H., Daum, N.,...Ehrhardt, C. (2014). The Cell Line NCI-H441 Is a Useful in Vitro Model for Transport Studies of Human Distal Lung Epithelial Barrier. *Molecular Pharmaceutics*, 11(3), 995-1006. <https://doi.org/10.1021/mp4006535>
- Salter, M. E., Zieger, P., Acosta Navarro, J. C., Grythe, H., Kirkevåg, A., Rosati, B. R., I., & Nilsson, E. D. (2015). An empirically derived inorganic sea spray source function incorporating sea surface temperature. 15, 11047–11066. <https://doi.org/10.5194/acp-15-11047-2015>, 2015
- Samet, J. M., Dominici, F., Currier, I., Coursac, I., & Zeger, S. L. (2000). Fine particulate air pollution and mortality in 20 U.S. cities, 1987-1994. *The New England Journal of Medicine*, 343(24), 1742-1749. <https://doi.org/10.1056/NEJM200012143432401>
- Samet, J. M., Dominici, F., Zeger, S. L., Schwartz, J., & Dockery, D. W. (2000). The National Morbidity, Mortality, and Air

Pollution Study. Part I: Methods and methodologic issues. *Research Reports (Health Effects Institute)*(94 Pt 1), 5-14; discussion 75-84.

- Samet, J. M., Rappold, A., Graff, D., Cascio, W. E., Berntsen, J. H., Huang, Y. C.,...Devlin, R. B. (2009). Concentrated ambient ultrafine particle exposure induces cardiac changes in young healthy volunteers. *American Journal of Respiratory and Critical Care Medicine*, 179(11), 1034-1042. <https://doi.org/10.1164/rccm.200807-1043OC>
- Samoli, E., Peng, R., Ramsay, T., Pipikou, M., Touloumi, G., Dominici, F.,...Katsouyanni, K. (2008). Acute effects of ambient particulate matter on mortality in Europe and North America: results from the APHENA study. *Environmental Health Perspectives*, 116(11), 1480-1486. <https://doi.org/10.1289/ehp.11345>
- Saraste, A. (1999). Morphologic criteria and detection of apoptosis. *Herz*, 24(3), 189-195. <https://doi.org/10.1007/BF03044961>
- Sato, H., Onose, J., Toyoda, H., Toida, T., Imanari, T., Sagai, M.,...Aoki, Y. (2001). Quantitative changes in glycosaminoglycans in the lungs of rats exposed to diesel exhaust. *Toxicology*, 166(3), 119-128. [https://doi.org/10.1016/s0300-483x\(01\)00453-x](https://doi.org/10.1016/s0300-483x(01)00453-x)
- Sawyer, K., Mundandhara, S., Ghio, A. J., & Madden, M. C. (2009). The Effects of Ambient Particulate Matter on Human Alveolar Macrophage Oxidative and Inflammatory Responses. *Journal of Toxicology and Environmental Health, Part A*, 73(1), 41-57. <https://doi.org/10.1080/15287390903248901>
- Saxena, R. K., Gilmour, M. I., & Hays, M. D. (2008). Isolation and quantitative estimation of diesel exhaust and carbon black particles ingested by lung epithelial cells and alveolar macrophages in vitro. *Biotechniques*, 44(6), 799-805. <https://doi.org/10.2144/000112754>
- Schaefer, J., Schulze, C., Marxer, E. E. J., Schaefer, U. F., Wohlleben, W., Bakowsky, U., & Lehr, C.-M. (2012). Atomic Force Microscopy and Analytical



- Ultracentrifugation for Probing Nanomaterial Protein Interactions. *ACS Nano*, 6(6), 4603-4614. <https://doi.org/10.1021/nn202657q>
- Schiefermeier-Mach, N., Heinrich, L., Lechner, L., & Perkhofer, S. (2023). Regulation of Surfactant Protein Gene Expression by *Aspergillus fumigatus* in NCI-H441 Cells. *Microorganisms*, 11(4).
- Schikowski, T., Adam, M., Marcon, A., Cai, Y., Vierkötter, A., Carsin, A. E.,...Künzli, N. (2014). Association of ambient air pollution with the prevalence and incidence of COPD. *European Respiratory Journal*, 44(3), 614-626. <https://doi.org/10.1183/09031936.00132213>
- Schroeder, W. H., & Urone, P. (1974). Formation of nitrosyl chloride from salt particles in air. *Environmental Science & Technology*, 8(8), 756-758. <https://doi.org/10.1021/es60093a015>
- Schuliga, M. (2015). NF-kappaB Signaling in Chronic Inflammatory Airway Disease. *Biomolecules*, 5(3), 1266-1283. <https://doi.org/10.3390/biom5031266>
- Schweitzer, K. S., Hatoum, H., Brown, M. B., Gupta, M., Justice, M. J., Beteck, B.,...Petrache, I. (2011). Mechanisms of lung endothelial barrier disruption induced by cigarette smoke: role of oxidative stress and ceramides. *American Journal of Physiology-Lung Cellular and Molecular Physiology*, 301(6), L836-L846. <https://doi.org/10.1152/ajplung.00385.2010>
- Seegeritz, C.-P., & Vallier, L. (2017). Chapter 9 - Cell Culture: Growing Cells as Model Systems In Vitro. In M. Jalali, F. Y. L. Saldanha, & M. Jalali (Eds.), *Basic Science Methods for Clinical Researchers* (pp. 151-172). Academic Press. <https://doi.org/https://doi.org/10.1016/B978-0-12-803077-6.00009-6>
- Sena, L. A., & Chandel, N. S. (2012). Physiological roles of mitochondrial reactive oxygen species. *Molecular Cell*, 48(2), 158-167. <https://doi.org/10.1016/j.molcel.2012.09.025>

- Sethi, S. (2010). Infection as a comorbidity of COPD. *European Respiratory Journal*, 35(6), 1209.  
<https://doi.org/10.1183/09031936.00081409>
- Shaw, C. A., Robertson, S., Miller, M. R., Duffin, R., Tabor, C. M., Donaldson, K.,...Hadoke, P. W. F. (2011). Diesel Exhaust Particulate–Exposed Macrophages Cause Marked Endothelial Cell Activation. *American Journal of Respiratory Cell and Molecular Biology*, 44(6), 840-851.  
<https://doi.org/10.1165/rcmb.2010-0011OC>
- Sherman, B. T., Hao, M., Qiu, J., Jiao, X., Baseler, M. W., Lane, H. C.,...Chang, W. (2022). DAVID: a web server for functional enrichment analysis and functional annotation of gene lists (2021 update). *Nucleic Acids Research*, 50(W1), W216-W221.  
<https://doi.org/10.1093/nar/gkac194>
- Shi, T., Duffin, R., Borm, P. J., Li, H., Weishaupt, C., & Schins, R. P. (2006). Hydroxyl-radical-dependent DNA damage by ambient particulate matter from contrasting sampling locations. *Environmental Research*, 101(1), 18-24.  
<https://doi.org/10.1016/j.envres.2005.09.005>
- Shoenfelt, J., Mitkus, R. J., Zeisler, R., Spatz, R. O., Powell, J., Fenton, M. J.,...Medvedev, A. E. (2009). Involvement of TLR2 and TLR4 in inflammatory immune responses induced by fine and coarse ambient air particulate matter. *Journal of Leukocyte Biology*, 86(2), 303-312.  
<https://doi.org/10.1189/jlb.1008587>
- Shouval, D. S., Ouahed, J., Biswas, A., Goettel, J. A., Horwitz, B. H., Klein, C.,...Snapper, S. B. (2014). Chapter Five - Interleukin 10 Receptor Signaling: Master Regulator of Intestinal Mucosal Homeostasis in Mice and Humans. In F. W. Alt (Ed.), *Advances in Immunology* (Vol. 122, pp. 177-210). Academic Press.  
<https://doi.org/https://doi.org/10.1016/B978-0-12-800267-4.00005-5>
- Shukla, A., Timblin, C., BeruBe, K., Gordon, T., McKinney, W., Driscoll, K.,...Mossman, B. T. (2000). Inhaled particulate matter causes expression of nuclear factor (NF)-kappaB-

- related genes and oxidant-dependent NF-kappaB activation in vitro. *American Journal of Respiratory Cell and Molecular Biology*, 23(2), 182-187. <https://doi.org/10.1165/ajrcmb.23.2.4035>
- Simons, R. K., Junger, W. G., Loomis, W. H., & Hoyt, D. B. (1996). Acute lung injury in endotoxic rats is associated with sustained circulating IL-6 levels and intrapulmonary cAMP activity and neutrophil recruitment-Role of Circulating TNF-alpha and IL-beta. *Shock*, 6(1).
- Singh, N., Gupta, V. K., Kumar, A., & Sharma, B. (2017). Synergistic Effects of Heavy Metals and Pesticides in Living Systems [Mini Review]. *Frontiers in Chemistry*, 5.
- Sittipunt, C., Steinberg, K. P., Ruzinski, J. T., Myles, C., Zhu, S., Goodman, R. B.,...Martin, T. R. (2001). Nitric oxide and nitrotyrosine in the lungs of patients with acute respiratory distress syndrome. *American Journal of Respiratory and Critical Care Medicine*, 163(2), 503-510. <https://doi.org/10.1164/ajrccm.163.2.2004187>
- Smit, R. (2014). Australian Motor Vehicle Emission Inventory for the Nation Pollution Inventory (NPI). *Uniquet Pty Ltd, St Lucia, Australia*.
- Smyth, T., Veazey, J., Eliseeva, S., Chalupa, D., Elder, A., & Georas, S. N. (2020). Diesel exhaust particle exposure reduces expression of the epithelial tight junction protein Tricellulin. *Particle and Fibre Toxicology*, 17(1), 52. <https://doi.org/10.1186/s12989-020-00383-x>
- Song, Q., Christiani, D. C., XiaorongWang, & Ren, J. (2014). The global contribution of outdoor air pollution to the incidence, prevalence, mortality and hospital admission for chronic obstructive pulmonary disease: a systematic review and meta-analysis. *International Journal of Environmental Research and Public Health*, 11(11), 11822-11832. <https://doi.org/10.3390/ijerph111111822>
- Soni, S., O'Dea, K. P., Abe, E., Khamdan, M., Shah, S. V., Sarathchandra, P.,...Takata, M. (2022). Microvesicle-Mediated Communication Within the Alveolar Space: Mechanisms of Uptake by Epithelial Cells and Alveolar

- Macrophages [Original Research]. *Frontiers in Immunology*, 13.
- Srinivasan, B., Kolli, A. R., Esch, M. B., Abaci, H. E., Shuler, M. L., & Hickman, J. J. (2015). TEER Measurement Techniques for In Vitro Barrier Model Systems. *Journal of Laboratory Automation*, 20(2), 107-126.  
<https://doi.org/10.1177/2211068214561025>
- Stading, R., Chu, C., Couroucli, X., Lingappan, K., & Moorthy, B. (2020). Molecular role of cytochrome P4501A enzymes in oxidative stress. *Current Opinion in Toxicology*, 20-21, 77-84.  
<https://doi.org/https://doi.org/10.1016/j.cotox.2020.07.001>
- Stapleton, H. M., Harner, T., Shoeib, M., Keller, J. M., Schantz, M. M., Leigh, S. D., & Wise, S. A. (2006). Determination of polybrominated diphenyl ethers in indoor dust standard reference materials. *Analytical and Bioanalytical Chemistry*, 384(3), 791-800.  
<https://doi.org/10.1007/s00216-005-0227-y>
- Steiner, S., Bisig, C., Petri-Fink, A., & Rothen-Rutishauser, B. (2016). Diesel exhaust: current knowledge of adverse effects and underlying cellular mechanisms. *Archives of Toxicology*, 90(7), 1541-1553.  
<https://doi.org/10.1007/s00204-016-1736-5>
- Stermann, T., Nguyen, T., Stahlmecke, B., Todea, A. M., Woeste, S., Hacheney, I.,...Rossi, A. (2022). Carbon nanoparticles adversely affect CFTR expression and toxicologically relevant pathways. *Scientific Reports*, 12(1), 14255.  
<https://doi.org/10.1038/s41598-022-18098-8>
- Stoller, J. K., & Aboussouan, L. S. (2005). Alpha1-antitrypsin deficiency. *The Lancet*, 365(9478), 2225-2236.  
[https://doi.org/10.1016/S0140-6736\(05\)66781-5](https://doi.org/10.1016/S0140-6736(05)66781-5)
- Stone, K. C., Mercer, R. R., Gehr, P., Stockstill, B., & Crapo, J. D. (1992). Allometric Relationships of Cell Numbers and Size in the Mammalian Lung. *American Journal of Respiratory Cell and Molecular Biology*, 6(2), 235-243.  
<https://doi.org/10.1165/ajrcmb/6.2.235>

- Stone, V., Miller, M. R., Clift, M. J. D., Elder, A., Mills, N. L., Møller, P.,...Cassee, F. R. (2017). Nanomaterials Versus Ambient Ultrafine Particles: An Opportunity to Exchange Toxicology Knowledge. *Environmental Health Perspectives*, 125(10), 106002. <https://doi.org/10.1289/EHP424>
- Straif, K., Benbrahim-Tallaa, L., Baan, R., Grosse, Y., Secretan, B., El Ghissassi, F.,...Group, W. I. A. f. R. o. C. M. W. (2009). A review of human carcinogens--Part C: metals, arsenic, dusts, and fibres. *Lancet Oncol*, 10(5), 453-454. [https://doi.org/10.1016/s1470-2045\(09\)70134-2](https://doi.org/10.1016/s1470-2045(09)70134-2)
- Stringer, B., Imrich, A., & Kobzik, L. (1995). Flow cytometric assay of lung macrophage uptake of environmental particulates. *Cytometry*, 20(1), 23-32. <https://doi.org/10.1002/cyto.990200106>
- Su, X., Tian, J., Li, B., Zhou, L., Kang, H., Pei, Z.,...Zhang, R. (2020). Ambient PM<sub>2.5</sub> caused cardiac dysfunction through FoxO1-targeted cardiac hypertrophy and macrophage-activated fibrosis in mice. *Chemosphere*, 247, 125881. <https://doi.org/10.1016/j.chemosphere.2020.125881>
- Sui, J., Xia, H., Zhao, Q., Sun, G., & Cai, Y. (2022). Long-Term Exposure to Fine Particulate Matter and the Risk of Chronic Liver Diseases: A Meta-Analysis of Observational Studies. *International Journal of Environmental Research and Public Health*, 19(16).
- Sun, L., Dong, S., Ge, Y., Fonseca, J. P., Robinson, Z. T., Mysore, K. S., & Mehta, P. (2019). DiVenn: An Interactive and Integrated Web-Based Visualization Tool for Comparing Gene Lists [Methods]. *Frontiers in Genetics*, 10.
- Sundblad, B.-M., Larsson, B.-M., Acevedo, F., Ernstgård, L., Johanson, G., Larsson, K., & Palmberg, L. (2004). Acute respiratory effects of exposure to ammonia on healthy subjects. *Scandinavian Journal of Work, Environment & Health*(4), 313-321. <https://doi.org/10.5271/sjweh.800>
- Suzuki, A. K., Tsubone, H., Sagai, M., & Kubota, K. (1983). Effects of low concentrations of and long-term exposures

- to nitrogen dioxide on rat arterial blood pH<sub>a</sub>, PaCO<sub>2</sub> and PaO<sub>2</sub>. *Japanese Journal of Hygiene*, 38(4), 758-763.
- Sykiotis, G. P., & Bohmann, D. (2010). Stress-activated cap'n'collar transcription factors in aging and human disease. *Science Signaling*, 3(112), re3. <https://doi.org/10.1126/scisignal.3112re3>
- Szklarczyk, D., Gable, A. L., Lyon, D., Junge, A., Wyder, S., Huerta-Cepas, J.,...Mering, Christian v. (2019). STRING v11: protein–protein association networks with increased coverage, supporting functional discovery in genome-wide experimental datasets. *Nucleic Acids Research*, 47(D1), D607-D613. <https://doi.org/10.1093/nar/gky1131>
- Søs Poulsen, S., Jacobsen, N. R., Labib, S., Wu, D., Husain, M., Williams, A.,...Halappanavar, S. (2013). Transcriptomic Analysis Reveals Novel Mechanistic Insight into Murine Biological Responses to Multi-Walled Carbon Nanotubes in Lungs and Cultured Lung Epithelial Cells. *PLOS ONE*, 8(11), e80452. <https://doi.org/10.1371/journal.pone.0080452>
- Tamaoki, J., Isono, K., Takeyama, K., Tagaya, E., Nakata, J., & Nagai, A. (2004). Ultrafine carbon black particles stimulate proliferation of human airway epithelium via EGF receptor-mediated signaling pathway. *American Journal of Physiology - Lung Cellular and Molecular Physiology*, 287(6), L1127-1133. <https://doi.org/10.1152/ajplung.00241.2004>
- Tan, S. P., & Piri, M. (2013). Modeling the Solubility of Nitrogen Dioxide in Water Using Perturbed-Chain Statistical Associating Fluid Theory. *Industrial & Engineering Chemistry Research*, 52(45), 16032-16043. <https://doi.org/10.1021/ie402417p>
- Tapia, V. L., Vasquez, B. V., Vu, B., Liu, Y., Steenland, K., & Gonzales, G. F. (2020). Association between maternal exposure to particulate matter (PM<sub>2.5</sub>) and adverse pregnancy outcomes in Lima, Peru. *Journal of Exposure Science & Environmental Epidemiology*, 30(4), 689-697. <https://doi.org/10.1038/s41370-020-0223-5>



- Tedgui, A., & Mallat, Z. (2006). Cytokines in Atherosclerosis: Pathogenic and Regulatory Pathways. *Physiological Reviews*, 86(2), 515-581. <https://doi.org/10.1152/physrev.00024.2005>
- Terzano, C., Di Stefano, F., Conti, V., Graziani, E., & Petroianni, A. (2010). Air pollution ultrafine particles: toxicity beyond the lung. *European Review of Medical and Pharmacological Sciences*, 14(10), 809-821.
- The World Health Organization. (2010). *Guidelines for Indoor Air Quality: Selected Pollutants*. World Health Organization Regional Office for Europe.
- Thompson, J. E. (2018). Airborne Particulate Matter: Human Exposure and Health Effects. *Journal of Occupational and Environmental Medicine*, 60(5), 392-423. <https://doi.org/10.1097/JOM.0000000000001277>
- Tian, L.-X., Tang, X., Zhu, J.-Y., Luo, L., Ma, X.-Y., Cheng, S.-W.,...Liang, H.-P. (2020). Cytochrome P450 1A1 enhances inflammatory responses and impedes phagocytosis of bacteria in macrophages during sepsis. *Cell Communication and Signaling*, 18(1), 70. <https://doi.org/10.1186/s12964-020-0523-3>
- Tian, Y., Denda-Nagai, K., Tsukui, T., Ishii-Schrade, K. B., Okada, K., Nishizono, Y.,...Irimura, T. (2022). Mucin 21 confers resistance to apoptosis in an O-glycosylation-dependent manner. *Cell Death Discovery*, 8(1), 194. <https://doi.org/10.1038/s41420-022-01006-4>
- Tobías, A., Caylà, J. A., Pey, J., Alastuey, A., & Querol, X. (2011). Are Saharan dust intrusions increasing the risk of meningococcal meningitis? *International Journal of Infectious Diseases*, 15(7), e503. <https://doi.org/10.1016/j.ijid.2011.03.008>
- Totlandsdal, A. I., Cassee, F. R., Schwarze, P., Refsnes, M., & Låg, M. (2010). Diesel exhaust particles induce CYP1A1 and pro-inflammatory responses via differential pathways in human bronchial epithelial cells. *Particle and Fibre Toxicology*, 7(1), 41. <https://doi.org/10.1186/1743-8977-7-41>

- Totsuka, Y., Higuchi, T., Imai, T., Nishikawa, A., Nohmi, T., Kato, T.,...Wakabayashi, K. (2009). Genotoxicity of nano/microparticles in in vitro micronuclei, in vivo comet and mutation assay systems. *Particle and Fibre Toxicology*, 6(1), 23. <https://doi.org/10.1186/1743-8977-6-23>
- Touloumi, G., Katsouyanni, K., Zmirou, D., Schwartz, J., Spix, C., de Leon, A. P.,...Ponka, A. (1997). Short-term effects of ambient oxidant exposure on mortality: a combined analysis within the APHEA project. *Air Pollution and Health: a European Approach. American Journal of Epidemiology*, 146(2), 177-185. <https://doi.org/10.1093/oxfordjournals.aje.a009249>
- Tran, V., Ledwith, M. P., Thamamongood, T., Higgins, C. A., Tripathi, S., Chang, M. W.,...Mehle, A. (2020). Influenza virus repurposes the antiviral protein IFIT2 to promote translation of viral mRNAs. *Nature Microbiology*, 5(12), 1490-1503. <https://doi.org/10.1038/s41564-020-0778-x>
- Tretina, K., Park, E.-S., Maminska, A., & MacMicking, J. D. (2019). Interferon-induced guanylate-binding proteins: Guardians of host defense in health and disease. *Journal of Experimental Medicine*, 216(3), 482-500. <https://doi.org/10.1084/jem.20182031>
- Tseng, J.-S., Chiang, C.-J., Chen, K.-C., Zheng, Z.-R., Yang, T.-Y., Lee, W.-C.,...Chang, G.-C. (2022). Association of Smoking With Patient Characteristics and Outcomes in Small Cell Lung Carcinoma, 2011-2018. *JAMA Network Open*, 5(3), e224830-e224830. <https://doi.org/10.1001/jamanetworkopen.2022.4830>
- Tsukue, N., Okumura, H., Ito, T., Sugiyama, G., & Nakajima, T. (2010). Toxicological evaluation of diesel emissions on A549 cells. *Toxicology in Vitro*, 24(2), 363-369. <https://doi.org/https://doi.org/10.1016/j.tiv.2009.11.004>
- Valdivia, A., Duran, C., & Martin, S. A. (2015). The role of Nox-mediated oxidation in the regulation of cytoskeletal dynamics. *Current Pharmaceutical Design*, 21(41), 6009-6022.



<https://doi.org/http://dx.doi.org/10.2174/1381612821666151029112624>

- van der Valk, J., Bieback, K., Buta, C., Cochrane, B., Dirks, W. G., Fu, J.,...Gstraunthaler, G. (2018). Fetal bovine serum (FBS): Past – present – future. *ALTEX - Alternatives to animal experimentation*, 35(1), 99-118. <https://doi.org/10.14573/altex.1705101>
- van Eeden, S. F., Tan, W. C., Suwa, T., Mukae, H., Terashima, T., Fujii, T.,...Hogg, J. C. (2001). Cytokines involved in the systemic inflammatory response induced by exposure to particulate matter air pollutants (PM(10)). *American Journal of Respiratory and Critical Care Medicine*, 164(5), 826-830. <https://doi.org/10.1164/ajrccm.164.5.2010160>
- Vaziri, N. D., & Sica, D. A. (2004). Lead-induced hypertension: Role of oxidative stress. *Current Hypertension Reports*, 6(4), 314-320. <https://doi.org/10.1007/s11906-004-0027-3>
- Veldhuizen, E. J., & Haagsman, H. P. (2000). Role of pulmonary surfactant components in surface film formation and dynamics. *Biochimica et Biophysica Acta*, 1467(2), 255-270. [https://doi.org/10.1016/s0005-2736\(00\)00256-x](https://doi.org/10.1016/s0005-2736(00)00256-x)
- Vella, G., Ritzmann, F., Wolf, L., Kamyschnikov, A., Stodden, H., Herr, C.,...Beisswenger, C. (2021). IL-17C contributes to NTHi-induced inflammation and lung damage in experimental COPD and is present in sputum during acute exacerbations. *PLOS ONE*, 16(1), e0243484. <https://doi.org/10.1371/journal.pone.0243484>
- Verboogen, D. R. J., Revelo, N. H., ter Beest, M., & van den Bogaart, G. (2019). Interleukin-6 secretion is limited by self-signaling in endosomes. *Journal of Molecular Cell Biology*, 11(2), 144-157. <https://doi.org/10.1093/jmcb/mjy038>
- Villamayor, L., López-García, D., Rivero, V., Martínez-Sobrido, L., Nogales, A., & DeDiego, M. L. (2023). The IFN-stimulated gene IFI27 counteracts innate immune responses after viral infections by interfering with RIG-I signaling [Original Research]. *Frontiers in Microbiology*, 14.

- Vis, M. A. M., Ito, K., & Hofmann, S. (2020). Impact of Culture Medium on Cellular Interactions in in vitro Co-culture Systems [Mini Review]. *Frontiers in Bioengineering and Biotechnology*, 8.
- Voisin, C., Aerts, C., Jakubczk, E., & Tonnel, A. B. (1977). [La culture cellulaire en phase gazeuse. Un nouveau modèle expérimental d'étude in vitro des activités des macrophages alvéolaires]. *Bulletin europeen de physiopathologie respiratoire*, 13(1), 69-82.
- Volk, H. E., Lurmann, F., Penfold, B., Hertz-Picciotto, I., & McConnell, R. (2013). Traffic-related air pollution, particulate matter, and autism. *JAMA Psychiatry*, 70(1), 71-77. <https://doi.org/10.1001/jamapsychiatry.2013.266>
- Voss, C., Schmid, O., Stoeger, T., Danielsen, P., Vogel, U., Seidel, C.,...Gat é, L. (2020). *SmartNanoTox - Deliverable 1.6: Report on in vitro and in vivo toxicological properties of NMs*.
- Waghray, M., Cui, Z., Horowitz, J. C., Subramanian, I. M., Martinez, F. J., Toews, G. B., & Thannickal, V. J. (2005). Hydrogen peroxide is a diffusible paracrine signal for the induction of epithelial cell death by activated myofibroblasts. *The FASEB Journal*, 19(7), 1-16. <https://doi.org/https://doi.org/10.1096/fj.04-2882fje>
- Walkey, C. D., Olsen, J. B., Song, F., Liu, R., Guo, H., Olsen, D. W. H.,...Chan, W. C. W. (2014). Protein Corona Fingerprinting Predicts the Cellular Interaction of Gold and Silver Nanoparticles. *ACS Nano*, 8(3), 2439-2455. <https://doi.org/10.1021/nn406018q>
- Wallaert, B., & Voisin, C. (1992). In vitro study of gas effects on alveolar macrophages. *Cell Biology and Toxicology*, 8(3), 151-156. <https://doi.org/10.1007/BF00130522>
- Wang, F., Li, C., Liu, W., & Jin, Y. (2012). Effect of exposure to volatile organic compounds (VOCs) on airway inflammatory response in mice. *The Journal of Toxicological Sciences*, 37(4), 739-748. <https://doi.org/10.2131/jts.37.739>

- Wang, J., Huang, J., Wang, L., Chen, C., Yang, D., Jin, M.,...Song, Y. (2017). Urban particulate matter triggers lung inflammation via the ROSMAPK- NF- $\kappa$ B signaling pathway. *Journal of Thoracic Disease; Vol 9, No 11 (November 29, 2017): Journal of Thoracic Disease (Quantitative Imaging of Thoracic Diseases)*.
- Wang, J., Smedje, G., Nordquist, T., & Norbäck, D. (2015). Personal and demographic factors and change of subjective indoor air quality reported by school children in relation to exposure at Swedish schools: A 2-year longitudinal study. *Science of The Total Environment*, 508, 288-296. <https://doi.org/https://doi.org/10.1016/j.scitotenv.2014.12.001>
- Wang, L., Gordon, R. A., Huynh, L., Su, X., Min, K.-H. P., Han, J.,...Ivashkiv, L. B. (2010). Indirect Inhibition of Toll-like Receptor and Type I Interferon Responses by ITAM-Coupled Receptors and Integrins. *Immunity*, 32(4), 518-530. <https://doi.org/https://doi.org/10.1016/j.immuni.2010.03.014>
- Wang, L., Li, M., Yu, S., Chen, X., Li, Z., Zhang, Y.,...Seinfeld, J. H. (2020). Unexpected rise of ozone in urban and rural areas, and sulfur dioxide in rural areas during the coronavirus city lockdown in Hangzhou, China: implications for air quality. *Environmental Chemistry Letters*, 18(5), 1713-1723. <https://doi.org/10.1007/s10311-020-01028-3>
- Wang, L., Liu, C., Meng, X., Niu, Y., Lin, Z., Liu, Y.,...Kan, H. (2018). Associations between short-term exposure to ambient sulfur dioxide and increased cause-specific mortality in 272 Chinese cities. *Environment International*, 117, 33-39. <https://doi.org/10.1016/j.envint.2018.04.019>
- Wang, L., Luo, D., Liu, X., Zhu, J., Wang, F., Li, B., & Li, L. (2021). Effects of PM<sub>2.5</sub> exposure on reproductive system and its mechanisms. *Chemosphere*, 264, 128436. <https://doi.org/https://doi.org/10.1016/j.chemosphere.2020.128436>

- Wang, Y., Wen, Y., Zhang, S., Zheng, G., Zheng, H., Chang, X.,...Hao, J. (2023). Vehicular Ammonia Emissions Significantly Contribute to Urban PM<sub>2.5</sub> Pollution in Two Chinese Megacities. *Environmental Science & Technology*, 57(7), 2698-2705. <https://doi.org/10.1021/acs.est.2c06198>
- Wani, A. L., Ara, A., & Usmani, J. A. (2016). Lead toxicity: a review. *Interdisciplinary Toxicology*, 8(2), 55-64. <https://doi.org/doi:10.1515/intox-2015-0009>
- Wathanavasin, W., Banjongjit, A., Phannajit, J., Eiam-Ong, S., & Susantitaphong, P. (2024). Association of fine particulate matter (PM<sub>2.5</sub>) exposure and chronic kidney disease outcomes: a systematic review and meta-analysis. *Scientific Reports*, 14(1), 1048. <https://doi.org/10.1038/s41598-024-51554-1>
- Watson, A., Madsen, J., & Clark, H. W. (2021). SP-A and SP-D: Dual Functioning Immune Molecules With Antiviral and Immunomodulatory Properties [Review]. *Frontiers in Immunology*, 11.
- Weber, A., Wasiliew, P., & Kracht, M. (2010). Interleukin-1 (IL-1) Pathway. *Science Signaling*, 3(105), cm1-cm1. <https://doi.org/10.1126/scisignal.3105cm1>
- Webster, J. D., & Vucic, D. (2020). The Balance of TNF Mediated Pathways Regulates Inflammatory Cell Death Signaling in Healthy and Diseased Tissues [Review]. *Frontiers in Cell and Developmental Biology*, 8.
- Wegmann, M., Renz, H., & Herz, U. (2002). Long-term NO<sub>2</sub> exposure induces pulmonary inflammation and progressive development of airflow obstruction in C57BL/6 mice: a mouse model for chronic obstructive pulmonary disease? *Pathobiology*, 70(5), 284-286. <https://doi.org/10.1159/000070743>
- Whitsett, J. A. (2018). Airway Epithelial Differentiation and Mucociliary Clearance. *Annals of the American Thoracic Society*, 15(Suppl 3), S143-S148. <https://doi.org/10.1513/AnnalsATS.201802-128AW>
- WHO. (2008). Guidelines for drinking-water quality, 3rd edition incorporating 1st and 2nd addenda. In (3 ed., Vol. 1).

- WHO. (2010). *WHO Guidelines for indoor air quality: selected pollutants*.  
<https://iris.who.int/bitstream/handle/10665/260127/9789289002134-eng.pdf?sequence=1>
- WHO. (2013). Review of evidence on health aspects of air pollution – REVIHAAP Project - Technical Report. *WHO Regional Office for Europe*.
- Wickremasinghe, M. I., Thomas, L. H., & Friedland, J. S. (1999). Pulmonary Epithelial Cells are a Source of IL-8 in the Response to *Mycobacterium tuberculosis*: Essential Role of IL-1 from Infected Monocytes in a NF- $\kappa$ B-Dependent Network. *The Journal of Immunology*, 163(7), 3936.
- Widdicombe, J. H., & Wine, J. J. (2015). Airway Gland Structure and Function. *Physiological Reviews*, 95(4), 1241-1319.  
<https://doi.org/10.1152/physrev.00039.2014>
- Wilkins, E. T. (1954). Air pollution and the London fog of December, 1952. *Journal of the Royal Sanitary Institute*, 74(1), 1-15; discussion, 15-21.
- Wippich, C., Rissler, J., Koppisch, D., & Breuer, D. (2020). Estimating Respirable Dust Exposure from Inhalable Dust Exposure. *Annals of Work Exposures and Health*, 64(4), 430-444. <https://doi.org/10.1093/annweh/wxaa016>
- Wittekindt, O. H. (2017). Tight junctions in pulmonary epithelia during lung inflammation. *Pflügers Archiv - European Journal of Physiology*, 469(1), 135-147.  
<https://doi.org/10.1007/s00424-016-1917-3>
- Wohlleben, W., Driessen, M. D., Raesch, S., Schaefer, U. F., Schulze, C., Vacano, B. v.,...Haase, A. (2016). Influence of agglomeration and specific lung lining lipid/protein interaction on short-term inhalation toxicity. *Nanotoxicology*, 10(7), 970-980.  
<https://doi.org/10.3109/17435390.2016.1155671>
- Wolf, J., Rose-John, S., & Garbers, C. (2014). Interleukin-6 and its receptors: A highly regulated and dynamic system. *Cytokine*, 70(1), 11-20.  
<https://doi.org/https://doi.org/10.1016/j.cyto.2014.05.024>

- Wong-Ekkabut, J., Xu, Z., Triampo, W., Tang, I. M., Tieleman, D. P., & Monticelli, L. (2007). Effect of lipid peroxidation on the properties of lipid bilayers: a molecular dynamics study. *Biophysical Journal*, 93(12), 4225-4236. <https://doi.org/10.1529/biophysj.107.112565>
- Wooding, D. J., Ryu, M. H., Hüls, A., Lee, A. D., Lin, D. T. S., Rider, C. F.,...Carlsten, C. (2019). Particle Depletion Does Not Remediate Acute Effects of Traffic-related Air Pollution and Allergen. A Randomized, Double-Blind Crossover Study. *Am J Respir Crit Care Med*, 200(5), 565-574. <https://doi.org/10.1164/rccm.201809-1657OC>
- World Health Organisation. (2007). Global surveillance, prevention and control of chronic respiratory diseases: a comprehensive approach. In. Geneva, Switzerland: WHO Press.
- World Health Organization. (2006). *Air quality guidelines: global update 2005: particulate matter, ozone, nitrogen dioxide and sulfur dioxide*. World Health Organization. Regional Office for Europe.
- World Health Organization. (2018). *Household air pollution and health*. Retrieved 30 July from <https://www.who.int/news-room/fact-sheets/detail/household-air-pollution-and-health>
- World Health Organization. (2021). *WHO global air quality guidelines: particulate matter (PM<sub>2.5</sub> and PM<sub>10</sub>), ozone, nitrogen dioxide, sulfur dioxide and carbon monoxide*. World Health Organization.
- Wottrich, R., Diabaté, S., & Krug, H. F. (2004). Biological effects of ultrafine model particles in human macrophages and epithelial cells in mono- and co-culture. *International Journal of Hygiene and Environmental Health*, 207(4), 353-361. <https://doi.org/10.1078/1438-4639-00300>
- Wu, S., Ni, Y., Li, H., Pan, L., Yang, D., Baccarelli, A. A.,...Guo, X. (2016). Short-term exposure to high ambient air pollution increases airway inflammation and respiratory symptoms in chronic obstructive pulmonary disease



- patients in Beijing, China. *Environment International*, 94, 76-82. <https://doi.org/10.1016/j.envint.2016.05.004>
- Wu, W., Jin, Y., & Carlsten, C. (2018). Inflammatory health effects of indoor and outdoor particulate matter. *Journal of Allergy and Clinical Immunology*, 141(3), 833-844. <https://doi.org/10.1016/j.jaci.2017.12.981>
- Wu, X., Ciminieri, C., Bos, I. S. T., Woest, M. E., D'Ambrosi, A., Wardenaar, R.,...Gosens, R. (2022). Diesel exhaust particles distort lung epithelial progenitors and their fibroblast niche. *Environmental Pollution*, 305, 119292. <https://doi.org/https://doi.org/10.1016/j.envpol.2022.119292>
- Wyer, K. E., Kelleghan, D. B., Blanes-Vidal, V., Schaubberger, G., & Curran, T. P. (2022). Ammonia emissions from agriculture and their contribution to fine particulate matter: A review of implications for human health. *Journal of Environmental Management*, 323, 116285. <https://doi.org/https://doi.org/10.1016/j.jenvman.2022.116285>
- Xing, W. J., Kong, F. J., Li, G. W., Qiao, K., Zhang, W. H., Zhang, L.,...Xu, C. Q. (2011). Calcium-sensing receptors induce apoptosis during simulated ischaemia-reperfusion in Buffalo rat liver cells. *Clinical and Experimental Pharmacology and Physiology*, 38(9), 605-612. <https://doi.org/10.1111/j.1440-1681.2011.05559.x>
- Yamamoto, N., Kan-o, K., Tatsuta, M., Ishii, Y., Ogawa, T., Shinozaki, S.,...Matsumoto, K. (2021). Incense smoke-induced oxidative stress disrupts tight junctions and bronchial epithelial barrier integrity and induces airway hyperresponsiveness in mouse lungs. *Scientific Reports*, 11(1), 7222. <https://doi.org/10.1038/s41598-021-86745-7>
- Yan, F., John, S. K., Wilson, G., Jones, D. S., Washington, M. K., & Polk, D. B. (2004). Kinase suppressor of Ras-1 protects intestinal epithelium from cytokine-mediated apoptosis during inflammation. *The Journal of Clinical Investigation*, 114(9), 1272-1280. <https://doi.org/10.1172/JCI21022>

- Yang, D., Chertov, O., Bykovskaia, S. N., Chen, Q., Buffo, M. J., Shogan, J.,...Oppenheim, J. J. (1999). Beta-defensins: linking innate and adaptive immunity through dendritic and T cell CCR6. *Science*, 286(5439), 525-528. <https://doi.org/10.1126/science.286.5439.525>
- Yin, P., Chen, R., Wang, L., Meng, X., Liu, C., Niu, Y.,...Kan, H. (2017). Ambient Ozone Pollution and Daily Mortality: A Nationwide Study in 272 Chinese Cities. *Environmental Health Perspective*, 125(11), 117006. <https://doi.org/10.1289/EHP1849>
- Ying, Z., Xie, X., Bai, Y., Chen, M., Wang, X., Zhang, X.,...Rajagopalan, S. (2015). Exposure to concentrated ambient particulate matter induces reversible increase of heart weight in spontaneously hypertensive rats. *Particle and Fibre Toxicology*, 12, 15. <https://doi.org/10.1186/s12989-015-0092-6>
- Yoon, H., Kim, S., Kim, O., & Song, J. (2021). Nitrogen dioxide increases the risk of mortality in idiopathic pulmonary fibrosis. *European Respiratory Journal*, 57(5), 2001877. <https://doi.org/10.1183/13993003.01877-2020>
- Yoon, H.-Y., Kim, S.-Y., Kim, O.-J., & Song, J. W. (2023). Nitrogen dioxide increases the risk of disease progression in idiopathic pulmonary fibrosis. *Respirology*, 28(3), 254-261. <https://doi.org/https://doi.org/10.1111/resp.14373>
- Yoshida, H., & Hunter, C. A. (2015). The Immunobiology of Interleukin-27. *Annual Review of Immunology*, 33(1), 417-443. <https://doi.org/10.1146/annurev-immunol-032414-112134>
- Yu, S., He, J., & Xie, K. (2023). Zonula Occludens Proteins Signaling in Inflammation and Tumorigenesis. *Int J Biol Sci*, 19(12), 3804-3815. <https://doi.org/10.7150/ijbs.85765>
- Yu, X., Yi, H., Guo, C., Zuo, D., Wang, Y., Kim, H. L.,...Wang, X. Y. (2011). Pattern recognition scavenger receptor CD204 attenuates Toll-like receptor 4-induced NF-kappaB activation by directly inhibiting ubiquitination of tumor necrosis factor (TNF) receptor-associated factor 6. *The*



- Journal of Biological Chemistry*, 286(21), 18795-18806.  
<https://doi.org/10.1074/jbc.M111.224345>
- Zanobetti, A., Schwartz, J., & Dockery, D. W. (2000). Airborne particles are a risk factor for hospital admissions for heart and lung disease. *Environmental Health Perspectives*, 108(11), 1071-1077.  
<https://doi.org/10.1289/ehp.001081071>
- Zemp, E., Elsasser, S., Schindler, C., Künzli, N., Perruchoud, A. P., Domenighetti, G.,...Zellweger, J. P. (1999). Long-term ambient air pollution and respiratory symptoms in adults (SAPALDIA study). The SAPALDIA Team. *American Journal of Respiratory Care Medicine*, 159(4 Pt 1), 1257-1266. <https://doi.org/10.1164/ajrccm.159.4.9807052>
- Zhang, J., Wei, Y., & Fang, Z. (2019). Ozone Pollution: A Major Health Hazard Worldwide [Review]. *Frontiers in Immunology*, 10.
- Zhang, R., Dai, Y., Zhang, X., Niu, Y., Meng, T., Li, Y.,...Zheng, Y. (2014). Reduced pulmonary function and increased pro-inflammatory cytokines in nanoscale carbon black-exposed workers. *Particle and Fibre Toxicology*, 11(1), 73. <https://doi.org/10.1186/s12989-014-0073-1>
- Zhang, T., Joubert, P., Ansari-Pour, N., Zhao, W., Hoang, P. H., Lokanga, R.,...Landi, M. T. (2021). Genomic and evolutionary classification of lung cancer in never smokers. *Nature Genetics*, 53(9), 1348-1359. <https://doi.org/10.1038/s41588-021-00920-0>
- Zhang, Z., Wang, J., & Lu, W. (2018). Exposure to nitrogen dioxide and chronic obstructive pulmonary disease (COPD) in adults: a systematic review and meta-analysis. *Environmental Science and Pollution Research*, 25(15), 15133-15145. <https://doi.org/10.1007/s11356-018-1629-7>
- Zhao, M., Ma, J., Li, M., Zhang, Y., Jiang, B., Zhao, X.,...Qin, S. (2021). Cytochrome P450 Enzymes and Drug Metabolism in Humans. *International Journal of Molecular Sciences*, 22(23).
- Zhou, Y., & Chen, J. J. (2021). STAT3 plays an important role in DNA replication by turning on WDHD1. *Cell &*

*Bioscience*, 11(1), 10. <https://doi.org/10.1186/s13578-020-00524-x>

- Zhou, Y., Murthy, J. N., Zeng, D., Belardinelli, L., & Blackburn, M. R. (2010). Alterations in Adenosine Metabolism and Signaling in Patients with Chronic Obstructive Pulmonary Disease and Idiopathic Pulmonary Fibrosis. *PLOS ONE*, 5(2), e9224. <https://doi.org/10.1371/journal.pone.0009224>
- Zitka, O., Skalickova, S., Gumulec, J., Masarik, M., Adam, V., Hubalek, J.,...Kizek, R. (2012). Redox status expressed as GSH:GSSG ratio as a marker for oxidative stress in paediatric tumour patients. *Oncol Lett*, 4(6), 1247-1253. <https://doi.org/10.3892/ol.2012.931>
- Öhlinger, K., Kolesnik, T., Meindl, C., Gallé, B., Absenger-Novak, M., Kolb-Lenz, D., & Fröhlich, E. (2019). Air-liquid interface culture changes surface properties of A549 cells. *Toxicology in Vitro*, 60, 369-382. <https://doi.org/https://doi.org/10.1016/j.tiv.2019.06.014>